Modelling and simulating excitation-energy transfer in light-harvesting antennae : a nonadiabatic perspective

Joachim Galiana

To cite this version:

Joachim Galiana. Modelling and simulating excitation-energy transfer in light-harvesting antennae : a nonadiabatic perspective. Theoretical and/or physical chemistry. Université de Montpellier, 2024. English. NNT : 2024UMONS001 . tel-04680925

HAL Id: tel-04680925
https://theses.hal.science/tel-04680925v1

Submitted on 29 Aug 2024

THÈSE POUR OBTENIR LE GRADE DE DOCTEUR
DE L'UNIVERSITÉ DE MONTPELLIER

En Chimie Théorique et Modélisation

École doctorale Sciences Chimiques Balard

Unité de recherche Institut Charles Gerhardt Montpellier

Modelling and Simulating Excitation-Energy Transfer in Light-Harvesting Antennae: a Nonadiabatic Perspective

Présentée par Joachim GALIANA
Le 05 juillet 2024

Sous la direction de Benjamin LASORNE

Devant le jury composé de

Chantal DANIEL, Directrice de Recherche Émérite, Université de Strasbourg, LCQS	Rapporteure
Graham WORTH, Professeur, University College London	Rapporteur
Morgane VACHER, Chargée de Recherche, Université de Nantes, CEISAM	Examinatrice
Martial BOGGIO-PASQUA, Directeur de Recherche, Université Toulouse III, LCPQ	Examinateur
Dahbia TALBI, Directrice de Recherche, Université de Montpellier, LUPM	Présidente du jury
David LAUVERGNAT, Directeur de Recherche, Université Paris-Saclay, ICP	Invité
Benjamin LASORNE, Directeur de Recherche, Université de Montpellier, ICGM	Directeur de thèse

UNIVERSITÉ
DE MONTPELLIER

Abstract (English)

Light-harvesting (LH) molecular antennae are known for their ability to absorb light in the UV-visible domain *via* their chromophores and to transfer the associated excitation energy down to an energy trap within the system to be used for different purposes (photocatalysis, enhanced light emission...).

In particular, the strong LH properties of poly(phenylene ethynylene) (PPE) dendrimers have been attributed to a unidirectional excitation-energy gradient along a molecular tree from the shortest branches (leaves: the chromophores) down to the longest branches (trunk: the energy trap). However, setting up a comprehensive atomistic simulation protocol of excitation-energy transfer (EET) in such π-conjugated macromolecules remains challenging to date, especially because of the large number of degrees freedom and the presence of many conical intersections responsible for nontrivial internal conversion among the manifold of electronic excited states.

The architectures of both primary chromophores and further units for EET are all based on the same chemical groups (benzenes and acetylenes), only with different substitution schemes and lengths. In this thesis, we have carried out various theoretical chemistry studies (regarding structure and dynamics) on several PPE building blocks so as to rationalize the nature and efficiency of the ultrafast dynamics EET process *via* a nonadiabatic chemical perspective.

First, we analyzed the properties of the electronic excited states for both isolated PPE-oligomers and the first generations of PPE-dendrimers using linear-response time-dependent density functional theory. After demonstrating the locally-excited character of electronic excited states, we explored their associated potential energy surfaces (PESs) and characterized their critical points (minima, transition states, and minimum-energy conical intersections).

Some particular attention was given to the optimization and characterization of the conical intersections, especially as regards the branching-space vectors and their decompositions on the basis of the normal modes of vibration of the studied molecules. Together with these characterizations, we parametrized vibronic-coupling Hamiltonian models consistent with a so-called diabatization by *ansatz* of the coupled electronic excited states. From them, we could run wavepacket quantum dynamics simulations based on

the multi-configuration time-dependent Hartree (MCTDH) formalism so as to simulate EET from first principles.

Our simulations confirmed the utmost importance of the acetylenic stretching modes for EET to occur. They also highlighted the relevance of the stretching and rock-bending quinoidal modes of the connecting nodes (twofold or threefold *meta*-substituted phenylenes) within the dendritic graph. Comparisons between symmetrical and asymmetrical units illustrated the role of the primary structure (symmetrical *meta*-substitution) of the chromophore for efficient light absorption and/or EET. In particular, we investigated the steady-state spectroscopy of the PPE-chromophore itself, and its unusual emission spectrum observed experimentally. Here, we faced the case of strongly nonadiabatically coupled electronic excited states in the Franck-Condon region, for which the Born-Oppenheimer approximation breaks down. We calculated the vibronic eigenstates in the excited-state manifold, having contributions within two bright electronic excited states, and evaluated the contributions to both absorption and emission spectra. The results of our modelling suggest that the observed emissive contribution is the one that has gone through a transfer from one electronic state to another.

Finally, we explored bottom-up approaches for modelling the coupled PESs of larger PPE-dendrimer units and simulating the EET process occuring through them. Our strategy made use of the knowledge of the isolated branches and of how their communication can be viewed as a weak coupling from one branch to another.

Abstract (Français)

Les antennes collectrices de lumière sont des molécules capables d'absorber la lumière du domaine UV-visible et de transférer l'énergie associée à cette excitation à une partie de la molécule où elle sera utilisée à des fins de photocatalyse ou d'émission augmentée, par exemple.

Les dendrimères de poly(phénylène éthynylène) (PPE) sont connus pour leur propriété de collecte de lumière, qui est attribuée à un gradient unidirectionnel d'énergie d'excitation le long du dendrimère : depuis les branches courtes (les feuilles, chromophores) vers les branches longues (le tronc, le piège énergétique). Cependant, la simulation atomistique exhaustive du phénomène de transfert d'énergie d'excitation (EET) dans de telles macromolécules π-conjuguées reste un challenge à ce jour, à cause du nombre de degrés de liberté ainsi que de la présence d'intersections coniques (CIs) responsables des nombreuses conversions internes entre les états électroniques excités du dendrimère.

La structure des chromophores primaires ainsi que des premières unités d'EET est basée sur les mêmes groupes d'atomes (benzènes et acétylènes), avec des schémas de substitution et des tailles différentes. Dans cette thèse, nous avons étudié théoriquement la structure et l'évolution dans le temps de plusieurs briques élémentaires de PPE, de façon à rationaliser la nature et l'efficacité de ce phénomène ultrarapide qu'est l'EET, en gardant une interprétation non-adiabatique et chimique du phénomène.

Dans un premier temps, nous avons caractérisé les états électroniques excités de différents oligomères de PPE, en utilisant la théorie de la fonctionnelle de la densité dépendante du temps. Après avoir démontré le caractère local des excitations électroniques, nous avons exploré les surfaces d'énergie potentielle (PESs) des états excités et caractérisé leurs points critiques (minima, états de transition et CIs d'énergie minimale).

Une attention particulière a été donnée à l'optimisation et à la caractérisation des CIs, en particulier pour ce qui est des vecteurs de l'espace de branchement et de leur décomposition dans la base des modes normaux des molécules étudiées. Parallèlement, nous avons paramétrisé des modèles de couplage vibronique pour les Hamiltoniens moléculaires de PPEs, en lien avec une diabatisation par *ansatz* des états électroniques couplés. Nous avons ensuite utilisé ces modèles pour étudier l'évolution temporelle de paquets d'ondes moléculaires, à l'aide du formalisme de Hartree multi-configurationnel dépendant du temps (MCTDH) pour simuler l'EET.

Nos simulations ont confirmé l'importance première des modes d'élongation acétyléniques pour l'EET. Nous avons également souligné la pertinence des modes d'élongation et de bascule quinoidaux pour les nœuds (benzènes di- ou tri-*meta*-substitués) du dendrimère. Une comparaison entre les unités symétrique et asymétrique de transfert a également illustré le rôle de la structure symétrique du chromophore primaire pour l'efficacité de l'absorption de lumière par le dendrimère. En particulier, nous avons étudié la spectroscopie stationnaire du chromophore, notamment pour comprendre son spectre d'émission non-usuel. Notre cas est celui d'états électroniques excités fortement couplés dans la région de Franck-Condon, où l'approximation de Born-Oppenheimer n'est pas valide. Nous avons calculé les états vibroniques dans les états excités et montré qu'ils ont des contributions vibrationnelles non-négligeables dans deux états électroniques optiquement actifs (donc potentiellement émissifs). Nos résultats suggèrent que la contribution d'émission observée expérimentalement est celle qui a subi un transfert d'un état électronique à un autre.

Finalement, nous avons exploré une approche ascendante de modélisation des PESs de dendrimères de PPE et de simulation de l'EET au sein de telles structures. Notre stratégie est basée sur la connaissance des branches isolées de PPE et du fait qu'elles soient faiblement couplées.

Acknowledgements

First, I would like to thank all the members of the jury for giving me the honor of examining my work. In particular, I thank Dr. Chantal Daniel and Pr. Graham A. Worth who accepted to be the rapporteurs for this thesis manuscript. I would like to thank Dr. Morgane Vacher, Dr. Martial Boggio-Pasqua, and Dr. Dahbia Talbi who accepted to be part of the jury of my thesis defence, and Dr. David Lauvergnat who accepted to attend the defence.

For the rest, I shall use French to express as accurately as possible my acknowledgements to all the persons that supported me and made this work possible.

Tout d'abord, je tiens à remercier le Ministère de l'Enseignement Supérieur et de la Recherche pour avoir financé ces travaux de thèse sous la forme d'un contrat doctoral, et l'Université de Montpellier pour avoir hébergé ce même contrat. Je remercie également l'Institut Charles Gerhardt Montpellier (ICGM), son directeur Eric Clot, ainsi que ses administrateur-ices et gestionnaires pour avoir permis que ces travaux se déroulent à l'institut dans des conditions optimales. Enfin, je remercie l'école doctorale Sciences Chimiques Balard pour le suivi de ma formation et pour le suivi du déroulement de ma thèse.

Je tiens à remercier personnellement mon directeur de thèse, Benjamin Lasorne, pour la confiance qu'il m'a accordée, son encadrement et sa disponibilité, son enthousiasme scientifique, sa gentillesse et sa direction, son attention aux détails, nos longues discussions sur la science ou non…[1] Je lui suis particulièrement reconnaissant pour ses nombreux conseils, scientifiques et personnels, pour la thèse et pour l'après-thèse, et finalement pour tout ce que j'ai appris sous sa direction. Je remercie également Gabriel Breuil, qui m'a co-encadré pendant mon stage de Master et m'a confié de nombreux outils indispensables à la réalisation de cette thèse.

Je souhaite remercier à nouveau Morgane Vacher, qui a accepté de m'initier à la dynamique moléculaire des états excités lors de mon premier stage de chimie théorique. Cette thèse est une juste continuation de la curiosité qu'elle a éveillée en moi pour ces sujets complexes.

Je remercie également tous les membres du département de Chimie Physique, Théorique et Modélisation de l'ICGM, à commencer par Marie-Liesse D. pour sa bienveillance. En particulier, je souhaite la remercier

---

[1] Liste non exhaustive.

pour m'avoir accordé sa confiance professionnelle, notamment par la représentation des étudiant-es au conseil scientifique du département, et pour m'avoir toujours encouragé à présenter mes résultats dans différents rassemblements scientifiques, en France comme à l'international. Je ne pourrais pas manquer de remercier Fabrice B. et son soutien informatique sans faille, sans lesquels aucun des calculs présentés ci-après n'aurait pu être réalisé. Je souhaite également remercier les enseignant-es de la faculté des sciences de Montpellier qui m'ont fait confiance pour que j'intervienne dans leur cours durant ces trois années. Je tiens notamment à remercier Christophe R. pour les nombreuses discussions autour des travaux dirigés de spectroscopie, tant sur la science elle-même que sur l'enseignement.

Merci aux membres du bureau N2G02 qui, depuis l'emménagement jusqu'à après la rédaction m'ont toujours motivé à venir mais qui m'ont surtout supporté presque trois ans : Arthur H. et Clara, Maxime, puis Defne et Loréna.[2] Leur importance a réellement été non-négligeable dans ce qui a permis de mener ces travaux et d'écrire cette thèse. En particulier, je remercie Defne et Loréna pour le magnifique *carton de vivres pour la rédaction*. Je souhaite également remercier les joueurs de belote qui ont égayé mes pauses à savoir principalement Bruno, Matthieu et Quentin, que je remercie aussi pour toutes les discussions tenues autour des cartes.

Je remercie également Arthur M. que j'ai eu la chance de pouvoir co-encadrer pendant son stage au laboratoire. Merci également à Diego, Joachim K., Lola, Alvina... et tous les autres que je n'aurais pas pu citer, pour les discussions scientifiques, les conseils et l'écoute, les cafés, les sorties.

Sur un plan plus personnel, je tiens particulièrement à remercier mon colocataire Arthur L., avec qui j'ai grandement apprécié de partager ces trois années et quelques de vie. Notamment, je le remercie pour son aide et sa compréhension lors des périodes difficiles. À ce sujet, je souhaite remercier ceux qui m'aident, m'écoutent, me soutiennent chaque jour, même à distance, depuis maintenant plus de six ans : Elise, Guillaume et Godefroy. Particulièrement, je remercie Godefroy sans qui je n'aurais pas écrit cette thèse en `org-mode`, sur `doom emacs`, avec une disposition de clavier bépo...

Enfin, je tiens à remercier mes parents et mes frères et sœurs pour leur compréhension lors de mes périodes silencieuses, et pour leur soutien d'une manière générale avant et pendant la thèse.

---

[2] Maxime m'a supporté pendant plus de trois ans, et réciproquement.

Table of Contents

List of Acronyms and Symbols

The next lists define the acronyms and most of the symbols that will be later used within the body of this document.

Acronyms

AA	Adiabatic approximation (in the context of LR-TD-DFT)
B3LYP	Three-parameters hybrid functional with Beck, Lee, Yang, and Parr correlation functionals
BFGS	Broyden-Fletcher-Goldfarb-Shanno
BO	Born-Oppenheimer
BS	Branching space
BSV	Branching-space vector
CAM	Coulomb attenuating method
CG	Composed gradient
CIS	Configuration interaction singles
CMF	Constant mean-field
CoIn	Conical intersection
COM	Center of mass
CS	Composed step
CT	Charge transfer
DC	Derivative coupling
DD	Direct dynamics
DFA	Density functional approximation
DFT	Density functional theory
DFVP	Dirac-Frenkel variational principle
DOF	Degree of freedom
DVR	Discrete variable representation
EET	Excitation-energy transfer
EOM	Equations of motion
ES	Excited state
ETDM	Electronic transition dipole moment
FBR	Finite basis representation
FC	Franck-Condon
FCF	Franck-Condon factor
FMS	Full multiple spawning
FT	Fourier transform
GA	Gradient average
GD	Gradient difference
GGA	Generalized-gradient approximation
GS	Ground state
HEOM	Hierarchical equations of motion
HF	Hartree-Fock (depending on the context)
HF	Hellmann-Feynman (depending on the context)
HK	Hohenberg-Kohn
HO	Harmonic oscillator
HOMO	Highest occupied molecular orbital
IS	Intersection space
KS	Kohn-Sham
LC	Long-range correction
LDA	Local-density approximation
LE	Locally-excited

LF	Laboratory frame
LHA	Light-harvesting antenna
LR	Linear response
LUMO	Lowest unoccupied molecular orbital
LVC	Linear vibronic coupling
MC-SCF	Multiconfiguration self-consistent field
MCTDH	Multiconfiguration time-dependent Hartree
MD	Molecular dynamics
MECI	Minimum-energy conical intersection
MinS$_\mathrm{n}$	Geometry of the minimum of the state S$_\mathrm{n}$
ML	Multi-layer
MQC	Mixed quantum classical
NAC	Nonadiabatic coupling
NACME	Nonadiabatic coupling matrix element
NACV	Nonadiabatic coupling vector
NM	Normal mode
NMV	Normal mode of vibration
NR	Newton-Raphson
NTO	Natural transition orbital
NTS	Non totally symmetric
PB	Primitive basis
PES	Potential energy surface
PPE	Poly(phenylene ethynylene)
QD	Quantum dynamics
QED	Quantum electrodynamics
QN	Quasi-Newton
QVC	Quadratic vibronic coupling
RI	Irreducible representation
RMSD	Root-mean-square deviation
SCF	Self-consistent field
SED	Squared energy difference
SHF	Single-hole function
SM	Standard method
SPF	Single-particle function
TD	Time-dependent
TD-DFT	Time-dependent density functional theory
TDA	Tamm-Dancoff approximation
TDH	Time-dependent Hartree
TDHF	Time-dependent Hartree-Fock
TDM	Transition dipole moment
TDSE	Time-dependent Schrödinger equation
TDVP	Time-dependent variational principle
TI	Time-independent
TISE	Time-independent Schrödinger equation
TS	Totally symmetric (depending on the context)
TS	Transition state (depending on the context)
TSH	Trajectory surface hopping
VCH	Vibronic coupling Hamiltonian
vMCG	Variational multiconfiguration Gaussian
VMF	Variable mean-field
XC	Exchange-correlation
ZPE	Zero-point energy

Physics Constants

ϵ_0	Permitivitty of the vacuum
$\hbar$	Reduced Planck constant
c	Speed of light in vacuum
e	Elementary charge
h	Planck constant
a_0	Bohr radius, Bohr constant
m_e	Mass of the electron
E_h	Hartree energy

Greek Symbols

$\bar{\nu}$	Wavenumber
χ	Linear-response function (depending on the context)
$\chi_{i_\kappa}^{(\kappa)}$	i_κ^th primitive basis function for degree of freedom κ (MCTDH)
χ_i^nu	Primitive basis function for degree of freedom i (depending on the context)

δF	"Differential" of the functional F
$\Delta\square$	Difference between two quantities
$\delta\square$	Infinitesimal variation of a function or difference between two quantities
$\Delta_{\_}$	Laplacian in a system of Cartesian coordinates (unless otherwise specified)
δ_{ij}	Kronecker symbol
ϵ_a	Energy of the spin-orbital φ_a (depending on the context)
ϵ_n	Excitation energy of site n (depending on the context)
Γ	Reducible or irreducible representation of a function (for group theory)
$\gamma_{\alpha\beta}$	Matrix elements of the reduced-density operator for a given molecular wavepacket expanded on electronic states α and β.
γ_{ij}	Second-order intra-state coupling parameter for the degrees of freedom i, j
κ	Index for the dynamical degrees of freedom (MCTDH)
κ_i	First-order intra-state coupling parameter for the degree of freedom i (energy gradient)
λ	Lagrange multiplier (depending on the context)
λ	Wavenumber (depending on the context)
$\lambda(t)$	Variational parameter for a given ansatz in the context of the time-dependent variational principle
λ_i	First-order inter-state coupling parameter for the degree of freedom i (coupling gradient)
$\Lambda_{\alpha\beta}$	Matrix elements in a given representation of the nonadiabatic couplings
μ_{ij}	Second-order inter-state coupling parameter for the degrees of freedom i, j
μ_i	Reduced mass associated to a displacement vector (example, a given normal mode i)
ν_i	Vibrational number related to the normal mode i
ω_i	Frequency (or wavenumber) for the normal mode i (energy gradient)
Φ	Configuration of SPFs, Hartree product (TDH)
$\Phi^{(\kappa)}$	Single-hole function for the degree of freedom κ (TDH)
ϕ_α^{ad}	Adiabatic electronic wavefunction for the electronic state α
ϕ_α^{dia}	Diabatic electronic wavefunction for the electronic state α (not unique)
ϕ_α^{el}	Generic electronic wavefunction for the electronic state α
$\Phi_{\mathbf{J}^\kappa}$	Single-hole configuration of SPFs associated to the holed composite indices $\mathbf{J}^\kappa$ (MCTDH)
$\Phi_{\mathbf{J}}$	Configuration of SPFs, Hartree product associated to the composite indices $\mathbf{J}$ (MCTDH)
$\Psi_l^{(\kappa)}$	Single-hole function for the degree of freedom κ and index l (MCTDH)
Ψ^{BO}	Molecular wavefunction as a Born-Oppenheimer product
Ψ_m^{mol}	Generic molecular wavefunction
$\psi_\alpha(\cdot)$	Nuclear wavefunction (time-independent) on state α
$\psi_\alpha(\cdot, t)$	Nuclear wavepacket (time-dependent) on state α
ρ	One-electron density (DFT and TD-DFT)
$\boldsymbol{\rho}^{(\kappa)}$	SPFs reduced density matrix (MCTDH)
τ	Damping time in the context of autocorrelation functions

τ	Trust radius in the context of geometry optimization
θ	Rotation angle
$\varphi^{(\kappa)}$	Single-particle function for the degree of freedom κ (TDH)
φ^{el}	Generic electronic wavefunction
φ_a	Spin-orbital function
$\varphi^{(\kappa)}_{j_\kappa}$	j_κ^{th} single-particle function for the degree of freedom κ (MCTDH)
$\widehat{\rho}$	Density operator
$\widehat{\boldsymbol{\mu}}$	Electric dipole moment operator
$\widehat{\boldsymbol{\mu}}^{\mathsf{el}}_{if}$	Electronic transition dipole moment operator between electronic states i and f

Roman Symbols

$\mathbf{A}(t)$	A-vector, expansion coordinates for the configurations in MCTDH
$\mathbf{C}$	Matrix representation of the molecular orbitals in a given basis of atomic orbitals
$\mathbf{D}$	Transformation matrix from mass-weighted Cartesian coordinates to internal coordinates
$\mathbf{d}$	Shift vector between two geometries given in a system of normal coodinates
$\mathbf{E}$	Electric field
$\mathbf{F}$	Matrix representation of the Fock operator in a given basis of atomic orbitals
$\mathbf{F}_{\alpha\beta}$	Matrix elements in a given representation of the first-order nonadiabatic couplings
$\mathbf{g}$	Gradient of a given objective function (depending on the context)
$\mathbf{g}^{\mathsf{ad}}$	Hellmann-Feynman gradient difference vector
$\mathbf{H}$	Matrix representation of the Hamiltonian operator
$\mathbf{h}^{\mathsf{ad}}$	Hellmann-Feynman derivative coupling vector
$\mathbf{I}$	Inertia tensor
$\mathbf{J}$	Duschinsky matrix (overlap matrix between two sets of normal modes at different geometries)
$\mathbf{K}$	Mass-weighted Hessian (second energy derivative)
$\mathbf{L}^{\mathsf{mw}}$	Matrix definition of the normal modes (the columns are eigenvectors of $\mathbf{K}$)
$\mathbf{L}^{\mathsf{mw}}_i$	Vector definition of the mass-weighted Cartesian displacements associated to the normal mode i
$\mathbf{L}_{\mathsf{Cart},i}$	Vector definition of the Cartesian displacements associated to the normal mode i
$\mathbf{O}$	Principal axis-frame for a given geometry, defined from the inertia tensor
$\mathbf{P}$	Matrix representation of an orthogonal projector onto a given subspace
$\mathbf{Q}$	Collection of coordinates of the nuclei in a system of normal coordinates
$\mathbf{R}$	Collection of coordinates of the nuclei in a system of Cartesian coordinates
$\mathbf{r}$	Collection of coordinates of the electrons in a system of Cartesian coordinates
$\mathbf{R}^{\mathsf{mw}}$	Collection of coordinates of the nuclei in a system of mass-weighted Cartesian coordinates
$\mathbf{R}_A$	Coordinates of the nucleus A in a system of Cartesian coordinates
$\mathbf{r}_i$	Coordinates of the electron i in a system of Cartesian coordinates
$\mathbf{S}$	Overlap matrix for a given basis of atomic orbitals
$\mathbf{s}$	Gradient of the mean energy; gradient average
$\mathbf{U}$	Orthogonal matrix for change of basis

$\mathbf{V}$	Matrix representation of the Hamiltonian operator in the adiabatic basis set
$\mathbf{W}^{(n)}$	Approximate Hessian obtained by an update scheme (step n)
$\mathbf{x}_i$	Spin and coordinates of the electron i in a system of Cartesian coordinates
$\mathcal{E}[\phi]$	Energy functional in Hartree-Fock theory
$\mathcal{H}$	Hilbert space
$\mathcal{L}$	Lagrangian functional
$\mathcal{M}$	Submanifold of a given Hilbert space
$\mathcal{T}_{u(t)}\mathcal{M}$	Tangent space for the submanifold of ansätze $u(t)$ within a given Hilbert space
$\widehat{\mathcal{F}}$	Fock operator
$\widehat{\mathcal{J}}$	Coulombic operator
$\widehat{\mathcal{K}}$	Exchange operator
$\hat{g}^{(\kappa)}$	Gauge freedom constraint operator for SPFs of the degree of freedom κ (MCTDH)
$\widehat{H}$	Hamiltonian operator
$\widehat{O}$	Generic operator
$\hat{P}$	Operator for the orthogonal projection onto a given subspace
$\hat{p}_i$	Momentum operator for a given degree of freedom i
$\hat{T}$	Kinetic energy operator (derivative operator)
$\hat{x}_i$	Position operator for a given degree of freedom i
$a(t)$	Pre-factor of the Hartree product in MCTDH
$C(t)$	Autocorrelation function
$C_{\alpha\beta}$	Coherence between electronic states α and β
$d_{\alpha i}(t)$	Expansion coefficient along the degree of freedom i of the nuclear wavepacket for the electronic state α
$E[\rho]$	Energy functional in density functional theory
$E^{(\alpha)}$	Zero-order term in the potential energy of diabatic state α
f	Oscillator strengh (in length-gauge)
$f(\cdot;\square)$	Function of the variable $\cdot$ parametrically-defined by the parameter $\square$
$F[f(\cdot)]$	Functional of the function f for the variable $\cdot$
f_{xc}	Exchange correlation kernel in the context of density functional theory
$G_{\alpha\beta}$	Matrix elements in a given representation of the second-order nonadiabatic couplings
g_{κ}	Gauge freedom constraint for SPF of the degree of freedom κ (TDH)
$H_{\alpha\beta}$	Matrix elements in a given representation of the Hamiltonian operator
J_{nm}	Excitonic coupling between sites n and m
k_i	Mass-weighted curvature for the degree of freedom i
k_{EET}	Excitation-energy transfer rate
$L(\cdot)$	Squared error function to be minimized in least-square fitting procedures
M_A	Mass of the nucleus A
m_i	Mass of the electron i
P_{α}	Population of the electronic state α
R_{DA}	Donor-acceptor distance
T	Period for a given periodic function (depending on the context)
T	Propagation or simulation time (depending on the context)
t	Time
$u(t)$	Generic ansatz in the context of the time-dependent variational principle
V	Potential energy operator (multiplicative

	operator)
V_α	Adiabatic potential energy for the electronic state α
v_{ne}	External potential in the context of density functional theory
v_{xc}	Exchange correlation potential in the context of density functional theory
$w(\cdot)$	Weight functions in least-square fitting procedures
$W^{(\alpha,\beta)}$	Zero-order term in the inter-state coupling between diabatic states α, β
Z_A	Atomic number of the nucleus A

Other Symbols

$\left\langle\widehat{\mathcal{H}}\right\rangle$	Mean field Hamiltonian (TDH)
$\left\langle\widehat{\mathcal{H}}\right\rangle_{kl}^{(\kappa)}$	Mean field Hamiltonian matrix elements (MCTDH)
$\left\langle\widehat{O}\right\rangle$	Expectation value for a given operator
$\langle\cdot\|$	"Bra" (row vector) for a given quantum state
$\dot{\Box}$	Alternative definition for time derivative
$\|\cdot\rangle$	"Ket" (column vector) for a given quantum state
$\|\|\mathbf{u}\|\|$	Norm of the vector $\mathbf{u}$
$\mathrm{d}f$	Differential of the function f
$\nabla_{\_}$	Gradient in a given system of coordinates
∂	Partial variation of a given function or quantity (defining partial derivatives)
$\propto$	Proportional to a given quantity
$\Box^*$	Complexe conjugate of $\Box$
$\Box^\dagger$	Conjugate transpose operation
$\Box^{\mathsf{el}}$	Related to the electronic coordinates and electronic motions
$\Box^{\mathsf{mol}}$	Related to the electronic and nuclear coordinates and electronic and nuclear motions
$\Box^{\mathsf{nu}}$	Related to the nuclear coordinates and nuclear motions
$\Box^{\mathsf{T}}$	Transpose operation
$\Box_{\mathsf{eq}}$	Related to a given equilibrium position

Chapter 1

General Introduction

Light-matter interactions are ubiquitous in our daily life: the mechanism of vision, the photosynthesis of plants, the electroluminescence behind flat screens... For each of these light-matter interactions, light induces transitions between molecular states of matter. Both these transitions and molecular states are central in the domains of photophysics (modifying the properties of matter *via* an excitation) or photochemistry (making chemical reactions *via* an excitation).

Among all the applications of light-matter interactions, we are here interested in the ability of some molecular edifices to *harvest light*, on which relies for instance the phenomenon of photosynthesis. In plant photosynthesis, chlorophyll molecules absorb natural light (continuous spectrum from the sun) and transfer the associated energy to a reaction center, where it is used to reduce $\mathrm{CO_2}$ (through a non trivial cycle of chemical reactions, the Calvin cycle). We shall now define *light-harvesting antennae*, which are molecular edifices able to absorb light and to transfer the associated excitation energy either to a different part of the antenna itself or to other molecules for a specific purpose. In the case of natural light-harvesting antennae, this purpose is *in-vivo* catalysis for photosynthesis-like processes, occuring at a so-called reaction center. Among the most studied natural edifices capable of such excitation-energy transfer (EET), we mention the light-harvesting complexes in the purple bacteria (with high-symmetry ring antennae) [1], in the green sulfur bacteria (without apparent symmetry in the antenna) [2] or in the plant cryptochromes [3]. In the case of artificial light-harvesting antennae, the use of the excitation energy can vary, for photocatalysis or for enhanced emission of light from a fluorophore. In either case, light-harvesting antennae must ensure an *efficient and ultrafast* EET, from the absorption of light to the use of the excitation energy by the photosyntethic complex. The ability to absorb light mostly depends on the so-called *chromophore* groups of the antennae. The *efficiency* of EET is measured by the ratio (or quantum yield) of useful work (or energy) at the reaction center (depending on the application of the antenna) over the energy associated to the photons absorbed by the chromophores. The closer to one is the quantum yield, the better is the antenna as regards its application for EET. On the other hand, the ability to efficiently harvest light for these antennae relies on the *ultrafast* character for EET, which occurs on the subpicosecond (10^{-12} s) timescale in general [4].

The appeal for inspiring artificial light-harvesting antennae from the ones that exist in nature has been productive for decades, with creative synthetic molecular complexes exhibiting efficient light absorption and EET [5, 6]. On the other hand, the fundamental description of EET within both natural and new artificial light-harvesting antennae remains a challenge up to date.

1.1 Mechanisms of excitation-energy transfer (EET)

The nature of EET is not consensually described theoretically among all the possible applications it has. First, EET is defined as an energy transfer from a *donor*, assumed initially in one of its *excited states*, D^* to an *acceptor*, assumed initially in its *ground state* A

$$\mathrm{D}^* + \mathrm{A} \xrightarrow{\text{EET}} \mathrm{D} + \mathrm{A}^* \tag{1.1}$$

which can be studied as any chemical reaction. The first kinetics studies of EET in solids and aggregates (ensemble of molecules capable of EET) were led by Förster and Dexter, which proposed two mechanisms schematized in fig. 1.1, a) and b), respectively [7–9].

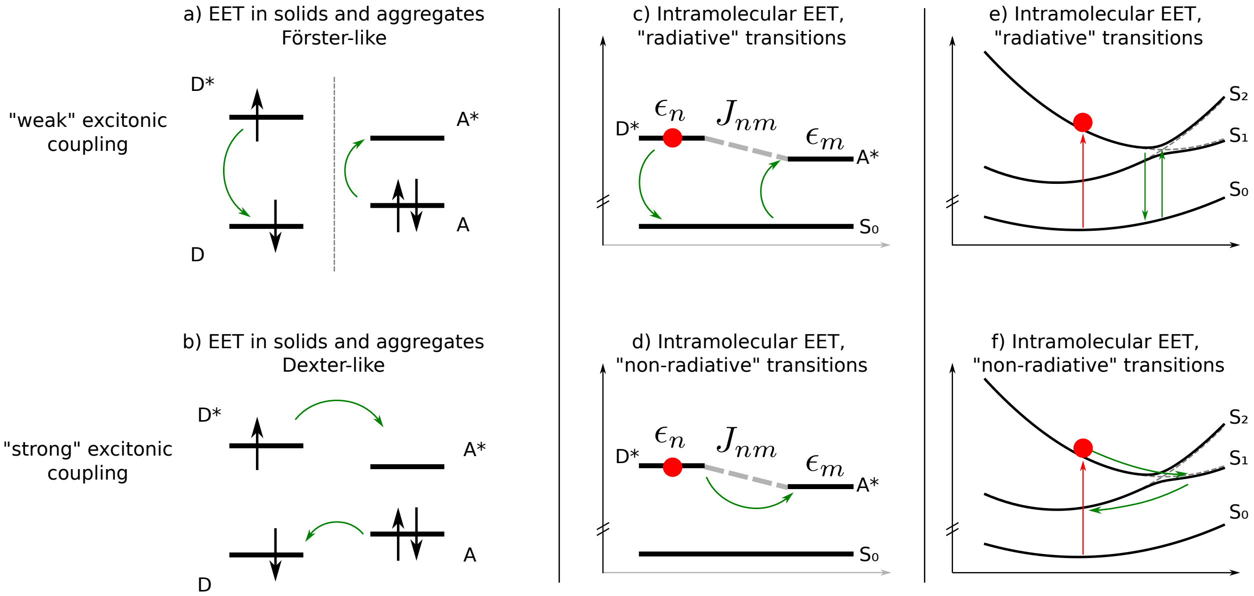

Figure 1.1: Schematic representations of the Förster-like (through-space excitonic coupling) and Dexter-like (through-bond excitonic coupling) mechanism in a) and b), respectively. Associated interpretations for intramolecular excitonic sites are given in c) and d), where the red dot is the initial excited donor state. Finally, the nonadiabatic and chemical interpretation of intramolecular EET *via* the use of excited-state potential energy surfaces is illustrated in e) and f).

The ground and excited states of the donor and acceptor are schematized by their highest occupied and lowest unoccupied molecular orbitals (HOMO, LUMO), and we call *excitons* the electron-hole pairs responsible for the excited donor or excited acceptor. The two mechanisms differ from the way this *exciton* (quasiparticle) is transferred; in particular, the *excitonic coupling* strength is different. In the Förster mechanism, the transfer occurs *via* a simultaneous de-excitation of the donor and excitation of the acceptor. In this limit of *weak excitonic coupling*, the transfer is indirect between the donor and acceptor excited states and occurs *via* simultaneous radiative electronic transitions (absorption and emission). As such, the kinetics depends on the orientation of the electronic transition dipole moments of the donor and the acceptor. On the other hand, the Dexter mechanism involves a transfer of electron within the excited states of the donor and the acceptor. The excitonic coulping is too strong to be considered as a perturbation, and the transfer kinetics now depends, to some extent, on the overlap between the frontier orbitals (highest occupied and lowest unoccupied) of the donor and the acceptor.

The Förster and Dexter theories give different rates k_{EET} for the EET process. Both rates depend, to some extent, on the overlap between the fluorescence spectrum of the donor and the absorption spectrum of the acceptor. The main difference is that the Dexter rate decreases exponentially with the donor-acceptor distance R_{DA}, and is proportional to donor-acceptor frontier orbitals interactions, while the Förster rate decreases with R_{DA}^{-6}. These differences discriminates the two mechanisms in a long-range/through-space (Förster) mechanism and short-range/through-bond (Dexter) mechanism.

Origin of the excitonic coupling, choice of an excitonic Hamiltonian

The origin of excitonic coupling in the Förster-Dexter models of EET kinetics was criticized, notably in the case of intramolecular EET (covalently bonded donor and acceptor), when applied to natural light-harvesting antennae [10]. In particular, the short-range mechanism was re-investigated by Harcourt and Scholes in the view of *ab initio* quantum chemistry (electronic structure calculations) [11–13]. The role of Coulombic and exchange integrals, and more generally the nature of the excitonic states for EET was rephrased in terms of local excitation (LE) and charge transfer (CT) states.

In the cases of LE states, the Frenkel excitonic Hamiltonian model,

$$\widehat{H} = \sum_{n} \epsilon_n \left|n\right\rangle \left\langle n\right| + \sum_{n<m} J_{nm} \left(\left|n\right\rangle \left\langle m\right| + \left|m\right\rangle \left\langle n\right|\right), \tag{1.2}$$

was perhaps established as a more rigorous and explicit starting point for understanding the EET among ensembles of molecules [14, 15]. Similarly to the previous models, it relies on the definition of *excitons*, here electronic LE excited states $\left|n\right\rangle$ for the site n of the molecular aggregate. The excitation energy of a site is ϵ_n and the excitonic coupling, which eventually induces excitation-energy transfers, is J_{nm}, see fig. 1.1, c and d). In essence, these schemes are reminiscent of a Jablonski diagram where the excitonic states are the electronic states, and the excitonic coupling is responsible for internal conversions.

The interaction between the excitonic sites and their complex environment (solvent, biological medium, *etc.*) was first taken into account *via* a coupling between the electronic excited states and a harmonic bath (the complex environment to the excitons). In the simple case of one donor and one acceptor, the "bathed" Frenkel Hamiltonian model is reminiscent of the spin-boson model for a two-level system (excited donor + excited acceptor)

$$\widehat{H}_{\mathsf{S}} = H_{\mathsf{D}} \left|\mathsf{D}\right\rangle \left\langle\mathsf{D}\right| + H_{\mathsf{A}} \left|\mathsf{A}\right\rangle \left\langle\mathsf{A}\right| + H_{\mathsf{AD}} \left(\left|\mathsf{A}\right\rangle \left\langle\mathsf{D}\right| + \left|\mathsf{D}\right\rangle \left\langle\mathsf{A}\right|\right) \tag{1.3}$$

coupled to a harmonic bath

$$\widehat{H}_{\mathsf{B}} = \sum_{i}^{N} \frac{\hbar\omega_i}{2} \left(\hat{p}_i^2 + \hat{x}_i^2\right) \left(\left|\mathsf{D}\right\rangle \left\langle\mathsf{D}\right| + \left|\mathsf{A}\right\rangle \left\langle\mathsf{A}\right|\right) \tag{1.4}$$

of N oscillators with frequencies ω_i. In spin-boson Hamiltonian models, the coupling between the system (the excitons) and the bath (the vibrations) is linear with the position of the modes and diagonal with respect to the excitons (it does not couple directly two excitons)

$$\widehat{H}_{\mathsf{SB}} = \sum_{i}^{N} \kappa_i^{(\mathsf{D})} \hat{x}_i \left|\mathsf{D}\right\rangle \left\langle\mathsf{D}\right| + \kappa_i^{(\mathsf{A})} \hat{x}_i \left|\mathsf{A}\right\rangle \left\langle\mathsf{A}\right| . \tag{1.5}$$

In other words, the excitons (LE excited states of the donor and the acceptor) can be interpreted as an ensemble of spins (two-level systems, donor and acceptor excited states) which are placed in a bath of bosons (vibrations in molecules, phonons in solids). Both Frenkel and spin-boson Hamiltonian models are very well suited for the study of quantum dynamics in open systems which include energy dissipation with an environment (here the harmonic bath). For instance, the time evolution of the populations of the different electronic states can be calculated using the Redfield equation [4, 16]. Other strategies, based on approximate solutions of the time-dependent Schrödinger equation have also been used for evaluating the kinetics of electron transfer and energy transfer [3, 17, 18].

From excitonic states to nonadiabatically coupled electronic states

In these first attempts of modelling of EET with the Frenkel Hamiltonian model or of D-A systems with a spin-boson model, the excitonic coupling (the inter-state coupling) is constant. In particular, there is no explicit coupling between the electronic states and the nuclear coordinates of the molecules. For intramolecular processes, the absence of explicit electron-nuclei coupling boils down to the assumption that the EET is mostly due to the interaction with the environment, through *tuning terms* (linear parameters in the system-bath interaction) and/or through *intramolecular vibrational energy redistribution* (quadratic, harmonic terms in the bath).

From these approximations, a natural extension is the use of a variable excitonic coupling. Two strategies were proposed: either modify the Harcourt theory to allow an *ad hoc* variation of the excitonic coupling [19] or modelling the gradient of the excitonic coupling with respect to some nuclear displacements. The latter strategy is directly linked to the vibronic coupling Hamiltonian models, where the off-diagonal terms explicitly depend on displacements associated to the nuclear displacements, originally proposed by Köppel and co-workers [20]. Historically, these models were used for understanding nonadiabatic effects and photoinduced phenomena in systems where conical intersections in the excited states are ubiquitous [21–23].

Using a vibronic coupling model thus provides a nonadiabatic and chemical interpretation of intramolecular EET. Herein, we aim at describing the EET process between a donor and an acceptor as a photoinduced chemical reaction, with an initial excitation (on the donor states) and with subsequent internal conversions toward a specific final state (possibly, the acceptor state). To do so, we have to know explicitly the potential energy surfaces (PESs) of the light-harvesting system (with the donor and the acceptor), see fig. 1.1, e and f). More importantly, we have to assess the form and the magnitude of the nonadiabatic couplings, which we identify, in an intramolecular regime, to the excitonic couplings responsible for the transfer of both population and energy from the donor to the acceptor, here with a diabatic perspective.

From the first theory of Förster to the vibronic coupling Hamiltonian models, a wide variety of mechanisms has been proposed for both identifying the origin of excitonic coupling and evaluating the kinetics of excitation-energy transfer. This variety also reflects the plurality of light-harvesting systems, both natural and artificial, exhibiting efficient and ultrafast (subpicosecond) excitation-energy transfer. We now present one of the most promising class of artificial light-harvesting antennae, the dendrimers of poly(phenylene ethynylenes).

1.2 Poly(phenylene ethynylene) light-harvesting dendrimers

Poly(phenylene ethynylene) dendrimers (PPE-dendrimers) are macromolecular *dendritic* systems composed of benzenes and acetylenes with different substitution schemes and lengths. They consist in *molecular trees* where the *leaves* are the functionalized diphenylacetylene (DPA) fragments at the periphery of the molecules, see fig. 1.2.

We mention both compact and extended PPE-dendrimers, with equal lengths for all branches or increasing lengths from the periphery to the core, see fig. 1.2 a) and b), respectively. The structure of PPE-dendrimers is very similar to Bethe (or Cayley) mathematical dendritic graphs. The two sites of the dendritic graph are benzenes and acetylenes. We define the *branches* of the graph as linear poly-*para*-substituted benzenes and the *nodes* as di- or tri-*meta*-substituted benzenes (see fig. 1.3).

In PPE-dendrimers, each *node* is a tri-*meta*-substituted phenylene, connecting the leaves (benzenes at the periphery) to the rest of the dendrimer, up to the core. However, one could imagine an incomplete dendrimer, with simply di-*meta*-substituted nodes. To retrieve the analogy with photosynthetic complexes, the nodes (with the leaves, or chromophores) and branches form the light-harvesting complexes, while the core is the reaction center for the bacteria or the plant.

Historical synthesis and design of the photophysical properties of PPE-dendrimers

The first synthetic routes for PPE-dendrimers (both compact and extended), proposed by Xu and Moore [24, 25], are responsible for the dendritic nature, and allow one to control the form and the generation (or size) of the final dendrimer.

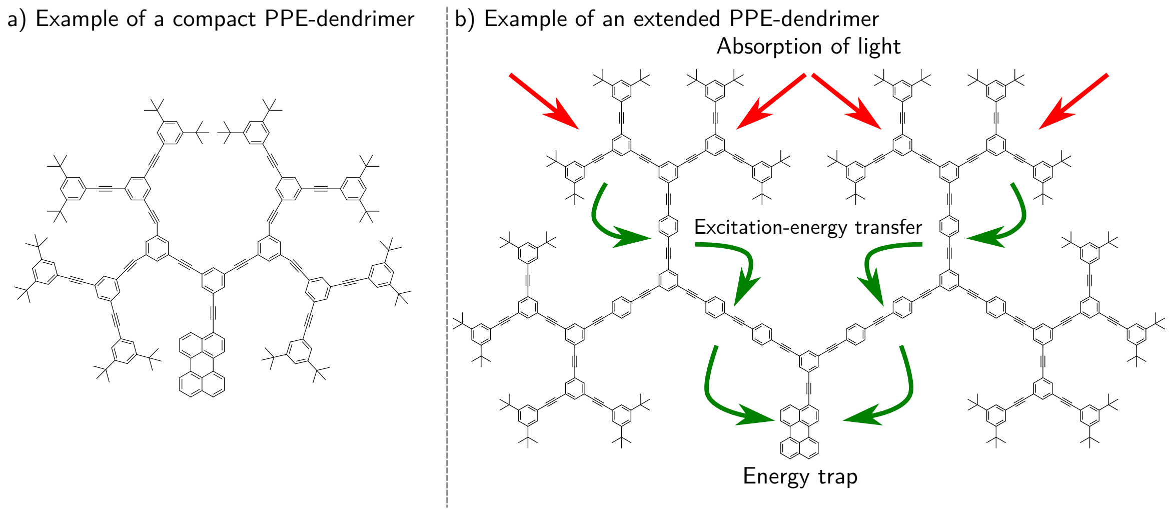

Figure 1.2: Examples of a) compact PPE-dendrimer of diphenylacetylene: all the branches have the same lengths (only DPA unit) and b) extended PPE-dendrimer of diphenylacetylene: from the periphery to the core, the branches are longer (DPA at the periphery and increasingly *para*-substituted DPA units to the core). This specific generation of PPE-dendrimer is called the nano-star. For the extended PPE-dendrimer, the simplified mechanism of light absorption (red arrows on the chromophores) and excitation-energy transfer (green arrows), funnelled to the core, is given. For both molecules, the energy trap is here a perylene unit (well-known fluorophore).

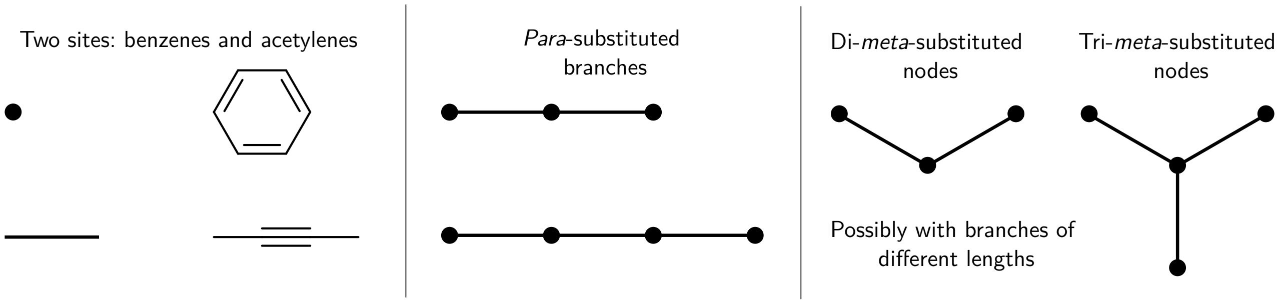

Figure 1.3: Definition of the sites, branches, and nodes for the description of the structure of PPE-dendrimers as Bethe dendritic graphs.

The compact dendrimers (fig. 1.2, panel a)), composed only of branches of the same lengths, are able to absorb light with a large number of equivalent chromophores (here DPA units). In the view of the Frenkel Hamiltonian model, a large number of excitonic states would be defined, each associated to one of the DPA units on the graph [26, 27]. The excitation-energy transfer is thus entropically favored, as a photoinduced exciton has no reason to stay localized and will explore the graph (statistically).

Among the extended dendrimers synthesized by Moore, we focus in this work on the infamous example of the so-called nano-star (fig. 1.2, panel b). Its design is simple: rather than using equivalent chromophores in the entire dendrimer, the idea is to separate energetically the excitons by varying the length of the branches. The longer is the branch, the longer is the conjugation and thus the lower is the excitonic energy [28–31]. A unidirectional energy gradient is thus obtained, from the periphery (leaves) to the core (energy trap) of the dendrimer, and the excitation-energy transfer is now energetically favored. We shall now discuss the properties and characterization of extended PPE-dendrimers only.

Joint theoretical and experimental efforts on understanding the extended dendrimer

The first estimations of the quantum yield of the PPE-dendrimers, in particular the nano-star, were proposed by Devadoss, Shortreed, and co-workers [32–34], with near-to-one quantum yield from excitations at 310 nm, 353 nm, and 372 nm (absorption of light by the DPA unit, the 3-ring branch, and the 4-ring branch). They also estimated that EET was at least two orders of magnitude faster for the extended PPE-dendrimers than for the compact PPE-dendrimers. The local character of these excitations was evidenced experimentally from steady-state spectroscopy [35]. Later, Palma and co-workers proposed the first joint theoretical and experimental study of the nano-star [36]. They estimated the dependence of the absorption spectrum on the temperature and in particular on the conformations of the nano-star.

The nature of the excitonic coupling between the previously stated local excitations was investigated by Martinez and co-workers [19, 37]. The electronic excitations of PPE-dendrimers were also studied by Huang and co-workers, who compared the results obtained from different electronic structure theories and discussed the excitonic states in the view of locally-excited (LE) and charge transfer (CT) states [38]. Finally, the vibronic spectra of the PPE-dendrimer building blocks were obtained with sufficient resolution to assess the optically active normal modes for transitions toward the LE excited states [39, 40]. This was further rationalized by Ho and co-workers for the *para*-substituted branches and for the smaller di-*meta*-substituted PPE [41, 42]. In particular, they unveiled a *pseudofragmentation* scheme for electronic excitations and vibrational modes, based on a pair of almost degenerate electronic states. On the other hand, the excited-state dynamics of DPA itself was studied. Long-lived excited states leading to cis-trans isomerization of DPA units in PPE-oligomers were characterized, both experimentally [43–45] and theoretically [46, 47]. In a recent work of Breuil and co-workers, these “dark” states were identified as a possible alternative for the EET to occur [48].

Up to now, the mentioned studies of PPE-dendrimers are mostly “stationary”, that is they rely on experimental steady-state spectroscopy or electronic structure calculations for given geometries.

Some playground for nonadiabatic molecular dynamics

Finally, the various experimental studies on PPE-dendrimers concluded on the prominent role of the localized excitations in the molecule, which was comforted by different theoretical approaches. The mechanism of the excitation-energy transfer exhibited by the nano-star was yet difficult to assess, in particular because no direct experiments nor direct atomistic simulations were available to probe EET. In particular, the question about the through-space (Förster-like) or through-bond (Dexter-like) character of the transfer was not clearly answered [19, 37, 49].

In 2009, Fernandez-Alberti and co-workers proposed the first atomistic simulations of EET in a PPE-oligomer (the smallest asymmetrical *meta*-substituted PPE), *via* direct nonadiabatic molecular dynamics [50]. They extended their strategy to other extended PPE-oligomers and concluded on several aspects of the EET mechanism [51–54]. First, the role of the excitonic coupling can be understood as a consequence of the presence of conical intersections between the electronic excited states. The funneling of excitation-energy transfer through the PPE-dendrimers was attributed to its molecular vibrations, in particular the acetylenic elongations, which connect together the locally-excited electronic states, and thus favor the *through-bond* mechanism. Overall, their simulations estimate that the intramolecular EET in PPEs occurs quite efficiently (near 100% of transfer from the initially photoexcited state to the higher-energy electronic state) and in an ultrafast manner (under $100\,\mathrm{fs}$).

The PPE-oligomers were finally found to be quite interesting *playgrounds* for the study of nonadiabatic quantum dynamics methods. For instance, it has been used to study the reliability of open quantum system dynamics [18, 55] or of nonadiabatic excited-state molecular dynamics [56–61].

1.3 A nonadiabatic and chemical perspective for the study of dendrimers

As we have seen, the PPE-dendrimers have been extensively studied both experimentally and theoretically for their EET abilities. However, the very nature and mechanisms of the photoinduced EET occuring within the dendrimer and its building blocks are still open to debate. In particular, the explicit simulations in time of the photoinduced EET has only been made possible, over the last decade, *via* direct molecular dynamics simulations.

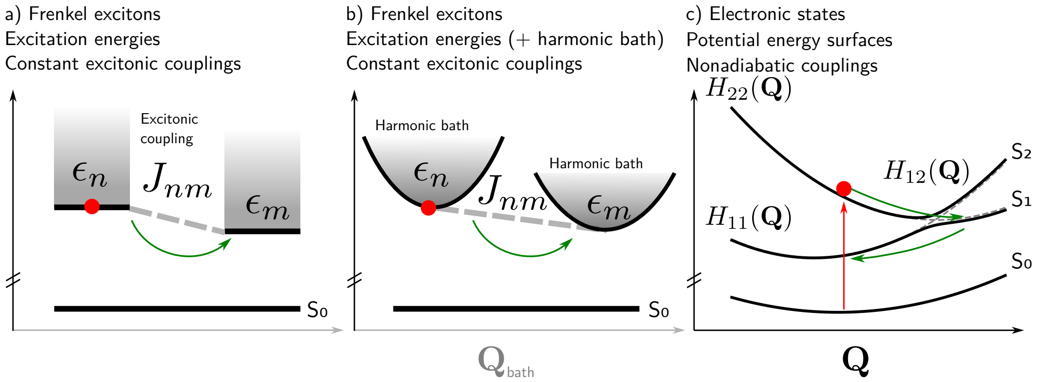

Figure 1.4: Strategies for modelling excitation-energy transfer (EET) occuring from an initially excited donor (red dot). a) Frenkel exciton model, with constant excitation energies and excitonic couplings. b) Same with an additional harmonic bath for the vibrations of either of the excitons. c) Interpretation of EET throught the lens of potential energy surfaces for the electronic excited states

The objective of this thesis is the modelling and simulation of excitation-energy transfer in PPE-oligomers, the building-blocks of the PPE-dendrimers and the nano-star. It is intended as a starting point for bridging the first theoretical developments using the Frenkel Hamiltonian model for PPE-dendrimers (fig. 1.4 panels a) and b)) with the direct dynamics simulations of PPE-oligomers.

To do so, we first characterize the electronic excitations in the PPE-oligomers and the nonadiabatic couplings between them, by extensive vibrational analysis of the *ab initio* (from electronic structure theory) potential energy surfaces (PESs) (fig. 1.4 panel c)). Then, we propose models of PESs that account for the most important features of the *ab initio* PESs and use them to simulate as explicitly as possible the photoinduced phenomena of interest in a selection of PPE-oligomers, see fig. 1.5. The characterization of nonadiabatic couplings and the modelling of PESs are intrinsically linked in this work, as we make use of Hamiltonian models to *diabatize* the electronic states and to take into account their coupling.

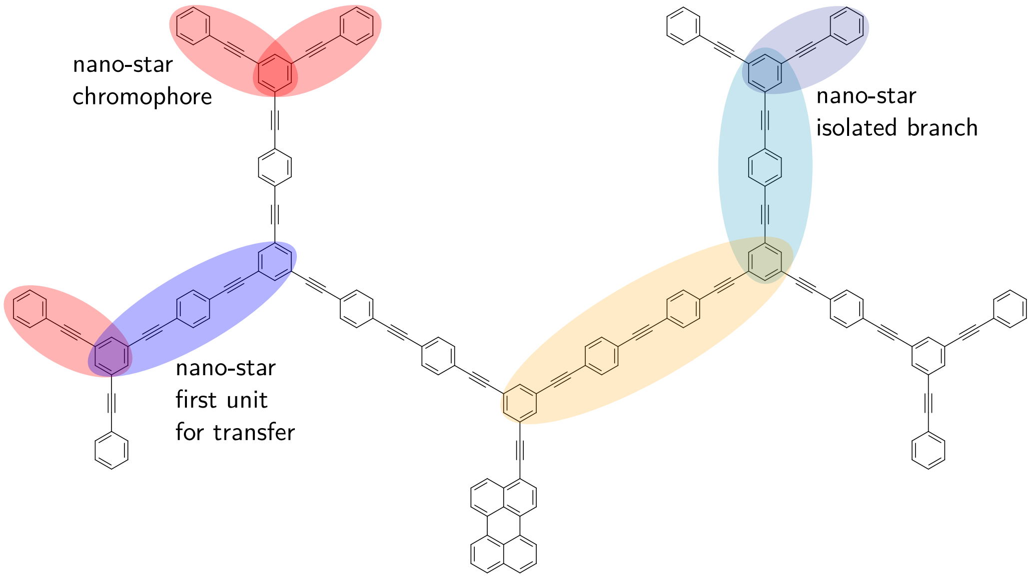

Figure 1.5: Structure of the simplified nano-star studied in this work. The nano-star chromophore is highlighted, along with two examples of the nano-star *units* for transfer, the first one at the periphery and the "full" extended branch from the periphery to the core.

This manuscript is organized in three parts. In part I, we present the background for running nonadiabatic quantum dynamics calculations for systems such as PPE-oligomers. We define the molecular Hamiltonian and the nuclear motions (chapter 2) and give the equations of motion for the propagation of nuclear wavepackets within the multiconfiguration time-dependent Hartree formalism (chapter 3). A particular attention is given to the description of electronic degeneracy, which is ubiquitous in this work. Theoretical insights and computational details about the electronic structure calculations are also given (chapter 4).

In part II, we use this theoretical framework to study both steady-state spectroscopy features and real-time evolutions of photo-excited PPE-oligomers. Our focus is first on the chromophore, the symmetrically *meta*-substituted PPE, for which we investigate an unusual fluoresence spectrum (chapter 5). In particular, we raise the question of the difficult prediction of fluorescence experiments for molecules with strongly nonadiabatically coupled electronic states near the Franck-Condon region. Then, we study the smallest PPE-oligomers capable of energy transfer, and apply our theoretical framework to the estimation of the quantum yield, the timescale and the mechanism of EET (chapters 6 and 7). Our analyses allow us to identify the most prominent modes for EET to occur and to describe how the excess energy from the initial excitation is distributed in the molecular vibrations.

Finally, in part III, we give the outlook for the present work, with our current developments as regards the description of EET in an entire PPE-dendrimer. First, we discuss the influence of local excitations on the EET, in particular in the case of symmetrically *meta*-substituted PPE-oligomers (chapter 8). We also raise the question of the physical meaning of electronic-state coherences for initially pure states or superpositions of states. Then, we discuss the feasibility of a bottom-up strategy to model large PPE-oligomers, eventually dendrimers (chapter 9). This strategy is intermediate between the Frenkel-exciton Hamiltonian and the linear vibronic coupling Hamiltonian models, with a definition of the Frenkel-exciton on the isolated fragments of the nano-star, and an *ab initio* estimation of the excitonic coupling.

Chapitre 1

Introduction Générale

Les interactions lumière-matière sont omniprésentes dans notre vie de tous les jours : pour notre vision, dans la photosynthèse des plantes, dans les écrans plats *via* l'électroluminescence... Pour chacune de ces interactions lumière-matière, la lumière induit des transitions entre des états moléculaires de la matière. Ces états moléculaires et ces transitions sont les objets d'étude centraux dans le domaine de la photophysique (modifier les propriétés de la matière *via* une excitation) ou de la photochimie (provoquer et contrôler des réactions chimiques *via* une excitation).

Parmi toutes les applications des interactions lumière-matière, nous nous intéressons ici à la capacité de certaines molécules à *collecter la lumière*, abilité sur laquelle repose notamment le phénomène de la photosyntèse. Pendant la photosynthèse, les molécules de chlorophylle absorbent la lumière naturelle (le spectre continu émis par le soleil) et transfèrent l'énergie associée jusqu'à un centre réactionnel, où cette énergie sera utilisée pour réduire le CO_2 de l'atmosphère (au travers d'un cycle non trivial de réactions chimiques, le cycle de Calvin). Nous définissons maintenant les *antennes collectrices de lumière* comme des édifices moléculaires capables d'absorber la lumière et de transférer l'énergie d'excitation associée soit à une autre partie de l'antenne elle-même, soit à d'autres molécules pour un usage spécifique. Dans le cas d'antennes collectrices de lumière naturelles, cet usage est la catalyse *in-vivo* pour les processus semblables à la photosynthèse, qui se déroulent dans le centre réactionnel de ces systèmes. Parmi les édifices naturels capables d'un tel transfert d'énergie d'excitation (EET) les plus étudiés, nous citons les complexes de collecte de lumière dans la bactérie pourpre [1], dans la bactérie *chlorobiota* [2] ou dans les cryptochromes [3]. Dans le cas d'antennes collectrices de lumière artificielles, l'utilisation de l'énergie collectée peut varier, par example pour faire de la photocatalyse ou pour créer une intensification d'émission d'un fluorophore. Dans tous les cas, les antennes collectrices de lumière doivent assurer un EET *efficace et ultra-rapide*, depuis l'absorption de la lumière jusqu'à l'utilisation de l'énergie d'excitation par le complexe photosynthétique. La faculté à absorber la lumière dépend principalement des groupes *chromophore* de ces antennes. L'efficacité de l'EET se mesure quant à elle par le rapport (ou rendement quantique) du travail énergétique utile au centre réactionnel (dépendant de l'application voulue pour l'antenne) par l'énergie associée aux photons absorbés par les chromophores. Plus le rendement quantique est proche de un, meilleure est l'antenne en ce qui concerne l'application pour faire de l'EET. Aussi, l'efficacité de la collecte de lumière par ces antennes repose sur le caractère ultra-rapide pour l'EET, qui se déroule sous l'échelle de la picoseconde (10^{-12} s) en général [4].

L'attrait pour inspirer des antennes collectrices de lumière artificielles sur celles qui existent dans la nature a été productif depuis les années 1990, avec le design de complexes moléculaires synthétiques créatifs pour faire de l'EET [5, 6]. En revanche, parallèlement à l'avancée de ces synthèses, la description fondamentale de l'EET au sein à la fois des antennes naturelles et des antennes artificielles est restée un challenge encore jusqu'à aujourd'hui.

1.1 Les mécanismes de transfert d'énergie d'excitation (EET)

La nature même de l'EET n'est pas consensuellement décrite théoriquement parmi toutes les applications que l'EET possède. Avant tout, l'EET est défini comme un transfert d'énergie depuis un *donneur*, supposé initialement dans un de ses états excités, D^* vers un *accepteur*, supposé initialement dans son état fondamental A

$$\text{D}^* + \text{A} \xrightarrow{\text{EET}} \text{D} + \text{A}^*. \tag{1.1}$$

Ce transfert peut alors être étudié comme une réaction chimique. Les premières études cinétiques théoriques de l'EET dans les solides et les aggrégats (ensemble de molécules capables d'EET), ont été menées par Förster et Dexter, qui ont proposé deux mécanismes, schématisés dans la fig. 1.1, a) et b), respectivement [7–9].

Les états fondamentaux et excités du donneur et de l'accepteur sont schématisés par leurs orbitales moléculaires hautes occupées et basses vacantes (HOMO, LUMO). Nous appelons *excitons* les paires d'électron-trou responsables du donneur excité et de l'accepteur excité. Les deux mécanismes diffèrent dans la façon dont l'*exciton* (la quasi-particule) est transféré ; en particulier, la force du *couplage excitonique* y est différente. Dans le mécanisme type Förster, le transfert se produit *via* une désexcitation du donneur en simultané d'une excitation de l'accepteur. Dans cette limite de *faible couplage excitonique*, le transfert est indirect entre les états excités du donneur et de l'accepteur, et se déroule donc *via* des transitions électroniques radiatives (absorption et émission de lumière) simultanées. Dès lors, la cinétique dépend de l'orientation relative des moments de transition électronique du donneur et de l'accepteur. De l'autre côté, le mécanisme type Dexter implique un transfert d'électron directement au sein des états excités entre le donneur et l'accepteur. Le couplage excitonique est alors trop fort pour être considéré comme une perturbation et la cinétique du transfert dépend maintenant du recouvrement entre les orbitales frontières (HOMO, LUMO) du donneur et de l'accepteur.

Les théories de Förster et Dexter donnent différentes constantes de vitesse k_{EET} pour les processus

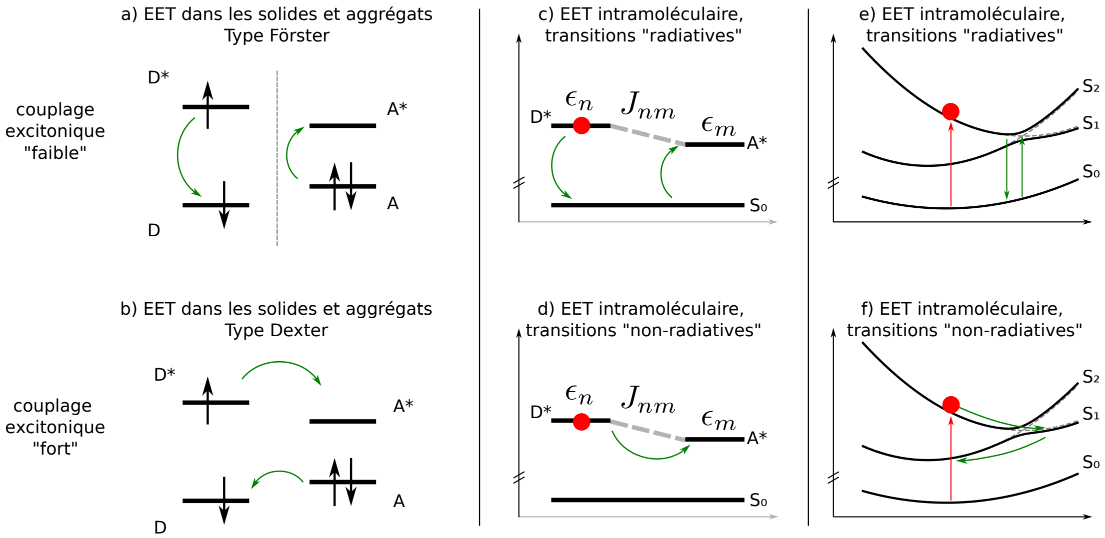

Figure 1.1 – Représentation schématique des mécanismes de type Förster (couplage excitonique à travers l'espace) et de type Dexter (couplage excitonique à travers les liaisons), a) et b), respectivement. Les interprétations associées pour les sites excitoniques intra-moléculaires sont données dans c) et d), où le point rouge symbolise l'état initial excité sur le donneur. Finalement, une interprétation chimique et non-adiabatique de l'EET intra-moléculaire, en utilisant les surfaces d'énergie potentielle pour les états excités, est illustrée en e) et f).

d'EET. Les deux constantes dépendent dans une certaine mesure du recouvrement entre le spectre de fluorescence du donneur et le spectre d'absorption de l'accepteur. En revanche, la principale différence est que la constante de Dexter décroît exponentiellement avec la distance donneur-accepteur R_{DA}, et est proportionnelle aux interactions entre les orbitales frontières du donneur et de l'accepteur, tandis que la constante de Förster décroît avec R_{DA}^{-6}. Ces différences permettent notamment de séparer les deux mécanismes en une famille de mécanismes longue-portée/à travers l'espace (Förster) et une famille de mécanismes courte-portée/à travers les liaisons (Dexter).

Origine du couplage excitonique, choix d'un Hamiltonien excitonique

L'origine du couplage excitonique dans les modèles de type Förster-Dexter pour la cinétique de l'EET a été critiquée, notamment dans le cas de l'EET intra-moléculaire (liaison covalente entre le donneur et l'accepteur) appliqué aux antennes collectrices de lumière dans la nature [10]. En particulier, le mécanisme courte-portée a été reformulé par Harcourt et Scholes en termes de quantités accessibles en chimie quantique, *via* des calculs de structure électronique [11–13]. Le rôle des intégrales de Coulomb et d'échange et plus généralement la nature des états excitoniques pour l'EET ont été reformulés en termes d'excitations locales (LE) et d'états à transfert de charge (CT).

Dans le cadre d'états LE, le Hamiltonien excitonique *de Frenkel*

$$\widehat{H} = \sum_{n} \epsilon_n \left|n\right\rangle \left\langle n\right| + \sum_{n<m} J_{nm} \left(\left|n\right\rangle \left\langle m\right| + \left|m\right\rangle \left\langle n\right|\right), \tag{1.2}$$

a depuis été établi comme le plus rigoureux et plus explicite point de départ pour comprendre l'EET au sein d'ensembles de molécules [14, 15]. Comme les modèles précédents, le Hamiltonien de Frenkel repose sur la définition d'*excitons*, ici des états électroniques localement excités $|n\rangle$ pour le site n de l'aggrégat de molécules. Nous définissons l'énergie d'excitation d'un site, ϵ_n et le couplage excitonique, J_{nm}, qui induit finalement les transferts d'énergie d'excitation entre les excitons, voir fig. 1.1, c) et d). En substance, ces schémas peuvent rappeler un diagramme de Jablonski où les états excitoniques seraient les états électroniques singulets ; les couplages excitoniques sont alors responsables des conversions internes entre les états électroniques.

L'interaction entre les sites excitoniques et leur environnement complexe (le solvant, le milieu biologique, *etc.*) est d'abord prise en compte par un couplage entre les états electroniques excités et un bain vibrationnel harmonique (qui symbolise l'environnement des excitons). Dans le cas simplifié d'un donneur et d'un accepteur, le Hamiltonien de Frenkel couplé à un bain rappelle le modèle spin-boson pour un système à deux niveaux (donneur excité et accepteur excité)

$$\widehat{H}_{\mathsf{S}} = H_{\mathsf{D}} \left|\mathsf{D}\right\rangle \left\langle\mathsf{D}\right| + H_{\mathsf{A}} \left|\mathsf{A}\right\rangle \left\langle\mathsf{A}\right| + H_{\mathsf{AD}} \left(\left|\mathsf{A}\right\rangle \left\langle\mathsf{D}\right| + \left|\mathsf{D}\right\rangle \left\langle\mathsf{A}\right|\right) \tag{1.3}$$

couplé à un bain harmonique

$$\widehat{H}_{\mathsf{B}} = \sum_{i}^{N} \frac{\hbar\omega_i}{2} \left(\widehat{p}_i^2 + \widehat{x}_i^2\right) \left(\left|\mathsf{D}\right\rangle \left\langle\mathsf{D}\right| + \left|\mathsf{A}\right\rangle \left\langle\mathsf{A}\right|\right) \tag{1.4}$$

de N oscillateurs avec les fréquences ω_i. Dans un Hamiltonien de modèle spin-boson, le couplage entre le système (les excitons) et le bain (les vibrations) est linéaire par rapport à la position des modes, et diagonal par rapport aux excitons (il ne couple pas directement deux excitons différents)

$$\widehat{H}_{\mathsf{SB}} = \sum_{i}^{N} \kappa_i^{(\mathsf{D})} \widehat{x}_i \left|\mathsf{D}\right\rangle \left\langle\mathsf{D}\right| + \kappa_i^{(\mathsf{A})} \widehat{x}_i \left|\mathsf{A}\right\rangle \left\langle\mathsf{A}\right| . \tag{1.5}$$

En d'autres termes, les excitons (états électroniques LE du donneur et de l'accepteur) peuvent être interprétés comme un ensemble de spins (systèmes à deux niveaux pour les états excités du donneur et de l'accepteur) placés dans un bain de bosons (vibrations en moléculaire, phonons en solides). Les modèdes de Hamiltonien de Frenkel et de Hamiltonien spin-boson sont tous les deux adaptés à des études de dynamique quantique en systèmes ouverts, qui incluent une dissipation de l'énergie du système dans un environnement (ici le bain harmonique). Par exemple, l'évolution temporelle de la population des différents états électroniques peut être calculée en utilisant l'équation de Redfield [4, 16]. D'autres stratégies, basées sur les solutions de l'équation de Schrödinger dépendante du temps, ont été utilisées pour évaluer la cinétique du transfert d'électron et du transfert d'énergie [3, 17, 18].

Des états excitoniques aux états électroniques non-adiabatiquement couplés

Dans ces premières tentatives de modélisation de l'EET avec un Hamiltonien de Frenkel, ou de systèmes D-A avec un modèle spin-boson, le couplage excitonique (le couplage inter-états) est constant. En particulier, il n'y a pas de couplage entre les états électroniques *via* les coordonnées nucléaires des molécules. Pour les processus intra-moléculaires, l'absence de couplage électron-noyau revient à supposer que l'EET est complètement dû aux interactions avec l'environnement, *via* des *tuning terms* (paramètres linéaires dans l'interaction système-bain) et/ou *via* la redistribution intra-moléculaire de l'énergie vibrationnelle (termes quadratiques, ou harmoniques, dans le bain). À partir de ces approximations, une extension naturelle est donc l'utilisation d'un couplage excitonique variable. Deux stratégies ont été proposées : soit modifier la théorie de Harcourt pour autoriser une variation *ad hoc* du couplage excitonique [19] ; soit estimer directement le gradient du couplage excitonique par rapport aux déplacements nucléaires. Cette dernière stratégie est en réalité directement reliée aux modèles de Hamiltonien de couplage vibronique, où les termes hors-diagonaux dépendent explicitement des déplacements associés aux déplacements nucléaires, originairement proposés par Köppel [20]. Historiquement, ces modèles ont été utilisés pour comprendre des effets non-adiabatiques et des phénomènes photo-induits dans des systèmes où les intersections coniques entre états excités sont répandues [21–23].

L'utilisation d'un modèle de couplage vibronique permet d'avoir une interprétation non-adiabatique et chimique du phénomère étudié, ici l'EET. Nous cherchons dans ce travail à décrire le processus d'EET entre un donneur et un accepteur comme s'il s'agissait d'une réaction chimique photo-induite, avec une excitation initiale (sur l'état excité d'un des donneurs) et des conversions internes vers un état final spécifique (idéalement l'état accepteur). Pour ce faire, nous avons à déterminer explicitement les surfaces d'énergie potentielle (PESs) des antennes collectrices de lumière (avec le donneur et l'accepteur), voir fig. 1.1, e) et f). Plus important encore, nous devons déterminer la forme et la force des couplages non-adiabatiques que nous identifions, dans le cas du régime intra-moléculaire, aux couplages excitoniques responsables du transfert de population et d'énergie du donneur vers l'accepteur (avec un point de vue diabatique).

Ainsi, de la première théorie de Förster vers les modèles de couplage vibronique, un grande variété de mécanismes a été proposée, pour l'identification de l'origine du couplage excitonique comme pour l'évaluation de la cinétique du transfert d'énergie d'excitation. Cette variété reflète également la variété de systèmes (naturels et artificiels) capables de collecter la lumière et d'effectuer un transfert d'énergie d'excitation efficace et ultra-rapide (sous la picoseconde). Nous présentons maintenant l'une des familles les plus prometteuses d'antennes artificielles de collecte de lumière, les dendrimères de poly(phénylène éthynylènes).

1.2 Dendrimères de poly(phénylène éthynylènes), collecteurs de lumière

Les dendrimères de poly(phénylène éthynylène) (dendrimères de PPEs) sont des systèmes dendritiques macro-moléculaires composés de benzènes et d'acétylènes avec différents schémas de substitution et différentes longueurs. Ils ressemblent à des *arbres moléculaires* où les *feuilles* sont des fragments diphénylacétylènes (DPAs, éventuellement fonctionalisés) à la périphérie des molécules, voir fig. 1.2.

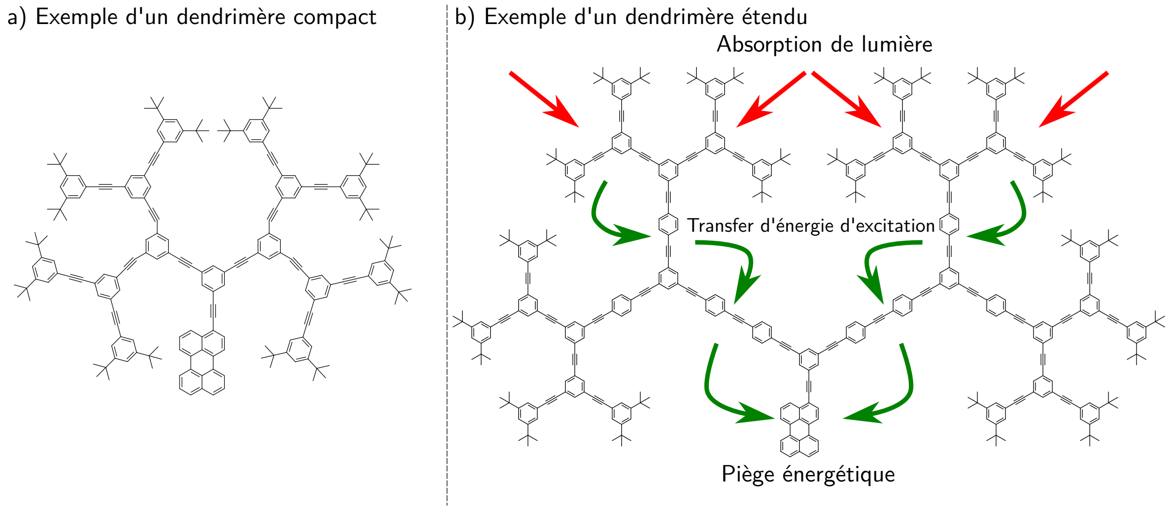

Figure 1.2 – Exemples de a) un dendrimère de PPEs compact, où toutes les branches ont la même longueur (seulement des unités DPA) et b) un dendrimère de PPEs étendu, où de la périphérie au cœur de la molécule, les branches sont de plus en plus longues. Cette génération spécifique de dendrimère de PPEs est appelée la *nano-star*. Pour le dendrimère de PPEs étendu, le mécanisme simplifié d'absorption de lumière (flèches rouges sur les chromophores) et de transfert d'énergie d'excitation (flèches vertes), canalisé vers le cœur, est aussi donné. Pour les deux molécules, le piège énergétique est ici une unité pérylène (un fluorophore bien connu).

Nous mentionnons à la fois les dendrimères de PPEs compacts et étendus, avec des longueurs égales ou des longueurs croissantes de la périphérie au cœur, voir fig. 1.2 a) et b), respectivement. La structure des dendrimères de PPEs est très similaire aux graphes mathématiques dits graphes dendritiques de Bethe (ou Cayley) où les deux sites du graphe dendritique sont des benzènes et des acétylènes. Nous définissons également les *branches* du graphes (les benzènes linéairement poly-*para*-substitués) et les *nœuds* (les benzènes di- ou tri-*meta*-substitués), voir fig. 1.3.

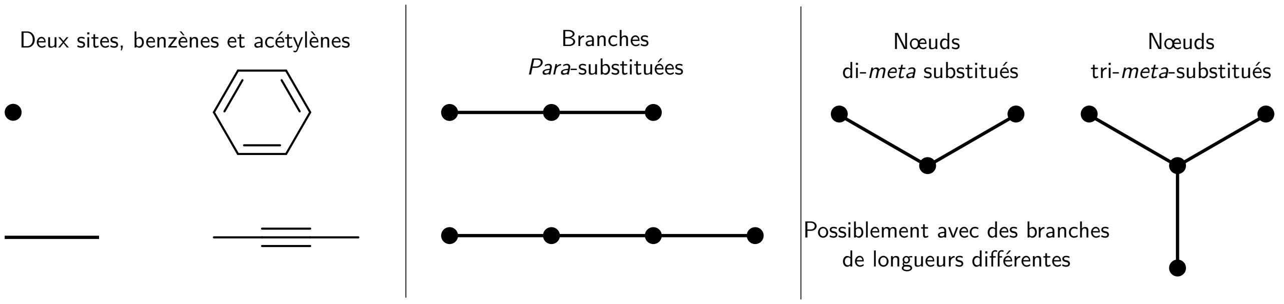

Figure 1.3 – Définition des sites, branches et nœuds pour la description de la structure des dendrimères de PPEs comme des graphes de Bethe.

Dans les dendrimères de PPEs, chaque *nœud* est un phénylène tri-*meta*-substitué, qui connecte les feuilles (benzènes à la périphérie) au reste du dendrimère jusqu'au cœur. Cependant, on pourrait imaginer un dendrimère incomplet, avec des nœuds simplement di-*meta*-substitués. Pour retrouver l'analogie avec les complexes photosynthétiques, les nœuds (avec les feuilles, ou les chromophores) et les branches sont les complexes de collecte de lumière, alors que le cœur (le piège énergétique) est le centre réactionnel de la bactérie ou de la plante.

Synthèse historique et design des propriétés photophysiques des dendrimères de PPEs

Les premières routes synthétiques des dendrimères de PPEs (à la fois compacts et étendus) proposées par Xu et Moore [24, 25] sont responsables de leur nature dendritique, et permettent de contrôler la génération (autrement dit la taille et l'étendue) du dendrimère final.

Les dendrimères compacts (fig. 1.2, a)) composés seulement de branches de mêmes longueurs, sont capables d'absorber la lumière par un large nombre de chromophores équivalents (ici des unités DPA). Du point de vue du Hamiltonien de Frenkel, autant d'états électroniques excités seraient définis que d'unités DPA du graphe [26, 27]. Le transfert d'énergie d'excitation est alors entropiquement favorisé, puisqu'un exciton photo-induit n'aurait pas de raison de rester localisé et explorerait statistiquement le reste du graphe.

Opposés aux dendrimères compacts, les dendrimères étendus ont été conçus et synthétisés (fig. 1.2, b)) avec l'exemple courant de la *nano-star*. Leur design est simple : plutôt que d'utiliser un seul type de chromophore pour tout le dendrimère, l'idée est de séparer énergétiquement les excitons, en faisant varier la longueur des branches. Plus une branche est longue, plus la conjugaison est grande et plus l'énergie d'excitation du fragment considéré est basse [28–31]. On obtient en fait un gradient unidirectionnel d'énergie, depuis la périphérie (les feuilles, énergie d'excitation « haute ») vers le cœur (piège énergétique, énergie d'excitation « basse ») du dendrimère, et le transfert d'énergie d'excitation est alors énergétiquement favorisé. Nous ne discuterons à partir de maintenant que les propriétés et la caractérisation des dendrimères de PPEs étendus.

Des efforts théoriques et expérimentaux pour la compréhension des dendrimères étendus

Les premières estimations de rendement quantique de l'EET dans les dendrimères de PPEs, en particulier dans la *nano-star*, ont été proposées par Devadoss, Shortreed et Swallen [32–34], avec un rendement estimé proche de un depuis les excitations à $310\,\mathrm{nm}$, $353\,\mathrm{nm}$ et $372\,\mathrm{nm}$ (absorption de lumière par l'unité DPA ou par des branches à trois ou quatre benzènes). Ils ont également estimé que l'EET était au moins deux ordres de grandeur plus rapide pour les dendrimères de PPEs étendu (où l'EET est favorisé énergétiquement) que pour les dendrimères compacts (où l'EET est favorisé entropiquement). Le caractère local des excitations dans la *nano-star* a ensuite été mis en évidence expérimentalement par spectrosocpie stationnaire [35]. En 2010, Palma et coll. ont proposé la première étude à la fois théorique et expérimentale de la *nano-star*. Ils ont notamment reproduit son spectre d'absorption et estimé l'effet de la température et en particulier des conformations de la *nano-star* sur le spectre.

La nature du couplage excitonique entre les excitations locales précédemment mentionnées a été investiguée par Martinez et coll. [19, 37]. Les excitations électroniques des dendrimères de PPEs ont également été étudiées par Huang et coll., qui comparent les résultats obtenus par différentes méthodes de structure électronique et proposent une description des états excitoniques en termes d'excitations locales et d'états à transfert de charge (LE et CT) [38]. En 2004, finalement, les spectres UV-visible des blocs élémentaires des dendrimères de PPEs ont été obtenus avec une résolution suffisante pour estimer les modes normaux optiquement actifs pour des transitions électroniques vers les excitations locales [39, 40]. Ces résultats de spectroscopie stationnaire ont été rationalisés théoriquement par Ho et Lasorne pour les branches *para*-substituées et pour le plus petit des PPEs di-*meta*-substitués [41, 42]. En particulier, ils ont proposé un schéma de *pseudofragmentation* pour les états électroniques excités et pour les modes vibrationels de ces molécules, basé sur une paire d'états électroniques excités presque dégénérés. D'un autre côté, la dynamique des états excités de la plus petite unité, le DPA, a été étudiée. Des états excités à longue durée de vie, menant à une isomérisation cis-trans du DPA dans des oligomères de PPEs ont été caractérisés, à la fois expérimentalement [43–45] et théoriquement [46,47]. Enfin dans un travail récent de Breuil et Lasorne, ces états, qui ne sont pas capables d'émettre de la lumière, ont été identifiés comme une possible route alternative pour l'EET [48]. Jusque là, les études mentionnées étaient principalement des études « stationnaires », c'est à dire de spectroscopie expérimentale UV-visible ou des calculs de structure électronique pour des géométries données des molécules.

Un bac à sable pour la dynamique moléculaire non-adiabatique

Finalement, les nombreuses études expérimentales sur les dendrimères de PPEs concluent sur le rôle majeur des excitations localisées dans la molécule, qui sont confortées par différentes études théoriques. Le mécanisme de transfert d'énergie d'excitation par la *nano-star* est cela-dit toujours difficile à estimer, en particulier puisque très peu d'expériences directes et de simulations atomistiques directes sont disponibles pour sonder la molécule pendant l'EET. En particulier, le débat sur la nature du transfert comme se faisant à travers l'espace (type Förster) ou à travers les liaisons (type Dexter) n'a pas été clairement fermé [19, 37, 49].

En 2009, Fernandez-Alberti et coll. ont proposé la première simulation atomistique de l'EET dans un oligomère de PPEs (le plus petit des PPEs asymétriquement *meta*-substitués), *via* des calculs de dynamique moléculaire non-adiabatique [50]. Ils ont notamment étendu leur stratégie à d'autres oligomères de PPEs et ont conclu sur plusieurs aspects du mécanisme de l'EET [51–54]. D'abord, le rôle du couplage excitonique peut être compris comme une conséquence de la présence d'intersections coniques entre les états électroniques excités. La canalisation, par l'EET, du transfert de l'énergie d'excitation au travers du dendrimère de PPEs a été attribuée aux vibrations moléculaires et en particulier à celles des liaisons acétyléniques, qui connectent les états électroniques localement excités et favorisent ainsi un mécanisme de transfert par les liaisons. En général, ces simulations estiment un rendement quantique à quasiment 100% pour l'EET après une photo-excitation de l'état localement excité le plus haut, le tout de façon ultra-rapide (en moins de $100\,\mathrm{fs}$).

Les oligomères de PPEs ont finalement été retenus comme des bacs à sables intéressants pour l'étude de méthodes de dynamique quantique non-adiabatique. Ils ont notamment été utilisés pour étudier la fiabilité de certaines méthodes de dynamique moléculaire dans des systèmes quantiques ouverts [18, 55] ou de dynamique moléculaire non-adiabatique en système fermé [56–61].

1.3 Une vision chimique et non-adiabatique pour l'étude des dendrimères

Comme nous l'avons vu, les dendrimères de PPEs ont été largement étudiés, à la fois expérimentalement et théoriquement, pour leur capacité à faire de l'EET. Cependant, le caractère même et les mécanismes de l'EET photo-induit qui se produit dans les dendrimères de PPEs et leurs blocs élémentaires sont toujours en débat. En particulier, les simulations explicites et résolues en temps de l'EET ont seulement été rendues possible lors de la dernière décennie *via* des simulations directes (ou *on-the-fly*) de dynamique moléculaires dans les états excités.

L'objectif de cette thèse est la modélisation et la simulation du transfert d'énergie d'excitation dans différents oligomères de PPEs (les blocs élémentaires de la *nano-star*). Ces modélisations sont destinées à être un point de départ pour faire le lien entre i) les premiers développements théoriques, qui utilisent le Hamiltonien de Frenkel pour les dendrimères de PPEs (fig. 1.4 a) and b)) ; et ii) les simulations directes de dynamique moléculaire non-adiabatique des oligomères de PPEs pendant l'EET.

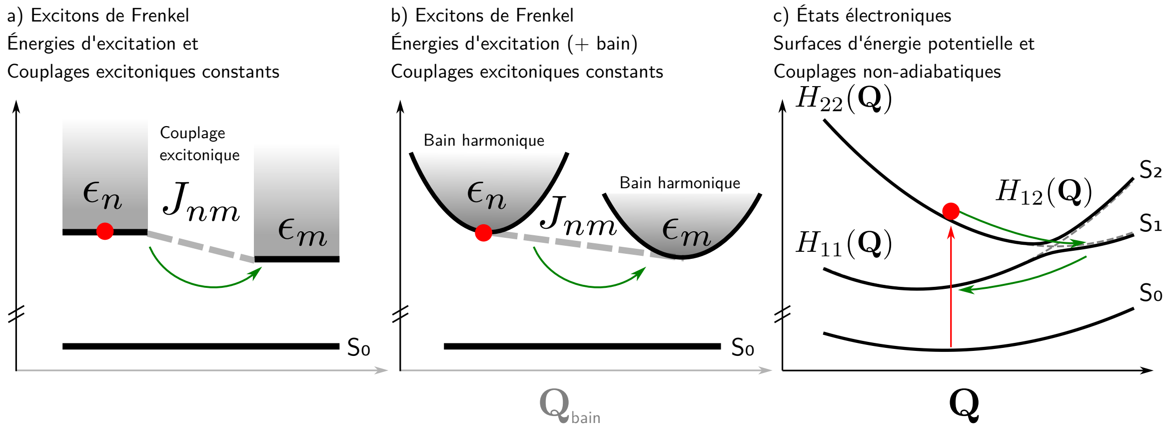

Figure 1.4 – Différentes stratégies pour la modélisation du transfert d'énergie d'excitation (EET) se produisant depuis un donneur initialement excité (point rouge). a) Modèles d'excitons de Frenkel, avec des énergies d'excitation et un couplage excitonique constants. b) *Idem* avec un bain harmonic additionnel pour les vibrations de chacun des excitons. c) Interprétation de l'EET au travers des surfaces d'énergie potentielle pour des états électroniques excités, avec une dépendance explicite des surfaces et du couplage par rapport aux vibrations.

Pour ce faire, nous caractérisons d'abord les excitations électroniques dans les oligomères de PPEs et les couplages non-adiabatiques entre eux (fig. 1.4, c), part une analyse vibrationnelle des PESs *ab initio* (obtenues par des calculs de structure électronique). Ensuite, nous proposons des modèles de PESs, qui prennent en compte les principales caractéristiques des PESs *ab initio*, afin de simuler aussi explicitement que possible les phénomènes photo-induits dans une sélection d'oligomères de PPEs, voir fig. 1.5. La caractérisation des couplages non-adiabatiques et la modélisation des PESs sont intrinsèquement liées ici, puisque nous utilisons des modèles de Hamiltonien de couplage vibronique pour *diabatiser* les états électroniques et prendre en compte leurs couplages.

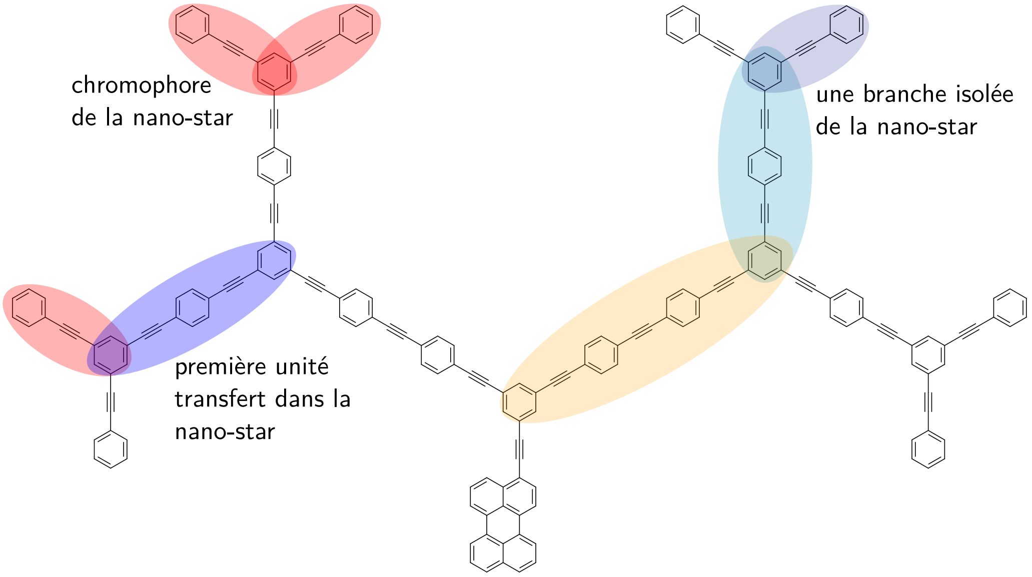

Figure 1.5 – Structure d'une *nano-star* simplifiée, étudiée dans ce travail. Le chromophore de la *nano-star* est repéré (rouge), avec deux exemples des unités de transfert (le premier à la périphérie en rouge et bleu, et la branche étendue « complète » de la périphérie jusqu'au cœur).

Ce manuscrit s'organise en trois parties. Dans la partie I, nous présentons le contexte théorique nécessaire pour réaliser des calculs de dynamique quantique non-adiabatique, pour des systèmes tels que les oligomères de PPEs. Nous définissons le Hamiltonien moléculaire ainsi que les mouvements des noyaux (chapitre 2) et donnons les équations du mouvement pour la propagation des paquets d'ondes nucléaires dans le formalisme de Hartree multiconfigurationel dépendant du temps (chapitre 3). Une attention particulière est portée sur la description de la dégénérescence entre états électroniques, qui est omniprésente dans ce travail. Une présentation de la théorie ainsi que des détails computationnels pour les calculs de structure électronique est également donnée (chapitre 4).

Dans la partie II, nous utilisons ce cadre théorique pour étudier des propriétés de spectroscopie stationnaire ainsi que l'évolution temporelle de différents oligomères de PPEs photo-excités. Nous nous intéressons d'abord au chromophore, le PPE symétriquement *meta*-substitué, pour lequel nous enquêtons sur le spectre non-usuel de fluorescence (chapitre 5). En particulier, nous posons la question de la prédiction difficile des expériences de fluorescence pour des molécules dont les états électroniques excités sont fortement couplés près de la région de Franck-Condon. Ensuite, nous étudions les plus petits oligomères de PPEs capables de faire de l'EET, et nous appliquons notre cadre théorique de simulation à l'estimation du rendement quantique, de l'échelle de temps et du mécanisme de l'EET (chapitres 6 and 7). Nos analyses nous permettent d'identifier les modes les plus importants pour que l'EET se déroule, et nous décrivons comment l'énergie d'excitation, en excès, est redistribuée au sein des vibrations moléculaires.

Finalement, dans la partie III, nous donnons les perspectives du travail présenté jusque là, avec l'état des lieux de nos développements actuels pour la description de l'EET dans un dendrimère de PPEs. D'abord, nous discutons l'influence d'excitations locales sur l'EET, en particulier dans le cas d'oligomères de PPE symétriquement *meta*-substitués (chapitre 8). Nous relevons également la question du sens physique des cohérences entre états électroniques pour des excitations initialement pures ou de superposition d'états. Enfin, nous discutons la faisabilitié d'une stratégie de modélisation « par le bas » pour les oligomères de PPEs et finalement pour les dendrimères (chapitre 9). Cette stratégie se veut intermédiaire entre l'utilisation d'un Hamiltonien de Frenkel et l'utilisation d'un Hamiltonien de couplage vibronique, avec la définition d'excitons de Frenkel basée uniquement sur les fragments linéaires isolés, ainsi que sur l'estimation du couplage excitonique autour d'intersections coniques bien identifiées.

Part I

Theoretical Background, Modelling, and Numerical Details

Intermediate Abstract

The atomistic time-dependent simulations of photoinduced excitation-energy transfer (EET) within poly(phenylene ethynylenes) (PPE) oligomers require some important theoretical background. Indeed, treating EET in the view of nonadiabatic molecular dynamics involves an interplay of both electronic structure calculations and quantum dynamics simulations, for which we choose grid-based methods here, hence requiring advanced knowledge on the potential energy surfaces of the studied systems.

The chapter 2 aims at defining, without loss of generality, the molecular Hamiltonian and its representations, and at highlighting the difficulties that exist for the description of nuclear motions in the case of degenerate electronic states. In particular, we will focus on the characterization of minimum-energy conical intersections and on setting up models to take them into account for subsequent quantum dynamics simulations.

In chapter 3, we present the multiconfiguration time-dependent Hartree (MCTDH) formalism for the variational propagation of nuclear wavepackets and some of its extensions, which will be used in this work. Together with the definition of the MCTDH ansatz for the wavefunction, we discuss the time-dependent variational principle and the derivation of the equation of motions for the propagation of nuclear wavepackets. Some details are given as regards the wavefunction analysis.

Finally, in chapter 4, we present the necessary background for electronic structure theory. We mostly discuss the use of density functional theory and its linear-response time-dependent extension for probing the electronic excited states in molecules. The computational details and the level of theory retained for this work are finally explicited.

Chapter 2

The Molecular Hamiltonian and its Representations

"Ça, c'est simplement Jahn-Teller second ordre !"

– Benjamin Lasorne, *Day one of this PhD*

In this chapter, we define the molecular Hamiltonian, the main ingredient for the time-independent and time-dependent Schrödinger equations. When studying quantum systems such as atoms and molecules, the Hamiltonian is the mathematical object denoted $\widehat{H}$ that contains the physical information about the system. Through this work, we will discuss different Hamiltonians, from the Coulomb molecular Hamiltonian to the vibronic coupling Hamiltonian models.

2.1 The molecular Hamiltonian and its kinetic energy operator

2.1.1 General definitions and notations

The non-relativistic Coulomb Hamiltonian for a molecule with N nuclei and n electrons is

$$\begin{aligned}\widehat{H}^{\text{mol}}(\mathbf{r},\mathbf{R}) &= \widehat{T}^{\text{el}}(\mathbf{r}) + \widehat{T}^{\text{nu}}(\mathbf{R}) + \widehat{V}^{\text{el-el}}(\mathbf{r}) + \widehat{V}^{\text{el-nu}}(\mathbf{r},\mathbf{R}) + \widehat{V}^{\text{nu-nu}}(\mathbf{R}) \\ &= \sum_{i=1}^{n} -\frac{\hbar^2}{2m_e}\nabla^2_{\mathbf{r}_i} + \sum_{A=1}^{N} -\frac{\hbar^2}{2M_A}\nabla^2_{\mathbf{R}_A} + \frac{1}{2}\sum_{i}^{n}\sum_{j\neq i}^{n}\frac{e^2}{4\pi\epsilon_0}\frac{1}{\|\mathbf{r}_j-\mathbf{r}_i\|} \\ &+ \sum_{i=1}^{n}\sum_{A=1}^{N} -\frac{Z_A e^2}{4\pi\epsilon_0}\frac{1}{\|\mathbf{R}_A-\mathbf{r}_i\|} + \frac{1}{2}\sum_{A=1}^{N}\sum_{B\neq A}^{N}\frac{Z_A Z_B e^2}{4\pi\epsilon_0}\frac{1}{\|\mathbf{R}_B-\mathbf{R}_A\|}\end{aligned} \tag{2.1}$$

where

- $\square^{\text{el}}$ and $\square^{\text{nu}}$ stand for functions of electronic and nuclear coordinates (and possibly the gradients with respect to these coordinates), respectively;
- T and V for kinetic energies and potential energies, respectively;
- $\mathbf{r}$ and $\mathbf{R}$ are the collections of electronic and nuclear coordinates, respectively;
- $\hbar$, m_e and ϵ_0 are the reduced Planck constant, the mass of the electron, and the permitivitty of the vacuum, respectively;
- M_A, Z_A are the mass and atomic number, respectively, of the nucleus A.

For derivatives with respect to electronic or nuclear coordinates, we define the gradient operators $\nabla_{\mathbf{r}_i}$ and $\nabla_{\mathbf{R}_A}$, respectively, and the Laplacians (here for Cartesian coordinates) $\Delta_{\mathbf{r}_i} = \nabla^2_{\mathbf{r}_i}$ and $\Delta_{\mathbf{R}_A} = \nabla^2_{\mathbf{R}_A}$. We now use atomic units which are defined such that numerically, in this new system of units

$$\hbar = m_e = \frac{e^2}{4\pi\epsilon_0} = 1 \tag{2.2}$$

and we define the fine-structure constant $\alpha = \frac{e^2}{4\pi\epsilon_0\hbar c}$. The Coulomb Hamiltonian is thus recast as

$$\begin{aligned}\widehat{H}^{\text{mol}}(\mathbf{r},\mathbf{R}) = &\sum_{i=1}^{n} -\frac{1}{2}\nabla^2_{\mathbf{r}_i} + \sum_{A=1}^{N} -\frac{1}{2M_A}\nabla^2_{\mathbf{R}_A} \\ &+ \frac{1}{2}\sum_{i}^{n}\sum_{j\neq i}^{n}\frac{1}{\|\mathbf{r}_j-\mathbf{r}_i\|} + \sum_{i=1}^{n}\sum_{A=1}^{N} -Z_A\frac{1}{\|\mathbf{R}_A-\mathbf{r}_i\|} + \frac{1}{2}\sum_{A=1}^{N}\sum_{B\neq A}^{N} Z_A Z_B\frac{1}{\|\mathbf{R}_B-\mathbf{R}_A\|}\end{aligned} \tag{2.3}$$

where energies are in hartree $E_{\mathsf{h}} = \alpha^2 m_e c^2$, lengths in bohr $a_0 = \hbar/(m_e \alpha c)$, and masses in mass of the electron m_e.

The present Coulomb molecular Hamiltonian, which is a non-relativistic approximation, is valid in the absence of external electromagnetic fields (field-free Hamiltonian, for instance for the electric field $\mathbf{E} = 0$). However, in the context of photophysics, we study molecular systems in the presence of external fields (for instance for the electric field $\mathbf{E} \neq 0$), which ideally must be described by quantum electrodynamics (QED). The field-matter interaction (for instance the light-matter interaction $-\widehat{\boldsymbol{\mu}} \cdot \mathbf{E}$, with the electric dipole moment $\widehat{\boldsymbol{\mu}}$) is taken into account in QED *via* quantization of the field, which is out of the scope of this thesis. Herein, the field-matter interaction is treated as a perturbation to the Coulomb molecular Hamiltonian and we further discuss it in section 2.3.

In this simple and general formulation of the Hamiltonian, the system of coordinates is Cartesian in the laboratory frame (LF). For now, only Cartesian coordinates are used; in the next sections of this work, mass-weighted coordinates and internal coordinates will also be discussed. Among the Cartesian coordinates, we distinguish degrees of freedom associated to the nuclei ($\mathbf{R}$) and to the electrons ($\mathbf{r}$). Unless otherwise specified, the basic description of the systems we are interested in relies on this non-relativistic Coulomb molecular Hamiltonian, such that we neglect the effects of the spin-orbit coupling. Possible relativistic effects (heavy atoms, orthogonal π-conjugated systems) would be taken into account as corrections to the Coulomb Hamiltonian. In the following, we often refer to the Coulomb molecular Hamiltonian simply as the molecular Hamiltonian.

In the Schrödinger picture of quantum mechanics, we look for the molecular eigenenergies E_m of the molecular system described by $\widehat{H}^{\mathsf{mol}}$ by solving the time-independent Schrödinger equation,

$$\forall m,\ \widehat{H}^{\mathsf{mol}}(\mathbf{r}, \mathbf{R}) \Psi_m^{\mathsf{mol}}(\mathbf{r}, \mathbf{R}) = E_m \Psi_m^{\mathsf{mol}}(\mathbf{r}, \mathbf{R}) \tag{2.4}$$

where $\Psi_m^{\mathsf{mol}}(\mathbf{r}, \mathbf{R})$ are the eigenstates of the molecular system. In the same picture, the time evolution of the molecular system is given by the time evolution of the total wavefunction $\Psi^{\mathsf{mol}}(\mathbf{r}, \mathbf{R}, t)$ which satisfies the time-dependent Schrödinger equation,

$$\widehat{H}^{\mathsf{mol}}(\mathbf{r}, \mathbf{R}) \Psi^{\mathsf{mol}}(\mathbf{r}, \mathbf{R}, t) = i\hbar \frac{\partial}{\partial t} \Psi^{\mathsf{mol}}(\mathbf{r}, \mathbf{R}, t). \tag{2.5}$$

The usual follow-up of the derivation for the description of a molecular system for a quantum chemist is the use of the *Born-Oppenheimer approximation* for separating nuclear and electronic degrees of freedom. In a few words and symbols, the Born-Oppenheimer adiabatic approximation consists in writing the molecular wavefunction as a simple product of a unique time-independent electronic wavefunction φ^{el} and a time-dependent nuclear wavefunction χ^{nu}

$$\Psi^{\mathsf{mol}}(\mathbf{r}, \mathbf{R}, t) \simeq \Psi^{\mathsf{BO}}(\mathbf{r}, \mathbf{R}, t) = \varphi^{\mathsf{el}}(\mathbf{r}; \mathbf{R}) \chi^{\mathsf{nu}}(\mathbf{R}, t) \tag{2.6}$$

where the electronic wavefunction is generally a solution to the time-independent Schrödinger equation $\varphi^{\mathsf{el}}(\mathbf{r}; \mathbf{R}) = \phi_\alpha^{\mathsf{el}}(\mathbf{r}; \mathbf{R})$, discussed later on. The variables after the semicolon in $f(\square; \square)$ define "external" parametric variables for the function f. Here, this implies that the electronic wavefunction is parametrized by the nuclear coordinates; that is, there is one wavefunction of the electronic coordinates for each set of nuclear coordinates. The Born-Oppenheimer approximation then allows us to separate one electronic state from the others, and to solve the time-dependent Schrödinger equation for this electronic state and its associated time-dependent nuclear wavefunction. However, electronic states degeneracies (conical intersections) are ubiquitous in this work, and the application of Born-Oppenheimer-like approximations is rarely valid. For this reason, we now discuss the interplay of electronic and nuclear motions through the definitions of adiabatic and (quasi)-diabatic states. The Born-Oppenheimer and adiabatic approximations will be further discussed after defining the nuclear motions.

2.1.2 Electronic and nuclear motions

The previously discussed Born-Oppenheimer wavefunction, with simple separation of electronic and nuclear degrees of freedom, is usually justified by comparing the *masses* associated to both types of degrees of freedom ($M_A \gg m_e$). Although this rationale is really practical, it is not completely rigorous. The validation or not of the Born-Oppenheimer types of approximation relies on the different timescales for the *motions* of the electronic and nuclear degrees of freedom. This implies that not only the ratio of the *masses* is important, but also the spatial derivatives (hence the nuclear kinetic energy operators). In this section, we propose to discuss as rigorously as possible the separation of the nuclear and electronic degrees of freedom and the physical and mathematical conditions required to do so.

The first incentive for separating electronic and nuclear motions is to write the molecular Hamiltonian as

$$\widehat{H}^{\mathsf{mol}}(\mathbf{r},\mathbf{R}) = \widehat{T}^{\mathsf{nu}}(\mathbf{R}) + \widehat{H}^{\mathsf{el}}(\mathbf{r};\mathbf{R}). \tag{2.7}$$

This separation is based on the separation of nuclear-related derivatives only, since the derivative operators for the nuclei coordinates are gathered in the kinetic energy operator $\widehat{T}^{\mathsf{nu}}(\mathbf{R})$. The time-independent Schrödinger equation for the *electronic* Hamiltonian now defines the electronic wavefunctions of the adiabatic states

$$\widehat{H}^{\mathsf{el}}(\mathbf{r},\mathbf{R})\phi^{\mathsf{el}}_{\alpha}(\mathbf{r};\mathbf{R}) = V_{\alpha}(\mathbf{R})\phi^{\mathsf{el}}_{\alpha}(\mathbf{r};\mathbf{R}),\ \forall\mathbf{R}. \tag{2.8}$$

The electronic wavefunctions $\phi^{\mathsf{el}}_{\alpha}(\mathbf{r};\mathbf{R})$ form an orthonormal basis $\forall\mathbf{R}$ (discussed in section 2.2.2) and they still depend on the nuclear degrees of freedom. This dependence is said to be *parametric* as discussed earlier, and is only due to multiplicative operators varying with $\mathbf{R}$ in the electronic Hamiltonian.

The art of quantum chemistry is to treat the electronic Hamiltonian and in particular the *electronic repulsion* term (2-electron term), and will be the focus of chapter 4. The electron kinetic energy and nuclear potential energies are, usually, not the most challenging part to treat because they only consists in 1-electron terms. On the other hand, it is the domain of molecular dynamics to solve the time-dependent Schrödinger equation for the full molecular Hamiltonian and in particular for the nuclear kinetic energy operator $\widehat{T}^{\textsf{nu}}(\mathbf{R})$.

The molecular wavefunction associated to the molecular Hamiltonian eq. (2.7) can be written with the Born-Huang expansion

$$\Psi^{\textsf{mol}}(\mathbf{r},\mathbf{R},t)=\sum_{\alpha,\ \textsf{el}}\psi_\alpha(\mathbf{R},t)\phi^{\textsf{el}}_\alpha(\mathbf{r};\mathbf{R}). \tag{2.9}$$

We find here an expression of the molecular wavefunction as a sum-of-product of nuclear wavepackets $\psi_\alpha(\mathbf{R},t)$ and electronic wavefunctions $\phi^{\textsf{el}}_\alpha(\mathbf{r},\mathbf{R})$. Strictly speaking, the nuclear wavepackets can be further expanded in a basis of time-independent nuclear wavefunctions $\chi^{\textsf{nu}}_i(\mathbf{R})$

$$\psi_\alpha(\mathbf{R},t)=\sum_{i,\ \textsf{nu}}d_{\alpha i}(t)\chi^{\textsf{nu}}_i(\mathbf{R}). \tag{2.10}$$

As such, the molecular wavefunction can be somewhat seen as a “direct-product” of

- an orthonormal basis of electronic wavefunctions $\{\phi^{\textsf{el}}_\alpha(\mathbf{r};\mathbf{R})\}$;
- an orthonormal basis of nuclear wavefunctions $\{\chi^{\textsf{nu}}_i(\mathbf{R})\}$;

and reads

$$\Psi^{\textsf{mol}}(\mathbf{r},\mathbf{R},t)=\sum_{\alpha,\ \textsf{el}}\sum_{i,\ \textsf{nu}}d_{\alpha i}(t)\chi^{\textsf{nu}}_i(\mathbf{R})\phi^{\textsf{el}}_\alpha(\mathbf{r};\mathbf{R}). \tag{2.11}$$

The previous expression can be seen as a generic form of ansätze for solving the time-dependent Schrödinger equation with grid-based quantum dynamics (see chapter 3).

Injecting the Born-Huang expression of the molecular wavefunction eq. (2.9) (with sum over α) into the time-dependent Schrödinger equation and integrating over the electronic degrees of freedom (with $\left\langle\phi^{\textsf{el}}_\beta;\mathbf{R}\right|$), we have

$$\sum_\alpha\left\langle\phi^{\textsf{el}}_\beta;\mathbf{R}\,\middle|\,\widehat{H}^{\textsf{mol}}(\mathbf{R})\psi_\alpha(\mathbf{R},t)\,\middle|\,\phi^{\textsf{el}}_\alpha;\mathbf{R}\right\rangle_{\textsf{el}}=i\sum_\alpha\left\langle\phi^{\textsf{el}}_\beta;\mathbf{R}\,\middle|\,\phi^{\textsf{el}}_\alpha;\mathbf{R}\right\rangle_{\textsf{el}}\frac{\partial}{\partial t}\psi_\alpha(\mathbf{R},t) \tag{2.12}$$

In this expression, we used the Dirac notation $\langle a\,|\,b\rangle_{\textsf{el}}$ to designate the integration over the electronic degrees of freedom $\int a^*(\mathbf{r})b(\mathbf{r})\mathrm{d}\mathbf{r}$. Again, the parametric dependence on nuclear degrees of freedom is given for the electronic bras $\langle\square;\mathbf{R}|$ and kets $|\square;\mathbf{R}\rangle$. The right-hand-side sum simplifies to one term (in β) because of the orthogonality of the electronic wavefunctions. The left-hand side is further “simplified” by looking closely to the effect of the nuclear kinetic energy operator (KEO)

$$\widehat{T}^{\textsf{nu}}(\mathbf{R})=\sum_{A=1}^{3N}-\frac{1}{2M_A}\frac{\partial^2}{\partial R_A^2} \tag{2.13}$$

on the nuclear-electronic wavefunction products. We now use the indices $A=1\ldots3N$ for the $3N$ nuclear degrees of freedom, where the mass M_A is the same for the three coordinates (x,y,z) of each atom. For the first-order derivatives, we find

$$\frac{\partial}{\partial R_A}\left(\psi_\alpha\phi^{\textsf{el}}_\alpha\right)=\left(\frac{\partial}{\partial R_A}\psi_\alpha\right)\phi^{\textsf{el}}_\alpha+\psi_\alpha\left(\frac{\partial}{\partial R_A}\phi^{\textsf{el}}_\alpha\right) \tag{2.14}$$

and consequently for the second-order derivatives

$$\frac{\partial^2}{\partial R_A^2}\left(\psi_\alpha\phi_\alpha^{\text{el}}\right) = \left(\frac{\partial^2}{\partial R_A^2}\psi_\alpha\right)\phi_\alpha^{\text{el}} + 2\left(\frac{\partial}{\partial R_A}\psi_\alpha\right)\left(\frac{\partial}{\partial R_A}\phi_\alpha^{\text{el}}\right) + \psi_\alpha\left(\frac{\partial^2}{\partial R_A^2}\phi_\alpha^{\text{el}}\right). \tag{2.15}$$

Again, multiplying to the right by $\phi_\beta^{\text{el}*}$ the previous relations and integrating over the electronic degrees of freedom (electronic bra-ket notation) yields

$$\left\langle \phi_\beta^{\text{el}};\mathbf{R}\middle|\frac{\partial}{\partial R_A}\psi_\alpha\phi_\alpha^{\text{el}};\mathbf{R}\right\rangle_{\text{el}} = \left(\frac{\partial}{\partial R_A}\psi_\alpha\right)\left\langle \phi_\beta^{\text{el}};\mathbf{R}\middle|\phi_\alpha^{\text{el}};\mathbf{R}\right\rangle_{\text{el}} + \psi_\alpha\left\langle \phi_\beta^{\text{el}};\mathbf{R}\middle|\frac{\partial}{\partial R_A}\phi_\alpha^{\text{el}};\mathbf{R}\right\rangle_{\text{el}} \tag{2.16}$$

and

$$\begin{aligned}\left\langle \phi_\beta^{\text{el}};\mathbf{R}\middle|\frac{\partial^2}{\partial R_A^2}\psi_\alpha\phi_\alpha^{\text{el}};\mathbf{R}\right\rangle_{\text{el}} &= \left(\frac{\partial^2}{\partial R_A^2}\psi_\alpha\right)\left\langle \phi_\beta^{\text{el}};\mathbf{R}\middle|\phi_\alpha^{\text{el}};\mathbf{R}\right\rangle_{\text{el}} \\ &+ 2\left(\frac{\partial}{\partial R_A}\psi_\alpha\right)\left\langle \phi_\beta^{\text{el}};\mathbf{R}\middle|\frac{\partial}{\partial R_A}\phi_\alpha^{\text{el}};\mathbf{R}\right\rangle_{\text{el}} \\ &+ \psi_\alpha\left\langle \phi_\beta^{\text{el}};\mathbf{R}\middle|\frac{\partial^2}{\partial R_A^2}\phi_\alpha^{\text{el}};\mathbf{R}\right\rangle_{\text{el}}.\end{aligned} \tag{2.17}$$

Let us define notations for the nuclear-space derivatives of the electronic states

$$F_{\alpha\beta}^{(A)}(\mathbf{R}) = \left\langle \phi_\alpha^{\text{el}};\mathbf{R}\middle|\frac{\partial}{\partial R_A}\phi_\beta^{\text{el}};\mathbf{R}\right\rangle_{\text{el}} \tag{2.18}$$

and for the second-order derivatives

$$G_{\alpha\beta}^{(A)}(\mathbf{R}) = \left\langle \phi_\alpha^{\text{el}};\mathbf{R}\middle|\frac{\partial^2}{\partial R_A^2}\phi_\beta^{\text{el}};\mathbf{R}\right\rangle_{\text{el}}. \tag{2.19}$$

Using this, we rewrite eq. (2.17) as

$$\begin{aligned}\left\langle \phi_\beta^{\text{el}};\mathbf{R}\middle|\frac{\partial^2}{\partial R_A^2}\psi_\alpha(\mathbf{R},t)\phi_\alpha^{\text{el}};\mathbf{R}\right\rangle_{\text{el}} &= \delta_{\beta\alpha}\left(\frac{\partial^2}{\partial R_A^2}\psi_\alpha(\mathbf{R},t)\right) \\ &+ 2F_{\beta\alpha}^{(A)}(\mathbf{R})\left(\frac{\partial}{\partial R_A}\psi_\alpha(\mathbf{R},t)\right) \\ &+ G_{\beta\alpha}^{(A)}(\mathbf{R})\psi_\alpha(\mathbf{R},t).\end{aligned} \tag{2.20}$$

In the context of adiabatic electronic wavefunctions, the previously derived nuclear dependence of the electronic wavefunctions are known as first- and second-order non-adiabatic couplings (NACs) $F_{\alpha\beta}^{(A)}(\mathbf{R})$ and $G_{\alpha\beta}^{(A)}(\mathbf{R})$, respectively. Their effect is often grouped together within the non-adiabatic coupling matrix elements in the kinetic energy operator, as

$$\Lambda_{\alpha\beta}(\mathbf{R}) = -\sum_{A=1}^{3N}\frac{1}{M_A}F_{\alpha\beta}^{(A)}(\mathbf{R})\frac{\partial}{\partial R_A} - \sum_{A=1}^{3N}\frac{1}{2M_A}G_{\alpha\beta}^{(A)}(\mathbf{R}) \tag{2.21}$$

which can be defined in a matrix-vector form if mass-weighted coordinates are used instead of Cartesian coordinates. For now, we keep the unspecified electronic basis set and continue the derivation by inserting the previous relation eq. (2.20) in eq. (2.12)

$$\boxed{\begin{aligned}i\hbar\frac{\partial}{\partial t}\psi_\beta(\mathbf{R},t) = &\left(\sum_A -\frac{\hbar^2}{2M_A}\frac{\partial^2}{\partial R_A^2} + H_{\beta\beta}^{\text{el}}(\mathbf{R}) - \sum_A\frac{\hbar^2}{2M_A}G_{\beta\beta}^{(A)}(\mathbf{R})\right)\psi_\beta(\mathbf{R},t) \\ &+\sum_{\alpha\neq\beta}\left(H_{\beta\alpha}^{\text{el}}(\mathbf{R}) - \sum_A\frac{\hbar^2}{2M_A}\left(2F_{\beta\alpha}^{(A)}(\mathbf{R})\frac{\partial}{\partial R_A} + G_{\beta\alpha}^{(A)}(\mathbf{R})\right)\right)\psi_\alpha(\mathbf{R},t)\end{aligned}} \tag{2.22}$$

Equation (2.22) describes the general propagation of a nuclear wavepacket $\psi_\beta(\mathbf{R}, t)$ and is the basis of discussion for both fully quantum and mixed quantum-classical dynamics. The first term (first parenthesis) describes the evolution of the nuclear wavepacket on state β relatively to the electronic surface β, while the second term includes (potential and/or kinetic) *coupling* between the electronic surface β and all other electronic surfaces (labeled $\alpha \neq \beta$). From here, two classes of molecular dynamics method can be defined. Quantum "wavepacket-based" dynamics keep the *wavepacket character* for the nuclear degrees of freedom; classical "trajectory-based" dynamics approximate the wavepacket definition with *ensembles of classical trajectories* for the nuclear motions. In quantum dynamics calculations, the complexity of the nuclear kinetic energy operator $\hat{T}^{\text{nu}}$ strongly depends on the choice for the coordinate system, which is discussed in section 2.4. In trajectory-based dynamics, the nuclear motions satisfy Newton's classical equations of motion, with forces parametrized or defined from quantum mechanical quantities, hence the *mixed quantum-classical* qualification for such methods when several electronic states are coupled (nonadiabatic context).

In both quantum dynamics and mixed quantum-classical methods, the representation for the electronic degrees of freedom is crucial, and is discussed in section 2.2. In particular, this choice is heavily related to the electronic structure methods available, because of the evaluation of the electronic Hamiltonian matrix representation ($H^{\text{el}}_{\alpha\beta}$) and the non-adiabatic coupling vectors (NACVs).

In this work, only quantum dynamics calculations are considered, based on the multi-configuration time-dependent Hartree (MCTDH) formalism, which is presented and discussed in chapter 3. A brief discussion of the place of MCTDH within the landscape of molecular dynamics will also be given there.

Take-home messages

1. The molecular Hamiltonian has been explicited, and the molecular, electronic and nuclear wavefunctions have been defined.
2. We defined the nuclear motions from the effect of the nuclear kinetic energy operator of the molecular wavefunction.
3. We explicited the theoretical propagation of nuclear wavepackets, eq. (2.22), for which the electronic representation is crucial.

2.2 Electronic representations and basis sets

According to the Born-Oppenheimer approximation, the electronic structure problem is crucial and comes first for all molecular dynamics simulations, and generally consists in solving the time-independent Schrödinger's equation (TISE) for the electronic degrees of freedom that we recall here

$$\widehat{H}^{\text{el}}(\mathbf{r},\mathbf{R})\phi_\alpha^{\text{el}}(\mathbf{r};\mathbf{R}) = V_\alpha(\mathbf{R})\phi_\alpha^{\text{el}}(\mathbf{r};\mathbf{R}) \tag{2.23}$$

where the eigenfunctions $\phi_\alpha^{\text{el}}(\mathbf{r};\mathbf{R})$ of the electronic Hamiltonian $\widehat{H}^{\text{el}}(\mathbf{r},\mathbf{R})$ are called the adiabatic electronic states, at any $\mathbf{R}$, and $V_\alpha(\mathbf{R})$ are the adiabatic potential energy surfaces (PESs). In this section, the superscript $\square^{\text{el}}$ will be replaced by $\square^{\text{ad}}$ on relevant quantities (except operators). By definition, the matrix of the electronic Hamiltonian is diagonal in the adiabatic representation, and the matrix elements of the (nuclear-)space derivatives of the adiabatic states define the non-adiabatic couplings, previously stated in eqs. (2.18) and (2.19). In other words, the adiabatic representation yields a diagonal matrix for what comes from the electronic Hamiltonian (defining the adiabatic PESs) and a full matrix for the nuclear kinetic energy operator. Within the adiabatic basis set representation, two very similar approximations are found: the adiabatic approximation and the Born-Oppenheimer approximation. The Born-Oppenheimer approximation consists in strictly neglecting all the nuclear-space derivatives of the electronic states (the NACs)

$$F_{\alpha\beta}^{\text{ad},(A)} \simeq 0 \text{ and } G_{\alpha\beta}^{\text{ad},(A)} \simeq 0 \tag{2.24}$$

while the adiabatic approximation allows in principle the second-order corrections in the diagonal elements of the kinetic energy operator $G_{\alpha\alpha}^{\text{ad},(A)}$ to be non-zero (diagonal Born-Oppenheimer corrections, DBOC). As a consequence of these approximations, the equation for the propagation of nuclear wavepackets eq. (2.22) reads

$$i\frac{\partial}{\partial t}\psi_\beta(\mathbf{R},t) = \left(\sum_{A=1}^{3N} -\frac{\hbar^2}{2M_A}\frac{\partial^2}{\partial R_A^2} + V_\beta(\mathbf{R}) + \lambda\left(\sum_{A=1}^{3N} -\frac{\hbar^2}{2M_A}G_{\beta\beta}^{(A)}(\mathbf{R})\right)\right)\psi_\beta(\mathbf{R},t) \tag{2.25}$$

with $\lambda = 0, 1$ in the Born-Oppenheimer and adiabatic approximations, respectively. The propagation of a nuclear wavepacket for a given electronic state β is now independent from the other electronic states $\alpha \neq \beta$.

As mentioned, the difference in masses of electrons and nuclei is not a sufficiently strong condition to ensure the approximations of eq. (2.24). In particular, the regions of molecular geometries for which two or more electronic states are degenerate break down the Born-Oppenheimer or adiabatic approximations, as we will illustrate now with the off-diagonal Hellmann-Feynman theorem.

2.2.1 The diagonal and off-diagonal Hellmann-Feynman theorems

The Hellmann-Feynman theorem is widely used for computing the nuclear forces (or gradients) using the information of the adiabatic states and the nuclear-derivatives of the electronic Hamiltonian within the adiabatic-type approximations

$$\frac{\partial V_\alpha}{\partial R_A}(\mathbf{R}) = \left\langle \phi_\alpha^{\text{ad}};\mathbf{R}\left|\frac{\partial \widehat{H}^{\text{el}}}{\partial R_A}(\mathbf{R})\right|\phi_\alpha^{\text{ad}};\mathbf{R}\right\rangle_{\text{el}} . \tag{2.26}$$

In addition, an off-diagonal Hellmann-Feynman theorem is easily derived. First, considering two adiabatic electronic states and differentiating (with respect to the nuclear degrees of freedom) their orthonormal condition

$$\left\langle \phi_\alpha^{\text{ad}};\mathbf{R} \middle| \phi_\beta^{\text{ad}};\mathbf{R} \right\rangle_{\text{el}} = \delta_{\alpha\beta} \tag{2.27}$$

one finds

$$\left\langle \frac{\partial}{\partial R_A}\phi_\alpha^{\text{ad}};\mathbf{R} \middle| \phi_\beta^{\text{ad}};\mathbf{R} \right\rangle_{\text{el}} + \left\langle \phi_\alpha^{\text{ad}};\mathbf{R} \middle| \frac{\partial}{\partial R_A}\phi_\beta^{\text{ad}};\mathbf{R} \right\rangle_{\text{el}} = 0 \tag{2.28}$$

so that $F_{\alpha\beta}^{\text{ad},(A)} = -F_{\beta\alpha}^{\text{ad},(A)*}$. Then for the Hamiltonian matrix elements,

$$\begin{aligned}\frac{\partial}{\partial R_A}\left(\left\langle \phi_\alpha^{\text{ad}};\mathbf{R} \middle| \widehat{H}(\mathbf{R}) \middle| \phi_\beta^{\text{ad}};\mathbf{R} \right\rangle_{\text{el}} \right) = & \left\langle \frac{\partial}{\partial R_A}\phi_\alpha^{\text{ad}};\mathbf{R} \middle| \widehat{H}(\mathbf{R}) \middle| \phi_\beta^{\text{ad}};\mathbf{R} \right\rangle_{\text{el}} \\ & + \left\langle \phi_\alpha^{\text{ad}};\mathbf{R} \middle| \frac{\partial}{\partial R_A}\widehat{H}(\mathbf{R}) \middle| \phi_\beta^{\text{ad}};\mathbf{R} \right\rangle_{\text{el}} \\ & + \left\langle \phi_\alpha^{\text{ad}};\mathbf{R} \middle| \widehat{H}(\mathbf{R}) \middle| \frac{\partial}{\partial R_A}\phi_\beta^{\text{ad}};\mathbf{R} \right\rangle_{\text{el}} .\end{aligned} \tag{2.29}$$

Using the fact that the adiabatic states are the exact eigenfunctions of the electronic Hamiltonian and eq. (2.28), we continue

$$\begin{aligned}0 = & -V_\alpha(\mathbf{R}) \left\langle \phi_\alpha^{\text{ad}};\mathbf{R} \middle| \frac{\partial}{\partial R_A}\phi_\beta^{\text{ad}};\mathbf{R} \right\rangle_{\text{el}} + \left\langle \phi_\alpha^{\text{ad}};\mathbf{R} \middle| \frac{\partial}{\partial R_A}\widehat{H}(\mathbf{R}) \middle| \phi_\beta^{\text{ad}};\mathbf{R} \right\rangle_{\text{el}} \\ & + V_\beta(\mathbf{R}) \left\langle \phi_\alpha^{\text{ad}};\mathbf{R} \middle| \frac{\partial}{\partial R_A}\phi_\beta^{\text{ad}};\mathbf{R} \right\rangle_{\text{el}} .\end{aligned} \tag{2.30}$$

Finally we find for the first-order NACV, for $\alpha \neq \beta$

$$\boxed{F_{\alpha\beta}^{\text{ad},(A)} = \frac{\left\langle \phi_\alpha^{\text{ad}};\mathbf{R} \middle| \frac{\partial}{\partial R_A}\widehat{H}(\mathbf{R}) \middle| \phi_\beta^{\text{ad}};\mathbf{R} \right\rangle_{\text{el}}}{V_\beta(\mathbf{R}) - V_\alpha(\mathbf{R})}} \tag{2.31}$$

which is thus singular when $V_\beta(\mathbf{R}) - V_\alpha(\mathbf{R}) = 0$. In such regions and looking back to the electronic and nuclear equations of motion eq. (2.22), the kinetic energy operator diverges and the propagation becomes unpraticable. For working with eq. (2.22) in the presence of degenerate electronic states, it is then necessary to choose an electronic representation that is not the adiabatic one. In this context, we now present the concept of quasi-diabatic states and their use for representing the potential energy surfaces and couplings in a smooth way with respect to $\mathbf{R}$.

2.2.2 Transformations to and from adiabatic electronic states

2.2.2.1 Arbitrary working electronic states and adiabaticity

Let us define some orthonormal basis of two “working” electronic states $\{|\phi_1;\mathbf{R}\rangle, |\phi_2;\mathbf{R}\rangle\}$, in which the electronic Hamiltonian matrix reads

$$\mathbf{H}(\mathbf{R}) = \begin{bmatrix} H_{11}(\mathbf{R}) & H_{12}(\mathbf{R}) \\ H_{21}(\mathbf{R}) & H_{22}(\mathbf{R}) \end{bmatrix} \tag{2.32}$$

with all the matrix elements being real-valued (such that $H_{12}(\mathbf{R}) = H_{21}(\mathbf{R})$). For the sake of simplicity, we shall rewrite the "working" Hamiltonian as an averaged-trace matrix and a traceless matrix

$$\mathbf{H}(\mathbf{R}) = S(\mathbf{R})\mathbb{1} + \begin{bmatrix} -D(\mathbf{R}) & W(\mathbf{R}) \\ W(\mathbf{R}) & D(\mathbf{R}) \end{bmatrix} \tag{2.33}$$

with

$$S(\mathbf{R}) = \frac{H_{11}(\mathbf{R}) + H_{22}(\mathbf{R})}{2}, \tag{2.34}$$

$$D(\mathbf{R}) = \frac{H_{22}(\mathbf{R}) - H_{11}(\mathbf{R})}{2} \tag{2.35}$$

and

$$W(\mathbf{R}) = H_{12}(\mathbf{R}) = H_{21}(\mathbf{R}). \tag{2.36}$$

For the purpose of this section, we do not need to further specify the coordinate system nor the actual dependence of the previous quantities with respect to the coordinates. We only require the matrix elements of $\widehat{H}$ to be smoothly varying with the nuclear coordinates. We can write the adiabatic electronic states as a unitary transformation of the "working" electronic states, for instance with a rotation parametrized with the angle $\theta(\mathbf{R})$

$$\left|\phi_1^{\text{ad}};\mathbf{R}\right\rangle = \cos\theta(\mathbf{R})\left|\phi_1;\mathbf{R}\right\rangle + \sin\theta(\mathbf{R})\left|\phi_2;\mathbf{R}\right\rangle \tag{2.37a}$$

$$\left|\phi_2^{\text{ad}};\mathbf{R}\right\rangle = -\sin\theta(\mathbf{R})\left|\phi_1;\mathbf{R}\right\rangle + \cos\theta(\mathbf{R})\left|\phi_2;\mathbf{R}\right\rangle. \tag{2.37b}$$

The unitary transformation, satisfying $\mathbf{U}^\dagger(\mathbf{R})\mathbf{U}(\mathbf{R}) = \mathbf{U}(\mathbf{R})\mathbf{U}^\dagger(\mathbf{R}) = \mathbb{1}$ is here a rotation

$$\mathbf{U}(\mathbf{R}) = \begin{bmatrix} \cos\theta(\mathbf{R}) & -\sin\theta(\mathbf{R}) \\ \sin\theta(\mathbf{R}) & \cos\theta(\mathbf{R}) \end{bmatrix} \tag{2.38}$$

and allows us to write the transformation in a vector-matrix form for the electronic states[1]

$$\Big(|\phi_1^{\text{ad}};\mathbf{R}\rangle \quad |\phi_2^{\text{ad}};\mathbf{R}\rangle\Big) = \Big(|\phi_1;\mathbf{R}\rangle \quad |\phi_2;\mathbf{R}\rangle\Big)\,\mathbf{U}(\mathbf{R}), \text{ with } \quad U_{ij} = \langle\phi_i\,|\,\phi_j^{\text{ad}}\rangle \tag{2.39}$$

and for the matrix representations of the Hamiltonian

$$\mathbf{V}(\mathbf{R}) = \mathbf{U}^\dagger(\mathbf{R})\mathbf{H}(\mathbf{R})\mathbf{U}(\mathbf{R}), \tag{2.40}$$

where $\mathbf{V}(\mathbf{R})$ is the (ordered) diagonal matrix of the adiabatic energies. In other words, the diagonalization of the "working" Hamiltonian boils down to the evaluation of the rotation angle $\theta(\mathbf{R})$. We rewrite the diagonal matrix of the adiabatic energies

$$\mathbf{V}(\mathbf{R}) = \begin{bmatrix} V_1(\mathbf{R}) & 0 \\ 0 & V_2(\mathbf{R}) \end{bmatrix} = \Sigma(\mathbf{R})\mathbb{1} + \begin{bmatrix} -\Delta V(\mathbf{R}) & 0 \\ 0 & \Delta V(\mathbf{R}) \end{bmatrix} \tag{2.41}$$

---

[1] We stress here that with more than two electronic states, the transformation $\mathbf{U}$ needs only to be unitary; for the two-state case, the form of a rotation matrix is convenient.

with

$$\Sigma(\mathbf{R}) = \frac{V_1(\mathbf{R}) + V_2(\mathbf{R})}{2} \tag{2.42}$$

and

$$\Delta V(\mathbf{R}) = \frac{V_2(\mathbf{R}) - V_1(\mathbf{R})}{2} \geq 0. \tag{2.43}$$

Let us note that the averaged-trace identity matrix in $\mathbf{H}(\mathbf{R})$ is unchanged by any rotation and in particular by $\mathbf{U}(\mathbf{R})$, such that

$$S(\mathbf{R}) = \Sigma(\mathbf{R}). \tag{2.44}$$

As a consequence, we can define the unitary transformation from the remaining traceless matrix directly. Evaluating the matrix products in eq. (2.40), we identify the so-called *adiabaticity conditions*

$$D(\mathbf{R}) \sin 2\theta(\mathbf{R}) + W(\mathbf{R}) \cos 2\theta(\mathbf{R}) = 0 \tag{2.45a}$$

$$D(\mathbf{R}) \cos 2\theta(\mathbf{R}) - W(\mathbf{R}) \sin 2\theta(\mathbf{R}) = \Delta V(\mathbf{R}) \tag{2.45b}$$

These equations simply define the *conditions* for transforming a given “working” electronic basis set into the adiabatic electronic basis set. One can find the solutions for the adiabaticity conditions eq. (2.45)

$$\frac{\sin 2\theta(\mathbf{R})}{\cos 2\theta(\mathbf{R})} = \tan 2\theta(\mathbf{R}) = -\frac{W(\mathbf{R})}{D(\mathbf{R})} \tag{2.46a}$$

$$\sqrt{D(\mathbf{R})^2 + W(\mathbf{R})^2} = \Delta V(\mathbf{R}) \geq 0. \tag{2.46b}$$

Thus, the adiabatic energies are found as the eigenvalues of the “working” Hamiltonian

$$\boxed{V_{1,2}(\mathbf{R}) = \Sigma(\mathbf{R}) \pm \Delta V(\mathbf{R}) = S(\mathbf{R}) \pm \sqrt{D(\mathbf{R})^2 + W(\mathbf{R})^2}} \tag{2.47}$$

and the associated adiabatic electronic states (associated eigenvectors) can be obtained using the parametrized angle satisfying

$$\boxed{\cos 2\theta(\mathbf{R}) = \frac{D(\mathbf{R})}{\Delta V(\mathbf{R})}, \quad \sin 2\theta(\mathbf{R}) = -\frac{W(\mathbf{R})}{\Delta V(\mathbf{R})}, \quad \tan 2\theta(\mathbf{R}) = -\frac{W(\mathbf{R})}{D(\mathbf{R})}.} \tag{2.48}$$

We note that the effect of the rotation on the “working” electronic states is related to its effect on the Hamiltonian matrix representation. Indeed, while the electronic states undergo a rotation of angle $\theta(\mathbf{R})$, the traceless matrix elements of $\mathbf{H}(\mathbf{R})$ (D and W) undergo a rotation of angle $-2\theta(\mathbf{R})$.

The previous derivations are used hereafter for illustrating two purposes. First we will present the particular case of quasi-diabatic electronic states for the electronic representation. Then, we will discuss the properties of crossing potential energy surfaces and in particular of conical intersections.

2.2.2.2 The case of (quasi-)diabatic electronic states

Until here, we have described the adiabatic representation for the electronic states, for which the off-diagonal terms of the nuclear kinetic energy operator are non-zero and diverge in the region of electronic state degeneracy (eq. (2.31)). On the other hand, *diabatic electronic states* are defined as a different set of electronic states for which

$$\Lambda^{\text{dia}}_{\alpha\beta}(\mathbf{R}) = 0. \tag{2.49}$$

These general conditions can be expressed in terms of the adiabatic-to-diabatic unitary transformation (from n adiabatic states to n diabatic states) $\mathbf{U}^{\text{dia}}(\mathbf{R})$ defined in a similar way to eq. (2.38) (for two states). This transformation is such that the (non-diagonal) Hamiltonian representation $\mathbf{H}^{\text{dia}}(\mathbf{R})$ and the (diagonal matrix of) adiabatic potential energies are linked through the relation

$$\mathbf{V}(\mathbf{R}) = \mathbf{U}^{\text{dia}\dagger}(\mathbf{R})\mathbf{H}^{\text{dia}}(\mathbf{R})\mathbf{U}^{\text{dia}}(\mathbf{R}). \tag{2.50}$$

It can be shown (see Ref [62]) that the effect of the transformation for the first-order non-adiabatic coupling matrix is

$$\mathbf{F}^{\text{ad}}(\mathbf{R}) = \mathbf{U}^{\text{dia}\dagger}(\mathbf{R})\mathbf{F}^{\text{dia}}(\mathbf{R})\mathbf{U}^{\text{dia}}(\mathbf{R}) + \mathbf{U}^{\text{dia}\dagger}(\mathbf{R})\frac{\partial}{\partial \mathbf{R}}\mathbf{U}^{\text{dia}}(\mathbf{R}). \tag{2.51}$$

The diabaticity conditions eq. (2.49) imply that

$$\mathbf{F}^{\text{dia}}(\mathbf{R}) \simeq 0. \tag{2.52}$$

Injecting eq. (2.52), we find the diabaticity conditions in terms of the adiabatic-to-diabatic unitary transformation

$$\mathbf{F}^{\text{ad}}(\mathbf{R}) \simeq \mathbf{U}^{\text{dia}\dagger}(\mathbf{R})\frac{\partial}{\partial \mathbf{R}}\mathbf{U}^{\text{dia}}(\mathbf{R}). \tag{2.53}$$

Applying this to the previous case of two electronic states, the conditions can be further rewritten with respect to the nuclear-space derivatives of the rotation angle $\theta^{\text{dia}}(\mathbf{R})$

$$F^{\text{ad},(A)}_{12}(\mathbf{R}) \simeq -\frac{\partial}{\partial R_A}\theta^{\text{dia}}(\mathbf{R}). \tag{2.54}$$

For the diabaticity conditions to be strictly fulfilled, a complete (infinite) basis set of electronic states is required, which is impracticable in practice. For this reason, the diabaticity condition is always only approximately fulfilled in molecular systems (of more than two nuclei)[2] and the electronic states are called *quasi-diabatic electronic states*. In the rest of this work, only quasi-diabatic states are discussed, and for the sake of simplicity, we shall call them *diabatic* states [62, 63]. As a matter of fact, we even do not have a direct usage of the diabatic states, because of the diabatization procedure that we use (that is, we do not explicitly check $\Lambda^{\text{dia}} = 0$).

The ways of obtaining approximate diabatic states are numerous and cannot be comprehensively cited here. Nonetheless we cite the main families of methods. First, for the (most common) case of two electronic states, one can directly line-integrate the NAC vector with eq. (2.54) [64]. However, the results for this direct method may depend on the integration path. Some authors also proposed to propagate the adiabatic-to-diabatic transformation matrix $\mathbf{U}^{\text{dia}\dagger}$ within on-the-fly dynamics calculations [65, 66].

---

[2] For diatomics, there is only one internal coordinate $R = ||\mathbf{R}_1 - \mathbf{R}_2||$ and no conical intersections and no path dependence for integrating eq. (2.54)

Other methods based on explicitly knowing the adiabatic wavefunctions for instance using block-diagonalization of the electronic Hamiltonian, have been developed, first by Pacher, Köppel and Cederbaum [67, 68]. In particular, this was explored for multiconfiguration wavefunction electronic structure methods by Atchity and Ruedenberg [69] and applied for triatomic molecules [70, 71]. It was further generalized later by Nakamura and Truhlar [72–74]. Block-diagonalization was also recently reused as an analysis tool for building PESs [75, 76].

The second main family is the so-called *diabatization by ansatz* and is the retained method in this work [20, 77, 78]. The main strategy behind diabatization by ansatz consists in fitting vibronic-coupling Hamiltonian models to *ab initio* data. The matrix elements of the "working" Hamiltonian models $\mathbf{H}^{\mathrm{el}}(\mathbf{R})$ are smooth functions of the nuclear coordinates. The advantages of it is that the focus of the diabatization is on the PESs, and therefore only requires information about the adiabatic energies or associated derivatives with respect to the nuclear coordinates. For instance this is compatible with electronic structure methods that are not based on wavefunctions, such as reduced-density methods. The drawback is shared with the main advantage, which is that one does not work directly with the electronic excited states as mathematical nor numerical objects, and thus have no direct access to the diabatic states.

Apart from mathematical definitions and problems, let us sum up in a few words the concept of diabatic states as we use them in this work.

Take-home messages

1. Diabatic states are electronic states associated to "slowly" and smoothly varying potential energy surfaces with respect to the nuclear coordinates, as opposed to the adiabatic potential energy surfaces. The aim is to eliminate the singularity in the kinetic energy operator (*kinetic couplings*) for geometries around energy degeneracy, replacing it with off-diagonal terms in the electronic Hamiltonian (*potential couplings*).
2. From a chemist point of view, we follow the electronic states based on a specific character (diabatic view: symmetry labels, resonant Lewis structures, localized excitations) rather than based on energy ordering (adiabatic view: spectroscopic ordering).

2.3 Interaction with an external field

In the previous sections, we defined molecular eigenstates, which are expanded in the basis of electronic states and nuclear wavepackets, and are studied quantum mechanically. One of the purposes of this thesis is not only the description of the molecular states but also their interaction with an external field. In particular, for both steady-state and time-resolved studies of photoinduced phenomena, we may be interested in the interaction with an external electric field, $\mathbf{E} \neq 0$. This interaction must be dealt with and we choose to include it in our simulations as a perturbation to the molecular Hamiltonian. Thus, the molecular states are treated quantum mechanically, but the electric field and its interaction with the molecular states will be included classically.

2.3.1 Semi-classical interaction with the electric field

Let us introduce an external monochromatic electronic field $\mathbf{E}(z,t)$ of wavelength λ (and frequency $\nu = \frac{c}{\lambda}$ with c the speed of light in vacuum) polarized along the unitary vector $\mathbf{x}$, travelling along $\mathbf{z}$. The associated angular frequency and wavenumber are $\omega = 2\pi\nu$ and $k = \frac{2\pi}{\lambda}$, respectively, such that

$$\mathbf{E}(z,t) = E_x \cos{(\omega t - kz)}\mathbf{x} = E_x \cos{(\omega t - \frac{2\pi z}{\lambda})}\mathbf{x}. \tag{2.55}$$

Here, we will neglect the effect of the magnetic field for its interaction with the electrons and the nuclei. Thus, we only consider the classical electric field, for which the potential energy of interaction with a set $\{q_i, \mathbf{r}_i\}$ of charged particles (here, all electrons and nuclei) gives the interaction Hamiltonian

$$\widehat{H}^{\mathsf{ext}}(t) = -E_x \sum_i q_i x_i \cos{(\omega t - \frac{2\pi z_i}{\lambda})}. \tag{2.56}$$

For our purposes, electric fields involved in transitions between molecular states will be characterized with a wavelength much larger than the size of the molecules.[3] This legitimates the *long-wave approximation*, which neglects the space variation of the electric field,

$$\widehat{H}^{\mathsf{ext}}(t) \simeq -E_x \sum_i q_i x_i \cos{(\omega t)} \tag{2.57}$$

that can be rewritten effectively as

$$\widehat{H}^{\mathsf{ext}}(t) = -\widehat{\boldsymbol{\mu}}(\mathbf{r},\mathbf{R}) \cdot \mathbf{E} \tag{2.58}$$

where $\widehat{\boldsymbol{\mu}}(\mathbf{r},\mathbf{R})$ is the dipole moment operator of the molecule and $\mathbf{E}$ is the electric field. We note that this is the usual semi-classical picture for the electric field interaction, with length-gauge; analogous equations can be found for the velocity-gauge. Considering the interaction of the molecule with the electric field only by adding eq. (2.58) to the molecular Hamiltonian eq. (2.1) is the *dipole approximation*. Unless otherwise specified, in the rest of this thesis, we always assume the dipole approximation to be valid.

2.3.2 Transition dipole moments and the Condon approximation

The first-order perturbative dipole approximation for the interaction of the molecule with the electric field is standard and allows us to simply treat the electric field as a first-order perturbation to the reference

---

[3] For the UV-visible transitions, the order of magnitude of the wavelength is $\lambda \simeq 100\,\mathrm{nm}$ while the molecular sizes range from $0.1\,\mathrm{nm}$ to $1\,\mathrm{nm}$.

molecular Hamiltonian. As such, the transition probabilities between the molecular states can be evaluated from the transition dipole moments (TDMs) matrix elements,

$$\mathsf{TDM}_{if} = \left\langle \Psi_i^{\mathsf{mol}} \middle| \widehat{\boldsymbol{\mu}}(\mathbf{r},\mathbf{R}) \middle| \Psi_f^{\mathsf{mol}} \right\rangle , \tag{2.59}$$

where i and f are the labels for the initial state and final state, respectively. Here, the braket notation accounts for the integration over both electronic and nuclear degrees of freedom. Assuming separable molecular states (that is, adiabatic electronic states within the Born-Oppenheimer approximation or locally diabatic states), one can separate the electronic and nuclear degrees of freedom

$$\begin{aligned} \left\langle \Psi_i^{\mathsf{mol}} \middle| \widehat{\boldsymbol{\mu}}(\mathbf{r},\mathbf{R}) \middle| \Psi_f^{\mathsf{mol}} \right\rangle &\simeq \left\langle \psi_i^{\mathsf{nu}}\phi_i^{\mathsf{el}} \middle| \widehat{\boldsymbol{\mu}}^{\mathsf{el}}(\mathbf{r}) + \widehat{\boldsymbol{\mu}}^{\mathsf{nu}}(\mathbf{R}) \middle| \psi_f^{\mathsf{nu}}\phi_f^{\mathsf{el}} \right\rangle \\ &= \left\langle \psi_i^{\mathsf{nu}}\phi_i^{\mathsf{el}} \middle| \widehat{\boldsymbol{\mu}}^{\mathsf{el}}(\mathbf{r}) \middle| \psi_f^{\mathsf{nu}}\phi_f^{\mathsf{el}} \right\rangle + \left\langle \psi_i^{\mathsf{nu}}\phi_i^{\mathsf{el}} \middle| \widehat{\boldsymbol{\mu}}^{\mathsf{nu}}(\mathbf{R}) \middle| \psi_f^{\mathsf{nu}}\phi_f^{\mathsf{el}} \right\rangle . \end{aligned} \tag{2.60}$$

Now using different notations for the integration over the electronic and nuclear degrees of freedom, the second term of eq. (2.60) reads

$$\left\langle \psi_i^{\mathsf{nu}}\phi_i^{\mathsf{el}} \middle| \widehat{\boldsymbol{\mu}}^{\mathsf{nu}}(\mathbf{R}) \middle| \psi_f^{\mathsf{nu}}\phi_f^{\mathsf{el}} \right\rangle = \left\langle \psi_i^{\mathsf{nu}} \middle| \widehat{\boldsymbol{\mu}}^{\mathsf{nu}}(\mathbf{R}) \middle| \psi_f^{\mathsf{nu}} \right\rangle_{\mathsf{nu}} \underbrace{\left\langle \phi_i^{\mathsf{el}};\mathbf{R} \middle| \phi_f^{\mathsf{el}};\mathbf{R} \right\rangle_{\mathsf{el}}}_{=\delta_{if}} \tag{2.61}$$

and is non-zero when considering that the transition does not change the electronic state. This leads to the study of (ro)vibrational spectroscopy, with the transition probabilities being governed by the matrix elements of the nuclear transition dipole moment $\left| \left\langle \psi_i^{\mathsf{nu}} \middle| \widehat{\boldsymbol{\mu}}^{\mathsf{nu}}(\mathbf{R}) \middle| \psi_f^{\mathsf{nu}} \right\rangle_{\mathsf{nu}} \right|^2$. On the other hand the first term of eq. (2.60) is

$$\left\langle \psi_i^{\mathsf{nu}}\phi_i^{\mathsf{el}} \middle| \widehat{\boldsymbol{\mu}}^{\mathsf{el}}(\mathbf{r}) \middle| \psi_f^{\mathsf{nu}}\phi_f^{\mathsf{el}} \right\rangle = \left\langle \psi_i^{\mathsf{nu}} \middle| \left\langle \phi_i^{\mathsf{el}};\mathbf{R} \middle| \widehat{\boldsymbol{\mu}}^{\mathsf{el}}(\mathbf{r}) \middle| \phi_f^{\mathsf{el}};\mathbf{R} \right\rangle_{\mathsf{el}} \middle| \psi_f^{\mathsf{nu}} \right\rangle_{\mathsf{nu}} = \left\langle \psi_i^{\mathsf{nu}} \middle| \widehat{\boldsymbol{\mu}}_{if}^{\mathsf{el}}(\mathbf{R}) \middle| \psi_f^{\mathsf{nu}} \right\rangle_{\mathsf{nu}} \tag{2.62}$$

where we defined $\widehat{\boldsymbol{\mu}}_{if}^{\mathsf{el}}(\mathbf{R})$ the electronic transition dipole moment (ETDM) between the initial and final electronic states. The probability of vibrational-electronic transitions (vibronic transitions) is evaluated by computing the expectation value of the ETDM with respect to the nuclear wavefunctions.

Let us consider the initial state is the electronic ground state of a given molecule, and the geometry $\mathbf{R} = \mathbf{R}_{\mathsf{eq}}$ of the molecule is the minimum of the electronic ground state. The ETDM can be expanded as a Taylor series along a set of nuclear coordinates corresponding to the normal modes ($\mathbf{Q}$ instead of $\mathbf{R}$) of the molecule (defined later on in section 2.4)

$$\boldsymbol{\mu}_{0f}^{\mathsf{el}}(\mathbf{Q}) = \boldsymbol{\mu}_{0f}^{\mathsf{el}}(\mathbf{Q}_{\mathsf{eq}}) + \sum_{i}^{3N-6} \left(\left. \frac{\partial \boldsymbol{\mu}_{0f}^{\mathsf{el}}}{\partial Q_i} \right|_{\mathsf{eq}} \right) (Q_i - Q_{i,\mathsf{eq}}) + \cdots \tag{2.63}$$

The zeroth order in eq. (2.63) leads to the *Condon approximation* [79, 80] when computing the ETDM toward an excited state and the associated vibronic spectrum. In particular, one can integrate the ETDM over the nuclear degrees of freedom and obtain within the so-called *Franck-Condon framework* [81]

$$\left\langle \psi_i^{\mathsf{nu}} \middle| \boldsymbol{\mu}_{if}^{\mathsf{el}}(\mathbf{R}) \middle| \psi_f^{\mathsf{nu}} \right\rangle_{\mathsf{nu}} \simeq \boldsymbol{\mu}_{0f}^{\mathsf{el}}(\mathbf{Q}_{\mathsf{eq}}) \left\langle \psi_0^{\mathsf{nu}} \middle| \psi_f^{\mathsf{nu}} \right\rangle_{\mathsf{nu}} . \tag{2.64}$$

Within an harmonic approximation for the nuclear wavefunctions, the squared overlaps $\left|\left\langle \psi_i^{\text{nu}} \middle| \psi_f^{\text{nu}} \right\rangle_{\text{nu}}\right|^2$ are known as the Franck-Condon factors and constitute the most straigthforward way of computing stationary vibronic spectra toward excited states in a time-independent framework [82, 83]. The first-order terms in eq. (2.63) are known as the Herzberg-Teller approximation of the ETDM and are necessary when the zeroth order is zero for symmetry-forbidden transition within the electronic states (also known as *intensity borrowing*). The previous approximations can be generalized with electronic excited states as initial states and electronic ground state as the final state for emission.

For our purposes, we will see that the ETDM can in general be approximated to the zeroth order. In particular when using diabatic electronic states and associated diabatic ETDM, their nuclear variations are assumed to be small at best or smooth at worst, with respect to the nuclear degrees of freedom.

Take-home messages

1. We apply the perturbative dipole approximation to take into account the interaction between the molecules and the electric field.
2. We use the Condon approximation (constant electronic transition dipole moments) to compute vibronic spectra within the Born-Oppenheimer approximation or when using diabatic electronic states.

2.4 The choice of coordinates

Until now, the coordinates of the nuclei were always given in the Cartesian laboratory-frame or were unspecified. Within the previous sections, the derivation (and in particular the nuclear-space derivatives) obtained for Cartesian coordinates are valid for any system of rectilinear coordinates. However, the results obtained are true for any system of coordinates. In this section, we briefly sum up the choices to be made for the coordinate system (**coords**) in molecular dynamics. Going back to nuclear wavepacket dynamics, the numerical implementations for eq. (2.22) strongly depend on the choice of the system of coordinates, as regards many aspects.

First, the ansatz for the wavepacket $\psi_\beta(\mathbf{coords}, t)$ can be adapted to the coordinates. For instance in wavepacket-based quantum dynamics, the wavepacket is expanded in a basis of primitive functions: Gauss-Hermite functions in the case of normal coordinates. On the other hand, in trajectory-based dynamics, the wavepacket is approximated by an ensemble of nuclear trajectories, for which the Cartesian coordinates are more natural. Next, the matrix of the nuclear kinetic energy operators, including the NACs (for the same electronic state or different ones), are also strongly determined by the choice of coordinates. In a molecular system, normal coordinates (associated to the normal modes of the equilibrium geometry of a given molecule) yield a simple diagonal, harmonic oscillator type for the kinetic energy operator, similarly to Cartesian coordinates. The kinetic energy operator is however more complicated for a polyspherical and curvilinear system of coordinates.

In addition, for grid-based quantum dynamics, the potential energies $H^{\text{el}}_{\alpha\alpha}(\textbf{coords})$ or $H^{\text{el}}_{\alpha\beta}(\textbf{coords})$ of the electronic Hamiltonian must be known. This part is strongly dependent on the phenomenon to be studied, and the choice of coordinates must allow for a correct description of the associated potential energy surfaces. For instance, for chemical reactivity (bond breaking), one expects strong anharmonic potential energies for which complicated system of coordinates can be really convenient. On the other hand, for phenomena involving only small nuclear displacements, the normal modes of vibration are expected to be relevant (for both kinetic energy and potential energy). Hence, for grid-based quantum dynamics, the choice of coordinates is in general a trade-off between simplicity for the kinetic energy operators or simplicity for the electronic state potential energies (similarly to the choice between adiabatic and diabatic representations). The more separable is the nuclear Hamiltonian representation (kinetic energy and potential energy parts in Hamiltonian), the more adapted the coordinates are for quantum dynamics (less correlation). As we will see later on, this is not a problem in this work because of the use of separable Hamiltonian models, with normal coordinates only.

We, hereafter, briefly describe the most common systems of coordinates, starting from the *Cartesian coordinates* to find *internal coordinates*, of interest for geometry optimization problems (minima, transition states). Next, we define *normal coordinates*, with a particular focus on the normal modes of vibrations, which we use in this work used for exploring PESs and for defining the nuclear wavepackets.

2.4.1 From Cartesian coordinates to internal coordinates

Suppose that we have a set of N nuclei having masses $\{M_1, \cdots, M_N\}$, for which the $3N$ Cartesian coordinates are collected in

$$\widetilde{\mathbf{R}} = \left(\underbrace{\widetilde{R}_{1x}, \widetilde{R}_{1y}, \widetilde{R}_{1z}}_{\widetilde{\mathbf{R}}_1}, \cdots, \underbrace{\widetilde{R}_{Nx}, \widetilde{R}_{Ny}, \widetilde{R}_{Nz}}_{\widetilde{\mathbf{R}}_N} \right)^{\mathsf{T}} \tag{2.65}$$

with respect to a Galilean laboratory-fixed frame (x, y, z) with fixed origin O (independent of the molecule). As the Coulomb molecular Hamiltonian is invariant by translation, one can always translate the coordinates of the nuclei so that the center of mass is superimposed with the origin of the coordinates, the so-called space-fixed frame (repeating the nuclei masses for x, y and z)

$$\widetilde{\mathbf{R}}_{\text{COM}} = \frac{\sum_A M_A \widetilde{\mathbf{R}}_A}{\sum_A M_A} \quad \text{and} \quad \mathbf{R} = \widetilde{\mathbf{R}} - \widetilde{\mathbf{R}}_{\text{COM}}. \tag{2.66}$$

From there, we define *mass-weighted* translation vectors; for the x-components

$$\widetilde{\mathbf{D}}_1 = \left(\sqrt{M_1}, 0, 0 \cdots \sqrt{M_N}, 0, 0 \right)^{\mathsf{T}} \tag{2.67}$$

and equivalently for the y- and z-components, in vectors $\widetilde{\mathbf{D}}_2$ and $\widetilde{\mathbf{D}}_3$, respectively. With the same idea, we define *mass-weighted* rotational vectors; for the rotation around x

$$\widetilde{\mathbf{D}}_4 = \begin{pmatrix} \left(G_{1y}O_{13} - G_{1z}O_{12}\right)\sqrt{M_1} \\ \left(G_{2y}O_{13} - G_{2z}O_{12}\right)\sqrt{M_2} \\ \vdots \\ \left(G_{Ny}O_{13} - G_{Nz}O_{12}\right)\sqrt{M_N} \end{pmatrix} \tag{2.68}$$

and equivalently for rotations around y and z in vectors $\widetilde{\mathbf{D}}_5$ and $\widetilde{\mathbf{D}}_6$, respectively, with $\mathbf{O}$ the matrix of eigenvectors (columns) of the inertia tensor

$$\mathbf{I} = \begin{bmatrix} I_{xx} & I_{xy} & I_{xz} \\ I_{yx} & I_{yy} & I_{yz} \\ I_{zx} & I_{zy} & I_{zz} \end{bmatrix} = \sum_A \begin{bmatrix} M_A\left(R_{Ay}^2 + R_{Az}^2\right) & -M_A\left(R_{Ax}R_{Ay}\right) & -M_A\left(R_{Ax}R_{Az}\right) \\ -M_A\left(R_{Ay}R_{Ax}\right) & M_A\left(R_{Ax}^2 + R_{Az}^2\right) & -M_A\left(R_{Ay}R_{Az}\right) \\ -M_A\left(R_{Az}R_{Ax}\right) & -M_A\left(R_{Az}R_{Ay}\right) & M_A\left(R_{Ax}^2 + R_{Ay}^2\right) \end{bmatrix}. \tag{2.69}$$

$\mathbf{O}$ defines the principal-axis frame for the molecular geometry, and $\mathbf{G}_A$ are the coordinates of nuclei A in this frame

$$\mathbf{G}_A = \mathbf{R}_A\mathbf{O}. \tag{2.70}$$

The vectors $\widetilde{\mathbf{D}}_{i=1\ldots6}$ define the mass-weighted translation and rotation vectors. If normalized they represent the so-called translational and rotational normal modes $\mathbf{D}_i$. This first separation of translational and rotational motions is often referred to as the definition of the Eckart frame, or the body-fixed frame, and provides the definition of Euler angles. In practice for a definition of internal coordinates or later on normal coordinates, the previous transformations are common. It is for instance the case for the vibrational analysis in the `Gaussian` package, where the six vectors previously defined are used to produce the remaining $N_{\text{vib}} = 3N-6$ vectors from a Schmidt orthogonalization, providing the tranformation matrix $\mathbf{D}$ from mass-weighted Cartesian coordinates (with the diagonal matrix of nuclear masses $\mathbf{M}$)

$$\mathbf{R}^{\text{mw}} = \mathbf{M}^{\frac{1}{2}}\mathbf{R} \tag{2.71}$$

to internal coordinates

$$\mathbf{s} = \mathbf{D}\mathbf{R}^{\text{mw}}. \tag{2.72}$$

These internal coordinates are not uniquely defined. In general, it is only an intermediate step either for the diagonalization of a Hessian matrix, yielding the normal modes of the molecule at the given geometry or for optimization steps in gradient-descent and quasi-Newton algorithms. In this work, we prefer the use of the singular-value decomposition for the determination of the internal coordinates instead of a Schmidt orthogonalization, only because of its simpler general implementation.

On a final note of this section, let us inspect the derivatives associated to mass-weighted coordinates for a function $f(\mathbf{R}^{\text{mw}})$ (for instance the energy)

$$\frac{\partial f}{\partial R_A^{\text{mw}}}(\mathbf{R}^{\text{mw}}) = \frac{1}{\sqrt{M_A}}\frac{\partial f}{\partial R_A}(\mathbf{R}) \tag{2.73}$$

where this can be shown using the chain rule for instance. It is then to be noted that in a mass-weighted Cartesian frame, coordinates are weighted with $\mathbf{M}^{1/2}$ while successive derivatives are weighted with $\mathbf{M}^{-1/2}$.

2.4.2 Introduction to normal coordinates

Although Cartesian coordinates are simple to use for having an unambiguous geometry of a molecule or for the derivation of general theorems in quantum chemistry and quantum dynamics, they are in general not adapted to practical studies. For instance in this work, we study vibrational motions from both time-independent and time-dependent perspectives. The natural system of coordinates for these are the normal coordinates, which are molecule-dependent and can be computed for each geometry of the molecule, based on the harmonic approximation for the nuclear displacements around an equilibrium geometry. Other studies, focused on chemical reactivity and bond breaking/bending might require more involved system of coordinates, such as Jacobi coordinates or poly-spherical coordinates. In other words, normal coordinates are well-suited for small amplitude motions, while large amplitude motions require more involved system of coordinates.

For the purpose of defining normal coordinates, let us suppose that the lower lying electronic state (electronic ground state) satisfies the Born-Oppenheimer approximation and is well-separated from any other electronic state, with potential energy $V(\mathbf{R})$. We assume that this potential has a minimum (set as the zero energy), and we choose a translation such that this minimum (the equilibrium geometry) is at $\mathbf{R}_{\text{eq}} = 0$. The potential can be expressed as a Taylor series of the displacements $\mathbf{X} = \mathbf{R} - \mathbf{R}_{\text{eq}}$

$$V(\mathbf{X}) = \frac{1}{2}\sum_{i=1}^{3N}\sum_{j=1}^{3N} \left.\frac{\partial^2 V}{\partial X_i \partial X_j}\right|_0 X_i X_j + \cdots \tag{2.74}$$

where i runs over all the coordinates ((x, y, z) for nucleus A), and where the gradient is zero because we expand the potential around an equilibrium geometry. Using mass-weighted displacements (similarly to mass-weighted Cartesian coordinates, $x_i = \sqrt{M_i} X_i$), the nuclear Hamiltonian takes the form

$$\widehat{H}(\mathbf{x}) = -\frac{\hbar^2}{2}\sum_{i=1}^{3N} \frac{\partial^2}{\partial x_i^2} + \frac{1}{2}\sum_{i=1}^{3N}\sum_{j=1}^{3N} \left.\frac{\partial^2 V}{\partial x_i \partial x_j}\right|_0 x_i x_j . \tag{2.75}$$

The mass in the kinetic energy term is now directly taken into account in the nuclear derivatives; on the other hand, the potential energy term is invariant under mass-weighting. As of now, the Hamiltonian is not separable with respect to the coordinates, because of cross-terms $x_i x_j$ in the potential energy term. The solution is thus to diagonalize the matrix (for i, j indices) of the nuclear second derivatives of the potential (that is, the Hessian matrix)

$$K_{ij} = \frac{\partial^2 V}{\partial x_i \partial x_j} \tag{2.76}$$

which has $3N$ eigenvalues and eigenvectors, k_i and $\mathbf{L}_i^{\text{mw}}$, that define the normal coordinates[4]

$$Q_i = \sum_{i}^{3N} L_{i,j}^{\text{mw}} x_j \tag{2.77}$$

---

[4] A training `jupyter-notebook` for vibrational analysis of equilibrium geometries is available online at `https://github.com/jwjgaliana/toolbox-qcqd/tree/main/fchk2NormalModes`.

where $\mathbf{L}^{\text{mw}}$ is an orthogonal matrix. We must stress here that the newly defined normal coordinates are still rectilinear coordinates, as they are obtained from linear combinations of Cartesian coordinates. The Hamiltonian representation within this set of coordinates is now separable

$$\widehat{H}(\mathbf{Q}) = -\frac{\hbar^2}{2}\sum_{i}^{3N}\frac{\partial^2}{\partial Q_i^2} + \frac{1}{2}\sum_{i}^{3N} k_i Q_i^2. \tag{2.78}$$

The normal-mode displacements and associated mass-weighted curvatures (k_i) define the vibrations and associated frequencies ($\omega_i = \sqrt{k_i}$, where the reduced mass is $\mu_i = 1$ when using mass-weighted coordinates) of the molecule for a given geometry. For this separable Hamiltonian, the vibrational eigenenergy depends on the vibrational numbers ν_i

$$E_{\text{vib}} = \sum_i E_{\nu_i} = \sum_i \hbar\omega_i\left(\nu_i + \frac{1}{2}\right) \tag{2.79}$$

with the associated zero-point energy

$$E_{\text{ZPE}} = \sum_i \frac{1}{2}\hbar\omega_i. \tag{2.80}$$

It is to be noted that normal coordinates are generally better defined by *a priori* transforming the Hessian to an internal coordinates basis set, so as to better separate translational/rotational modes from vibrational modes.[5] Let us stress that the normal modes of vibration obtained from a mass-weighted Hessian are not adapted to displacements in a non-mass-weighted Cartesian system of coordinates. In particular, in the rest of this work, we distinguish

- the normal modes of vibration: a rigorously orthonormal basis set (mass-weighted);
- the Cartesian displacements associated to normal modes of vibrations: a normalized (but nonorthogonal) set of vectors for which the coordinates have been "de-mass-weighted".

Unless otherwise specified, in the following, each time a projection is made on normal modes, it is on the normal modes of vibration; each time a displacement is made, it is from the Cartesian displacements.

Take-home messages

1. We make the choice of normal coordinates (adapted to the normal modes of vibration of a given molecule) for the rest of this work.
2. From the time-independent perspective, the normal modes of vibration are used to compute UV-visible spectra (vibronic properties) from computing the overlaps between vibrational wavefunctions of initial and final states.

---

[5] Translational and rotational modes have zero-valued eigenvalues, resulting in $3N-6$ or $3N-5$ non-zero eigenvalues in general or for linear molecules, respectively.

3. From the time-dependent perspective, the normal coordinates are used for the definition of practical primitive basis sets (Gauss-Hermite functions) for low-energy and small-amplitude motions.

2.5 Conical intersections and models of potential energy surfaces

In the rest of this chapter and unless otherwise specified, we now choose nuclear coordinates expressed in the system of normal coordinates. Thus, all previously defined quantities having nuclear dependence on $\mathbf{R}$ are now explicitly functions of the normal coordinates $\mathbf{Q}$. In particular, let us inspect the halved energy difference for the case of two adiabatic electronic states

$$\Delta V(\mathbf{Q}) = \frac{V_2(\mathbf{Q}) - V_1(\mathbf{Q})}{2} \geq 0 \tag{2.81}$$

and suppose there exists a geometry $\mathbf{Q}_\mathsf{X}$ for which

$$\Delta V(\mathbf{Q}_\mathsf{X}) = 0. \tag{2.82}$$

This geometry is called a conical intersection (CoIn) and is the focus of this section. We shall briefly describe the important features of CoIns from an adiabatic PESs point of view and illustrate that with plausible but simple diabatic models of PESs. Then, we will present the advances in finding CoIns and in particular a minimum-energy conical intersection (MECI). Finally, we will present the diabatic models we retain for diabatization by ansatz around conical intersections.

2.5.1 Conical intersections, adiabatic and diabatic representations

As we already stated before, CoIn geometries exhibit a singular character in the adiabatic electronic states, as the off-diagonal kinetic energy operator

$$\mathbf{F}^{\mathsf{ad}}_{12}(\mathbf{Q}) = \frac{\left\langle \phi^{\mathsf{ad}}_1; \mathbf{Q} \middle| \frac{\partial}{\partial \mathbf{Q}} \widehat{H}^{\mathsf{el}}(\mathbf{Q}) \middle| \phi^{\mathsf{ad}}_2; \mathbf{Q} \right\rangle}{V_2(\mathbf{Q}) - V_1(\mathbf{Q})} \tag{2.83}$$

which indeed diverges at the exact locus $\mathbf{Q}_\mathsf{X}$ of a CoIn. With the adiabatic representation, we define the Hellmann-Feynman gradient difference (GD) vector

$$\begin{aligned} \mathbf{g}^{\mathsf{ad}}(\mathbf{Q}) &= \frac{1}{2}\left(\left\langle \phi^{\mathsf{ad}}_2; \mathbf{Q} \middle| \frac{\partial}{\partial \mathbf{Q}} \widehat{H}^{\mathsf{el}}(\mathbf{Q}) \middle| \phi^{\mathsf{ad}}_2; \mathbf{Q} \right\rangle - \left\langle \phi^{\mathsf{ad}}_1; \mathbf{Q} \middle| \frac{\partial}{\partial \mathbf{Q}} \widehat{H}^{\mathsf{el}}(\mathbf{Q}) \middle| \phi^{\mathsf{ad}}_1; \mathbf{Q} \right\rangle \right) \\ &= \frac{1}{2}\left(\frac{\partial V_2}{\partial \mathbf{Q}} - \frac{\partial V_1}{\partial \mathbf{Q}} \right) = \frac{\partial}{\partial \mathbf{Q}}(\Delta V)(\mathbf{Q}) \end{aligned} \tag{2.84}$$

and the Hellmann-Feynman derivative coupling (DC) vector

$$\mathbf{h}^{\mathsf{ad}}(\mathbf{Q}) = \left\langle \phi^{\mathsf{ad}}_1; \mathbf{Q} \middle| \frac{\partial}{\partial \mathbf{Q}} \widehat{H}^{\mathsf{el}}(\mathbf{Q}) \middle| \phi^{\mathsf{ad}}_2; \mathbf{Q} \right\rangle = 2\Delta V(\mathbf{Q}) \mathbf{F}^{\mathsf{ad}}_{12}(\mathbf{Q}) \tag{2.85}$$

Let us suppose that we are at the exact CoIn geometry, $\Delta V(\mathbf{Q}_\mathsf{X}) = 0$. At this geometry, the given expression of the GD vector eq. (2.84) may be ill-defined because $\Delta V(\mathbf{Q})$ is no longer differentiable everywhere around $\mathbf{Q}_\mathsf{X}$. On the PESs, this can be understood by looking closely at the locus of the CoIn, where a double-cone cusp is found for the upper and lower surfaces. In the following, we further illustrate this using a toy model of diabatic Hamiltonian.

We reuse the "working" Hamiltonian and electronic states defined in section 2.2.2.1 and suppose it is a sufficiently diabatic representation

$$\mathbf{H}(\mathbf{Q}) = S(\mathbf{Q})\mathbb{1} + \begin{bmatrix} -D(\mathbf{Q}) & W(\mathbf{Q}) \\ W(\mathbf{Q}) & D(\mathbf{Q}) \end{bmatrix}. \tag{2.86}$$

The associated eigenvalues and energy difference are

$$V_{1,2}(\mathbf{Q}) = \Sigma(\mathbf{Q}) \pm \Delta V(\mathbf{Q}) = S(\mathbf{Q}) \pm \sqrt{D(\mathbf{Q})^2 + W(\mathbf{Q})^2} \tag{2.87a}$$

$$\Delta V(\mathbf{Q}) = \sqrt{D(\mathbf{Q})^2 + W(\mathbf{Q})^2}. \tag{2.87b}$$

At $\mathbf{Q} = \mathbf{Q}_\mathsf{X}$, to ensure $\Delta V(\mathbf{Q}_\mathsf{X}) = 0$, we must have

$$D(\mathbf{Q}_\mathsf{X}) = 0 \text{ and } W(\mathbf{Q}_\mathsf{X}) = 0 \tag{2.88}$$

Three main gradients are thus identified for the characterization of a CoIn. The gradient of the *tuning* D between the diabatic electronic states, which *tunes* the diabatic states so that their energies get closer. The gradient of the *coupling* W between the diabatic electronic states, which *couples* the diabatic states so that their characters get closer. And finally the gradient of the average energy S, which defines the *tilt* of the CoIn.

The energy difference ΔV can simply be seen as a function of the tuning and the coupling values, D and W respectively. In this case, we can have a first-order expansion of the energy difference in terms of D and W. Accordingly, the energy degeneracy is lifted linearly around the CoIn geometry when moving along the gradients of D and W (hence ultimately the coordinates $\mathbf{Q}$ that makes D and W change to first order). These two gradients form a 2-dimensional space in which the energy difference is lifted linearly from the CoIn geometry. This 2-dimensional space in the nuclear space is called the branching space or branching plane, and is spanned by two (non-uniquely defined) branching-space vectors. They correspond to the diabatic equivalent of the GD and DC vectors defined for the adiabatic electronic states. We stress again here that because the degeneracy is lifted along two directions only, there remain $3N-8$ dimensions in nuclear space for which the degeneracy is conserved. As a consequence, when one finds a conical intersection, it is not unique. This is the concept of the conical intersection seam, a $3N-8$ subspace in which conical intersections are linked together. Because there is no uniqueness of a conical intersection, one can always try to find the minimum-energy CoIn within a seam, like any other critical points in PES. This is the subject of the section section 2.5.2, on finding minimum-energy conical intersections (MECIs).

2.5.1.1 Evaluation of the branching-space vectors without the electronic states

Concerning the derivative coupling $\mathbf{h}^{\text{ad}}$ defined in eq. (2.85), although not directly ill-defined away from degeneracy points, it is not routinely obtained in all electronic structure methods. In particular, single-reference methods of evaluation of the electronic excited states, in our case the time-dependent density functional theory (chapter 4) exhibit two main problems. First, because it is based on the linear-response of the electronic ground state, it cannot describe adequatly a degeneracy between the electronic ground state and one electronic excited state. For this reason, in the following, we only present results regarding the degeneracy between electronic excited states; the electronic ground state is always supposed to be well-separated from the electronic excited states (and it is for the molecules studied here). Next, among the electronic excited states, the derivative coupling is never obtained exactly, as opposed to wavefunction methods where it can be evaluated from the derivatives of configuration interaction vectors and orbitals. Different strategies have been proposed (and benchmarked) for estimating and evaluating the DC vector and how to use its approximation for molecular dynamics, in particular for trajectory-based dynamics calculations [84]. In this work, we evaluate the DC vector using energy derivatives only, based on the proposition of Gonon and co-workers [85]. The idea is to reconstruct the branching-space vectors from the knowledge of the Hessian of the squared energy difference ΔV^2. Indeed, the squared energy difference is a regular function having a minimum at a CoIn geometry, and it is differentiable at the locus of a CoIn. Furthermore, because we know that $\Delta V = 0$ is lifted to first order around a CoIn through only two directions, the Hessian of $\Delta V^2 = 0$ must have two non-zero eigenvalues at a CoIn. Let us write the successive derivatives of the squared energy difference

$$\frac{\partial}{\partial Q_j}(\Delta V^2)(\mathbf{Q}) = 2\Delta V(\mathbf{Q}) \underbrace{\frac{\partial}{\partial Q_j}(\Delta V)(\mathbf{Q})}_{g_j^{\text{ad}}(\mathbf{Q})} = 2\Delta V(\mathbf{Q}) g_j^{\text{ad}}(\mathbf{Q}) \tag{2.89}$$

and

$$\frac{\partial^2}{\partial Q_i Q_j}(\Delta V^2)(\mathbf{Q}) = 2\Delta V(\mathbf{Q}) \frac{\partial^2}{\partial Q_i Q_j}(\Delta V)(\mathbf{Q}) + 2 g_i^{\text{ad}}(\mathbf{Q}) g_j^{\text{ad}}(\mathbf{Q}) \tag{2.90}$$

which can be rewritten in matrix-vector form, defining $\mathbf{K}_{\text{SED}}$ the Hessian matrix of the squared energy difference and dropping the coordinate dependence

$$\mathbf{K}_{\text{SED}} = \Delta V(\mathbf{K}_2 - \mathbf{K}_1) + 2\left(\mathbf{g}^{\text{ad}} \mathbf{g}^{\text{ad},\text{T}}\right), \tag{2.91}$$

where $\mathbf{K}_i$ is the Hessian for the adiabatic electronic state i at the CoIn. The first term is thus simply the difference in the adiabatic Hessians of the considered electronic excited states, times the halved energy difference. The second term is the dyadic product of the adiabatic halved gradient difference with itself. Diagonalizing $\mathbf{K}_{\text{SED}}$ yields some type of vibrational analysis of the squared difference energy. Far from a point of degeneracy, negative non-zero eigenvalues are found and correspond to directions along which the energy difference can be further minimized. Close to a point of degeneracy, two non-zero eigenvalues

$l_{1,2}$ should be found and the associated orthogonal eigenvectors $\mathbf{u}_{1,2}$ correspond, once scaled and up to a rotation, to the branching-space vectors. Indeed, by construction, these eigenvectors are orthonormal

$$\mathbf{u}_i \cdot \mathbf{u}_j = \delta_{ij} \tag{2.92}$$

and can be re-scaled

$$\mathbf{x}_i = \sqrt{\frac{l_i}{2}}\mathbf{u}_i. \tag{2.93}$$

so that they have the physical meaning of an energy gradient. At a CoIn geometry, the pair of vectors $(\mathbf{x}_1, \mathbf{x}_2)$ spans the same subspace as the branching-space vectors $(\mathbf{g}^{\text{ad}}, \mathbf{h}^{\text{ad}})$ and both pairs are thus related through a rotation.[6] We note that the Hessian of the squared energy difference can be written, at a CoIn geometry, as a dyadic sum of the branching-space vectors (spectral decomposition)

$$\mathbf{K}_{\text{SED}} = 2\left(\mathbf{x}_1\mathbf{x}_1^{\mathsf{T}} + \mathbf{x}_2\mathbf{x}_2^{\mathsf{T}}\right). \tag{2.94}$$

2.5.1.2 Visual inspection of conical intersections

Now, let us focus on illustrating the properties of the "working" diabatic Hamiltonian with a two-dimensional case of a given CoIn with a very simple expansion and toy-model

$$\begin{aligned} S(X,Y) &= \text{"tilt"} \times X + 3X^2 + 3Y^2 \\ D(X,Y) &= Y \\ W(X,Y) &= X. \end{aligned} \tag{2.95}$$

The average energy is harmonic, with equal curvatures ($= 6$ for the toy-model) for X and Y coordinates. The tilt parameter is turned on or off and prescribes the presence or not of a gradient for the average energy. The *tuning* is linear in Y and the *coupling* is linear in X. The locus of the CoIn is simply here $(X,Y) = 0$. The adiabatic and diabatic surfaces for these models (with zero tilt and with non-zero tilt) are given in fig. 2.1 with two different ranges for the (X,Y) plane.

Looking at the adiabatic surfaces for the zero-tilt case: the surfaces seem governed by the quadratic average energy far from $(X,Y) = 0$ (upper panel), but close to this point the surfaces happen to have a linear double-cone shape (lower panel). On the other hand, the diabatic surfaces are simple paraboloids in X and Y, with non-zero position for their minima. In this thesis, we mostly encounter two topologies of CoIns, characterized by symmetrical and asymmetrical double wells on the lowest potential energy surface. We illustrate it again with two-dimensional models, for a symmetrical double-well

$$\begin{aligned} S(X,Y) &= 3X^2 + 3Y^2 \\ D(X,Y) &= 2Y \\ W(X,Y) &= X \end{aligned} \tag{2.96}$$

---

[6] A training `jupyter-notebook` for implementing and manipulating a simple numerical branching-space is available online `https://github.com/jwjgaliana/toolbox-qcqd/tree/main/fchk2NumericalBranchingSpace`.

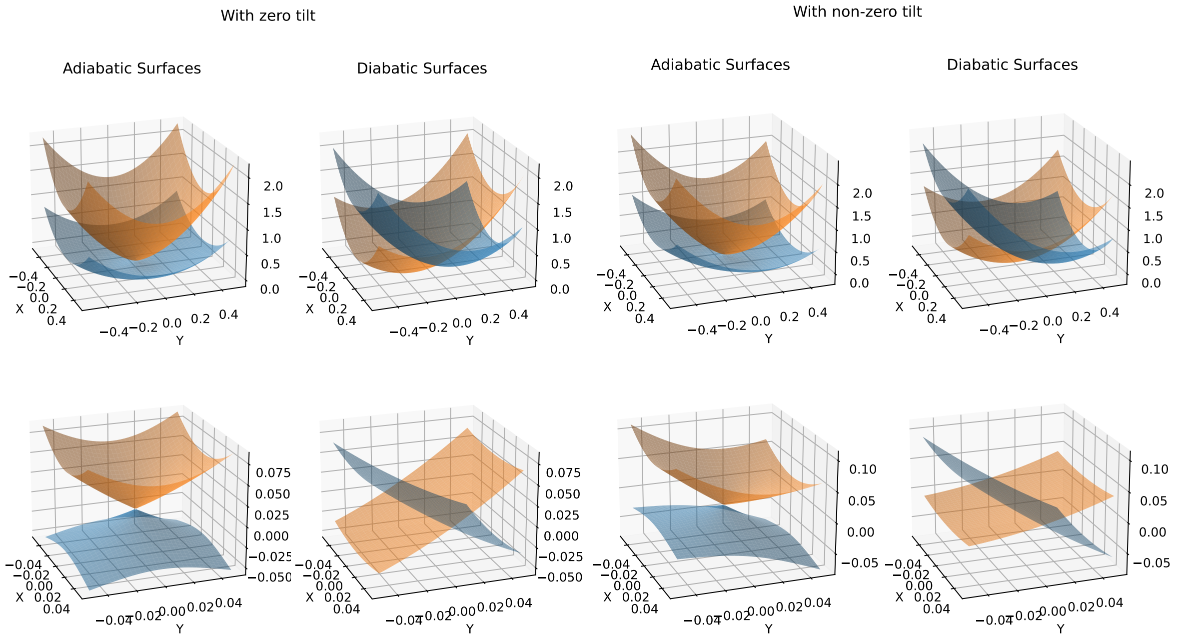

Figure 2.1: Adiabatic and diabatic potential energy surfaces for simple models of conical intersections, without (left) and with (right) tilt.

and for an asymmetrical double-well

$$\begin{aligned} S(X,Y) &= X + Y + 3X^2 + 3Y^2 \\ D(X,Y) &= X + 2Y \\ W(X,Y) &= Y \end{aligned} \tag{2.97}$$

The adiabatic and diabatic surfaces for these models (symmetrical and asymmetrical) are given in fig. 2.2 with, again, two different ranges fo the (X, Y) plane. On the left, the symmetrical double-well correspond to an anisotropic conical intersection (coupling on Y greater than tuning on X) with similar curvatures. On the right, the asymmetrical double-well corresponds to an example of tuning along both directions and coupling along one, with a tilt.

The accurate description of high-dimensional PESs of crossing electronic excited states around conical intersections is a challenging task and one of the main aspect of the present thesis. In the following, we briefly present strategies for finding the MECI for a given pair of electronic states and present the principal ideas of vibronic coupling Hamiltonian models for the diabatic states around CoIns.

2.5.2 Geometry optimization of MECI

Formally, the optimization of a MECI geometry between two electronic states can be seen as a constrained optimization of the average energy $S(\mathbf{R})$, under the constraint that the energy difference is zero. This boils down to

$$\min_{\Delta V(\mathbf{R}) \leq \epsilon} S(\mathbf{R}) \tag{2.98}$$

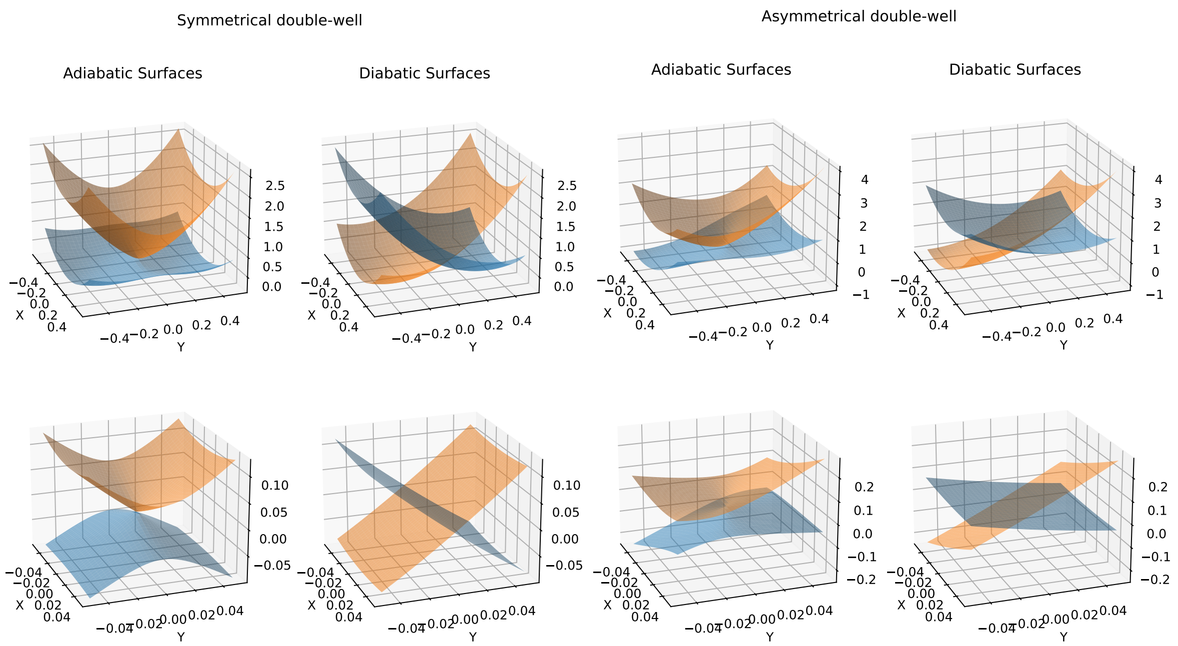

Figure 2.2: Adiabatic and diabatic potential energy surfaces for simple models of anisotropic conical intersections; symmetrical (left) and asymmetrical (right) double-well.

where ϵ is a convergence criterion for the energy difference. Depending on the algorithm chosen, the other optimization criteria will be the root mean square and maximum absolute value of the optimizing gradient and of the nuclear displacements. Historically, the first algorithms were proposed in 1993 by Manaa and Yarkony (with Lagrange multipliers) [86] and in 1994 by Bearpark, Robb and Schlegel (without Lagrange multiplier) [87]. During this work, we mostly used home-made implementations of a family of without-Lagrange-multiplier algorithms. These implementations are based on the propositions of the composed gradient (CG) and composed steps (CS) algorithms developed non-exhaustively by Bearpark, Sicilia, Ruiz-Barragan, and co-workers [87–89].

In the following, all quantities depend on the nuclear coordinates that we express in the Cartesian system of coordinates $\mathbf{R}$ and we drop this dependence for the sake of readability. Let us define the gradient average $\mathbf{s}$ for two electronic states, labeled a and b, as

$$\mathbf{s} = \frac{\partial}{\partial \mathbf{R}} S = \frac{\partial}{\partial \mathbf{R}} \left(\frac{V_a + V_b}{2} \right) = \frac{1}{2} \left(\frac{\partial V_a}{\partial \mathbf{R}} + \frac{\partial V_b}{\partial \mathbf{R}} \right) \tag{2.99}$$

and re-define

$$\mathbf{u}_1 = \frac{\mathbf{g}^{\text{ad}}}{||\mathbf{g}^{\text{ad}}||} \text{ and } \mathbf{u}_2 = \frac{\mathbf{h}^{\text{ad}}}{||\mathbf{h}^{\text{ad}}||} \tag{2.100}$$

the normalized branching-space vectors (BS vectors) for the considered electronic states. Because the BSVs are the vectors along which the degeneracy is lifted to first order, one strategy is to follow the negative of the gradient average (in order to decrease the energy average) but projected out of the BS, to stay in the intersection space (IS). This is done by defining the projector onto the BS

$$\mathbf{P}_{\text{BS}} = \mathbf{u}_1 \mathbf{u}_1^{\text{T}} + \mathbf{u}_2 \mathbf{u}_2^{\text{T}} \tag{2.101}$$

which holds if the BS vectors are defined such that $\mathbf{u}_1^{\mathsf{T}}\mathbf{u}_2 = 0$.[7] Similarly, we define the projector onto the intersection-space (IS), the complementary space to the branching-space

$$\mathbf{P}_{\mathsf{IS}} = \mathbb{1} - \mathbf{u}_1\mathbf{u}_1^{\mathsf{T}} - \mathbf{u}_2\mathbf{u}_2^{\mathsf{T}}. \tag{2.102}$$

We can now define the *gradient of the seam* which is the gradient of the average energy projected onto the intersection-space

$$\mathbf{g}_{\mathsf{IS}} = \mathbf{P}_{\mathsf{IS}}\mathbf{s} \tag{2.103}$$

Ideally, one can think of a gradient-descent algorithm (first-order) optimization algorithm that uses the gradient of the seam to optimize the energy average and to satisfy the constraint in energy difference. Two problems are encountered doing so. First, the raw gradient of the seam does not guarantee that the energy difference will be minimized. Indeed, the projection out of the branching space (if adequately described) only guarantees that the energy difference will not vary much. Thus, such an algorithm is bad for approaching the CoIn seam, because no effort on the gradient is dedicated to changing the energy difference. Second, due to the first-order character of the algorithm, the convergence might be very slow.

For the first problem of approaching the CoIn seam, one common strategy is to use as a gradient for the optimization a *composed gradient*, which is numerically relevant for optimizing both the energy difference and the energy average

$$\mathbf{g}_{\mathsf{CG}} = \mathbf{g}_{\mathsf{IS}} + \mathbf{f}(\mathbf{g}^{\mathsf{ad}}) \tag{2.104}$$

where the second term is a function of the gradient difference vector. Usually, this function is simply proportional to the direction of the gradient difference. Common choices are for instance

$$\mathbf{f}(\mathbf{g}^{\mathsf{ad}}) = 2\Delta V\mathbf{g}^{\mathsf{ad}} \tag{2.105a}$$

$$\text{or } = 2\alpha\Delta V\mathbf{g}^{\mathsf{ad}} \tag{2.105b}$$

$$\text{or } = 2\frac{\Delta V}{||\mathbf{g}^{\mathsf{ad}}||}\frac{\mathbf{g}^{\mathsf{ad}}}{||\mathbf{g}^{\mathsf{ad}}||} \tag{2.105c}$$

Historically, the first expression was proposed as it is the gradient of the (well-defined) squared energy difference ΔV^2. The second (with $\alpha \in \mathbb{R}^+$) and third expressions have been proposed because of their better convergence performance. In the following and unless otherwise specificied, we use the proposition eq. (2.105c) which is the best prediction for finding $\Delta V^2 \simeq 0$. With the composed gradient algorithm, the optimization step is a trade-off, through the value of ΔV, between

- following the gradient difference ($\mathbf{f}(\mathbf{g}^{\mathsf{ad}})$) when the energy difference is large;
- following the gradient of the seam ($\mathbf{g}_{\mathsf{IS}}$) when the energy difference is small

although the gradient used for computing the displacements from one geometry to the next is unique.

---

[7] Let us note here that for two column vectors $\mathbf{u}$ and $\mathbf{v}$, we write their dyadic product $\mathbf{u}\mathbf{v}^{\mathsf{T}}$ and their scalar product $\mathbf{u}^{\mathsf{T}}\mathbf{v}$.

For the second problem, the usually implemented extension of the gradient-descent is the Newton-Raphson (NR) search, which is a second-order search. For an objective function $\mathrm{E}(\mathbf{R})$ to be minimized associated to the gradient $\mathbf{g}_{\mathsf{CG}}$, we use a second-order Taylor expansion

$$\mathrm{E}(\mathbf{R}+\Delta\mathbf{R}) = \mathrm{E}(\mathbf{R}) + \mathbf{g}_{\mathsf{CG}}^{\mathsf{T}}\Delta\mathbf{R} + \frac{1}{2}\Delta\mathbf{R}^{\mathsf{T}}\mathbf{K}\Delta\mathbf{R} \tag{2.106}$$

where $\mathbf{K}$ is the Hessian of the objective function and $\Delta\mathbf{R}$ is the coordinates change between two consecutive optimization steps. In particular, if a minimum is seeked, the gradient of the objective function (expanded to first-order) is seeked to be zero

$$0 = \mathbf{g}_{\mathsf{CG}}(\mathbf{R}+\Delta\mathbf{R}) = \mathbf{g}_{\mathsf{CG}}(\mathbf{R}) + \mathbf{K}\Delta\mathbf{R} \tag{2.107}$$

so that the NR predicted change in coordinates is

$$\Delta\mathbf{R}^{\mathsf{NR}} = -\mathbf{K}^{-1}\mathbf{g}_{\mathsf{CG}}. \tag{2.108}$$

In practice, in optimization algorithms (and in particular in quantum chemistry), the Hessian is rarely known at each step of the optimization. It is rather updated from gradient information. In the case of geometry optimization, the iterative scheme of Broyden-Fletcher-Goldfarb-Shanno (BFGS) is often used [90]. It consists in the calculation of an approximate Hessian $\mathbf{W}^{(n+1)}$ at step $n+1$ knowing the approximate Hessian $\mathbf{W}^{(n)}$ at step n and the change in gradients $\Delta\mathbf{g}_{\mathsf{CG}} = \mathbf{g}_{\mathsf{CG}}^{(n+1)} - \mathbf{g}_{\mathsf{CG}}^{(n)}$ and coordinates $\Delta\mathbf{R} = \Delta\mathbf{R}^{(n+1)} - \Delta\mathbf{R}^{(n)}$ from step n to step $n+1$. The BFGS Hessian update reads

$$\mathbf{W}^{(n+1)} = \mathbf{W}^{(n)} + \frac{\Delta\mathbf{g}\Delta\mathbf{g}^{\mathsf{T}}}{\Delta\mathbf{g}^{\mathsf{T}}\Delta\mathbf{R}} - \frac{\mathbf{W}^{(n)}\Delta\mathbf{R}\Delta\mathbf{R}^{\mathsf{T}}\mathbf{W}^{(n),\mathsf{T}}}{\Delta\mathbf{R}^{\mathsf{T}}\mathbf{W}^{(n)}\Delta\mathbf{R}}. \tag{2.109}$$

The advantages of an Hessian update such as the BFGS scheme is twofold. First, the updated Hessian is always invertible, by construction, if the initial Hessian is. Indeed, it is recursively built from a matrix that is invertible and two dyad products which are invertible. Second, the updated Hessian allows us to have a second-order algorithm without computing the Hessian at each step, which is computationally expensive in electronic structure methods. With the use of an approximate Hessian instead of an exact Hessian, the NR search eq. (2.108) is rather called a quasi-Newton search

$$\Delta\mathbf{R}^{\mathsf{QN},(n+1)} = -\left(\mathbf{W}^{(n+1)}\right)^{-1}\mathbf{g}_{\mathsf{CG}}^{(n+1)}. \tag{2.110}$$

In general, the second-order expansion and the use of an approximate Hessian are valid only in a certain region around the current geometry. The change in coordinates $\Delta\mathbf{R}$ is thus estimated by minimizing the model of the objective function under a size constraint

$$\min_{||\Delta\mathbf{R}||\leq\tau} E(\mathbf{R}+\Delta\mathbf{R}) \tag{2.111}$$

Finally, we mention that we tried a recently imagined Lagrange-multiplier algorithm, which avoids the knowledge of the derivative coupling, proposed by Joubert-Doriel and co-workers [91]. We give more details about it in appendix A.

2.5.3 Vibronic coupling Hamiltonian models around conical intersections

As we have seen, in the presence of CoIns (MECI or not), the adiabatic representation for the electronic states is not convenient because of the ill-defined kinetic energy operator. For quantum dynamics simulations, it is then necessary to work with a different basis set of the electronic states, which we will call a diabatic basis set $\{\phi_\alpha^{\text{dia}}(\mathbf{Q})\}$ (see above) in the following. The matrix representation of the electronic Hamiltonian is full (but symmetric) in the previous basis of n electronic states

$$\mathbf{H}^{\text{dia}}(\mathbf{Q}) = \begin{bmatrix} H_{11}(\mathbf{Q}) & H_{12}(\mathbf{Q}) & \cdots & H_{1n}(\mathbf{Q}) \\ H_{21}(\mathbf{Q}) & \ddots & & \vdots \\ \vdots & & \ddots & \vdots \\ H_{n1}(\mathbf{Q}) & \cdots & \cdots & H_{nn}(\mathbf{Q}) \end{bmatrix} \tag{2.112}$$

where all the matrix elements are assumed to be smoothly varying with the nuclear coordinates (here normal mode coordinates). First, without any assumption on the nature of the diabatic states, the diabatic Hamiltonian elements can be expanded as Taylor series around a reference point. A convenient choice for this reference is the minimum of the electronic ground state (the Franck-Condon point, FC point), definining $\mathbf{Q} = 0$ with $\mathbf{Q}$ the normal coordinates associated to the N equilibrium normal modes i (reference harmonic approximation). Doing so we have

$$H_{\alpha\alpha}(\mathbf{Q}) = \sum_{i=1}^{N} \frac{1}{2} k_i^{(0)} Q_i^2 + E^{(\alpha)} + \sum_{i=1}^{N} \kappa_i^{(\alpha)} Q_i + \sum_{i=1}^{N}\sum_{j=1}^{N} \frac{1}{2} \gamma_{ij}^{(\alpha)} Q_i Q_j + \cdots \tag{2.113a}$$

$$H_{\alpha\beta}(\mathbf{Q}) = W^{(\alpha,\beta)} + \sum_{i=1}^{N} \lambda_i^{(\alpha,\beta)} Q_i + \sum_{i=1}^{N}\sum_{j=1}^{N} \frac{1}{2} \mu_{ij}^{(\alpha,\beta)} Q_i Q_j + \cdots \tag{2.113b}$$

The zeroth- and first-order parameters correspond to a diabatic version of

- the vertical transition energy, $E^{(\alpha)}$ for state α;
- the vertical energy gradient, $\boldsymbol{\kappa}^{(\alpha)}$ for state α;

and

- the constant coupling $W^{(\alpha,\beta)}$ between states α and β;
- the inter-state coupling gradient $\boldsymbol{\lambda}^{(\alpha,\beta)}$ between states α and β.

Let us note here that the constant coupling is in general nullyfied by building diabatic electronic states that coincide/match with the adiabatic electronic states at the reference point (typically the minimum of the electronic ground state).

The quadratic diagonal terms $\mathbf{k}^{(\alpha)} = \mathbf{k}^{(0)} + \boldsymbol{\gamma}^{(\alpha,\alpha)}$ have a particular role in the expansion as they are necessary for the harmonic approximation for the excited states PES. Indeed, with this framework of normal coordinates, the kinetic energy operator and the diagonal quadratic terms define the harmonic oscillators for each normal mode. The first-order diagonal terms allow us to take into account the shift between the harmonic oscillator of the reference state and of the other diabatic states. Using only the harmonic approximation and the first-order terms in the Taylor expansion consists in the linear vibronic coupling (LVC) Hamiltonian model. Strictly speaking however, the LVC Hamiltonian uses the same curvatures for the reference state and the other diabatic states ($\mathbf{k}^{(\alpha)} = \mathbf{k}^{(0)}$).

On the other hand, the bilinear diagonal terms $\boldsymbol{\gamma}$ and $\boldsymbol{\mu}$ allow us to take into account the *primary* Duschinsky effect between the normal modes. This is the usual mode mixing of the ground state equilibrium normal modes, to describe the excited state equilibrium normal modes. The bilinear off-diagonal terms describe a *secondary* Duschinsky effect, which is caused by the non-negligible vibronic coupling. Including these bilinear terms yield the quadratic vibronic coupling (QVC) Hamiltonian model.

The vibronic coupling Hamiltonian (VCH) models given in eq. (2.113) serve as parametrized surrogate models for diabatization by ansatz [20, 77]. We thus stress again here that this diabatization scheme does not yield the diabatic electronic states, but only diabatize the potential energy surfaces. The most popular usage of the VCH models is to fit the different parameters on *ab initio* electronic structure calculations of the adiabatic electronic states. The aim is to find reliable VCH parameters to reproduce the (ill-defined around CoIns) adiabatic PESs, and using the underlying (smooth) diabatic PES models for the quantum dynamics calculation. Another strategy relies not on fitting the VCH parameters but on identifying them locally to adiabatic energy gradients or adiabatic Hessians, for instance. Both strategy will be used in this work.

For now, the parameters are non-necessarily zero for all the normal modes of the system of interest. When electronic diabatic states can be associated to irreducible representations (for molecular geometries having symmetry), normal modes have specific parameters according to their associated irreducible representations and those of the electronic states. We illustrate this with the case of two electronic states in the following section.

2.5.3.1 Two-state case, with symmetry-adapted electronic states

We consider a molecular geometry that is optimized in the electronic ground state, and assume that it belongs to a given non-trivial Abelian symmetry point group (for instance $\mathrm{C_{2v}}$). The adiabatic excited states at this geometry thus belong to irreducible representations (IRs, for instance $\mathrm{A_1}$ or $\mathrm{B_2}$). The equilibrium normal modes are also labelled with respect to IRs. Let us assume that adiabatic states ($\mathrm{S_a}$ and $\mathrm{S_b}$) are close in energy and strongly coupled, with different IRs

$$\Gamma_a^{\mathrm{ad}} \neq \Gamma_b^{\mathrm{ad}}. \tag{2.114}$$

A VCH model can be derived for describing this pair of coupled adiabatic excited states. In particular, a symmetry-adapted basis of diabatic states can be chosen as underlying states of the VCH model, with IRs

$$\Gamma_a^{\mathrm{dia}} = \Gamma_a^{\mathrm{ad}} \quad \text{and} \quad \Gamma_b^{\mathrm{dia}} = \Gamma_b^{\mathrm{ad}}. \tag{2.115}$$

At the origin (reference or equilibrium geometry), the diabatic energy gradients must be totally symmetric, hence they must have non-zero components only along normal modes of the totally-symmetric IR Γ_{TS}. In the same way, the diabatic inter-state coupling gradient must have non-zero components along the normal modes satisfying

$$\Gamma_a^{\mathsf{dia}} \otimes \Gamma_{\mathsf{NM}_i} \otimes \Gamma_b^{\mathsf{dia}} \supset \Gamma_{\mathsf{TS}}. \tag{2.116}$$

Because the symmetry point group is assumed Abelian, the IR for the normal modes satisfies $\Gamma_{\mathsf{NM}} = \Gamma_a \otimes \Gamma_b$. For instance, within the Abelian symmetry point-group C_{2v} and with two adiabatic electronic states of IRs A_1 and B_2:

- the diabatic energy gradients are expanded along the normal modes of symmetry A_1;
- the diabatic inter-state coupling gradient are expanded along the normal modes of symmetry B_2.

It can be further generalized for second-order bilinear terms, with products of same IRs modes for γ parameters and products of A_1 and B_2 modes for μ parameters. Prototypical examples on the pyrazine or butatriene cations can be found in Ref [78, 92]. A similar model will be used in chapters 5 and 7 of this work. We stress that although the symmetry-adapted diabatic states are a natural choice for the diabatic states, one can always use a rotation of the diabatic basis set, associated to a change of the Hamiltonian representation.

2.5.3.2 Two-state case, without symmetry-adapted electronic states

As opposed to the previous case, we now consider

$$\Gamma_a^{\mathsf{ad}} = \Gamma_b^{\mathsf{ad}}. \tag{2.117}$$

In this case, both the diabatic energy gradients and inter-state coupling gradient have non-zero components along the same totally-symmetric normal modes. For instance, within the symmetry point-group C_S and with two adiabatic electronic states beloging to A', all the normal modes belonging to A' contribute to the diagonal and off-diagonal parameters of the VCH model. In this case, a systematic strategy is to express the Hamiltonian using the gradient average $\mathbf{s}$, the gradient difference $\mathbf{g}$ and the inter-state coupling $\mathbf{h}$ vectors components

$$H^{\mathsf{dia}}(\mathbf{Q}) = \begin{bmatrix} E^{(a)} & 0 \\ 0 & E^{(b)} \end{bmatrix} + \sum_i \left(s_i Q_i \mathbb{1} + \begin{bmatrix} -g_i Q_i & h_i Q_i \\ h_i Q_i & g_i Q_i \end{bmatrix} + \frac{1}{2} \begin{bmatrix} k_i^{(a)} Q_i^2 & 0 \\ 0 & k_i^{(b)} Q_i^2 \end{bmatrix} \right) \tag{2.118}$$

which is reminiscent of a LVC model with different curvatures for the two diabatic states. Compared to the case with symmetry, the parameters of the branching plane can be associated to a pair of branching-space vectors determined from the adiabatic electronic states at the reference point. Again, any rotation of these branching-space vectors or of the underlying diabatic states is valid, so that some choice is required here. A similar strategy has been used in [93] and will be applied in chapter 6 of this work.

Take-home messages

1. Conical intersections are molecular geometries at which at two least adiabatic electronic states are degenerate. They are characterized by an intersection space (seam of degeneracy) and a branching space (spanned by two vectors, the branching-space vectors).
2. The branching-space vectors are linked to the Hellmann-Feynman gradient difference and derivative coupling vectors (hence to the nonadiabatic couplings).
3. They can be evaluated numerically using only the nuclear derivatives of the energy of the two considered states.
4. Minimum-energy conical intersections can be found by using constrained optimization of the mean energy; algorithms that do not require explicitly the nonadiabatic couplings have been implemented.
5. Vibronic coupling Hamiltonian models can be used to describe the potential energy surfaces around conical intersection, and serve as ansätze for diabatization procedures.

Chapter 3

Quantum Dynamics and Variational Equations of Motion

In this chapter, we discuss the solutions of the time-dependent Schrödinger equation in the context of the propagation of multi-dimensional molecular wavepackets. In particular, we focus on the use of the multiconfiguration time-dependent Hartree (MCTDH) method, and present the main aspects of its usage. This presentation is strongly inspired from the first review on the MCTDH formalism, Ref [94] (for physical and numerical details) and on the textbook *Applications of Quantum Dynamics in Chemistry*, Ref [95]. Unless otherwise specified, all quantum dynamics calculations presented in this work are run with the MCTDH implementation of the `Quantics` package [96].

3.1 Time-dependent Schrödinger equation and variational principle

The time-dependent Schrödinger equation reads

$$i\hbar \frac{\partial}{\partial t}\Psi(\mathbf{Q},t) = \widehat{H}\Psi(\mathbf{Q},t), \tag{3.1}$$

where $\Psi(\mathbf{Q},t)$ is the time-dependent wavefunction (*i.e.* wavepacket) describing the quantum state of interest, with $\mathbf{Q}$ the dynamical degrees of freedom, and $\widehat{H}$ is the Hamiltonian of the system (here time-independent). For the rest of this chapter, let us consider $\hbar = 1$ for the sake of simplicity (which boils down to the use of adimensional physical quantities and atomic units in particular). The aim of this chapter is the discussion of the differential equation eq. (3.1) from mathematical and numerical perspectives. Detailed discussions of the Hamiltonian and its representations, and of the coordinates, as well as their physical meaning were the subject of chapter 2.

Equation (3.1) does not have analytical solutions for systems of many particles in general. The aim of quantum dynamics (QD) is thus to solve (or propagate) the time-dependent Schrödinger equation (TDSE) eq. (3.1), with various strategies and approximations. In this section, we focus on solving the TDSE eq. (3.1) without using mixed quantum-classical approximations, that is by entirely treating all the degrees of freedom (electronic and nuclear) as quantum degrees of freedom. Thus, for now, the degrees of freedom in $\mathbf{Q}$ are unspecified as regards their nuclear or electronic character. To numerically solve the problem of variationally propagating an approximate wavefunction in time, one requires two main pre-requisites:

- an approximate ansatz for the wavefunction $\Psi(\mathbf{Q},t)$;
- a time-dependent variational principle,

which will result in optimal approximate solutions of the TDSE.

In this chapter, we first present the variational principle for solving the time-dependent Schrödinger equation and then define the three most common ansätze for the wavefunction. Next, we discuss the equations of motion emerging from these definitions, with a focus on the MCTDH equations of motion. Finally, we give an overview of the extensions of MCTDH, in particular for including a large number of degrees of freedom.

3.1.1 The time-dependent variational principle

Without loss of generality, let us define the functional $|\Psi(t)\rangle = |\Psi[\lambda(t)]\rangle$, as a given ansatz for the multi-dimensional wavepacket, with complex-valued variational parameters $\lambda(t)$. The simplest expression of a time-dependent variational principle (TDVP) is the Dirac-Frenkel variational principle (DFVP),

$$\left\langle \delta\Psi \middle| \widehat{H} - i\frac{\partial}{\partial t} \middle| \Psi \right\rangle = 0. \tag{3.2}$$

Here, $\delta\Psi$ represents the mathematical extension of the differential variation to a functional and is determined by the infinitesimal changes in the variational parameters, $\delta\lambda(t)$. Given a functional form (an ansatz) of $\Psi(t)$ as $\Psi[\lambda(t)]$ and from the condition assumed in eq. (3.2), one is able to produce the equations of motion related to the variational parameters of $\Psi(t)$, $\lambda(t)$, that is, an expression for $\frac{\partial\lambda}{\partial t}(t)$ (ordinary differential equations for $\lambda(t)$). The ansatz $|\Psi[\lambda(t)]\rangle$ will be optimized (satisfying the time-dependent variational principle) to be the best approximation of the exact wavefunction (which satisfies the exact time-dependent Schrödinger equation). The TDVP is further discussed in section 3.4.1.

3.1.2 The choice of the ansatz for numerical calculations

We now have to define the functional form of the ansatz for the time-dependent wavefunction. In the following, unless otherwise specified, we define

- f the number of dynamical degrees of freedom, such that $\mathbf{Q} = (Q_1, \cdots, Q_\kappa, \cdots, Q_f)$;
- $i_\kappa = 1, \cdots, N_\kappa$ the index of the (orthonormal) so-called primivite basis functions $\chi_{i_\kappa}^{(\kappa)}(Q_\kappa)$ for the degree of freedom (DOF) κ. In this work, the primitive basis functions are Gauss-Hermite functions, solutions of the one-dimensional quantum harmonic oscillator (other choices are possible).
- $j_\kappa = 1, \cdots, n_\kappa$ the index of single-particle functions (SPFs) that we define below.

Time-dependent Hartree and standard method

The time-dependent Hartree (TDH) ansatz is a simple Hartree product with a time-dependent complex pre-factor

$$\Psi^{\mathsf{TDH}}(Q_1, \cdots, Q_f, t) = a(t) \prod_{\kappa=1}^{f} \varphi^{(\kappa)}(Q_\kappa, t), \tag{3.3}$$

where we define the time-dependent single-particle functions (SPFs)

$$\varphi^{(\kappa)}(Q_\kappa, t) = \sum_{i_\kappa=1}^{N_\kappa} B_{i_\kappa}^{(\kappa)}(t)\chi_{i_\kappa}^{(\kappa)}(Q_\kappa). \tag{3.4}$$

For each degree of freedom, we define a single SPF which is a time-dependent linear combination of the primitive basis functions associated to the considered degree of freedom. Both the pre-factor and the SPFs are time-dependent ($a(t)$ and $B_{i_\kappa}^{(\kappa)}(t)$). The analogous method in quantum chemistry problems is the time-dependent Hartree-Fock (TDHF) method, for which the wavefunction is antisymmetric instead of a simple Hartree product. The roles of SPFs and primitive basis functions are then similar to the roles of molecular orbitals and atomic orbitals, respectively.

On the other hand, the "standard method" (SM) ansatz is a sum-of-product expansion of the wavefunction

$$\Psi^{\mathsf{SM}}(Q_1, \cdots, Q_f, t) = \sum_{i_1=1}^{N_1} \sum_{i_2=1}^{N_2} \cdots \sum_{i_f=1}^{N_f} C_{i_1 i_2 \cdots i_f}(t) \prod_{\kappa=1}^{f} \chi_{i_\kappa}^{(\kappa)}(Q_\kappa), \tag{3.5}$$

where the $\chi_{i_\kappa}^{(\kappa)}(Q_\kappa)$ is is the i_κ^{th} primitive basis functions for the degree of freedom κ. If the primitive basis set is complete, the results are numerically exact (same as *full configuration interaction* in electronic structure theory). There are no SPFs, but we consider a linear combination (defined with the $C_{i_1 i_2 \cdots i_f}(t)$, or $\mathbf{C}$ tensor) of all the configurations generated from the primitive basis functions. Only the $\mathbf{C}$ tensor is time-dependent, but its size is the very limit of the "standard method", as it depends directly on the number of degrees of freedom and the size of the primitive basis (scaling in N^f if $N_\kappa = N \quad \forall \kappa$). This exponential scaling is often referred to as the *curse of dimensionality*. To overcome this problem, one solution is to build an ansatz that benefits from both the TDH and the SM strategies: a multiconfiguration ansatz with an efficient contraction of the associated configuration tensor $\mathbf{C}$. Other solutions may be found by *optimizing* basis functions to use smaller basis sets or in pruning the ansatz (non-direct-product basis set or selected configurations) [97–99].

Multiconfiguration time-dependent Hartree

The multiconfiguration time-dependent Hartree (MCTDH) ansatz is also a sum-of-product expansion

$$\Psi^{\mathsf{MCTDH}}(Q_1, \cdots, Q_f, t) = \sum_{j_1=1}^{n_1} \sum_{j_2=1}^{n_2} \cdots \sum_{j_f=1}^{n_f} A_{j_1 j_2 \cdots j_f}(t) \prod_{\kappa=1}^{f} \varphi_{j_\kappa}^{(\kappa)}(Q_\kappa, t), \tag{3.6}$$

where we now define different sets of single-particle functions (with indices $j_\kappa = 1, \cdots, n_\kappa$) as

$$\varphi_{j_\kappa}^{(\kappa)}(Q_\kappa, t) = \sum_{i_\kappa}^{N_\kappa} B_{i_\kappa}^{(\kappa, j_\kappa)}(t) \chi_{i_\kappa}^{(\kappa)}(Q_\kappa). \tag{3.7}$$

By setting $n_1 = n_2 = \cdots = n_f = 1$ from the MCTDH ansatz, we retrieve the TDH ansatz (allowing only one TDH configuration, *i.e* one Hartree product). Compared with TDH, the tensor $\mathbf{A}(t)$ is a generalization of the pre-factor $a(t)$, and is stored numerically as a vector, generally called A-*vector* in the following. While TDH is the time-dependent version of the self-consistent field algorithm, MCTDH is a time-dependent version of multiconfiguration self-consistent field (MCSCF) methods in quantum chemistry. By setting $n_\kappa = N_\kappa$ from the MCTDH ansatz, we retrieve the "standard method" ansatz and only have a unitary transformation between the primitive basis set and the SPFs basis set. This unitary transformation is physically irrelevant and can be fixed, such that in the case $n_\kappa = N_\kappa$, the SPFs basis is time-independent and similar to the primitive basis. The advantage of MCTDH is of course to take a SPFs basis set smaller than the primitive basis set, leading to fewer equations of motion and a smaller coefficient tensor.

For the sake of readability, let us introduce the compact notations

$$\begin{aligned} \mathbf{J} &= (j_1, \cdots, j_f) && \text{composite indices} \\ \mathbf{A}_\mathbf{J} &= A_{j_1 \cdots j_f} && \text{corresponding } A\text{-vector} \\ \Phi_\mathbf{J} &= \prod_{\kappa=1}^{f} \varphi_{j_\kappa}^{(\kappa)} && \text{configuration (Hartree product).} \end{aligned} \tag{3.8}$$

The MCTDH ansatz now reads

$$\Psi^{\mathsf{MCTDH}}(Q_1, \cdots, Q_f, t) = \sum_\mathbf{J} \mathbf{A}_\mathbf{J}(t) \Phi_\mathbf{J}(Q_1, \cdots, Q_f, t), \tag{3.9}$$

where the multiconfiguration character of the ansatz is made clearer.

Until now, the electronic degrees of freedom are implicit. In particular, eq. (3.9) is implicitly given for the propagation of the wavepacket on a single electronic state. If several electronic states (denoted with the kets $|\alpha\rangle$) are considered, the MCTDH ansatz is

$$\left|\Psi^{\mathsf{single}}(Q_1, \cdots, Q_f, t)\right\rangle = \sum_\alpha \sum_\mathbf{J} \mathbf{A}_{\mathbf{J}\alpha}(t) \Phi_\mathbf{J}(Q_1, \cdots, Q_f, t) \, |\alpha\rangle \tag{3.10}$$

where the A-vector is now also indexed with the electronic degrees of freedom α. This simple extension is called the single-set formalism; the SPFs sets are uniquely defined for all the electronic states (and thus not indexed with α). On the other hand, indexing the SPFs sets with α yields the multi-set formalism, for which different SPFs sets are defined for each electronic states

$$\left|\Psi^{\mathsf{multi}}(Q_1, \cdots, Q_f, t)\right\rangle = \sum_\alpha \sum_{\mathbf{J}^\alpha} \mathbf{A}_{\mathbf{J}^\alpha}(t) \Phi_\mathbf{J}^{(\alpha)}(Q_1, \cdots, Q_f, t) \, |\alpha\rangle \tag{3.11}$$

where the indices $\mathbf{J}^\alpha$ are indexed with α, but not directly the A-vector. In general, the multi-set formalism is better suited for the propagation of wavepackets on electronic states with very different potential energies. Both formalisms will be used in this work but for the sake of simplicity, in this chapter we discuss the MCTDH method within the single-set formalism, eq. (3.9), only.

Take-home messages

1. The time-dependent variational principle is given for an unspecified ansatz.
2. Three ansätze are defined, for the "standard method", the time-dependent Hartree (TDH), and the multiconfiguration time-dependent Hartree (MCTDH) formalisms.
3. For the MCTDH ansatz, compact notations are defined and both single-set and multi-set formalisms are explicited.

3.2 Derivation of the equations of motion

In this section, we derive the variational equations of motion for the TDH ansatz Then, we give the analogous equations of motion for the MCTDH ansatz and discuss them. We choose to derive only the TDH ansatz as being more straightforward than for MCTDH but similar in essence. In the following and for the sake of readability, we discard the coordinate dependence on dynamical degrees of freedom $\mathbf{Q}$ in the notations.

3.2.1 Derivation for the TDH ansatz

For the derivation of the equations of motion, we need the definition of the TDH ansatz, eq. (3.3), and the Dirac-Frenkel variational principle, eq. (3.2). Because of the product-form of the ansatz, there is not a unique definition of $\Psi(t)$. Indeed, a phase factor can be attributed either to a SPF Hartree product or to the pre-factor, and compensated in the other terms[1]. We thus impose constraints separetely on each SPF

$$i \left\langle \varphi^{(\kappa)}(t) \,\middle|\, \dot{\varphi}^{(\kappa)}(t) \right\rangle = g_\kappa(t) \tag{3.12}$$

where the functions g_κ must be real-valued for the norms of the SPFs to stay constant.[2] From now on, we shall assume $g_\kappa(t) \in \mathbb{R}$ and $\left\langle \varphi^{(\kappa)}(0) \,\middle|\, \varphi^{(\kappa)}(0) \right\rangle = 1$ such that $\langle \Phi(t) \,|\, \Phi(t) \rangle = 1$. We will see at the end of the derivation that straighforward choices can be made for g_κ. This will be referred to as the gauge freedom in the following.

Let us rewrite the TDH ansatz as

$$\Psi(t) = a(t)\Phi(t) \tag{3.13}$$

and define $\Phi^{(\kappa)}$ the single-hole function for each DOF κ as

$$\Phi^{(\kappa)}(t) = \prod_{\nu \neq \kappa} \varphi^{(\nu)}(t) \tag{3.14}$$

such that

$$\Phi(t) = \varphi^{(\kappa)}(t)\Phi^{(\kappa)}(t) \quad \forall \kappa. \tag{3.15}$$

These notations for the complete configuration Φ as a product of the single-particle function $\varphi^{(\kappa)}$ and the single-hole function $\Phi^{(\kappa)}$ will be widely used in the following derivation.

From time differentiation of eq. (3.13), we find

$$\begin{aligned} \dot{\Psi} &= \dot{a} \prod_{\kappa=1}^{f} \varphi^{(\kappa)} + a \sum_{\kappa=1}^{f} \dot{\varphi}^{(\kappa)} \prod_{\nu \neq \kappa} \varphi^{(\nu)} \\ &= \dot{a}\Phi + a \sum_{\kappa=1}^{f} \dot{\varphi}^{(\kappa)} \Phi^{(\kappa)} \end{aligned} \tag{3.16}$$

---

[1] A naive example is for b a non-zero complex number, for which $\varphi^{(1)}\varphi^{(2)} = (b\varphi^{(1)})\left(\frac{\varphi^{(2)}}{b}\right)$. During time evolution, without any specification, there is no certainty that b stays associated to these two SPFs in this way.

[2] The proof reads $\frac{\partial}{\partial t}\left\langle \varphi^{(\kappa)} \,\middle|\, \varphi^{(\kappa)} \right\rangle = \left\langle \dot{\varphi}^{(\kappa)} \,\middle|\, \varphi^{(\kappa)} \right\rangle + \left\langle \varphi^{(\kappa)} \,\middle|\, \dot{\varphi}^{(\kappa)} \right\rangle = 2\Re\left(\left\langle \varphi^{(\kappa)} \,\middle|\, \dot{\varphi}^{(\kappa)} \right\rangle\right) = 2\Im\left(g_\kappa\right)$ which gives a constant norm for $\varphi^{(\kappa)}$ if g_κ is real-valued.

where we defined the following notation for time-derivative $\dot{f} = \frac{\partial f}{\partial t}$. In an analogous way, the variation of the functional Ψ with respect to its functional parameters, a and $\varphi^{(\kappa)}$ reads

$$\delta\Psi = \underbrace{(\delta a)\,\Phi}_{\text{pre-factor variation}} + \underbrace{a\sum_{\kappa=1}^{f}\left(\delta\varphi^{(\kappa)}\right)\Phi^{(\kappa)}}_{\text{SPF variations}}. \tag{3.17}$$

We can now apply the Dirac-Frenkel variational principle eq. (3.2) separately with respect to δa and $\delta\varphi^{(\kappa)}$. For the variation along the pre-factor, δa

$$\begin{aligned}
0 &= \left\langle \delta\Psi(\text{pre-factor}) \,\middle|\, \widehat{H} - i\frac{\partial}{\partial t} \,\middle|\, \Psi \right\rangle \\
&= \left\langle \delta a\Phi \,\middle|\, \widehat{H} - i\frac{\partial}{\partial t} \,\middle|\, a\Phi \right\rangle \\
&= \left\langle \delta a\Phi \,\middle|\, \widehat{H} \,\middle|\, a\Phi \right\rangle - i\left\langle \delta a\Phi \,\middle|\, \dot{a}\Phi + a\sum_{\kappa=1}^{f}\dot{\varphi}^{(\kappa)}\Phi^{(\kappa)} \right\rangle \\
&= (\delta a)^{*}a\left\langle \Phi \,\middle|\, \widehat{H} \,\middle|\, \Phi \right\rangle - i(\delta a)^{*}\dot{a}\left\langle \Phi \,\middle|\, \Phi \right\rangle - i(\delta a)^{*}a\left\langle \Phi \,\middle|\, \sum_{\kappa=1}^{f}\dot{\varphi}^{(\kappa)}\Phi^{(\kappa)} \right\rangle.
\end{aligned} \tag{3.18}$$

Using $\langle \Phi \,|\, \Phi \rangle = 1$, $\left\langle \Phi \,\middle|\, \widehat{H} \,\middle|\, \Phi \right\rangle = E$ and $\left\langle \Phi \,\middle|\, \dot{\varphi}^{(\kappa)}\Phi^{(\kappa)} \right\rangle = \left\langle \varphi^{(\kappa)} \,\middle|\, \dot{\varphi}^{(\kappa)} \right\rangle$ we get

$$0 = aE - i\dot{a} - ia\sum_{\kappa=1}^{f}\left\langle \varphi^{(\kappa)} \,\middle|\, \dot{\varphi}^{(\kappa)} \right\rangle. \tag{3.19}$$

Using the definition eq. (3.12) of the constraints g_κ, we arrive to the first equation of motion, for the pre-factor $a(t)$

$$i\dot{a} = \left(E - \sum_{\kappa=1}^{f} g_\kappa\right)a. \tag{3.20}$$

For the variation along the SPF $\delta\varphi^{(\kappa)}$

$$\begin{aligned}
0 &= \left\langle \delta\Psi(\text{SPF } \kappa) \,\middle|\, \widehat{H} - i\frac{\partial}{\partial t} \,\middle|\, \Psi \right\rangle \\
&= \left\langle a\left(\delta\varphi^{(\kappa)}\right)\Phi^{(\kappa)} \,\middle|\, \widehat{H} - i\frac{\partial}{\partial t} \,\middle|\, a\Phi \right\rangle \\
&= \underbrace{\left\langle a\left(\delta\varphi^{(\kappa)}\right)\Phi^{(\kappa)} \,\middle|\, \widehat{H} \,\middle|\, a\Phi \right\rangle}_{\textcircled{a}} - \underbrace{i\left\langle a\left(\delta\varphi^{(\kappa)}\right)\Phi^{(\kappa)} \,\middle|\, \dot{a}\Phi \right\rangle}_{\textcircled{b}} - \underbrace{i\left\langle a\left(\delta\varphi^{(\kappa)}\right)\Phi^{(\kappa)} \,\middle|\, a\sum_{\nu=1}^{f}\dot{\varphi}^{(\nu)}\Phi^{(\nu)} \right\rangle}_{\textcircled{c}}.
\end{aligned} \tag{3.21}$$

We note that the notations for indices in the differentiation of Ψ (ket side) must be different (ν) than the one for the varied SPF (bra side), κ. The first term reads

$$\begin{aligned}
\textcircled{a} &= |a|^2\left\langle \left(\delta\varphi^{(\kappa)}\right)\Phi^{(\kappa)} \,\middle|\, \widehat{H} \,\middle|\, \Phi \right\rangle \\
&= |a|^2\left\langle \left(\delta\varphi^{(\kappa)}\right)\right| \left\langle \Phi^{(\kappa)} \,\middle|\, \widehat{H} \,\middle|\, \Phi^{(\kappa)} \right\rangle \left|\varphi^{(\kappa)}\right\rangle \\
&= |a|^2\left\langle \left(\delta\varphi^{(\kappa)}\right) \,\middle|\, \widehat{\mathcal{H}}^{(\kappa)} \,\middle|\, \varphi^{(\kappa)} \right\rangle
\end{aligned} \tag{3.22}$$

where we define the mean-field Hamiltonians

$$\widehat{\mathcal{H}}^{(\kappa)} = \left\langle \Phi^{(\kappa)} \,\middle|\, \widehat{H} \,\middle|\, \Phi^{(\kappa)} \right\rangle \tag{3.23}$$

obtained upon integrating the Hamiltonian over all DOFs but κ. Each mean-field Hamiltonian $\widehat{\mathscr{H}}^{(\kappa)}$ acts on the SPFs of the degree of freedom κ. The second term reads

$$\begin{aligned}
\textcircled{b} &= i a^* \dot{a} \left\langle \left(\delta\varphi^{(\kappa)}\right) \Phi^{(\kappa)} \,\middle|\, \Phi \right\rangle \\
&= i a^* \dot{a} \left\langle \left(\delta\varphi^{(\kappa)}\right) \,\middle|\, \varphi^{(\kappa)} \right\rangle \\
&= |a|^2 \left(E - \sum_{\nu=1}^{f} g_\nu \right) \left\langle \left(\delta\varphi^{(\kappa)}\right) \,\middle|\, \varphi^{(\kappa)} \right\rangle \text{ using eq. (3.20) with index } \nu.
\end{aligned} \tag{3.24}$$

Finally, the last term reads

$$\begin{aligned}
\textcircled{c} &= i|a|^2 \left\langle \left(\delta\varphi^{(\kappa)}\right) \Phi^{(\kappa)} \,\middle|\, \sum_{\nu=1}^{f} \dot{\varphi}^{(\nu)} \Phi^{(\nu)} \right\rangle \\
&= i|a|^2 \sum_{\nu=1}^{f} \left\langle \left(\delta\varphi^{(\kappa)}\right) \Phi^{(\kappa)} \,\middle|\, \dot{\varphi}^{(\nu)} \Phi^{(\nu)} \right\rangle
\end{aligned} \tag{3.25}$$

and because $\left\langle \left(\delta\varphi^{(\kappa)}\right) \Phi^{(\kappa)} \,\middle|\, \dot{\varphi}^{(\nu)} \Phi^{(\nu)} \right\rangle = \left\langle \left(\delta\varphi^{(\kappa)}\right) \varphi^{(\nu)} \,\middle|\, \dot{\varphi}^{(\nu)} \varphi^{(\kappa)} \right\rangle$ we find

$$\begin{aligned}
\textcircled{c} &= i|a|^2 \sum_{\nu=1}^{f} \left\langle \left(\delta\varphi^{(\kappa)}\right) \varphi^{(\nu)} \,\middle|\, \dot{\varphi}^{(\nu)} \varphi^{(\kappa)} \right\rangle \\
&= i|a|^2 \left\langle \left(\delta\varphi^{(\kappa)}\right) \,\middle|\, \dot{\varphi}^{(\kappa)} \right\rangle + i|a|^2 \sum_{\nu\neq\kappa}^{f} \left\langle \left(\delta\varphi^{(\kappa)}\right) \varphi^{(\nu)} \,\middle|\, \dot{\varphi}^{(\nu)} \varphi^{(\kappa)} \right\rangle \\
&= i|a|^2 \left\langle \left(\delta\varphi^{(\kappa)}\right) \,\middle|\, \dot{\varphi}^{(\kappa)} \right\rangle + i|a|^2 \sum_{\nu\neq\kappa}^{f} \left\langle \varphi^{(\nu)} \,\middle|\, \dot{\varphi}^{(\nu)} \right\rangle \left\langle \left(\delta\varphi^{(\kappa)}\right) \,\middle|\, \varphi^{(\kappa)} \right\rangle \\
&= i|a|^2 \left\langle \left(\delta\varphi^{(\kappa)}\right) \,\middle|\, \dot{\varphi}^{(\kappa)} \right\rangle + |a|^2 \sum_{\nu\neq\kappa}^{f} g_\nu \left\langle \left(\delta\varphi^{(\kappa)}\right) \,\middle|\, \varphi^{(\kappa)} \right\rangle .
\end{aligned} \tag{3.26}$$

In the end, collecting $\textcircled{a} = \textcircled{b} + \textcircled{c}$ we find

$$\begin{aligned}
\left\langle \left(\delta\varphi^{(\kappa)}\right) \,\middle|\, \widehat{\mathscr{H}}^{(\kappa)} \,\middle|\, \varphi^{(\kappa)} \right\rangle = &\left(E - \sum_{\nu=1}^{f} g_\nu \right) \left\langle \left(\delta\varphi^{(\kappa)}\right) \,\middle|\, \varphi^{(\kappa)} \right\rangle \\
&+ i \left\langle \left(\delta\varphi^{(\kappa)}\right) \,\middle|\, \dot{\varphi}^{(\kappa)} \right\rangle + \sum_{\nu\neq\kappa}^{f} g_\nu \left\langle \left(\delta\varphi^{(\kappa)}\right) \,\middle|\, \varphi^{(\kappa)} \right\rangle .
\end{aligned} \tag{3.27}$$

The two sums cancel with only the κ index remaining so that we can rewrite

$$i \left\langle \left(\delta\varphi^{(\kappa)}\right) \,\middle|\, \dot{\varphi}^{(\kappa)} \right\rangle = \left\langle \left(\delta\varphi^{(\kappa)}\right) \,\middle|\, \widehat{\mathscr{H}}^{(\kappa)} \,\middle|\, \varphi^{(\kappa)} \right\rangle - (E - g_\kappa) \left\langle \left(\delta\varphi^{(\kappa)}\right) \,\middle|\, \varphi^{(\kappa)} \right\rangle \tag{3.28}$$

which defines the coupled equations of motion for the SPFs. For the whole derivation, $(\delta\varphi^{(\kappa)})$ was arbitrary, so we can finally write the full set of coupled equations of motion for the TDH ansatz

$$i\dot{a} = \left(E - \sum_{\kappa=1}^{f} g_\kappa \right) a \tag{3.29a}$$

$$i\dot{\varphi}^{(\kappa)} = \left(\widehat{\mathscr{H}}^{(\kappa)} - E + g_\kappa \right) \varphi^{(\kappa)}. \tag{3.29b}$$

The most common choice for the constraints is $g_\kappa = 0$ so that

$$\boxed{i\dot{a} = Ea} \tag{3.30a}$$

$$\boxed{i\dot{\varphi}^{(\kappa)} = \left(\widehat{\mathscr{H}}^{(\kappa)} - E \right) \varphi^{(\kappa)}} \tag{3.30b}$$

3.2.2 Equations of motion for the MCTDH ansatz

With the MCTDH ansatz, we have a similar problem of no uniquely defined expansion of the wavefunction that we had for TDH. To lift the ambiguity, we define the contraint operators $\hat{g}^{(\kappa)}$ for the SPFs

$$i\left\langle \varphi_l^{(\kappa)} \middle| \dot{\varphi}_j^{(\kappa)} \right\rangle = \left\langle \varphi_l^{(\kappa)} \middle| \hat{g}^{(\kappa)} \middle| \varphi_j^{(\kappa)} \right\rangle \tag{3.31}$$

that we can choose to be Hermitian if the SPFs are to remain orthogonal. This is easily shown by time differentiating the overlap matrix between the SPFs. Typically, in the general implementation of MCTDH, we choose $\hat{g}^{(\kappa)} = 0$.

Again, the ansatz can be rewritten as an expansion in terms of single-hole functions, that are useful for the definition of many MCTDH-related quantities. We can rewrite the multi-dimensional wavepacket as a sum over the indices of SPFs for one degree of freedom κ

$$\Psi = \sum_{l}^{n_\kappa} \left|\varphi_l^{(\kappa)}\right\rangle \left\langle \varphi_l^{(\kappa)} \middle| \Psi \right\rangle_\kappa = \sum_{l=1}^{n_\kappa} \varphi_l^{(\kappa)} \Psi_l^{(\kappa)} \tag{3.32}$$

where we define $\Psi_l^{(\kappa)}$ the single-hole function for the DOF κ

$$\Psi_l^{(\kappa)} = \sum_{j_\kappa} A_{J_l^\kappa} \Phi_{J^\kappa} \tag{3.33}$$

with the following compact index definitions

$$\begin{aligned}
J^\kappa &= (j_1, \cdots, j_{\kappa-1}, j_{\kappa+1}, \cdots, j_f) && \text{compact indices with hole at index } \kappa \\
J_l^\kappa &= (j_1, \cdots, j_{\kappa-1}, l, j_{\kappa+1}, \cdots, j_f) && \text{compact indices with index } l \text{ instead of index } j_\kappa \\
\Phi_{J^\kappa} &= \prod_{\nu=1,\nu\neq\kappa}^{f} \varphi_{j_\nu}^{(\nu)} && \text{single-hole configuration}
\end{aligned} \tag{3.34}$$

which are the analogous of the SPFs compact notations eq. (3.8) for the single-hole functions. In simple words, the wavefunction can be expressed as a sum (over the index of SPFs of one degree of freedom) of products of each SPF of the set with a wavefunction "holed" for this SPF. Let us note that with these definitions, we have simple expressions of the variation of the ansatz with respect to its functional parameters:

$$\frac{\delta\Psi}{\delta \mathbf{A_J}} = \Phi_\mathbf{J} \text{ with eq. (3.9)} \tag{3.35a}$$

$$\frac{\delta\Psi}{\delta \varphi_j^{(\kappa)}} = \Psi_j^{(\kappa)} \text{ with eq. (3.32).} \tag{3.35b}$$

The linear variation along the A-vector gives the associated configuration (partial linearity), the linear variation along one SPF gives the associated single-hole function.

Let us introduce MCTDH-related quantities necessary for writing the MCTDH equations of motion. From the single-hole functions, we define the mean-field Hamiltonians

$$\left\langle \mathcal{H} \right\rangle_{kl}^{(\kappa)} = \left\langle \Psi_k^{(\kappa)} \middle| \widehat{H} \middle| \Psi_l^{(\kappa)} \right\rangle . \tag{3.36}$$

Compared with TDH, we now have matrices of mean-field Hamiltonians for each degree of freedom. Similarly, we define the reduced density matrices from the single-hole functions

$$\rho^{(\kappa)}_{kl} = \left\langle \Psi^{(\kappa)}_{k} \middle| \Psi^{(\kappa)}_{l} \right\rangle . \tag{3.37}$$

Finally, for each degree of freedom we define the projector onto the corresponding set of SPFs

$$\hat{P}^{(\kappa)} = \sum_{j=1}^{n_\kappa} \left| \varphi^{(\kappa)}_{j} \right\rangle \left\langle \varphi^{(\kappa)}_{j} \right| . \tag{3.38}$$

With these definitions, we give the equations of motion for the MCTDH ansatz

$$\boxed{i\dot{\mathbf{A}}_{\mathbf{J}} = \sum_{\mathbf{L}} \left\langle \Phi_{\mathbf{J}} \middle| \widehat{H} \middle| \Phi_{\mathbf{L}} \right\rangle \mathbf{A}_{\mathbf{L}}} \tag{3.39a}$$

$$\boxed{i\dot{\varphi}^{(\kappa)}_{j} = \left(\hat{1} - \hat{P}^{(\kappa)}\right) \sum_{k,l=1}^{n_\kappa} \left(\boldsymbol{\rho}^{(\kappa)-1}\right)_{jk} \left\langle \widehat{\mathcal{H}} \right\rangle^{(\kappa)}_{kl} \varphi^{(\kappa)}_{l}.} \tag{3.39b}$$

We can also define *vectors* of SPFs

$$\boldsymbol{\varphi}^{(\kappa)} = \left(\varphi^{(\kappa)}_{1} \cdots \varphi^{(\kappa)}_{n_\kappa} \right)^{T} \tag{3.40}$$

and give a more compact second set of equations

$$i\dot{\boldsymbol{\varphi}}^{(\kappa)} = \left(\hat{1} - \hat{P}^{(\kappa)}\right) \boldsymbol{\rho}^{(\kappa)-1} \left\langle \boldsymbol{\mathcal{H}} \right\rangle^{(\kappa)} \boldsymbol{\varphi}^{(\kappa)}. \tag{3.41}$$

Let us compare the TDH and MCTDH equations of motion. The propagation of the A-vector eq. (3.39a) in MCTDH is equivalent to the propagation of the TDH pre-factor eq. (3.30a). The main difference is that eq. (3.39a) depends on the matrix elements $\left\langle \Phi_{\mathbf{J}} \middle| \widehat{H} \middle| \Phi_{\mathbf{L}} \right\rangle$ for all configurations of MCTDH (secular-type equations), rather than simply on the energy of the one propagated configuration in TDH. The propagation of SPFs is also more complicated for MCTDH, where the projector and density reduced density matrix for the propagated degrees of freedom are also required, on top of the mean-field operators.

Take-home messages

1. We have used the TDH ansatz and the TD variational principle to derive the equations of motion (EOM) in the case of one configuration of SPFs (Hartree product). The EOM include one equation for the pre-factor and a set of coupled equations for the SPFs.
2. We defined the quantities related to the MCTDH ansatz (namely, the matrices of mean-field Hamiltonians, the MCTDH density and the operator for the MCTDH projection) and presented the equations of motion of MCTDH as a generalization of TDH.

3.3 MCTDH computational details and wavefunction analysis

We now briefly discuss the computational details for integrating the ordinary differential equations for the variational parameters $A_J(t)$ and $\varphi_j^{(\kappa)}(t)$, which define the MCTDH equations of motion. Two main numerical aspects will be discussed: the representation of the multi-dimensional wavepacket and the integration of the equations of motion. These discussions are quite general and are not necessarily specific to the use of the MCTDH ansatz.

3.3.1 Representation of the wavepacket

As we have seen in section 3.1.2, the ansätze (SM, TDH or MCTDH) are defined with respect to $\left\{\chi_j\right\}_j$, a set of orthogonal *primitive basis* functions (for MCTDH, see eq. (3.7)). This way of representing the wavefunction or the wavepacket Ψ is called the *finite basis representation* (FBR): the wavefunction is explicitly expanded in a (finite) direct-product of time-independent basis sets. These functions are in general chosen as solutions of simple eigenvalue model problems, for example the particle-in-a-box (sine functions) or, herein, the harmonic oscillator (Gauss-Hermite functions). One advantage of the FBR is that the effect of differential operators ($\frac{\partial}{\partial x}$ for the degree of freedom x) is simple, and known explicitly, on the primitive basis functions. On the other hand, for instance in the case of MCTDH, the FBR for the wavefunction boils down to knowing the A-vector (definition of the configurations of SPFs) and the B-vector (definition of the SPFs with respect to the primitive basis). However, such a representation is not adapted for evaluating multiplicative operators, such as in the operator for the potential energy.

As a consequence, another representation of the wavefunction must be found to be compatible with the multiplicative operators, for instance V, at a given point x_i

$$(V\Psi)_i = (V\Psi)(x_i) = V(x_i)\Psi(x_i). \tag{3.42}$$

One way of defining the grid points x_i is the use of the *discrete variable representation* (DVR). The DVR is a representation of the wavefunction with DVR functions, obtained from the FBR functions (they are linked together with a unitary transformation) and centered around the DVR points. The DVR points and DVR functions are obtained *via* the diagonalization of the matrix representation of the coordinate operator (for a given degree of freedom) in the FBR.

In practice, we use a given primitive basis to define the wavefunction (at any time) in the FBR. The DVR is computed accordingly to the choice of the primitive basis and its size, such that a spatial grid is defined for the calculation, for which the value of the wavefunction is known for each grid point. The FBR serves all calculations involving differential operators; the DVR serves all calculations involving multiplicative operators and wavefunction spatial analysis.

3.3.2 Propagation and relaxation

We are now aware of two representations for the wavefunction, adapted to differential and multiplicative operators, respectively. In addition, we have derived (or assume we know) the equations of motions for the variational parameters of a given ansatz (here, MCTDH). For MCTDH, solving the equations of motion is twofold. First, as in any method for solving the time-dependent Schrödinger equation, one has to choose an *integrator* for evaluating the formal, ideal, solution

$$\Psi(t) = \exp\left(-i\widehat{H}t\right)\Psi(t=0) \tag{3.43}$$

given that the initial state $\Psi(t=0)$ is known. For MCTDH, this boils down to integrating the (coupled) first-order differential equations, eqs. (3.39a) and (3.39b). In the context of quantum dynamics, the integration of the equations of motion is also called propagation. Different integration (or propagation) algorithms exist and we mention for instance the split-operator scheme, the Runge-Kutta scheme and the short iterative Lanczos (SIL) scheme. The integration algorithm can be different for the equations of motion of the A-vector or of the SPFs.

Second, the propagation of the MCTDH equations of motion is very expensive because of the evaluation, at each step, of the matrix $\left\langle \Phi_{\mathbf{J}} \middle| \widehat{H} \middle| \Phi_{\mathbf{L}} \right\rangle$ for the integration of the A-vector and of the mean-field matrices $\left\langle \widehat{\mathscr{H}} \right\rangle_{kl}^{(\kappa)}$ for the integration of the SPFs. In addition, these matrices also couple the equations of motion together. This explicit and straigthforward update of the mean-field matrices, at each step of the simulation, is called the *variable mean-field* approach (VMF). An approximation for speeding up the calculations is the *constant mean-field* approach (CMF) which, in essence, consists in updating the mean-field matrices less often. This approximate mean-field update holds in general because the mean-field matrices vary slowly compared to the wavefunction. The gain is twofold: the matrices are not to be computed at each time-step and the differential equations of the A-vector decouples (and becomes linear) from the ones of the SPFs (which stay non-linear).

We now briefly present the propagation schemes used in this work. As regards the practical calculations, we are interested in three types of calculations. The first two are time evolution (real-time propagation) and simple relaxation (negative imaginary-time propagation) of the system. The simple relaxation is a way to use propagation to find the lowest vibronic eigenstate having non-zero overlap with the initial guess (used to find the vibronic ground eigenstate). The last calculation is the improved relaxation, which allows one to access vibronic excited eigenstates rather than only the vibronic ground eigenstate.

Unless otherwise specified, the CMF approach is used for real-time propagation and improved relaxation. In these cases, we integrate the A-vector with the already mentioned SIL integrator and the SPFs with the Bulirsch-Stoer (BS) integrator for real-time propagation and for improved relaxation. The use of different integration schemes is adapted to the linear and non-linear nature of the equations of motion for the A-vector and the SPFs, respectively. The VMF approach is used in the case of simple relaxation (imaginary-time propagation) and the Adam-Bashforth-Moulton (ABM) integration scheme is used for both

A-vector and SPFs. Further details are beyond of the present scope, and can be found in Refs [94, 95].

3.3.3 Time-resolved and energy-resolved wavefunction analysis

In this section, we briefly present how to analyse the observables from the wavefunction (obtained from either propagation or relaxation) for time-resolved (expectation values) and energy-resolved (spectra) applications. We note that most of these analyses require the knowledge of the wavefunction on a given spatial grid, hence the definition and use of the DVR.

3.3.3.1 Diabatic and adiabatic populations

As we have seen in chapter 2, the molecular wavefunction can be expanded in the basis of the electronic states

$$|\Psi(\mathbf{Q},\mathbf{t})\rangle = \sum_{\beta} \Psi_{\beta}(\mathbf{Q},t) \left|\phi_{\beta}^{\text{el}};\mathbf{Q}\right\rangle , \tag{3.44}$$

where the many-body electronic basis set is chosen as being orthonormal for all $\mathbf{Q}$,

$$\left\langle \phi_{\beta}^{\text{el}};\mathbf{Q} \middle| \phi_{\alpha}^{\text{el}};\mathbf{Q}\right\rangle_{\text{el}} = \delta_{\beta\alpha}, \tag{3.45}$$

such that $\delta_{\beta\alpha}$ is the Kronecker symbol. The Dirac's "bra-ket"-notation corresponds here to an implicit integration over the electronic degrees of freedom, while the nuclear degrees of freedom (positions; $\mathbf{Q}$) have to be specified explicitly. The previous definitions are general and do not require the use of an MCTDH wavepacket. However, we must still assume that the electronic basis set is diabatic, $|\phi_{\alpha}^{\text{el}}\rangle = |\phi_{\alpha}^{\text{dia}}\rangle$. The corresponding density operator is defined as

$$\hat{\rho}(\mathbf{Q},t) = |\Psi(\mathbf{Q},t)\rangle \langle\Psi(\mathbf{Q},t)| , \tag{3.46}$$

which expands as

$$\hat{\rho}(\mathbf{Q},t) = \sum_{\beta}\sum_{\alpha} \Psi_{\beta}(\mathbf{Q},t)\Psi_{\alpha}^{*}(\mathbf{Q},t) \left|\phi_{\beta}^{\text{dia}};\mathbf{Q}\right\rangle \left\langle\phi_{\alpha}^{\text{dia}};\mathbf{Q}\right| . \tag{3.47}$$

"Bra-ket"-type electronic integration brings the following discrete density matrix representation,

$$\rho_{\beta\alpha}(\mathbf{Q},t) = \left\langle \phi_{\beta}^{\text{dia}};\mathbf{Q} \middle| \hat{\rho}(\mathbf{Q},t) \middle| \phi_{\alpha}^{\text{dia}};\mathbf{Q}\right\rangle_{\text{el}} = \Psi_{\beta}(\mathbf{Q},t)\Psi_{\alpha}^{*}(\mathbf{Q},t). \tag{3.48}$$

Now, integrating the density operator over the nuclear degrees of freedom (integrating over $\mathbf{Q}$) yields a reduced-density representation,

$$\gamma_{\beta\alpha}(t) = \int_{\mathbf{Q}} \Psi_{\beta}(\mathbf{Q},t)\Psi_{\alpha}^{*}(\mathbf{Q},t)\mathrm{d}\mathbf{Q}. \tag{3.49}$$

The diabatic electronic populations are thus defined as

$$P_{\beta}(t) = \gamma_{\beta\beta}(t) = \int_{\mathbf{Q}} |\Psi_{\beta}(\mathbf{Q},t)|^{2}\mathrm{d}\mathbf{Q}, \tag{3.50}$$

and the diabatic electronic coherences satisfy

$$C_{\beta\alpha}(t) = \gamma_{\beta\alpha}(t) = \gamma^*_{\alpha\beta}(t) = C^*_{\alpha\beta}(t), \tag{3.51}$$

for $\alpha \neq \beta$.

In the rest of this chapter, Dirac's "Bra-ket"-notation will no longer be used for integration over the electronic degrees of freedom. Hence, and unless otherwise specified, we shall now use $\langle \square \,|\, \square' \rangle$ only as a shorthand notation so as to refer to the integration over $\mathbf{Q}$ (the nuclear degrees of freedom). With this in mind, we get for the populations

$$P_\beta(t) = \left\langle \Psi_\beta \,\middle|\, \Psi_\beta \right\rangle (t), \tag{3.52}$$

and for the coherences (for the diabatic states $\alpha \neq \beta$)

$$C_{\alpha\beta}(t) = \left\langle \Psi_\beta \,\middle|\, \Psi_\alpha \right\rangle (t). \tag{3.53}$$

Let us notice that when dealing with two-level electronic systems, the evaluation of such magnitudes in practice simply involves to get the expectation values of Pauli operators over time.

Now, since the representation of the wavepacket is diabatic in MCTDH, the evaluation of adiabatic populations is to be done *a posteriori*, computing at each time of the propagation the adiabatic transformation and integrating the resulting multi-dimensional adiabatic wavepackets over the DVR grid, which is known to be a challenging task on the numerical front. Unless otherwise specified, the adiabatic populations discussed in this work are obtained thanks to the recent implementation of the time-dependent discrete variable representation (TD-DVR) formalism in the `Quantics` analysis programs for single-set calculations [100, 101].

3.3.3.2 A note on the expectation values of state-specific operators

Given an operator $\widehat{O}$ acting on $\mathbf{Q}$ and with no off-diagonal term among the electronic manifold, the expectation value of $\widehat{O}$ for the system is

$$\begin{aligned}\left\langle \widehat{O} \right\rangle &= \frac{\left\langle \Psi \middle| \widehat{O} \middle| \Psi \right\rangle}{\left\langle \Psi \,\middle|\, \Psi \right\rangle} = \sum_\beta \left\langle \Psi_\beta \middle| \widehat{O} \middle| \Psi_\beta \right\rangle \\ &= \sum_\beta P_\beta \frac{\left\langle \Psi_\beta \middle| \widehat{O} \middle| \Psi_\beta \right\rangle}{\left\langle \Psi_\beta \,\middle|\, \Psi_\beta \right\rangle} = \sum_\beta P_\beta \left\langle \widehat{O} \right\rangle_\beta ,\end{aligned} \tag{3.54}$$

assuming $\langle \Psi \,|\, \Psi \rangle = 1$ and where the electronic populations (weights) are $P_\beta = \left\langle \Psi_\beta \,\middle|\, \Psi_\beta \right\rangle$. The expectation value for the whole system can thus be interpreted as a population-weighted sum of state-specific expectation values $\left\langle \widehat{O} \right\rangle_\beta$ (with state-occurence probability weights, the populations P_β). In other words, two types of state-specific expectation values can be discussed:

- normalized (state-specific) expectation values

  $$\left\langle \widehat{O} \right\rangle_\beta = \frac{\left\langle \Psi_\beta \middle| \widehat{O} \middle| \Psi_\beta \right\rangle}{\left\langle \Psi_\beta \,\middle|\, \Psi_\beta \right\rangle}, \tag{3.55}$$

  which are "intensive" expectation values in the sense that they cannot be added together;

- population-weighted (for any state-contribution) expectation values

$$\left\langle \Psi_\beta \middle| \widehat{O} \middle| \Psi_\beta \right\rangle = P_\beta \left\langle \widehat{O} \right\rangle_\beta , \tag{3.56}$$

  which are "extensive" expectation values in the sense that they can be added together to obtain the full expectation value upon adding the contributions for all the electronic states.

In single-set calculations, the population-weighted expectation values are directly obtained, and must be normalized to access the state-specific expectation values. Normalized state-specific expectation values are required when studying the system in some given electronic state during a phenomenon that involves population transfer.

Conceptually speaking, state-specific expectation values correspond to what could be measured ideally (for example, a bond length, assuming specific knowledge of the electronic state). In contrast, a state-contribution expectation value is already weighted by the probability of observing the state and tells us how much it partially contributes to a global observable (for example to the total energy).

3.3.3.3 Autocorrelation functions and power spectra

On the other hand, real-time propagations also allow us to access energy-resolved quantities, such as spectroscopic properties *via* a linear-response analysis. We define the autocorrelation function

$$C(t) = \langle \Psi(0) \,|\, \Psi(t) \rangle \tag{3.57}$$

for which, unless otherwise specified, the so-called $t/2$-trick is used (valid only for real-valued initial wavepackets)

$$C(t) = \langle \Psi(t/2)^* \,|\, \Psi(t/2) \rangle \tag{3.58}$$

The Fourier transform of the autocorrelation function yields the so-called power spectrum associated to the propagation

$$I(\omega) \propto \int_{-\infty}^{+\infty} C(t) \exp{(i\omega t)} \mathrm{d}t. \tag{3.59}$$

Because the propagation time is finite, the autocorrelation function is multiplied by a decaying function

$$g(t) = \cos^n(\pi t/2T), \tag{3.60}$$

where T is the propagation time, and n is an integer, set to $n = 1$ in our calculations. Overall, this function filters the signal and reduces the presence of the Gibbs phenomenon (unphysical oscillations and negative intensities). Additionally, the autocorrelation function is multiplied by a Gaussian function characterized by the damping time

$$\tau = \frac{2\sqrt{2 \log 2}}{\Delta\omega} \tag{3.61}$$

to simulate the experimental full width at half-maximum (FWHF) of the peaks, $\Delta\omega$. In the rest of this work, such intensity spectra are referred to as power spectra.[3] Unless otherwise specified, we use the Condon approximation for the diabatic states, such that there is no explicit account of the dependence on the nuclear geometry of electronic transition dipole moments. As such, we will directly identify the previously defined power spectra as absorption and emission steady-state spectra.

Take-home messages

1. FBR and DVR have been defined.
2. Computational details for both propagation and relaxation calculations are given.
3. The diabatic populations and coherences have been defined. The adiabatic populations are computed using the TD-DVR approach.
4. Expectation values are analysed in terms of the choice of normalization. State-specific and state-contribution expectation values have been defined.
5. Power spectra have been defined in the case of real-time propagation, using the associated autocorrelation function.

3.4 Additional discussion, extensions of MCTDH

3.4.1 A geometric interpretation of the TD variational principle

General reformulation of the TD variational principle

In this section, we discuss the geometric interpretation of the Dirac-Frenkel variational principle, applicable for the different ansätze presented above [102,103]. We recall the abstract formulation of the Dirac-Frenkel variational principle

$$\left\langle \delta u \middle| \widehat{H} - i\frac{\partial}{\partial t} \middle| u \right\rangle = 0 \tag{3.62}$$

where without any assumption, u lies in a complex Hilbert space $\mathcal{H}$. Let $\mathcal{M}$ be a Kähler submanifold of $\mathcal{H}$ and $u \in \mathcal{M}$ the chosen ansatz ($u = \Psi^{\text{TDH}}$, Ψ^{SM}, or Ψ^{MCTDH}). The exact solution would be $\Psi(\mathbf{x}, t)$ (satisfying the time-dependent Schrödinger equation), function of the degrees of freedom $\mathbf{x}$ and of the

---

[3] A training `jupyter-notebook` for the use of autocorrelation functions to compute power spectra in the case of UV-visible steady-state spectroscopy is available at https://github.com/jwjgaliana/toolbox-qcqd/tree/main/autocorrelation2spectrum.

time t. The function $u(\mathbf{x},t)$ is the approximation of the exact solution

$$u(\mathbf{x};\boldsymbol{\lambda}(t)) = u[\boldsymbol{\lambda}(t)](\mathbf{x}) \simeq \Psi(\mathbf{x},t) \tag{3.63}$$

where the ansatz $u(\mathbf{x},t)$ is a holomorphic functional of the variational complex-valued parameters $\boldsymbol{\lambda}(t)$, such that $u(\mathbf{x},t) = u[\boldsymbol{\lambda}(t)](\mathbf{x})$. From now on, we discard the dependence on the degrees of freedom $\mathbf{x}$. Assuming $u(t)$ is complex-differentiable (holomorphic functional) with respect to the parameters $\boldsymbol{\lambda}(t)$, we denote $\mathcal{T}_{u(t)}\mathcal{M}$ the complex linear tangent space of $\mathcal{M}$ at $u(t)$, consisting in of all the derivatives with respect to the parameters $\boldsymbol{\lambda}(t)$

$$\mathcal{T}_{u(t)}\mathcal{M} = \text{span}\left(\left\{\frac{\partial u}{\partial \lambda_i}\right\}_i\right). \tag{3.64}$$

The variations of $u(t)$ are then

$$\delta u = \sum_i \frac{\partial u}{\partial \lambda_i}\delta\lambda_i \in \mathcal{T}_{u(t)}\mathcal{M}. \tag{3.65}$$

We stress here that the previously presented ansätze satisfy a condition of “contact” for the tangent space. In simple words, the ansatz can be written in terms of linear variations with respect to its own variational parameters (partial linearity, see the role of $a(t)$ in TDH or $A_{\mathbf{J}}(t)$ in MCTDH).

The Dirac-Frenkel variational principle can also be rephrased in the following terms. The function of time u is found at every time t so that its time derivative $\frac{\partial u}{\partial t}$ satisfies

$$\left\langle \delta u \middle| \widehat{H}u - i\frac{\partial u}{\partial t}\right\rangle = 0 \quad \forall \delta u \in \mathcal{T}_{u(t)}\mathcal{M}. \tag{3.66}$$

Using the Dirac-Frenkel variational principle for all the variations $\delta\lambda_i$, we find the differential equations satisfied by the variational parameters. Let us notice that the time derivative of $u(t)$ also depends on the time derivatives of λ_i,

$$\frac{\partial u}{\partial t} = \sum_i \frac{\partial u}{\partial \lambda_i}\frac{\partial \lambda_i}{\partial t} \in \mathcal{T}_{u(t)}\mathcal{M} \tag{3.67}$$

so that solving the equations of motion for the variational parameters $\lambda_i(t)$ is solving the equations of motion for $u(t)$. Solving the equations of motion for $u(t)$ at a given time t thus yields the time derivative $\frac{\partial u}{\partial t} \in \mathcal{T}_{u(t)}\mathcal{M}$, which can then be propagated.

Geometric interpretation of the TD variational principle

Let us give a geometric interpretation of the DFVP through the discussion of the real part of eq. (3.66). The time derivative obtained from the equations of motion $\frac{\partial u}{\partial t}(t)$ satisfies

$$\frac{\partial u}{\partial t}(t) = \arg \min_{w \in \mathcal{T}_{u(t)}\mathcal{M}} \left(\left|\left|\widehat{H}u(t) - iw(t)\right|\right|\right). \tag{3.68}$$

In other words, within the Dirac-Frenkel variational principle, $\frac{\partial u}{\partial t}$ is the orthogonal projection of $\frac{1}{i}\widehat{H}u$ onto the tangent space $\mathcal{T}_{u(t)}\mathcal{M}$ (see fig. 3.1). Note that $\frac{1}{i}\widehat{H}u$ does not necessarily lies in $\mathcal{M}$ nor in $\mathcal{T}_{u(t)}\mathcal{M}$, such that it can not be described with $u(t)$ or $\frac{\partial u}{\partial t}(t)$. Compared to the variational principle used in the

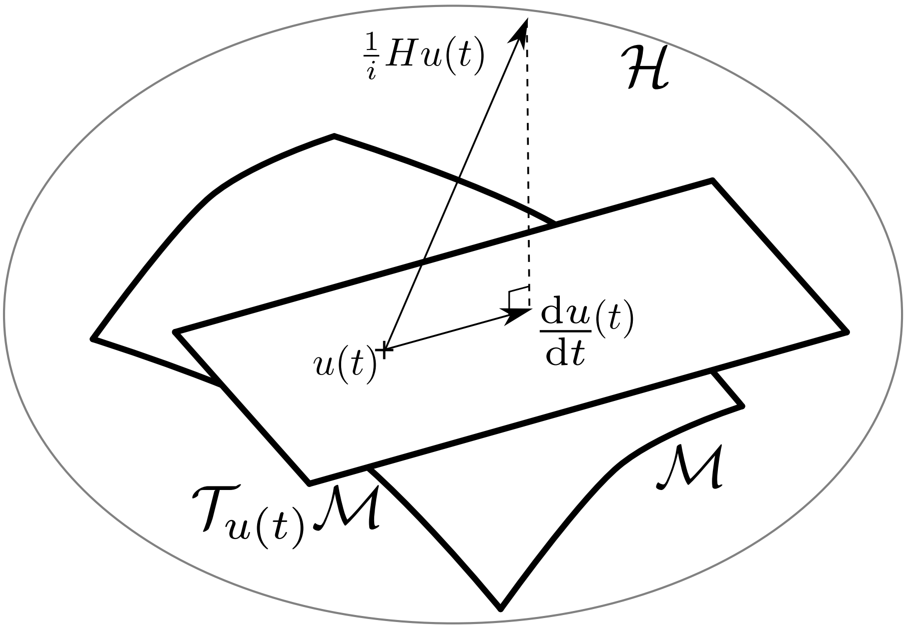

Figure 3.1: Geometric interpretation of the Dirac-Frenkel variational principle, representing the Hilbert space $\mathcal{H}$, the ansatz and its manifold $u(t) \in \mathcal{M}$, and the tangent space of the ansatz $\mathcal{T}_{u(t)}\mathcal{M}$. Reproduced from Lubich, **2008** [102]

context of the time-independent Schrödinger equation, this interpretation consists in an error minimization in the tangent plane $\mathcal{T}_{u(t)}\mathcal{M}$.

The Dirac-Frenkel variational principle is one out of various variational approximations of quantum dynamics. The error made by the choice of the Dirac-Frenkel variational principle and the ansatz $u(t)$ is upper bounded, and this error bound is found to be

$$||u(t) - \Psi(t)|| \leq \int_0^t \text{dist}\left(\frac{1}{i\hbar}\widehat{H}u(s),\, \mathcal{T}_{u(s)}\mathcal{M}\right) \mathrm{d}s. \tag{3.69}$$

The theory of the Dirac-Frenkel variational principle and its variants is still an active field for error estimates in applied mathematics [104]. More could be said about the simplecticity of the present variational principle but is out of the scope of this work. For a recent review of the mathematical aspects of the time-dependent variational principle, see Ref [105].

3.4.2 Including more degrees of freedom

MCTDH is very well suited for medium-size systems, typically less than 10 degrees of freedom. In practice, two criteria are limiting when looking for higher dimensionality. The first one is the size of the primitive basis set, which is important for the SPF equations of motion and also all the post-treatement calculations. The second one and most important is the number of SPFs which directly gives the number of coupled equations of motion. The more the SPFs, the longer the calculation. When the system has too high dimensionality, or requires an important number of SPFs, the calculation might simply be infeasible. In this work, two strategies may be employed (mode-combination and multi-layer MCTDH), both having strong similarities.

3.4.2.1 Mode combination

In the first definition of the MCTDH ansatz (eq. (3.6)), one set of SPFs is defined for each degree of freedom, and the SPFs are simple linear combinations of primitive basis functions of a single coordinate. However, the MCTDH equations of motion do not require the SPFs to depend on a single coordinate. A set of SPFs can be defined for a group of degrees of freedom and depend on several coordinates. For instance, let us define a set of SPFs for a group $\mathbf{Q}_\lambda$ of three *primitive* coordinates $(q_{\lambda,1}, q_{\lambda,2}, q_{\lambda,3})$

$$\begin{aligned} \varphi_j^\lambda(\mathbf{Q}_\lambda, t) &= \varphi_j^\lambda((q_{\lambda,1}, q_{\lambda,2}, q_{\lambda,3}), t) \\ &= \sum_{i_1,i_2,i_3}^{N_1,N_2,N_3} B^{(\lambda,j)}_{i_1,i_2,i_3}(t)\chi^{(\lambda,1)}(q_{\lambda,1})\chi^{(\lambda,2)}(q_{\lambda,2})\chi^{(\lambda,3)}(q_{\lambda,3}). \end{aligned} \tag{3.70}$$

In the previous expression, the SPFs set is adapted to a *combined* degree of freedom λ, involving the initial degrees of freedom (λ, i). Usually to reach convergence, the set of SPFs for the combined mode $(\tilde{n})$ is bigger than the set of one isolated non-combined mode (n) but much smaller than the size of the direct-product of the sets of SPFs of the non-combined modes (n^3). Although the number of SPFs to propagate is significantly reduced when using mode combination, the propagation of the newly defined multi-dimensional SPFs takes more computational power and time (notably because of the evaluation of multi-dimensional integrals). As a consequence, the mode-combination strategy alone is typically limited to the combination of up to three degrees of freedom, otherwise the combination becomes inefficient.

In the end, mode-combination is a good strategy for medium-dimensional systems, typically for contracting a 15-dimensional basis of the initial SPFs to an 8-dimensional basis of mode-combined SPFs. Yet, the propagation of MCTDH wavepackets in high-dimensional systems is still difficult, or unfeasible, for more degrees of freedom.

3.4.2.2 Multi-layer MCTDH

The strategy behind multi-layer (ML) MCTDH consists in expanding the SPFs (SPFs of the *upper* layer $z-1$) in another set of time-dependent functions (SPFs of the *lower* layer z) [106–108]

$$\varphi_m^{z-1,(\kappa_{\mathsf{up}})}(Q_{\kappa_{\mathsf{up}}^{z-1}}, t) = \sum_{j_1}^{n_1^z}\cdots\sum_{j_{p^z}}^{n_{p^z}^z} A^{z,m}_{j_1\cdots j_{p^z}}(t)\prod_{\kappa_{\mathsf{low}}=1}^{p^z}\varphi^{z,(\kappa_{\mathsf{low}})}_{j_{\kappa_{\mathsf{low}}}}(Q^z_{\kappa_{\mathsf{low}}}, t) \tag{3.71}$$

with combined modes $Q_{\kappa_{\mathsf{up}}^{z-1}} = \left(Q_1^z, \cdots, Q_{p^z}^z\right)$. For instance, the first layer would be

$$\Psi^{(\kappa)}(Q_\kappa, t) = \sum_{j_1}^{n_1^1}\cdots\sum_{j_{p^1}}^{n_{p^1}^1} A^1_{j_1\cdots j_{p^1}}(t)\prod_{\kappa=1}^{p^1}\varphi^{1,(\kappa)}_{j_\kappa}(Q^1_\kappa, t) \tag{3.72}$$

in the same manner as in MCTDH. The first difference is that the second layer is not the last one. In other words, the first SPFs are not expanded in the primitive basis set but in a new basis set of different SPFs

$$\varphi_m^{1,(\lambda)}(Q^1_\lambda, t) = \sum_{j_1}^{n_1^2}\cdots\sum_{j_{p^2}}^{n_{p^2}^2} A^{2,m}_{j_1\cdots j_{p^2}}(t)\prod_{\lambda=1}^{p^2}\varphi^{2,(\lambda)}_{j_\lambda}(Q^2_\lambda, t) \tag{3.73}$$

and iteratively until the last layer for which the SPFs are expanded in the primitive basis set. In practice and in the rest of this work, we do not explicitly formulate the ML-MCTDH ansatz as its form is very system-dependent. Instead, we give the associated so-called *ML-tree*, representing the layers of SPFs and associated size of basis sets.

There are many benefits from using the ML-MCTDH ansatz. The first one is to allow for the propagation of wavepackets for more than about tens of degrees of freedom. Without an ML-strategy, the length of the A-vector would simply be too large, as it depends on the size of the direct-product of the first-layer SPFs basis sets. The calculation rapidly becomes impracticable (exponential scaling, *curse of dimensionality*). The second benefit is to speed-up calculations that would be possible in MCTDH but slow, at a reduced cost in accuracy. Indeed, in practice the multi-layer MCTDH ansatz is a way to prune the space spanned by the SPFs and the configurations. The convergence must be carefully checked when using ML-MCTDH over an MCTDH calculation. Thanks to this speeding-up, the third benefit is that one can work with combined modes at the lowest layer instead of one-dimensional degrees of freedom. This allows one to retrieve some correlation between the degrees of freedom within the mode-combined SPFs, at some negligible computational cost (calculation of the associated multi-dimensional integrals, practicable for combination of two or three modes).

The practical use and advantages of ML-MCTDH for the purposes of this thesis will be discussed in the results part of the manuscript.

Take-home messages

1. The time-dependent variational principle, and in particular its geometric interpretations, can be related to the time-independent variational principle as an error minimization.
2. The obtention of equations of motion from the time-dependent variational principle can be generalized to any "well-behaved" ansatz.
3. The MCTDH formalism can be directly used with combined modes in order to treat systems with a larger number of degrees of freedom.
4. A more general extension of it is known as the multi-layer variant of MCTDH, where MCTDH is recursively used to propagate "hierarchical combinations" of modes at different levels (layers).

3.4.3 MCTDH in the landscape of nonadiabatic molecular dynamics methods

To conclude, let us discuss the place of MCTDH, in terms of advantages and limits, in the landscape of the nonadiabatic molecular dynamics (NAMD) methods (for closed quantum systems). We note that this discussion is not meant to be an exhaustive review of the nonadiabatic dynamics methods. In fig. 3.2, we schematize the strategies behind trajectory-based quantum dynamics (surface hopping, for instance), wavepacket dynamics (MCTDH here), and Gaussian wavepacket dynamics.

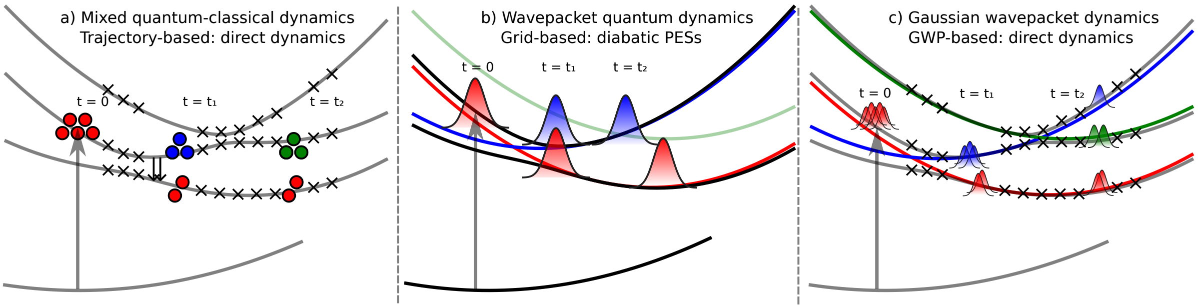

$$\Psi(\mathbf{Q},t) = \sum_{\mathbf{J}} A_{\mathbf{J}}(t)\Phi_{\mathbf{J}}(\mathbf{Q},t)$$

Distribution $\{\mathbf{x}_{\mathbf{J}}(t), \mathbf{p}_{\mathbf{J}}(t)\}$

$$\Phi_{\mathbf{J}}(\mathbf{Q},t) = \prod_{\kappa=1}^{f} \varphi_{j_\kappa}^{(\kappa)}(Q_\kappa,t)$$

$$\Phi_{\mathbf{J}}(\mathbf{Q},t) = g(\mathbf{Q};\{\mathbf{x}_{\mathbf{J}}(t),\mathbf{p}_{\mathbf{J}}(t)\})$$

Figure 3.2: Schematic representation of the main families of (a) mixed quantum-classical dynamics methods, and (b) and (c) wavepacket quantum dynamics methods. The cross symbols represent symbolically the interface with direct dynamics calculations, hence no explicit parametrization of the potential energy surfaces.

Grid-based and wavepacket nonadiabatic molecular dynamics methods

As already mentioned, MCTDH is a grid-based and wavepacket propagation method for running quantum dynamics calculations, see fig. 3.2, panel b). It relies notably on

1. the definition of an explicit grid of points (both spatially and in the functional space, DVR and FBR, respectively);
2. and the knowledge of diabatic potential energy surfaces and inter-state couplings on the grid and as analytic functions.

Thanks to the explicit and variational ("exact" at convergence) propagation of the wavepacket, based on the time-dependent Schrödinger equation ("first principles"), MCTDH is often used as a reference for benchmarking other quantum dynamics methods. However, the strengths of the method are also its biggest weaknesses: the grids are exponentially growing with the number of degrees of freedom (so-called *curse of dimensionality*), and the required prior knowledge of the diabatic Hamiltonians prevents the use of MCTDH as a predicting tool on itself, for instance as regards chemical reactivity. Exact grid-based quantum dynamics methods are thus particularly indicated for the calculation of electronic and/or vibrational spectra, or any other problems with "small amplitude" nuclear displacements. Situations with large amplitudes or strong geometry changes require either a more involved choice of the system coordinates, hence more complicated nuclear KEO and parametrization of the PESs, or a completely different strategy.

Trajectory-based nonadiabatic molecular dynamics

Among the alternatives to grid-based methods, there is the family of direct dynamics (or *on-the-fly*) methods, in which the energies, gradients and couplings are evaluated *on-the-fly* during the propagation. The most prominent advantages are twofold. First, the prior parametrization of the PESs and their diabatization is avoided, and the choice of the coordinates is less important. Second, and most importantly, the propagation is more "blind", in the sense that the "wavepacket" is allowed to explore channels of relaxation that could have not been predicted with prior parametrization of the PESs. The main drawback is that the limitations on the system size and number of degrees of freedom are now due to electronic structure calculations, which are to be run at each step of the propagation. Another limitation, related again to the electronic structure but shared with the parametrization of the PESs, is the evaluation and propagation of the nonadiabatic couplings [84] and the reliability of the electronic structure method used.

Among the most popular direct dynamics methods are the mixed quantum-classical methods based on trajectory surface hopping (TSH), see fig. 3.2, panel a) [109,110]. In TSH, the wavepacket is approximated to an ensemble of trajectories (characterized by their positions and momenta, the distribution $\{\mathbf{x}(t), \mathbf{p}(t)\}$), while the electronic superpositions mostly serve the calculation of the probabilities to "hop" from one state to another (see for instance Tully fewest switches surface hopping algorithm) [109, 111]. However, such trajectory-based methods suffer difficulties to account for many quantum effects. Indeed, in mixed quantum-classical methods, the nuclear degrees of freedom are not propagated quantum mechanically, but classically. As such, the coherence of the electronic wavepacket might be overestimated (the superposition of electronic states is attributed to a "classical" trajectory), and *decoherence* corrections must be applied (see a recent review from Subotnik and co-workers [112]). On the other hand, the coherence of the nuclear wavepackets are usually neglected because the trajectories are uncoupled.

A promising solution to join the best of both worlds from grid-based and direct dynamics methods has been designed by using Gaussian wavepacket dynamics (originating from the seminal work of Heller [113, 114]). In particular, the variational multiconfiguration Gaussian wavepacket method (vMCG) takes advantage of a superposition of Gaussian wavepackets (see fig. 3.2 panel c)) to both:

1. account for an accurate description and propagation of the wavepackets (vMCG)
2. evaluate (and diabatize) the electronic excited states and their PESs in an *on-the-fly* fashion (using Gaussians moments) (direct-dynamics, DD-vMCG)

In DD-vMCG, the Gaussian wavepackets are propagated with the time-dependent Schrödinger equation, but their centers are the closest one can find to classical trajectories, which allows the PESs to be computed *on-the-fly* [115, 116]. Another strategy is to directly propagate these Gaussian wavepackets as classical trajectories, as proposed by Martinez and co-workers in the full multiple spawning (FMS) method [117].

“Hierarchy” of the nonadiabatic molecular dynamics methods

As regards the comparison of *fitting PES* or *on-the-fly or direct* strategies for grid-based and trajectory-based methods, a comprehensive discussion is provided in Ref [118]. For the discussion of the “exactness” of the propagation methods, the wide diversity of nonadiabatic quantum dynamics methods (which have not been exhaustively mentioned here) is explicited with a rather clear hierarchy in Ref [119]. In particular, the exact factorization has been shown to provide such a hierarchy, from exact to mixed quantum-classical methods [120].

On a final note, for the rest of this work, we study isolated molecular systems through the definition of dimensionally reduced models and we propagate the associated wavepackets explicitly *via* MCTDH and its extensions (mode combination and multi-layer) only.

Chapter 4

Electronic Structure Theory

In this chapter, we briefly present the electronic structure problem and discuss the ways of solving the time-independent Schrödinger equation. The aim of this chapter is to give a minimal background for the discussion of the electronic structure calculations presented through this work. In particular, the problem of many-body electronic structure is herein discussed *via* the derivations of the effective one-body Hartree-Fock theory and the density functional theory. My personal research project was not focused on the developement of electronic structure methods nor on directly assessing their validity. However, electronic structure calculations comes first in this work both for characterizating the systems and phenomena of interest and for modelling tools for bridging electronic structure and quantum dynamics. As such, this chapter is thought as a minimal guide for enlightened users of electronic structure methods interested in the study of electronic excited states in isolated molecules. It is organized as follows. First, we recall the time-independent electronic Schrödinger equation and discuss the difficulty of dealing with the electronic-repulsion term (two-body term). Then, the Hartree-Fock theory for solving the Schrödinger equation is presented for both ground and excited electronic states. This presentation is extended to the density functional theory and its time-dependent flavor, along with a brief discussion of the existing approximate functionals. Finally, we summarize computational details as regards the electronic structure calculations done in the rest of this work.

4.1 Position of the problem

Let us consider again the time-independent Schrödinger equation (TISE), at some given molecular geometry (implicit here), for the electronic wavefunction, which will be the focus of this chapter

$$\forall\alpha,\ \widehat{H}^{\text{el}}(\mathbf{x})\phi^{\text{el}}_{\alpha}(\mathbf{x}) = E_{\alpha}\phi^{\text{el}}_{\alpha}(\mathbf{x}) \tag{4.1}$$

where we consider the n-electron Hamiltonian and wavefunction in the position and spin representation with $\mathbf{x} = (\mathbf{r}, \boldsymbol{\sigma})$ the space coordinates and the spin coordinates of the n electrons. The n-electron Hamiltonian only contains one-electron and two-electron terms

$$\begin{aligned}\widehat{H}^{\text{el}}(\mathbf{x}) &= \underbrace{\sum_i^n -\frac{1}{2}\nabla^2_{\mathbf{r}_i} - \sum_i^n\sum_A^N \frac{Z_A}{||\mathbf{R}_A - \mathbf{r}_i||}}_{h_i,\ \text{one-electron term}} \underbrace{+ \sum_i^n\sum_{j>i}^n \frac{1}{||\mathbf{r}_j - \mathbf{r}_i||}}_{g_{ij},\ \text{two-electron term}} \\ &= \widehat{T}^{\text{el}} + \widehat{V}^{\text{el-nu}} + \widehat{V}^{\text{el-el}}\end{aligned} \tag{4.2}$$

where we dropped the constant nuclear-nuclear interaction $\widehat{V}^{\text{nu-nu}}$. The kinetic energy of the electrons and the electronic-nuclear interaction (the first two terms) are one-electron terms and do not represent the challenging part in electronic structure theory. The third term is the electronic repulsion $\frac{1}{r_{ij}} = \frac{1}{||\mathbf{r}_j - \mathbf{r}_i||}$ and its role is the focus of this section. From eq. (4.2), there are two main families of approximations. The first family is composed of *ab initio* methods, solving the time-independent Schrödinger equation for $\widehat{H}^{\text{el}}$ which requires approximations because of the two-electron term. On the other hand, one can use "empirical" models for $\widehat{H}^{\text{el}}$ and parametrize these models against experimental or *ab initio* data, which is related to, for instance, tight-binding methods for estimating electronic properties. In this work, as regards electronic structure calculations we focus on *ab initio* methods and discard tight-binding-like methods.

4.2 Hartree-Fock theory

4.2.1 Variational approach for the electronic ground state

The Hartree-Fock theory is a variational method for which the ansatz for the electronic wavefunction is built from a Slater determinant, so as to account for the antisymmetry property of the wavefunction but with minimal correlation.

The Rayleigh-Ritz time-independent variational principle for the expectation value of the energy of the electronic ground state, defined as the functional

$$\mathcal{E}[\phi^{\text{el}}] = \frac{\left\langle \phi^{\text{el}} \middle| \widehat{H}^{\text{el}} \middle| \phi^{\text{el}} \right\rangle}{\left\langle \phi^{\text{el}} \middle| \phi^{\text{el}} \right\rangle} \quad \text{with} \quad \left\langle \phi^{\text{el}} \middle| \phi^{\text{el}} \right\rangle = 1 \tag{4.3}$$

consists in finding the optimized electronic wavefunction that minimizes the energy $\mathcal{E}$ (under the normalization constraint for the wavefunction). The problem formally consists in the minimization of the Lagrangian functional

$$\mathcal{L}[\phi^{\text{el}}, \lambda] = \left\langle \phi^{\text{el}} \middle| \widehat{H}^{\text{el}} \middle| \phi^{\text{el}} \right\rangle - \lambda \left(\left\langle \phi^{\text{el}} \middle| \phi^{\text{el}} \right\rangle - 1 \right) \tag{4.4}$$

where the Lagrange multiplier λ ensures the constraint that the electronic wavefunction is normalized at stationarity. The optimized electronic wavefunction is found for the stationary conditions

$$\delta \mathcal{L} = 0 \tag{4.5}$$

which can be rewritten in terms of variations for the ansatz and for the Lagrange multiplier, leading to

$$\left\langle \delta\phi_0^{\text{el}} \middle| \widehat{H}^{\text{el}} - \lambda_0 \middle| \phi_0^{\text{el}} \right\rangle = 0 \tag{4.6}$$

for real valued wavefunctions. In the previous equation, the optimal Lagrange multiplier λ_0 occurs to be the minimized energy $\mathcal{E}_0$ of the electronic ground state within the accessible Hilbert submanifold for the chosen ansatz. We note that eq. (4.6) is simply a different formulation of the stationary conditions for the Lagrangian and resembles the Dirac-Frenkel variational principle presented in chapter 3. Let us now define the ansatz for the electronic wavefunction ϕ^{el} used for the Hartree-Fock theory, as a Slater determinant

$$\phi^{\text{el}}(\mathbf{x}_1, \cdots, \mathbf{x}_n) = \frac{1}{\sqrt{n!}} \begin{vmatrix} \tilde{\varphi}_1(\mathbf{x}_1) & \cdots & \tilde{\varphi}_n(\mathbf{x}_1) \\ \vdots & \ddots & \vdots \\ \tilde{\varphi}_1(\mathbf{x}_n) & \cdots & \tilde{\varphi}_n(\mathbf{x}_n) \end{vmatrix} . \tag{4.7}$$

The functions $\tilde{\varphi}_a$ are the spin-orbitals and are the functions effectively optimized to access the minimum energy of the ground electronic state and the associated electronic wavefunction. Again, the problem of finding $\mathcal{E}$ can be rewritten as minimizing the Lagrangian

$$\mathcal{L}[\{\tilde{\varphi}_a\}, \{\epsilon_{ba}\}] = \mathcal{E}[\{\tilde{\varphi}_a\}] - \sum_a^n \sum_b^n \epsilon_{ba} \left(\langle \tilde{\varphi}_a \,|\, \tilde{\varphi}_b \rangle - \delta_{ab} \right) \tag{4.8}$$

where the objective function $\mathcal{E}[\phi^{\text{el}}] = \mathcal{E}[\{\tilde{\varphi}_a\}]$ is minimized under the constraints that the spin-orbitals form an orthonormal basis set. The associated Lagrange multiplier ϵ_{ba} have the dimension of energy. From this point, it can be shown through infinitesimal variation of the spin-orbitals that the previous minimization problem is equivalent to satisfying (stability conditions)

$$\widehat{\mathcal{F}}(i)\tilde{\varphi}_a(i) = \sum_b^n \epsilon_{ba}\tilde{\varphi}_b(i) \tag{4.9}$$

where $\widehat{\mathcal{F}}$ is the associated one-electron (for the i^{th} electron), so-called Fock operator. It is defined as

$$\widehat{\mathcal{F}}(i) = \hat{h}(i) + \sum_{b,\text{ occupied}} \widehat{\mathcal{J}}_b(i) - \widehat{\mathcal{K}}_b(i) \tag{4.10}$$

where $\hat{h}(i)$ is the one-electron core Hamiltonian, $\widehat{\mathcal{J}}_b(i)$ and $\widehat{\mathcal{K}}_b(i)$ are the Coulomb and exchange one-electron operators, respectively. It can be shown that the Fock operator is invariant to an arbitrary unitary rotation (*gauge freedom*) and that the Fock matrix in the basis set $\{\tilde{\varphi}_a\}$ can be diagonalized such that the Fock operator has a diagonal matrix representation in a new so-called canonical basis set $\{\varphi_a\}$

$$\widehat{\mathcal{F}}(i)\varphi_a(i) = \epsilon_a\varphi_a(i). \tag{4.11}$$

The latter formulation is thus a practical way of solving the variational principle as a pseudo eigenvalue problem. Now, as electrons are indistinguishable and we only have one- and two-electron terms to consider, let us consider the previous "pseudo-"eigenvalue problem (non-linear) for "electron 1" only. Solving the linear many-body Schrödinger equation now boils down to solving a set of one-electron non-linear pseudo-eigenvalue problems, with the subtelty that the Fock operator $\widehat{\mathcal{F}}(1)$ depends on all the occupied spin-orbitals. The Fock operator can be rewritten as the sum of the core-Hamiltonian operator $\hat{h}(1)$ for one electron and an effective potential operator $v^{\text{HF}}(1)$, caused by all other electrons, having the role of an approximation of the electron-electron repulsion term. This way, the Hartree-Fock theory is clearly identified as a mean-field theory and the energy is finally obtained as

$$\mathcal{E}_0 = \sum_a \epsilon_a - \frac{1}{2}\sum_a \sum_b \langle ab \,\|\, ab \rangle_{\text{2el}} \tag{4.12}$$

which requires the evaluation of the two-electron integrals

$$\langle ab \,\|\, ab \rangle_{\text{2el}} = \left\langle \varphi_a(1) \,\middle|\, \widehat{\mathcal{J}}_b(1) \,\middle|\, \varphi_a(1) \right\rangle - \left\langle \varphi_a(1) \,\middle|\, \widehat{\mathcal{K}}_b(1) \,\middle|\, \varphi_a(1) \right\rangle \tag{4.13a}$$

$$\left\langle \varphi_a(1) \,\middle|\, \widehat{\mathcal{J}}_b(1) \,\middle|\, \varphi_a(1) \right\rangle = \int\int \varphi_a^*(\mathbf{x}_1)\varphi_b^*(\mathbf{x}_2)\frac{1}{r_{12}}\varphi_a(\mathbf{x}_1)\varphi_b(\mathbf{x}_2)\mathrm{d}\mathbf{x}_1\mathrm{d}\mathbf{x}_2 \tag{4.13b}$$

$$\left\langle \varphi_a(1) \,\middle|\, \widehat{\mathcal{K}}_b(1) \,\middle|\, \varphi_a(1) \right\rangle = \int\int \varphi_a^*(\mathbf{x}_1)\varphi_b^*(\mathbf{x}_2)\frac{1}{r_{12}}\varphi_b(\mathbf{x}_1)\varphi_a(\mathbf{x}_2)\mathrm{d}\mathbf{x}_1\mathrm{d}\mathbf{x}_2 \tag{4.13c}$$

where we defined handy notations $\langle ij \| kl \rangle_{2\text{el}}$ for two-electron integrals (integration of r_{12}^{-1}) by giving only the index of the spin-orbitals. This notation is the usual physicist's notation; different notations for two-electrons integrals have been proposed elsewhere [121].

The Hartree-Fock equations eq. (4.11) are not strictly a linear eigenvalue problem, as stated above, because of the dependence of the Fock operator on all the occupied spin-orbitals. On a practical aspect, the equations are solved iteratively, until self-consistency is reached. In other words, an initial guess of spin-orbitals is made to build the Fock operator matrix representation, which is diagonalized to produce new spin-orbitals, used in the next step as the initial guess and so on. Self-consistency criteria can be chosen as convergence within an energy threshold or as unchanged spin-orbitals. This procedure is referred to as the self-consistent field (SCF) procedure in quantum chemistry programs. Numerically, the procedure is implemented through the Roothaan equations (in the context of closed-shell and restricted spin-orbitals) which are the matrix reformulation of the Hartree-Fock equations eq. (4.11) given a non-orthonormal atomic orbital basis set $\{\chi_\mu\}$,

$$\mathbf{FC} = \mathbf{SC}\boldsymbol{\epsilon}. \tag{4.14}$$

In equation eq. (4.14), $\mathbf{F}$ is matrix representation of the Fock operator in the set of atomic orbitals; $\mathbf{S}$ is the overlap matrix for the non-orthogonal set of atomic orbitals and $\mathbf{C}$ is the matrix defining the molecular orbitals as linear combinations of the atomic orbitals. Finally, $\boldsymbol{\epsilon}$ is the diagonal matrix for the "energies" of the molecular orbitals.

4.2.2 Configuration interaction and linear-response for the electronic excited states

In the previous section, we accessed the many-body electronic ground state energy and wavefunction using a mono-determinental ansatz. Let us assume this Hartree-Fock solution for the time-independent Schrödinger equation and build the configuration interaction singles (CIS) wavefunction from mono-excited Slater determinants

$$\phi^{\text{el,CIS}}(\mathbf{x}_1, \dots, \mathbf{x}_n) = \sum_a \sum_r c_a^r \phi_a^r(\mathbf{x}_1, \dots, \mathbf{x}_n) \tag{4.15}$$

where ϕ_a^r is obtained from the Hartree-Fock solution by promoting an electron from the occupied orbital a to the unoccupied orbital r (a single excitation). This simple CIS formalism allows us to define the excitation energies ω_{CIS} from the electronic ground state to the electronic excited states from the eigenvalue problem

$$\mathbf{AX} = \boldsymbol{\omega}\mathbf{X} \tag{4.16}$$

where $\mathbf{A}$ is the matrix representation of the electronic Hamiltonian eq. (4.2) in the basis of the mono-excited determinants, $\mathbf{X}$ is the matrix of the CIS expansion coefficients for the different excited states and $\boldsymbol{\omega}$ the diagonal matrix of the associated CIS excitation energies $\omega_n \propto E_n - E_0$. However, CIS being limited to singles, it is only an approximate formulation of the exact full configuration interaction, which is generally not practical. Yet, CIS is still a convenient way to think of the electronic transitions that we will further discuss within the theory of linear-response of approximate electronic structure methods.

Let us go back to Hartree-Fock theory, and assume an electronic ground state wavefunction ϕ_0 for the unperturbed electronic Hamiltonian. A common strategy to find the electronic transitions from this electronic ground state is to evaluate the linear-response of the wavefunction due to an external perturbation representing a periodic electric field. Such a perturbative treatement, formulated in the frequency-domain, yields first-order response equations for the HF theory

$$\begin{pmatrix} \mathbf{A} & \mathbf{B} \\ \mathbf{B}^* & \mathbf{A}^* \end{pmatrix} \begin{pmatrix} \mathbf{X}_n \\ \mathbf{Y}_n \end{pmatrix} = \omega_n \begin{pmatrix} 1 & 0 \\ 0 & -1 \end{pmatrix} \begin{pmatrix} \mathbf{X}_n \\ \mathbf{Y}_n \end{pmatrix} \tag{4.17}$$

where $\mathbf{A}$ and $\mathbf{B}$ are formed from the knowledge of the spin-orbitals of the electronic ground state calculation

$$A_{ar,bs} = (\epsilon_r - \epsilon_a)\delta_{ab}\delta_{rs} + \langle rb \,\|\, as\rangle \tag{4.18a}$$

$$B_{ar,bs} = \langle rs \,\|\, ab\rangle \,. \tag{4.18b}$$

Equation (4.17) is often referred to as the time-dependent Hartree-Fock (TDHF) equation although it is derived as a linear-response equation. Its solutions yield a pair of an electronic excitation $\mathbf{X}_n$ and an electronic de-excitation $\mathbf{Y}_n$, related to the excitation energy ω_n. These excitations and de-excitations are related to resonance *versus* anti-resonance terms obtained in the transition probability between two electronic states when considering the time-dependent perturbation theory.

We stress here that the problem of finding the electronic excited states is not solved directly but rather through the determination of the electronic transitions from an initial electronic ground state. We note that the eigenvalue problem 4.17 can be derived equivalently from the equations of motion; the linear-response of the wavefunction to a perturbation; or the random-phase approximation (RPA). In essence, for a given theory of the electronic ground state, the linear-response theory and first order spectral response to a time-dependent perturbation yield an eigenvalue problem for the electronic transitions. Hartree-Fock thus has its time-dependent extension, related to the CIS formalism when the de-excitations terms are neglected. In the next section, we will present a similar formalism evaluating electronic transitions within the context of the density functional theory (DFT).

Take-home messages

1. The Hartree-Fock equations for the electronic ground state are obtained by solving the time-independent variational principle for a Slater determinant built from spin-orbitals.
2. The Hartree-Fock equations are solved iteratively (SCF algorithms) and expressed in matrix-vector forms (Roothaan equations).
3. The electronic excited states can be approximated to the solutions of Casida-like equations (see below), a linear-response of the Hartree-Fock electronic ground state.

4.3 Density functional theory

Electronic structure methods based on the wavefunction are computationally expensive and become not practical for large systems. In this section, we present the density functional theory (DFT) and the associated density functional approximations (DFAs) for solving the electronic structure problem.

4.3.1 DFT for the electronic ground state

This section is strongly inspired from the lectures of J. Toulouse and their recent review on density functional theory and approximations [122].

4.3.1.1 One-electron density and universal functional

The electronic structure problem, within the non-relativistic limit, is concerned with the kinetic energy for the electron $\hat{T}^{\text{el}}$, the electron-electron interaction $\hat{V}^{\text{el-el}}$ and the external potential from the nuclei $\hat{V}^{\text{el-nu}}$ (see eq. (4.2)). The external potential is what defines the molecular system, from the knowledge of the nucleus positions, and is a multiplicative operator for which the representation in position is $v_{\text{ne}}(\mathbf{r})$ for one electron at position $\mathbf{r}$ (often called the external potential $v_{\text{ext}}(\mathbf{r})$). Having this and assuming an exact solution to the Schrödinger equation, one obtains the electronic wavefunction for the electronic ground state $\phi^{\text{el}}(\mathbf{x}_1, \dots, \mathbf{x}_n)$ (with $\mathbf{x}_i = (\mathbf{r}_i, \sigma_i)$), and can further define the one-electron density

$$\rho(\mathbf{r}) = \rho(\mathbf{r}_1) = n \int |\phi(\mathbf{x}_1, \mathbf{x}_2, \dots, \mathbf{x}_n)|^2 \mathrm{d}\sigma_1 \mathrm{d}\mathbf{x}_2 \cdots \mathrm{d}\mathbf{x}_n. \tag{4.19}$$

The one-electron density is a reduced-density function formed from the wavefunction integrated over all spin coordinates and over the position of all the electrons except one (chosen as the first one here, but all are indistinguishable) and is the focus interest of DFT. In a few words, given the external potential, the electronic wavefunction and the one-electron density are consequently obtained

$$v_{\text{ne}}(\mathbf{r}) \longrightarrow \rho(\mathbf{r}). \tag{4.20}$$

The first theorem of foremost importance for DFT is the first Hohenberg-Kohn (HK) theorem, for which the proposition is that this mapping can be inverted [123]. In other word, by only knowing the ground-state density $\rho(\mathbf{r})$ for an n-electron system, one is able to recover the underlying external potential (up to a constant)

$$\rho(\mathbf{r}) \longrightarrow v_{\text{ne}}(\mathbf{r}), \tag{4.21}$$

and consequently all observables of the n-electron system. Mathematically speaking, the external potential (and thus any observable for the n-electron system) is a functional of the density

$$v_{\text{ne}} = v[\rho], \tag{4.22}$$

and the ground state wavefunction for the external potential is also a functional of the density, such that the rest of the electronic Hamiltonian can also be evaluated as a functional of the density

$$F[\rho] = \left\langle \phi^{\text{el}}[\rho] \middle| \hat{T}^{\text{el}} + \hat{V}^{\text{el-el}} \middle| \phi^{\text{el}}[\rho] \right\rangle . \tag{4.23}$$

The previous functional of the density is called the "universal" functional of DFT in the sense that it does not depend on the external potential. Altogether we finally write the functional for the energy of the ground state

$$E[\rho] = F[\rho] + \int v_{\text{ne}}(\mathbf{r})\rho(\mathbf{r})\mathrm{d}\mathbf{r} \tag{4.24}$$

satisfying the variational principle such that

$$E_0 = \min_{\rho} \left(F[\rho] + \int v_{\text{ne}}(\mathbf{r})\rho(\mathbf{r})\mathrm{d}\mathbf{r} \right). \tag{4.25}$$

The optimum obtained for the minimal ground state energy E_0 is the optimal density of the electronic ground state $\rho_0(\mathbf{r})$ for the given potential $v_{\text{ne}}(\mathbf{r})$. The latter proposition is often referred to as the second HK theorem. Compared to the variational principle for the wavefunction (4-n spin-space parameters), we have here a tremendous simplification with a variational principle for the density (3 spatial parameters). Although this functional is universal in principle, it is an impossible task to have a practical use of it formally, in particular because of the kinetic energy of the electron within the n-electron system. Indeed, even if the universal functional exists, it is not known explicitly.

4.3.1.2 The Kohn-Sham method

A first approximation scheme was proposed shortly after the HK theorem: the Kohn-Sham (KS) scheme [124]. The main idea behind the KS method is to replace the many-body problem of interacting electrons with a simpler system of "non-interacting" electrons having the exact same electron density. The universal functional is rewritten as

$$F[\rho] = T_{\text{S}}[\rho] + E_{\text{Hxc}}[\rho]. \tag{4.26}$$

The second term, the Hartree-exchange-correlation energy, is the focus of the density functional approximations (DFAs) and is discussed later on. The advantage of the previous mapping is the evaluation of the first term, the kinetic energy for the electrons $T_{\text{S}}[\rho]$, which can now be simply evaluated with a variational principle with mono-determinantal wavefunctions.

$$T_{\text{S}}[\rho] = \min_{\phi \in \mathcal{S}_{\rho}^{n}} \left\langle \phi \middle| \hat{T}^{\text{el}} \middle| \phi \right\rangle = \left\langle \phi[\rho] \middle| \hat{T}^{\text{el}} \middle| \phi[\rho] \right\rangle \tag{4.27}$$

where $\mathcal{S}_{\rho}^{n}$ is the mathematical space of all the n-electron mono-determinantal wavefunctions having density ρ. The energy of the electronic ground state is then

$$E_0 = \min_{\phi \in \mathcal{S}_{\rho}^{n}} \left\langle \phi \middle| \hat{T}^{\text{el}} + \hat{V}^{\text{el-nu}} \middle| \phi \right\rangle + E_{\text{Hxc}}[\rho_{\phi}] \tag{4.28}$$

with, at the minimum, the optimal density ρ_0 of the electronic ground state, but with the subtelty that ϕ_0 is *not* the wavefunction of the ground state. For the Hartree-exchange-correlation energy functional, let us decompose again

$$\begin{aligned} E_{\mathsf{Hxc}}[\rho] &= E_{\mathsf{H}}[\rho] + E_{\mathsf{x}}[\rho] + E_{\mathsf{c}}[\rho] \\ &= \frac{1}{2}\int \frac{\rho(\mathbf{r}_1)\rho(\mathbf{r}_2)}{|\mathbf{r}_1 - \mathbf{r}_2|}\mathrm{d}\mathbf{r}_1\mathrm{d}\mathbf{r}_2 + E_{\mathsf{x}}[\rho] + E_{\mathsf{c}}[\rho] \end{aligned} \tag{4.29}$$

where the first term (Hartree energy) is the classical Coulombic interaction between two electron densities and the other two terms are exchange and correlation functionals, respectively, and must be approximated.

On practical terms, as for the HF approximation and its derivation, the minimization problem is effectively solved using spin-orbitals so that the density, hence the energy, are functionals of the spin-orbitals

$$E[\{\varphi_i\}] = \sum_i^n \int \varphi_i^*(\mathbf{r}) \left(-\frac{1}{2}\nabla_{\mathbf{r}}^2 + v_{\mathsf{ne}}(\mathbf{r})\right) \varphi_i(\mathbf{r})\mathrm{d}\mathbf{r} + E_{\mathsf{Hxc}}[\rho] \tag{4.30}$$

with

$$\rho(\mathbf{r}) = \sum_i^n |\varphi_i(\mathbf{r})|^2. \tag{4.31}$$

Similarly to the constrained variational approach for deriving the HF equations, the variational principle leads to the KS equations

$$\underbrace{\left(-\frac{1}{2}\nabla_{\mathbf{r}}^2 + v_{\mathsf{ne}}(\mathbf{r}) + v_{\mathsf{Hxc}}(\mathbf{r})\right)}_{h_{\mathsf{S}},\ \text{one-electron operator}} \varphi_i(\mathbf{r}) = \epsilon_i \varphi_i(\mathbf{r}). \tag{4.32}$$

The KS equations resembles the canonical HF equations, only with a new potential that is the Hartree-exchange-correlation potential

$$v_{\mathsf{Hxc}}(\mathbf{r}) = \frac{\delta E_{\mathsf{Hxc}}[\rho]}{\delta \rho(\mathbf{r})} \tag{4.33}$$

obtained from the extension of the derivation to the Hartree-exchange-correlation functional. It is to be noted that the existence of such a potential is not guaranteed in general, and is known as the v-representability problem, or condition, which is the main issue of KS-DFT.

In the exact same way as in HF equations, the solution of KS equations are found iteratively, until self-consistency of the density is reached. In practice, a basis set of atomic orbitals is given and the equivalent of the Roothaan equations for the KS one-electron operator $\hat{h}_{\mathsf{S}}$ are found and solved. Compared to the HF approximation and the Roothaan equations, using DFT "only" requires defining an Hartree-exchange-correlation functional. If the functional E_{Hxc} is exact, the DFT energy and density for the electronic ground state are exact, but in practice, only approximate functionals for exchange and correlation energies are accessible, hence used.

4.3.1.3 Exchange-correlation approximations

In this section, we briefly review the historical approximation types for the exchange-correlation functionals, from the simplest to the more involved ones. These density functional approximations (DFAs) have historically been illustrated as the *rungs of a Jacob's ladder*, the lowest rung being closer to the Hartree theory and the highest rung being closer to the many-body perturbation theory [122]. The first approximation was proposed together with the non-interacting mapping by Kohn and Sham [124] and is the *local*-density approximation (LDA)

$$E_{\mathsf{xc}}^{\mathsf{LDA}} = \int \rho(\mathbf{r})\epsilon^{\mathsf{UEG}}(\rho(\mathbf{r}))\mathrm{d}\mathbf{r} \tag{4.34}$$

where $\epsilon^{\mathsf{UEG}}(\rho(\mathbf{r}))$ is the exchange-correlation energy per particle for an uniform electron gas (UEG) at the given density $\rho(\mathbf{r})$. The latter energy per particle is decomposed in an exchange contribution, computed analytically, and a correlation contribution which can only be estimated numerically.

The second rung in the ladder of DFAs is the family of generalized-gradient approximation (GGA) functionals of the form

$$E_{\mathsf{xc}}^{\mathsf{GGA}} = \int e_{\mathsf{xc}}^{\mathsf{GGA}}(\rho(\mathbf{r}), \nabla\rho(\mathbf{r}))\mathrm{d}\mathbf{r}. \tag{4.35}$$

Compared to LDA functionals, the GGA functionals are said to be *semilocal* due to the use of the local gradient of the density $\nabla\rho(\mathbf{r})$ on top of the local density $\rho(\mathbf{r})$. Far from being comprehensive, we cite

- the B88 exchange functional (Becke 1988 [125]), which is a correction to LDA using the modulus of the density gradient $|\nabla\rho(\mathbf{r})|$ and is fitted to Hartree-Fock exchange energies of rare-gas atoms;
- the LYP correlation functional (Lee-Yang-Parr 1988 [126]), which is a density functional depending on the density $\rho(\mathbf{r})$, the square of the density gradient $(\nabla\rho(\mathbf{r}))^2$ and the Laplacian of the density $\nabla^2\rho(\mathbf{r})$.

An extension of GGA (meta-GGA) was later introduced by adding dependency on the non-interactive kinetic energy density, re-inserting kinetic energy from the orbitals of the KS single-determinant wavefunction.

The next rung of the Jacob ladder consists in the hybrid functionals, where hybrid implies using a mix of Hartree-Fock exchange energy and exchange and/or correlation from LDA and GGA functionals. Within this family, Becke proposed a three-parameter hybrid (3H) approximation [127, 128]

$$E_{\mathsf{xc}}^{\mathsf{3H}}[\phi] = aE_{\mathsf{x}}^{\mathsf{HF}}[\phi] + bE_{\mathsf{x}}^{\mathsf{GGA}}[\rho_\phi] + (1-a-b)E_{\mathsf{x}}^{\mathsf{LDA}}[\rho_\phi] + cE_{\mathsf{c}}^{\mathsf{GGA}}[\rho_\phi] + (1-c)E_{\mathsf{c}}^{\mathsf{LDA}}[\rho_\phi] \tag{4.36}$$

where the energy functionals are here functionals of the mono-determinantal wavefunction ϕ consistent with the density ρ_ϕ. One example of a 3H functional is the hybrid B3LYP [129] and is a mix of the previously cited B88 exchange and the LYP correlation functionals ($(a, b, c) = (0.20, 0.72, 0.81)$).

Another common hybrid approximation is the simpler in form one-parameter hybrid (1H) [130] and adapted to any lower approximation

$$E_{\mathsf{xc}}^{\mathsf{1H}}[\phi] = aE_{\mathsf{x}}^{\mathsf{HF}}[\phi] + (1-a)E_{\mathsf{x}}^{\mathsf{LDA/GGA}}[\rho_\phi] + aE_{\mathsf{c}}^{\mathsf{LDA/GGA}}[\rho_\phi]. \tag{4.37}$$

A trade-off for a must be found, and it is generally taken around 0.25 based on fitted experimental data. The B97 (Becke 97 [131]) family of functionals is an example of 1H hybrid functional with GGA initial approximation.

Up to these hybrid functionals, DFAs are still usually bad appproximations for electronic ground and excited states of large molecules or for charge-transfer systems, for instance. One important step toward the last rungs of Jacob's ladder for DFAs is the long-range correction (LC), which is proposed in the range-separated scheme for hybrid functionals. There are different range-separated schemes, but the initial idea is to have a mix of exchange functional from HF and the targeted DFA using a parameter (previously denoted a) that depends on r_{12}

$$E_{\text{x}}^{\text{LC}} = E_{\text{x}}^{\text{lr,HF}}[\phi] + E_{\text{x}}^{\text{sr,DFA}}[\rho_{\phi}] + E_{\text{c}}^{\text{DFA}}[\rho_{\phi}] \tag{4.38}$$

where the long-range (lr) and short-range (sr) exchange functionals are calculated using long-range and short-range electron-electron interactions

$$w_{\text{ee}}^{\text{lr}}(r_{12}) = \frac{\text{error-function}(\mu r_{12})}{r_{12}} \text{ and } w_{\text{ee}}^{\text{sr}} = \frac{1}{r_{12}} - w_{\text{ee}}^{\text{lr}}(r_{12}) \tag{4.39}$$

where μ parametrizes the degree of *separation* [132]. The LC scheme was further extended to 3H and 1H hybrid functionals, using the long-range and short-range versions of the exchange functionals. This is the case of the Coulomb attenuating method (CAM)

$$\begin{aligned} E_{\text{xc}}^{\text{CAM}}[\phi] &= aE_{\text{x}}^{\text{sr,HF}}[\phi] + bE_{\text{x}}^{\text{lr,HF}}[\phi] \\ &\quad + (1-a)E_{\text{x}}^{\text{sr,DFA}}[\rho_{\phi}] + (1-b)E_{\text{x}}^{\text{lr,DFA}}[\rho_{\phi}] + cE_{\text{c}}^{\text{GGA}}[\rho_{\phi}] + (1-c)E_{\text{c}}^{\text{LDA}}[\rho_{\phi}] \end{aligned} \tag{4.40}$$

for which the most known application is the CAM-B3LYP functional, extensively used in this work. Compared to B3LYP, the parameters of CAM are the same for correlation but slightly different for exchange ($a = 0.19$, $b = 0.65$) and the LC parameter is $\mu = 0.33\, {a_0}^{-1}$ [133]. For 1H hybrid functional, we cite the ω-B97X functional which is the LC corrected B97 functional with re-optimized parameters $a = 0.16$, $b = 1$ and $\mu = 0.3\, {a_0}^{-1}$ [134].

In this thesis, we almost exclusively used range-separated hybrid functionals for the electronic ground and excited states. Unless otherwise specified, the preferred functional is CAM-B3LYP. Some side projects to this work suggested the use of different range-separated hybrid functionals such as the family of ω-B87 functionals for the electronic excited states.

Take-home messages

1. The density functional theory (DFT) uses the one-electron density, rather than the electronic wavefunction, to minimize the energy of the electronic ground state.
2. The Hohenberg-Kohn theorems allows one to rewrite the external potential as a functional of the density, and to minimize the energy accordingly.
3. The Kohn-Sham (KS) scheme defines a mapping of the many-body problem for the electrons with a system of non-interacting electrons.

4. With the KS scheme, the kinetic energy functional is easily computed, and only the exchange-correlation potential must be approximated.
5. The approximations for exchange-correlation potentials are numerous, and we choose, as regards our calculations, the CAM-B3LYP functional (range-separated hybrid functional).

4.3.2 Linear-response time-dependent DFT and electronic excited states.

In the previous section, we described DFT and usual DFAs for the electronic ground state. In this section, we briefly present how DFT has been extended for studying electronic excited states and transition energies, within the framework of the linear-response time-dependent DFT (LR-TD-DFT). This presentation is strongly inspired from the review article of M. E. Casida and M. Huix-Rotllant [135] and the book chapter *Introduction to TDDFT* of E. Gross and N. Maitra [136].

Similarly to Hohenberg and Kohn theorems, TD-DFT has for fundation the Runge and Gross (RG) theorems. The first one states that the time-dependent electron density $\rho(\mathbf{r},t)$ and the initial wavefunction $\phi^0 = \phi(t=0)$ determines the external potential (up to an additive function of time only)

$$v_{\text{ext}}(\mathbf{r},t) \longleftrightarrow \rho(\mathbf{r},t) \text{ given } \phi^0. \tag{4.41}$$

The difference compared with HK first theorem is the dependence on the information at $t=0$ or within the functional formalism

$$v_{\text{ext}}(\mathbf{r},t) = v[\rho,\phi^0], \tag{4.42}$$

where the external potential now includes both the electron-nuclear potential and the external time-dependent perturbation (such as electromagnetic radiations). Analogous to the time-independent case and the Kohn-Sham scheme, one can consider the RG theorem in the case of non-interacting electrons

$$v_{\text{KS}}(\mathbf{r},t) \longleftrightarrow \rho(\mathbf{r},t) \text{ given } \phi^0_{\text{KS}} \tag{4.43}$$

where the density is the same as in the case of the interacting electrons. The so-called KS potential can be rewritten as

$$v_{\text{KS}}[\rho,\phi^0_{\text{KS}}](\mathbf{r},t) = v_{\text{ext}}[\rho,\phi^0](\mathbf{r},t) + E_{\text{H}}[\rho] + v_{\text{xc}}[\rho,\phi^0,\phi^0_{\text{KS}}](\mathbf{r},t) \tag{4.44}$$

retrieving the external potential, the Hartree potential and a new exchange-correlation potential, functional of the density and of the initial states for interacting electrons and non-interacting electrons. The new KS scheme for the time-dependent Schrödinger equation now gives the time-dependent KS equations

$$\left[-\frac{\nabla^2_{\mathbf{r}}}{2} + v_{\text{KS}}[\rho,\phi^0_{\text{KS}}](\mathbf{r},t)\right]\varphi_i(\mathbf{r},t) = i\frac{\partial\varphi_i(\mathbf{r},t)}{\partial t}. \tag{4.45}$$

However, the conditions for the existence of the exchange-correlation functional $v_{\text{xc}}[\rho,\phi^0,\phi^0_{\text{KS}}]$ are not trivial and constitute an important fundamental question in TD-DFT [137]. Furthermore, it is a highly complicated mathematical object and is, in the context of the TD-DFT presented here, strongly simplified. The most current approximation is the “Adiabatic Approximation”. Let us stress here that the “Adiabatic Approximation” in the context of TD-DFT is not the same as the adiabatic approximation in the context of nuclear motions. It consists in neglecting all *memory* or *history* effects in the exchange-correlation functional (Markovian-like approximation), thus writing

$$v_{\mathsf{xc}}[\rho,\phi^0,\phi^0_{\mathsf{KS}}] \simeq v^{\mathsf{AA}}_{\mathsf{xc}}[\rho_t](\mathbf{r}) = \frac{\delta E_{\mathsf{xc}}[\rho_t]}{\delta\rho_t(\mathbf{r})}. \tag{4.46}$$

In other words, the time-dependent exchange-correlation potential only depends on the functional derivative of the exchange-correlation functional at time t with respect to the density at time t.

Although TD-KS equations could be propagated in time, the problem is more easily solved, for weak external perturbation, within the linear-response (LR) formalism. Let us begin with the LR formalism for the interacting system, with the underlying ϕ_0 wavefunction for the electronic ground state. Let us assume that the initial state is the electronic ground state of the system, and assume that we have the following separation for the external potential

$$v_{\mathsf{ext}}(\mathbf{r},t) = v_{\mathsf{ext},0}(\mathbf{r}) + \delta v_{\mathsf{ext}}(\mathbf{r},t). \tag{4.47}$$

The response of the time-dependent density to the external perturbation $\delta v_{\mathsf{ext}}(\mathbf{r},t)$ is

$$\rho(\mathbf{r},t) = \rho_0(\mathbf{r}) + \rho_1(\mathbf{r},t) + \rho_2(\mathbf{r},t) + ... \tag{4.48}$$

For the linear-response formulation of TD-DFT, we are simply interested in the first-order term

$$\rho_1(\mathbf{r},t) = \int_0^{+\infty} \mathrm{d}t' \int \chi(\mathbf{r},t,\mathbf{r}',t')\delta v_{\mathsf{ext}}(\mathbf{r}',t')\mathrm{d}\mathbf{r}' \tag{4.49}$$

where we define the so-called density-density linear-response function χ

$$\chi(\mathbf{r},t,\mathbf{r}',t') = \left.\frac{\delta\rho(\mathbf{r},t)}{\delta v_{\mathsf{ext}}(\mathbf{r}',t')}\right|_{v_{\mathsf{ext},0}}. \tag{4.50}$$

Using the completeness relation for the excited states of the unperturbed electronic Hamiltonian and a Fourier transform one can write the previous response function in the frequency-domain

$$\chi(\mathbf{r},\mathbf{r}',\omega) = \lim_{\eta\to 0^+}\sum_{\alpha\neq 0}\left[\frac{\langle\phi_0\,|\,\hat\rho(\mathbf{r})\,|\,\phi_\alpha\rangle\,\langle\phi_\alpha\,|\,\hat\rho(\mathbf{r}')\,|\,\phi_0\rangle}{\omega-\omega_\alpha+i\eta} - \frac{\langle\phi_0\,|\,\hat\rho(\mathbf{r}')\,|\,\phi_\alpha\rangle\,\langle\phi_\alpha\,|\,\hat\rho(\mathbf{r})\,|\,\phi_0\rangle}{\omega+\omega_\alpha+i\eta}\right]. \tag{4.51}$$

In the previous expression, the electronic excited state wavefunctions ϕ_α and associated excitation energies $\omega_\alpha = E_\alpha - E_0$ would be the solutions of the CIS eigenvalue problem eq. (4.16). The poles of the density-density linear-response function in the frequency domain theoretically give the excitation energies. In particular, we find again the resonance ($\propto (\omega-\omega_\alpha)^{-1}$) and anti-resonance ($\propto (\omega+\omega_\alpha)^{-1}$) with respect to the frequency of the perturbation (see for instance first-order time-dependent perturbation theory in Ref [138]).

Now, we want to take advantage of TD-DFT by using the KS scheme of non-interacting electrons, which yield the same time-dependent density. The definition of the response function holds for the non-interacting system, yielding

$$\chi_{\mathsf{KS}}(\mathbf{r},t,\mathbf{r}',t') = \left.\frac{\delta\rho(\mathbf{r},t)}{\delta v_{\mathsf{KS}}(\mathbf{r}',t')}\right|_{v_{\mathsf{KS},0}} \tag{4.52}$$

for which we can also give the frequency-space representation, introducing the spin-orbitals for the electronic ground state of the non-interacting system

$$\chi_{\mathsf{KS}}(\mathbf{r},\mathbf{r}',\omega) = \lim_{\eta\to 0^+}\sum_a\sum_r (f_a - f_r)\frac{\varphi_a^{(0)*}(\mathbf{x})\varphi_r^{(0)}(\mathbf{x})\varphi_r^{(0)*}(\mathbf{x}')\varphi_a^{(0)}(\mathbf{x}')}{\omega - (\epsilon_r - \epsilon_a) + i\eta} \tag{4.53}$$

where $f_{a,r}$ are occupation numbers for the orbitals $\varphi_{a,r}$ with energies $\epsilon_{a,r}$. The problem is now that the poles of the KS density-density linear-response function are not the ones of the true density-density response function eq. (4.51). We must take into account the exchange-correlation potential and the so-called exchange-correlation kernel f_{xc}

$$f_{\mathsf{xc}}[\rho_0](\mathbf{r},t,\mathbf{r}',t') = \left.\frac{\delta v_{\mathsf{xc}}^{\mathsf{AA}}[\rho](\mathbf{r},t)}{\delta\rho(\mathbf{r}',t')}\right|_{\rho=\rho_0} = \left.\frac{\delta^2 E_{\mathsf{xc}}[\rho](\mathbf{r},t)}{\delta\rho(\mathbf{r}'t')\delta\rho(\mathbf{r},t)}\right|_{\rho=\rho_0}. \tag{4.54}$$

to correct the response function. Assuming this is known, the true density-density response function is, within the TD-KS scheme

$$\begin{aligned}\chi[\rho_0](\mathrm{r},t,\mathrm{r}',t') &= \chi_{\mathsf{KS}}[\rho_0](\mathrm{r},t,\mathrm{r}',t')\\ &+ \int \mathrm{d}t_1 \int \mathrm{d}\mathbf{r}_1 \int \mathrm{d}t_2 \int \mathrm{d}\mathbf{r}_2 \chi_{\mathsf{KS}}[\rho_0](\mathrm{r},t,\mathrm{r}_1,t_1)\\ &\times \left[\frac{\delta(t_1-t_2)}{|r_1-r_2|} + f_{\mathsf{xc}}[\rho_0](\mathbf{r}_1,t_1,\mathbf{r}_2,t_2)\right]\chi[\rho_0](\mathrm{r}_2,t_2,\mathrm{r}',t')\end{aligned} \tag{4.55}$$

which is known as a Dyson-like equation [136].

Having the KS orbitals for the ground state, the previous problem can be reformulated in terms of matrix-vector equations. The excitation energies can be found by solving the Casida equations

$$\begin{pmatrix}\mathbf{A} & \mathbf{B}\\ \mathbf{B}^* & \mathbf{A}^*\end{pmatrix}\begin{pmatrix}\mathbf{X}_n\\ \mathbf{Y}_n\end{pmatrix} = \omega_n\begin{pmatrix}1 & 0\\ 0 & -1\end{pmatrix}\begin{pmatrix}\mathbf{X}_n\\ \mathbf{Y}_n\end{pmatrix} \tag{4.56}$$

where $\mathbf{A}$ and $\mathbf{B}$ are obtained from the difference energy for KS orbitals and from the expectation values of the exchange-correlation kernel

$$A_{ar,bs} = (\epsilon_r - \epsilon_a)\delta_{ab}\delta_{rs} + \langle rb\,|\,as\rangle + \langle rb\,|\,f_{\mathsf{xc}}\,|\,as\rangle \tag{4.57a}$$

$$B_{ar,bs} = \langle rs\,|\,ab\rangle + \langle rs\,|\,f_{\mathsf{xc}}\,|\,ab\rangle \tag{4.57b}$$

where $\langle ij\,|\,f_{\mathsf{xc}}\,|\,kl\rangle$ consists in the two-electron Coulomb integrals with the exchange-correlation kernel instead of r_{12}^{-1}. Thus, we find similar equations for TD-HF (eq. (4.17)) and TD-DFT (eq. (4.56)), with $\mathbf{A}$ and $\mathbf{B}$ defined with r_{12}^{-1} and f_{xc} for TD-HF and TD-DFT, respectively. Similarly, the solutions of eq. (4.56) are twofold, with the onward transitions $\mathbf{X}_n$ and the backward transitions $\mathbf{Y}_n$. Neglecting the latter is known as the Tamm-Dancoff approximation (TDA), which in practice corresponds to $\mathbf{B} = \mathbf{0}$. Such a final approximation yields approximate CIS-type equations (eq. (4.16)) for the KS orbitals.

For the rest of this work, when we refer to TD-DFT calculations, we refer to the use of the working equations derived by Casida for the LR-TD-DFT [135, 139]. Unless otherwise specificed, there are no other approximations done for the ground and excited electronic structure of the molecule of interest. To go beyond some approximations, we mention the recent advances of the use of the Bethe-Salpeter equation formalism for quantum chemistry [140, 141].

Take-home messages

1. The Runge-Gross theorems allow one to rewrite the time-dependent external potential as a functional of the time-dependent density and of the initial electronic ground state.
2. The Kohn-Sham scheme is also extended to the time-dependent flavor The time-dependent exchange-correlation potential depends on both the electronic ground state of the interacting and non-interacting systems (memory effects).
3. The adiabatic approximation consists in neglecting all memory effects in the exchange-correlation potentials.
4. The linear-response theory, applied to the TD-DFT within the adiabatic approximation, yields the Casida equations, for which the solutions are the electronic excitations and de-excitations.
5. The most important limits of TD-DFT is the estimation of the transition energy toward charge transfer states and the absence of double excitations.

4.4 Computational and practical details

We briefly expose the computational details for all the electronic structure calculations presented in this thesis. Unless otherwise specified, the `Gaussian16` package (revision `A.03` [142]) has been used for all calculations. In general, we use the DFT for the electronic ground state and the linear-response TD-DFT for the electronic excited states. The TDA is in general turned off, such that the TD-DFT calculations are to be interpreted as a true linear response from the excitation of the electronic ground state. The chosen level of theory is CAM-B3LYP/6-31+G* for which the validity (for the electronic transitions of the molecules of interest here) has been assessed against experiments [41, 42, 143]. The functional CAM-B3LYP is a range-separated hybrid functional, defined in section 4.3.1.3. The basis of atomic orbitals is 6-31+G*

which belongs to the family of Gaussian-type atomic orbitals (GTOs), or Pople basis sets [144, 145]. The number “6” stands for the use of six Gaussian functions to describe the orbitals associated to the core shell of the atoms. The numbers “31” stand for the use a split-valence double-zeta scheme for the valence electrons of the atoms. The orbitals are polarized (superscript *) by adding d orbitals for the atoms with a np^x valence shell. Diffuse orbitals ($+$) are added (adding $n+1$-type orbitals for atoms with a nl^x valence shell) [146, 147].

Geometry optimizations for minima and transition states are done using the widely used optimization algorithm of Schlegel [148] and its variants implemented in `Gaussian16`. As regards energy derivatives, the energy gradients and Hessians are computed analytically for ground and electronic excited states [149, 150]. For TD-DFT calculations, the electronic transition dipole moments (ETDMs) are also obtained for each transition. The oscillator strengths are given in the “length gauge” [151].

Finally, steady-state spectroscopy calculations in the framework of the Franck-Condon principle (Born-Oppenheimer and Condon approximations) are done using the FCHT module with the adiabatic Hessians flavor [82, 152, 153]. The Franck-Condon (zeroth order in the ETDM) and Herzberg-Teller (first order in the ETDM, for symmetry-forbidden electronic transitions) contributions to the absorption and emission electronic (and vibronically resolved) spectra can thus be computed.

Part II

Quantum Dynamics Simulations around PPEs' Conical Intersections

Intermediate Abstract

In this part, we characterize three poly(phenylene ethynylene) (PPE) oligomers that are building blocks for the light-harvesting PPE-dendrimer presented in chapter 1. For the three cases, we characterize the electronic excited states *via* their excitation energies and chemical characters, as well as their minima, transition states and minimum-energy conical intersection geometries.

In chapter 5, we focus on the chromophores of PPE-dendrimers (the symmetrically di-*meta*-substituted phenylene) and their steady-state spectroscopy properties. In particular, we devise models of potential energy surfaces for the strongly-coupled electronic excited states of the chromophore unit. These models serve for running nonadiabatic quantum dynamics to investigate the vibronic eigenstates of the molecule and identify the involved electronic-vibrational (vibronic) transitions for both absorption and emission spectra.

In chapter 6, we propose a framework for studyding excitation-energy transfer (EET) in the first unit of PPE-oligomer that exhibit it: the asymmetrical di-*meta*-substituted phenylene node with branches of two and three phenyl rings, respectively. We identify the most prominent nuclear motions to correctly describe the EET process and propose a time-resolved analysis of correlated electronic and vibrational transfers. We also propose an extension toward a more systematic construction of high-dimensional models of EET in such molecules.

Finally, in chapter 7, we extend the previous framework of characterization for EET to the first generation of PPE-dendrimers. The molecule of interest is now a tri-substituted phenylene node, where more excitation channels are available for the absorption of light than in the previously studied unit. Similarly, we identify the main features of the mechanism of EET within a more involved landscape of both electronic excited states and vibrations in the molecule.

Parts of the results presented for the chromophore and for the first unit for EET have been published [154, 155].

Chapter 5

The Chromophore of the PPE-dendrimers, 1,3-bis(phenylethynyl)benzene

> *"Les états électroniques, ils sont ce qu'ils sont. Mais..."*
>
> – Benjamin Lasorne, *Everyday of this PhD*

As we have seen in the chapter 1, π-conjugated dendrimers are known for their light-harvesting properties, for which the efficiency depends on two crucial ingredients: the nature of the chromophores and the graph structure of the dendrimer skeleton. A common choice for the dendrimer skeleton is an extended structure, where the chromophores are the "leaves" of a "tree-like" dendrimer with longer "branches" from the periphery to the core of the light-harvesting molecule. In this thesis, we study extended dendrimers of poly(phenylene ethynylenes) (PPEs) where the chromophores and the skeleton are made of the same "sites", *para*-conjugated benzenes and acetylenes. The primary chromophores in PPE-dendrimers are diphenylacetylenes (DPAs or tolane, called p2 in the following) and the features of PPE-dendrimers stem from the local excitations (LE) on the peripheral DPAs, p2 units.

This chapter focusses on the characterization and study of this first (chromophore) building block of the PPE-dendrimers. More rigorously, the effective chromophores of the PPE-dendrimers are the 1,3-bis(phenylethynyl)benzene fragments (called m22 in the following), which – in fact – can be seen as two DPAs units sharing one central *meta*-substituted phenylene ring [42]. The principal aim of this study is to explore plausible explanations for the rather unusual UV-visible spectra of the m22 PPE-oligomer. The first observation is the strong resemblance between the absorption spectra of the simple unit p2 and the symmetrically *meta*-substituted unit m22 (fig. 5.1, blue lines).

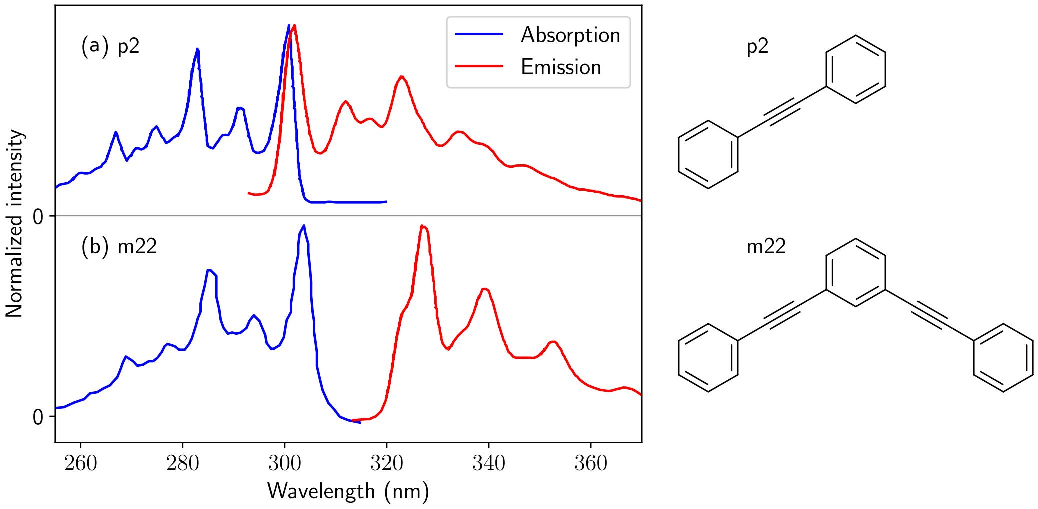

Figure 5.1: Left: Absorption (blue lines) and emission (red lines) experimental spectra of diphenylacetylene (panel a, p2) and 1,3-bis(phenylethynyl)benzene (panel b, m22), measured at $-198\,°\mathrm{C}$ $(75\,\mathrm{K})$. Data reproduced with permission from Q. Chu and Y. Pang, Spectrochim. Acta A **60**, 1459 (2004) [39]. Right: Lewis structures at the ground-state equilibrium geometry of diphenylacetylene (p2) and 1,3-bis(phenylethynyl)benzene (m22).

This *additivity* of the UV-visible spectra was already identified more generally in PPE-dendrimers with p2 primary units, and was attributed to the LE character of the excited states of m22. This was further rationalized *via* a *pseudofragmentation* scheme of m22 into two p2 units sharing a central ring, consistent with the electronic state characters [19, 42]. Thus, the absorption of light by the chromophore m22 simply boils down, from this point of view, to the absorption of light by two distinct but equivalent p2 units.

On the other hand, steady-state UV-visible spectroscopy shows that the emission spectrum of m22 is completely different from the emission spectrum of p2 (fig. 5.1, red lines) [19, 37, 39]. The difference between the maxima of absorption and emission (the *Stokes shift*) in m22 was measured at low temperature as $\Delta\bar{\nu} \simeq 2300\,\mathrm{cm}^{-1}$. As can be seen from the UV-visible spectra, this Stokes shift does not correspond to the usual hypothesis of strong changes in equilibrium geometry, which generally holds for bell-shaped absorption and emission spectra (see fig. 5.2).

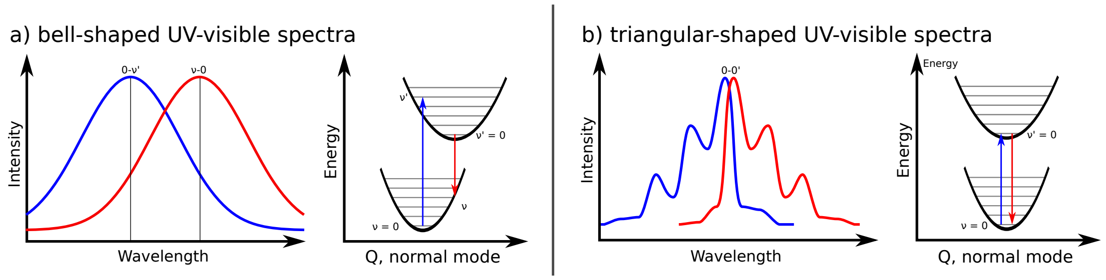

Figure 5.2: Schematic representation of usual absorption and emission vibronic spectra (blue and red lines), with simplified one-dimensional potential energy profiles for strongly shifted (a) and unshifted (b) harmonic oscillators for the electronic ground and excited states.

We thus qualify this shift as being unusual and attribute this character to the fact that it is absent from the UV-visible spectra of p2 and that it cannot be reproduced theoretically within the framework of Born-Oppenheimer and harmonic approximations, as we will further discuss.

This chapter is organized as follows. First, we discuss in section 5.1 the molecular geometries, the excited-state properties, and the normal modes of vibration of the m22 molecule. In section 5.2, we describe simple and low-dimensional modes of coupled diabatic states for studying m22 beyond the Born-Oppenheimer approximation, and propose a simple extension to medium-dimensional models in section 5.3. Finally in section 5.4, we give outlooks for this work and explain how it articulates with the next chapters.

5.1 Time-independent characterization

The electronic ground state and first electronic excited states of 1,3-bis(phenylethynyl)benzene (m22) have already been studied theoretically in previous works. In particular, Emmeline K. Ho and Gabriel Breuil first explored the potential energy surfaces (PESs) and associated electronic states of *para*-substituted oligomers of PPE pn ($n = 2, \dots, 7$) [41] and of the symmetrically *meta*-substituted PPE m22 [42]. In this section, we greatly benifit from their work and present again the most important properties of the electronic states of m22. In particular, we will describe the critical points of the PESs of m22 (minima, transition states, and minimum-energy conical intersections) and the normal modes of vibration of the molecule. This serves as a starting point for discussing all variants of *meta*-substituted PPEs that we have studied in the rest of the thesis.

We briefly recall the computational details. We use DFT and TD-DFT for evaluating electronic ground-state and excited-state energy derivatives, respectively, at the CAM-B3LYP/6-31+G* level of theory (see chapter 4 for more details). The validity of this level of theory for *para*-substituted PPEs has been assessed against experiments [41, 143].

5.1.1 Electronic states and vibrational analysis

The minimum of the electronic ground state is a C_{2v} molecular geometry ($N_{\text{at}} = 36$) and is consistent with the Lewis structure shown in fig. 5.1, right panel. The structure of the local acetylene and phenylene moieties is that of their individual electronic ground state (alternated $\mathrm{C}-\mathrm{C}\equiv\mathrm{C}-\mathrm{C}$ and aromatic patterns, respectively). The singlet electronic excited states from vertical transitions have different symmetry and belong to irreducible representations of the C_{2v} point group (A_1, A_2, B_1, or B_2). The most important pairs of molecular orbitals involved in the transitions $S_0 \longrightarrow S_1$ and $S_0 \longrightarrow S_2$ are shown in fig. 5.3. The first two singlets S_1 and S_2 (vertical transition energies $E = 4.43\,\text{eV}$ and $4.47\,\text{eV}$, respectively) have B_2 and A_1 symmetry, respectively and are almost degenerate ($\Delta E = 0.04\,\text{eV}$) at this geometry. Let us note already that at this C_{2v} geometry, the density differences and the transition densities, also shown in fig. 5.3, are delocalized over the whole molecule and are consistent with the symmetry of the considered excited state.[1]

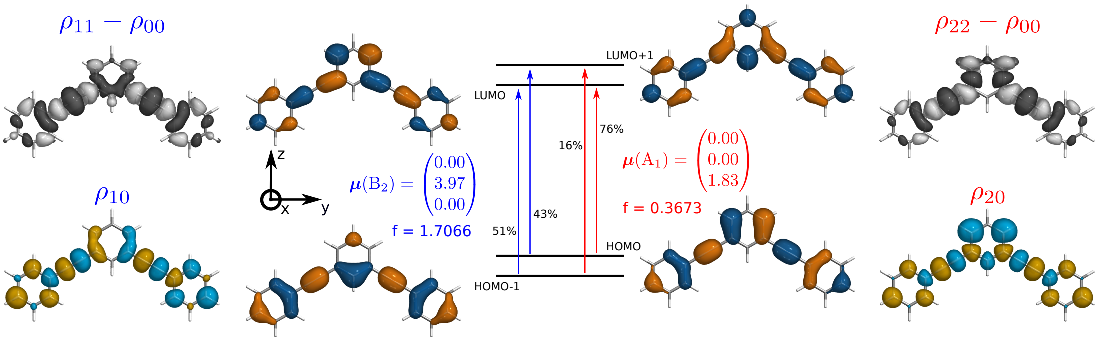

Figure 5.3: HOMO-1, HOMO, LUMO, and LUMO+1 Khon-Sham molecular orbitals at the minimum of the electronic ground state MinS_0. The electronic transition dipole moments (ETDMs) are given (in atomic units) for the first two vertical transitions. The vertical ETDM from S_0 to $S_1 = {}^1B_2$ (in blue) is polarized along the y-axis. The vertical ETDM from S_0 to $S_2 = {}^1A_1$ (in red) is polarized along the z-axis. The main two one-electron transitions between the molecular orbitals are given, with the corresponding weights. The density differences and the transition densities from the ground state to both excited states are also shown (grey/white and cyan/yellow isovalues, respectively).

We also computed the normal modes of vibration ($N_{\text{vib}} = 102$), which belong to the irreducible representations of the C_{2v} point group. Let us note already that the in-plane modes belong to either the A_1 or B_2 irreducible representations. Unless otherwise specified, the normal modes of vibration are computed

---

[1] A program for the re-construction of the transition density using the NTO calculation implemented in the `Gaussian16` package is available at `https://github.com/jwjgaliana/toolbox-qcqd/blob/main/TransitionDensity.py`

after prior i) separation of the translational and rotational normal modes and ii) projection in a basis of internal coordinates.

In the rest of this chapter, this geometry will be referred to as the Franck-Condon (FC) geometry (or MinS$_0$) and the normal modes, accordingly, will also be referred to as the FC normal modes or S$_0$ normal modes. This will have its importance later on for understanding the issue of mode mixing in the electronic excited states. In this work, we focus on the in-plane normal modes of vibration (symmetry A$_1$ and B$_2$ in the C$_{2v}$ point group). A selection of relevant in-plane normal modes is shown in fig. 5.4, illustrated by their associated Cartesian displacements from the minimum geometry of S$_0$. The main characteristics of these normal modes are gathered in table 5.1.

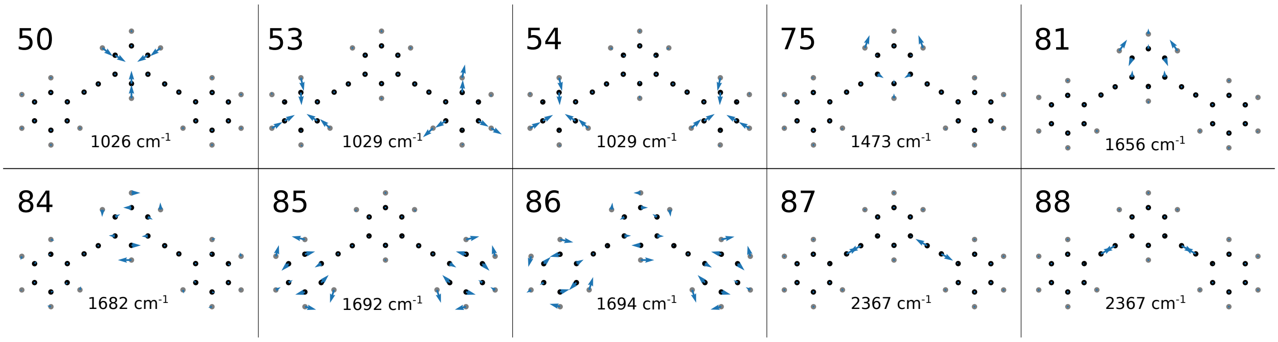

Figure 5.4: Geometry of m22 at MinS$_0$ (carbon and hydrogen nuclei in black and grey, respectively) and Cartesian displacements (blue arrows) associated to a selection of 10 normal modes of vibration. These normal modes are either A$_1$ (50, 54, 75, 81, 85, and 88) or B$_2$ (53, 84, 86, and 87) in the C$_{2v}$ point group.

Table 5.1: Symmetry label in the C$_{2v}$ point group, chemical nature, frequency (wavenumber in cm^{-1}) and reduced masses (in AMU) of a reduced selection of 10 in-plane normal modes of vibration at the FC geometry of m22.

Mode	50	53	54	75	81	84	85	86	87	88
Symmetry	A$_1$	B$_2$	A$_1$	A$_1$	A$_1$	B$_2$	A$_1$	B$_2$	B$_2$	A$_1$
Nature	Tria.	Tria.	Tria.	Quin.	Quin.	Quin.	Quin.	Quin.	Acet.	Acet.
$\bar{\nu}$ (cm^{-1})	1026	1029	1029	1473	1656	1682	1692	1694	2367	2367
μ (AMU)	6.2	6.2	6.2	3.7	5.5	5.9	5.8	5.9	12.0	12.0

In particular, we will distinguish four types of prominent modes:

- phenylene triangular stretching modes (50, 53 and 54);
- quinoidal stretching modes (81, 85 and 86);
- anti-quinoidal rock-bending modes (75, 84);
- and acetylenic stretching modes (87 and 88).

Each mode considered in this chapter is either A_1 or B_2 in the $\mathrm{C}_{2\mathrm{v}}$ point group (in-plane totally or non-totally symmetric modes) or A' in the C_s point group (totally symmetric, in-plane modes). This selection of normal modes is based on prior identification of the optically active modes in steady-state absorption spectroscopy [41, 42].

Within the $\mathrm{C}_{2\mathrm{v}}$ molecular geometries, the PES of the first electronic excited state S_1 has two transitions states, of B_2 and A_1 symmetry, respectively. Their energies in the first excited state are $E^{\mathrm{TS}}(\mathrm{B}_2) = 4.25\,\mathrm{eV}$ and $E^{\mathrm{TS}}(\mathrm{A}_1) = 4.29\,\mathrm{eV}$ with imaginary frequencies $\omega^{\mathrm{TS}}(\mathrm{B}_2) = i4890\,\mathrm{cm}^{-1}$, and $\omega^{\mathrm{TS}}(\mathrm{A}_1) = i15\,110\,\mathrm{cm}^{-1}$. The imaginary frequency associated to the two TS geometries are consistent with the closeness to a CoIn seam. What we mean is that the strong "negative" value of the TS curvature (imaginary frequency) is caused by the second order Jahn-Teller effect, which makes negative the curvature of the lower lying excited state. The Cartesian displacements associated to the imaginary frequency of both TS are given in fig. 5.5. The two normal modes with imaginary frequencies are similar in their displacements together, and also with the non-totally symmetric acetylenic normal mode in S_0.

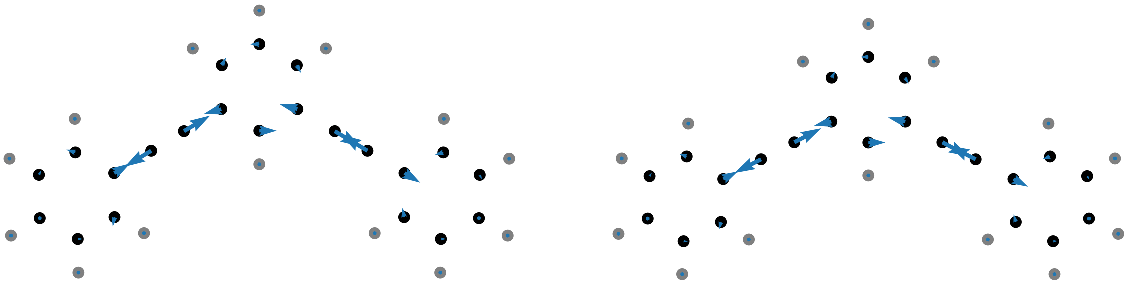

Figure 5.5: B_2 Cartesian displacements associated to the imaginary frequency of each of the two transition states (TS) B_2 and A_1 (left and right, respectively) in the first excited states of m22.

In addition, the PES of the S_1 excited state has two equivalent mirror-image C_s minima with $E = 4.12\,\mathrm{eV}$. Each of these minima is consistent with a local excitation (LE) on either of the p2 *pseudo* fragments of m22 (left and right, for instance, in the chosen orientation), see fig. 5.6 for the Lewis structures and fig. 5.7 for the interpolation between two geometries.

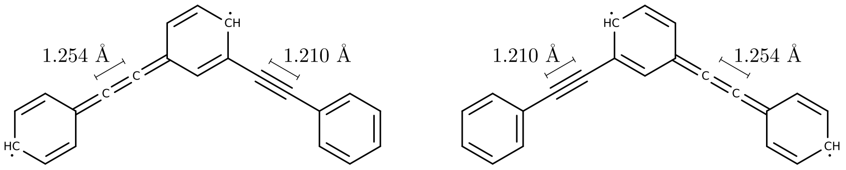

Figure 5.6: Lewis structures at the C_s geometry of the two equivalent minima of the electronic excited state S_1. Distances of the acetylenic bonds are given in Å.

Accordingly, the symmetry of the excited state is A' at the minima of S_1. The underlying molecular transition involves the promotion of an electron from a bonding to an antibonding orbital with respect to the acetylenic bond, consistent with an intermediate cumulenic $\mathrm{C}=\mathrm{C}=\mathrm{C}=\mathrm{C}$ bonding pattern for the equilibrium geometry MinS_1. With the symmetry-breaking from $\mathrm{C}_{2\mathrm{v}}$ to C_s, the S_1 normal modes are now localized on one or the other of the p2 *pseudo* fragments.

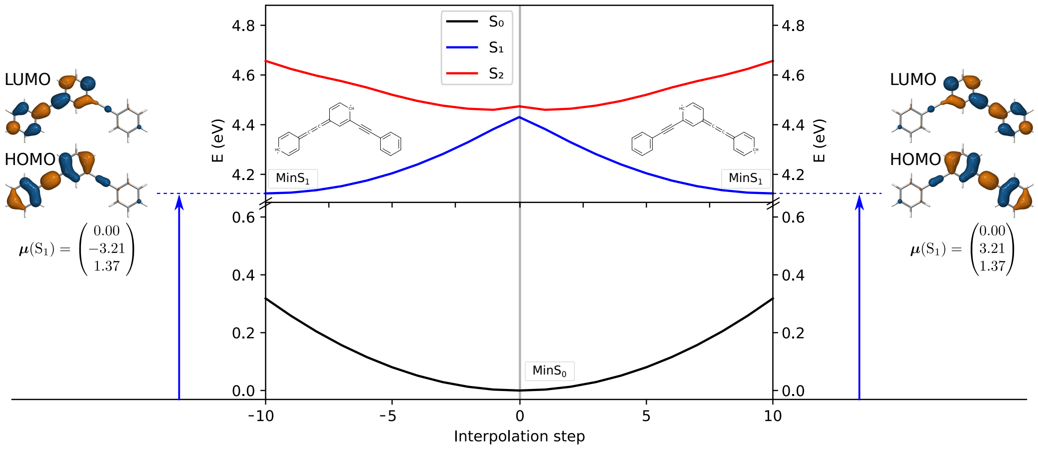

Figure 5.7: 1D-cut of the S_0, S_1, and S_2 PES from the FC geometry to the MinS_1 geometries (left and right). The HOMO-LUMO transition (82% of the $S_0 \longrightarrow S_1$ transition) is also represented at the minima of S_1, with the associated electronic transition dipole moment $\boldsymbol{\mu}(S_1)$ (in atomic units) in the standard axes of the C_{2v} point group.

Finally, to better understand the topology of the S_1-S_2 *coupled* PESs, we search for the minimum-energy conical intersection (MECI) between the two considered states. The MECI is optimized by minimizing the energy average $\bar{E}$ under the constraint that the energy difference $\Delta E = \frac{E(S_2)-E(S_1)}{2}$ is below a given threshold ($\Delta E < 5 \times 10^{-5}\, E_h$). Hence at the MECI geometry, the gradient average vector

$$\mathbf{s} = \frac{\partial}{\partial \mathbf{Q}} \left(\frac{E(S_1) + E(S_2)}{2} \right) \tag{5.1}$$

is zero in the intersection space at the MECI and the remaining non-zero part of $\mathbf{s}$ in the branching plane characterizes the *tilt* of the MECI. We found the optimized geometry of the S_1-S_2 MECI as a C_{2v} molecular geometry with $\bar{E} = \frac{E(S_1)+E(S_2)}{2} = 4.29\,\text{eV}$, in agreement with previous work [42]. Further characterization of the MECI arises from the nature of the branching-space vectors. The MECI couples a pair of B_2 and A_1 electronic states, through a pair of branching-space vectors that also belong to B_2 and A_1 irreducible representations. From an adiabatic point of view for this two electronic states, at any C_{2v} molecular geometry, the gradient difference (GD) vector $\mathbf{g}$ is totally symmetric (A_1) and the derivative coupling (DC) vector $\mathbf{h}$ is non-totally symmetric (B_2). This condition for the DC vector comes from the nature of the symmetry-adapted electronic states B_2 and A_1

$$\Gamma(S_1) = B_2 \text{ and } \Gamma(S_2) = A_1 \text{ so that } \Gamma(S_1) \otimes \Gamma(S_2) = B_2. \tag{5.2}$$

As described in chapter 2, the branching-space vectors $(\mathbf{x}_1, \mathbf{x}_2)$ can be obtained upon the diagonalization of the Hessian of the squared energy difference $\mathbf{K}_{\text{SED}}$. By construction, the re-scaled eigenvectors $(\mathbf{x}_1, \mathbf{x}_2)$ are orthogonal. In addition, the Hellmann-Feynman DC and GD vectors belong to the irreducible representations B_2 and A_1, respectively and are orthogonal. As a result, the re-scaled eigenvectors $(\mathbf{x}_1, \mathbf{x}_2)$

directly identify to the branching-space vectors DC and GD, namely $(\mathbf{h}, \mathbf{g})$. We illustrate the Cartesian displacements associated to the DC and GD vectors in fig. 5.8, left and right, respectively. As stated previously, the DC vector $\mathbf{h}$ is B_2 and from visual comparison with the S_0 normal modes, it is mostly a linear combination of the non-totally symmetry acetylenic stretching mode 87 and the anti-quinoidal rock-bending mode 84. On the other hand, the GD vector $\mathbf{g}$ is A_1 and mostly a linear combination of the central quinoidal stretching mode 81 and the totally symmetric acetylenic stretching mode 87. Similarly, the gradient average vector $\mathbf{s}$, related to the *tilt* of the MECI, is A_1. We project the GD and DC vectors onto S_0 normal modes and give the corresponding components of the branching-space vectors, along with the proportion to the total vectors, in table 5.2.

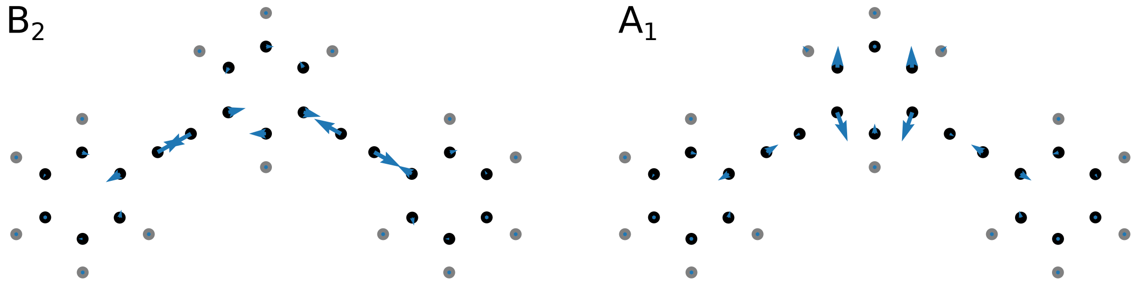

Figure 5.8: Geometry of m22 at the S_1-S_2 MECI (carbon and hydrogen nuclei in black and grey, respectively) and Cartesian displacements (blue arrows) associated the numerical evaluation of the branching-space vectors (BSV) of the MECI at this geometry. The BSV on the left and right are associated to the highest and lowest non-zero eigenvalues of the Hessian of the squared energy difference, respectively.

Table 5.2: Projection of the derivative coupling, gradient difference, and gradient average vectors ($\mathbf{h}$, $\mathbf{g}$, and $\mathbf{s}$, respectively) along the selected S_0 normal modes of vibration. Associated contributions to the full vectors are given in the last three columns (in percentages). Columns to the right give the mass-weighted shift between the critical point geometries of the PESs and the FC geometry of m22 (in $a_0\sqrt{m_e}$).

Mode	Sym.	$\mathbf{h}$	$\mathbf{g}$	$\mathbf{s}$	$\%\mathbf{h}$	$\%\mathbf{g}$	$\%\mathbf{s}$	FC-MinS_1	FC-TS(B2)	FC-TS(A1)	FC-MECI
50	A_1	0.000	-0.021	-0.021	0.0	1.3	1.4	-4.897	-4.132	-6.965	-6.749
53	B_2	0.071	0.000	0.000	0.6	0.0	0.0	3.883	0.000	0.000	0.000
54	A_1	0.000	-0.011	-0.010	0.0	0.4	0.3	-4.851	-5.121	-3.311	-4.196
75	A_1	0.000	0.077	0.074	0.0	17.8	17.9	-0.987	-2.125	1.795	1.712
81	A_1	0.000	-0.119	-0.115	0.0	42.6	42.7	-4.014	-2.777	-7.888	-7.688
84	B_2	-0.383	0.000	0.000	17.8	0.0	0.0	-6.882	0.000	0.000	0.000
85	A_1	0.000	0.067	0.064	0.0	13.6	13.4	-4.110	-5.120	-2.654	-2.702
86	B_2	-0.066	0.000	0.000	0.5	0.0	0.0	-1.274	0.000	0.000	0.000
87	B_2	-0.776	0.000	0.000	72.9	0.0	0.0	7.254	0.000	0.000	0.000
88	A_1	0.000	-0.059	-0.055	0.0	10.4	9.8	-7.593	-7.904	-6.599	-6.894
Sum					91.8	86.0	85.6				

From this selection of relevant critical points in the adiabatic PESs of S_1 and S_2, we notice that the transition state geometries (C_{2v}) are really close to the S_1-S_2 minimum-energy conical intersection (MECI), with energy differences below 0.1 eV. On the other hand, the MinS_1 geometries (C_s) exhibit much larger energy difference. This is the basis for our discussion of the S_1-S_2 PES of m22: from a C_{2v} geometry toward a C_s geometry, the electronic degeneracy is strongly lifted. On the other hand, along a line of C_{2v} geometries, the electronic degeneracy is slowly varying. The energy landscape for the S_1 and S_2 electronic state is summarized in fig. 5.9 with 2D-interpolations from the FC geometry to i) the MECI geometry and ii) the MinS_1 geometries.

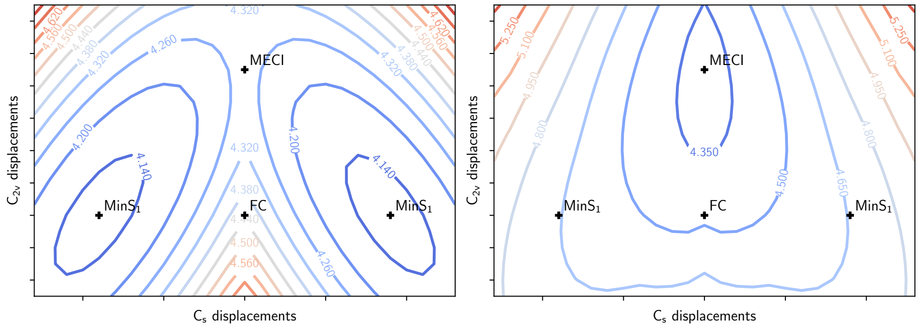

Figure 5.9: 2D-interpolations of S_1 and S_2 PESs from the FC geometry to MinS_1 minima (C_s displacements) and from the FC geometry to the MECI (C_{2v} displacements).

We gather in table 5.3 the energy of the electronic ground and excited states for the discussed critical points in the PESs of m22 (minima, TS, and MECI). The geometry of these points is compared to the geometry of MinS_0. To do so, we compute the mass-weighted shift vector of the coordinates of the current geometry (minima, TS, MECI) from the reference geometry (MinS_0)

$$\Delta\mathbf{R}^{\text{mw}} = (\mathbf{R}(\text{current}) - \mathbf{R}(\text{reference})) \cdot \mathbf{M}^{\frac{1}{2}} \tag{5.3}$$

and project it onto the normal modes of vibration of MinS_0

$$d_i = \Delta\mathbf{R}^{\text{mw}} \cdot \mathbf{L}_i^{\text{mw}}(\text{S}_0) \quad \forall i \text{ normal mode.} \tag{5.4}$$

In general, we shall give these "shift components" in mass-weighted atomic units, $a_0\sqrt{m_e}$. Such quantities are gathered in the last columns of table 5.2 for the previously mentioned S_0 normal modes of vibrations. In the following, we often refer to these shifts with respect to the FC geometry to describe the PESs of m22. For instance, from the column-entry "FC-MinS_1" in table 5.2 we read that the C_s minimum of S_1 is displaced of about $\pm 7\, a_0\sqrt{m_e}$ along both acetylenic stretching normal modes of S_0 (87 and 88). This is consistent with a localized excitation on one of the p2 *pseudo* fragment. Indeed, the $\pm$ combinations of 87 and 88 yield localized acetylenic stretching modes on the left or right p2 *pseudo* fragments. This is also consistent with the mode mixing between the normal modes of S_0 at MinS_0 and the normal modes of S_1 at MinS_1.

Table 5.3: Adiabatic energies (in eV) of the electronic ground state and first two electronic excited states for a selection of critical points in p2 and m22. The minimum of the electronic ground state is taken as the reference energy for each molecule. For transition-state geometries, the imaginary frequency is also given (in cm^{-1}). The lengths of the acetylenic bonds are given ($d(\mathrm{C}\equiv\mathrm{C})$ in Å). For m22 MinS$_1$, the value (in bold) is given for the $\mathrm{C}\equiv\mathrm{C}$ bond in the excited part of the molecule; the other bond length is 1.210 Å.

Geometry	$E(\mathrm{S}_0)$	$E(\mathrm{S}_1)$	$E(\mathrm{S}_2)$	$E(\mathrm{S}_2)-E(\mathrm{S}_1)$	ω^{TS}	$d(\mathrm{C}\equiv\mathrm{C})$
p2 MinS$_0$	0.00	4.48	5.08	0.60		1.210
p2 MinS$_1$	0.32	4.14	4.84	0.70		1.255
m22 MinS$_0$	0.00	4.43	4.47	0.04		1.210
m22 MinS$_1$	0.32	4.12	4.66	0.54		**1.254**
m22 TS B$_2$	0.18	4.25	4.33	0.08	$\mathrm{i}4890$	1.233
m22 TS A$_1$	0.19	4.29	4.30	0.01	$\mathrm{i}15110$	1.229
m22 MECI	0.19	4.29	4.29	$<$ 0.0001		1.230

Take-home messages

1. The MinS$_0$ geometry of the m22 molecule is a C$_{2v}$ molecular geometry and exhibit almost degenerate vertical excitations toward the S$_1$ and S$_2$ states, of symmetry B$_2$ and A$_1$, respectively.
2. The S$_1$ PES has two transition states in the C$_{2v}$ molecular space and two equivalent ("left" and "right") minima in the C$_s$ molecular space.
3. The MECI between the S$_1$ and S$_2$ states has been found, with a branching space mostly expanded on the B$_2$ acetylenic stretching (for the derivative coupling) and on the A$_1$ quinoidal stretching (for the gradient difference). The MECI connects the two "left" and "right" LE states of the m22 molecule.
4. In the following, one choice for a pair of diabatic states will be this pair of localized excited states, both having A' symmetry in the C$_s$ point group. Another choice for a pair of diabatic states will be the electronic states having A$_1$ or B$_2$ symmetry. In contrast to the pair of localized diabatic states, the A$_1$ and B$_2$ diabatic states will be referred to as delocalized because they belong to irreducible representations of the C$_{2v}$ point group.

5.1.2 Describing the PESs around the MECI

Until now, we only described the S_1 and S_2 PESs from optimized critical points or interpolations between them. From now on, we start exploring the high-dimensional PESs of m22 *via* 1D- or 2D- cuts (profiles and surfaces, respectively) along specific directions. Choices have to be made regarding:

- the reference point for the PES cut origin;
- the direction to follow from the reference point.

In the following, we often refer to PES cuts as "rigid scans" along given directions (typically, normal-mode Cartesian displacements, or combinations of them). For this section, we consider PES cuts along the branching-space vectors, from the MECI, see fig. 5.10.

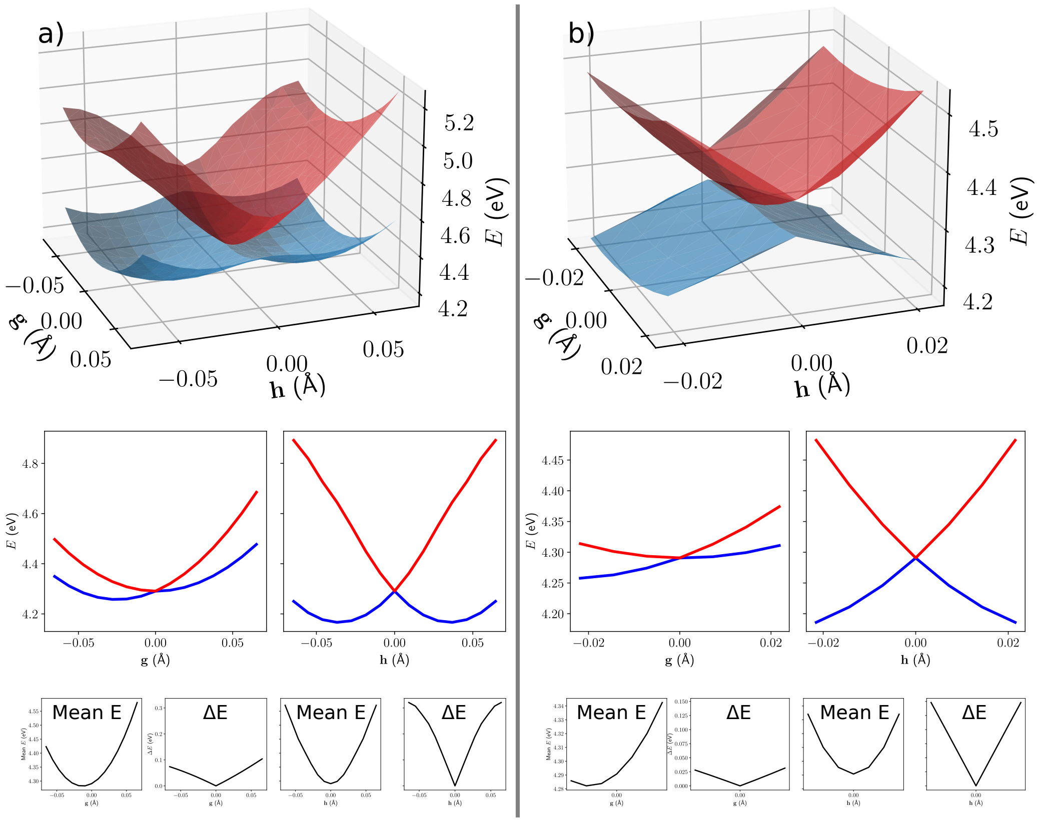

Figure 5.10: Upper panels: 2D-cuts of the S_1 and S_2 adiabatic PESs along the branching-space vectors $\mathbf{h}$ and $\mathbf{g}$, from the MECI geometry. Lower panels: 1D-cuts along $\mathbf{h}$ (lower left) and $\mathbf{g}$ (lower right) vectors from the MECI geometry. The right panels (b) present a zoomed representation of the PESs (smaller displacements) around the MECI (linear regime).

In other words, we explore the branching plane around the MECI. With our symmetry-based definitions, the A_1 GD vector $\mathbf{g}$ connects roughly the C_{2v} MECI and the two C_{2v} transitions states which are apparent minima of S_1 (either A_1 or B_2) in the C_{2v} subspace projected out of the DC vector $\mathbf{h}$. These C_{2v} geometries will be identified as minima of delocalized diabatic electronic states. The DC vector $\mathbf{h}$ connects the C_{2v} geometry of the MECI to the two equivalent minima in the C_s point group. As expected, the energy profiles are even with respect to the non-totally symmetric displacements (DC, coupling vector $\mathbf{h}$ expanded along B_2 normal modes) and arbitrary with respect to the totally symmetric displacements (GD, tuning vector $\mathbf{g}$ expanded along A_1 normal modes).

5.1.3 A first note on localized *vs.* delocalized representations

Localized representations of molecular orbitals and normal modes of vibration

As we pointed out, two types of molecular geometries are relevant in the S_1 PES of m22: C_{2v} and C_s geometries. Consequently, the molecular orbitals and normal modes of vibration adapt to the C_{2v} symmetry (they are delocalized) or to the C_s symmetry (they are localized). When the reference is the FC geometry, the delocalized electronic and vibrational properties are natural. On the other hand, the localized properties arise naturally when the reference is one or the other of the two equivalent C_s minima in S_1. However, both delocalized or localized properties can be used to characterize the two types of geometries. For instance, it has been shown that the frontier orbitals at the FC geometry can be combined together to form localized orbitals on the two p2 *pseudo* fragments [19, 42]. Indeed, the normalized sum and difference of the delocalized pairs of HOMO-1/HOMO and LUMO/LUMO+1 at the FC geometry lead to molecular orbitals localized on one or the other of the two p2 *pseudo* fragments (see fig. 5.11). The localized orbitals obtained at the FC geometry are in very good agreement with the localized orbitals obtained in C_s geometries for the minima of S_1.

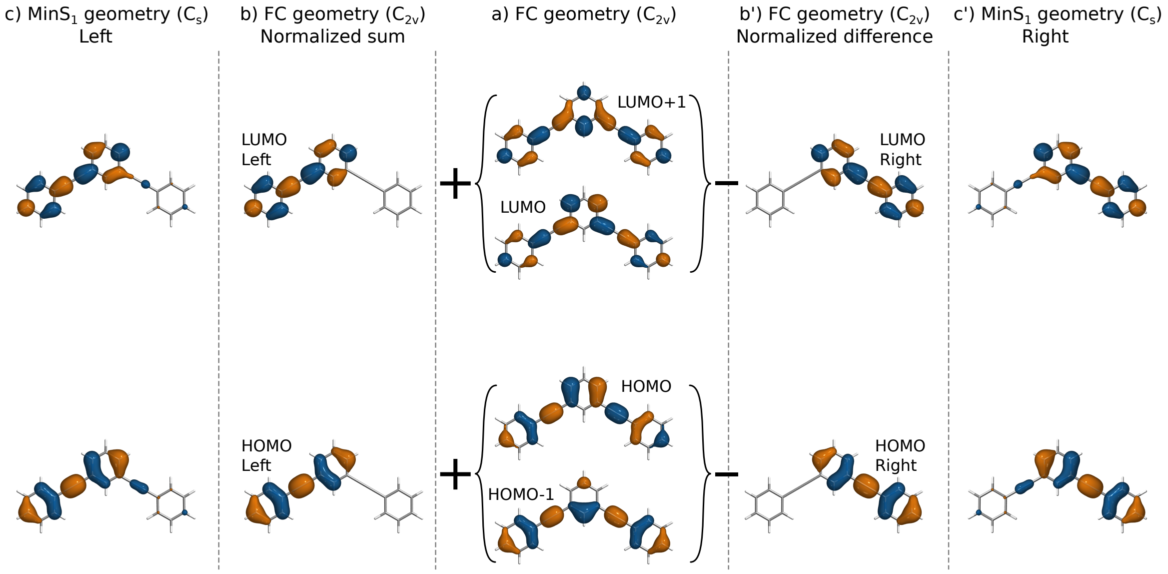

Figure 5.11: a) Delocalized orbitals HOMO-1, HOMO, LUMO, and LUMO+1 at the FC geometry of m22. b) and b') Localized orbitals obtained as the combinations [sum and difference] of (HOMO-1, HOMO) and (LUMO and LUMO+1) at the FC geometry of m22. c) and c') Localized orbitals HOMO and LUMO at the MinS$_1$ geometries of m22 [left and right].

We also observe a localization of the normal modes of vibration computed at the minima of S_1 compared to the S_0 normal modes. This is related to what is usually referred to as mode mixing. At MinS_1, the new normal modes can be expressed in the basis of the S_0 normal modes. More specifically, the overlaps between the two basis sets can be gathered in a single orthogonal matrix, the Duschinsky matrix, such that the displacements along the S_1 normal modes $\mathbf{Q}'$ are expressed as

$$\mathbf{Q}' = \mathbf{J}\mathbf{Q} + \mathbf{d} \tag{5.5}$$

where $\mathbf{J}$ is the Duschinsky matrix, $\mathbf{Q}$ are the displacements along the S_0 normal modes and $\mathbf{d}$ is the shift vector, defined in eq. (5.4). The Duschinsky matrix is the generalization of a rotation matrix for the $3N-6$ normal mode coordinates, transforming displacements viewed from the S_0 normal modes to displacements viewed from the S_1 normal modes. A visual example for this is the transformation of the acetylenic stretching modes 87 and 88. For instance, as regards the acetylenic stretching displacements, we find from the Duschinsky matrix the approximate relations

$$\begin{aligned} Q'_{87} &\simeq 0.99 \times (\cos 42° Q_{87} - \sin 42° Q_{88}) + d_{87} + \sum_{i \neq 87,88} J_{87,i} Q_i, \\ Q'_{88} &\simeq 0.99 \times (\sin 42° Q_{87} + \cos 42° Q_{88}) + d_{88} + \sum_{i \neq 87,88} J_{88,i} Q_i. \end{aligned} \tag{5.6}$$

Thus, modes 87 and 88 at the MinS_1 geometry are approximately (for 99% of the displacements) a rotation of modes 87 and 88 at the MinS_0 geometry, with an angle of about $42°$. Up to a scaling factor, the two pairs of modes are indeed related through plus and minus linear combinations, similarly to the localization strategy used for the molecular orbitals. The main explanation for such simple combinations lies in underlying symmetries (for orbitals and normal modes) of the central benzene (which involves E-type degenerate frontier orbitals and normal modes).

Localized *vs.* delocalized electronic states and potential energy surfaces

Until now, we have characterized the m22 molecule through its PESs critical points and associated normal modes of vibration. We have identified local excitations yielding two equivalent C_s minima, linked together *via* a MECI lying within the C_{2v} molecular geometries. The full picture allows us to understand the first two adiabatic excited states of the molecule as either

- a coupled pair of delocalized, symmetry-adapted, diabatic excited states, $^1A_1$ and $^1B_2$;
- or a coupled pair of equivalent localized diabatic excited states, "right" or "left", $\frac{1}{\sqrt{2}}\left(^1A_1 \pm {}^1B_2\right)$.

We have seen that the main directions for linking the MinS_0, MinS_1/MinS_1' and TS(B_2), TS(A_1), and MECI geometries are in principle the branching-space vectors GD and DC, $\mathbf{g}$ and $\mathbf{h}$, respectively. In the following, we will often refer to either delocalized or localized electronic states. Let us discuss this concept on simple "toy Hamiltonian models" of the generic form

$$H^{\text{deloc}} = S\mathbb{1} + \begin{bmatrix} -D & W \\ W & D \end{bmatrix} \text{ and } H^{\text{loc}} = S\mathbb{1} + \begin{bmatrix} -W & D \\ D & W \end{bmatrix} \tag{5.7}$$

where we suppose here that D and W are smooth functions of the coordinates and are obtained to first order upon displacements along the GD vector $\mathbf{g}$ and the DC vector $\mathbf{h}$, respectively. Similarly, the function S is obtained to first order upon displacements along the gradient average vector $\mathbf{s}$. Let us assume for the sake of simplicity that the shared average potential S bears all quadratic (harmonic) terms and that D and W only consist in linear terms or bilinear cross terms. For $\mathbf{g}$ and $\mathbf{h}$ totally and non-totally symmetric, respectively, the first Hamiltonian in eq. (5.7) consists in a delocalized representation of the PESs, and the second one in a localized representation of the same PESs. Both pair of underlying diabatic states are linked together *via* a Nikitin rotation ($45°$ for the electronic states, $90°$ for the $\mathbf{h}$ and $\mathbf{g}$ vectors) which preserves the adiabatic PESs.

We illustrate the toy models of Hamiltonian with a schematic representation of the associated diabatic potential energies in fig. 5.12 (left for delocalized, right for localized). For a double-well shaped potential energy along the DC vector $\mathbf{h}$, a strong coupling W (linear with respect to $\mathbf{h}$) must exist, and in such a case the delocalized (unshifted along $Q_{\mathbf{h}}$) diabatic states are almost degenerate but strongly coupled (red lines). After a Nikitin rotation, the roles of the GD and DC vectors are swapped, such that we have now the situation of two localized (shifted along $Q_{\mathbf{h}}$) diabatic states (blue lines) but only weakly coupled (*via* the GD vector).

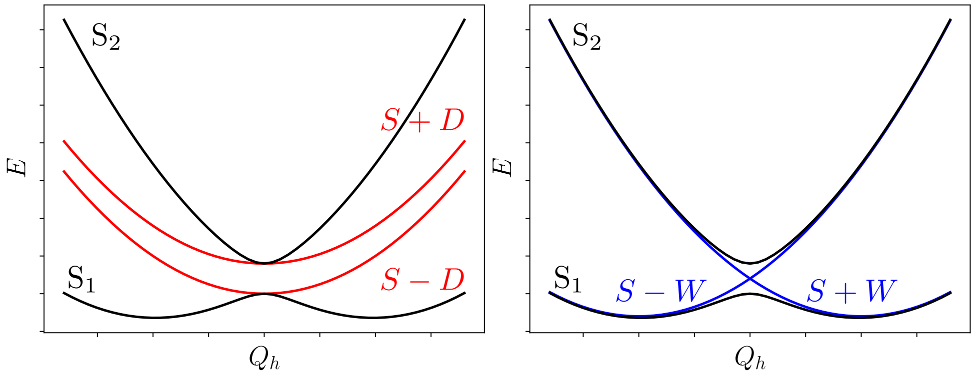

Figure 5.12: Schematic representations of *delocalized* (red) and *localized* (blue) diabatic potential energies, with the same coordinate Q_h. As Q_h linear terms only appear in the W function, Q_h is a coupling coordinate in the delocalized case and a tuning coordinate in the localized case.

Take-home messages

1. The CoIn seam in the S$_1$/S$_2$ manifold is *induced by symmetry* in the sense that the two electronic states are of different symmetry at the MECI geometry.
2. Two equivalent representations, *localized* and *delocalized*, can be used for either i) the electronic states and consequently ii) the molecular orbitals and iii) the normal modes of vibration.

3. They describe the same adiabatic PESs, and are linked together *via* a Nikitin rotation ($45°$) for the electronic states, and role swapping (rotation $90°$) for the branching-space vectors (hence, coupling and tuning vectors).
4. In section 5.2, we will use the convenient delocalized representation to parametrize models of PESs for the S_1/S_2 manifold.

5.1.4 Vibronic spectra within the Franck-Condon framework

We now discuss our first attempts at reproducing the experimental steady-state spectra for m22. One common method is the time-independent framework, where the transitions probabilities are evaluated through the calculation of Franck-Condon factors (FCFs). The usual framework, for instance implemented in the `Gaussian` package, uses the Born-Oppenheimer approximation, the Franck-Condon approximation (Franck-Condon framework), and the harmonic approximation to compute the FCFs [82, 152, 153]. In the following, we often use the notations $n^{v(\mathrm{es})}_{v(\mathrm{gs})}$ where n is the normal mode of vibration for which a transition is observed with vibrational numbers v(es) and v(gs) in the excited and ground states, respectively. For instance, the notation 87^1_0 corresponds to a transition from the electronic ground state with $v_{87}(\mathrm{gs}) = 0$ to the electronic excited state with $v_{87}(\mathrm{es}) = 1$. The 0-0 transition on the other hand is 0^0_0, also termed the band origin, and is unique, with all active modes involved (vibrational overlap $\langle 0 \cdots 0 \,|\, 0 \cdots 0 \rangle$)

Results from Franck-Condon factors calculations

In fig. 5.13 we compare the (low temperature) experimental spectra (a) to the theoretical absorption and emission spectra obtained within the Franck-Condon framework (b and c). We first describe the absorption spectra (blue lines). We observe in spectra b) and c) a difference for the position of the 0^0_0 transition (vibrational overlap $\langle 0 \,|\, 0 \rangle$ for the 0^0_0 transition), compared to the most intense transition in the experimental absorption spectrum.

This difference for the 0^0_0 transition (a few nm) is only a measure of the accuracy of the level of theory for predicting the excitation energies. Yet, we have a good agreement for the vibrational progression of the absorption spectra (comparing a) and b) for instance). The spectra in c) are obtained by “trimming” the spectra in b), selecting only the transitions involving the ten most-relevant normal modes of vibration presented above (the other active modes being mostly triangular quinoidal modes). We can thus note that the small number of selected modes already accounts for most of the vibrational progression in the absorption spectrum. Now looking at absorption *vs.* emission (blue *vs.* red lines), the theoretical spectra exhibit the most intense peak in absorption and in emission is the same wavelength (and is attributed to the 0^0_0 band-origin transition in both cases), with no Stokes shift at all. The next most intense in both absorption and emission spectra are obtained for vibronic transitions involving quinoidal stretching modes

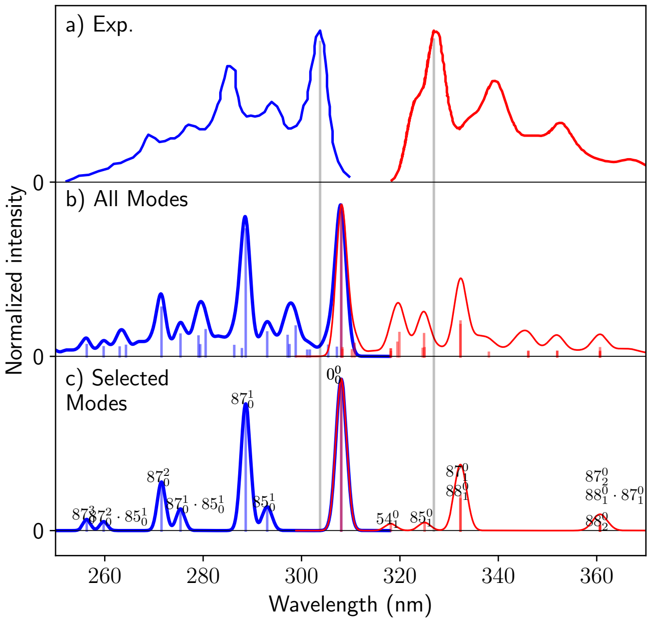

Figure 5.13: Absorption (blue lines) and emission (red lines) steady-state spectra of m22. a) Experimental spectra measured at $-198\,°C$ ($75\,K$). Data reproduced with permission from Q. Chu and Y. Pang, Spectrochim. Acta A **60**, 1459 (2004) [39]. b) Theoretical spectra obtained within the Franck-Condon framework with account of all normal modes of vibration. c) Theoretical spectra obtained by "trimming" with a certain selection of the most prominent normal modes (triangular, quinoidal, and acetylenic nature).

(85) and acetylenic stretching modes (87, 88).

We clearly identify the 0_0^0 transition as the most intense at $0\,K$ from the FCFs calculation, in both absorption and emission spectra. A usual Stokes shift would arise from n_0^v [and/or n_v^0] transitions (strong vibrational overlap $\langle 0 \,|\, v \rangle$ for the mode n), in absorption [and/or emission] for instance, that are greater than the 0_0^0 transition (see again ideal bell-shaped absorption and emission spectra in fig. 5.2)

The main objective of the rest of this chapter is thus to reproduce the Stokes shift that is absent from *routine* Franck-Condon factors calculations of the vibronic spectra. First, we rationalize the observed steady-state spectroscopy problem with a simple 1D model of double-well shaped potential energy profile and 1D Franck-Condon factors.

A minimalistic rationalization of the present problem

We know that the PES of the first excited state of m22 is a double-well with respect to nuclear displacements along some of the B_2 normal modes (in particular along the acetylenic stretching mode with wavenumber $\bar{\nu} \simeq 2300\,\text{cm}^{-1}$). The absorption spectrum is almost not affected by this PES shape, since the absorption spectrum of m22 is the same as the one of p2 (both experimentally and theoretically). Emission is more involved.

Let us consider a centered harmonic potential in the electronic ground state and of the two symmetrically shifted, "uncoupled", harmonic potential energy in the first excited state (L, left and R right, see fig. 5.14).

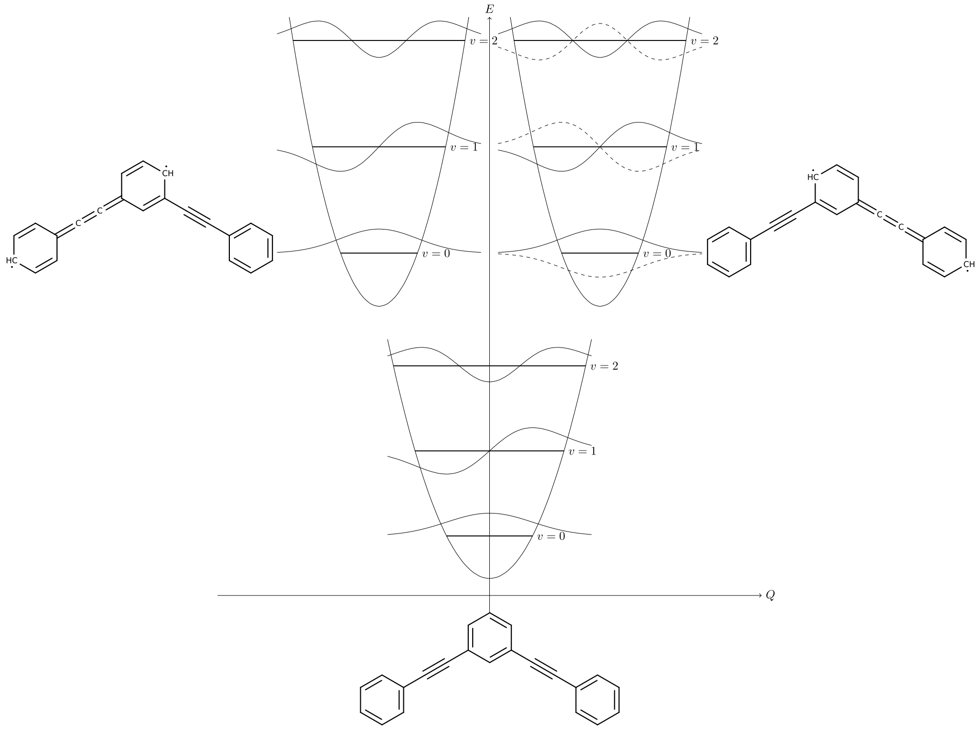

Figure 5.14: Schematic representation of the model harmonic potential energies in the electronic ground and first excited state along a non-totally symmetric displacement.

The potential energies for the two uncoupled electronic excited states represent the two locally excited states in m22, with left and right p2 *pseudo* fragments. With no coupling between the two excited wells, a simple description of the first two vibrational states in the electronic excited states (tunnelling pair) are the renormalized sum and difference of the left and right first vibrational states (neglecting the overlap)

$$|0_{\mathsf{S}}\rangle \simeq \frac{|0_{\mathsf{L}}\rangle + |0_{\mathsf{R}}\rangle}{\sqrt{2}}, \tag{5.8a}$$

$$|0_{\mathsf{A}}\rangle \simeq \frac{|0_{\mathsf{L}}\rangle - |0_{\mathsf{R}}\rangle}{\sqrt{2}} \tag{5.8b}$$

where S and A subscripts stand for symmetric and anti-symmetric, respectively. The two vibrational states are degenerate if the wells are uncoupled. Let us assume we know the 1D FCFs for the left and right wells, separately. With the uncoupled scheme, we can compute the new *generalized* Franck-Condon factors between the ground-state vibrational contributions $|0\rangle$ or $|1\rangle$ and the excited state vibrational contributions $|0_{\mathsf{S,A}}\rangle$. Indeed, we have, using $\langle 0\,|\,0_{\mathsf{L}}\rangle = \langle 0\,|\,0_{\mathsf{R}}\rangle$

$$|\langle 0\,|\,0_{\mathsf{S}}\rangle|^2 = \left(\frac{\langle 0\,|\,0_L\rangle + \langle 0\,|\,0_R\rangle}{\sqrt{2}}\right)^2 \tag{5.9a}$$

$$= \frac{1}{2}\left(\langle 0\,|\,0_L\rangle^2 + \langle 0\,|\,0_R\rangle^2 + 2\,\langle 0\,|\,0_L\rangle\,\langle 0\,|\,0_R\rangle\right) \tag{5.9b}$$

$$= 2|\langle 0\,|\,0_L\rangle|^2 = 2|\langle 0\,|\,0_R\rangle|^2 \tag{5.9c}$$

and using $\langle 1\,|\,0_{\mathrm{L}}\rangle = -\,\langle 1\,|\,0_{\mathrm{R}}\rangle$

$$
\begin{aligned}
|\,\langle 1\,|\,0_A\rangle\,|^2 &= \left(\frac{\langle 1\,|\,0_L\rangle - \langle 1\,|\,0_R\rangle}{\sqrt{2}}\right)^2 && (5.10a)\\
&= \frac{1}{2}\left(\langle 1\,|\,0_L\rangle^2 + \langle 1\,|\,0_R\rangle^2 - 2\,\langle 1\,|\,0_L\rangle\,\langle 1\,|\,0_R\rangle\right) && (5.10b)\\
&= 2|\,\langle 1\,|\,0_L\rangle\,|^2 = 2|\,\langle 1\,|\,0_R\rangle\,|^2. && (5.10c)
\end{aligned}
$$

As a result, the Franck-Condon factors of an uncoupled symmetric double-well shaped harmonic potential boil down to twice the Franck-Condon factors of the separate simple-well harmonic potential. Thus, the transition probability $|\langle 1\,|\,0_A\rangle|^2$ has no reason to be greater than the transition probability $|\langle 0\,|\,0_S\rangle|^2$ if there is not already an unusual Stokes shift for the simple-well situation. Yet, this contribution to the emission spectrum might not be negligible, as in the case of m22.

Thus, for the cases of m22 and p2, we know from the experiments that the simple-well situation (isolated p2) exhibits no Stokes shift. The main idea developed in this chapter is that the vibronic eigenstate in the excited state manifold resembles to some extent a $|0_A\rangle$ vibrational state and that this odd character is possible because of the presence of a conical intersection in the excited state.

Take-home messages

1. It is expected from the simulation of vibronic spectra *via* FCFs calculations that the Stokes shift is not reproduced. Indeed, we identified two distinct localized minima in S_1 for the m22 molecule (that were very similar to locally excited p2 *pseudo* fragment), linked together *via* a MECI with the second excited state S_2.
2. Thus, the absorption spectrum is correctly reproduced because it is as if the absorption took place from the symmetrical ground state to one or the other of the two p2 *pseudo* fragments.
3. The simulation of emission in the Franck-Condon framework is rationalized in the same way: it is as if the emission took place from *one and only one* of the two excited p2 *pseudo* fragments, toward the symmetrical electronic ground state.
4. In the following, we make (and intend to test) the hypothesis that the most intense transition for emission is a of the type ”$n_1^{0,\mathrm{A}}$”, that is, a non-negligible overlap between the first anti-symmetric vibrational state (in the excited states) and the first vibrational state (in the ground state).

We now illustrate this hypothesis with a more rigourous model, explicitly taking into account the coupling between the two electronic states, beyond the Born-Oppenheimer approximation.

5.2 The use of quantum dynamics for steady-state spectroscopy

In this section, we describe vibronic coupling Hamiltonian (VCH) models for the first two electronic excited states of the m22 molecule. We explore the use of linear vibronic coupling (LVC) and quadratic vibronic coupling (QVC) Hamiltonian models, originally proposed by Köppel and co-workers [20]. With these diabatic-by-ansatz, "coupled", PESs, we run nonadiabatic quantum dynamics to estimate plausible contributions to the absorption and emission spectra. Let us stress that the use of quantum dynamics to evaluate transition probabilities from the autocorrelation function has been widely used in the context of absorption, where the initial state is in general not challenging to describe [78, 92]. Here, we extend this strategy to the context of emission spectra, where the nature of the transitions is more complicated to understand notably as regards spontaneous *vs.* stimulated emission.

LVC and QVC for a pair of A_1/B_2 electronic states

We recall that the first two electronic excited states are $^1B_2$ and $^1A_1$ at the FC geometry, respectively. We choose as a pair of diabatic states this pair of so-called crude-adiabatic states at the FC geometry. Neglecting all out-of-plane motions, we restrict ourselve to the study of C_{2v} and C_s planar molecular geometries (A_1 coordinates preserve symmetry, B_2 coordinates break left/right symmetry). The general QVC Hamiltonian model for the B_2 and A_1 delocalized electronic states is

$$\begin{aligned}\hat{H}^{\mathsf{dia}} = {} & \left(\hat{T}_{\mathsf{nu}}(\mathbf{Q})\right)\mathbb{1}_2 + \begin{bmatrix} E^{(1)}(\mathbf{Q}=0) & 0 \\ 0 & E^{(2)}(\mathbf{Q}=0) \end{bmatrix} + \sum_i \begin{bmatrix} \frac{1}{2}k_i^{(1)}Q_i^2 & 0 \\ 0 & \frac{1}{2}k_i^{(2)}Q_i^2 \end{bmatrix} \\ & + \sum_{\substack{i \\ \Gamma_i = \mathsf{A}_1}} \begin{bmatrix} \kappa_i^{(1)}Q_i & 0 \\ 0 & \kappa_i^{(2)}Q_i \end{bmatrix} + \sum_{\substack{i \\ }}\sum_{\substack{j \\ j\neq i, \Gamma_i\otimes\Gamma_j = \mathsf{A}_1}} \begin{bmatrix} \frac{1}{2}\gamma_{i,j}^{(1)}Q_iQ_j & 0 \\ 0 & \frac{1}{2}\gamma_{i,j}^{(2)}Q_iQ_j \end{bmatrix} \\ & + \sum_{\substack{i \\ \Gamma_i = \mathsf{B}_2}} \begin{bmatrix} 0 & \lambda_iQ_i \\ \lambda_iQ_i & 0 \end{bmatrix} + \sum_{\substack{i \\ }}\sum_{\substack{j \\ \Gamma_i\otimes\Gamma_j = \mathsf{B}_2}} \begin{bmatrix} 0 & \frac{1}{2}\mu_{i,j}Q_iQ_j \\ \frac{1}{2}\mu_{i,j}Q_iQ_j & 0 \end{bmatrix}. \end{aligned} \tag{5.11}$$

The eigenvalues of the above Hamiltonian at a given geometry are to be compared with the adiabatic energies obtained from electronic structure calculation (*ab initio* data) at the same geometry. The diabatic parameters can be fitted to the *ab initio* data by computing the eigenvalues of the model (global fit from *ab initio* data). Alternatively, the diabatic parameters can be directly identified to energy derivatives such as gradient vectors, branching-space vectors, and (after some manipulations) Hessians (local fit from *ab initio* data). In either case, in this quite general model,

1. the first matrix represents the kinetic energy operator for the normal modes of vibration (no cross terms), identical for both diabatic states;
2. the second matrix represents vertical transition energies at the reference point $\mathbf{Q} = 0$ from the ground state to the two diabatic excited states;

3. the third matrix represents what would be the distortion matrix in the Franck-Condon framework (diagonal change of curvature between the normal modes in the ground state and in the diabatic excited states);
4. the fourth matrix represents the gradients of energy for the diabatic excited states at the reference point (first-order, linear terms);
5. the fifth matrix represents the gradient of the diabatic inter-state coupling at the reference point (first-order, linear terms);
6. the sixth matrix represents to some extent the normal mode mixing between the S_0 normal modes and the normal modes of the diabatic excited states for modes of same symmetry only (*primary Duschinsky transformation*);
7. the seventh matrix represents to some extent the normal mode mixing between the S_0 normal modes and the normal modes of the diabatic excited states for modes of different symmetry only (*secondary Duschinsky transformation*).

The *primary Duschinsky transformation* is the usual normal mode mixing observed between electronic states of identical symmetry. Indeed, in such a case, all molecular geometries have the same symmetry point group C_{2v}. As a consequence, the Hessian matrices are block-diagonal with symmetry-adapted blocks and the mode mixing occurs only within groups of modes that have the same symmetry (A_1 with A_1, B_2 with B_2). On the other hand, in a case where S_0 normal modes allow symmetry-breaking to occur from one group to another (here, C_{2v} to C_s), the Hessian matrices in the low-symmetry geometries are not block-diagonal with respect to the S_0 normal modes. In particular in our case, this leads to mode mixing between S_0 normal modes of different symmetry (B_2 and A_1). The most striking example of secondary Duschinsky transformation is the localization of the acetylenic stretching modes from the S_0 normal modes to the S_1 normal modes, explicited in eq. (5.6). This will be made clearer when discussing the PESs of the LVC model *vs.* the PESs of the QVC model in a reduced 3-dimensional model of m22 electronic excited states.

The numerical parameters obtained for the LVC and QVC Hamiltonian models presented in this chapter are gathered in appendix B. They are the ready-to-use numerical parameters for encoding the operator files in the `Quantics` package. However, as much as possible, in the corpus of this thesis we present VCH parameters *via* more natural and easy-to-compare equivalent parameters. In particular, for the curvature parameters $k_i^{(s)}$ we give the associated frequency $\omega_i^{(s)}$ in cm^{-1}. Additionally, for the numerical parameters of the diabatic gradients $\kappa_i^{(s)}$ and the inter-state coupling gradient components $\lambda_i^{(rs)}$, we give the characteristic shifts

$$d_i^{(s)} = -\frac{\kappa_i^{(s)}}{k_i^{(s)}} \text{ and } d_i^{(rs)} = \pm\frac{2\lambda_i^{(rs)}}{k_i^{(r)} + k_i^{(s)}} \tag{5.12}$$

in mass-weighted atomic units. The latter shifts are for instance to be compared with the shift vector present in the Duschinsky transformation. When given, the bilinear parameters associated to cross terms in the

QVC Hamiltonian model are given directly in atomics units and can be compared, after some manipulations (second-order Jahn-Teller effect due to the coupling), with adiabatic Hessians from electronic structure calculations.

Definition and role of the electronic ground state for quantum dynamics simulations

In this section, we make use of LVC and QVC Hamiltonian models for a minimal (1+2)-state 3-dimensional model. As of now and until otherwise specified, we will only consider the electronic ground state as completely uncoupled to the electronic excited states (hence the "(1+2)-state" notation). This is compatible with the *sudden approximation* for the electronic excitation. This way, the electronic ground state, although explicitly defined, only serves

- for defining initial wavepackets for sudden excitations toward the electronic excited states;
- or for representing the propagated wavepackets in the S_0 normal-mode basis set.

We already note that the explicit treatement of S_0-S_i couplings ($i > 0$), to go toward explicit excitations from the ground to the excited states, is an outlook of the present study, and will be shortly mentioned in chapter 8.

The present section is structured as follows. First, we describe the model and how it is parametrized to reproduce the adiabatic PESs from *ab initio* data. A first comparison is made between LVC and QVC sets of parameters and the effect of QVC on the PES models is discussed. Next, quantum dynamics simulations are presented and discussed for the two following purposes: finding the vibronic eigenstates and elucidating the early dynamics of the reduced model with different initial states. From this, the power spectra for absorption and emission are discussed in terms of plausible contributions to the total vibronic spectra.

5.2.1 Simple models of potential energy surfaces

We, hereby, choose 3 modes among the S_0 normal modes which are

- the non-totally symmetric acetylenic stretching mode, 87 (B_2);
- the totally symmetric acetylenic stretching mode, 88 (A_1);
- and the totally symmetric quinoidal stretching mode on the central benzene, 81 (A_1).

The two acetylenic stretching modes are chosen as we expect them to be the main actors for the presence of the unusual Stokes shift ($\Delta\bar{\nu}_{\text{Stokes}}$ is of about $2300\,\text{cm}^{-1}$, close to the wavenumber of the acetylenic stretching modes, $2360\,\text{cm}^{-1}$ and $2100\,\text{cm}^{-1}$ at MinS_0 and MinS_1, respectively). Thus, the inter-state coupling gradient will be defined only for the B_2 acetylenic stretching mode. The diabatic gradient (hence diabatic gradient difference) will expand in the plane (Q_{81}, Q_{88}), such that the CoIn seam is oblique in this plane.

Fitting procedure

The starting geometry for PESs cuts (or rigid scans) is here the geometry of the optimized MECI. As a consequence, all critical points in the PES models are only *apparent* critical points from the point of view of the optimized MECI, which is the only fully optimized geometry. In other words, all coordinates are frozen at the coordinates of the MECI, except for the three chosen modes

$$\mathbf{Q}^{\text{3D}} = (Q_1 \dots, Q_i, \dots, Q_{3N-6}) \text{ with } \begin{cases} Q_i & = Q_i \in \mathbb{R} \text{ if } i \in (81, 87, 88) \\ Q_i & = Q_{i,X} \text{ otherwise.} \end{cases} \tag{5.13}$$

Still, to compare with *ab initio* energy derivatives, we expand the L/QVC models from the *apparent* FC geometry (that is at $(Q_{81}, Q_{87}, Q_{88}) = (0, 0, 0)$). At this geometry, we compare the *apparent* vertical transition energies and vertical gradients with the *ab initio* ones of the fully optimized FC geometry.

2D-cuts of PESs are generated by incrementing Cartesian displacements along two desired normal modes. 1D-cuts are enough for adjusting the first-order parameters (diabatic gradients and inter-state coupling gradient) while 2D-cuts are necessary for evaluating bilinear terms (cross terms with respect to different normal modes). Since the geometries are $\text{C}_{2\text{v}}$ for any cuts where $Q_{87} = 0$, the diabatic electronic states keep their B_2 or A_1 symmetry, and can be identified to S_1 and S_2 adiabatic states, up to relabelling before and after the crossing of the MECI. As such, one can adjust the diagonal (symmetry-preserving) diabatic parameters independently from the off-diagonal (symmetry-breaking) parameters. The fitting procedure minimizes the following function for the symmetry-preserving parameters

$$\begin{gathered} L(E^{(1)}, E^{(2)}, \boldsymbol{\kappa}, \boldsymbol{\gamma}, \mathbf{k}_{81}, \mathbf{k}_{88}) = \\ \sum_{n, Q_{87}=0} \left[\left(H_{11}[E^{(1)}, \boldsymbol{\kappa}^{(1)}, \boldsymbol{\gamma}^{(1)}](\mathbf{Q}^{\text{3D}}(n)) - E_{\text{A}_1}(n) \right)^2 + \left(H_{22}[E^{(2)}, \boldsymbol{\kappa}^{(2)}, \boldsymbol{\gamma}^{(2)}](\mathbf{Q}^{\text{3D}}(n)) - E_{\text{B}_2}(n) \right)^2 \right], \end{gathered} \tag{5.14}$$

and allows for the optimization of both B_2 and A_1 diabatic surfaces simultaneously. Then, taking the resulting parameters for granted, the eigenvalues of the full LVC and QVC models are fitted to the *ab initio* data from 2D-cuts (87,81) and (87,88) so as to optimize the parameters related to the non-totally symmetric normal mode 87. Again, the parameters are obtained through a least-square fitting procedure minimizing the function

$$\begin{gathered} L(\lambda_{87}, \boldsymbol{\mu}, \mathbf{k}_{87}) = \\ \sum_{n} \left[\left(V_1[\lambda_{87}, \boldsymbol{\mu}, \mathbf{k}_{87}](\mathbf{Q}^{\text{3D}}(n)) - E_{\text{S}_1}(n) \right)^2 + \left(V_2[\lambda_{87}, \boldsymbol{\mu}, \mathbf{k}_{87}](\mathbf{Q}^{\text{3D}}(n)) - E_{\text{S}_2}(n) \right)^2 \right], \end{gathered} \tag{5.15}$$

where $V_1(\mathbf{Q}^{\text{3D}})$ and $V_2(\mathbf{Q}^{\text{3D}})$ are the eigenvalues of the Hamiltonian models. The resulting parameters are presented in table 5.4 *via* their natural equivalent quantities when possible.

We note that the presented LVC and QVC sets of parameters are obtained independently, that is: we do not take the LVC parameters for granted to optimize the additional bilinear parameters of the QVC model. We can compare the two sets of parameters. First the additional QVC parameters have little to no effect

Table 5.4: LVC and QVC model parameters obtained upon fitting *ab initio* calculations. The curvatures $k_i^{(s)}$ are illustrated with the associated frequency $\omega_i^{(s)}$ in cm^{-1}. Parameters associated to the first-order expansion (λ_i or $\kappa_i^{(k)}$) are given by the associated characteristic shift in the mass-weighted framework for displacement along the normal-mode directions. Parameters associated to the second-order bilinear terms ($\gamma_{i,j}^{(k)}$ or $\mu_{i,j}$) are given directly in atomic units. Superscripts (1) and (2) refer to diabatic excited states A$_1$ and B$_2$, respectively, coincident with S$_2$ and S$_1$ at the FC geometry. The corresponding LVC and QVC parameters in mass-weighted atomic units are gathered in appendix B.

Parameter	Equivalent	Value (LVC)	Value (QVC)	Unit
$E^{(1)}$	–	4.405	4.407	eV
$E^{(2)}$	–	4.380	4.379	eV
$\kappa_{81}^{(1)}$	$d_{81}^{(1)}$	7.900	8.203	$a_0\sqrt{m_e}$
$\kappa_{81}^{(2)}$	$d_{81}^{(2)}$	3.094	3.059	$a_0\sqrt{m_e}$
$\kappa_{88}^{(1)}$	$d_{88}^{(1)}$	-7.205	-7.365	$a_0\sqrt{m_e}$
$\kappa_{88}^{(2)}$	$d_{88}^{(2)}$	-8.274	-8.289	$a_0\sqrt{m_e}$
λ_{87}	d_{87}	7.417	6.569	$a_0\sqrt{m_e}$
$\gamma_{81,88}^{(1)}$	–	0	-2.594×10^{-6}	$E_\mathrm{h}/({a_0}^2 m_e)$
$\gamma_{81,88}^{(2)}$	–	0	-0.512×10^{-6}	$E_\mathrm{h}/({a_0}^2 m_e)$
$\mu_{87,81}$	–	0	-1.084×10^{-6}	$E_\mathrm{h}/({a_0}^2 m_e)$
$\mu_{87,88}$	–	0	-11.867×10^{-6}	$E_\mathrm{h}/({a_0}^2 m_e)$
$k_{81}^{(1)}$	$\omega_{81}^{(1)}$	1515	1513	cm^{-1}
$k_{81}^{(2)}$	$\omega_{81}^{(2)}$	1552	1549	cm^{-1}
$k_{88}^{(1)}$	$\omega_{88}^{(1)}$	2274	2274	cm^{-1}
$k_{88}^{(2)}$	$\omega_{88}^{(2)}$	2281	2280	cm^{-1}
$k_{87}^{(1)}$	$\omega_{87}^{(1)}$	2200	2212	cm^{-1}
$k_{87}^{(2)}$	$\omega_{87}^{(2)}$	2201	2171	cm^{-1}

on the vertical transition energies at the apparent FC geometry and the frequencies. Only the frequency of the coupling normal mode 87 is significantly different ($2201\,$cm^{-1} in LVC *vs.* $2171\,$cm^{-1} in QVC). On the other hand, the flexibility offered by bilinear terms (γ and μ) slightly affects the first-order gradient and coupling parameters (κ and λ). In particular again in the case of the coupling normal mode 87, the linear coupling parameter is reduced of one unity, which is compensated by the secondary Duschinsky term between both acetylenic stretching modes, $\mu_{87,88}$. In the following, we will see that both the LVC and QVC models correctly reproduce the adiabatic PESs, and we will now make more explicit the effect of this strong bilinear coupling term for the acetylenic stretching modes.

Comparison of the fitted energies to the *ab initio* data

Let us first illustrate the results for the LVC model. The 1D-cuts from the MECI along the A$_1$ normal modes 81, 88, and the B$_2$ normal mode are shown in fig. 5.15 with the corresponding diabatic potential energies (blue for A$_1$, red for B$_2$).

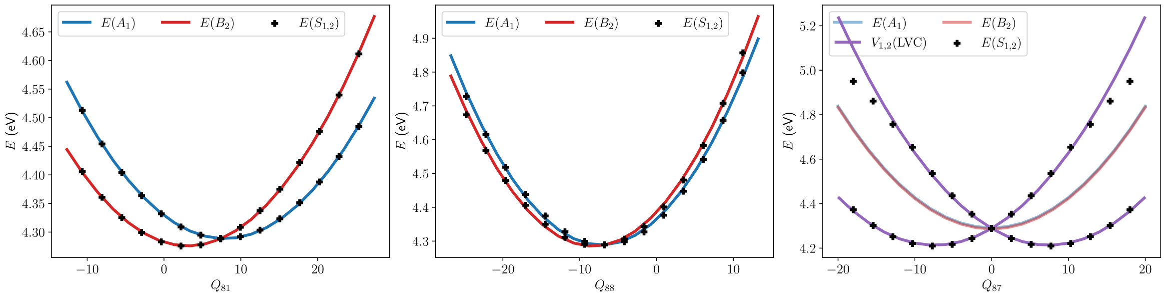

Figure 5.15: Adiabatic energies from electronic structure calculations (symbol $+$) and diabatic potential energies for the pair of delocalized diabatic states (blue and red lines) along Cartesian displacements associated to the A$_1$ normal modes 81, 88, and the B$_2$ normal mode 87. The adiabatic energies (eigenvalues) for the LVC Hamiltonian model are also given for the B$_2$ normal mode 87 (purple lines). For unspecified coordinates, the values are those at the MECI; all coordinates are mass-weighted and given in atomic units.

Let us already notice that the symmetry-adapted diabatic states are fully degenerate along the symmetry-breaking normal modes. For these 1D-cuts (here only along 87), the localized diabatic states are better adapted to the adiabatic surfaces. In addition, the localized diabatic states are simply obtained by rotating the already parametrized model, such that the exact same set of parameters is valid, only with different diabatic Hamiltonian matrix elements. In particular, the roles of the inter-state coupling gradient $\boldsymbol{\lambda}$ and of the gradient difference $\frac{\boldsymbol{\kappa}^{(2)}-\boldsymbol{\kappa}^{(1)}}{2}$ are swapped. In the case of symmetry-preserving normal modes, the adiabatic energies coincide with the potential energies of the pair of delocalized diabatic states A$_1$ and B$_2$. In the case of a symmetry-breaking normal mode, the adiabatic energies coincide with the potential energies of the pair of localized diabatic states.

As expected from the contributions of the chosen normal modes to the *ab initio* derivative coupling vector, the B$_2$ normal mode 87 strongly "digs" the PESs into a double-well shaped potential energy profile, from the MECI. Similarly, the A$_1$ normal modes 81 and 88 lift the degeneracy from the MECI, with a stronger effect of the quinoidal mode 81 for the CoIn seam. The physical relevance of the 3-dimensional model can be further evaluated by comparing the critical points of the reduced dimensional adiabatic surfaces and of the fully optimized adiabatic surfaces. Such energies are gathered in table 5.5.

The adiabatic PESs for the 2D-cuts are shown in fig. 5.16, again for the LVC model only. As we have already discussed, the LVC and QVC parameters show little difference for the zeroth and first order terms. The main difference lies in the coupling parameters related to the non-totally symmetric acetylenic stretching. The effect of the non-negligible cross term $\mu_{87,88}$ is illustrated in fig. 5.17 by looking at the 2D-cut (87,88) of the S$_1$ PES in both LVC and QVC cases. For the case of LVC, the two potential energy

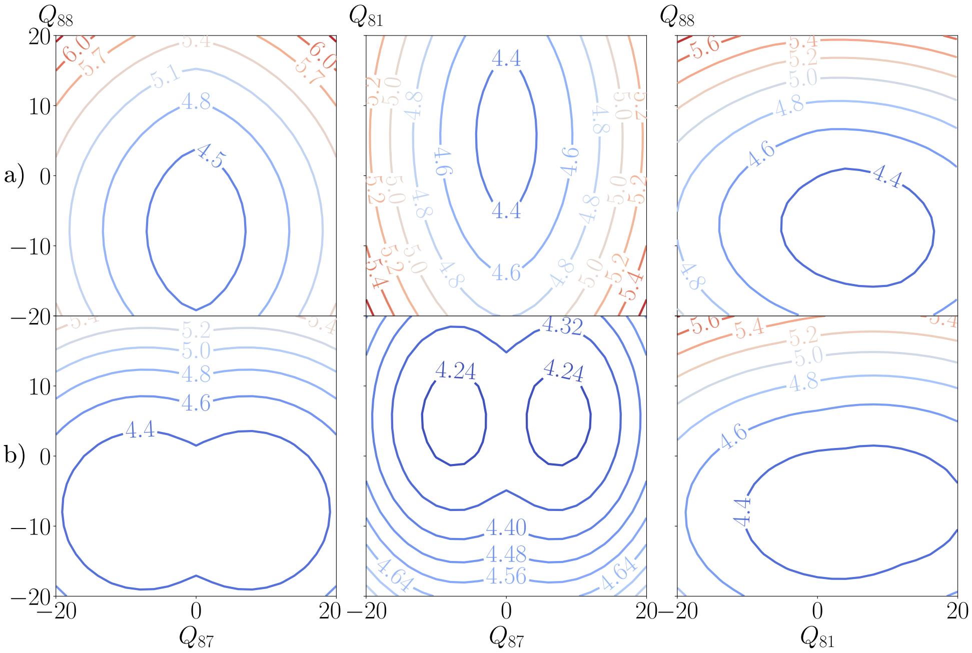

Figure 5.16: Adiabatic PESs of the LVC model (in eV) of electronic states S$_1$ (a) and S$_2$ (b) for the 2D cuts (81,87), (87,81) and (81,88), from left to right. Energy is given in eV, as inset in the contour lines. For unspecified coordinates, the values are those at the MECI; all coordinates are mass-weighted and given in atomic units.

wells in the S$_1$ have their main axes aligned with the original directions of the normal modes. However, we know from the vibrational analysis at the MinS$_1$ geometries that in such a region of the PES (the two equivalent wells of the MinS$_1$), the normal modes are localized. In particular, we explicited them as the normalized sum and difference of the delocalized S$_0$ normal modes, *via* a Duschinsky transformation. The strong $\mu_{87,88}$ parameter translates this strong (yet expected) Duschinsky effect on the PESs. Now with the QVC PESs, the two wells have been rotated so that their main axes are aligned with the sum and difference of the initial S$_0$ normal modes and directions (which are closer to the true directions of the S$_1$ normal modes). Yet, we expect the effect of such a rotation to be rather small on the physics of the system, as the two rotated axes are almost equivalent. Indeed, the two acetylenic stretching modes have similar frequencies, such that the wells are almost isotropic ellipsoids along modes 87 and 88.

Table 5.5: Energies (in eV) of the critical points in the *ab initio* PESs (CAM-B3LYP/6-31+G* level of theory) and in the parametrized 3-dimensional LVC PES models or QVC PES models.

Critical Point	MinS$_1$	TS(B$_2$)	TS(A$_1$)	$E_{S_1}(\mathbf{0})$	$E_{S_2}(\mathbf{0})$	MECI
CAM-B3LYP/6-31+G*	4.12	4.25	4.29	4.43	4.47	4.29
LVC Model	4.209	4.273	4.288	4.380	4.405	4.29
QVC Model	4.208	4.272	4.286	4.379	4.407	4.29

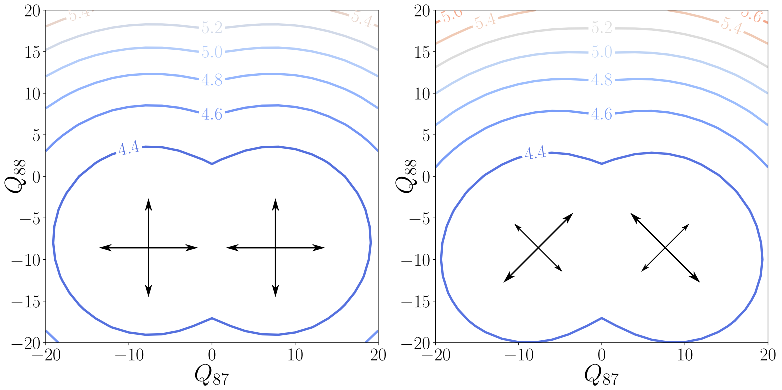

Figure 5.17: PESs of the first excited state in the LVC (left) and the QVC (right) models for the 2D cut (87,88) (B_2 and A_1 acetylenic stretching modes, respectively). Energy is given in eV, as inset in the contour lines. Central arrows correspond to the directions of the main axes of the ellipsoids along both coordinates. For unspecified coordinates, the values are those at the MECI; all coordinates are mass-weighted and given in atomic units.

Take-home messages

1. We have sucessfully parametrized LVC and QVC Hamiltonian models for a (1+2)-state 3-dimensional model, so as to reproduce the most important features of the S_1/S_2 manifold as regards the presence of the MECI (explicitly included in the data set).
2. Although the dimensionality of the model is strongly reduced, the criticial points of the S_1/S_2 manifold are comparable, in energy, with the previously described fully optimized geometries.
3. Little to no physically relevant effect, at such low-dimensionality, was attributed to the bilinear terms of the QVC Hamiltonian.

5.2.2 Understanding fluorescence in strongly nonadiabatically coupled manifold

We use the previously described (1+2)-state 3-dimensional PES models to run wavepacket dynamics calculations. The MCTDH multi-set formalism is used for the definition of the molecular wavefunction. Corresponding numerical details are presented in table 5.6. The primitive basis (PB) functions are Gauss-Hermite functions of the mass-weighted coordinates and the size of the basis is chosen so as to have a relevant range for the spatial grid (about $\pm 40\, a_0 \sqrt{m_e}$). In the following, propagations in imaginary time (simple relaxation) and in real time (wavepacket dynamics) are done (time of simulation $200\,$fs, printing of the output files every $0.5\,$fs and printing of the wavefunction every $1\,$fs).

Table 5.6: Single-particle functions (SPFs) and primitive basis (PB) parameters for the relaxation and propagation of nuclear wavepackets. Setting the reduced masses for the primitive basis harmonic oscilator functions to 1.0 is relevant when using mass-weighted coordinates.

Coordinates	Basis type	Size of the basis	Eq. position	Frequency	Reduced mass	SPFs
Q_{81}	HO	15	0.0	1655 cm^{-1}	1.0	multi-set 8,8,8
Q_{87}	HO	15	0.0	2365 cm^{-1}	1.0	multi-set 8,8,8
Q_{88}	HO	15	0.0	2365 cm^{-1}	1.0	multi-set 8,8,8

First, imaginary-time propagations allow us to probe the vibronic eigenstates within the coupled electronic manifold. Beyond the Born-Oppenheimer approximation, the vibronic eigenstates expand in the chosen basis for the electronic excited states. In the presented delocalized representation for the VCH models, the electronic excited states are the diabatic delocalized states $^1\mathrm{A}_1$ and $^1\mathrm{B}_2$. We have for the vibronic eigenstates

$$\Psi_k^{(\mathrm{exc})}(\mathbf{q},\mathbf{Q}) = \psi_{\mathrm{A}_1,k}(\mathbf{Q})\phi_{\mathrm{A}_1}(\mathbf{q};\mathbf{Q}) + \psi_{\mathrm{B}_2,k}(\mathbf{Q})\phi_{\mathrm{B}_2}(\mathbf{q};\mathbf{Q}) \tag{5.16}$$

where $\mathbf{Q} = \mathbf{Q}^{\mathrm{ND}}$ are the N nuclear degrees of freedom included in the model and $\mathbf{q}$ are the electronic degrees of freedom. Numerically, the electronic degrees of freedom are treated *via* a dedicated set of single-particle functions (SPFs) for which the index is the index of the electronic states. Thus, the electronic degrees of freedom are now implicit, and we discard them in the following. The underlying electronic states $\phi_{\mathrm{A}_1}(\mathbf{Q})$ and $\phi_{\mathrm{B}_2}(\mathbf{Q})$ are quasi-diabatic states, which vary moderately and smoothly (ideally not at all to first-order) with the nuclear degrees of freedom $\mathbf{Q}^{\mathrm{ND}}$. The vibronic eigenstates in the electronic ground state are obtained more easily than in the excited state manifold, as the diabatic electronic ground state does not couple to other states (Born-Oppenheimer approximation for the electronic ground state).

Definition and choice of the initial states

The *sudden approximation* implies to use the ground-state vibrational wavepacket as a starting point, directly projected onto one of the electronic excited state (diabatic states here). Thus, the trivial initial states from sudden approximation are

$$\begin{aligned} \Psi_{\mathrm{A}_1}(\mathbf{Q}^{3\mathrm{D}}, t=0) &= \psi_{\mathrm{GS}}^{(0)}(\mathbf{Q}^{3\mathrm{D}})\phi_{\mathrm{A}_1}^{\mathrm{dia}} \\ \Psi_{\mathrm{B}_2}(\mathbf{Q}^{3\mathrm{D}}, t=0) &= \psi_{\mathrm{GS}}^{(0)}(\mathbf{Q}^{3\mathrm{D}})\phi_{\mathrm{B}_2}^{\mathrm{dia}}, \end{aligned} \tag{5.17}$$

where electronic degrees of freedom are implicit because of the *a priori* diabatization. In the following, we discuss the obtention of vibronic eigenstates in the excited-state manifold and the autocorrelation functions for the two initial states in eq. (5.17). However, let us already note that two other *sudden approximation* are valid, if one switches to the localized representation of the diabatic states. The initial states would then rather be

$$\begin{aligned}\Psi(\mathbf{Q}^{3\mathrm{D}}, t=0) &= \psi_{\mathrm{GS}}^{(0)}(\mathbf{Q}^{3\mathrm{D}})\phi_{\mathrm{L}}^{\mathrm{dia}} = \psi_{\mathrm{GS}}^{(0)}(\mathbf{Q}^{3\mathrm{D}})\frac{\phi_{\mathrm{A}_1}^{\mathrm{dia}} + \phi_{\mathrm{B}_2}^{\mathrm{dia}}}{\sqrt{2}} \\ \Psi(\mathbf{Q}^{3\mathrm{D}}, t=0) &= \psi_{\mathrm{GS}}^{(0)}(\mathbf{Q}^{3\mathrm{D}})\phi_{\mathrm{R}}^{\mathrm{dia}} = \psi_{\mathrm{GS}}^{(0)}(\mathbf{Q}^{3\mathrm{D}})\frac{\phi_{\mathrm{B}_2}^{\mathrm{dia}} - \phi_{\mathrm{A}_1}^{\mathrm{dia}}}{\sqrt{2}}.\end{aligned} \tag{5.18}$$

The use of localized or delocalized initial states is further discussed in chapter 8, and has be explored in Ref [55].

Obtention of the vibronic eigenstates in the S_1/S_2 manifold

The two delocalized initial states eq. (5.17) yield, after an imaginary time of about $20\,\mathrm{fs}$, two quasi-degenerate ($\Delta E = 0.0076\,\mathrm{eV}$) but distinct lowest-energy vibronic eigenstates in the S_1/S_2 manifold. Although imaginary time has no physical relevance, the short time indicates a short number of steps to variationally optimize the vibronic eigenstates from the guesses that are the initial states.

Let us compare for the two states the transition energy (with respect to the ZPE of the electronic ground state in the 3D model), the diabatic populations (presented in table 5.7) and the shapes of the wavefunctions (shown in fig. 5.18).[2]

Table 5.7: Vibronic eigenstates energies and diabatic populations. The transition energy is computed upon setting the energy reference to the zero-point energy of the 3D model, $E = 0.396\,\mathrm{eV}$

	Vibronic state	Total energy (eV)	Transition energy (eV)	P_{A_1}	P_{B_2}
LVC	$\Psi_{\mathrm{exc}}^{(0)}$	4.576	4.180	0.20	0.80
	$\Psi_{\mathrm{exc}}^{(1)}$	4.584	4.188	0.78	0.22
QVC	$\Psi_{\mathrm{exc}}^{(0)}$	4.576	4.176	0.19	0.81
	$\Psi_{\mathrm{exc}}^{(1)}$	4.584	4.187	0.77	0.23

Clearly from the populations and from the shapes of the nuclear wavefunction contributions, the two states form a complementary pair of quasi-degenerate states. In the following, we use *even* and *odd* adjectives for reference to the parity with respect to the B_2 normal mode 87.

The first vibronic state, obtained *via* the initially fully populated state B_2, has even contributions in the B_2 state and odd contributions to the A_1 state. The shape of the even contributions are almost unchanged compared with the shape of the initial wavefunction (they almost stay $|v=0\rangle$), and the wavefunction is simply shifted toward the MECI position. The shape of the odd contributions are almost $|v=1\rangle$, centered at the MECI but with density maxima shifted toward the minima of the S_1 PES. The even and odd parities in the targeted state and non-targeted state (B_2 and A_1 respectively) are expected. Indeed, the wavefunction staying (diabatically) on the initial surface does not experience the coupling coordinate 87.

---

[2] Because we discuss here the vibronic eigenstates, hence stationary states, of the parametrized models, we talk about time-independent wavefunctions rather than wavepackets.

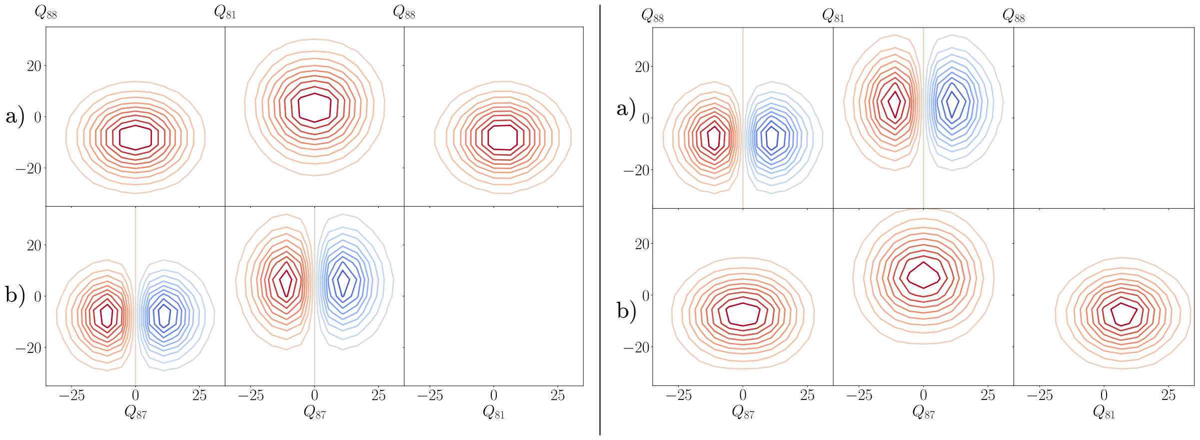

Figure 5.18: Vibrational contributions in diabatic electronic states B_2 (a) and A_1 (b) for the first (left) and second (right) vibronic eigenstates of the coupled S_1/S_2 manifold, in planes (87,81), (87,88), and (81,88) from left to right. For unspecified coordinates, the values are those at the MECI; all coordinates are mass-weighted and given in atomic units. The blank panels correspond to the wavefunctions having the B_2 coordinate 87 in the nodal plane and thus zero contribution.

The wavefunction that is transferred from the initial surface to the non-targeted surface does so *via* the coupling coordinate 87, which is B_2, hence a change of parity after the transfer. The same observation holds for the second vibronic eigenstates, only by changing the roles of A_1 and B_2 states.

In other words, although the propagation occurs in imaginary time, the relaxation can be seen as the equilibrium of a "transfer of excitation" from one diabatic excited state to the other. The initial wavefunction conserves 80% of its initial electronic population in the final vibronic eigenstate, with little to no variation of shape compared to the ground state. About 20% of the initial wavefunction is transferred to the other excited state, and undergoes a change of symmetry due to the B_2 character of the coupling coordinate. This means that the coupling criteria (energy difference and coupling strength) are strong enough so that the vibronic eigenstates necessarily have non-negligible contributions in both diabatic states. To compare with the adiabatic point of view in textbook vibronic spectroscopy, one could invoke the Herzberg-Teller terms (intensity borrowing from other states through vibronic coupling), which cannot be seen as a perturbation here.

Vibrational interaction diagram for the vibronic transitions

We propose to interpret again the first two vibronic eigenstates as an interaction diagram comparable to a molecular orbital diagram. In fig. 5.19, we represent the first two uncoupled vibronic eigenstates on the B_2 and A_1 surfaces (left and right, respectively) and the first two coupled vibronic eigenstates for the B_2/A_1 (S_1/S_2) manifold. The interaction diagram and in particular the twofold vibrational character of the vibronic eigenstates allows us to propose a first attribution of the vibronic transitions expected in steady-state absorption and emission (blue and red arrows).

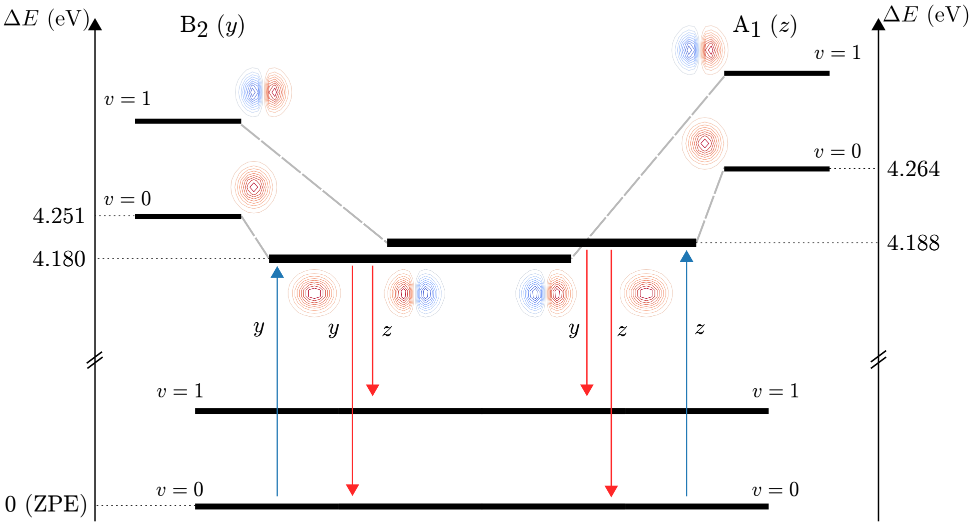

Figure 5.19: Representation of the vibronic eigenstates as interacting two-state(A_1, B_2)-two-body(Q_{87}, Q_{88}) vibronic wavefunction components. The vibrational number v refers to the excitation number of the non-totally symmetric normal mode of vibration 87. The nuclear wavefunction contributions are shown in the plane (87,88).

For absorption, the initial state will unambiguously be $\psi^{(0)}_{\mathsf{GS}}(\mathbf{Q}^{3\mathsf{D}})$ in the electronic ground state. Such a vibrational wavefunction, which is simply written $|v_{81}, v_{87}, v_{88}\rangle = |0, 0, 0\rangle$, is even with respect to all nuclear degrees of freedom. This vibrational wavefunction will thus overlap with all even contributions in the vibronic eigenstates of the S_1/S_2 manifold. Such overlaps are possible from S_0 to the B_2 state (polarized along y) or from S_0 to the A_1 state (polarized along z), for which we know that both are bright states, from their oscillator strengths at the FC geometry. These overlaps yield first the 0^0_0 transition, schematized in fig. 5.19 (blue arrows) and give the associated band origin in the absorption spectrum. As we will see later, the next transitions will depend first on excitations for the A_1 normal modes, $|v_{81}\rangle$ or $|v_{88}\rangle \neq 0$ (vibrational progression).

For emission, two cases arise for each vibronic eigenstates of the S_1/S_2 manifold. Focussing on the lowest one, two vibrational contributions associated to the two diabatic states (B_2 polarized along y, A_1 polarized along z) are present. The "initial state" for emission is thus not so unambiguously defined as in S_0, in particular in the case of spontaneous emission. However, we can think of two direct contributions

- "emitting" from the even vibrational contribution, on the y-polarized B_2 diabatic state;
- or "emitting" from the odd vibrational contribution, on the z-polarized A_1 diabatic state

where the transition probabilities for both cases will be determined, similarly to the case of absorption, by the overlap between vibrational wavefunctions (fig. 5.19 red arrows). The first contribution overlaps first and mostly with the $|v_{81}, v_{87}, v_{88}\rangle = |0, 0, 0\rangle$ in the electronic ground state, yielding the same 0^0_0 transition than is absorption. The second contribution overlaps first and mostly with the $|v_{81}, v_{87}, v_{88}\rangle = |0, 1, 0\rangle$ in the electronic ground state, yielding a "n^0_1" transition with $n = 87$, thus shifted compared to the 0^0_0

transition of $\bar{\nu}_{87} = 2360\,\mathrm{cm}^{-1}$. Note that in "$n_1^0$", the superscript $\square^0$ refers to one of the vibrational contributions (the odd one, here) of the lowest vibronic eigenstates. The vibronic progression in both contributions to the emission occurs, as expected, due to the non-zero overlaps with the next vibrational states in the electronic ground state.

A word on higher excited vibronic eigenstates

Until now, the first two vibronic eigenstates have beeen represented and discussed in terms of the shape of their vibrational contributions. The next excited vibronic eigenstates are found using the improved relaxation algorithm (see the end of this chapter, table 5.13 for results from the LVC model and table 5.14 for results form the QVC model, with comparison in table 5.15). The sizes of the primitive bases and the SPF bases have been augmented so that the wavefunction remains centered with respect to the B$_2$ normal mode. Without this, the nuclear space is not large enough for the high excitations to be correctly described. Even with a large basis (51 HO basis functions and 21 SPFs per degrees of freedom and per state), we note that there is some "leakage" of the nuclear wavefunction at the spatial boundaries for the highly excited states.

From table 5.13, we see indeed that the first two vibronic eigenstates (column "relax=0") are the lowest pair of vibronic eigenstates previously identified, and are mostly excited along 87 in the 20% populated state. The other excitation numbers are always lower than 0.40 for these states. The next vibronic eigenstates, on the other hand, maintain $\langle n_{87} \rangle_{\mathrm{A}_1 \text{ or } \mathrm{B}_2} \simeq 0$ or 1 but also have close-to-one excitation numbers for the A$_1$ normal modes. These excitations lead to the two vibronic progressions from the 0_0^0 transition along 81 and 88, namely the 81_0^v and 88_0^v transitions.

Obtention of the absorption and emission spectra

The power spectra for absorption and emission contributions can be computed directly *via* the Fourier transform of the autocorrelation functions of the adequate propagated wavepackets. The different initial states and calculations schematically correspond to the illustrated transitions in fig. 5.19. First, let us focus on the two real-time propagations (pure A$_1$ or B$_2$ initial states) in the excited-state manifold.

In particular, we are first interested in the early dynamics trajectories, up to $25\,\mathrm{fs}$. We propose to approximate the "trajectories" of the wavepackets to the evolution of their center position in the 2D-cut (81,88), because they are centered with respect to the normal coordinate 87. In fig. 5.20 a), we illustrate again the PESs with A$_1$ and B$_2$ diabatic potential energies and recall the positions of the MECI and transitions states. The unspecified coordinates is the normal coordinate 87, set to 0, such that the first two adiabatic energies are always either the diabatic potential energy of the A$_1$ or B$_2$ states. The populations of the diabatic and adiabatic states are also illustrated as functions of time, fig. 5.20 b).

Around the FC point, the initially pure diabatic states consist in a 40:60 superposition of the pair of S$_1$ and S$_2$ states (due to the coupling along the normal mode 87). The trajectories start from the (apparent)

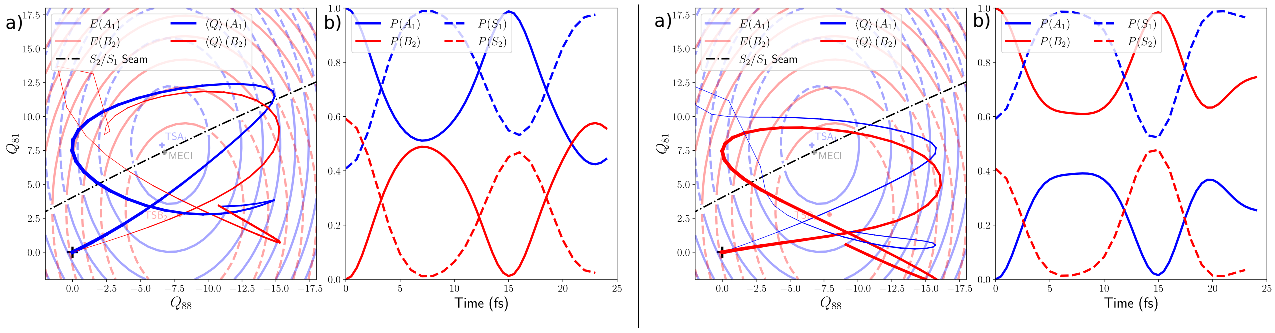

Figure 5.20: (a) Trajectories of the centers of the wavepackets in the 2D-cut (81,88) up to 25 fs in the LVC model. The linewidth of the "trajectory" in each diabatic state at a given time is proportional to the associated population at this time. Diabatic PESs A_1 and B_2 in blue and red, respectively; adiabatic PESs S_1 and S_2 in dashed and plain lines, respectively. (b) Diabatic (plain lines) and adiabatic (dashed lines) populations. Left and right panels show the propagations for an initial state on A_1 and for an initial state on B_2, respectively.

FC geometry. We observe that for initially pure states A_1 and B_2, the population is rapidly transferred to the initially unpopulated state and that the two diabatic trajectories follow different gradients. The seam of CoIns is also represented, and is parallel to neither the 81 nor the 88 axis. In addition, we observe that the wavepackets cross the seam twice within the first 25 fs, which is consistent with the strong oscillations between populations of the adiabatic states S_1 and S_2. We stress here the importance of mode 81 in the description of the seam. Indeed, with a model reduced to acetylenic vibrations only (87 and 88), the initial state would be on the wrong side of the seam with respect to the FC geometry (the seam is oblique in the (Q_{81}, Q_{88}) plane).

We now discuss the direct obtention of power spectra from real-time propagations. For each power spectrum, we illustrate two different broadening choices. A first illustration is obtained with a damping time $\tau = 100$ fs, yielding highly-resolved power spectra. A second illustration is obtained with a damping time $\tau = 19$ fs which is more realistic for comparison with low but non-zero temperature experiments.

The two previously described "trajectories" (precisely, wavepacket dynamics) yield two distinct but equivalent contributions to the absorption spectra. Both contributions are physically relevant as both are obtained upon *sudden excitation* toward an optically bright state in the FC region. The two contributions are shown in fig. 5.21 (left), where the transition energies are obtained with respect to the zero-point energy in the electronic ground state. Contributions to the emission spectrum are evaluated through the propagation of the vibrational wavefunction on the A_1 and B_2 diabatic states of the first two quasi-degenerate vibronic eigenstates (fig. 5.21 center and right). As a result, we illustrate a total of four distinct plausible contributions to the emission spectrum.

The main spectroscopic data of our simulations are collected in table 5.8. We stress that up to now, the theoretical spectra have not been shifted to match experimental data. The wavelength position for the

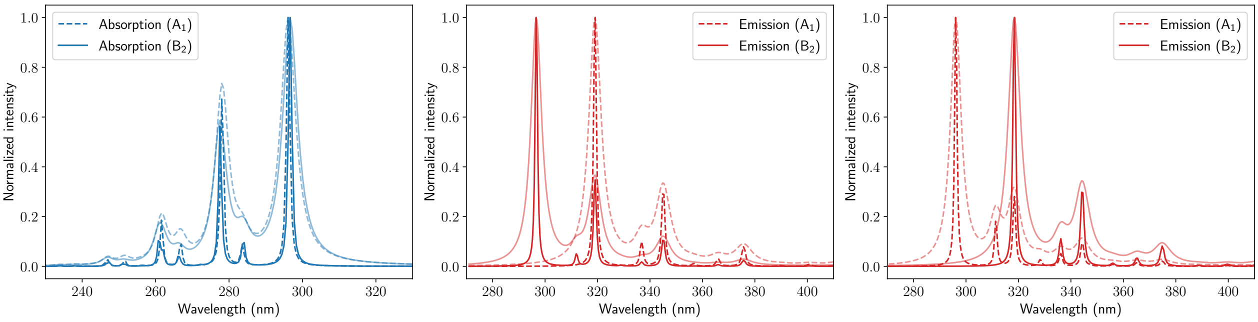

Figure 5.21: Left: simulated contributions to the absorption spectrum from electronic ground state to electronic excited state B_2 (plain lines) and A_1 (dashed lines). Center: simulated contributions to the emission spectrum from vibrational wavefunctions on B_2 (plain lines) and A_1 (dashed lines) of the first vibronic eigenstate. Right: simulated contributions to the emission spectrum from vibrational wavefunctions of B_2 (plain lines) and A_1 (dashed lines) of the second vibronic eigenstate. Pale and dark colors indicate the use of damping times $19\,\mathrm{fs}$ and $100\,\mathrm{fs}$, respectively. All results are for the LVC model.

main transitions and associated vibronic progressions are given within each contribution. Both absorption contributions yield the same transition energies and associated wavelengths. The 0_0^0 transition occurs at $296\,\mathrm{nm}$. For emission, we find two contributions with the most intense transition at $296\,\mathrm{nm}$ and $297\,\mathrm{nm}$, consistent with the 0_0^0 transition. These contributions are called *non-Stokes* contributions in the rest of the text. More importantly, we find two contributions for which the most intense transition is at $319\,\mathrm{nm}$ which is consistent with a 87_1^0 transition. These contributions are called *Stokes* contributions in the rest of the text. With respect to the maximum in absorption, these two contributions are shifted to the red wavelengths by $23\,\mathrm{nm} \equiv 2400\,\mathrm{cm}^{-1}$, which is, expectedly, consistent with the *loss* of an acetylenic vibrational quantum.

Table 5.8: Spectroscopic data for theoretical absorption and emission spectra in the LVC model, before any comparison with the experiments. One row is given for absorption as both computed spectra are identical for reading the transition energies. The four contributions to the emission spectrum are given next. The most intense transition for each contribution is given in bold. The second transition with low intensity is given in parenthesis. Associated vibronic progression are given with respect to the most intense transition of each contribution.

Spectrum contribution	λ_{max} (nm)	First vibronic progression (cm^{-1})
Absorption	**296**, (284), 278	–, (1430), 2190
Emission		
$\Psi_{\text{exc}}^{(0)}$, non-Stokes	**297**, (312), 319	–, (1620), 2320
$\Psi_{\text{exc}}^{(0)}$, Stokes	**319**, (337), 345	–, (1670), 2360
$\Psi_{\text{exc}}^{(1)}$, non-Stokes	**296**, (311), 318	–, (1630), 2340
$\Psi_{\text{exc}}^{(1)}$, Stokes	**319**, (336), 344	–, (1590), 2280

Comparison to the experiments

We now compare the results of our calculations to experimental spectra obtained at low-temperature ($-198\,°\mathrm{C} \equiv 75\,\mathrm{K}$) in fig. 5.22 [39]. The theoretical spectra are now all shifted in energy so that the band origins from the theoretical absorption ($297\,\mathrm{nm}$) and from the experimental absorption ($304\,\mathrm{nm}$) match. The associated wavelength shift (again, applied for all spectra) of $7.3\,\mathrm{nm}$ consist in fact in an (homogeneous) energy shift of $\Delta E = 0.10\,\mathrm{eV}$ and $\Delta\bar{\nu} = 818\,\mathrm{cm}^{-1}$. This (small) shift is, firstly, attributed to the not-perfect accuracy of the reduced model for reproducing the PESs and, second, to the level of theory for the electronic structure. For instance, the minima of S_1 in the LVC model are $0.09\,\mathrm{eV}$ higher than the actual fully optimized minima of S_1, which is consistent with higher transition energies overall for the theoretical spectra.

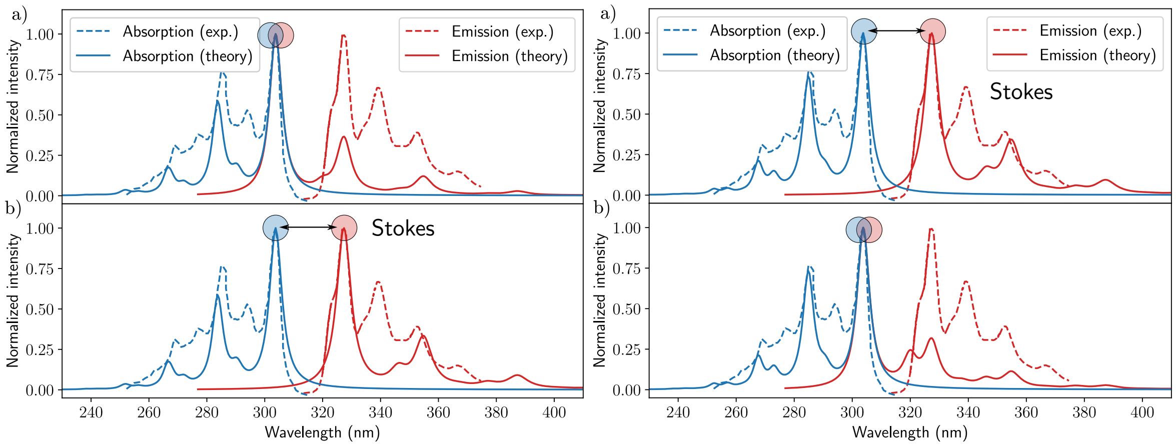

Figure 5.22: Theoretical absorption spectrum reproduced in (a) and (b), theoretical emission spectrum from a given (first or second) vibronic eigenstate, contributions of B_2 (a) and of A_1 (b). Left: absorption and emission toward and from the first vibronic eigenstate. Right: absorption and emission toward and from the second vibronic eigenstate. Blue and red circles indicate the maxima for the theoretical absorption and emission spectra. Realistically broadened bands are obtained using a damping time $\tau = 19\,\mathrm{fs}$. Experimental absorption and emission spectra (dashed lines in (a) and (b)) are reproduced from Spectrochim. Acta A 60, 1459 (2004) [39]. Copyright 2003 Elsevier B.V.

Overall, the absorption spectrum is correctly reproduced from what we can expect from a 3-dimensional model. We will see in the next section that these results are easily quantitatively improved by simply adding physically relevant degrees of freedom. On the other hand, the main unexplained feature of the experimental emission (the unusual Stokes shift), is not completely solved. Indeed, the study of the first vibronic eigenstates in the nonadiabatically coupled S_1/S_2 manifold results in an ambiguous initial state and indicates two types of contributions to the emission spectrum. The *non-Stokes* contributions are obtained and are expected to be prominent in steady-state spectroscopy, as if we had two different, uncoupled diabatic states. Indeed, vibronic eigenstates have most of the electronic population associated to the even vibrational contributions, which ultimately yield the *non-Stokes* contributions. The *Stokes* contributions are always identified as coming from wavepackets having undergone transfer from one diabatic state to another, caused by the non-zero and strong coupling between them. Let us mention here that the two diabatic states can be distinguished theoretically by their different polarization (y-axis for B_2, z-axis for A_1).

Concluding remarks

It is not trivial to understand which contributions or combination of contributions should or could be directly compared to the steady-state spectroscopy experiments. Indeed, the pair of vibronic eigenstates is sufficiently close so that we cannot expect only one of the two to be the "emissive state". Thus even if the ETDMs of both diabatic states were taken into account, the similar roles of B_2 and A_1 states would imply that both Stokes and non-Stokes contributions have non-negligible transition probabilities. An explanation could be found on the reliability of the *ab initio* data to estimate the L/QVC parameters such that the percentages of *transferred* wavefunction is clearly underestimated. However, non-Stokes contributions being similar to the absorption contributions, if the transfer were strong enough for Stokes contributions to be prominent, the 0_0^0 transition in absorption would also be too small compared to the 87_0^1 transition.

On a final note, we presented here a plausible interpretation for the presence of an unusual Stokes shift in the fluorescence spectrum of m22. However, our results are not in agreement with the usual way that spontaneous emission in fluorescence spectroscopy is understood. Indeed we expect, from our modelling, two differently polarized (and orthogonal) contributions to the emission spectrum, which would hold in the case of a "long-lived coherence" from absorption to emission. It is as if the emissive species conserved history about their initial excitation. This "long-lived coherence" should not occur in fluorescence experiments, and is still to be evaluated, both theoretically and experimentally. For the theoretical outlooks, one can first estimate the importance of the missing nuclear degrees of freedom (section 5.3), and second, can go toward simulating time-resolved fluorescence or angle-resolved (poralized-resolved) fluorescence. Of course, the latter meets with experimental outlooks, and have not been explored yet, to our knowledge.

Take-home messages

1. By relaxing 3-dimensional nuclear wavepackets in the (1+2) 3-dimensional LVC (or QVC) models, we identified a "tunnelling" pair of vibronic eigenstates, having non-negligible contributions in both electronic excited states (y- and z-polarized).
2. We characterized two different contributions (*Stokes* and *non-Stokes*) to the emission spectrum with (equivalently)
    - the identification of the possible vibronic transitions between the electronic ground state and the excited state manifold;

- a direct evaluation of the power spectra for absorption and emission.

3. The resulting absorption and *Stokes*-emission spectra are in good agreement with the experiments, although the absence of the *non-Stokes*-emission spectrum is not yet understood from our modelling

5.3 Toward higher dimensionality

We extend the previous study to a higher-dimensional LVC model, taking into accounts 10 normal modes in total. At our level of theory for the electronic structure, the ten selected modes account for almost 90% of the branching-space vectors components and most of the shifts from the FC geometry toward critical points of the S_1/S_2 PESs. In terms of vibrational nature, our choice of ten modes is a selection among the most optically active triangular (stretching), quinoidal (stretching) and anti-quinoidal (rock-bending), and acetylenic (stretching) normal modes of vibration, with ground-state wavenumbers ranging around $1100\,\mathrm{cm}^{-1}$, $1650\,\mathrm{cm}^{-1}$, and $2300\,\mathrm{cm}^{-1}$, respectively.

5.3.1 Systematic LVC model for the potential energy surfaces

In this section, and contrarily to the previous model, the reference point (origin) for PES cuts is the optimized FC geometry. The choice has been made so as to rely only on the optimized FC geometry in order to have a more transferable/systematic procedure for building simple models of PESs in PPE-oligomers. Indeed, as we will see in the next chapters, the optimization of the MECI is not easily guaranteed for other PPE-oligomers.

Let us note that, herein, the superscripts for diabatic quantities (1) and (2) correspond to the delocalized states B_2 and A_1, respectively, consistent with their ordering at the FC geometry. Also, because the FC geometry is fully included in the model, we take the vertical transition energies $E^{(s)}(\mathbf{Q}=0)$ for granted for the fitting procedure. Therefore, the reduced coordinates are now

$$\mathbf{Q}^{\text{10D}} = (Q_1 \dots, Q_i, \dots, Q_{3N-6}) \text{ with } \begin{cases} Q_i & = Q_i \in \mathbb{R} \text{ if } i \in (50, 53, 54, 75, 81, 84, 85, 86, 87, 88) \\ Q_i & = 0 \text{ otherwise.} \end{cases} \tag{5.19}$$

Because we generated the 1D-cuts from the FC geometry which is also the reference point of the LVC model, and because the model has no bilinear terms, we can fit the parameters of each profile independently of the others. For A_1 profiles we minimize the functions

$$\begin{aligned} L(k_i^{(1)}, k_i^{(2)}, \kappa_i^{(1)}, \kappa_i^{(2)}) = & \sum_n w^{(1)}(n) \left(V_1[k_i^{(1)}, k_i^{(2)}, \kappa_i^{(1)}, \kappa_i^{(2)}](Q_i(n)) - E_{\mathrm{S}_1}(n) \right)^2 \\ & + \sum_n w^{(2)}(n) \left(V_2[k_i^{(1)}, k_i^{(2)}, \kappa_i^{(1)}, \kappa_i^{(2)}](Q_i(n)) - E_{\mathrm{S}_2}(n) \right)^2 , \end{aligned} \tag{5.20}$$

and for B_2 profiles the following functions

$$L(k_i^{(1)},k_i^{(2)},\lambda_i)=\sum_n w^{(1)}(n)\left(V_1[k_i^{(1)},k_i^{(2)},\lambda_i](Q_i(n))-E_{S_1}(n)\right)^2 + \sum_n w^{(2)}(n)\left(V_2[k_i^{(1)},k_i^{(2)},\lambda_i](Q_i(n))-E_{S_2}(n)\right)^2 . \tag{5.21}$$

Note that we added weight functions to the fitting procedure for better robustness of the overall fit, with

$$w^{(1)}(n)=\exp\left(-\frac{E_{S_1}(n)-E_{S_1}(\mathbf{Q}=0)}{\left|E_{S_1}(n_{\text{max}})-E_{S_1}(\mathbf{Q}=0)\right|}\right) \tag{5.22}$$

which gives importance to S_1 for the regions near the apparent S_1 minima of the profiles and

$$w^{(2)}(n)=\exp\left(-\frac{\Delta E(n)}{\Delta E(n_{\text{min}})^2}\right) \tag{5.23}$$

which gives importance to S_2 for the regions near conical intersections (with $\Delta E(n)=E_{S_2}(n)-E_{S_1}(n)$) For each mode, we give in fig. 5.23 the 1D-cut, the results from the fitting procedure for the concerned 1D-cut and the weights used to obtain such results. Overall, we obtain a very good agreement between the *ab initio* PESs and the model of PESs along the 1D-cuts.

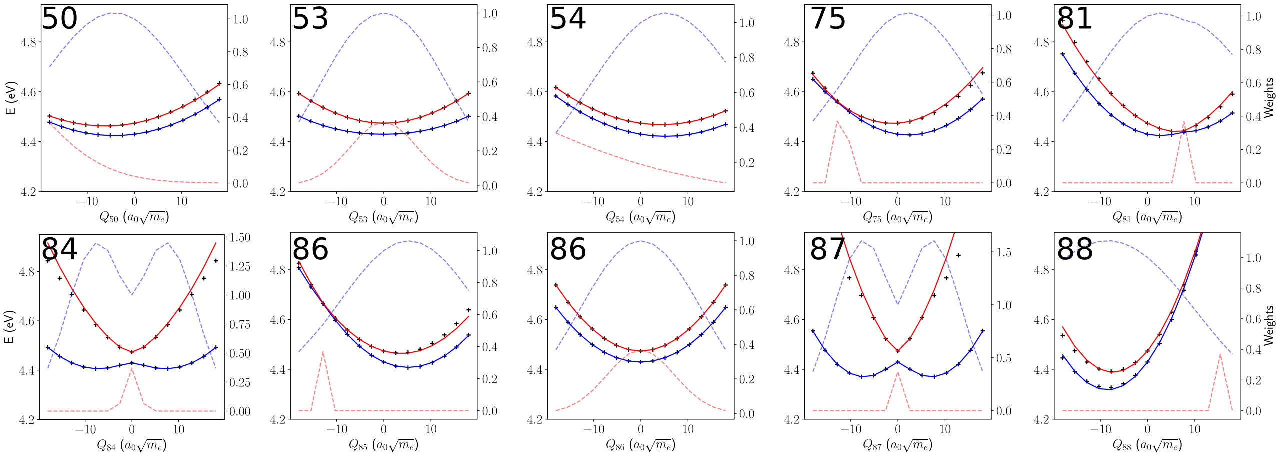

Figure 5.23: Adiabatic energies (in eV) from electronic structure calculations (symbol +) and from the 2-state 10-dimensional LVC model, along Cartesian displacements associated to the selection of S_0 normal modes. For unspecified coordinates, the values are those at the FC geometry (0); all coordinates are mass-weighted and given in atomic units. The weights functions used in the fitting procedure are also given (dashed lines) with ranges specified in the right axis of each figure.

The LVC parameters are given in table 5.9. Let us already note that the results for the modes 81, 87, and 88 are comparable between the 3D and 10D models, although the reference geometry for 1D-cuts was not the same. Again, we assess the validity of the LVC model by searching for the critical points (minima, transition states, and MECI) within the PES of the reduced model. Such critical points are described in table 5.10. A good agreement is found when comparing fully optimized geometries, with overall better described minima in S_1 for the 10-dimensional model than for the 3-dimensional model, as expected.

Table 5.9: Frequency (in cm^{-1}) and characteristic shift (in $a_0\sqrt{m_e}$) of the energy gradient and inter-state coupling gradient for the delocalized representation of the LVC model, obtained upon fitting 1D-cuts through the 10 selected modes. The parameters $\omega_i^{(s)}$ correspond to curvatures $k_i^{(s)}$. The parameters $d_i^{(s)}$ correspond to energy gradients $\kappa_i^{(s)}$. The parameters $d_i^{(12)}$ correspond to inter-state coupling gradient λ_i. The vertical transition energies are those obtained from electronic structure calculation at the FC geometry. The corresponding LVC and parameters in mass-weighted atomic units are gathered in appendix B.

Mode i	Symmetry	$\omega_i^{(1)}$	$\omega_i^{(2)}$	$d_i^{(1)}$	$d_i^{(2)}$	$d_i^{(12)}$
50	A1	1014	1005	4.318	6.185	0.0
53	B2	1034	1014	0.0	0.0	3.843
54	A1	1026	1027	-5.274	-4.347	0.0
75	A1	1445	1477	-2.283	1.061	0.0
81	A1	1640	1546	-2.747	-7.31	0.0
84	B2	1533	1780	0.0	0.0	-7.251
85	A1	1670	1608	-5.242	-3.706	0.0
86	B2	1629	1623	0.0	0.0	1.478
87	B2	2316	2387	0.0	0.0	-7.155
88	A1	2346	2380	8.487	7.318	0.0

Table 5.10: Characteristics of the critical points obtained in the PESs of the 10-dimensional LVC Hamiltonian model. The first part of the table gathers the energy (in eV) for the two adiabatic states for the 10-dimensional geometries of the critical points. The second part of the table gives the critical-point positions in normal coordinates (in $a_0\sqrt{m_e}$), with respect to the FC geometry.

	$E(\mathrm{S}_1)$	$E(\mathrm{S}_2)$	ΔE	50	53	54	75	81	84	85	86	87	88
MinS$_1$	4.176	4.688	0.256	-4.798	-3.513	5.008	1.358	4.356	7.325	4.637	-1.462	7.112	-7.981
MinS$_2$	4.301	4.324	0.012	-6.185	0.000	4.347	-1.061	7.310	0.000	3.706	0.000	0.000	-7.318
TS(B$_2$)	4.273	4.351	0.039	-4.318	0.000	5.274	2.283	2.747	0.000	5.242	0.000	0.000	-8.487
TS(A$_1$)	4.301	4.324	0.012	-6.185	0.000	4.347	-1.061	7.310	0.000	3.706	0.000	0.000	-7.318
MECI	4.329	4.330	$<$ 0.001	-7.148	0.518	2.271	-2.330	8.734	-0.010	2.576	-0.064	0.051	-6.700

5.3.2 A first step toward high-dimensional quantum dynamics

We run similar dynamics calculations as in the case of the 3-dimensional model. Because of the number of degrees of freedom, a scheme for the contraction of the SPFs basis set has to be chosen. For the sake of simplicity and because the number of modes is not overwhelming, we choose to use the MCTDH ansatz with simple mode combination. Four combined modes are defined by combining

- the triangular modes (50, 53 and 54);
- the quinoidal and anti-quinoidal modes of the central phenylene ring (75, 81 and 84);

- the quinoidal modes of the peripheral phenylene rings (85 and 86);
- and the acetylenic modes (87 and 88).

This choice was made so as to have overall good convergence (conservation of energy and conservation of centers of wavepackets along B_2 normal modes to 0, *i.e.* no symmetry breaking) within a reasonable computational cost (about 1 h of human-time on a 16-core machine, for 200 fs of simulation). The numerical parameters for the definition of the MCTDH wavepackets are given in table 5.11.

Table 5.11: Single-particle functions (SPFs) and primitive basis (PB) parameters for the relaxation and propagation of nuclear wavepackets. The degrees of freedom are grouped in four combined modes to reduce the computational cost of the propagation. Setting the reduced masses for the primitive basis harmonic oscilator functions to 1.0 is relevant when using mass-weighted coordinates.

Coordinates	Basis type	Size of the basis	Eq. position	Frequency	Reduced mass	Comb Mode	SPFs
Q_{50}	HO	15	0.0	1026 cm^{-1}	1.0	#1	17
Q_{53}	HO	15	0.0	1029 cm^{-1}	1.0	#1	
Q_{54}	HO	15	0.0	1029 cm^{-1}	1.0	#1	
Q_{75}	HO	15	0.0	1473 cm^{-1}	1.0	#2	21
Q_{81}	HO	15	0.0	1656 cm^{-1}	1.0	#2	
Q_{84}	HO	15	0.0	1682 cm^{-1}	1.0	#2	
Q_{85}	HO	15	0.0	1692 cm^{-1}	1.0	#3	13
Q_{86}	HO	15	0.0	1694 cm^{-1}	1.0	#3	
Q_{87}	HO	15	0.0	2367 cm^{-1}	1.0	#4	13
Q_{88}	HO	15	0.0	2367 cm^{-1}	1.0	#4	

The energies and populations of the first two vibronic eigenstates in the S_1/S_2 manifold are presented in table 5.12. Let us notice that the transferred population is more important for this 10-dimensional model than for the 3-dimensional model, with 25% and 40% of transferred population for the first two eigenstates, respectively.

Table 5.12: Vibronic eigenstates energy and diabatic populations. The transition energy is computed by setting the energy reference to the zero-point energy of the 10D model, $E = 0.993\,\mathrm{eV}$

Vibronic state	Total energy (eV)	Transition energy (eV)	P_{A_1}	P_{B_2}
$\Psi^{(0)}_{\mathrm{exc}}$	5.138	4.145	0.75	0.25
$\Psi^{(1)}_{\mathrm{exc}}$	5.161	4.168	0.40	0.60

The contributions to the absorption and emission spectra are also computed and shown in fig. 5.24 toward and from the first two vibronic eigenstates. The vibrational structure of the absorption spectrum is in good agreement with the experiments, thanks to the additional modes compared to the 3-dimensional model. This agreement is better for the low-energy vibronic transitions, and the differences (compared with the experiments) for higher-energy transitions can be attributed to anharmonicity. We find again, as expected, the same Stokes and non-Stokes contributions.

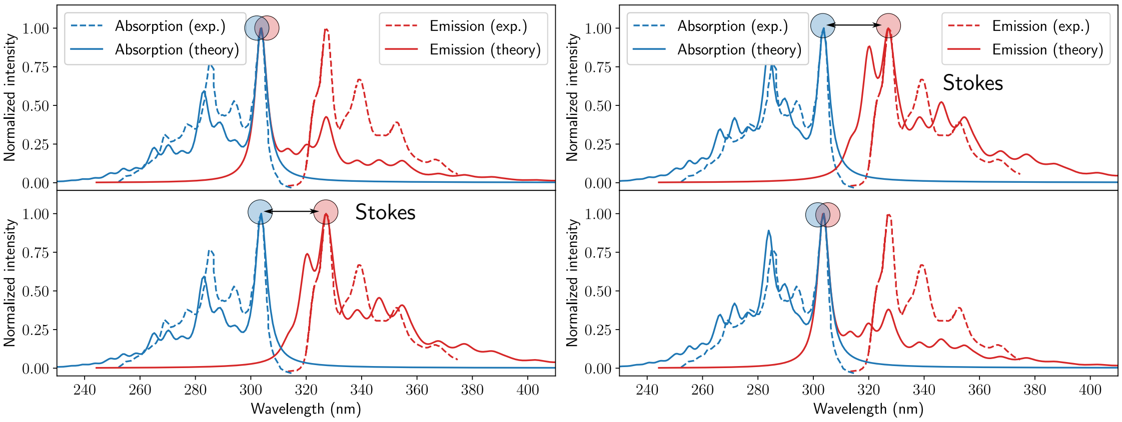

Figure 5.24: Theoretical absorption spectrum reproduced in (a) and (b), theoretical emission spectrum from a given (first or second) vibronic eigenstate, contributions of B_2 (a) and of A_1 (b). Left: absorption and emission toward and from the first vibronic eigenstate. Right: absorption and emission toward and from the second vibronic eigenstate. Blue and red circles indicate the maxima for the theoretical absorption and emission spectra. Realistically broadened bands are obtained using a damping time $\tau = 19\,\text{fs}$. Experimental absorption and emission spectra (dashed lines in (a) and (b)) are reproduced from Spectrochim. Acta A 60, 1459 (2004) [39]. Copyright 2003 Elsevier B.V.

The non-Stokes contributions share the vibrational structure with the absorption spectrum. However, the Stokes contributions now exhibit an intense transition at $320\,\text{nm}$, before the “0-1” transition 87^0_1 (associated to the non-totally symmetric acetylenic stretching normal mode). This new transition is another “0-1” transition, 84^0_1 associated to the anti-quinoidal rock-bending mode 84. It is expected to be intense because of the strength of the coupling along the mode 84. Indeed the transferred wavepacket has almost $|v = 1\rangle$ vibrational contribution along both modes 84 and 87. In the experiments, such a band is not directly observed, but we note the presence of a shoulder in the blue-region of the most intense band of emission. At the moment, our main hypothesis is that the parametrization and the level of theory we used for the electronic structure calculations may overestimate the coupling along the normal mode 84. It is also possible that the LVC model is too simple to take into account strong coupling along several directions, with the same order of magnitude.

With the same idea as when looking at early dynamics, we can study the “trajectory” of the center of the wavepackets for the two different excitations and along the various normal modes of vibration. We propose to evaluate the state-specific expectation value of the position operators as functions of time, see fig. 5.25. More importantly, we can check that the wavepackets are centered with respect to the B_2 normal modes of vibration (not breaking symmetry). This is also a check for validating the choice of the primitive basis set contraction (the choice of the combined modes and associated SPFs basis size). Indeed we observed that the position along the B_2 normal modes is one of the first observable to significantly diverge when the calculation is not converged enough because of primitive or SPFs basis choices (unphysical symmetry breaking).

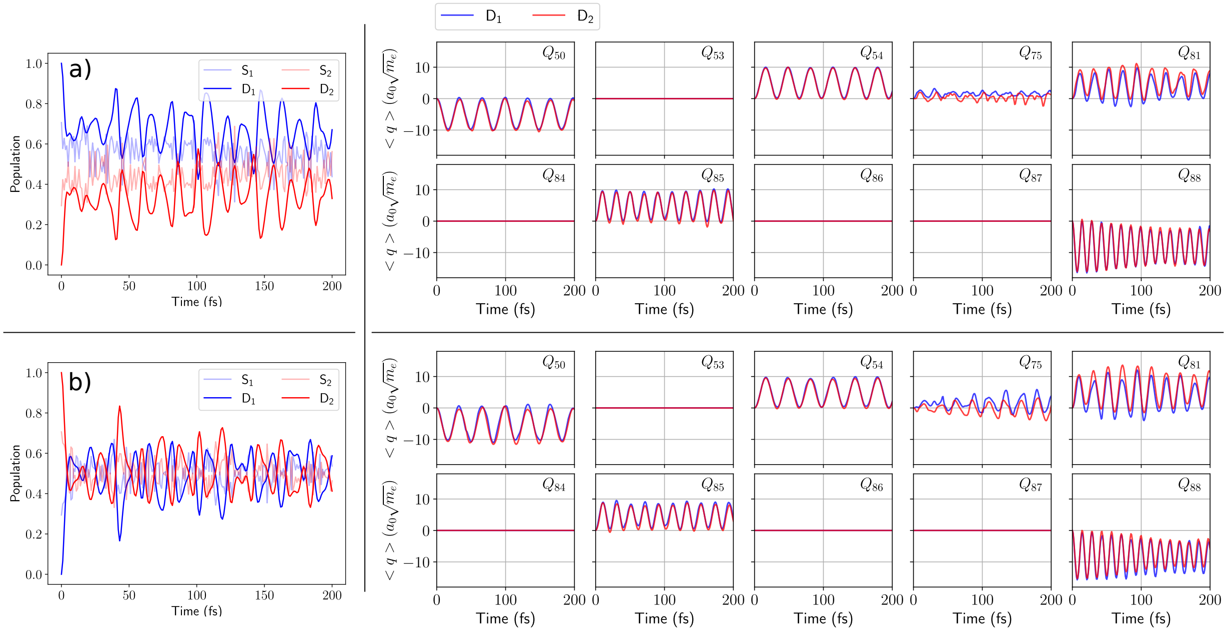

Figure 5.25: Left: Time evolution of the population of the diabatic (plain lines) and adiabatic states (in transparency). Right: Time evolution of the state-specific expectation values of the position operator in diabatic states $D_1 = B_2$ (blue lines) and $D_2 = B_1$ (red lines) for the different normal modes of vibration in the 10-dimensional model. Labels a) and b) refer to initial excitation on the diabatic state B_2 and A_1, respectively.

Again, we observe the similar role of the B_2 and A_1 diabatic states after an initial excitation on a pure diabatic state. Overall, the symmetry properties of the excited wavepacket is maintained (as expected). Such analysis of the trajectory of the wavepackets will come handy in the following for studying:

- the use of more complicated initial states and of possible symmetry-breaking for the wavepackets propagation (see chapter 8);
- the electronic-vibrational communication in excitation-energy transfer in asymmetrically substituted PPE-oligomers and for comparision to mixed quantum-classical dynamics.

Take-home messages

1. We successfully extended our strategy for the simulation of absorption and emission spectra for the case of strongy nonadiabatically coupled electronic excited states to medium-

dimensionality (ten degrees of freedom) for both the PES models and the wavepackets dynamics.

2. Our results are qualitatively improved, as expected by taking into account more optically active modes, but the absence of the *non-Stokes* contribution in the absorption is yet to be explained.

Let us now conclude on our quantitative results for both the low- and medium-dimensional studies of 1,3-bis(phenylethynyl)benzene.

5.4 Concluding remarks

5.4.1 Fluorescence in the context of nonadiabatically coupled electronic excited states

We presented here the first quantum dynamics study of 1,3-bis(phenylethynyl)benzene (m22) *via* explicit wavepacket propagation. This study aimed at the exploration and characterization of the adiabatic PESs of m22; the diabatization and choice of models (3-dimensional LVC/QVC and 10-dimensional LVC) of such PESs; and the modelling of absorption and emission properties in the context of a nonadiabatic process. Our results are summarized and compared with time-independent simulations of vibronic spectra and with the low-temperature experimental UV-visible spectra in fig. 5.26, left. The spectra are slightly shifted so that the most intense band (identified as a band-origin 0_0^0 transition) in absorption matches between experiments and theory (fig. 5.26, right).

We find that the case of m22 is a striking example of a breaking of the Born-Oppenheimer approximation with significant effect on the observed vibronic spectra. Indeed, the results from time-independent spectra simulations, within the Born-Oppenheimer approximation, reproduce the absorption (blue lines) but also the associated mirror-imaged emission (*non-Stokes* spectra, green lines). This result for emission is completely off compared to the experimental fluorescence, yet matches the expected emission spectrum of the single diphenylacetylene fragments. On the other hand, our modeling unveiled plausible contributions, induced by the presence of a conical intersection between S_1 and S_2, which are consistent with the experimentally observed Stokes shift (*Stokes* spectra, red lines).

However and as already stated, our simulations cannot discriminate between *non-Stokes* and *Stokes* contributions to the emission spectrum. With our results and comparison to the experiments, we find that the description of fluorescence experiments is ambiguous is the case of strongly nonadiabatically coupled electronic excited states, for which complicated vibronic eigenstates exist.

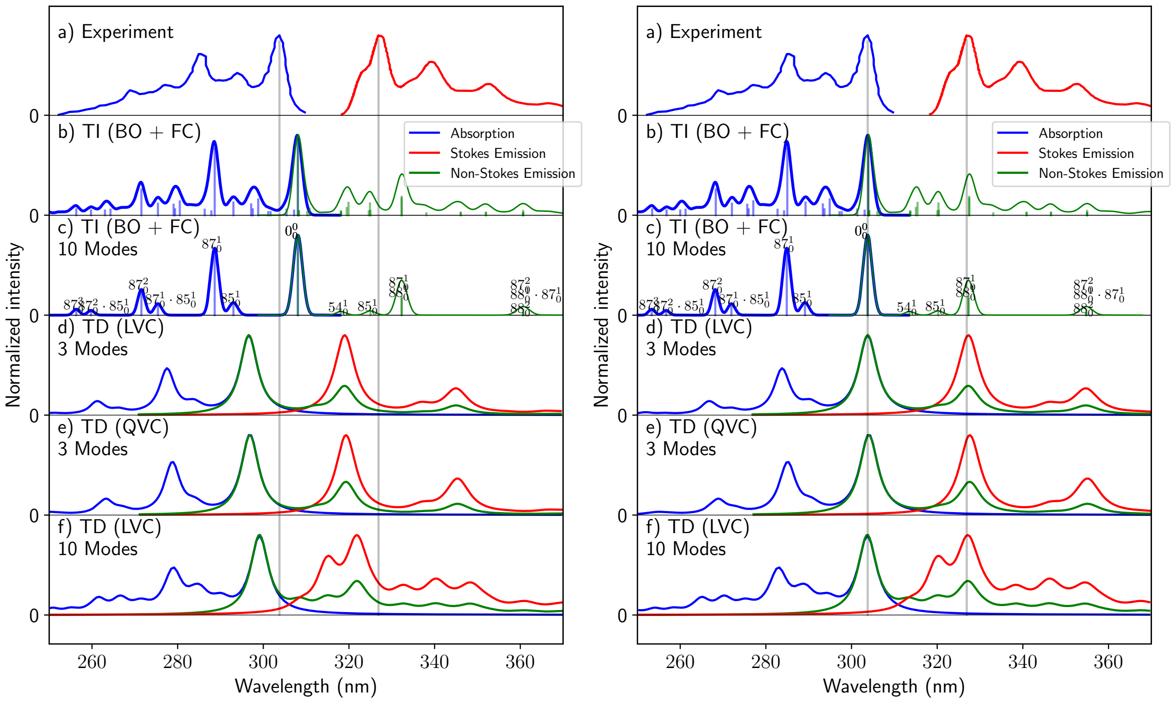

Figure 5.26: Comparison of absorption (in blue) and emission (in green or red) spectra from the experiments, panel a), and from different types of simulations, panels b) to f). For emission, we distinguish *non-Stokes* and *Stokes* contributions, in green and red, respectively. To the left, all theoretical spectra are unshifted in energy. To the right, all theoretical spectra are shifted (within each panel) such that the maximum of theoretical absorption matches the maximum of experimental absorption. Panels b) and c) are obtained from routine time-independent Franck-Condon calculation with only ten modes selected in c). Panels d) and e) are obtained from time-dependent calculations with the 3-dimensional models (LVC and QVC, respectively). Panel f) is obtained from time-dependent calculations with the 10-dimensional model (LVC).

5.4.2 Outlook for theoretical and experimental studies

This study objectives were to have a complete understanding of the m22 emission spectrum and to reproduce the experimental Stokes shift. We were able, as of now, to propose a rationalization of such an energy shift. We also hope that we have correctly raised the question of the relevant nature of the non-trivial initial state for spontaneous emission in the context of strongly nonadiabatically coupled electronic excited states. In particular, this question calls for further theoretical and experimental studies.

First, theoretically: can we better understand the process of spontaneous emission with such an ill-behaved system with respect to the Born-Oppenheimer approximation and Franck-Condon principle? The first improvement could come from scientific communities working on explicitly including the electric field to molecular physics simulations. Indeed, the presented study is limited to the approximation of sudden excitations, with no explicit light-matter couplings between the electronic ground state and the targeted electronic excited states. Having a time-resolved characterization of the electronic (or more specifically vibronic) excitations from the electronic ground to the excited states would help us to better tackle the rationalization of the evolution of the initial wavepackets.

Complementary work already started regarding this question, *via* the use of simple LVC models and hierarchical equations of motion (HEOM) [55], will not be directly presented here but is an outlook of this work. On the other hand, the explicit simulation of spontaneous emission *via* quantum electrodynamics (quantization of the electric field and of the vacuum state) is also out of the scope of this thesis.

Second, experimentally: is there a way to discriminate the theoretically identified Stokes and non-Stokes contributions? The theoretical contributions involved in our simulations of the UV-visible spectra of m22 are associated to well-defined polarizations. However, steady-state spectroscopy experiments are not supposed to depend on the orientation of the molecule, in particular in solution (free rotational averaging). The question raised is now the very nature of fluorescence obtained experimentally for m22: is it spontaneous emission; a sort of stimulated emission; a Raman resonant-like emission? New experiments such as time-resolved fluorescence (for a study of electronic coherence) and angle-resolved fluorescence (for a study of polarization) might help us to address the question. In any case, we can confess that no answer has been provided to us over the last couple of years.

5.4.3 The role of the symmetry of the chromophore as regards excitation-energy transfer

Replacing the chromophore m22 in the context of the light-harvesting PPE-dendrimers, what is the role of the coupled electronic excited states? As we have seen, the S_1/S_2 manifold of m22 can be seen as a pair of localized states, which correctly fits the *additive* property of the absorption spectrum expected in a PPE-dendrimer. More importantly, the oscillator strength of the first excited state $(f = 1.71)$ in the m22 PPE-oligomer (a *pseudo* dimer of p2) is enhanced compared to the oscillator strength of the first excited state $(f = 0.93)$ in the isolated p2 PPE-oligomer. In addition, the second excited state of the m22 PPE-oligomer, with almost identical excitation energy, is also bright, which gives a second channel of initial excitation as regards excitation-energy transfer.

In other words, the symmetrically substituted chromophores in the PPE-dendrimers are likely to absorb more efficiently the light, with close-to-degeneracy excited states in the UV spectral domain and enhanced oscillator strengths compared to isolated diphenylacetylenes. The role of the symmetry for the efficiency of the chromophore as regards the transfer of absorbed energy will be studied in part III, chapter 7, where we study the tri-*meta*-substituted PPE-oligomer with the chromophore m22 linked with an energy-trap.

5.A Table of characteristics for the vibronic excited eigenstates

Table 5.13: Energy, diabatic populations and wavepacket centers for vibronic eigenstates obtained from initialization on A_1 (top table) or B_2 (bottom table) for the LVC model. The vibronic eigenstates have been obtained *via* improved relaxation. To ensure better convergence, the primitive basis and SPFs basis sets have been augmented (51 HO basis functions for the PB and multi-set (1,21,21) for the SPFs)

Relax=n	0	1	2	3	4	5	6	7	8	9
From initial state A_1										
Energy (eV)	4.188	4.372	4.556	4.473	4.556	5.275	5.296	5.286	6.512	6.51
$\mathcal{P}_{\mathrm{A}_1}$	0.781	0.758	0.741	0.736	0.741	0.618	0.526	0.595	0.595	0.578
$\mathcal{P}_{\mathrm{B}_2}$	0.219	0.242	0.259	0.264	0.259	0.382	0.474	0.405	0.405	0.422
$\langle Q_{87}\rangle_{\mathrm{A}_1}$ (a.u.)	0	0	0	-0.002	-0	0.011	0.004	-0.008	-0.008	0.024
$\langle Q_{87}\rangle_{\mathrm{B}_2}$ (a.u.)	0	0	0.001	-0.008	-0	-0.01	-0.002	-0.016	-0.015	0.016
$\langle Q_{81}\rangle_{\mathrm{A}_1}$ (a.u.)	7.177	8.997	10.605	6.767	10.605	5.338	5.438	5.273	6.052	6.11
$\langle Q_{81}\rangle_{\mathrm{B}_2}$ (a.u.)	5.55	-0.186	-4.271	6.106	-4.27	6.966	5.688	6.724	5.681	5.43
$\langle Q_{88}\rangle_{\mathrm{A}_1}$ (a.u.)	-7.34	-7.327	-7.317	-9.661	-7.317	-8.426	-6.848	-7.606	-6.799	-6.594
$\langle Q_{88}\rangle_{\mathrm{B}_2}$ (a.u.)	-7.793	-7.893	-7.954	-1.457	-7.954	-6.331	-8.668	-7.702	-8.867	-9.106
$\langle n_{87}\rangle_{\mathrm{A}_1}$	0.098	0.116	0.132	0.304	0.132	2.221	2.238	2.532	3.182	3.35
$\langle n_{87}\rangle_{\mathrm{B}_2}$	1.049	1.061	1.069	1.208	1.069	2.638	2.361	2.755	3.614	3.849
$\langle n_{81}\rangle_{\mathrm{A}_1}$	0.196	1.274	2.344	0.185	2.344	0.438	0.136	0.257	2.183	2.17
$\langle n_{81}\rangle_{\mathrm{B}_2}$	0.118	0.745	1.486	0.144	1.486	0.447	0.138	0.284	2.152	2.13
$\langle n_{88}\rangle_{\mathrm{A}_1}$	0.291	0.29	0.289	1.287	0.289	1.968	2.231	1.772	4.24	4.11
$\langle n_{88}\rangle_{\mathrm{B}_2}$	0.328	0.336	0.342	0.415	0.342	1.845	2.38	1.938	4.339	4.119
From initial state B_2										
Energy (eV)	4.180	4.367	4.555	4.555	4.555	5.304	5.305	5.300	6.531	6.522
$\mathcal{P}_{\mathrm{A}_1}$	0.195	0.224	0.251	0.251	0.251	0.505	0.459	0.602	0.562	0.512
$\mathcal{P}_{\mathrm{B}_2}$	0.805	0.776	0.749	0.749	0.749	0.495	0.541	0.398	0.438	0.488
$\langle Q_{87}\rangle_{\mathrm{A}_1}$ (a.u.)	0	0	0	0	0	-0.016	0	0.005	0.011	-0.004
$\langle Q_{87}\rangle_{\mathrm{B}_2}$ (a.u.)	0	0	0	0	0	-0.02	0	0.008	0.016	0
$\langle Q_{81}\rangle_{\mathrm{A}_1}$ (a.u.)	5.256	10.899	15.096	15.096	15.096	5.54	5.229	5.565	6.067	5.723
$\langle Q_{81}\rangle_{\mathrm{B}_2}$ (a.u.)	3.706	2.265	0.799	0.799	0.799	5.38	5.253	6.461	5.346	5.271
$\langle Q_{88}\rangle_{\mathrm{A}_1}$ (a.u.)	-7.709	-7.613	-7.543	-7.543	-7.543	-8.17	-8.891	-7.156	-8.007	-9.056
$\langle Q_{88}\rangle_{\mathrm{B}_2}$ (a.u.)	-8.152	-8.157	-8.161	-8.161	-8.161	-7.298	-6.85	-8.348	-7.25	-6.342
$\langle n_{87}\rangle_{\mathrm{A}_1}$	1.048	1.06	1.07	1.07	1.07	1.938	1.899	2.024	2.901	2.821
$\langle n_{87}\rangle_{\mathrm{B}_2}$	0.088	0.107	0.131	0.131	0.131	1.288	1.255	2.012	3.184	3.042
$\langle n_{81}\rangle_{\mathrm{A}_1}$	0.106	1.21	2.289	2.289	2.289	0.14	0.128	0.139	2.108	2.19
$\langle n_{81}\rangle_{\mathrm{B}_2}$	0.053	0.996	1.934	1.934	1.934	0.144	0.139	0.191	2.055	2.16
$\langle n_{88}\rangle_{\mathrm{A}_1}$	0.321	0.313	0.307	0.307	0.307	2.593	2.754	2.351	4.781	4.91
$\langle n_{88}\rangle_{\mathrm{B}_2}$	0.358	0.359	0.36	0.36	0.36	3.361	3.284	2.883	4.746	4.571

Table 5.14: Energy, diabatic populations and wavepacket centers for vibronic eigenstates obtained from initialization on A_1 (top table) or B_2 (bottom table) for the QVC model. The vibronic eigenstates have been obtained *via* improved relaxation. To ensure better convergence, the primitive basis and SPFs basis sets have been augmented (51 HO basis functions for the PB and multi-set (1,21,21) for the SPFs)

Relax=n	0	1	2	3	4	5	6	7	8	9
From initial state A_1										
Energy (eV)	4.187	4.369	4.442	4.442	4.485	5.265	5.264	5.266	6.535	6.553
$\mathcal{P}_{A_1}$	0.77	0.742	0.651	0.647	0.688	0.613	0.589	0.631	0.512	0.455
$\mathcal{P}_{B_2}$	0.23	0.258	0.349	0.353	0.312	0.387	0.411	0.369	0.488	0.545
$\langle Q_{87}\rangle_{A_1}$ (a.u.)	0	0	0	-0.015	0	-0.006	-0.019	0.011	0.013	-0.012
$\langle Q_{87}\rangle_{B_2}$ (a.u.)	0	0	-0.046	-0.032	0	0.01	0.034	-0.014	0.022	-0.028
$\langle Q_{81}\rangle_{A_1}$ (a.u.)	6.869	9.103	4.867	4.806	6.237	3.875	3.758	3.955	5.49	4.748
$\langle Q_{81}\rangle_{B_2}$ (a.u.)	5.098	-1.333	7.895	7.914	5.388	8.44	8.106	8.735	4.752	4.94
$\langle Q_{88}\rangle_{A_1}$ (a.u.)	-8.026	-7.838	-5.128	-5.148	-10.951	-7.583	-6.958	-7.552	-10.296	-11.037
$\langle Q_{88}\rangle_{B_2}$ (a.u.)	-9.179	-9.544	-14.473	-14.347	-2.686	-9.999	-10.832	-10.116	-6.856	-6.684
$\langle n_{87}\rangle_{A_1}$	0.104	0.134	0.582	0.6	0.417	0.922	1.036	0.847	5.172	4.283
$\langle n_{87}\rangle_{B_2}$	1.056	1.08	1.328	1.333	1.26	2.019	2.182	1.889	5.519	4.135
$\langle n_{81}\rangle_{A_1}$	0.18	1.251	0.167	0.166	0.162	0.521	0.41	0.547	0.942	0.598
$\langle n_{81}\rangle_{B_2}$	0.1	0.67	0.246	0.247	0.113	0.544	0.417	0.601	0.655	0.515
$\langle n_{88}\rangle_{A_1}$	0.348	0.342	0.558	0.541	1.3	3.152	3.111	3.183	3.729	5.133
$\langle n_{88}\rangle_{B_2}$	0.454	0.494	1.18	1.154	0.328	2.765	2.753	2.902	3.537	4.996
From initial state B_2										
Energy (eV)	4.176	4.364	4.552	4.552	4.552	5.301	5.303	5.303	6.589	6.597
$\mathcal{P}_{A_1}$	0.194	0.218	0.242	0.242	0.242	0.274	0.274	0.274	0.46	0.453
$\mathcal{P}_{B_2}$	0.806	0.782	0.758	0.758	0.758	0.726	0.726	0.726	0.54	0.547
$\langle Q_{87}\rangle_{A_1}$ (a.u.)	0	0	0	0	0	0.024	0.011	-0.009	-0.011	0.024
$\langle Q_{87}\rangle_{B_2}$ (a.u.)	0	0	0	0	0	-0.007	0.005	-0.005	-0.004	0.023
$\langle Q_{81}\rangle_{A_1}$ (a.u.)	4.815	9.849	13.928	13.928	13.927	5.59	5.695	5.682	5.846	5.873
$\langle Q_{81}\rangle_{B_2}$ (a.u.)	3.437	2.196	0.866	0.866	0.866	3.467	3.458	3.466	4.177	4.089
$\langle Q_{88}\rangle_{A_1}$ (a.u.)	-9.131	-8.96	-8.803	-8.803	-8.803	-11.12	-9.437	-9.41	-10.047	-10.112
$\langle Q_{88}\rangle_{B_2}$ (a.u.)	-8.799	-8.799	-8.804	-8.804	-8.804	-7.936	-8.55	-8.559	-7.302	-7.355
$\langle n_{87}\rangle_{A_1}$	1.052	1.059	1.068	1.068	1.068	1.675	1.521	1.527	5.751	5.816
$\langle n_{87}\rangle_{B_2}$	0.096	0.11	0.13	0.13	0.13	0.385	0.326	0.329	4.36	3.958
$\langle n_{81}\rangle_{A_1}$	0.09	1.182	2.256	2.256	2.256	0.288	0.388	0.377	0.474	0.512
$\langle n_{81}\rangle_{B_2}$	0.046	1.003	1.95	1.95	1.95	0.127	0.158	0.155	0.6	0.699
$\langle n_{88}\rangle_{A_1}$	0.45	0.434	0.419	0.419	0.419	3.588	3.526	3.525	3.698	3.631
$\langle n_{88}\rangle_{B_2}$	0.418	0.418	0.419	0.419	0.419	4.059	4.14	4.14	4.792	5.132

Table 5.15: Relative difference between the values obtained from the LVC and QVC models, tables 5.13 and 5.14.

Relax=n	0	1	2	3	4	5	6	7	8	9
From initial state $\mathrm{A_1}$										
Energy (eV)	0.024	0.069	2.566	0.698	1.583	0.190	0.608	0.380	0.352	0.656
$\mathcal{P}_{\mathrm{A_1}}$	1.429	2.156	13.825	13.756	7.703	0.816	10.696	5.705	16.211	27.033
$\mathcal{P}_{\mathrm{B_2}}$	4.783	6.202	25.788	25.212	16.987	1.292	15.328	9.756	17.008	22.569
$\langle Q_{87}\rangle_{\mathrm{A_1}}$	0	0	0	-86.667	0	-283.333	-121.053	172.727	161.538	-300.000
$\langle Q_{87}\rangle_{\mathrm{B_2}}$	0	0	-102.174	-75.000	0	200.000	105.882	-14.286	168.182	-157.143
$\langle Q_{81}\rangle_{\mathrm{A_1}}$	4.484	1.164	117.896	40.803	70.034	37.755	44.705	33.325	10.237	28.686
$\langle Q_{81}\rangle_{\mathrm{B_2}}$	8.866	-86.047	154.098	22.846	179.250	17.464	29.830	23.022	19.550	9.919
$\langle Q_{88}\rangle_{\mathrm{A_1}}$	-8.547	-6.520	-42.687	-87.665	-33.184	-11.117	-1.581	-0.715	-33.965	-40.256
$\langle Q_{88}\rangle_{\mathrm{B_2}}$	-15.100	-17.299	-45.042	-89.845	-196.128	-36.684	-19.978	-23.863	-29.332	-36.236
$\langle n_{87}\rangle_{\mathrm{A_1}}$	5.769	13.433	77.320	49.333	68.345	140.889	116.023	198.937	38.476	21.784
$\langle n_{87}\rangle_{\mathrm{B_2}}$	0.663	1.759	19.503	9.377	15.159	30.659	8.203	45.844	34.517	6.917
$\langle n_{81}\rangle_{\mathrm{A_1}}$	8.889	1.839	1303.593	11.446	1346.914	15.931	66.829	53.016	131.741	262.876
$\langle n_{81}\rangle_{\mathrm{B_2}}$	18.000	11.194	504.065	41.700	1215.044	17.831	66.906	52.745	228.550	313.592
$\langle n_{88}\rangle_{\mathrm{A_1}}$	16.379	15.205	48.208	137.893	77.769	37.563	28.287	44.329	13.703	19.930
$\langle n_{88}\rangle_{\mathrm{B_2}}$	27.753	31.984	71.017	64.038	4.268	33.273	13.549	33.218	22.675	17.554
From initial state $\mathrm{B_2}$										
Energy (eV)	0.024	0.069	2.566	0.698	1.583	0.190	0.608	0.380	0.352	0.656
$\mathcal{P}_{\mathrm{A_1}}$	1.429	2.156	13.825	13.756	7.703	0.816	10.696	5.705	16.211	27.033
$\mathcal{P}_{\mathrm{B_2}}$	4.783	6.202	25.788	25.212	16.987	1.292	15.328	9.756	17.008	22.569
$\langle Q_{87}\rangle_{\mathrm{A_1}}$	0	0	0	-86.667	0	-283.333	-121.053	172.727	161.538	-300.000
$\langle Q_{87}\rangle_{\mathrm{B_2}}$	0	0	-102.174	-75.000	0	200.000	105.882	-14.286	168.182	-157.143
$\langle Q_{81}\rangle_{\mathrm{A_1}}$	4.484	1.164	117.896	40.803	70.034	37.755	44.705	33.325	10.237	28.686
$\langle Q_{81}\rangle_{\mathrm{B_2}}$	8.866	-86.047	154.098	22.846	179.250	17.464	29.830	23.022	19.550	9.919
$\langle Q_{88}\rangle_{\mathrm{A_1}}$	-8.547	-6.520	-42.687	-87.665	-33.184	-11.117	-1.581	-0.715	-33.965	-40.256
$\langle Q_{88}\rangle_{\mathrm{B_2}}$	-15.100	-17.299	-45.042	-89.845	-196.128	-36.684	-19.978	-23.863	-29.332	-36.236
$\langle n_{87}\rangle_{\mathrm{A_1}}$	5.769	13.433	77.320	49.333	68.345	140.889	116.023	198.937	38.476	21.784
$\langle n_{87}\rangle_{\mathrm{B_2}}$	0.663	1.759	19.503	9.377	15.159	30.659	8.203	45.844	34.517	6.917
$\langle n_{81}\rangle_{\mathrm{A_1}}$	8.889	1.839	1303.593	11.446	1346.914	15.931	66.829	53.016	131.741	262.876
$\langle n_{81}\rangle_{\mathrm{B_2}}$	18.000	11.194	504.065	41.700	1215.044	17.831	66.906	52.745	228.550	313.592
$\langle n_{88}\rangle_{\mathrm{A_1}}$	16.379	15.205	48.208	137.893	77.769	37.563	28.287	44.329	13.703	19.930
$\langle n_{88}\rangle_{\mathrm{B_2}}$	27.753	31.984	71.017	64.038	4.268	33.273	13.549	33.218	22.675	17.554

Chapter 6

The First Unit for Excitation-Energy Transfer in PPE-dendrimers

"Is this gradient, or this Hessian, mass-weighted? Should it be mass-weighted? and this displacement? What is its reduced mass? ..."

– Benjamin and me, *Every two weeks*

As already mentioned, dendrimers of poly(phenylene ethynylenes) (PPEs) exhibit efficient light-harvesting features. In chapter 5, we presented the chromophore of PPE-dendrimers, 1,3-bis(phenylethynyl)benzene (m22), for which the absorption properties were qualified as *additive* with respect to the two local diphenylenacetylene (p2) *pseudo* fragments. Although we have seen that the emission properties of m22 were more difficult to understand and reproduce, the local *pseudofragmentation* scheme is enough to understand the efficiency of m22 as a chromophore for light-harvesting dendrimers. In this chapter, we are now interested in the process of excitation-energy transfer: how is the energy, associated to light absorption by the chromophore, transferred within the molecule? In particular, atomistic simulations of the EET with explicit treatement of the initial excitation and the excitation transfer are challenging tasks. For answering these questions more practically, we focus on the first unit of excitation-energy transfer (EET) in PPE-dendrimers: the asymmetrically *meta*-substituted benzene (called m23 in the following, see fig. 6.1).

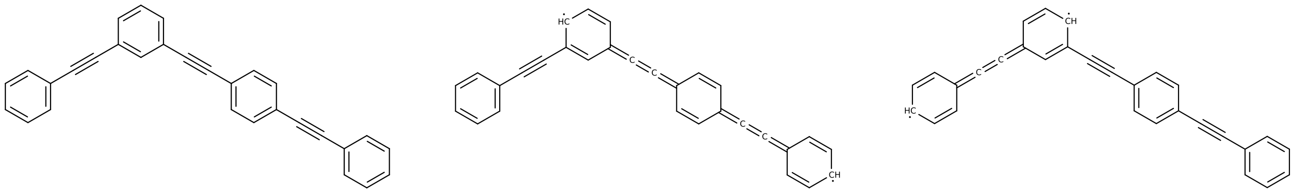

Figure 6.1: From left to right, representative Lewis structures of the minimum of the electronic ground state, the minimum of the first electronic excited state and the minimum of the second electronic excited state of the asymmetrically *meta*-substituted benzene.

The origin of EET in PPE-dendrimers and oligomers, among them m23, has been extensively studied both experimentally and theoretically. In the PPE-dendrimers, the role of the energy gradient (due to the different lengths of the branches) was first identified as central for the experimentally observed ultrafast EET [32,33,156,157]. In addition, the origin of the energy gradient, associated to local excitations (LE) for the excited states, was evidenced experimentally [34,35] and rationalized theoretically with Frenkel excitonic models [30, 31]. As regards the electronic structure of PPE-oligomers, Huang and co-workers proposed an extensive theoretical analysis of the excited states of m23 [38], and showed the reliability of CAM-B3LYP TD-DFT (compared to its computational cost) to reproduce the main features of the electronic excited states. On the other hand, Fernandez-Alberti and co-workers proposed, for m23 and other *meta*-substituted PPEs, the first fully atomistic and time-resolved simulations of EET in PPE-oligomers, *via* trajectory-based nonadiabatic molecular dynamics (trajectory surface hopping, TSH). Their direct-dynamics simulations unveiled ultrafast EET (within 30 fs after excitation) and highlighted the role of acetylenic bonds in the observed ultrafast and efficient EET [50, 51, 56, 58]. The transient absorption of m23 has also been simulated, using similar mixed-quantum classical nonadiabatic dynamics, and was proposed as a spectral fingerprint of EET [59].

In this chapter, we propose the simulation of EET *via* quantum wavepackets propagation, in the first unit of energy transfer of the PPE-dendrimer, m23. First in section 6.1 we interpret again the process of EET *via* electronic structure calculations, which gives us a simple stationary picture of EET within m23 (and is easily generalized to larger PPE-branches, see Ref [54]). In particular, we examine the EET through the lens of conical intersections and strongly nonadiabatically coupled electronic excited states. Next, we make use of this characterization to build dimensionally reduced vibronic coupling Hamiltonian (VCH) models in section 6.2, with the particular context of a conical intersection that is not induced by the symmetry of the electronic states. In section 6.3, we simulate the process of EET in our model, and analyse it *via* time-resolved studies of the correlations between electronic and nuclear quantities, energy decomposition and redistribution, and electronic coherence and decoherence. Finally, we explore different strategies to include most of the nuclear degrees of freedom and evaluate their influence on our modelling of EET.

6.1 Time-independent characterization

The level of theory (CAM-B3LYP/6-31+G*), is identical to the previous study of m22.

6.1.1 Electronic states and vibrational analysis

The minimum of the S_0 electronic ground state is a C_s molecular geometry ($N_{\text{at}} = 48$). The Lewis structure is, similarly to the case of m22, consistent with ground state acetylenic and aromatic patterns for the local acetylenes and benzenes. At this minimum of S_0 (FC geometry), the vertical transition energies (VTEs) for the first two singlet electronic states are $E(S_1) = 3.88$ eV and $E(S_2) = 4.45$ eV, respectively. We give the frontier orbitals and the most important transitions toward the two electronic states in fig. 6.2.

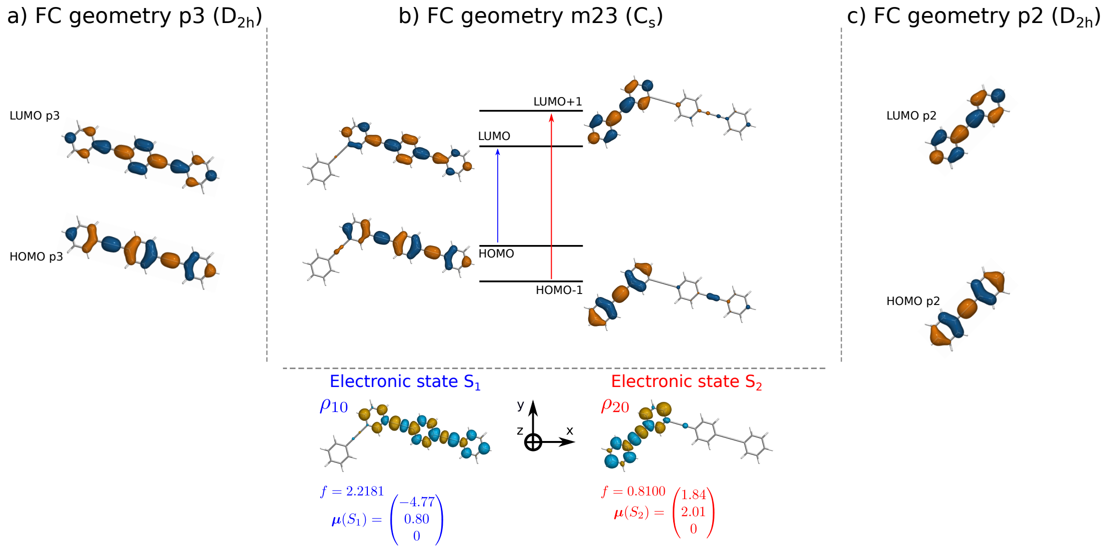

Figure 6.2: First frontier orbitals for the isolated p3 and p2 fragments (a and c, respectively) and for the m23 molecule (b) at the minimum geometry of S_0 in each case. For m23 (b), the most intense transition for a vertical transition toward S_1 (blue) and S_2 (red) is represented, with the associated electronic transition density, electric transition dipole moment (it atomic units), and oscillator strength.

S_1 is mainly obtained from a HOMO/LUMO transition (82%) and S_2 is mainly obtained from a HOMO-1/LUMO+1 transition (61%). For comparison, the first vertical transition energy in the isolated p3 and p2 fragments are $E(S_1, p3) = 3.90\,\text{eV}$ and $E(S_1, p2) = 4.48\,\text{eV}$, respectively (within $0.03\,\text{eV}$ the same as in m23). The frontier orbitals of the isolated fragments are also given in fig. 6.2 (all calculations are done at the same level of theory). We find that the *meta*-substitution sufficiently breaks the conjugation so that the first two electronic excited states at the FC geometry are ideally localized excitons. This contrasts with the symmetrically *meta*-substituted phenylene m22 where the electronic states were delocalized over the two fragments at the FC geometry, although localized excitons were obtained for the minima of its first excited state. Thus for m23, directly at the FC geometry and consistently, as we will see, with the minima of S_1 and S_2, the first pair of electronic excited states are a pair of localized excitons, which is the basis for future diabatic models.

We illustrate again the (local) excitonic character of the pair (S_1, S_2) by showing the transition densities toward the two electronic excited states, which are non-negligible only on the p3 and p2 *pseudo* fragments, respectively. Accordingly, both electronic excited states are bright, with the LE state on p3 having a stronger oscillator strength ($f(S_1) = 2.22$ and $f(S_2) = 0.81$) (and compare well with the oscillator strenths of the isolated p3 and p3 fragments, $f(\text{p3}) = 1.92$ and $f(\text{p2}) = 0.93$).

Normal modes for the electronic ground state

The normal-mode displacements at the FC geometry are adapted to the C_s point group, with in-plane and out-of-plane normal modes. In this chapter, we focus on the in-plane normal modes (A' symmetry label). In particular, and similarly to the study of m22, we are interested in quinoidal, anti-quinoidal, and acetylenic modes, for which the frequencies vary from $1600\,\text{cm}^{-1}$ to $2360\,\text{cm}^{-1}$. We show in fig. 6.3 the Cartesian displacements associated to eight of these quinoidal and acetylenic normal modes, along with a scheme of the associated most representative internal coordinates, and give the frequencies and reduced masses for these modes in table 6.1.

Although the electronic excited states are localized on the p2 and p3 *pseudo* fragments, the normal modes are not completely localized. For instance, as regards the acetylenic stretching modes (118, 119, and 120) we observe that 118 is mostly localized on the p3 fragment, but neither 119 nor 120 are perfectly localized on either the p3 or p2 fragments. However, a simple re-combination of the normal modes 119 and 120 yields a pair of more local modes adapted to the isolated fragments, for instance with 119 being the asynchronous stretching of the p3-acetylenic bonds and 120 being fully localized on the p2-acetylenic bond (fig. 6.4).

Critical points of the excited-state PESs

The minimum of the first electronic excited state S_1 is unambiguous, with energy $E(S_1) = 3.61\,\text{eV}$. The minimum of S_2 is obtained with energy $E(S_2) = 4.17\,\text{eV}$. The minimum of the second electronic excited

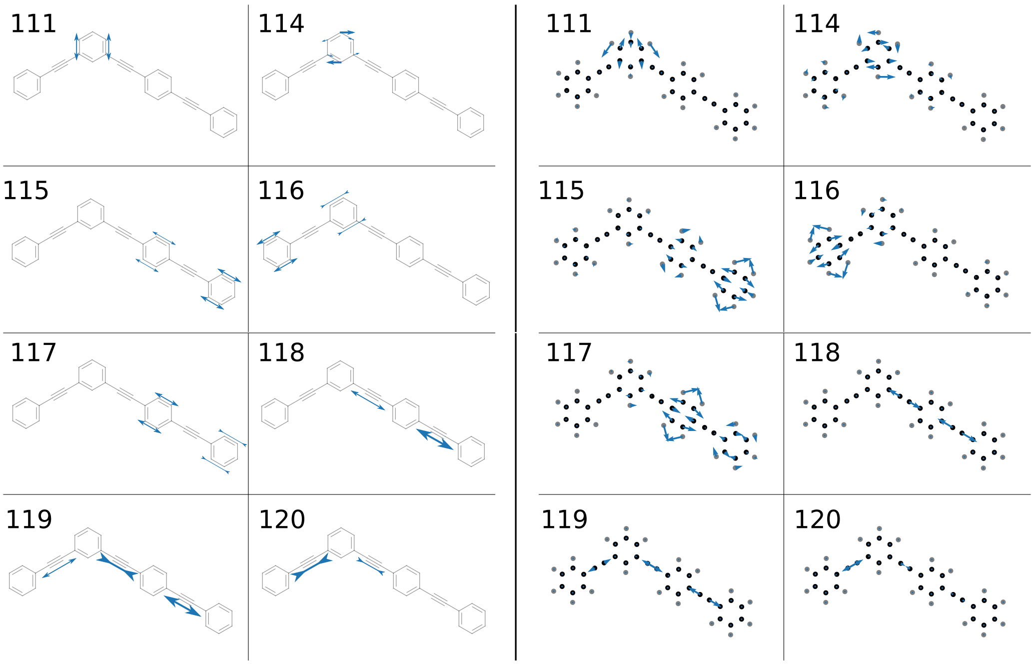

Figure 6.3: Left: Schematic representation of the main internal displacements associated to the 8 selected normal modes of vibration at the FC geometry of m23. Right: rigorous normalized Cartesian displacements associated to the 8 selected normal modes of vibration at the same geometry.

Table 6.1: Frequencies and reduced masses of the normal modes of vibration associated to quinoidal and acetylenic displacements in m23. The numbering of the normal modes is associated to the frequency-ordering of the normal modes computed at MinS$_0$. The normal modes at other geometries are sorted so as to satisfy the most overlap with the normal modes of the ground state geometry. The mass-weighted shifts between the minimum of S$_0$ and the minima of S$_1$, S$_2$ and the MECI are also given. The contributions of the normal modes to the $\mathbf{g}$, $\mathbf{h}$, and gradient average $\mathbf{s}$ vectors at the MECI are given in the last columns, with the sum of the 8-dimensional model contributions.

	Frequency (cm^{-1})			Reduced mass (u)			Shift ($a_0\sqrt{m_e}$)			Contrib. to		
Mode (S$_0$)	MinS$_0$	MinS$_1$	MinS$_2$	MinS$_0$	MinS$_1$	MinS$_2$	MinS$_1$	MinS$_2$	MECI	%$\mathbf{g}$	%$\mathbf{h}$	%$\mathbf{s}$
111	1656	1616	1539	5.47	4.62	2.64	2.28	5.57	15.61	0	36	21
114	1682	1635	1768	5.87	4.97	7.54	-5.17	4.57	3.79	18	2	5
115	1689	1697	1675	5.77	6.09	5.71	5.76	2.19	-1.49	1	9	7
116	1693	1690	1633	5.87	5.78	5.22	-1.10	-2.72	-0.40	0	3	1
117	1699	1664	1688	6.04	5.50	5.82	-6.00	-1.15	1.82	3	6	8
118	2359	2267	2299	12.00	11.99	11.98	8.07	1.00	-0.97	28	6	31
119	2366	2023	2289	12.00	11.72	11.98	0.85	-2.36	-0.75	14	11	0
120	2367	2357	3279	12.00	12.00	3.03	0.82	8.02	7.32	26	2	7
Sum(8D)										90	75	80

state S$_2$ is more complicated to obtain because, as we will see, it is rather close to the S$_1$/S$_2$ conical intersection seam. We gather the vertical transition energies and the energy of the minima in table 6.2 for

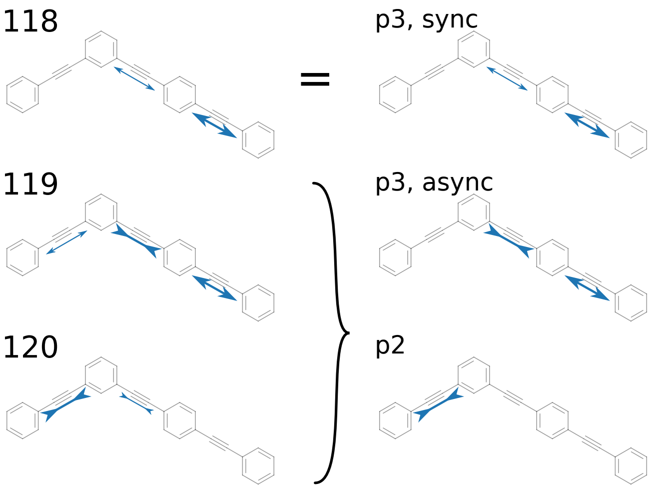

Figure 6.4: Schematic representation of the main internal displacements associated to the acetylenic normal modes of vibration at the FC geometry of m23 and proposition of approximate localization on the p3 and p2 fragments.

m23 and the isolated fragments p3 and p2, along with the lengths of the acetylenic bonds in the molecules. Let us note again the separation between the p3 and p2 *pseudo* fragments of m23 by noticing that the energy of the minima of S_1 and S_2 correspond to the energy of the minima of the S_1 in the isolated p3 and p2 fragments, $3.62\,$eV and $4.14\,$eV, respectively. The bond lengths are also elongated (from alternate to cumulenic pattern) accordingly to the localized excitations.

Table 6.2: Adiabatic energies (in eV) of the electronic ground state and first two electronic excited states for a selection of critical points in isolated fragments p3 and p2 and in m23. The minimum of the electronic ground state is taken as the reference energy for each molecule. The lengths of the acetylenic bonds are given ($d(\mathrm{C}\equiv\mathrm{C})$ in Å) and the values are bold when it is intermediate between acetylenic and cumulenic bond patterns. Labels [p2], [p3-in] and [p3-ext] refer for m23 to the acetylenic bond of the p2 *pseudo* fragment and of the inner and external acetylenic bonds of the p3 *pseudo* fragment.

Geometry	$E(\mathrm{S}_0)$	$E(\mathrm{S}_1)$	$E(\mathrm{S}_2)$	$E(\mathrm{S}_2)-E(\mathrm{S}_1)$	$d(\mathrm{C}\equiv\mathrm{C})$[p2]	$d(\mathrm{C}\equiv\mathrm{C})$[p3-in]	$d(\mathrm{C}\equiv\mathrm{C})$[p3-ext]
p3 MinS_0	0.00	3.90	4.81	0.91	–	1.210	1.210
p3 MinS_1	0.26	3.62	4.80	1.18	–	1.233	1.233
p2 MinS_0	0.00	4.48	5.08	0.60	1.210	–	–
p2 MinS_1	0.32	4.14	4.84	0.70	1.255	–	–
m23 MinS_0	0.00	3.88	4.45	0.57	1.210	1.210	1.210
m23 MinS_1	0.27	3.61	4.61	1.00	1.210	**1.233**	**1.233**
m23 MinS_2	0.23	3.99	4.17	0.18	**1.245**	1.214	1.213
m23 MECI	0.47	4.30	4.30	$< 5\mathrm{e}^{-4}$	**1.240**	1.214	1.204

Let us note that the normal modes of vibration obtained for the MinS_1 and MinS_2 geometries are different from the normal modes of MinS_0. Before being able to compare the normal modes from one equilibrium geometry to another, the normal modes have to be ordered with a shared criterion. Indeed, within the sets of A' or A" normal modes, mixing is allowed between all modes. Furthermore, with the localized geometrical distorsion on the p3 and p2 *pseudo* fragments, there is no guarantee that the normal modes of similar nature from S_0 to S_1 or S_2 equilibrium geometries keep exactly the same frequency-ordering. As a consequence, we re-order the modes obtained at $MinS_1$ and $MinS_2$ such that they have the best individual overlap with the normal modes of $MinS_0$ (which can be related to an analysis of the Duschinsky matrices).

The frequencies and reduced masses of the (selected) normal modes at $MinS_0$, $MinS_1$ and $MinS_2$ geometries are gathered in table 6.1 after re-ordering. As regards the S_1 normal modes, they are very similar to the S_0 normal modes, only with the expected softening of the synchronous p3-acetylenic stretching normal mode. For the S_2 normal modes on the other hand, the discussion is more involved. Indeed, because of the relative closeness to a conical intersection seam ($\Delta E = E(S_2) - E(S_1) = 0.18$ eV at the minimum of S_2; the optimized MECI is discussed below), some modes have their frequencies particularly exalted. This is for instance the case of the p2-acetylenic stretching normal mode 120 (last mode 138 before re-ordering with maximum overlap with 120 in S_0 normal modes), for which the frequency is exalted to $3280\,\text{cm}^{-1}$. As a consequence, this mode is also strongly mixing with $\mathrm{C-H}$ normal modes because of the closeness in frequency, which explains the lowering of its reduced mass and a relatively low overlap with the acetylenic normal mode 120 in S_0 normal modes (yet it is the maximum overlap). For the rest of this chapter and unless otherwise specified, we only work with the S_0 normal modes for which there is no ambiguity of ordering. The shifts between the $MinS_0$ and other critical points of the S_1/S_2 surfaces of m23, along the S_0 normal modes, are also given in table 6.1

Take-home messages

1. The minimum of the electronic ground state of the m23 molecule is a C_s geometry, with vertical transition to S_1 and S_2 that are both bright and localized (LE) on the p3 or p2 *pseudo* fragments, respectively.

2. The minima in the S_1/S_2 PESs maintain this LE character. In particular, the minima S_1 and S_2 are comparable with the minima of S_1 in the isolated p3 or p2 fragments, respectively.

3. The pair of LE states can thus be seen as a pair of excitonic states, sharing one central benzene.

4. The minimum of the PES of S_2 and the associated normal modes of vibration suggest the presence of a nearby conical intersection with the S_1 state.

6.1.2 Nonadiabatically coupled electronic states of same symmetry

Anticipating the study of excitation-energy transfer (EET), let us discuss the possibility of a strong coupling between the localized excitations (S_1 and S_2 localized on p3 and p2 *pseudo* fragments, respectively) *via* the search of the MECI for the S_1/S_2 manifold.

A note on the algorithms for MECI optimization

The optimization of the MECI in m23 was done using a modified home-implementation of the hybrid composed-gradient/composed-step algorithm of Sicilia and co-workers [88]. The main aspects of the optimization algorithm have been presented in section 2.5.2. Our implementation differs from the ones in the literature mostly because of the evaluation of the branching-space vectors, herein obtained numerically from the Hessian of the squared energy difference [85].

We note here that the S_1/S_2 MECI of m23 is more difficult to optimize because the electronic states have the same symmetry (see appendix A). More strikingly, we observed for PPE-oligomers that finding a conical intersection (with no criterion on the average energy) by strictly following the gradient difference was much more complicated in the case of same-symmetry electronic states. We did not have time to rigorously explore these problems for the molecules of interest, but intend to improve the algorithm for MECI search for PPE-oligomers in the future.

Characterization of the S_1/S_2 MECI

The optimized MECI is obtained with the average energy $\bar{E} = 4.30\,\text{eV}$ and the energy difference $\Delta E = E(\text{S}_2) - E(\text{S}_1) = 0.0003\,\text{eV}$. The branching-space vectors (BSVs) obtained numerically from the diagonalization of the Hessian of the squared energy difference $\mathbf{K}_{\text{SED}}$ are illustrated in fig. 6.5 *via* the Cartesian displacements associated to its eigenvectors $(\mathbf{u}_1, \mathbf{u}_2)$ (which have been defined in chapter 2). For the rest of this chapter, we label $\mathbf{g}$ and $\mathbf{h}$ the re-scaled vectors $\mathbf{u}_1$ and $\mathbf{u}_2$ associated to the highest and lowest non-zero positive eigenvalues of $\mathbf{K}_{\text{SED}}$. By construction, $\mathbf{g}$ and $\mathbf{h}$ are orthogonal. However they are not unambiguously defined, since any arbitrary combination of the two vectors spans the same branching plane. In the case of m23, the two electronic states are of identical symmetry A' in C_s, such that there is no symmetry guidance for the BSVs. From the adiabatic point of view, both the GD and DC vectors are totally symmetric in the C_s point group. In other words, the BSVs have the same symmetry and the criterion of orthogonality alone is not enough to identify them to the Hellmann-Feynman branching-space vectors ("adiabatic" GD and DC).[1]

---

[1] In the case of a conical intersection between two electronic states of different symmetry, a pair of orthogonal BSVs is adapted to the irreducible representations of the molecular geometry symmetry. This is the case for m22 (C_{2v} point group), where the Hellmann-Feynman BSVs, GD and DC vectors, can be identified to A_1 and B_2 vectors, and can thus be expanded along either A_1 and B_2 normal modes, respectively.

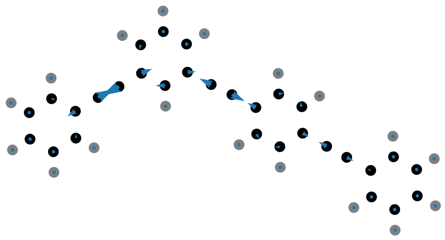

Figure 6.5: Geometry of m23 at the S_1-S_2 MECI (carbon and hydrogen nuclei in black and grey, respectively) and Cartesian displacements (blue arrows) associated the numerical evaluation of the branching-space vectors of the MECI at this geometry. The BSVs on the left and right are associated to the highest and lowest non-zero eigenvalues of the Hessian of the squared energy difference, respectively.

The definition of $\mathbf{g}$ and $\mathbf{h}$ vectors as short and long axis of the branching plane, respectively, can thus be further modified so as to find a more relevant pair of underlying diabatic states. However, this first choice should already be quite consistent with a pair of weakly coupled localized diabatic states on the p3 and p2 *pseudo* fragments. The 2D-cut in the PES through directions of the branching plane $(\mathbf{g}, \mathbf{h})$ is shown in fig. 6.6. Contrary to the branching plane of the symmetrically substituted phenylene, the branching plane of m23 leans toward a strongly favored minimum for S_1 (associated to a local excitation on the p3 branch). In terms of underlying diabatic states, this means that the GD vector favors the diabatic state localized on the p3 *pseudo* fragment and that the tuning between the electronic states is predominant compared to the coupling.

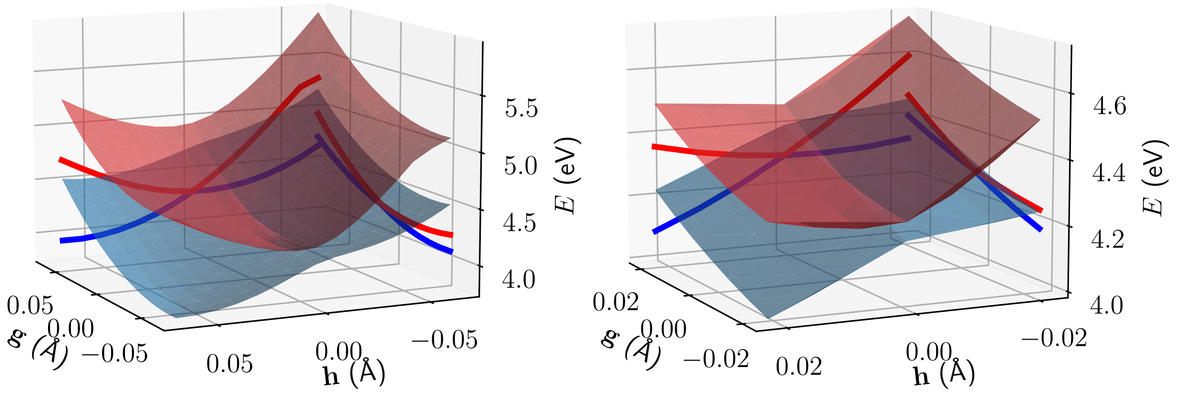

Figure 6.6: 2D-cuts of adiabatic potential energy surfaces along the branching-space vectors $\mathbf{h}$ and $\mathbf{g}$, from the MECI geometry. The right panel only present a zoomed illustration of the same PESs around the MECI.

We show the interpolation path between the FC geometry and the MECI geometry in fig. 6.7 (a). The direction of the interpolation path between the FC geometry and the MECI geometry preserves almost constant values for the oscillator strengths. The strongest oscillator strengths is expectedly attributed to the p3 *pseudo* fragment and associated diabatic state (in blue for $\Delta Q \geq 0$) while the lowest is attributed to the p2 *pseudo* fragment (in red for $\Delta Q \geq 0$). The use of Franck-Condon-type approximations for the localized diabatic states thus holds along this direction. The 1D-cuts from the MECI along the BSVs $\mathbf{g}$ and $\mathbf{h}$ are reproduced in fig. 6.7 (b,c). Let us notice again the particular character of the BSVs which are both totally symmetric, hence two profiles of arbitrary shape (no parity). The oscillator strengths also support this peculiarity. Starting from the MECI geometry, the pair of oscillator strengths appears to be "arbitrary". This is explained by the fact that the BSVs and the underlying diabatic states are defined up to an arbitrary rotation. From these "arbitrary" values, the direction $\mathbf{g}$ tends to couple the localized diabatic states (toward similar oscillator strengths) and the direction $\mathbf{h}$ tends to tune the localized diabatic states (toward different oscillator strengths).

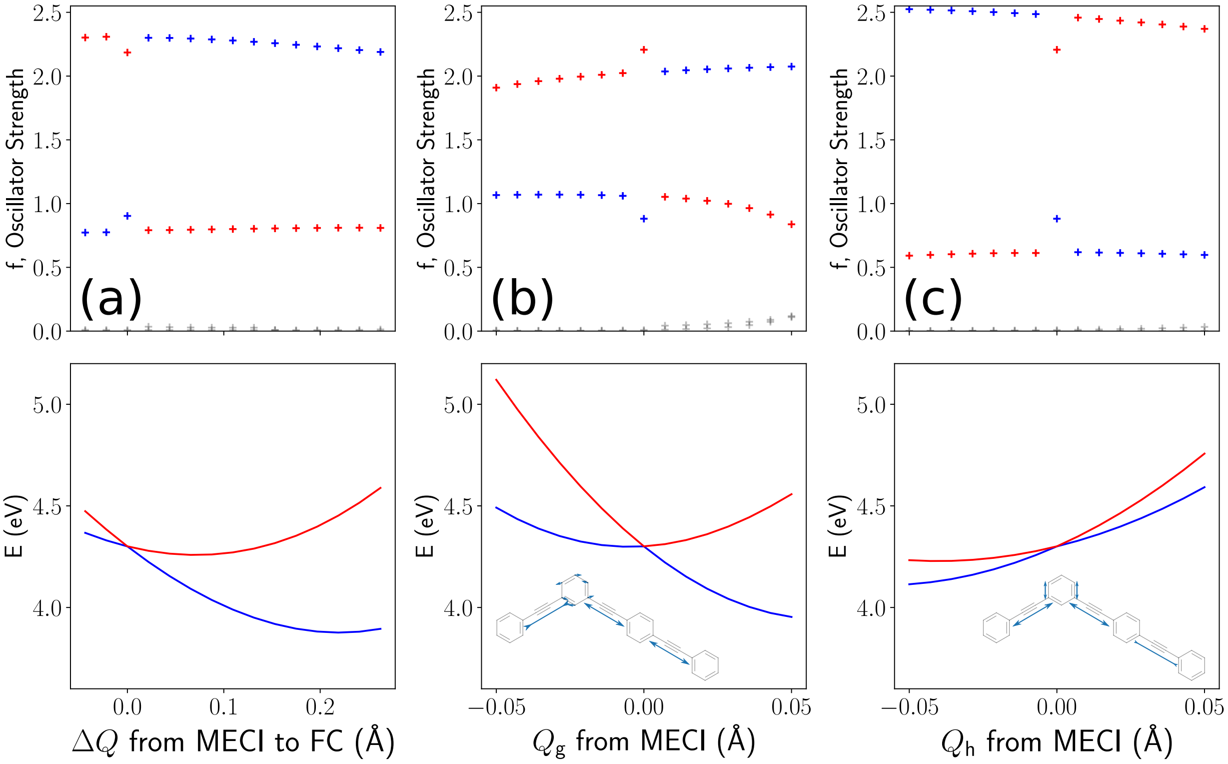

Figure 6.7: Oscillator strengths (top panels) and adiabatic energies (bottom panels) of the first two electronic excited states along: **(a)** the shift from the FC geometry to the MECI geometry; **(b, c)** the nuclear displacements along the branching-space vectors ($\mathbf{g}$: **(b)**; $\mathbf{h}$: **(c)**) from the MECI geometry (a shifted displacement from the MECI origin, $\Delta\mathbf{Q} = \mathbf{Q} - \mathbf{Q}_{\text{MECI}}$, was used for both profiles along either $\mathbf{g}$ or $\mathbf{h}$). The oscillator strengths of the next two (dark) electronic states are shown in grey for information.

The proportion of the BSVs $\mathbf{g}$ and $\mathbf{h}$ after projection on the selected 8 in-plane normal modes is given in the last columns of table 6.1. The same quantity is also given for the gradient average $\mathbf{s}$ at the geometry of the MECI. The BSVs and the gradient average are almost completely defined through displacements along the selected quinoidal and acetylenic modes (90%, 75%, and 80% respectively). This overall good description of the MECI characteristic directions will be the basis of discussion for the choice of the degrees of freedom included in the model for quantum dynamics simulations.

A stationary picture of EET

Finally, a simplified representation of the S_1/S_2 manifold is shown in fig. 6.8 *via* interpolations between the minima of S_1, of S_0 and the MECI.

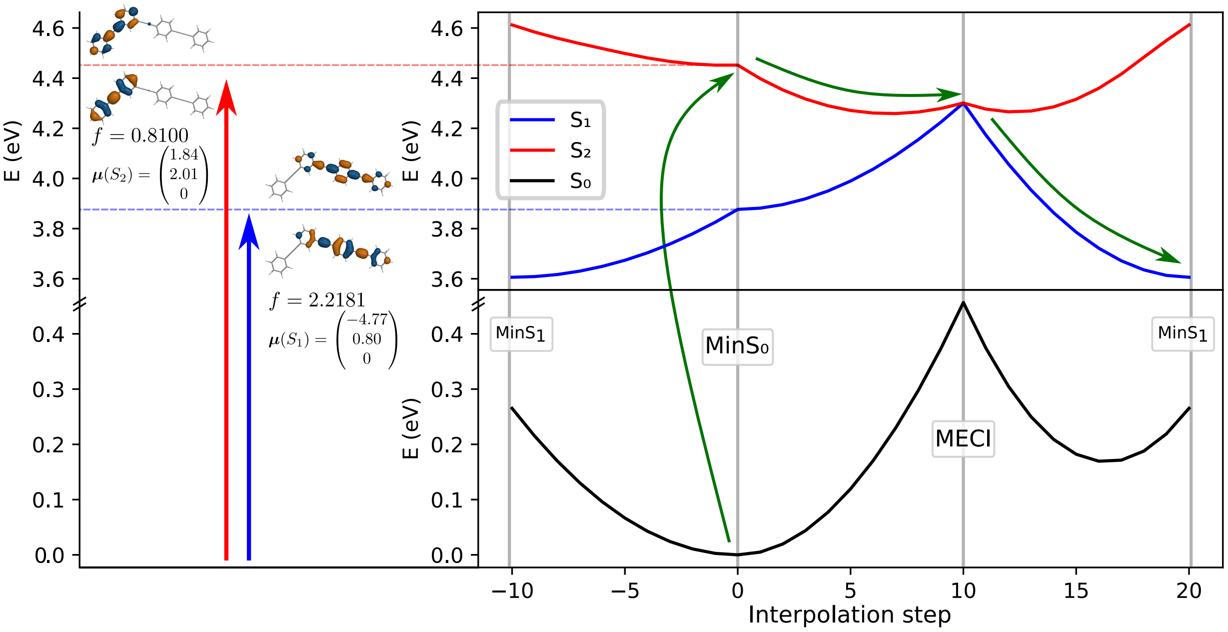

Figure 6.8: Left: oscillator strengths, electronic transition dipole moments (in atomic units), and NTOs for the first two vertical transitions at the minimum of S_0. Right: adiabatic energies of the electronic ground state and of the first two excited singlet states along linear interpolations between the minimum of S_1 (both at -10 and 20), the minimum of S_0 (at 0), and the MECI (at 10). The green arrows represent the idealized pathway for excitation-energy transfer (EET).

In fig. 6.8 left, we recall the vertical transitions from the FC geometry to the first two electronic excited states. The most important pair of NTOs ($> 90\%$ of contribution to the total transition) are shown for the two transitions. In fig. 6.8 right, the potential energy profiles allow for a first interpretation of the EET in m23 (green arrows). The photo-induced excitation on the p2 *pseudo* fragment (S_2 adiabatic state, bright) is transferred *via* radiationless transition to the p3 *pseudo* fragment (S_1 adiabatic state, also bright). From such surfaces, it can be inferred that the ultrafast transfer is facilitated by the fast and straightforward approach to the conical intersection seam after photo-excitation in S_2, with non-negligible coupling allowing for an efficient transfer.

Take-home messages

1. The S_1/S_2 MECI geometry has been optimized, and its branching plane characterized.
2. The MECI seems energetically accessible due to its closeness with the minimum geometry of the S_2 state.

3. Both BSVs (hence both gradient difference and derivative coupling) have non-negligible contributions along acetylenic stretching and quinoidal rock-bending normal modes of vibration.

It is the very aim of the rest of this chapter to propose a time-resolved study of EET with explicit propagation of the nuclear wavepackets.

6.2 Potential energy surfaces and steady-state spectroscopy

We choose, similarly to the case of m22, the linear vibronic coupling (LVC) Hamiltonian model to describe and reproduce the adiabatic PESs of the first two coupled excited states in m23. Because both electronic states have the same symmetry (A') in the C_s point group (thus restricting to displacements along in-plane modes), the choice of the diabatic states for the LVC is nontrivial. In the case of two electronic states of different symmetry, the choice of symmetry-adapted diabatic states allowed us to use the irreducible representations to discriminate between *coupling* modes (off-diagonal terms) and *tuning* modes (diagonal terms). Here the identical symmetry for the electronic states (and thus of the BSVs) implies that all A' (in-plane) normal modes can be involved in both diabatic potential energies and inter-state coupling, whatever the choice of the underlying diabatic states. The chosen model is the FC-centered LVC model

$$\begin{aligned}\mathbf{H} = \hat{T}_{\text{nu}}\mathbb{1} + \begin{bmatrix} E^{(1)} & 0 \\ 0 & E^{(2)} \end{bmatrix} + \sum_i \begin{bmatrix} k_i^{(1)}Q_i^2 & 0 \\ 0 & k_i^{(2)}Q_i^2 \end{bmatrix} \\ + \sum_i \begin{bmatrix} \kappa_i^{(1)}Q_i & 0 \\ 0 & \kappa_i^{(2)}Q_i \end{bmatrix} + \sum_i \begin{bmatrix} 0 & h_i'Q_i \\ h_i'Q_i & 0 \end{bmatrix}.\end{aligned} \tag{6.1}$$

The diagonal parameters define the diabatic potential energies, with the vertical transition energies (VTEs) at the FC geometry $E^{(s)}$, the vertical gradients $\kappa_i^{(s)}$ (providing equivalent shifts toward each diabatic potential energy minimum) and the curvatures $k_i^{(s)}$ (providing equivalent frequencies). The off-diagonal parameters are the h_i' components of an inter-state coupling vector $\mathbf{h}'$. Here, a difference is made between the BSV $\mathbf{h}$ obtained from the diagonalization of $\mathbf{K}_{\text{SED}}$ and the inter-(diabatic-)state coupling $\mathbf{h}'$. The definition of $\mathbf{h}'$ will be made clearer in the following, but can be seen as of now simply as a linear combination of the orthogonal BSVs ($\mathbf{g}$, $\mathbf{h}$). Although we do not use here bilinear terms, the model is strictly speaking between LVC and QVC because of the different curvatures for both diabatic potential energies. For the sake of simplicity, we will however refer to the model as an LVC Hamiltonian model.

Unless otherwise specified, we do not account for couplings between the electronic ground and excited states, assuming that the energy difference $\Delta E(\text{S}_1 - \text{S}_0)$ is large enough. Hence, the electronic ground state is simply parametrized with the harmonic approximation around the FC geometry, and the model will be reffered to as a (1+2)-state LVC model.

6.2.1 Parametrization of the LVC model

Herein, the parametrization of the 8-dimensional LVC model is done in two steps:

1. we first choose the inter-state coupling $\mathbf{h}'$ *via* a projection of the BSVs onto the eight selected normal modes of interest;
2. we then obtain the diagonal parameters upon fitting the adiabatic energies of the model to *ab initio* profiles along the selected normal modes.

To do so, *rigid scans* (1D-cuts in the PES) are computed for displacements along the Cartesian displacements of the selected normal modes from the FC geometry of the molecule, see $+$ symbols in fig. 6.9.

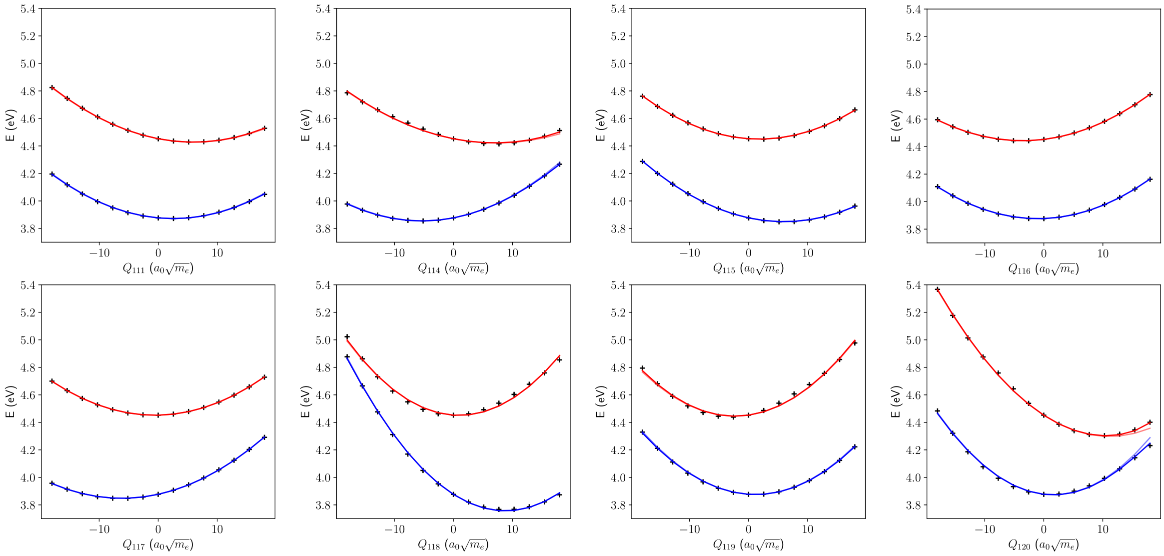

Figure 6.9: Adiabatic energies (in eV) from electronic structure calculations (symbol $+$) and from the 2-state 8-dimensional LVC model, along displacements associated to the selection of S_0 normal modes. For unspecified coordinates, the values are those at the FC geometry (0); all coordinates are mass-weighted and given in atomic units.

A motivated choice for fixing the inter-state coupling parameters

As we can see in fig. 6.9, the energy difference is quite large for each profile and the electronic states do not "accidentally" cross along following a single normal mode. This is the reason why we choose to *a priori* fix the inter-state coupling vector $\mathbf{h}'$ because the region around the FC geometry is quite far from the conical intersection seam. Indeed, we do know the position of the MECI with respect to the FC geometry (table 6.1, *Shift* columns) and the associated branching-plane directions $(\mathbf{g},\ \mathbf{h})$. To use both the knowledge of the position of the MECI and the lengths of the BSVs, we define a rotation $(\mathbf{g},\mathbf{h}) \rightarrow (\mathbf{g}',\mathbf{h}')$ parametrized with

$$\tan\theta = -\frac{\mathbf{h}\cdot\Delta\mathbf{Q}_X}{\mathbf{g}\cdot\Delta\mathbf{Q}_X}, \tag{6.2}$$

such that the $\mathbf{h}'$ vector is forced to be orthogonal to the shift $\Delta\mathbf{Q}_X$ between the FC geometry and the MECI geometry. We note that this choice is consistent with ensuring that diabatic and adiabatic states coincide at the FC geometry [93]. Indeed, with the chosen rotation and definition of $\mathbf{h}'$, the off-diagonal term in eq. (6.1) is zero at both the FC geometry and the MECI geometry. However, there is a subtelty in this statement. The zero-coupling at the two geometries depends on the dimensionality of the model. The parametrization of the rotation eq. (6.2) can *a priori* be done with the full-dimensional BSVs and FC-to-MECI shift vector; or with vectors reduced to a selection of normal modes. One could choose the full-dimensionality in the search of a generalized procedure. However for the sake of having a self-contained model, we choose to parametrize the rotation only within the reduced model. As a matter of fact, the rotation is only slightly varying when parametrized with full-dimensional vectors, 11-dimensional vectors (all quinoidal and acetylenic modes) and 8-dimensional vectors (selected modes), with $\theta = 18.82°,\ 14.84°$ and $14.58°$, respectively.

Fitting the parameters for the diabatic potential energies

Let us assume that the off-diagonal parameters are now fixed and discuss the fitting procedure for the rest of the parameters. In the "built-in" *ab initio* data set, the fully optimized geometry (FC geometry) is also the reference point for the LVC model. As a consequence, the VTEs can also be fixed for the fitting procedure, which allows us to have an unambiguous ordering of the diabatic excited states. Up to this point, the fitting procedure is quite similar to the procedure for building the 10-dimensional model of m22. The main difference are

- the absence of discrimination based on symmetry between *coupling* and *tuning* characters for the normal modes;
- and the choice of $\mathbf{h}'$, prior to any fitting procedure.

From a practical point of view, we fit the diagonal diabatic parameters of the profiles one by one. Thus, for one 1D-cut in the PES, we have a set of displaced geometries $\{\mathbf{Q}_{n,l}\}_{l\in\text{scan}} = \{(0,\cdots,Q_l,\cdots,0)\}_{l\in\text{scan}}$, each along only one normal mode. The parameters of the LVC Hamiltonian are thus obtained by fitting its eigenvalues (adiabatic energies) to the *ab initio energies* along each 1D-cut. This is implemented as a minimization of the least-square function for normal mode n,

$$\begin{aligned} &L(\kappa_n^{(1)},\kappa_n^{(2)},k_n^{(1)},k_n^{(2)}) = \\ &\sum_{s=1,2}\sum_{l\in\text{scan}}\left(V^{(s)}[E^{(1)},E^{(2)},\kappa_n^{(1)},\kappa_n^{(2)},k_n^{(1)},k_n^{(2)},h'_n](\mathbf{Q}_{n,l}) - E^{(s)}(\mathbf{Q}_{n,l})\right)^2 \end{aligned} \tag{6.3}$$

where $V^{(s)}[E^{(1)},E^{(2)},\kappa_n^{(1)},\kappa_n^{(2)},k_n^{(1)},k_n^{(2)},h'_n](\mathbf{Q}_{n,l})$ are the eigenvalues of the LVC Hamiltonian, and $E^{(s)}(\mathbf{Q}_{n,l})$ the *ab initio* energies at the displaced geometry $\mathbf{Q}_{n,l}$. Note again that the parameters h'_n are not optimized, and given as an input to the fitting procedure. The resulting parameters are given in table 6.3 in the form of "equivalent" magnitudes in terms of frequencies and shifts. The numerical values associated to $\kappa_n^{(1)}, \kappa_n^{(2)}, k_n^{(1)}, k_n^{(2)}, h'_n$ for implementing the operators used in quantum dynamics calculations are given in mass-weighted atomic units in appendix B.

Table 6.3: Equivalent quantities for LVC parameters obtained upon fitting *ab initio* calculations. Parameters associated with the harmonic (second-order) expansion ($k_i^{(n)}$) are provided in terms of the associated frequency, $\omega_i^{(n)}$. Parameters associated with the first-order expansion (h'_i and $\kappa_i^{(k)}$) are provided also in terms of their characteristic induced geometry shifts, $d_i'^{(12)} = -\frac{2h'_i}{k_i^{(1)}+k_i^{(2)}}$ and $d_i^{(k)} = -\frac{\kappa_i^{(k)}}{k_i^{(k)}}$. The corresponding LVC parameters in mass-weighted atomic units are gathered in appendix B.

Parameter	$k_i^{(1)}$	$k_i^{(2)}$	$\kappa_i^{(1)}$	$\kappa_i^{(2)}$	h'_i	Contrib. to		
Equivalent	$\omega_i^{(1)}$	$\omega_i^{(2)}$	$d_i^{(1)}$	$d_i^{(2)}$	$d_i'^{(12)}$	$\%\mathbf{h}'$	$\%\mathbf{g}'$	$\%\mathbf{s}$
Mode								
111	1650	1554	2.54	6.06	-1.92	14	1	6
114	1666	1437	-5.28	7.29	2.63	19	17	0
115	1648	1682	5.97	1.81	0.58	2	2	6
116	1684	1599	-1.00	-3.61	-0.71	2	1	2
117	1644	1692	-6.15	-0.55	-0.16	0	5	4
118	2345	2301	8.80	0.98	-0.62	7	37	37
119	2103	2157	1.16	-2.38	-1.46	29	5	1
120	2342	2108	1.62	11.10	1.46	27	32	44

The resulting PESs cuts of the optimized LVC model are compared to the *ab initio* calculations in fig. 6.9 (blue and red for the first and second electronic states, respectively). Both adiabatic and diabatic profiles are shown (in plain and transparent, respectively) and we notice the closeness, along the selected modes, for the two basis of electronic states. This illustrates the effect of $\mathbf{h}'$ for 1D-cuts along the normal modes, expected to be small in this region close to the FC geometry with a large energy difference.

The contribution of each mode to the inter-state coupling, the diabatic gradient difference, and the diabatic gradient average within our reduced 8-dimensional subspace are gathered in table 6.3. Such a decomposition highlights the importance of the acetylenic modes involving the p2 branch, 119 and 120. The latter two account together for more than the third of each of the three vectors within the reduced 8-dimensional model. The third acetylenic mode 118, localized on the p3 branch, contributes mostly to the gradient difference (tuning) and gradient average (tilting). The quinoidal modes of the central *meta*-substituted ring can also be qualified as strongly coupling (for 111, stretching mode) and strongly coupling and tuning (for 114, rock-bending mode). Let us already observe the separate role of these five normal modes and of the remaining three quinoidal normal modes (115, 116 and 117). Indeed, the first five modes strongly participate in the BSVs and gradient average and are thus important for the description of the coupling between the two localized electronic states. On the other hand, the quinoidal normal modes are important for correctly describing the minima in the first and second electronic excited states (table 6.1, *Shift* columns). In the next sections, we shall examine the effects of freezing or not such modes for quantum dynamics simulations of EET. Before that, let us discuss the validity of the LVC model for the eight selected normal modes.

6.2.2 Validation of the LVC model, PES characterization

We discuss here two types of *a posteriori* validation for the PESs of the LVC model: i) the comparison of the fully optimized and reduced-dimensional critical points of the S_1/S_2 manifold; and ii) the comparison of the gradient difference vector at the reference FC point and at the MECI. These two validations allows us to estimate how the choices of the reduced dimensionality and of neglecting the bilinear terms (identical BSVs at the FC and at the MECI) affect the accuracy for the adiabatic PESs.

Minima and MECI of the dimensionally reduced model of PESs

The optimized critical points within the LVC 8D model are in qualitative agreement with the critical points obtained from full-dimensional optimization in the *ab initio* PESs (see table 6.4 for comparison). In particular, the minima of the first and second adiabatic states in the model are less than $0.1\,$eV off in energy from the fully optimized geometries. Their shifts with respect to the FC geometry along the eight normal modes included in the model are in good qualitative agreement (see table 6.4). The same is found for the MECI (where the apparent MECI of the model was taken as the lowest average-energy crossing point optimized with an energy difference of $0.0001\,E_\mathrm{h} = 0.0027\,$eV).

Table 6.4: Energies in eV of the first two adiabatic excited states at the critical points in the *ab initio* PESs (at the CAM-B3LYP/6-31+G* level of theory) and in the LVC PESs model. Positions for the selected modes (with respect to the MinS$_0$ geometry) of the optimized critical points in the full-dimensional system and in the dimensionally reduced model are also given (in mass-weighted atomic units $a_0\sqrt{m_e}$).

	Energies		Shifts ($a_0\sqrt{m_e}$)							
Geometry	$E(S_1)$	$E(S_2)$	111	114	115	116	117	118	119	120
FullD MinS$_1$	3.61	4.62	2.28	-5.17	5.76	-1.10	-6.00	8.07	0.85	0.82
8D MinS$_1$	3.67	4.59	2.58	-5.43	5.94	-0.97	-6.14	8.83	1.27	1.55
FullD MinS$_2$	3.99	4.17	5.57	4.57	2.19	-2.72	-1.15	1.00	-2.36	8.02
8D MinS$_2$	4.03	4.24	5.95	7.19	1.79	-3.57	-0.54	1.01	-2.24	9.50
FullD MECI	4.30	4.30	15.61	3.79	-1.49	-0.40	1.82	-0.97	-0.75	7.32
8D MECI	4.41	4.41	16.74	4.51	-4.89	-0.99	4.88	-0.41	3.08	12.8

This clearly shows that the 8-dimensional model is an acceptable trade-off between size and accuracy, since relaxing the remaining 130 frozen modes out of a total of 138 only lowers typical energies by about

0.1 eV. In particular, the relaxation for the remaining 130 frozen modes is somewhat compensated through larger displacements in the 8-dimensional reduced model for the S_1 and S_2 minima. Let us note that the "optimized" position of the MECI in the reduced dimension is only indicative, because of the strong dependence of the optimization on the energy difference criterion and on the initial guess. For all the attempts, the coordinates stay similar to the ones given in table 6.4 with the energy average $\bar{E} = 4.41$ eV and energy difference $\Delta E < 5 \times 10^{-3}$ eV.

Validation of the parametrized rotation of the branching-space vectors

We can consider that a good agreement between the GD vector at the FC geometry and at the MECI is also a good *a posteriori* check of how the linear vibronic coupling model is relevant. In table 6.5 we compare the GD vector obtained from the fitted diabatic gradients $\mathbf{GD} = \frac{1}{2}\left(\boldsymbol{\kappa}^{(2)} - \boldsymbol{\kappa}^{(1)}\right)$ at the FC geometry and $\mathbf{g}'$, the rotated branching-space vector obtained along with $\mathbf{h}'$. We find that the two vectors are almost aligned, with no striking difference component by component. This illustrates that the branching plane at the FC and at the MECI can be taken as similar for the targeted pair of localized diabatic states. In particular, the BSVs suffer very little to no rotation from the FC to the MECI geometry (which could be associated to strong second-order bilinear coupling terms between both states).

Table 6.5: Halved gradient difference from the fitting procedure at the FC geometry $\mathbf{GD}(\mathrm{FC})$ and second branching-space vector $\mathbf{g}'$, counterpart of the first branching-space vector $\mathbf{h}'$ orthogonalized to the shift $\Delta\mathbf{Q}_X$ between FC geometry and MECI. Both quantities are given in thousandth of energy gradients given in mass-weighted atomic units $(\frac{E_h}{a_0\sqrt{m_e}})$

Mode	111	114	115	116	117	118	119	120
$\mathbf{GD}(\mathrm{FCP})$	-0.080	-0.308	0.115	0.066	-0.156	0.448	0.168	-0.420
$\mathbf{g}'(\mathrm{MECI})$	-0.083	-0.332	0.091	0.020	-0.142	0.443	0.290	-0.402
$\lvert\mathbf{GD}(\mathrm{FCP}) - \mathbf{g}'(\mathrm{MECI})\rvert$	0.003	0.024	0.024	0.046	0.024	0.005	0.122	0.018

6.2.3 Validation of the LVC model, steady-state spectroscopy

Another *a posteriori* validation of the LVC model consists in simulating the UV-visible absorption and emission spectra. Similarly to the steady-state spectroscopy study done in chapter 5 for the symmetrically substituted phenylene m22, we can compute different contributions to the absorption spectrum and to the emission spectrum.

Power spectra from the autocorrelation functions

For the simulation of absorption, two initial states are considered with the excitations toward the first or the second diabatic states D_1, D_2, respectively. Within the sudden approximation from the electronic ground state, these excitations correspond to promoting the vibrational ground state (an 8-dimensional Gaussian vibrational wavefunction) to the first diabatic state or the second diabatic state. Indeed, the BSVs rotation defined in eq. (6.2) ensures that the diabatic states match the adiabatic states at the FC geometry (reference of our model) as much as possible. In practice, the initial excitations on D_1 and D_2 yield 95%:5% and 5%:95% mixtures of the adiabatic states, respectively.

For now, let us focus on the excitation toward D_1 and D_2, which are diabatic states localized on the p3 and p2 *pseudo* fragments, respectively. From these, we find two different contributions to the absorption spectrum. For simulating emission, we first search for the vibronic ground state in the excited-state manifold. We find it to be unambiguously defined in the $\mathrm{S}_1/\mathrm{S}_2$ manifold, with mostly the D_1 state being populated (population $P(\mathrm{D}_1) = 0.99$) and mostly displaced along the normal modes involving the p3 *pseudo* fragment. This result is expected because the minimum of the S_1 surface is unique and strongly displaced along the p3 *pseudo* fragment normal modes, with large energy difference between the S_1 and S_2 states. In other words, the vibronic eigenstate of the $\mathrm{S}_1/\mathrm{S}_2$ manifold is comparable to the vibronic eigenstate of the S_1 state, uncoupled from other electronic states. The emission spectrum in then simply obtained by the propagation of the vibrational wavepacket of the D_1 state in the electronic ground state surface. Both absorption and emission power spectra are shown in fig. 6.10.

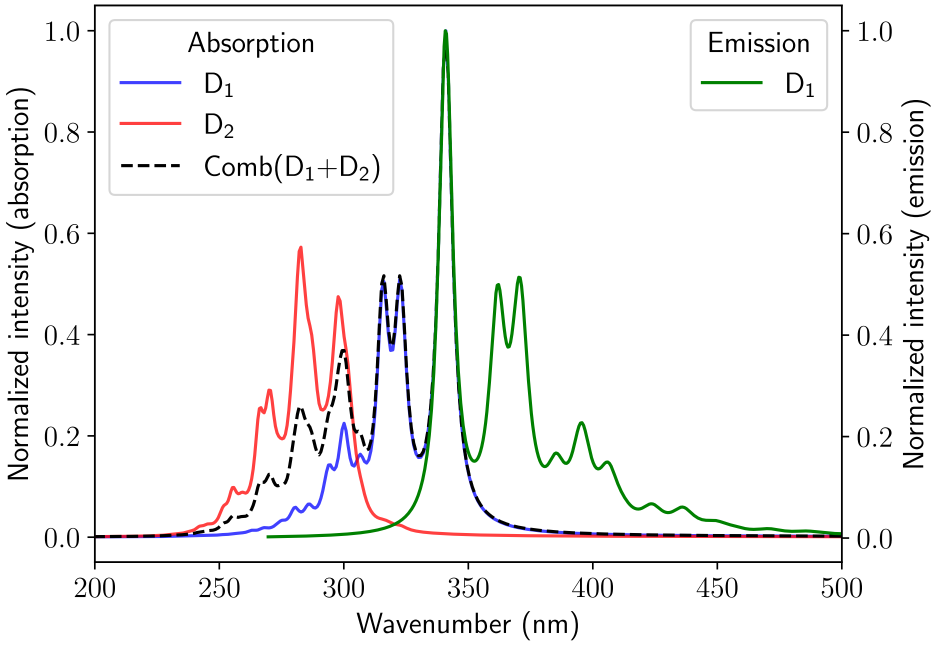

Figure 6.10: Power spectra contributions obtained from Fourier transform of the relevant autocorrelation functions. Contribution to absorption from the excitation of D_1, D_2, or both: plain blue, red lines, and dashed black line, respectively. Emission from the vibronic ground state in the (D_1, D_2) manifold: plain green line. The spectra are realistically broadened by using a damped autocorrelation function with damping time $\tau = 19\,\mathrm{fs}$.

There are two clearly distinct contributions to the absorption spectrum. As expected from PPE dendrimer building blocks, they match the vibronic progressions in the absorption spectra of the isolated p2 and p3 fragments, respectively, with the peculiarity for D_2 that the band origin is not the most intense transition (see discussion below and fig. 6.11). We observe typical mirror-image spectra between emission and the first absorption band, which is consistent with Kasha's rule in the context of triangular-shaped spectra (the band associated to the 0_0^0 transition is the most intense in both absorption and emission). For an estimation of what could be the total absorption spectrum of m23, we show in fig. 6.10 (black line) the sum of both contributions with the oscillator strengths of both excited states (at the FC geometry) as weighting factors.

Comparison of time-dependent *vs.* time-independent strategies

For further discussion of the power spectra, we compare the quantum dynamics results to absorption spectra simulated in the time-independent (TI) framework, as implemented in the `Gaussian16` package [82,152,153]. The absorption spectra of m23, p2, and p3 are computed, with full-dimensionality or reduced-dimensionality (RedDim) including the normal modes from the 8-dimensional (quinoinal and acetylenic) model.

Unfortunately, as of now, we have no direct comparison with experimental spectra for the isolated m23 molecule. The closest experiments we have are the attributions of the electronic transitions for the experimental absorption spectrum of the nano-star only [35, 36], later reproduced with Frenkel exciton Hamiltonian models [30]. The two contributions to our modelling of the absorption spectrum are comparable with the two most intense bands in the absorption spectrum of the nano-star (313 nm and 361 nm) with associated vibronic structure. Attention must be paid about the relative intensity between these two peaks. Indeed, in the nano-star the most intense peak is expectedly the one associated to local excitations on the p2 branches, which are more numerous than the p3 branches. In m23, because the oscillator strength of the first excited state (LE on p3) is larger than the oscillator strength of the second excited states (LE on p2), the most intense band is expectedly the transition at 340 nm–350 nm (for TD and TI spectra, respectively).

Take-home messages

1. A minimum (1+2)-state 8-dimensional LVC model has been parametrized for the S_1 and S_2 state of an asymmetrically *meta*-substituted PPE.
2. The validity of the PESs model has been assessed by comparison with fully optimized geometries of minima and MECI and by the calculation of steady-state absorption and emission spectra.

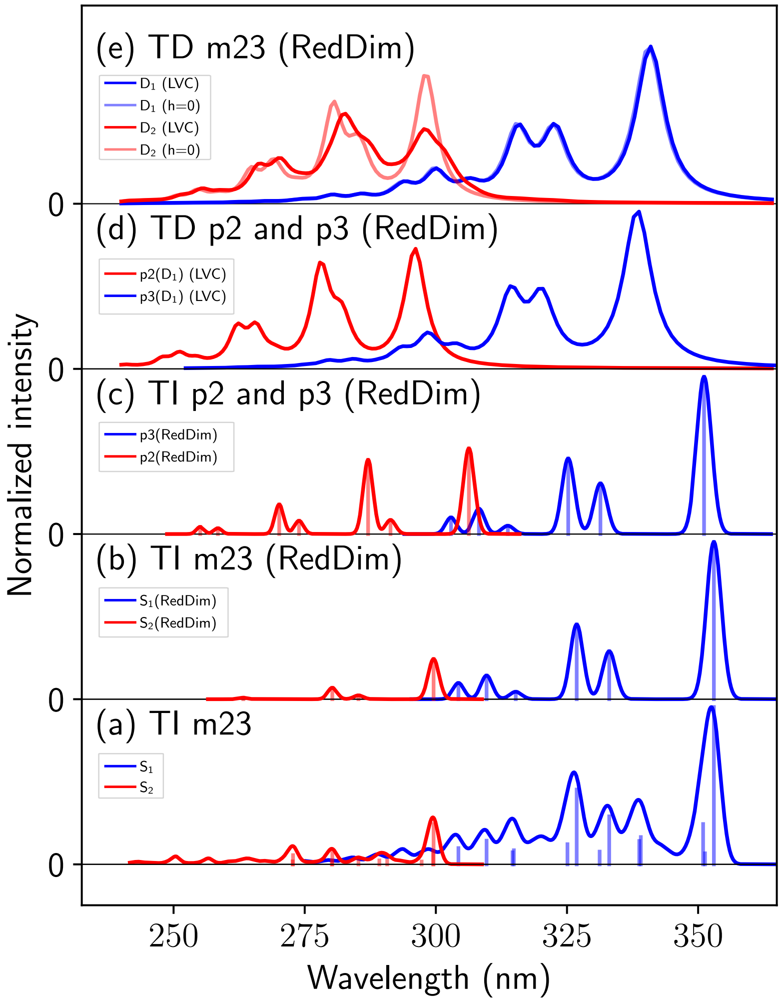

Figure 6.11: Calculated UV-visible spectra using a time-independent (TI) method giving Franck-Condon factors within the harmonic and Born-Oppenheimer approximations (a, b, c), and calculated power spectra using a time-dependent (TD) method beyond the Born-Oppenheimer approximation (d, e). **(a)** Full dimensional TI spectra between S_0 and S_1/S_2 (blue/red lines) of m23. **(b)** Reduced dimensional TI spectra between S_0 and S_1/S_2 (blue/red lines) of m23, selecting only transitions involving modes of the 8-dimensional model. **(c)** Reduced dimensional TI spectra between S_0 and S_1 in p3/p2 fragments (blue/red lines). **(d)** Reduced dimensional TD power spectra between S_0 and D_1 in p3/p2 fragments (blue/red lines). **(e)** Reduced dimensional TD spectra between S_0 and D_1/D_2 (blue/red lines) of m23 with and without coupling (plain and transparent lines).

6.3 Time-dependent study of excitation-energy transfer

In this section, we discuss the real-time dynamics of the (1+2)-state 8-dimensional model of m23. As already mentioned, we consider two limiting situations of *sudden excitations* of an initial vibronic state. In either case, the initial vibronic state is always the vibrational ground state of the electronic ground state (namely, an unshifted 8-dimensional Gaussian wavefunction), projected onto one of the diabatic states. The first situation is to excite the LE state associated with the p2 *pseudo* branch (D_2 state), with the aim of evaluating the existence, dynamics and efficiency of EET. The second situation is to excite the LE state associated with the p3 *pseudo* branch (D_3 state) in order to confirm the absence of reverse EET. Of course, the focus of this work is on the EET occuring from the D_2 to the D_1 state, hence the first situation.

This section is organized in two parts. First, we will discuss the (1+2)-state 8-dimensional model in terms of the role and requirement of the selected normal modes to reproduce an ultrafast, efficient excitation-energy transfer. This study is based on the parametrized 8-dimensional model, but we freeze some of the normal modes to evaluate their role. In a second part, we focus on the 8-dimensional model without frozen modes and explore the correlations between the dynamics of electronic population transfer and the dynamics of the nuclear-related quantities.

6.3.1 Requirements for ultrafast and efficient EET in m23

We hereby study the importance of the different normal modes for reproducing an ultrafast and efficient EET. We make use of the previously parametrized and discussed (1+2)-state 8-dimensional LVC model for the PES of m23, which will be the "parent" model for models with fewer degrees of freedom. To evaluate the importance of one normal mode (or one set of normal modes), we freeze the wavepacket in the direction associated to this considered normal mode. In the "parent" model, we recall that there are three acetylenic stretching modes, one anti-quinoidal rock-bending mode, and four quinoidal stretching modes (label 8D QuinAce.) From this set, we define three "child" models,

- a 3-dimensional model with only acetylenic modes (3D Ace.);
- a 5-dimensional model with only quinoidal and anti-quinoidal modes (5D Quin.);
- and a 5-dimensional model with the three acetylenic modes and both quinoidal and anti-quinoidal modes localized on the central benzene (5D QuinAce.).

For the "parent" model and the three "child" models, we show in fig. 6.12 the diabatic populations (panels a-b) and the adiabatic populations (panels c-d) after initial excitation of the diabatic state D_2 (mostly LE state on the p2 *pseudo* fragment). As the model is essentially a two-level system, we can focus on either the donor state (decaying state D_2 localized on p2) or the acceptor state (populating state D_1 localized on p3). Let us look at the population of the first diabatic state D_1 and the first adiabatic state S_1 (fig. 6.12, panels a and c).

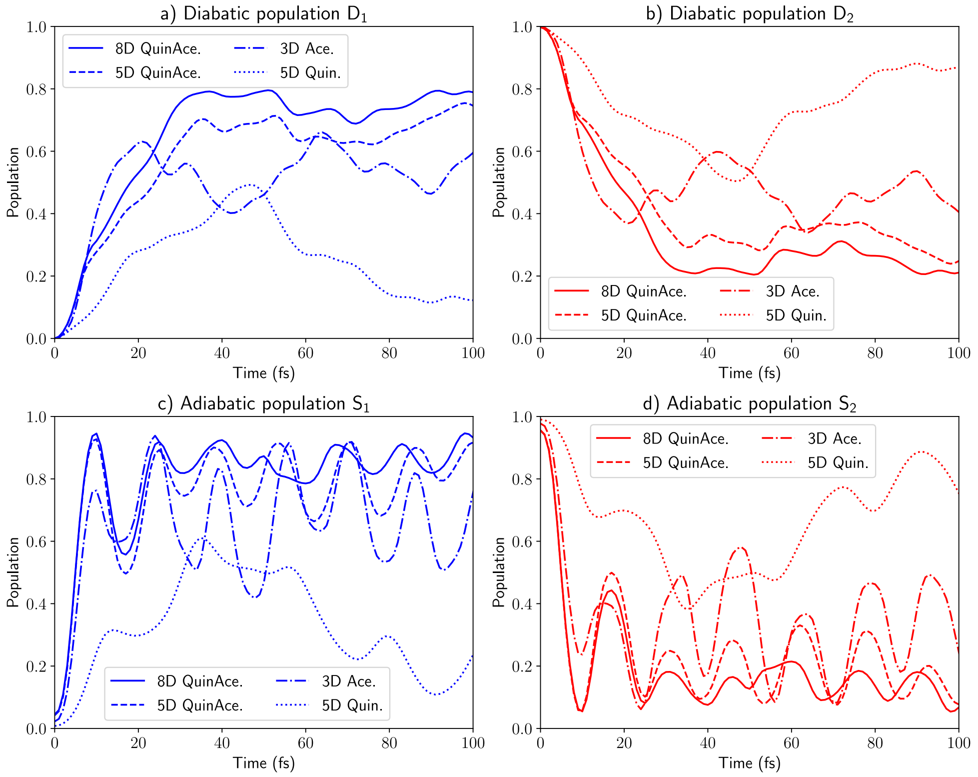

Figure 6.12: Diabatic populations (panels a-b) and adiabatic populations (panels c-d) after initial excitation of the diabatic state D_2 for the "parent" 8D QuinAce model and the "child" 3D Ace, 5D Quin, and 5D QuiAce models (solid, dashed, dotted-dashed, and dotted lines, respectively).

First, we notice that whatever the model, the population of the adiabatic state S_1 is strongly oscillating, while the population of the diabatic state D_1 is more monotonic and smoother. This is expected because the wavepackets are defined with respect to the diabatic states and their evolution is mostly governed by the diabatic gradients. On the other hand, the oscillations in the adiabatic population can be understood as multiple crossings of the conical intersection seam (for the PESs of the reduced models) by the propagated wavepacket.

The 8D QuinAce. "parent" model (blue and red plain lines) exhibits an ultrafast EET (within $25\,\mathrm{fs}$) with quite a strong quantum yield (from 0 diabatic population to 0.8, or from almost 0 adiabatic population to 0.9 in average). We note that the "final molecular state" is not clearly established here, with remaining oscillations in both diabatic and adiabatic populations, making it complicated to systematically evaluate the quantum yield. As of now, we attribute this still oscillating final molecular state to the low dimensionality of the model and hence to incomplete internal vibrational redistribution.

The "child" models corroborate, to some extent, this hypothesis. For instance, the 5D QuinAce. model is similar to the 8D QuinAce. model (blue and red dashed lines), only with the 3 non-central quinoidal modes being frozen. The quantum yield estimated from the diabatic populations is slightly lower than in the 8-dimensional model, but more strikingly the oscillations in the adiabatic populations are of higher amplitude. The EET still occurs, quite efficiently and within the same timescale, but a clear final state is not unambiguously reached. In particular, there are more possibilities for the system to transfer back the adiabatic population to the S_2 state.

This is even more striking for the 3D Ace. model (blue and red dashed-dotted lines). Indeed, it exhibits ultrafast EET but the quantum yield is reduced (0.6 at best) and the multiple crossings of the CoIn seam are non-negligible and are not attenuated with time. On the other hand, freezing the acetylenic modes but taking into account all the quinoidal modes (5D Quin. model, blue and red dotted lines) clearly affects the early dynamics after excitation, with no clear EET. Indeed, the transfer is slow and inefficient, for both diabatic and adiabatic populations.

Take-home messages

1. Altogether, we identify two main features for the EET in PPE-dendrimers:
    - the acetylenic modes play the central role for the EET to occur (in an ultrafast manner, within the first $25\,\mathrm{fs}$) as identified in the literature;
    - the quinoidal modes, in particular the ones localized on the central phenylene, stabilize the acceptor state D_1 (and consequently S_1) so that the EET is unidirectional and there is no transfer back to the initial donor state.
2. The latter feature will be further explored in the context of energy redistribution in the following section (focussing on the 8-dimensional model) and of internal vibrational redistribution with higher dimensionality in section 6.4.

6.3.2 A nonadiabatic perspective of EET: electron-nuclear correlations

In this section, we only discuss the results from the (1+2)-state 8-dimensional model with no further mode freezing.

6.3.2.1 Population transfer in a two-level system candidate for simulation of EET

Recalling the results from previous section, the excitation initialized on the D_2 state (local excitation on the p2 *pseudo* branch and mostly S_2 electronic state) is rapidly and quite monotonically transferred to the D_1 state (see fig. 6.13, left panel).

As regards the adiabatic populations, we observe that the S_2 population decays faster than the D_2 population, but undergoes two strong oscillations before starting to stabilize, within $25\,\mathrm{fs}$ after excitation. We interpret these oscillations as a double crossing of the conical intersection seam in our model, which could cause problems for simulations based on mixed quantum-classical method of nonadiabatic dynamics.

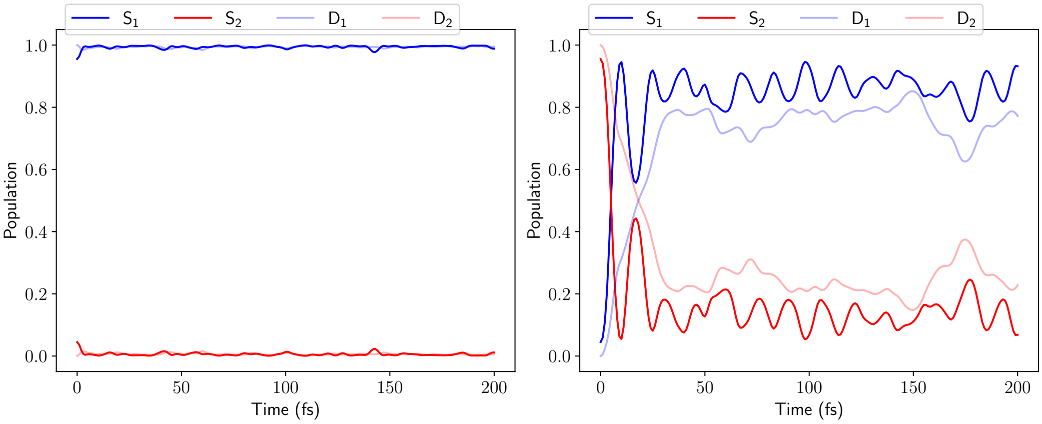

Figure 6.13: Time evolution of the populations of the first two adiabatic and diabatic states for different initial states (left: D$_1$, right: D$_2$) for the first 200 fs of simulation.

However, we stress that these oscillations and double crossing of the CoIn seam may be due to the low dimensionality of the present model.

Another way of characterizing the EET is the evolution of coherence between the electronic states (here for the simple case of a two-level system). The study of coherence in two-level (or more) systems for different PPEs will be further studied and discussed in chapter 8. Herein, we simply look for the coherence between the diabatic electronic states D$_1$ and D$_2$, which is obtained, interestingly enough, as the expectation values of Pauli matrices in the diabatic representation. The population difference and real/imaginary parts of the coherence are shown in fig. 6.14, up to 1000 fs.

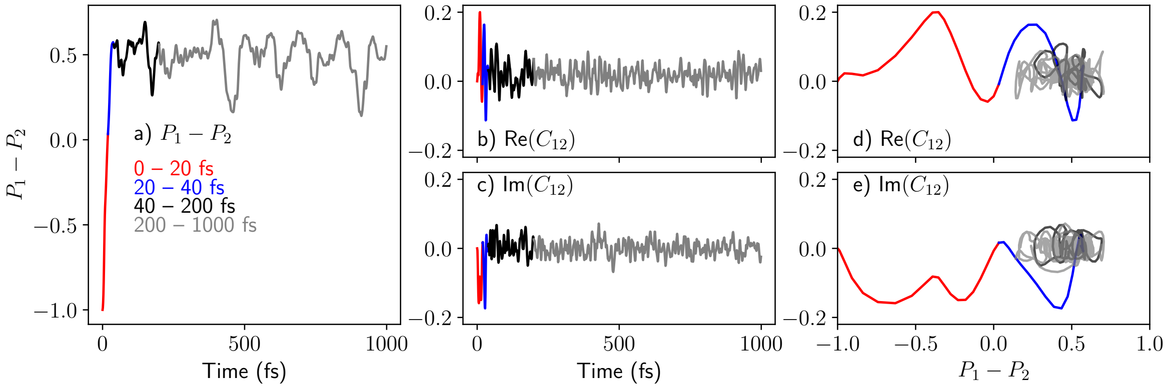

Figure 6.14: Time evolution of **(a)** the diabatic population difference, **(b)** the real part of the diabatic coherence, and **(c)** the imaginary part of the diabatic coherence. Real and imaginary parts of the diabatic coherence as functions of the diabatic population difference are shown in **(d)** and **(e)**, respectively. Colors correspond to different time windows after the initial excitation.

The coherence between the diabatic electronic states remains non-zero all along the simulation, with significant maxima during the EET process ($|C_{12}| = 0.20$). After the transfer, the system remains mostly in D$_1$ but is still exchanging population with D$_2$. We also illutrate the correlation between coherence and population difference in fig. 6.14 **(d)** and **(e)**.

We interpret this result as a signature of the nonadiabatic EET, with three distinct regimes. The first regime (red line, 0 fs to 20 fs) is the first part of the population inversion, leading to equalization of the diabatic populations. The second regime (blue line, 20 fs to 40 fs) is the completion of the population inversion, with the system ending up trapped in the lowest-lying diabatic excite state D_1. Finally, the late dynamics (black line, 40 fs to 200 fs and grey line 200 fs to 1000 fs) corresponds to oscillations in the region close to equilibrium for the system.

Take-home messages

1. In our modelling of EET, the population transfer from the donor state to the acceptor state occurs within 25 fs after the initial excitation, with significant quantum yield (80% for diabatic populations, 90% for the adiabatic populations).
2. For the diabatic states, the coherence and the population transfer are evolving smoothly during EET, and quite erratically when the final state is reached.
3. Such behaviors are still to be studied for the adiabatic states.

6.3.2.2 Analysis of EET in terms of internal coordinates

Let us now monitor the geometry of the molecule during excitation-energy transfer. In particular, in this section we are interested in two representations of the geometry changes during EET: *via* centers (expectation value of the position) of the nuclear wavepackets in the system of normal coordinates and *via* direct monitoring of the internal coordinates, in particular bond lengths.

Wavepacket "trajectories" and state-specific expectation value

As regards the center of the wavepackets, we distinguish the mean expectation value of the position operator $\langle q_i \rangle (t)$ and the state-specific expectation value $\langle q_i \rangle_s (t)$ of the same operator. A detailed note on these different definitions of expectation values as *contributions* (extensive) of a given electronic state to the total manifold or *measurements* (intensive) for the same given electronic state, independently of its population has been made in chapter 3, eq. (3.54) and after. Another relevant quantity for characterizing the nuclear wavepacket is the vibrational excitation number $\langle n_i \rangle_s (t)$, especially because our model and our dynamics simulations are built on the basis of normal modes of vibration. The state-specific expectation values of the position and vibrational number operators are shown in fig. 6.15 for the two distinct types of sudden excitations.

We first look at the results from the initial excitation on the p3-localized state, D_1 (fig. 6.15, left

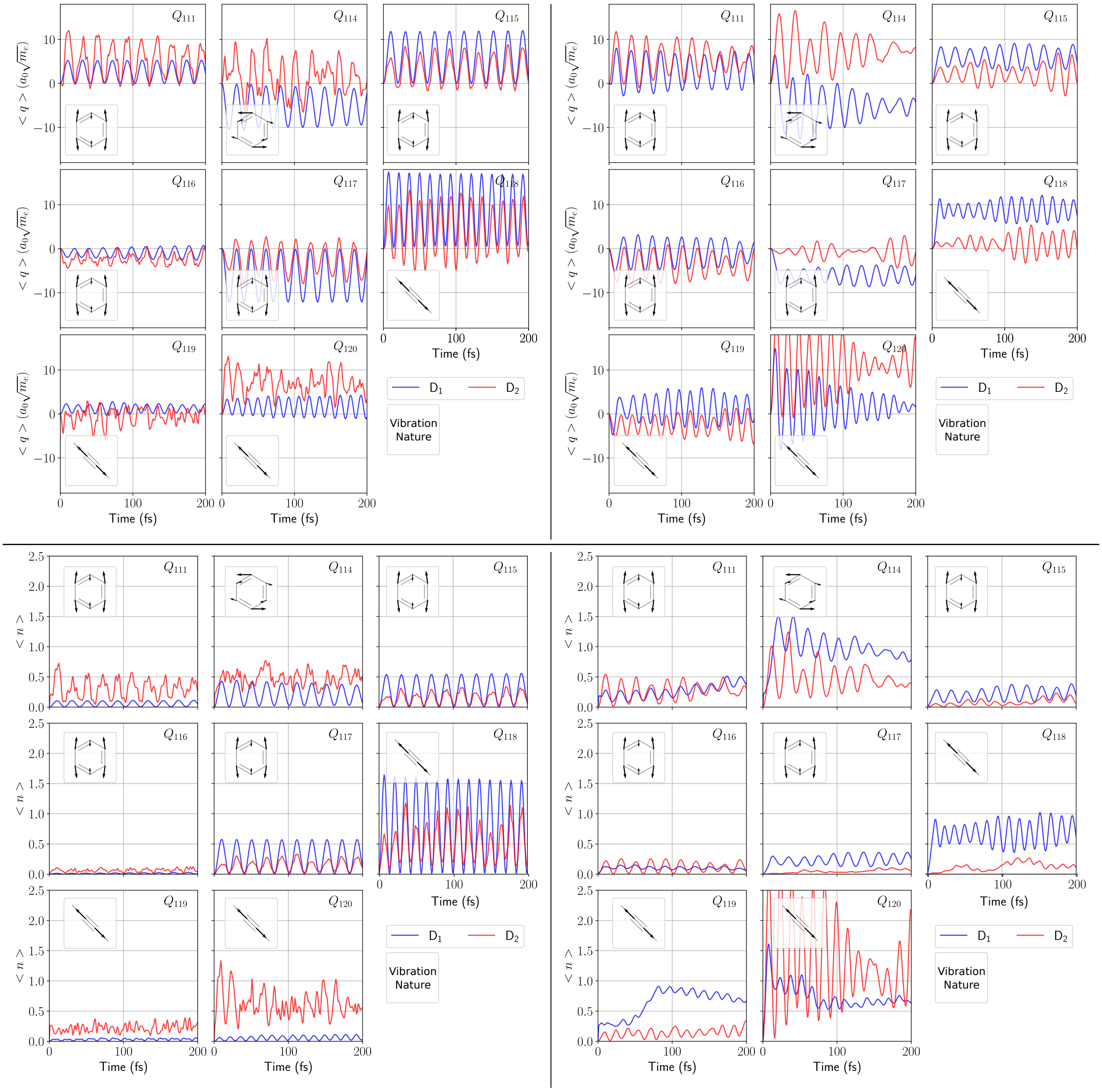

Figure 6.15: Results from initial sudden excitations on D$_1$ and D$_2$, left and right panels respectively. The time evolution of the expectation values of positions (in mass-weighted atomic units) is given in the top panels. The time evolution of the expectation values of the vibrational excitation numbers is given in the bottom panels. The expectation values are shown for diabatic states D$_1$ (blue line) and D$_2$ (red line) and for each normal mode. The nature of the vibration (quinoidal/acetylenic and stretching/rock-bending) is recalled for each normal mode; for the definition of the normal modes, see fig. 6.3.

panels).[2] Focussing first on the D$_1$-expectation values (blue lines), we observe little significant variations of the wavepacket center along the different normal modes. More precisely, the average of the wavepacket center for a given direction does not change in time, but oscillates as expected from the dynamics in a

---

[2] This simulation is the exact same as the one used in order to produce the power spectrum contribution from the D$_1$ state to the absorption spectrum.

quasi-harmonic well. Indeed, after promoting the initial 8-dimensional vibrational ground state of the S_0 surface to the D_1 surface, the system directly follows the gradient of D_1 and does not suffer the effect of the coupling from the CoIn seam (which is far from both FC and MinS_1 geometries). In addition, the standard deviation of the wavepacket [not shown here] stays almost constant, meaning that the wavepacket in the D_1 surface mostly maintains its shape during the propagation. Let us now mention the D_2-expectation values (red lines), which seem quite erratic. This is explained by the really small, close-to-zero population in the D_2 state (below 0.05 at every time of the simulation, fig. 6.13, left). Such state-specific quantities does not seem physically relevant here, because the system is quite correctly described by a single and harmonic surface D_1. This is further comforted by turning on and off the coupling for the simulation of the TD spectra toward the D_1 state, as previously illustrated in fig. 6.11 (a).

Now, the discussion of the EET situation (excitation on the D_2 state, fig. 6.15, right panels) yields much more interesting results as regards correlation between population transfer and nuclear motions. During the first few fs, the initial excitation on D_2 involves strong displacements along the anti-quinoidal rock-bending mode 114 and the (mostly-)p2-acetylenic stretching mode 120 (red lines). Both modes strongly participate in the model gradient difference $\mathbf{g}'$ vector (table 6.3). Accordingly, the D_2 diabatic energy gradient is important along these two modes within the reduced model, which is consistent with strong 114 and 120 displacements (and vibrational number) following initial excitation on the D_2 state. On the other hand, they also participate strongly in the model inter-state coupling vector $\mathbf{h}'$ such that their excitation is transferred to the D_1 state (blue lines) concomitantly to EET population transfer. In conjunction with this, the wavepacket shifts along the p3-localized modes (quinoidal mode 117 and acetylenic mode 118), which corresponds to a displacement toward the equilibrium geometry of the first diabatic state. In other words, the time evolution of $\langle q_i \rangle_s (t)$ for both states is consistent with the role of the corresponding modes in energy gradient and inter-state coupling vector.

Re-localization of the acetylenic normal modes

Although we clearly identify the conjunction between the population transfer and the changes in geometry (monitored, for now, *via* the positions of the wavepackets), our interpretation is not done in the localized representation for the normal modes (defined in fig. 6.4). We want to be sure to validate the interpretation of EET in m23 as a transfer between two p2 and p3 *pseudo* fragments, as if they were different but coupled molecules. To do so, we ensure a better localization of the acetylenic stretching normal modes 118, 119, and 120, following the schematic idea illustrated in fig. 6.4. We assume that the normal mode 118 is sufficiently localized on the p3 fragments. For the modes 119 and 120, we find the better combinations of the associated displacements so that the root-mean-square deviation (RMSD) of the displacements is minimized on the p2 or p3 *pseudo* fragments, respectively. We find completely localized modes with displacements labeled Q_{p2} and Q_{ASp3}, which, as indicate the labels, are localized on the p2 and p3 *pseudo* fragments, respectively. As expected from a *pseudofragmentation* scheme, the mode ASp3 is the asynchronous elongation of the p3-acetylenic bonds, that is the counterpart of the synchronous elongation of the p3-acetylenic bonds, 118. Another localization would be to combine 118 and 119 to find one mode per acetylenic bond.

Having the parameters for defining modes p2 and ASp3, we compute the associated expectation values, shown in fig. 6.16.

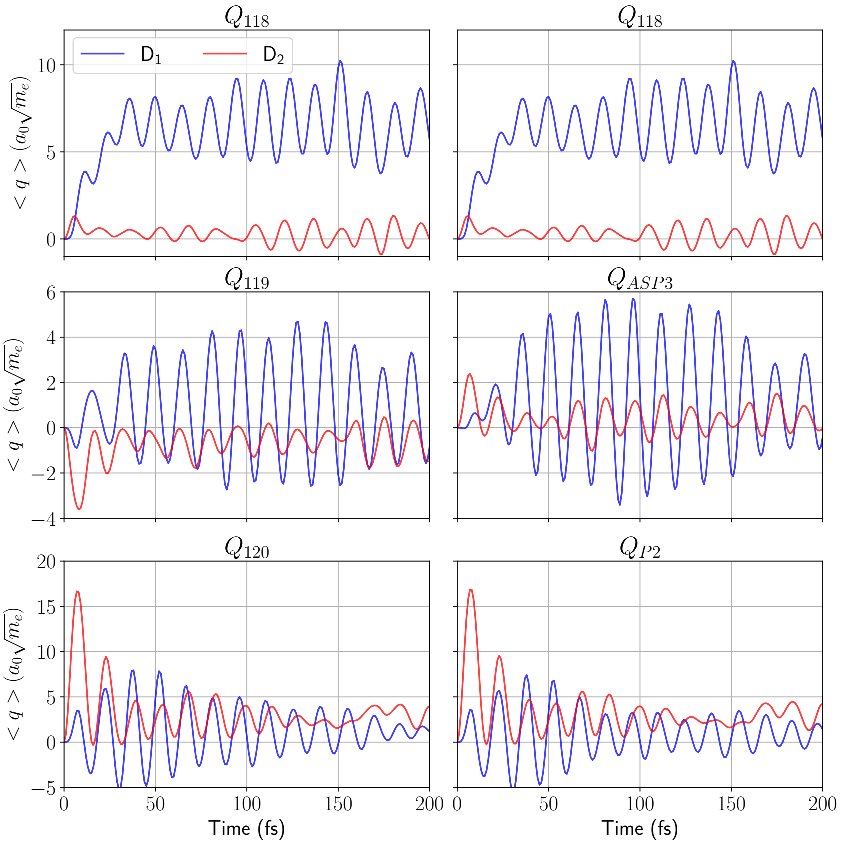

Figure 6.16: Time evolution of the expectation values of position in diabatic states D$_1$ and D$_2$ for an initial excitation on D$_2$, for normal modes (118, 119, 120) on the left and modes (118, Q_{p2}, Q_{ASp3}) on the right.

We notice a large-period oscillation for $\langle q_{\mathrm{ASp3}} \rangle (t)$, but in low amplitudes, with a periodic envelope of about 200 fs. For instance, looking at the expectation values for the D$_1$ state (blue lines), the signals for modes 119 and 120 (equivalent periods $T = 16.0$ fs and 14.8 fs, respectively), are almost added together for building the mode ASp3. The combination of the two quasi-periodic signals thus yields a beating signal, just as in accoustic or amplitude modulation. The carrier wave for the ASp3 signal has a period equivalent to oscillations for modes 119 and 120. For idealized cosine signals for 119 and 120 and with equal summation, we would find $T = 15.4$ fs and 395 fs for the carrier wave and the modulated wave (beating), respectively, which is quite consistent with the observation.[3] As regards $\langle q_{\mathrm{p2}} \rangle (t)$, its signal resembles the evolution of 120 because the coefficient in the linear combination of 119 and 120 is much greater for 120. We interpret this by the fact that 120 is mostly an acetylenic elongation on p2, contaminated with some

---

[3] using relations like

$$\cos 2\pi f_a t + \cos 2\pi f_b t = 2 \cos 2\pi \frac{f_a + f_b}{2} t \times \cos 2\pi \frac{f_b - f_a}{2} t \tag{6.4}$$

for two ideal cosine signals with frequencies $f_a \simeq f_b$.)

asynchronous elongation on p3.

Toward the monitoring of molecular geometry during EET

For better comparison with the literature of direct-dynamics simulations on systems such as m23 or related, we now illustrate the evolution of the internal coordinates during the EET process. First, let us define the displaced Cartesian coordinates

$$\Delta\mathbf{R}^{(s)}(t) = \sum_{i,\text{ modes}} \frac{\langle q_i \rangle_s (t)}{\sqrt{\mu_i}} \mathbf{L}_{\text{Cart},i}, \tag{6.5a}$$

$$\Delta\mathbf{R}(t) = \sum_{i,\text{ modes}} \frac{\langle q_i \rangle (t)}{\sqrt{\mu_i}} \mathbf{L}_{\text{Cart},i}, \tag{6.5b}$$

where $\mathbf{L}_{\text{cart,i}}$ and μ_i are the Cartesian displacements and reduced masses associated to the normal mode i. The state-specific displaced coordinates $\Delta\mathbf{R}^{(s)}(t)$ and total displaced coordinates $\Delta\mathbf{R}(t)$ are calculated by adding the Cartesian displacements of the normal modes weighted by the position of the center of the wavepacket. This analysis is closer to trajectory-based simulations. Indeed, we transform the initial output of quantum dynamics, which are wavepackets in the space of normal mass-weighted coordinates, back to trajectories or geometries in the Cartesian laboratory-frame. However, compared to mixed-quantum classical methods, the average trajectory is here unique for each simulation; more specifically, we have one "average trajectory" for each diabatic state.

Once the geometries are obtained, the relevant distances (bond lengths, or other internal coordinates) are easily computed knowing the numbering of the atoms. We focus here on the lengths of the acetylenic bonds, shown in fig. 6.17 for "early" and "late" dynamics in left and right panels respectively. We recall that the equilibrium length of the acetylenic bond is $1.21\,\text{Å}$ in the ground state of PPEs (with an alternated $\mathrm{C-C\equiv C-C}$ bonding pattern), and $1.25\,\text{Å}$ in the first excited state (toward an ideal cumulenic $\mathrm{C=C=C=C}$ bonding pattern) (see again table 6.2). These values are reported in fig. 6.17 with grey areas.

During the early dynamics, the p2 acetylenic bond is strongly distorted (fig. 6.17, **(a)**, black line) and is elongated beyond the equilibrium geometry of MinS$_1$. Within the first $25\,\text{fs}$, it oscillates back toward the equilibrium geometry of MinS$_0$. During the same time, the "internal" p3 acetylenic bond (the closest to the central phenylene) is elongated but exhibits large-amplitude oscillations with a period of about $150\,\text{fs}$ (fig. 6.17, **(b)**, black line). The "external" (or peripheral) p3 acetylenic bond is elongated during the same timescale (first $25\,\text{fs}$) but the high-amplitude oscillations begin only at $50\,\text{fs}$, with a similar period of $150\,\text{fs}$ (fig. 6.17, **(c)**, black line).

From a local, internal-bond, point of view, the excitation on the second excited state D$_2$ yields EET dynamics with two main features: i) strong elongation of the p2 acetylenic bond; ii) moderate elongation of the two p3 acetylenic bonds with asynchronous oscillations between the two bond lengths. These are consistent with previous studies of internal coordinates evolution during EET in m23 [50]. In the latter

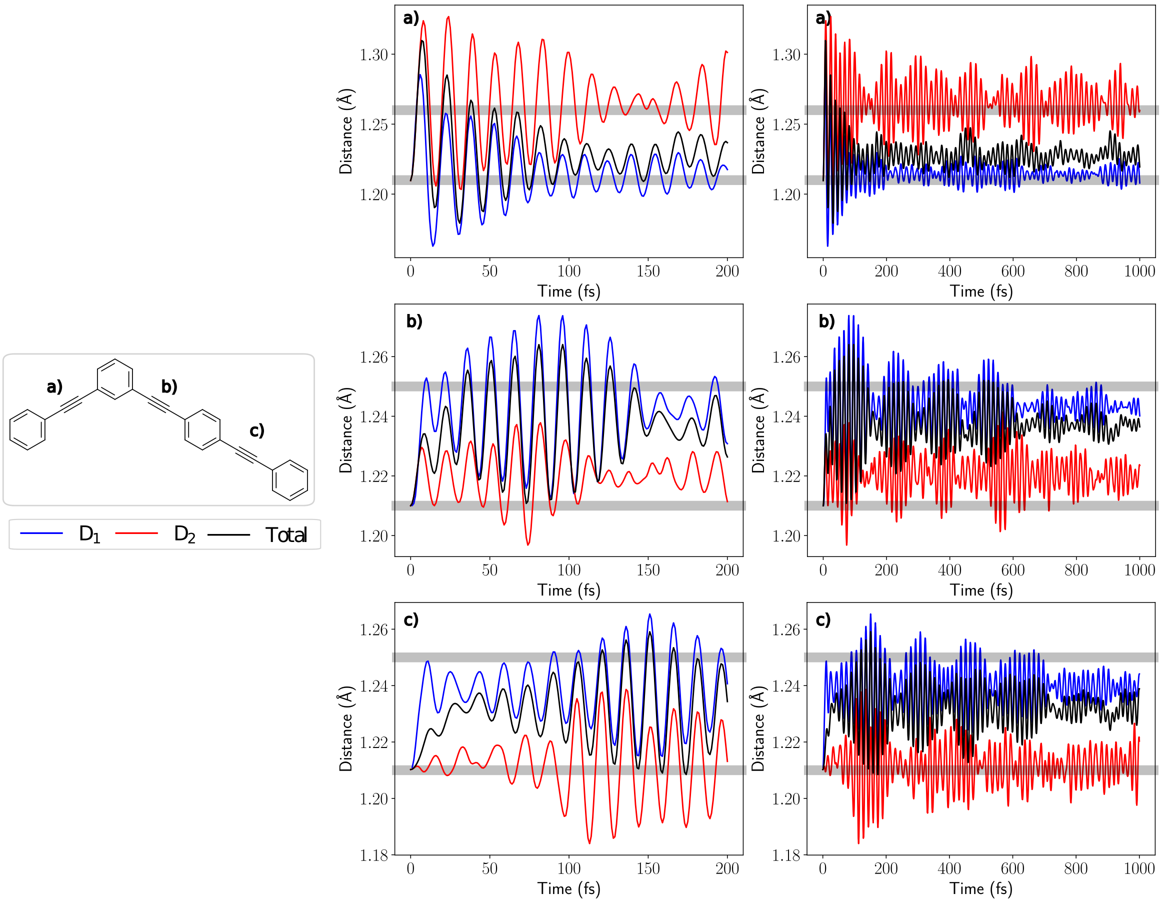

Figure 6.17: Time evolution of the lengths of the acetylenic bonds of m23 in either of the two diabatic states D$_1$ or D$_2$ (blue and red lines), or in total (black line). The "early" dynamics is shown in left panels (up to 200 fs) and the "late" dynamics is shown in right panels (up to 1000 fs). Grey areas represent the approximate equilibrium position of the acetylenic bond in the electronic ground and first excited states.

work, the authors used mixed quantum-classical dynamics with propagation of multiple trajectories and surface hopping. The trajectories are separated into two sets: effective (non back-hopping after) or non-effective (existing back-hopping) hops from S$_2$ to S$_1$. Our results are consistent with the set of effective-hop trajectories. Note that the large-amplitude oscillations for the p3 acetylenic bonds are maintained for about 600 fs in our simulations, with four quantum beats (which validates a period with the order of magnitude $\simeq 200$ fs).

Take-home messages

1. We simulated the early dynamics of EET in the (1+2)-state 8-dimensional model, and analysed the time evolution of both wavepacket expectation values and of the underlying molecular geometry.
2. We confirm the role of the acetylenic normal modes in the EET in both

- the early transfer of electronic population, *via* the p2-acetylenic vibrations
- the late trapping in the acceptor state, *via* the p3-acetylenic and, to some extent, p3-quinoidal vibrations.

6.3.2.3 Study of the internal vibronic redistribution of EET

We now analyze the EET process in m23 through the lens of the internal redistribution of energy. First, let us stress that the total energy

$$E_{\text{total}} = E_{\text{diabatic}}(t) + E_{\text{off-diagonal}}(t). \tag{6.6}$$

is conserved but that the total diabatic energy (the sum of the expectation values for all diagonal Hamiltonian operators in the two-state formalism) is not. In particular, it can be further decomposed

$$E_{\text{diabatic}}(t) = E_{\text{electronic}}(t) + E_{\text{vibrational}}(t). \tag{6.7}$$

The electronic and vibrational energy are then defined as

$$E_{\text{electronic}}(t) = P_1(t)E^{(1)}(t=0, \mathbf{Q}=0) + P_2(t)E^{(2)}(t=0, \mathbf{Q}=0), \tag{6.8a}$$

$$E_{\text{vibrational}}(t) = \sum_{s,\ \text{states}} P_s(t) \left(\sum_{i,\ \text{modes}} \left\langle T_{\text{nu},i} \right\rangle_s + \kappa_i^{(s)} \left\langle q_i \right\rangle_s (t) + \frac{1}{2} k_i^{(s)} \left\langle q_i^2 \right\rangle_s (t) \right). \tag{6.8b}$$

With these definitions, the electronic energy is the reservoir of energy in the constant part of the diabatic potential energies at the origin ($\mathbf{Q} = 0$) and the vibrational energy is the energy resulting from the nuclear displacements from the origin. In other words, the EET can also be interpreted from the perspective of a spin-boson Hamiltonian model. The spin-part relates to the local electronic excitations and the boson-part relates to the intra- and inter-state couplings, mediated through the nuclear displacements. Again, such an interpretation is facilitated by the fact that the present model is a two-level system.

Decomposition of the excess excitation energy

We illustrate the energy decomposition in fig. 6.18. From left to right we show the diabatic, electronic, and vibrational energies in the system. In fig. 6.18, center panel, black line, we measure that the total electronic energy decreases from $4.45\,\text{eV}$ (initial vertical transition energy) to approximately $3.9\,\text{eV}$. The excess energy (from the electronic state D_2) is expectedly transferred to the vibrational wavepacket as a vibrational energy fig. 6.18 (right panel, black line).

The decomposition of the vibrational energy in eq. (6.8b) allows for a discussion of the energy per state and per mode.

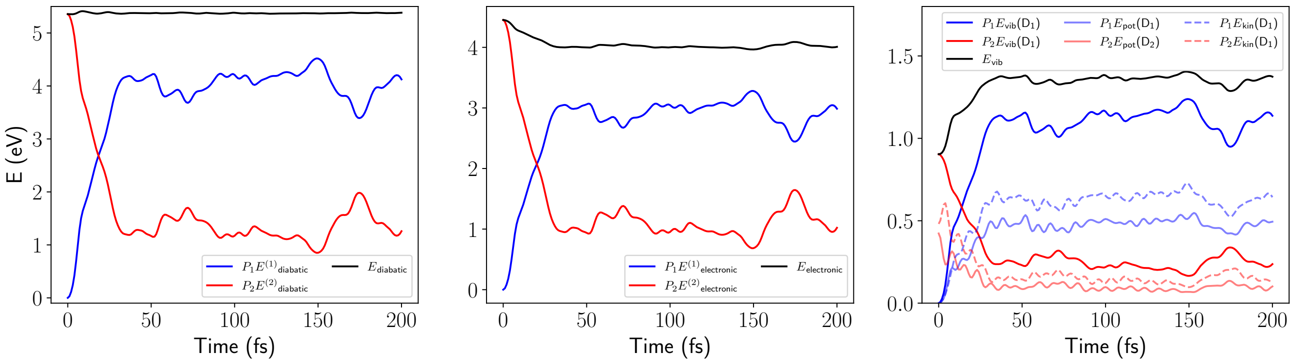

Figure 6.18: Time evolution of the diabatic (diagonal) energy and its decomposition. Contributions from diabatic states D_1 and D_2 are blue and red lines, respectively. Left: contributions to the total diabatic energy (black line). Center: contributions to the total electronic energy (black line). Right: contributions to the total vibrational energy (black line) from potential energy (transparent lines) and kinetic energy (dashed lines).

Decomposition of the vibrational energy and identification of the "most" active modes

We now look at the distribution of the excess vibrational energy in the different normal modes, comparing for each mode the average and specific kinetic energy, potential energy, and vibrational energy. The contributions of such quantities from the diabatic state D_1 are shown in fig. 6.19 (left).

At $t = 0\,\text{fs}$, all the vibrational energy is in state D_2, and is equal to the zero-point energy (ZPE) associated to the vibrational ground state of the ground electronic state of the molecule. In the first $25\,\text{fs}$, the vibrational energy in state D_2 is transferred to D_1.

The vibrational energies in D_2 of each mode are shown in fig. 6.19 (right) and quickly tend to an almost-zero residual energy, consistently with the D_2 vibrational energy, see fig. 6.18 (right). Only the p2-acetylenic mode 120 exhibits significant variations of potential energy and kinetic energy. On the other hand, the vibrational distribution in D_1 is no longer like a ZPE. In particular, the excess energy from the electronic reservoir is split into two groups, with spectator modes (115, 116, 117 and 118) and active (excited) modes (111, 114, 119, and 120) (panel **(a)** in fig. 6.19, left).

Energetically active degrees of freedom

The p2-acytelenic stretching mode 120 is highly excited in the initial state D_2, and its excitation is maintained in D_1 (most energetic mode), which denotes its importance in the reduced model for energy redistribution. The next two most energetic modes are the (almost) asynchronous p3-acetylenic stretching mode 119 and the central anti-quinoidal mode 114. We note that to some extent, the vibrational energy of the central quinoidal mode 111 also increases, although it seems to be more of a spectator mode.

It is clear from table 6.1 that the modes that contribute strongly to the inter-state coupling vector keep a significant vibrational excitation after the electronic transfer. On the contrary, the spectator modes

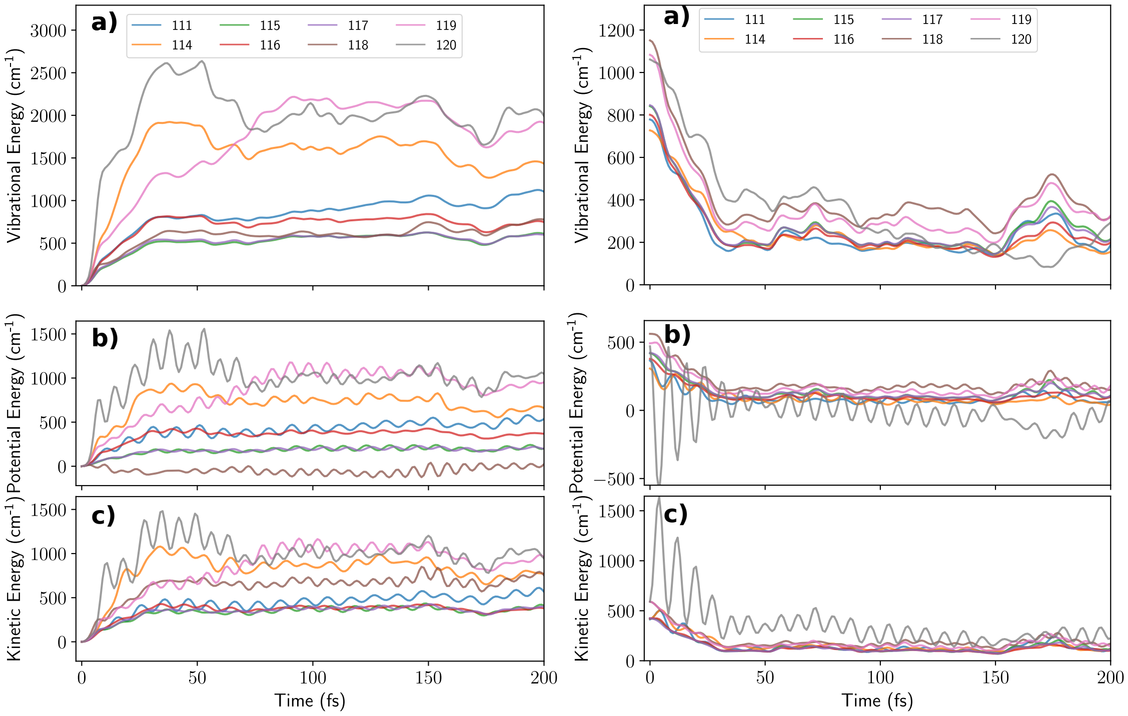

Figure 6.19: Time evolution of the vibrational, potential, and kinetic energy (a, b, and c, respectively) per mode for contributions from diabatic state D_1 (left) and diabatic state D_2 (right).

from the vibrational excitation perspective are only involved in the diagonal gradient vectors (both energy difference and gradient average vectors). From this internal vibrational redistribution of the excess electronic excitation, we indeed identify a clear separation between active and spectator modes within our model. This is also consistent with mixed quantum-classical trajectory-based dynamics calculations in analogous systems in the literature [158], for which two groups of modes are identified: i) active modes, which transiently store the excess energy during EET; and ii) spectator modes, which provide a "bath" of lowly-excited modes and contribute to dissipate the initial excess electronic energy in the late dynamics.

Estimation of the late dynamics (up to the ps)

With the present model, the thermal equilibration of the excess energy among all the normal modes is (expectedly) not reached even at longer times. The total (for the two diabatic states) vibrational energy per mode is shown in fig. 6.20 for up to 1000 fs.

Tuning-only modes appear to reach equilibrium with equipartition of the energy within the group (the four lowest-energy modes). However, the modes strongly involved in the inter-state coupling with the electronic reservoir are still out-of-equilibrium at longer times. This is related to the limits of the low dimensionality of the model and most importantly to the absence of interaction with the environment or low-frequency modes.

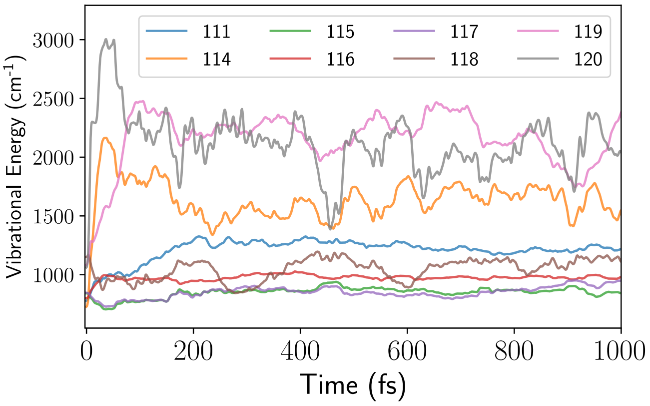

Figure 6.20: Time evolution of the vibrational energy per mode from both diabatic states D_1 and D_2 up to 1000 fs.

Take-home messages

1. We provided an energy decomposition analysis for the ultrafast EET in the nonadiabatically coupled electronic states of m23.
2. The first decomposition illustrates that the initial electronic excitation energy is rapidly transferred to the lower-lying excited state, but *via* its vibrational energy.
3. The decomposition of the vibrational energy for each modes yields interesting features of the energy transfer:
    - the population transfer is concomitant with a significant transient vibrational energy in the p2-acetylenic stretching mode (the donor fragment) and in the central phenylene rock-bending mode (the shared "articulation" between the donor and acceptor)
    - the excess excitation energy is, after the transfer, trapped mostly into the vibrational energies of the two previously mentioned modes and in the p3-asynchronous acetylenic stretching.
    - the other modes, mostly the quinoidal stretching, are rather spectator of the energy transfer but are important to stabilize the vibrational energy and the population in the acceptor state D_1.
4. This excitation energy transfer is sort of reminiscencent of the energy transfer in systems that can be separated into an active system and a passive bath (or of spin-boson models).

6.4 An attempt of high-dimensional quantum dynamics simulations

In this section we parametrize a high-dimensional LVC model for the S_1 and S_2 PESs of m23. The aim is to take into account all the $N = 93$ in-plane normal modes (A'), which are involved in both energy and coupling gradients for the first two electronic excited states (of symmetry A'). The selection of in-plane modes ranges from $11\,\mathrm{cm}^{-1}$ to $3244\,\mathrm{cm}^{-1}$ (large-scale displacements and C-H vibrations, respectively). The previously selected eight normal modes are included in this new model, only with a different parametrization procedure, that we further discuss in the following.

6.4.1 Parametrization of high-dimensional PESs

The aim of this section is to present a rather straightforward way of producing high-dimensional PESs for having a good estimation of the early and late dynamics for EET. As of now, we choose a model in-between the linear vibronic coupling (LVC) and quadratic vibronic coupling model (QVC), with all off-diagonal bilinear terms set to zero. The chosen model Hamiltonian (centered at the FC geometry) reads

$$\begin{aligned}\mathbf{H}(\mathbf{Q}) = \left(\hat{T}_{\text{nu}} + \sum_i \frac{1}{2} k_i^{(0)} Q_i^2\right) \mathbb{1} + \begin{bmatrix} E^{(1)}(\mathbf{Q}=0) & 0 \\ 0 & E^{(2)}(\mathbf{Q}=0) \end{bmatrix} + \sum_i \begin{bmatrix} \kappa_i^{(1)} Q_i & 0 \\ 0 & \kappa_i^{(2)} Q_i \end{bmatrix} \\ + \sum_i \begin{bmatrix} 0 & h'_i Q_i \\ h'_i Q_i & 0 \end{bmatrix} + \sum_i \sum_j \begin{bmatrix} \frac{1}{2}\gamma_{ij}^{(1)} Q_i Q_j & 0 \\ 0 & \frac{1}{2}\gamma_{ij}^{(2)} Q_i Q_j \end{bmatrix},\end{aligned} \tag{6.9}$$

where the first matrix (proportional to the identity matrix) is the harmonic reference, parametrized at the minimum of the electronic ground state. This slightly differs from the definition used for the diabatic curvatures in section 6.2, but is consistent with the first formulation of the LVC model (for instance in Refs [20, 78]). The curvatures of the electronic excited states are still allowed to be different together and with the electronic ground state because of the diagonal quadratic terms $\gamma_{ii}^{(s)}$. In other words, we model the PESs with a Taylor expansion to the second order for the diabatic potential energies and to the first order for the inter-state coupling. We note here that the most common Frenkel exciton Hamiltonian with a harmonic bath, often used for the simulation of EET in aggregates and solids, would resemble to the sum of the first three matrices in eq. (6.9).

A local fitting procedure *via* identification of energy derivatives

The procedure for the parametrization of the model Hamiltonian requires

- the knowledge of the vertical transtition energies, gradients, and Hessians at the FC geometry
- the knowledge of the position (with respect to the FC geometry) of the MECI and the branching-space vectors at this geometry.

The strategy for ensuring the diabatic and adiabatic states match at both FC and MECI geometries is similar to the one used in the 8-dimensional model. The BSVs $(\mathbf{g}, \mathbf{h})$ are rotated into a pair of BSVs $(\mathbf{g}', \mathbf{h}')$ such that

$$\mathbf{h}' \cdot \Delta\mathbf{Q}_X = 0 \tag{6.10}$$

with $\Delta\mathbf{Q}_X$ the position of the MECI with respect to the FC geometry. With the 93 selected normal modes, the parametrized rotation angle is $\theta = 18.82°$ and is the same than within full-dimensionality because out-of-plane normal modes do not participate in the $\mathbf{h}$ vector. Having parametrized the off-diagonal coupling, we now focus on the parameters for the diabatic potential energies. The diabatic energies at the FC geometry $E^{(s)}(\mathbf{Q} = 0)$ simply identify to the adiabatic vertical transition energies of S_1 and S_2. Similarly, the diabatic gradients are identified to the adiabatic vertical transition gradients of S_1 and S_2, projected onto the S_0 normal modes of vibration.

A note on the $\gamma^{(s)}$ matrices

The definition of the diabatic curvatures and bilinear cross-terms in the excited diabatic states is more involved. The matrices $\boldsymbol{\gamma}^{(s)}$ (which account for intra-state mode mixing) can not be directly identified to the adiabatic vertical transition Hessians of S_1 and S_2. Indeed, because we defined an inter-state coupling $\mathbf{h}'$, the choice of the diabatic Hessians (sum of the ground state Hessian $\mathbf{K}_{\mathsf{S}_0}$ and the $\boldsymbol{\gamma}^{(s)}$ matrices) must reflect the effect of the coupling for reproducing the adiabatic Hessians. To ensure this, we define the diabatic Hessians, according to a second-order Jahn-Teller-type formula

$$\begin{aligned}
\mathbf{K}_{\mathsf{S}_0} + \boldsymbol{\gamma}^{(1)} = \mathbf{K}_{\mathsf{D}_1} = \mathbf{K}_{\mathsf{S}_1} + 2\frac{\mathbf{h}'\mathbf{h}'^{\mathsf{T}}}{E(\mathsf{S}_2) - E(\mathsf{S}_1)}, \\
\mathbf{K}_{\mathsf{S}_0} + \boldsymbol{\gamma}^{(2)} = \mathbf{K}_{\mathsf{D}_2} = \mathbf{K}_{\mathsf{S}_2} - 2\frac{\mathbf{h}'\mathbf{h}'^{\mathsf{T}}}{E(\mathsf{S}_2) - E(\mathsf{S}_1)}.
\end{aligned} \tag{6.11}$$

Let us note that this “regularization” of the adiabatic Hessians into diabatic Hessians for the 93-dimensional model has numerically almost zero effect here. This is only because of the relatively strong energy difference at the FC geometry (which sort of nullifies the effect of the inter-state coupling at this geometry). We illustrate this in fig. 6.21 by showing the adiabatic Hessians of S_1 and S_2 and the diabatic Hessians of D_1 and D_2 (first two columns). All Hessians are projected onto the in-plane normal modes; in this representation, the most important values are on the diagonal. In other words, the normal modes of S_0 are almost an orthonormal basis for the Hessians of the excited states (almost diagonal matrices). The matrices $\boldsymbol{\gamma}^{(s)}$ represent the mixing (harmonic oscillator distortion for the diagonal elements) between the S_0 normal modes to describe the energy of the excited states to second order. They are also shown in fig. 6.21 (last two columns, where the Hessian $\mathbf{K}_{\mathsf{S}_0}$ has been substracted). Such an analysis can be linked to the calculation of Duschinsky matrices, only with the fact that here the excited states are evaluated at the same geometry as the ground state equilibrium geometry.

Let us notice for the mode-mixing matrices $\boldsymbol{\gamma}^{(s)}$ a particular structure with respect to the frequencies of the normal modes. There seem to be greater values (hence greater mode-mixing) for the group of quinoidal and acetylenic modes ($1600\,\mathrm{cm}^{-1}$ to $2400\,\mathrm{cm}^{-1}$) both between them and with the other modes. To some extent, this is also true for the triangular modes ($1000\,\mathrm{cm}^{-1}$ to $1600\,\mathrm{cm}^{-1}$), with important mode-mixing between them.

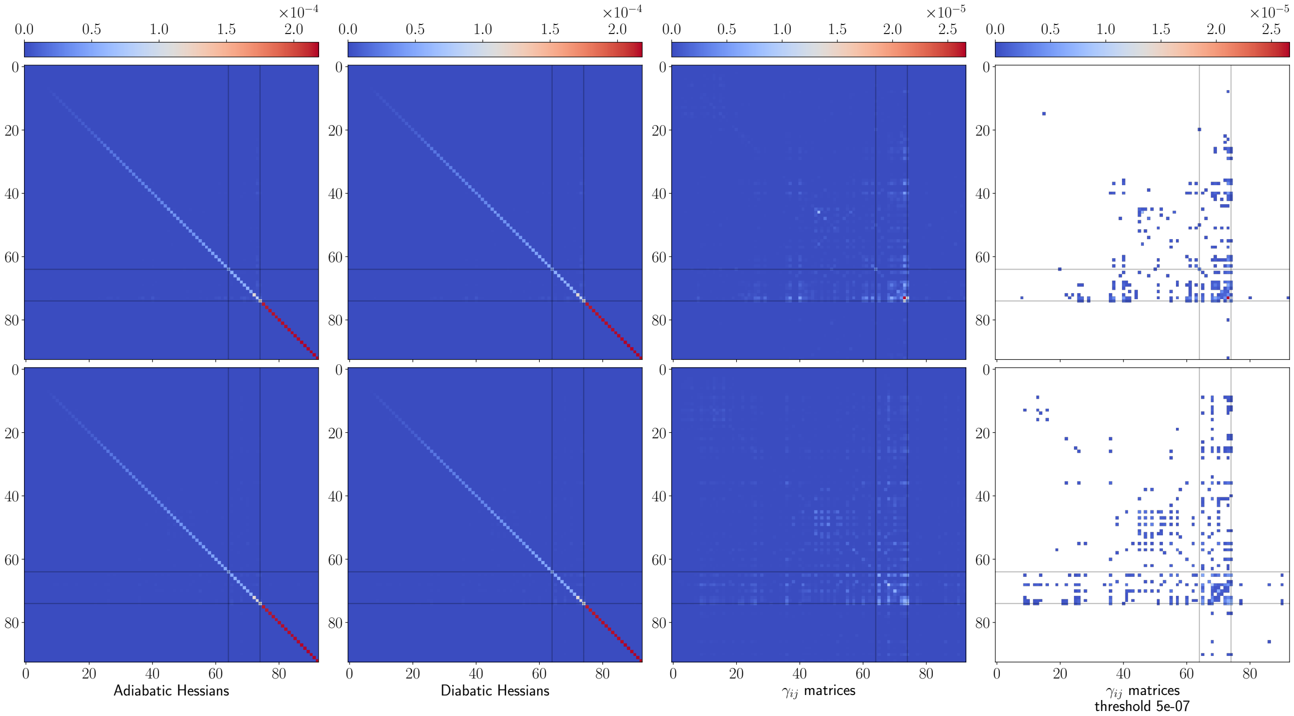

Figure 6.21: From left to right, i) adiabatic Hessians $\mathbf{K}_\mathrm{S}$ of S_1 and S_2 at the FC geometry; ii) constructed diabatic Hessians $\mathbf{K}_\mathrm{D}$ of D_1 and D_2 at the FC geometry; iii) mode-mixing matrices $\gamma^{(s)} = \mathbf{K}_{\mathrm{D}_s} - \mathbf{K}_{\mathrm{S}_0}$ for the two electronic states; iv) same with blanks where values are $\leq 5 \times 10^{-7}\,\frac{E_\mathrm{h}}{a_0^2 m_e}$ (unselected values). All Hessians are projected onto the normal modes computed at the FC geometry. The top and bottom panels correspond to the first and second excited states, respectively. The grey horizontal and vertical lines define the region of quinoidal, anti-quinoidal, and acetylenic normal modes.

This analysis will serve at least two (not completely unrelated) purposes:

- find mode-combination strategies for correctly taking into account the correlation between the strongly mixing modes;
- establish system-bath partitions with active modes (as regards spectroscopy and EET) and spectator modes.

Estimating the validity of the 93-dimensional LVC "plus" model

To evaluate the consistency of the model, we compare the energies of S_1 and S_2 for the S_1/S_2 PESs critical points with the one obtained from usual optimization. The energies for the minima of S_1, S_2 and the MECI are given in table 6.6.

We note the good agreement between the S_1 minimum in the 93-dimensional LVC model and the S_1 minimum in the fully-optimized PESs. The S_2 minimum in the 93-dimensional LVC model is really close to

Table 6.6: Energies in eV of the first two adiabatic and diabatic excited states at the critical points in the *ab initio* PESs (at the CAM-B3LYP/6-31+G* level of theory) and in the LVC models (8-dimensional and 93-dimensional). For the models, the optimization method is the COBYLA method inplemented in the `scipy` `python` library.

Model	Full-dimensional (*ab initio*)[a]			8-dimensional (LVC)			93-dimensional (LVC)		
Critical Point	S_1	S_2	MECI	S_1	S_2	MECI	S_1	S_2	MECI[b]
$E(S_1)$	3.61	3.99	4.30	3.67	4.00	4.40	3.62	4.13	–
$E(S_2)$	4.62	4.17	4.30	4.59	4.23	4.40	4.64	4.13	–
$\Delta E(S)$	1.01	0.18	$< 5e^{-4}$	1.08	0.23	$< 5e^{-3}$	1.02	$< 5e^{-3}$	–
$E(D_1)$	–	–	–	3.67	4.01	4.40	3.64	4.13	–
$E(D_2)$	–	–	–	4.59	4.22	4.40	4.62	4.13	–

[a] The diabatic states and their energies are not known from the *ab initio* calcultions.

[b] Up to now, the MECI has not been successfully found for the 93-dimensional model.

an S_1/S_2 conical intersection. However the MECI in the 93-dimensional model has not been found directly for now. Our model thus seems to underestimate by about 0.15 eV the energy of the MECI (or at least the energies within the intersection space), which seems superimposed with the minimum of the S_2 PES. As such, the model is clearly perfectible, but we continue with it for the rest of this chapter to evaluate the feasibility of high-dimensional quantum dynamics (HDQD) simulations in light-harvesting building-blocks (and eventually dendrimers).

Take-home messages

1. We proposed a systematic and straightforward parametrization of a high-dimensional (93 modes) vibronic coupling model, including linear off-diagonal (inter-state) couplings and bilinear diagonal (intra-state) couplings.
2. As only two reference geometries are used to parametrize the model. It is expectedly not perfect as regards the re-construction of the PESs of the S_1/S_2 manifold, in particular for the minima of S_2 and of the conical intersection.
3. However, we hope it correctly estimates i) the vertical transition gradients (for the initial states); ii) the inter-state coupling (for the early dynamics); and iii) the minimum of the acceptor state (for late dynamics).

6.4.2 Global fitting *vs.* local fitting, comparison of the 8-dimensional models

Before running high-dimensional quantum dynamics, we compare the EET dynamics simulated for the LVC parametrized *via* a global fit (fitting of *ab initio* PESs, section 6.2.2) and the LVC parametrized *via* a local fit (identification of energy derivatives, section 6.4.1). For this comparison, we extract the 8-dimensional *child* model from the 93-dimensional *parent* model, by freezing all unselected normal modes in quantum dynamics calculations.

We show in fig. 6.22 the population transfer dynamics of EET for simulations for which the matrices $\gamma_{ij}, i \neq j$ are adiabatically switched on from 0 (blue lines) to 1 (gray lines), and to 2 (red lines).

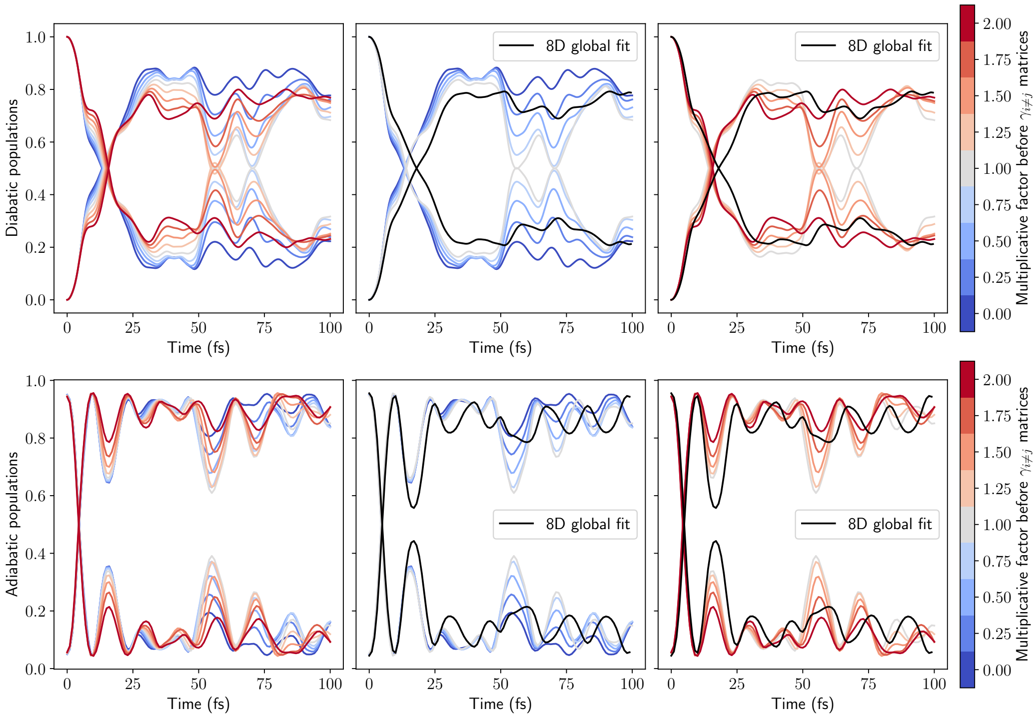

Figure 6.22: Diabatic and adiabatic populations of the first two excited states in various LVC models, in top and bottom panels, respectively. The results obtained from varying the $\gamma_{i\neq j}$ matrices from 0 (LVC models with different curvatures for the excited states but no mode mixing) to 1 (same with mode mixing) [in both left and center panels] and from 1 to 2 (articifially enhanced mode mixing) are shown [in both center and right panels] (colormap from blue to red).

The results obtained in section 6.2.2 from an 8-dimensional global fit of the S_1/S_2 PESs are recalled (black line). We want to examine the role of the intra-state bilinear couplings ($\gamma_{ij}, i \neq j$) and their relevance in low-dimensional models. For both diabatic and adiabatic populations, the early EET population transfer (up to 50 fs) seems to be only slightly affected by the variations on the $\gamma_{ij}, i \neq j$ matrices. In particular, we note that the diabatic population transfer is slightly faster when switching on, and enhancing, the mode mixing. This is likely due to the contribution of the $\gamma_{ij}, i \neq j$ parameters to the diabatic gradient difference, which really drives the early dynamics. Quite counter-intuitively, the diabatic quantum yield (again, before 50 fs) is higher for simulations with no mode mixing, while we would expect bilinear intra-state couplings to allow for more efficient relaxations in the S_1 electronic state. For longer times, we observe that the diabatic states mix again with a 50:50 population mix for the case of $1 \times \gamma_{ij}$, at both 55 fs and 70 fs.

Quite counter-intuitively again, the transfer is more monotonic in the extreme case of $0 \times \gamma_{ij}$ than in the (supposedly more realistic) case of $1 \times \gamma_{ij}$. A plausible explanation would be that accounting for the mode mixing *via* non-zero bilinear intra-state couplings is not accurate enough in low-dimensional system. Indeed, as we will see in section 6.4.3, with the same model $(1 \times \gamma_{ij})$ but without freezing any in-plane modes, there are no crossing in the diabatic states anymore. The same is found for the extreme case of $2 \times \gamma_{ij}$ which is an artificial enhancement of mode mixing.

Our interpretation is that accounting for mode mixing (that is, intra-state bilinear couplings) *via* a local fit of the excited-state Hessians might not be adapted to low-dimensional models. Indeed, with the *a priori* more realistic local fit parametrization $(1 \times \gamma_{ij})$, the results are significantly different from the global fit parametrization. This can be explained by the fact the γ_{ij} parameters are obtained for the full-dimensional system, so that they might be too important when used in a reduced model.

We note that these effects are not found to the same extent in the adiabatic population transfer, although the simulation of EET with $1 \times \gamma_{ij}$ also exhibits important crossings of the CoIn seam at both 55 fs and 70 fs.

6.4.3 Strategies for high-dimensional quantum dynamics and associated feasibility

We now discuss the feasibility of wavepacket propagation and associated analysis for high-dimensional PESs, wavepackets, and configuration spaces (spatial grids). Indeed, as mentioned in chapter 3, the equations of motion for MCTDH are tractable for less than ten degrees of freedom; the mode-combination strategy allows one to easily propagate up to 12-14 degrees of freedom, but the *curse of dimensionality* remains. Here, several tens of normal modes can not be propagated with simple MCTDH wavepackets and combined modes.[4] We thus choose the multi-layer strategy (ML-MCTDH) [106–108] for which the idea is to iteratively combine the modes in order to drastically reduce the number of configurations to be propagated and the associated mean-field matrices.

6.4.3.1 Construction of the ML-tree helped with chemical intuition

The problem we now face is: how should the 93 modes be combined, *i.e.* which "ML-tree" has to be defined. Unfortunately, there is no perfect nor unique answer. Then, we must define criteria for evaluating the validity of an ML-tree for a given high-dimensional quantum dynamics simulation.

We use here a simple approach, based on separating the modes with respect to their chemical character. To do so, the simplest separation uses the frequencies and the reduced masses of the normal modes. The first "guess" for the ML-tree is obtained by defining so-called "nodes" (group of modes or combined modes) and so-called "layers" (groups of same nodes at the same level). "Branches" are then defined as

---

[4] 93 degrees of freedom with 15 basis function each yield an absurd grid size of $\simeq 10^{109}$.

links between two nodes between consecutive layers. Let us start a tree with 4 nodes (first layer), that will ultimately contain modes belonging to the frequency-windows $0\,\mathrm{cm}^{-1}$ to $1000\,\mathrm{cm}^{-1}$, $1000\,\mathrm{cm}^{-1}$ to $1500\,\mathrm{cm}^{-1}$, $1500\,\mathrm{cm}^{-1}$ to $2300\,\mathrm{cm}^{-1}$, and $2400\,\mathrm{cm}^{-1}$ to $3400\,\mathrm{cm}^{-1}$. From each of these nodes, let us build 4 or 5 branches (toward the second layer) and again 3 or 4 branches (third layer). In each of the latter branch, we define a (2-by-2-) mode-combined MCTDH wavepacket for consecutive primitive degrees of freedom. The representation of this "guess" ML-tree is shown in fig. 6.23

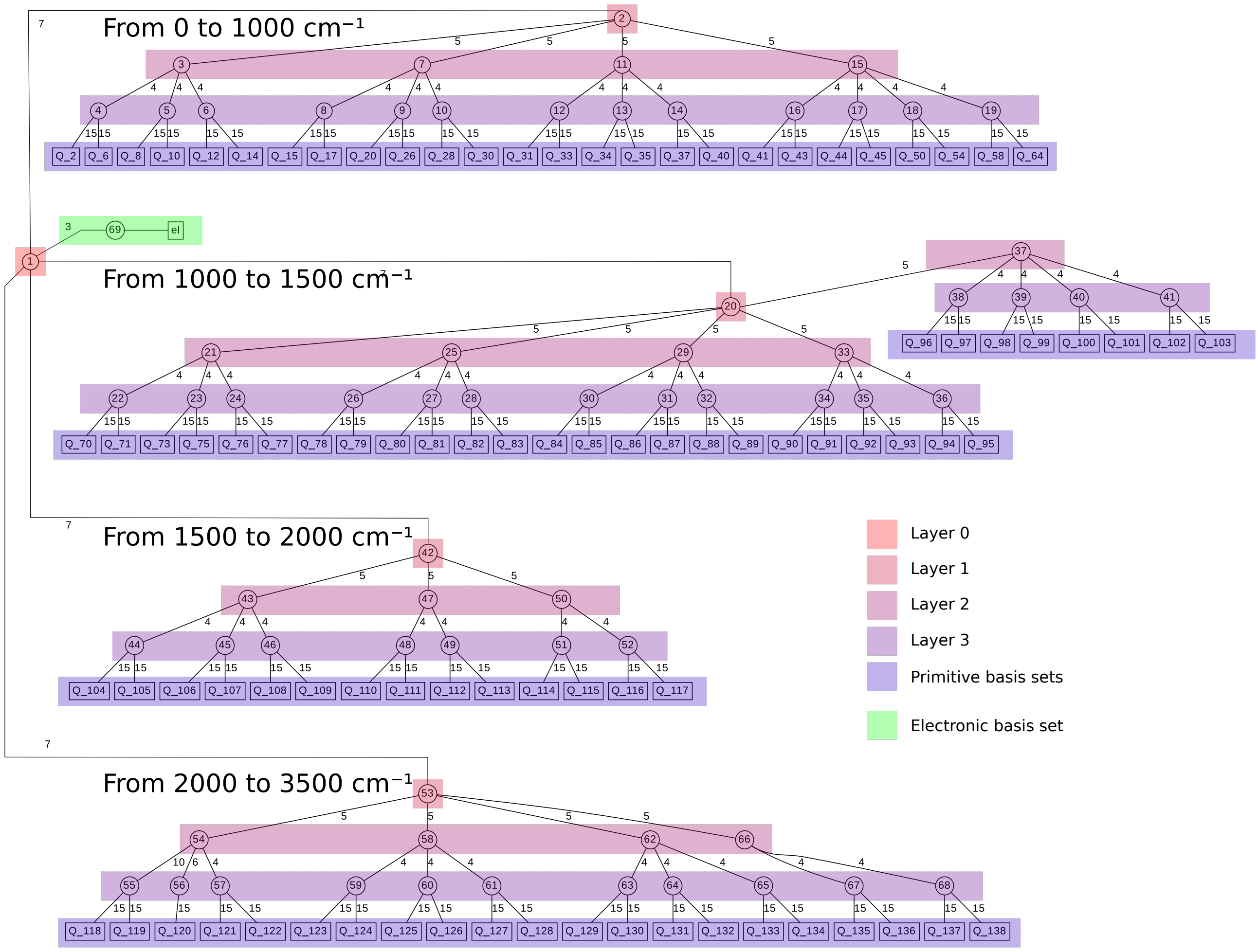

Figure 6.23: First guess of an ML-tree for the quantum dynamics simulations on the (1+2)-state 93-dimensional LVC model. The layer for the electronic states is given in green. The layers for the vibrational degrees of freedom are given in red to blue shading, from the top layer to the primitive basis, respectively. Nodes are in circles, primitive modes are in squares. The size of the basis set for each expansion (nodes or modes) is given above the corresponding node.

With small SPFs basis sets for each layer, the computational time is reasonable ($1\,\mathrm{h}$ of human-time, on a 16-core machine, for $10\,\mathrm{fs}$) and we can imagine the ML-tree to be iteratively optimized upon "convergence". The criteria that would define a not-optimized ML-tree are (non-exhaustively):

- obviously the absence of energy conservation;
- important natural population of the last SPFs for each node (or normal mode for the last layer),

analogous to MCTDH;

- or unphysical symmetry-breaking (in the case of PESs and initial states with symmetry).

The “variables” to be optimized are the very structure of the ML-tree (should we add branches, layers?); and the number of SPFs per node (or mode). Only the energy-conservation and low-natural-population criteria are used in the case of m23, as the wavepackets have no specific parity as regards the in-plane normal modes. For now, we only explore such an optimization by changing by hand the size of SPFs basis sets or the structure of the ML-tree (definition of the layers and the nodes).

Over the first $100\,\text{fs}$ of simulation (initial excitation on D_2 to simulate EET in m23), we evaluate the highest last natural population for each node. A typical value of highest last natural population for having converged diabatic expectation values (which is our main analysis tool here) is 1×10^{-3}. We show the highest last natural populations (multiplied by 1×10^{3}) for each nodes in fig. 6.24 (left panel for the simulation with the guess ML-tree). The same quantity is shown for two subsequent optimization steps “by-hand” in the other panels.

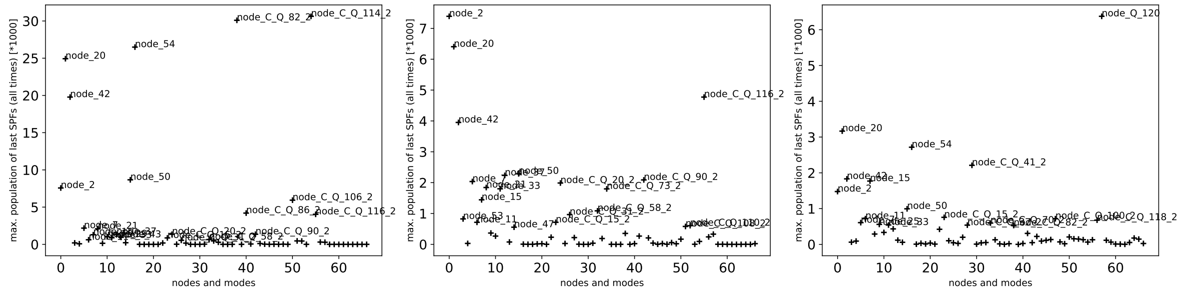

Figure 6.24: Highest last natural population (over $100\,\text{fs}$ propagation) for the set of SPFs of each node and mode of three ML-MCTDH calculations, with the same ML-tree but for different ”steps” of its ”optimization-by-hand” (increasing or decreasing the number of SPFs per nodes).

We observe that the guess ML-tree yields poorly converged wavepackets. In particular, there are highest last natural populations at 25×10^{-3} for nodes 20 and 42 which are the “core” nodes of the ML-tree, and for node 54 which is the node defining the wavefunction for the acetylenic normal modes (see fig. 6.23). From the left to the right panels, we successfully optimize the size of the SPFs basis sets for the unconverged nodes (and similarly for the “too much” converged nodes) to find “better” natural populations for the SPFs.

However, this comes with a significantly higher computational time, from left to right: $1.5\,\text{h}$, $12\,\text{h}$, and $80\,\text{h}$ with the same 16-core machine. In addition, we note that the energy conservation is more easily conserved with the initial guess of a naive tree than with the other two attempts (see fig. 6.25 left panel, with at the end $\Delta E = 7.3\,\text{meV}$, $13.4\,\text{meV}$, and $102.2\,\text{meV}$). As of now and with our present expertise of ML-MCTDH, we were not able to interpret properly such results on the energy conservation for, in our understanding, “better” converged wavepackets. However, let us note that for the three calculations, the population transfer is qualitatively the same overall, and quantitatively the same up to 30 fs (fig. 6.25, right panel).

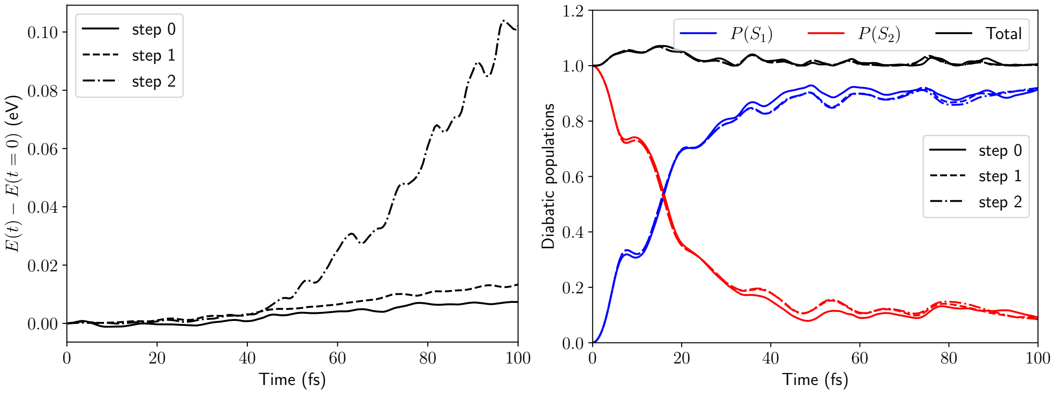

Figure 6.25: Left: time evolution of the difference in total energy compared to initial energy of the wavepacket, for the three "steps" of the ML-tree optimization. Right: time evolution of the diabatic populations (and their sum) of the D_1 and D_2 states for the three "steps" of the ML-tree optimization.

To conclude on this approach, clearly this ML-tree definition and optimization is too naive and inefficient, as the most-adapted ML-trees might be very different at different points of the dynamics. In particular in the case of EET, we have seen that at least three regimes are identified: initial excitation, inversion of electronic populations, and harmonic oscillations in the lower-lying diabatic state. The three regimes involve mainly one diabatic state, two diabatic states, and one diabatic state, respectively, and are very likely to behave differently as regards the "optimized" character of a given ML-tree. Choosing a complicated ML-tree for the most complicated regime would then be very expensive as regards the other regimes. One solution to circumvent this has been designed by Mendive-Tapia and co-workers and consists in the *ML-spawning algorithm*, which idea is to adapt the number of SPFs per mode in an on-the-fly fashion [159, 160]. This algorithm has been successfully used for the study of spin-boson Hamiltonian models [3] and is likely to be applicable in our case.

6.4.3.2 Potential solutions for systematic definitions of the ML-tree

Construction of the ML-tree helped with system-bath separations

In order to interpret the 93D model as an extension of the model based only on acetylenic and quinoidal modes, we aim to separate the normal modes in two sets:

- a set of 11 "active" normal modes (all quinoidal, anti-quinoidal and acetylenic modes of m23);
- a set of 82 "spectator" normal modes (all remaining in-plane modes).

In order to simplify the (1+2)-state LVC Hamiltonian in eq. (6.9), we set

$$h'_i = 0 \quad \forall i \ \in \text{spectator modes} \tag{6.12a}$$

$$\gamma_{ij}^{(s)} = 0 \quad \forall s \text{ and } \forall i, j \ \in \text{active modes and spectator modes, respectively} \tag{6.12b}$$

yielding an approximation where the active modes (A) define a "system" minimally coupled to the spectator modes (S), defining a "vibrational bath", with a "separable" diabatic Hamiltonian

$$\mathbf{H}(\mathbf{Q}) = \mathbf{H}_{\mathsf{A}}(\mathbf{Q}) + \mathbf{H}_{\mathsf{S}}(\mathbf{Q}). \tag{6.13}$$

Let us stress that even though we set to zero all "explicit" couplings between the active and the spectator modes (the diabatic Hamiltonian is separable, with no $\mathbf{H}_{\mathsf{AS}}(\mathbf{Q})$), the propagations of the two systems are still coupled.[5] To convince oneself, one can notice that the adiabatic Hamiltonian is not separable, due to the non-zero off-diagonal couplings. Another way of understanding this is to examine the commutator (discarding nuclear dependence)

$$[\mathbf{H}_{\mathsf{A}}, \mathbf{H}_{\mathsf{S}}] = \begin{pmatrix} 0 & H_{12,\mathsf{A}}\left(H_{22,\mathsf{S}} - H_{11,\mathsf{S}}\right) \\ H_{12,\mathsf{A}}\left(H_{22,\mathsf{S}} - H_{11,\mathsf{S}}\right) & 0 \end{pmatrix} \tag{6.14}$$

as examplified recently by Montorsi and co-workers [161]. This non-zero commutator is involved (theoretically) in the propagation of the active and spectator systems, so that the two systems cannot be seen as completely uncoupled.

We also propose an ML-tree adapted to this intermediate "system-bath" separation of the normal modes, based on groups of active (11D) and spectator modes (82D) (see fig. 6.26).

Toward systematic construction of the ML-tree using hierarchical clustering

Recent work from Mendive-Tapia proposed to build ML-trees based on an estimation of the correlation between the modes included in the calculations [162]. The idea is to use hierarchical clustering, which relies on two ingredients: i) the estimation of the *proximity* or distance between two elements (here modes); and ii) a *linkage criterion*. Herein, we estimate the distance using the angular distance formula as suggested in Ref [162]

$$\text{dist}_{ij} = \frac{2}{\pi} \arccos\left(\frac{\sum_l C_{li} C_{lj}}{\sqrt{\sum_l C_{li}^2}\sqrt{\sum_l C_{lj}^2}}\right) \tag{6.15}$$

where the $\mathbf{C}$ matrix is a correlation matrix. For our preliminary tests, we tried to estimate a "correlation" matrix between the S_0 normal modes using the $\gamma^{(s)}$ matrices. However, we note that the choice of $\gamma^{(\mathsf{s})}$ is quite arbitrary here, and we might want to use a matrix representing the correlation between the normal modes *via* the measure of mode mixing within the excited states.

Now, when the distance matrix is defined (for instance, the mean matrix of $\gamma^{(s)}$ matrices, shown in fig. 6.27), the linkage criterion allows us to build a *dendrogram* which represents an optimal (depending on

---

[5] ... under certain conditions: different curvatures and gradients for the two excited diabatic states.

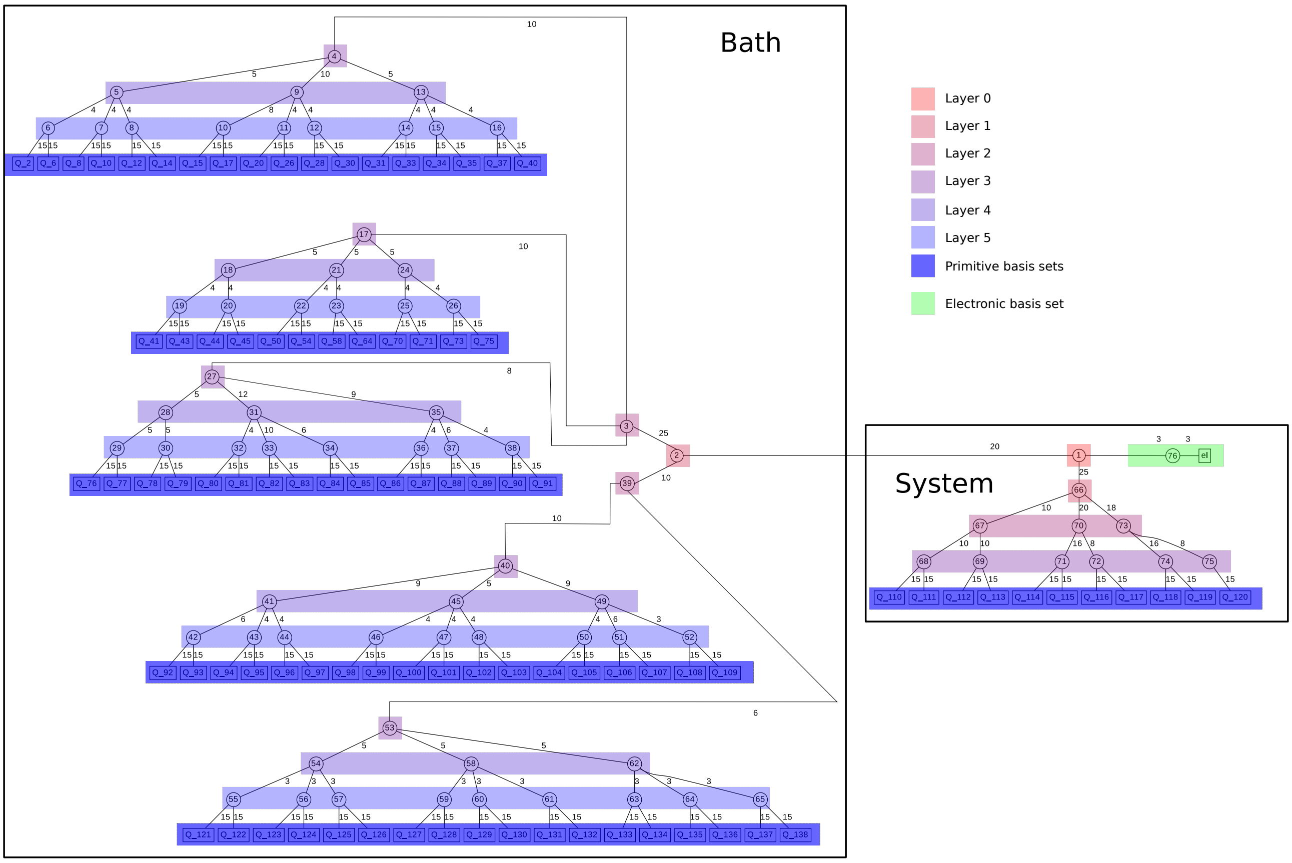

Figure 6.26: Proposition of an ML-tree for the quantum dynamics simulations on the (1+2)-state 93-dimensional LVC model with a system-bath separation based. The layer for the electronic states is given in green. The layers for the vibrational degrees of freedom are given from red, from the top layer to the primitive basis, respectively. Nodes are in circles, primitive modes are in squares. The size of the basis set for each expansion (nodes or modes) is given above the corresponding node.

the criterion) way of pairing (clustering) the initial modes together up to a final, unique node. An example of such a dendrogram in shown in fig. 6.28. With our measure of correlations, the distance matrix should be read as follows, for instance

- mode 58 is *close* to mode 118 (small distance, blue color in fig. 6.27); hence, the two modes must be close together in the dendrogram and must be paired (they are, see fig. 6.28, red branch, lower left)
- mode 75 is *close* to mode 119 (small distance, blue color in fig. 6.27); hence, the two modes must be close together in the dendrogram and must be paired (they are, see fig. 6.28, pink branch, lower right)
- *etc.*,

so that the closer modes are paired into clusters of two, which are paired again iteratively. Of course, the aim is not to interpret each distance and each branch of the dendrogram, but to hope for a reliable clustering from the correlation measure.

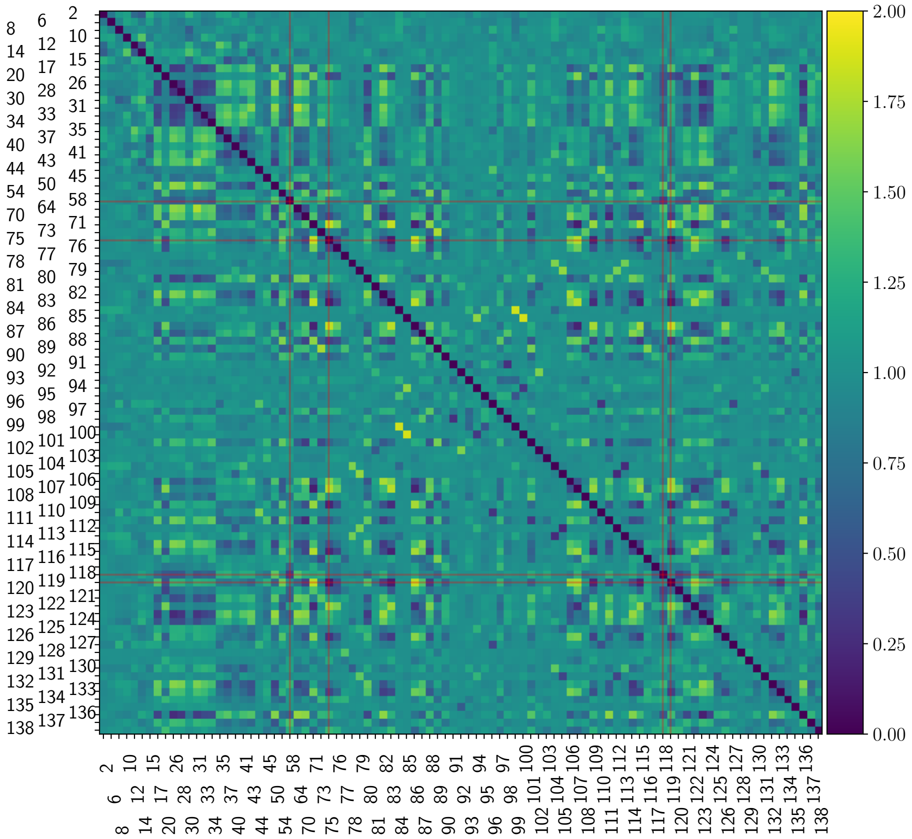

Figure 6.27: Distance matrix calculated with eq. (6.15) and $\mathbf{C} = \frac{1}{2}\left(\gamma^{(1)} + \gamma^{(2)}\right)$ for the 93 in-plane normal modes of the m23 molecule. The red lines are visual guides for the comparison of modes 58 and 75 with the acetylenic stretching modes 118 and 119.

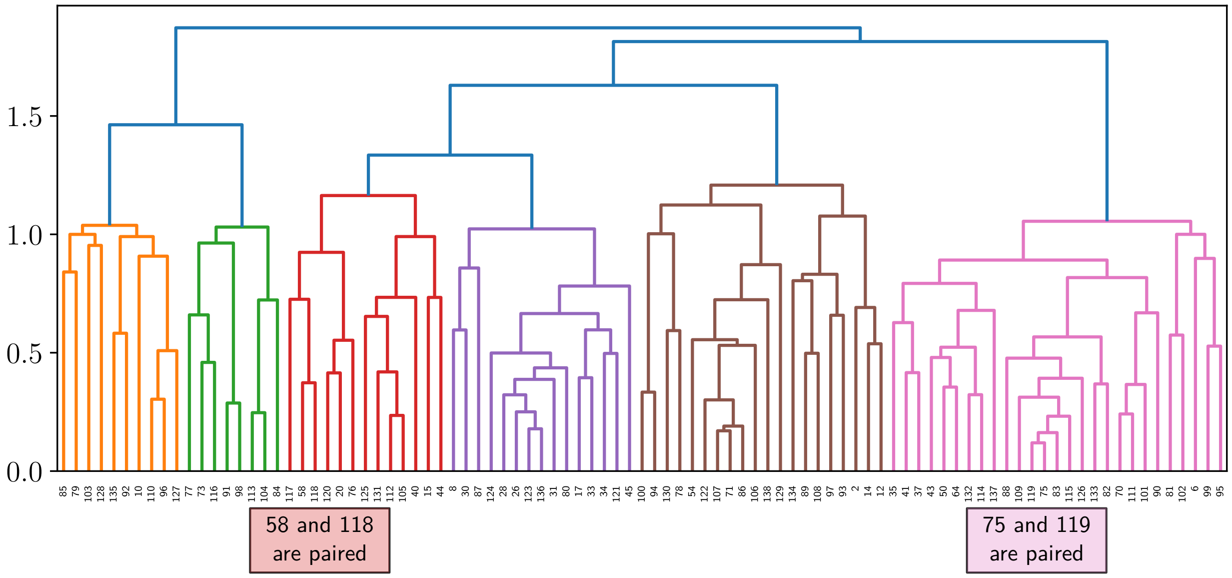

58 and 118 are paired

75 and 119 are paired

Figure 6.28: Dendrogram obtained from the distance matrix shown in fig. 6.27, illustrating the most efficient hierarchical clustering of the initial 93 in-plane normal modes into pairs up to a central node. Obtained using the functions of the `python` library `scipy.cluster.hierarchy`.

On a final note, building an ML-tree from the dendrogram directly is not trivial, but one can think of additional criteria so as to define the layers and the branches. This work is not done yet, and as of now we only tried to manually define an ML-tree [not shown here] that reflects the dendrogram. Yet, such hierarchical cluster analysis seems promising for studies of phenomena involving low-amplitude displacements in the excited-state, as the information for the correlation of the modes is directly found from vibrational analysis and from the Duschinsky matrices.

Take-home messages

1. We evaluated both
    - the relevance of high-dimensional PESs parametrized with energy derivatives alone;
    - the feasibility of associated high-dimensional wavepacket dynamics (with a proposition of a ”performing” ML-tree),

   for the specific case of intramolecular excitation-energy transfer, with up to 93 degrees of freedom.
2. We started a discussion on the relevance of the mode-mixing parameters for simulating EET and understanding its mechanism.
3. We also explored alternative strategies for the choice of the ML-tree (namely system-bath separations and hierarchical clustering).

6.5 Concluding remarks

6.5.1 Modelling and simulating EET in an asymmetrical PPE-oligomer

In this chapter, we presented the first quantum dynamics study of the asymmetrically substituted poly(phenylene ethynylene) (PPE) oligomer, the m23 molecule, which is the first unit of PPE for excitation-energy transfer (EET) in the PPE-dendrimers. We aimed for i) the characterization of electronic excited states of the molecule and of the normal modes of vibration, both in the electronic ground and excited states; and ii) an atomistic and time-resolved simulation of intramolecular EET within m23.

In particular, we showed, at our level of theory, the *excitonic* character of the first two electronic excited states and characterized their intersection (MECI and branching-space vectors). We re-interpreted the EET process, *via* a simple stationary picture, from an initial excitation on the donor state (localized transition density on the p2 *pseudo* fragment) to a transfer into the acceptor state (localized transition density on the p3 *pseudo* fragment, lower in energy). Strong of this knowledge, we parametrized low-dimensional models of PESs to estimate both the importance of the high-frequency normal modes of vibration in the transfer and the timescale of the process.

Most importantly, our results show that a minimal model of five modes with the acetylenic stretching and the central-quinoidal modes is enough to predict an ultrafast (within $25\,\mathrm{fs}$ after excitation) and efficient (80% quantum yield) excitation-energy transfer. The model is completed with other quinoidal modes, yielding an 8-dimensional model able to reproduce correctly both the transfer from the donor state to the acceptor state and the energy trapping in the acceptor state. Such results are obtained from the interpretation of the expectation values for both monitoring the molecular geometry and monitoring the energy distribution during the electronic population transfer.

6.5.2 A trade-off between fully explicit PESs and parametrizing costs

Our short-term outlooks are to extend this strategy for the atomistic simulation of EET to more realistic models, ideally to the full-dimensional system. However, even in this smallest unit for EET, full-dimensionality is $f = N_{\text{vib}} = 138$, which is untractable for both parametrization of the PESs and propagation of the nuclear wavepackets. In this chapter, we proposed a first attempt of high-dimensional quantum dynamics with all in-plane modes of the molecule ($f = 93$).

We based our parametrization procedure on local derivatives only, using two optimized geometries, the Franck-Condon geometry (for estimating the initial state for the dynamics) and the minimum-energy conical intersection geometry (for estimating the nonadiabatic coupling between the excited states). This strategy is clearly not adapted for explicitly reproducing the full-dimensional adiabatic PES of the excited state. However, it is an acceptable trade-off as an advanced (and easily parametrized) Frenkel-exciton Hamiltonian model. The model can also be seen in the fashion of a spin-boson system, only with an explicit and discrete bath (first quantization) made of the spectator normal modes. In particular, we started a discussion on the relevance of the intra-state bilinear coupling parameters (which reflects mode mixing) for both modelling and designing EET. Finally, we explored the feasibility of high-dimensional quantum dynamics calculations by discussing different strategies for the multi-layer combination of the numerous degrees of freedom.

Medium-term outlooks concern the parametrization of similarly advanced Frenkel-exciton Hamiltonian models for an arbitrary shape and size of the PPE-oligomer. We explicit our ideas for tackling this task in part III, chapter 9.

Chapter 7

The First Dendron of PPE-oligomers

We have presented in chapters 5 and 6 the two main ingredients for light-harvesting PPE-dendrimers. We first presented the chromophore m22, which consists in a symmetrically *meta*-substituted benzene with two bright electronic excited states able to collect light in the UV-visible domain. Then, the prototypical molecule m23, which is an articulation of p2 and p3 *pseudo* fragments, has been extensively studied. A simple and relatively low-dimensional model was able to reproduce the ability of the system to efficiently transfer excitation energy from the shortest branch (p2) to the longest branch (p3). For both systems, the importance of the acetylenic and quinoidal normal modes of vibration has been demonstrated as regards both steady-state spectroscopy properties and excitation-energy transfer features. In this chapter, we shall focus on the very first dendron of PPE-dendrimers for studying excitation-energy transfer (EET) in *oligo*-PPEs and PPE-dendrimers. The first dendron is the tri-*meta*-substituted benzene with two equivalent p2 *pseudo* fragments and one p3 *pseudo* fragment, denoted d223 in the rest of this chapter and shown in fig. 7.1. We stress already that different pseudofragmentation schemes can be used for the study of d223.

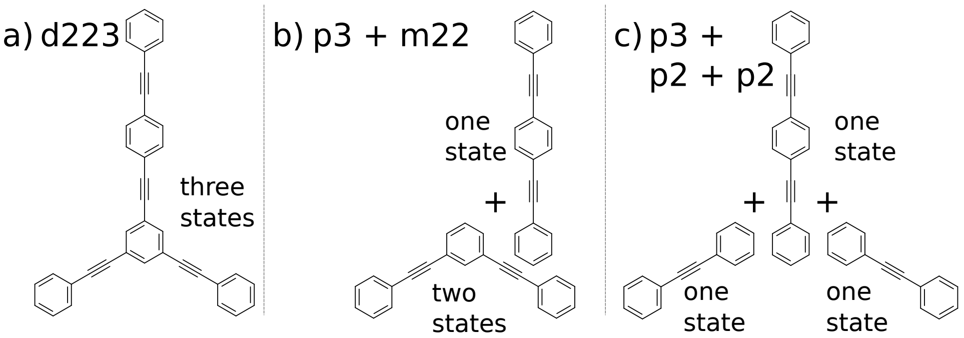

Figure 7.1: Ground-state Lewis structure of the first dendron of PPE-dendrimers, d223 (a), and schemes of *pseudofragmentation* for d223 as a p3 *pseudo* fragment and an m22 *pseudo* fragment (b), or as a p3 *pseudo* fragment and two p2 *pseudo* fragments (c).

The present chapter is organized as follows: in section 7.1, we briefly describe the electronic excited states of d223 and some of the most important features of the associated adiabatic PESs. In section 7.2, we propose (1+3)-state LVC Hamiltonian models for reproducing the PESs and NACs of d223, and use these models in section 7.3 to simulate EET in d223 and evaluate both its timescale and quantum yield.

The aim of this chapter is to make the first step toward simulating larger PPE-dendrimers prototypes. Numerous types of analysis have already been presented in chapter 6 and have been published, and will be directly re-used in this chapter (for instance, the wavepacket analysis in terms of the diabatic expectations values, the transformation into internal coordinates for trajectory-like monitoring...) [155].

7.1 Electronic excited states of a tri-*meta*-substituted PPE

The minimum of the electronic ground state (FC geometry) of d223 is a C_{2v} geometry. We examine the vertical transitions from the electronic ground state to the first four electronic singlet excited states, through the visual inspection of the NTOs and the transition densities, shown in fig. 7.2.

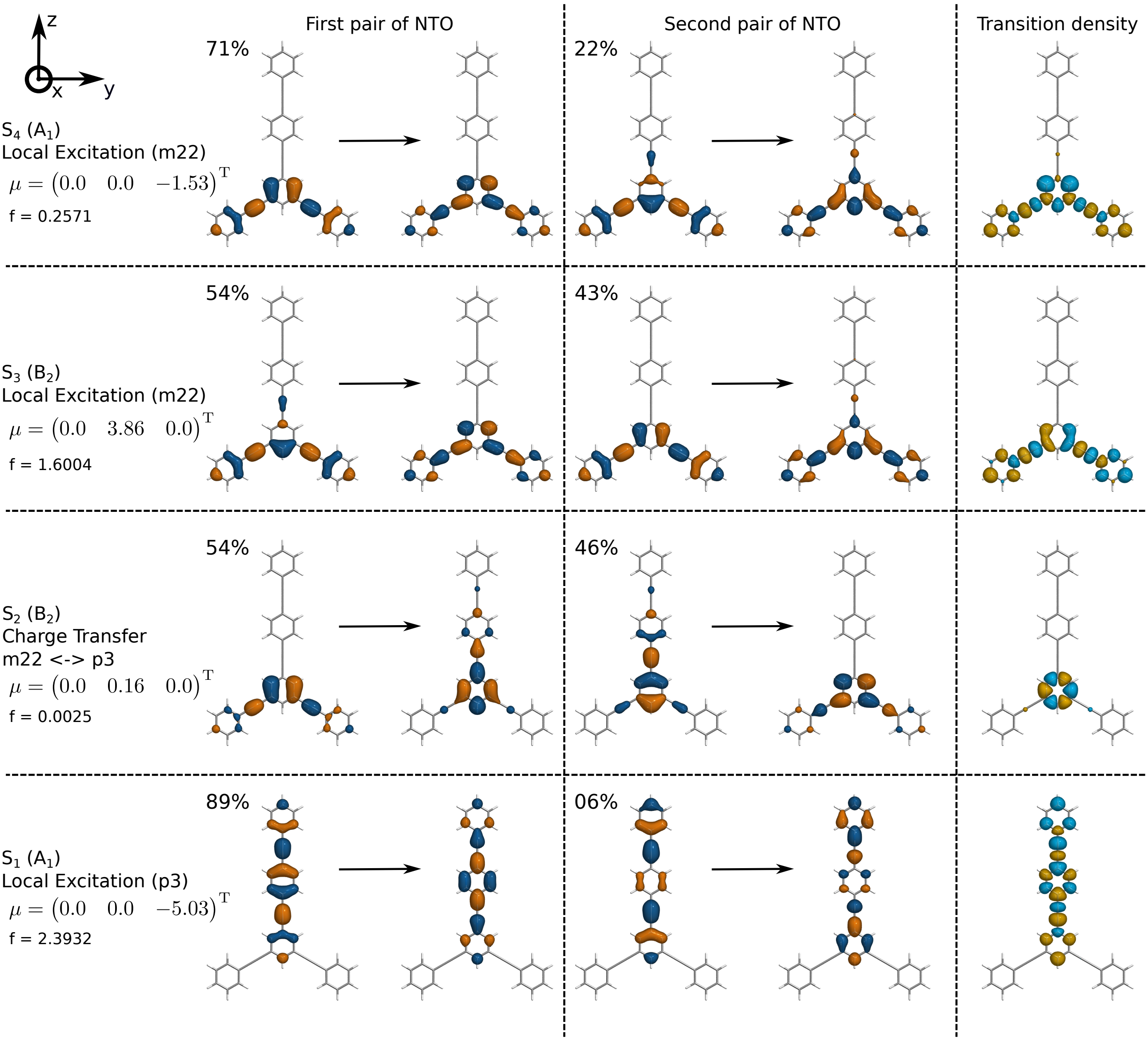

Figure 7.2: First two pairs of natural transition orbitals (NTOs) and the associated transition densities for the electronic states S$_1$ to S$_4$ at the mininum of the electronic ground state (vertical transitions). The electronic transition dipole moments (ETDMs) are also given, in atomic units and with respect to the axes for the C$_{2v}$ point group of symmetry.

The vertical transitions to S$_1$, S$_3$, and S$_4$ are similar to what is known for local excitations (LE) on the previously studied fragments. In particular, the first excited state has a non-negligible transition density localized on the p3 *pseudo* fragment and belongs to the A$_1$ irreducible representation (z-polarized). The third and fourth excited states have non-negligible transition densities on the m22 *pseudo* fragment and belong to B$_2$ and A$_1$ irreducible representations (y- and z-polarized), respectively. The NTOs involved are in very good agreement with the isolated m22 fragment. However, the second excited state is not a local excitation, but a charge transfer (CT) state with almost zero oscillator strength. The NTOs are not localized strictly on the same fragments (except for the contributions from the central benzene). The transition density clearly corroborates this, with only non-negligible density on the central benzene. As regards the state ordering, we note that it is the same for both CAM-B3LYP and ωB97XD functionals at the FC geometry optimized with CAM-B3LYP. We did not further investigate the state ordering for optimized geometries with ωB97XD.

Optimization of minima and transition states

As regards the critical points of the excited-state PESs, we give the energies for the minima and transition states in table 7.1.

Table 7.1: Adiabatic energies (in eV) of the electronic ground state and first four electronic excited states for a selection of critical points in d223. The minimum of the electronic ground state is taken as the reference energy for each molecule. The lengths of the acetylenic bonds are given ($d = d(\mathrm{C} \equiv \mathrm{C})$ in Å) and the values are set in bold when they are intermediate between acetylenic and cumulenic bonding patterns. Labels [p2], [p3-in] and [p3-ext] refer for d223 to the acetylenic bond of the p2 *pseudo* fragments and of the inner and external acetylenic bonds of the p3 *pseudo* fragment.

Geometry	Sym.	$E(\mathrm{S}_0)$	$E(\mathrm{S}_1)$	$E(\mathrm{S}_2)$	$E(\mathrm{S}_3)$	$E(\mathrm{S}_4)$	d[p2]	d[p3-in]	d[p3-ext]
p3 MinS_0	D_{2h}	0.00	3.90	4.81			–	1.210	1.210
p3 MinS_1	D_{2h}	0.26	3.62	4.80			–	**1.233**	**1.233**
p2 MinS_0	D_{2h}	0.00	4.48	5.08			1.210	–	–
p2 MinS_1	D_{2h}	0.32	4.14	4.84			**1.255**	–	–
m23 MinS_0	C_s	0.00	3.88	4.45			1.210	1.210	1.210
m23 MinS_1	C_s	0.27	3.61	4.61			1.210	**1.233**	**1.233**
m23 MinS_2	C_s	0.23	3.99	4.17			**1.245**	1.214	1.213
d223 MinS_0	C_{2v}	0.00	3.86	4.23	4.39	4.47	1.210	1.210	1.210
d223 MinS_1	C_{2v}	0.27	3.59	4.32	4.61	4.71	1.210	**1.233**	**1.232**
d223 MinS_2(CT)	C_{2v}	0.13	3.83	4.09	4.31	4.39	1.220	1.221	1.211
d223 MinS_2(LE)	C_s	0.23	3.98	4.14	4.24	4.66	**1.245**	1.214	1.213
d223 TS S_3	C_{2v}	0.17	3.99	4.17	4.22	4.35	**1.231**	1.211	1.210
d223 MinS_4	C_{2v}	0.14	3.94	4.16	4.26	4.32	**1.227**	1.212	1.212

In particular, let us notice that the minimum of the first excited state (C_{2v}) is really close in energy and character (same acetylenic bonding pattern) to the minimum of the first excited state of the isolated p3 fragment. The critical points of the higher-lying excited states are more complicated to examine. First, in S_2, we find one global minimum for the CT state (C_{2v}) and two equivalent local minima which are the minima of the LE states on the two p2 *pseudo* fragments (C_s). Then, we find a transition state (TS, with $\omega^{\mathrm{TS}} = i3440\,\mathrm{cm}^{-1}$) in S_3 and a minimum in S_4 (but with a strong frequency $\omega = 6070\,\mathrm{cm}^{-1}$ which indicates the presence of a nearby conical intersection). We note that the TS is really close in energy and character to the $MinS_2$ in the m23 molecule; in fact, it is as if the TS was a symmetrically-averaged geometry of two m23 *pseudo* fragments. The minima toward the p2 *pseudo* fragments are then obtained by following the displacements associated to the TS frequency. Interpolations between the $MinS_0$, $MinS_1$, TS of S_3, and $MinS_2$(LE) geometries are shown in fig. 7.3.

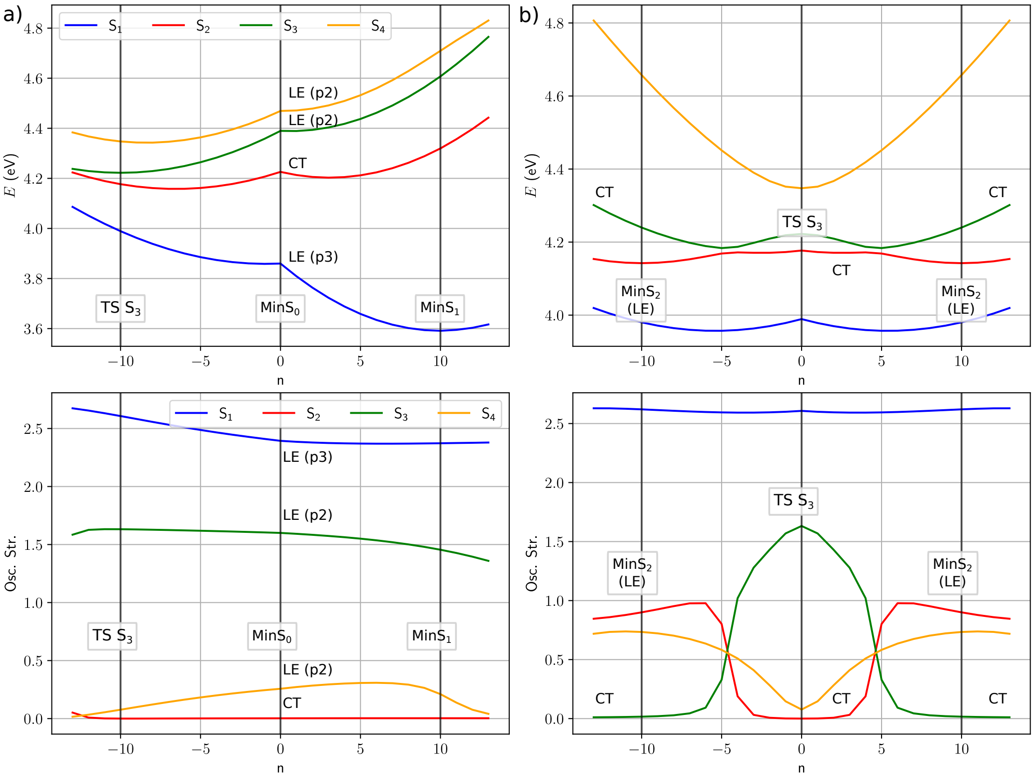

Figure 7.3: Adiabatic energies (top panels) and oscillator strengths (bottom panels) of the first four excited singlet states along linear interpolations. a) Interpolations between the TS of S_3 (at -10), the minimum of S_0 (at 0), and the minimum of S_1 (at 10). The characters of the vertical excitations at the $MinS_0$ geometry are also given. b) Interpolations between the TS of S_3 (at 0) and the (locally-excited) minima of S_2 (both at -10 and 10).

The C_{2v} symmetry is preserved from the TS of S_3 to the minimum of S_1, and the characters of the electronic excitations are maintained. In particular, the CT state and the S_2 state match all along the profile, fig. 7.3 panels a), and start slowly mixing only after the TS of S_3. On the other hand, the interpolation between the TS of S_3 and the LE minima of S_2 shows symmetry-breaking (from C_{2v} to C_s molecular geometries, hence the even shape of the potential energy) and avoided crossings (fig. 7.3, panels b). In particular, the S_2 and S_3 states change character (approximately halfway between the two optimized geometries), as we can see from the evolution of the oscillator strengths. The CT state matches with S_2 at the geometry of the TS and with S_3 at the LE minima of S_2. As a consequence, we note that the m22-like conical intersection seam does involve three adiabatic electronic states (S_2, S_3, and S_4) depending on the geometry. However, the coupling between the S_2 and S_3 states (CT and LE at the $MinS_0$) is expected to be small, and we will see with 1D-profiles along the normal modes of the $MinS_0$ that the CT state (either

S_2 or S_3) can be discarded for describing the m22-like conical intersections.

Optimization of conical intersections in the excited states of d223

In appendix A, we give details about the optimization of the MECIs within this manifold of electronic excited states. We briefly discuss the results of these optimizations here. We find three optimized MECI geometries in the first four excited states of d223. The lowest one is found at $\bar{E} = 4.161\,$eV, with a C_{2v} molecular geometry and involves electronic states S_1 and S_2, localized on the p3 and m22 *pseudo* fragments, respectively (see fig. 7.4, panel c)). Two equivalent, mirror-image, intermediate MECI between the electronic states S_2 and S_3 are found at $\bar{E} = 4.164\,$eV, with a C_s molecular geometry (see fig. 7.4, panel b)). In this case, S_2 resembles more a CT state, but has likely borrowed LE character from other LE states; S_3 is localized on the left or right p2 *pseudo* fragment. Finally, the expected m22-like MECI is found between the electronic states S_3 and S_4 at $\bar{E} = 4.340\,$eV, with a C_{2v} molecular geometry, both states being localized on the m22 *pseudo* fragment.

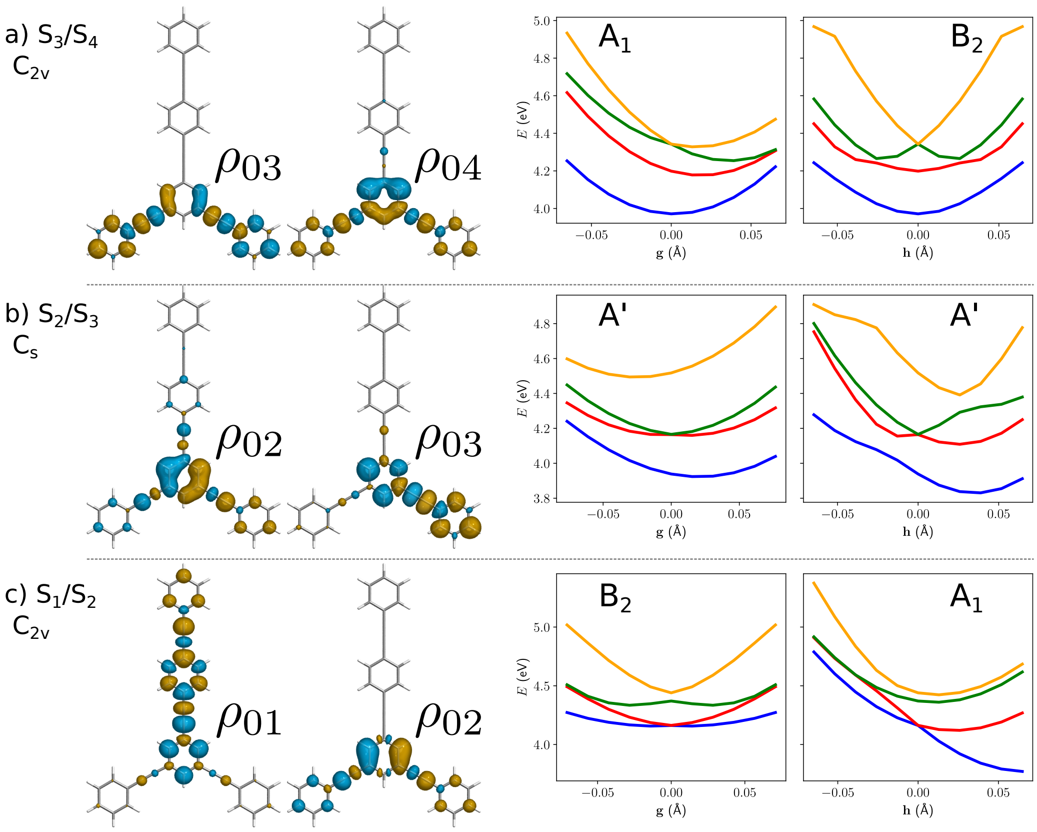

Figure 7.4: Transition densities at the geometry of the MECI and profiles along the associated branching-space vectors, for three MECIs in the excited states of d223: a) between S_3 and S_4; b) between S_2 and S_3; c) between S_1 and S_2.

Let us stress that we do not require the MECI geometries to build relevant vibronic coupling models, which is the focus of section 7.2. However, the characterization of such points will help us to understand which choices of diabatic states (and which inter-state couplings) are relevant.

Vibrational analysis at the Franck-Condon geometry

The Cartesian displacements associated to the quinoidal and acetylenic normal modes of vibration at the FC geometry are shown in fig. 7.5. This selection of normal modes will be used later on to build a (1+3)-state 10-dimensional model of PESs for the excited states of d223, and is similar to the reduced selection of modes presented in chapter 6.

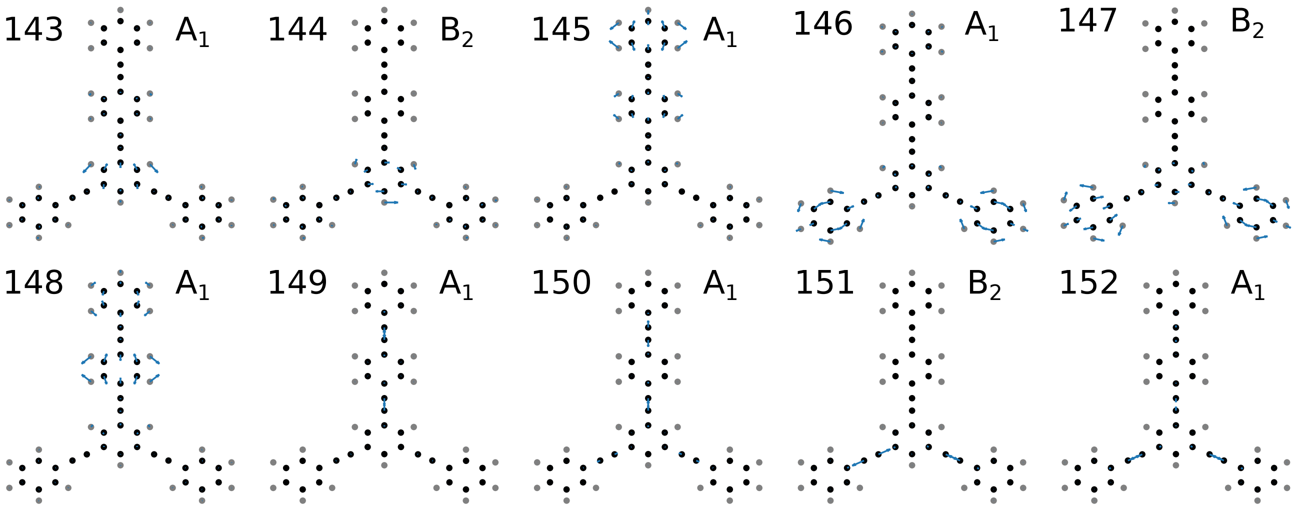

Figure 7.5: Geometry of d223 at MinS_0 (carbon and hydrogen nuclei in black and grey, respectively) and Cartesian displacements (blue arrows) associated to a selection of ten normal modes of vibration. These normal modes are either A_1 (143, 145, 146, 148, 149, 150, and 152) or B_2 (144, 147, and 151) in the C_{2v} point group.

Table 7.2: Frequencies and reduced masses for the selection of ten normal S_0 normal modes. The shifts (in $a_0\sqrt{m_e}$) from the FC geometry to other critical points in the excited-state PESs are also given.

	Symm.	Freq.	Red. mass	Shifts to minima and **TS** (in bold)					Shifts to MECIs		
		in cm^{-1}	in AMU	S_1	S_2(CT)	S_2(p2)	**S_3(B_2)**	S_4	S_1/S_2	S_2/S_3	S_3/S_4
143	A_1	1667	5.7	-4.588	-0.523	1.001	2.191	5.384	0.409	1.853	8.777
144	B_2	1667	5.7	0.000	0.000	6.630	0.000	0.000	0.000	-4.209	0.000
145	A_1	1689	5.8	-6.400	-0.778	-1.124	-0.583	-1.216	2.049	-0.568	-1.879
146	A_1	1692	5.8	0.515	1.207	3.473	4.833	2.314	1.961	2.732	0.135
147	B_2	1693	5.8	0.000	0.000	1.824	0.000	0.000	0.000	-1.596	0.000
148	A_1	1699	6.0	-6.318	-1.031	-0.767	-0.125	-0.945	2.134	-0.920	-1.723
149	A_1	2360	12.0	-7.895	-1.832	-0.883	0.089	-0.528	1.581	-0.952	-1.064
150	A_1	2367	12.0	-1.743	-1.220	1.171	1.886	1.498	0.301	0.623	1.365
151	B_2	2368	12.0	0.000	0.000	-5.588	0.000	0.000	0.000	3.814	0.000
152	A_1	2369	12.0	-1.064	-4.739	-6.140	-7.378	-5.830	-6.667	-6.272	-4.618

To briefly conclude on the electronic structure of d223, the oscillator strengths for the three LE states are similar to the oscillator strengths of electronic excited states in the isolated p3 and m22 fragments. As regards the light-harvesting ability for d223, the LE states on the m22 *pseudo* fragment offer more channels of excitation (the chromophore is more efficient) than in the case of m23 (where the oscillator strength of the LE state on the p2 *pseudo* fragment is significantly weaker). Now, the aim of this chapter is to extend the atomistic simulation of EET (with the nonadiabatic perspective) used for m23 to d223. In particular, in section 7.3 we will evaluate if the EET channels are similarly activated or not for the two molecules.

Take-home messages

1. We characterized the vertical transitions at the FC geometry and the excited-state PES critical points in the first dendron of PPEs, d223. We found that at the FC geometry, there are three LE states and one CT state.
2. The two LE states on the m22 *pseudo* fragment are two bright states, hence plausible excitation channels for EET. The third LE state on the p3 *pseudo* fragment is also bright, and is the acceptor state as regards EET.
3. Three different MECIs were optimized. The lowest and highest ones of them are reminiscent of the MECIs in m23 and in m22, respectively. The intermediate MECI seems to involve the CT state, but is in the same energy domain as the lowest MECI.
4. For the rest of this work, the CT state is discarded, but its influence must be investigated. As of now, we consider it as a plausible alternative route for EET.

7.2 Vibronic coupling Hamiltonian models for a three-state case

We hereby extend the previously discussed LVC Hamiltonian models to the three-state case. The corresponding LVC Hamiltonian, in a *delocalized* representation is

$$\mathbf{H}^{(\text{delocalized})} = \hat{T}_{\text{nu}}\mathbb{1} + \begin{bmatrix} H_{11}(\mathbf{Q}) & H_{12}(\mathbf{Q}) & H_{13}(\mathbf{Q}) \\ H_{21}(\mathbf{Q}) & H_{22}(\mathbf{Q}) & H_{23}(\mathbf{Q}) \\ H_{31}(\mathbf{Q}) & H_{32}(\mathbf{Q}) & H_{33}(\mathbf{Q}) \end{bmatrix}, \tag{7.1}$$

where the reference position for the functions of $\mathbf{Q}$ is the Franck-Condon geometry $\mathbf{Q} = 0$. The diabatic potential energies are expressed *via* Taylor series around the FC geometry for the FC normal modes

$$H_{nn}(\mathbf{Q}) = E^{(n)}(\mathbf{Q}=0) + \sum_{\substack{i \\ \text{A}_1 \text{ modes}}} \kappa_i^{(n)} Q_i + \sum_{\substack{i \\ \text{all modes}}} \frac{1}{2} k_i^{(n)} Q_i^2 \tag{7.2}$$

The inter-state couplings satisfy

$$H_{12}(\mathbf{Q}) = H_{21}(\mathbf{Q}),\ H_{23}(\mathbf{Q}) = H_{32}(\mathbf{Q}) \text{ and } H_{13}(\mathbf{Q}) = H_{31}(\mathbf{Q}) \tag{7.3}$$

which are linear functions of $\mathbf{Q}$ (see below). The choices for the diabatic states are the following:

- D_1 is the A_1 state corresponding to the LE state on p3;
- D_2 is the B_2 state of the pair of LE states corresponding to m22;
- D_3 is the A_1 state of the pair of LE states corresponding to m22

which is consistent with the ordering of the LE electronic excited states at the Franck-Condon geometry.

Again, we note that at the FC geometry, the S_2 state is a CT state. We discard it here as it seems to have little to no coupling with the other three states (at least there), and we identify, at the FC geometry, the three LE states to adiabatic states S_1, S_3, and S_4, respectively. Discarding the CT state can be seen as a prior (to the diabatization by ansatz) diabatization of the ensembles of LE and CT states. Here, it is simply done in 1D-cuts of the PESs by selecting the adiabatic states with non-zero oscillator strengths (the LE states) and separating out the close-to-zero oscillator strength (the CT state).

With this 3-state delocalized Hamiltonian model, there are three inter-state coupling vectors (or inter-state coupling gradients) to consider. The simplest coupling vector is the one for the electronic states D_2 and D_3, as there are the electronic states localized on the m22 fragment that has been studied already in chapter 5. D_2 and D_3 are the delocalized states B_2 and A_1, respectively, and the coupling between them is expanded along B_2 normal modes

$$H_{23}(\mathbf{Q}) = \sum_{\substack{i \\ \text{B}_2 \text{ modes}}} \lambda_i^{(23)} Q_i. \tag{7.4}$$

For the same reasons, the coupling vector between electronic states D_1 and D_2 is also of symmetry B_2, with

$$H_{12}(\mathbf{Q}) = \sum_{\substack{i \\ \text{B}_2 \text{ modes}}} \lambda_i^{(12)} Q_i. \tag{7.5}$$

The two couplings are zero by symmetry at C_{2v} molecular geometries (such as the FC geometry, here the reference point of the LVC Hamiltonian models).

The third coupling to consider is the coupling vector between the electronic states D_1 and D_3, that are delocalized states A_1 for the p3 *pseudo* fragment and A_1 for the m22 *pseudo* fragment, respectively. The coupling vector is thus of symmetry A_1 and yields

$$H_{13}(\mathbf{Q}) = \sum_{\substack{i \\ \text{A}_1 \text{ modes}}} \lambda_i^{(13)} Q_i. \tag{7.6}$$

Here, there is some flexibility because the coupling is for electronic states of the same symmetry (similar to the MECI without symmetry in the asymmetrically substituted PPE, m23). For the sake of simplicity, we consider that this coupling is linear with respect to the coupling vector $\boldsymbol{\lambda}^{(13)}$ and impose that there is no constant coupling between D$_1$ and D$_3$. In other words, the coupling H_{13} is also zero at the FC geometry $\mathbf{Q} = 0$. This choice is arbitrary and is not guaranteed (which is the case because of symmetry in the other two cases). It is convenient here for the fitting procedure and for further interpretation, since it ensures that the diabatic states D$_1$ and D$_3$ match the adiabatic states S$_1$ and S$_3$ at the FC geometry. As discussed below, it may even be set to zero everywhere in practice.

7.2.1 Parametrization of the LVC Hamiltonian model

We now present the fitting procedures for the parametrization of two LVC Hamiltonian models, with and without assuming $\boldsymbol{\lambda}^{(13)} = 0$. Similarly to the minimal 8-dimensional model of m23 discussed in chapter 6, we choose the ensemble of quinoidal stretching and anti-quinoidal rock-bending modes in addition to the four acetylenic stretching modes, resulting in a total of ten normal modes (shown in fig. 7.5). We explore the S$_1$–S$_4$ PESs *via* 1D-cuts along these normal modes (shown in fig. 7.6, symbols $+$). Let us notice that the shapes of the cuts along A$_1$ and B$_2$ normal modes are analogous to the shapes of the interpolations presented above, fig. 7.3 a) and b), respectively. In the case of 1D-cuts along A$_1$ normal modes, the weights are set equal for the three adiabatic states. In the case of 1D-cuts along the B$_2$ normal modes, the weight of the second adiabatic state (having the double-well shaped potential energy, displaced for the p2 *pseudo* fragments) is set to twice the weights of the other states.

The fitted LVC parameters are given in table 7.3, with and without the inter-state coupling H_{13} between the pair of A$_1$ electronic states.

Finally, let us mention that the presented (1+3)-state model is parametrized and given in a basis of delocalized diabatic states (with respect to the *pseudo* m22 fragment). One of the consequences is that the couplings between the p3 and p2 *pseudo* fragments are not directly comparable with the couplings obtained for the m23 molecule. However, a rotation applied to the three diabatic states allows us to consider an LVC Hamiltonian model for the localized fragments p3, p2 "left", and p2 "right"

$$\mathbf{H}^{(\text{localized})} = \begin{bmatrix} H_{11} & \frac{\sqrt{2}}{2}\left(H_{12}+H_{13}\right) & \frac{\sqrt{2}}{2}\left(H_{13}-H_{12}\right) \\ \frac{\sqrt{2}}{2}\left(H_{12}+H_{13}\right) & H_{23} & \frac{H_{33}-H_{22}}{2} \\ \frac{\sqrt{2}}{2}\left(H_{13}-H_{12}\right) & \frac{H_{33}-H_{22}}{2} & -H_{23} \end{bmatrix} + \begin{bmatrix} 0 & 0 & 0 \\ 0 & \frac{H_{22}+H_{33}}{2} & 0 \\ 0 & 0 & \frac{H_{22}+H_{33}}{2} \end{bmatrix} \tag{7.7}$$

with the parameters and functions $H_{ij}(\mathbf{Q})$ defined for the LVC for delocalized states (see eq. (7.1)). The newly defined coupling $H'_{23} = \frac{H_{33}-H_{22}}{2}$ now couples two localized states associated to the "left" and "right" p2 *pseudo* fragments. The couplings $H'_{12} = \frac{\sqrt{2}}{2}\left(H_{12}+H_{13}\right)$ and $H'_{13} = \frac{\sqrt{2}}{2}\left(H_{13}-H_{12}\right)$ are obtained accordingly to this rotation, and now represent the couplings between the LE-p3 state and the "left" and "right" LE-p2 states, respectively. They are equal along A$_1$ displacements and opposed along B$_2$ displacements. The associated inter-state coupling gradients are given in table 7.4 and compared to the case of delocalized diabatic states.

With all couplings allowed

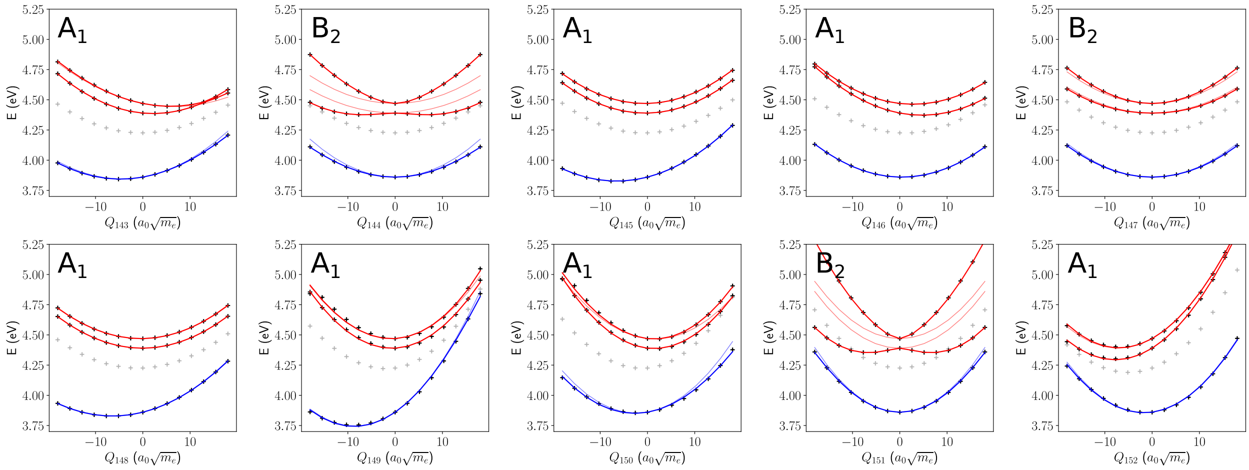

Without the H$_{13}$ coupling

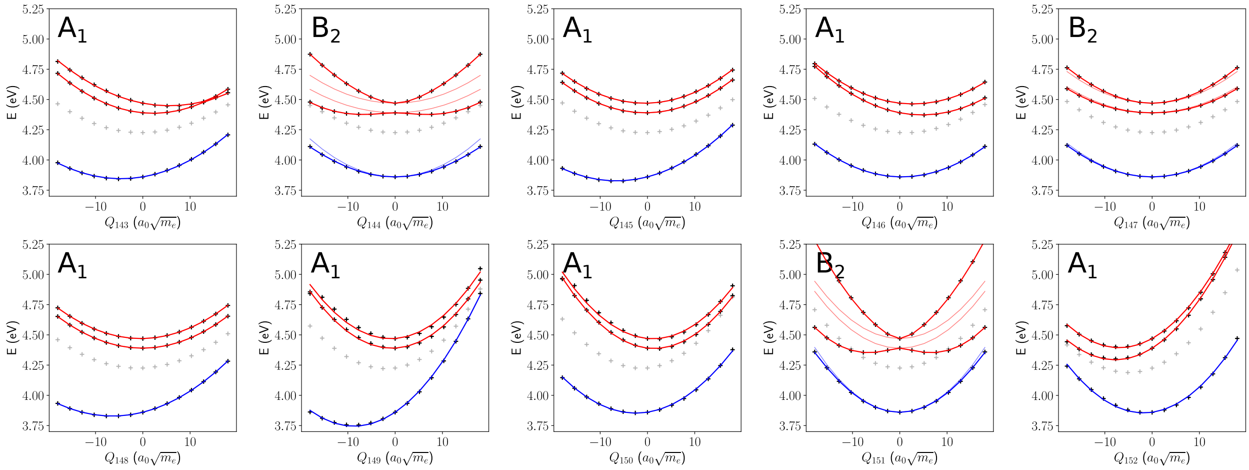

Figure 7.6: Adiabatic energies (in eV) from electronic structure calculations (black symbol $+$) and from the 3-state 10-dimensional LVC Hamiltonian model (blue and red lines), along Cartesian displacements associated to the selection of S$_0$ normal modes. For unspecified coordinates, the values are those at the FC geometry (0); all coordinates are mass-weighted and given in atomic units. The diabatic potential energies are also given in transparency. The adiabatic energy for the charge transfer state (discarded for the fitting procedure) is also shown (grey symbol $+$). The results with all coupling and without the $H_{13}(\mathbf{Q})$ coupling are given in top and bottom panels, respectively.

Table 7.3: Frequencies (in cm^{-1}) associated to the curvature parameters, and characteristic shifts (in $a_0\sqrt{m_e}$) associated to the energy gradients and inter-state coupling gradients for the delocalized representation of the 3-state LVC Hamiltonian models, obtained upon fitting 1D-cuts through the ten selected modes. The parameters $\omega_i^{(s)}$ correspond to curvatures $k_i^{(s)}$. The parameters $d_i^{(s)}$ correspond to energy gradients $\kappa_i^{(s)}$. The parameters $d_i^{(rs)}$ correspond to inter-state coupling gradients $\lambda_i^{(rs)}$. Results from both fitting procedures with and without the A$_1$ inter-state coupling gradient $\lambda_i^{(13)}$ are given. The B$_2$ parameters really are the same in either case because each profile is optimized independently from the others. The corresponding LVC parameters in mass-weighted atomic units are gathered in appendix B.

Mode i	Symmetry	$\omega_i^{(1)}$	$\omega_i^{(2)}$	$\omega_i^{(3)}$	$d_i^{(1)}$	$d_i^{(2)}$	$d_i^{(3)}$	$d_i^{(12)}$	$d_i^{(23)}$	$d_i^{(13)}$
143	A$_1$	1670	1687	1457	4.420	-2.217	-6.568	0.000	0.000	4.187
144	B$_2$	1853	1455	1585	0.000	0.000	0.000	5.811	-8.908	0.000
145	A$_1$	1652	1690	1690	6.529	0.427	0.536	0.000	0.000	-0.017
146	A$_1$	1690	1664	1656	-0.414	-4.702	-2.808	0.000	0.000	-0.047
147	B$_2$	1743	1529	1691	0.000	0.000	0.000	-3.382	-2.592	0.000
148	A$_1$	1657	1697	1688	6.341	0.083	0.372	0.000	0.000	-1.544
149	A$_1$	2369	2352	2282	8.541	0.687	0.783	0.000	0.000	1.555
150	A$_1$	2251	2344	2144	2.355	-1.396	-1.645	0.000	0.000	3.967
151	B$_2$	2420	2266	2275	0.000	0.000	0.000	1.884	-7.122	0.000
152	A$_1$	2359	2354	2328	1.683	7.826	7.196	0.000	0.000	1.427
Mode i	Symmetry	$\omega_i^{(1)}$	$\omega_i^{(2)}$	$\omega_i^{(3)}$	$d_i^{(1)}$	$d_i^{(2)}$	$d_i^{(3)}$	$d_i^{(12)}$	$d_i^{(23)}$	$d_i^{(13)} = 0$
143	A$_1$	1595	1687	1539	4.582	-2.217	-5.598	0.000	0.000	0.000
145	A$_1$	1652	1690	1690	6.529	0.427	0.536	0.000	0.000	0.000
146	A$_1$	1690	1664	1656	-0.414	-4.701	-2.808	0.000	0.000	0.000
148	A$_1$	1646	1697	1699	6.403	0.083	0.388	0.000	0.000	0.000
149	A$_1$	2319	2352	2333	8.721	0.687	0.941	0.000	0.000	0.000
150	A$_1$	2088	2344	2303	2.445	-1.396	-1.186	0.000	0.000	0.000
152	A$_1$	2329	2354	2358	1.805	7.826	6.938	0.000	0.000	0.000

Table 7.4: Charateristic shifts (in $a_0\sqrt{m_e}$) of the inter-state coupling gradients in the case of delocalized and localized diabatic states (D$_2$,D$_3$) for the m22 *pseudo* fragment.

Mode i	143	144	145	146	147	148	149	150	151	152
Symmetry	A$_1$	B$_2$	A$_1$	A$_1$	B$_2$	A$_1$	A$_1$	A$_1$	B$_2$	A$_1$
$d_i^{(12)}$	0.000	5.811	0.000	0.000	-3.382	0.000	0.000	0.000	1.884	0.000
$d_i^{(13)}$	4.187	0.000	-0.017	-0.047	0.000	-1.544	1.555	3.967	0.000	1.427
$d_i^{(\mathrm{loc},12)}$	2.580	4.109	-0.012	-0.033	-2.392	-1.086	1.067	2.567	1.332	0.998
$d_i^{(\mathrm{loc},13)}$	2.580	-4.109	-0.012	-0.033	2.392	-1.086	1.067	2.567	-1.332	0.998

Take-home messages

1. We parametrized two (1+3)-state 10-dimensional LVC Hamiltonian models for the three LE states of the d223 molecule. The difference between the two models is the definition of the H_{13} coupling, set explicitly to zero in one of the two models.
2. This choice has little to no effect as regards the 1D-cuts along the normal modes of vibration.
3. However, its physical relevance for modelling EET might be twofold:
    - in the delocalized representation, there is no reason for the coupling between the A_1 states to be zero
    - in the localized representation, the choice of no coupling boils down to no coupling between the p3 and the p2 *pseudo* fragments along A_1 modes.

7.3 Time-resolved simulation of EET in a tri-*meta*-substituted PPE-oligomer

The excitation-energy transfer (EET) in the d223 molecule consists in i) the excitation of electronic states localized on the m22 *pseudo* fragment (previously defined diabatic states D_2 and D_3) and ii) the transfer of the excitation-energy to the electronic state localized on the p3 *pseudo* fragment (previously defined diabatic state D_1). Unless otherwise specified, the three diabatic states are the delocalized (as regards the m22 *pseudo* fragment viewed as two p2 *pseudo* fragments) electronic states, for which two (1+3)-state 10-dimensional LVC Hamiltonian models have been parametrized in section 7.2. The two models correspond to two arbitrary choices for the definition (and subsequent parametrization) of the $\mathrm{A}_1/\mathrm{A}_1$ coupling H_{13}, for which the effects on the dynamics of EET are now discussed.

7.3.1 Comparison of EET with and without $\mathrm{A}_1/\mathrm{A}_1$ couplings

The comparison of the simulations with and without the $\mathrm{A}_1/\mathrm{A}_1$ coupling H_{13} (fig. 7.7 plain and dashed lines) suggests that the early dynamics is almost unchanged by this coupling.

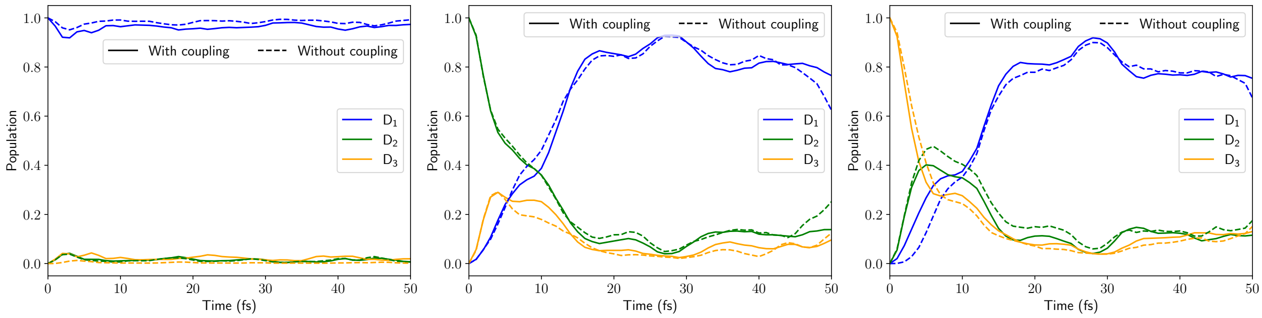

Figure 7.7: Time evolution (up to 50 fs) of the populations of the three diabatic excited states for different initial states, in the case of a (1+3)-state 10-dimensional LVC Hamiltonian model with all linear inter-state couplings allowed (plain lines) and without the A$_1$/A$_1$ inter-state coupling H_{13} (dashed lines). From left to right, initial states for the dynamics are D$_1$, D$_2$, and D$_3$, respectively.

Let us first focus on the results from the LVC Hamiltonian model "with coupling". Consistently with the donor-donor-acceptor scheme of d223, the two excitation channels (on donor states D$_2$ and D$_3$) have an analogous relaxation channel toward the D$_1$ state. The population of the acceptor D$_1$ (blue line) state reaches 50% around 15 fs in both cases, and oscillates around a maximum of 80% after 20 fs, irrespective of the initial excitation. The populations of the donor states D$_2$ and D$_3$ exhibit differences for the very early dynamics (due to the choice of the initial state) but show identical transient regimes after 5 fs. In both cases, some population is transferred between the two states in the very early dynamics up to 5 fs where the superposition of the donor states is sligtly in favor of the donor state D$_2$ (the B$_2$ state, coupling with the two other A$_1$ states). The resulting dynamics is a non-totally monotonic transfer from the excited donor state to the acceptor state, and a sort of transient accumulation in both donor states before the transfer is completed toward the acceptor state D$_1$. This is also noticeable by the slowdown in the population of the acceptor state D$_1$.

The two models, with and without A$_1$/A$_1$ coupling (plain and dashed lines) yield similar results for the early dynamics of the population transfer itself. A significant difference is obtained only as regards the initial excitation on the donor state D$_3$ (the A$_1$ state on the m22 *pseudo* fragment), where the transient population of the other donor state (D$_2$) is more important than with coupling. The excess of transient population here is comcomitant with the deficit of population in the acceptor state D$_1$. In other words, the presence of the coupling slightly speeds up the early transfer from initial excitation on D$_3$, most likely thanks to a more efficient direct transfer from the donor state D$_3$ to the acceptor state D$_1$. The effect of this modelling choice seems rather innocent in the present case of a donor-donor-acceptor dendrimer, because both donor states are somehow quite equivalent.

Let us now discuss how the population evolves after the transfer from the D$_2$/D$_3$ pair donor states to the acceptor state D$_1$, and compare the results for the models with and without the coupling H_{13} (fig. 7.8). Without the coupling H_{13}, the population of the D$_1$ state is allowed to transfer back to the D$_2$/D$_3$ manifold, at approximately $t = 50$ fs. An interpretation of this is that in the absence of the A$_1$/A$_1$

coupling H_{13}, the effect of the coupling H_{12} is too important compared to other (intra- or inter-state) couplings. However, the population is rapidly transferred again to the acceptor state D_1, thus only yielding an additional transient regime for the populations. Overall, both modelling choices lead to equivalent final states, but may have different detailed relaxation dynamics for the first 100 fs.

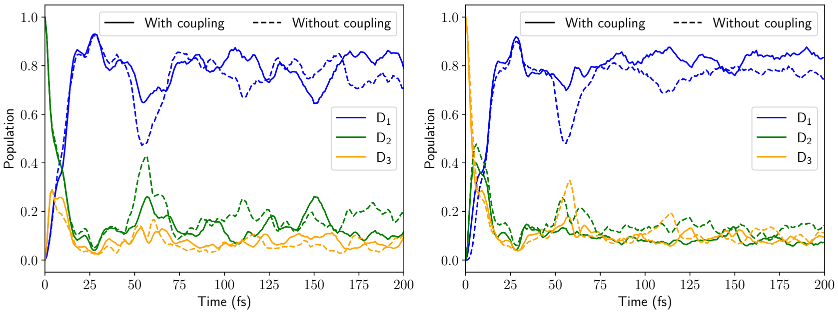

Figure 7.8: Time evolution (up to 200 fs) of the populations of the three diabatic excited states for different initial states, in the case of a (1+3)-state 10-dimensional LVC Hamiltonian model with all linear inter-state couplings allowed (plain lines) and without the $\mathrm{A}_1/\mathrm{A}_1$ inter-state coupling H_{13} (dashed lines). In left and right panels, the initial states for the dynamics D_2 and D_3, respectively.

To conclude on this comparison, we investigated here the effect of the $\mathrm{A}_1/\mathrm{A}_1$ coupling even though the underlying electronic states are not “first neighbours” in terms of adiabatic ordering. We also mention that in the case of “freezing” the H_{13} to zero without re-fitting the other parameters, the “late” dynamics behavior is similar to the case of $H_{13} = 0$ prior to the fitting procedure. We thus expect this coupling to be necessary for every situation where the chromophores (here m22) and the energy-“trap” (here p3) share non-negligible similar electronic transition densities (on the “linker” between the two fragments, here a benzene). This confirms the importance of the choice of the diabatic states and the activation or not of the coupling H_{13} to correctly model energy-trapping (the final state of excitation-energy transfer) in tri-*meta*-substituted dendrimer nodes. This holds here in a low-dimensional model (ten degrees of freedom out of 174) of the tri-*meta*-substituted PPE-oligomers, but further studies involving more degrees of freedom and the intra-state couplings (Duschinsky contributions) would be necessary to complement the present study and rule out any artefacts due to low dimensionality.

We clearly identified, in our simulations, three regimes, for which the effect of the H_{13} coupling is different. First, the very early dynamics (first transfer from the $\mathrm{D}_2/\mathrm{D}_3$ manifold to the D_1 acceptor state) has almost no dependence on the choice of the H_{13} coupling. The second regime (around 50 fs) exhibits a non-negligible superposition of the D_2 and D_3 donor states, and lasts longer in the case of no coupling between the D_3 and D_1 states. Finally, the late dynamics, where the wavepacket is definitely trapped in the acceptor state D_1, is the same for both situations, only with a time delay between them.

For the rest of this chapter, we will discuss only the results obtained with the (1+3)-state 10-dimensional LVC with all couplings, as it is the closer we have to an ideal excitation-energy transfer.

7.3.2 Electronic and vibrational monitoring of EET

Similarly to the study of EET in m23, we analyse the dynamics of the electronic populations and of the state-specific expectation values of nuclear-dependent operators for three initial state (D_1, D_2, and D_3).

7.3.2.1 Kinetics of the population transfer

The adiabatic and diabatic population dynamics for the three simulations are shown in fig. 7.9, up to $200\,\mathrm{fs}$. Again, the adiabatic populations are computed using the time-dependent DVR which yields approximate adiabatic populations. The reason why we choose a TD-DVR integration is that the DVR integration (with no speeding-up algorithm) for ten degrees of freedom takes more than a few hours for computing the adiabatic populations for each time step, while the TD-DVR adiabatic populations are obtained in about a minute. One consequence of the TD-DVR integration for the adiabatic populations is the rather non-smooth variations of the populations. However, for all three simulations, the adiabatic and diabatic populations are relatively close, except for the early dynamics. Another consequence is that there are numerically different results from TD-DVR integrations even for physically identical situations (example: initialization on “left” or “right” diabatic states, shown and discussed in chapter 8).

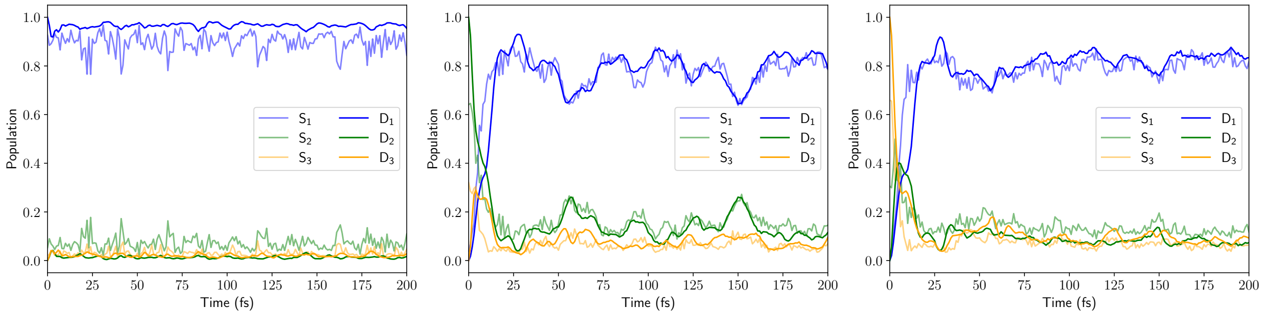

Figure 7.9: Time evolution (up to $200\,\mathrm{fs}$) of the populations of the first three adiabatic and diabatic states for different initial states, in the case of a (1+3)-state 10-dimensional LVC Hamiltonian model with all linear inter-state couplings allowed. From left to right, the initial states for the dynamics are D_1, D_2, and D_3, respectively.

We briefly recall that the initializations on D_2 or D_3 represent two distinct excitation channels of EET in d223, even though the probability of light absorption toward D_2 is stronger than the one toward D_3 (due to a significantly larger oscillator strength associated to D_2). In either case, the dynamics goes toward a similar relaxation channel, with ultrafast and very efficient EET (within $25\,\mathrm{fs}$, quantum yield of about 80%). The previously identified “transient” state in D_2 before almost entirely transferring population to D_1 is consistent with the fact that D_2 is intermediate in energy (at least around the Franck-Condon region and at the local minima of the p2 *pseudo* fragments) and is responsible for a non-negligible part of the coupling toward D_1 (for instance along the central-quinoidal rock-bending mode 144). In essence, the system d223 acts similarly to m23 being excited on its S_2 electronic states, but there are now twice more excitation channels (S_3 and S_4), with a clear enhancement of the oscillator strength thanks to the symmetrical substitution of the chromophore fragment. In the next section, we confirm the equivalent character between the EET from both excitation channels by monitoring the nuclear geometry during the population transfer.

7.3.2.2 “Trajectories” of EET, monitoring the molecular geometry

The expectation values of the position of the propagated wavepackets (so-called centers of the wavepackets) for the two excitation channels (initial state D_2 or D_3) are shown in fig. 7.10, for the ten selected normal modes.

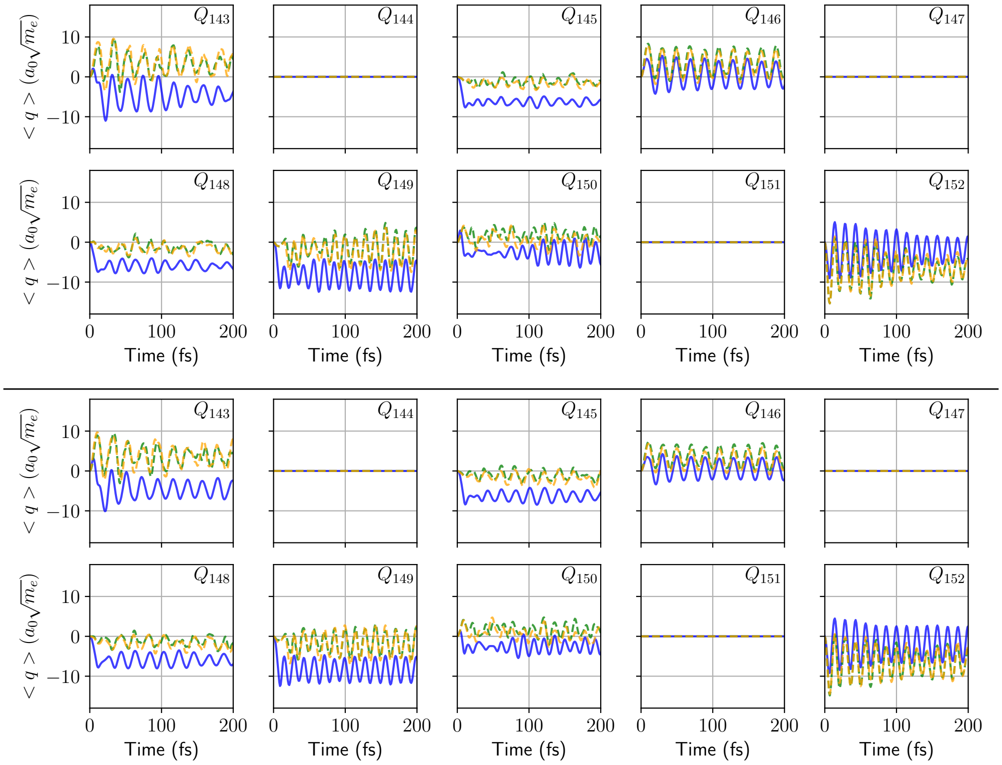

Figure 7.10: Time evolution of the expectation values of position (in mass-weighted atomic units) of the centers of the nuclear wavepackets in either of the three diabatic states D_1, D_2, and D_3 (blue, green, and orange lines). Dynamics initialized on D_2 and D_3 are shown in top and bottom panels, respectively.

Let us notice that the propagated wavepackets maintain their even character with respect to the normal modes that belong to the B_2 irreducible representation, which is a positive sign as regards the size of the grid and the spreading of the wavepackets. On the other hand, the wavepacket centers are significantly (and rapidly) moving, at least in the acceptor state D_1, along the A_1 normal modes. This is expected since the gradients along these modes are non-negligible, except to some extent for mode 146 (for which the displacements are less important). Most importantly, the trajectory of the centers of the wavepacket are very similar when comparing the two initial excitations. Again, this shows how the two channels of excitation lead to the same EET channel, with almost identical vibrational relaxations in the D_1 acceptor state from the two initial excitations.

As regards the internal coordinates, similar conclusions can be drawn. We show in fig. 7.11 the acetylenic bond lengths in all three diabatic states as well as in the total contribution to the molecular geometry. As expected from the visual inspection of the centers of the wavepackets, the internal coordinates have similar evolutions for the two excitation channels. We stress that although it is not trivial from visual inspection: the left and right panels are indeed (slightly) different.

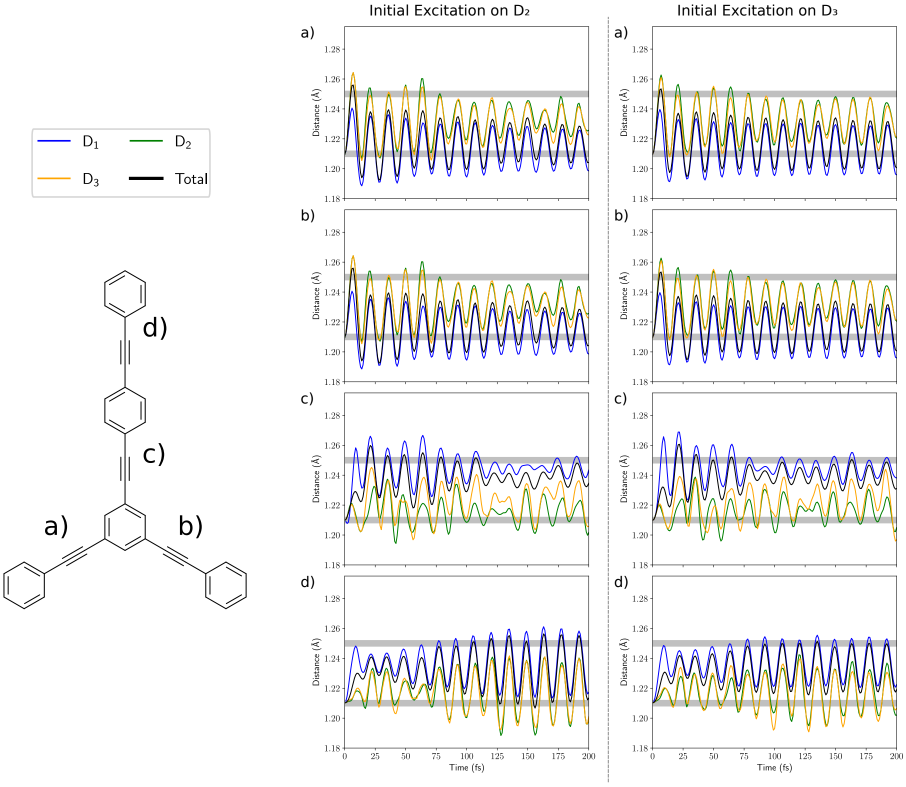

Figure 7.11: Time evolution of the lengths of the acetylenic bonds of d223 in either of the three diabatic states D_1, D_2, and D_3 (blue, green, and orange lines), or in total (black line). Grey areas represent the approximate equilibrium positions of the acetylenic bonds in the electronic ground and first excited states. Dynamics initialized on D_2 and D_3 are shown in left and right panels, respectively.

Up to now, there was no major difference between EET in m23 or in d223, except for the enhanced oscillator strength of the excitation channels in d223. However, there is another advantage of having a symmetrically substituted chromophore m22, as opposed to only one p2 *pseudo* fragment. This advantage can be seen in the initial distortion of the p2 *pseudo* fragments, fig. 7.11, panels a) and b). In either case of initial excitation (D_2 or D_3), the initial distortion is split into the two p2 acetylenic bond lengths on average, whereas in the case of d223 the initial excitation on D_2 yields a very strong distortion, going far beyond the excited-state bonding pattern. We expect this to be a signature of a smoother and more efficient internal redistribution of the excess electronic energy, helped by the fact that the initial vibrations are split into the whole m22 chromophore. In particular, we also expect this smoother internal redistribution to be responsible for fewer back-transfer of energy to the higher-excited states, as opposed what we observed in our simulations of EET in m23.

7.3.2.3 Intramolecular vibrational energy redistribution during EET

Our framework (closed quantum systems) is not well-suited for the study of energy redistribution and thermal equilibration in a medium. However, such phenomena happen in larger timescales compared to the ultrafast EET that we are facing here. As a result, we are interested in the early repartition of the photoinduced excess of electronic energy (the excitation energy from the donor states D_2 and D_3) within the normal modes of the acceptor state (D_1 here, localized on the p3 branch). In fig. 7.12, we show the vibrational energy mode per mode for the diabatic states D_1, D_2, and D_3, with initial excitation either on D_2 or D_3.

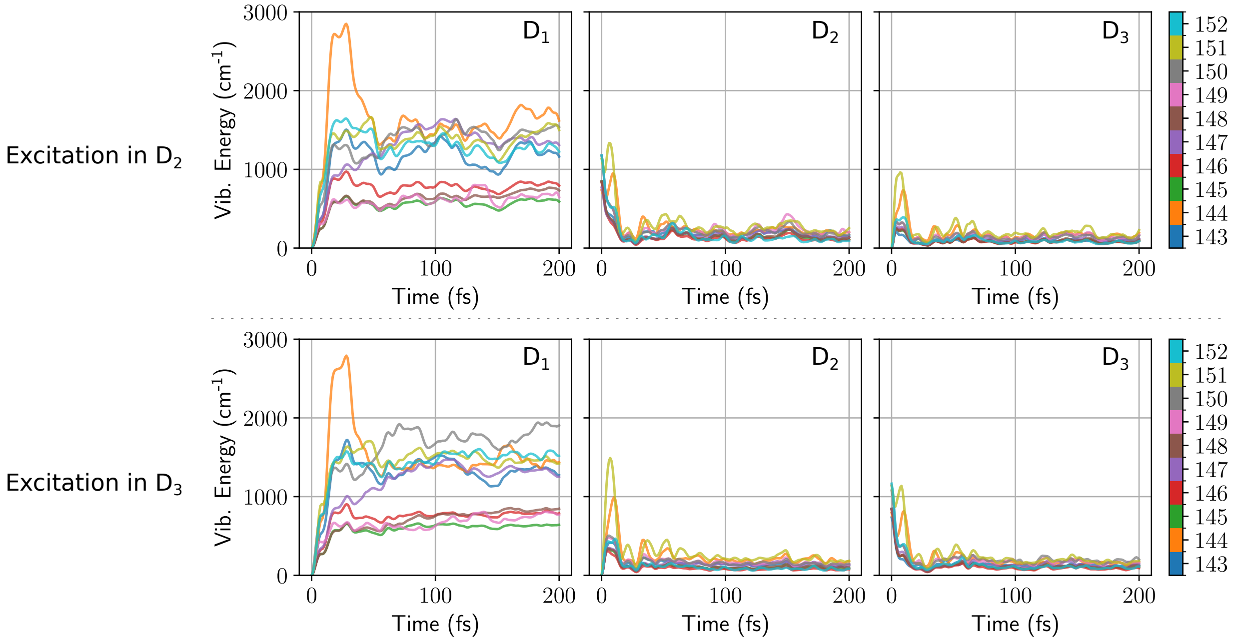

Figure 7.12: Vibrational energy (in cm^{-1}) per mode for contributions from the diabatic states D_1, D_2, and D_3 (left to right, respectively). The initial state is either D_2 or D_3 in top and bottom panels, respectively.

We recall that in the case of m23, the same vibrational energy analysis suggested that the p2-acetylenic stretching normal modes were strongly distorted and excited, and we associated the re-crossing of the conical intersection seam to these intense vibrational excitations. Here, we notice that the acetylenic stretching modes end up bearing a smaller part of the total excess energy coming from EET. In partical, the m22-asynchroneous stretching mode (151) is indeed distorted in the D_2 and D_3 states, but (expectedly from the internal coordinates analysis) its vibrational behavior stays reasonable (slightly above the zero-point energy) even at the crucial time of the electronic population transfer (around $15\,\mathrm{fs}$). On the other hand, the central-phenylene rock-bending mode 144 is also strongly excited; in particular at the time of the transfer from the pair of the donor states to the acceptor state (when the system reaches 80% of yield for EET), and is then stabilized with the other active modes.

Take-home messages

1. The photoinduced excess vibrational energy in the p2-acetylenic stretching modes is reduced compared to the asymmetrical *meta*-substituted PPE. This might be related to a more important stability of the d223 dendrons as regards photo-induced EET compared to the m23 oligomer (photo-protection).
2. The central-phenylene rock-bending mode is the most excited mode as regards EET in the acceptor state.

7.4 Concluding remarks

7.4.1 Modelling EET in a tri-*meta*-substituted node of the PPE-dendrimers

In this chapter, we characterized the electronic excited states of the first dendron of PPEs, namely d223. In particular, we modelled the PESs and NACs associated to the locally-excited states, and ran time-resolved simulations of the excitation-energy transfer after excitation of either of the two donor states of the chromophore (m22). The EET was found to occur with very similar relaxation channels for both situations (exciting the brightest or darkest states of the m22 *pseudo* fragment). The role of the coupling beween the A_1 p3-localized electronic state and the A_1 m22-localized electronic state was also investigated and our results suggest that it has a non-crucial, yet non-negligible, effect on the dynamics of the system, at least for low-dimensional models.

As regards the CT state, we did not account for its existence in the quantum dynamics simulations. The investigation of its importance for the EET mechanism is yet another debate, which opened first for the m23 molecule [38]. As regards our present framework (TD-DFT with CAM-B3LYP functional), we are not able to validate nor its energy nor its coupling with the LE states. Our estimation is for now limited to the estimation of the coupling at the MECI geometries where the CT state is involved. A first step toward this characterization has been done, and further comparisons with another tri-*meta*-substituted PPE-oligomer (the symmetrically substituted one, d222) might help us to identify its role. Such studies and comparisons are underway (and not shown here), with the supervision of the research internship of a 2^{nd}-year Master student on the characterization of the d222 molecule, bearing similar features.

However, results of the simulation of EET for the d223 dendron with only the LE states are quite similar to the simulation done for the m23 molecule. We would expect the effect of the CT state to be rather small on the dynamics of the system, maybe slowing down the dynamics *via* possible alternative but not "quenching" routes for EET ($LE_{2,3} \rightarrow LE_1$ *versus* $LE_{2,3} \rightarrow CT \rightarrow LE_1$).

7.4.2 Toward an explicit simulation of the EET

Our most short-term outlook is now the study of local (“left” or “right”) excitations for the d223 dendron, as it is a very convenient playground for it. Indeed, we have seen that the m22-like MECI couples a pair of delocalized states (localized on m22) that can also be seen as a pair of p2-localized states. Such excitations have already been explored for the same molecules within other frameworks (open quantum systems and hierarchical equations of motion) [18, 55]. We demonstrate in chapter 8 the feasibility of such excitations within our framework (MCTDH).

Part III

Outlook – Toward Electronic Excitations and Bottom-Up Approaches

Intermediate Abstract

In part II, we used nonadiabatic quantum dynamics to reproduce steady-state spectroscopy and to probe the EET dynamics in PPE-oligomers. We based our modelling on the prior characterization of the electronic excited states and their potential energy surfaces. Two of these oligomers have C_{2v} molecular geometries, such that there are two types of excitations for the chromophores: delocalized excitations or localized excitations.

In chapter 8, we discuss the influence on EET of initially localized or delocalized excitations, in the case of the first dendron of PPE-dendrimers. We investigate this effect in the view of "pure" delocalized electronic states or superpositions of them, and raise a question of the physical meaning of the coherence within the excited-state manifold.

In chapter 9, we propose a bottom-up strategy to model EET in an extended branch of the nano-star (with 2-, 3- and 4-ring fragments). Our strategy takes advantage of the easily characterized isolated linear fragments, which define localized Frenkel excitons. The excitonic coupling is estimated from the knowledge of isolated *meta*-substituted fragments and the characterization of conical intersections within their excited states.

Finally in chapter 10, we give concluding remarks for the present work.

Chapter 8

Toward Control of the Initial Electronic Excitations

In part II, we characterized the electronic locally-excited states (LE) of two symmetrically-substituted building blocks of the PPE-dendrimers, namely the m22 chromophore and d223 dendron. We discussed the importance, as regards the excitation channels of EET, of the C_{2v} molecular geometry for both molecules. Indeed in both cases, the m22-localized electronic states are *delocalized* over the whole m22 fragment, and the *delocalized* initial excitations are thus on either of the two delocalized states, belonging to A_1 or B_2 irreducible representations.

In this chapter, we present our most recent analysis of *local* initial excitations, in particular for the case of the d223 dendron, and evaluate the possible effect on the EET relaxation channel on localized rather than delocalized excitations. We also discuss such excitations from the analysis of diabatic (and adiabatic) coherences. We hope that such advances can lead to an extension of our framework that is compatible with the simulation of light pulses for the calculation of two-dimensional electronic and time-resolved spectroscopies.

8.1 Diphenylacetylene-localized excitations, the case of d223

We have seen in chapter 5 that the chromophore m22 has an absorption spectrum similar to the isolated p2 fragments (diphenylacetylene), which was rationalized by the nature of the first pair of electronic excited states [42]. In the PPE-dendrimer, this corresponds, in terms of Frenkel excitons, to an ensemble of p2 *pseudo* fragments able to absorb light, simultaneously or not, and able to transfer the associated excitation-energy *via* the m23 or d223 units. Herein, we evaluate the EET mechanism from this starting point of a local excitation on only one of the p2 *pseudo* fragments.

8.1.1 Transformation from delocalized to localized states

To study such local excitations, we already mentioned that another choice of diabatic electronic states was possible. Indeed, we showed that for the 3-state model of d223, the Nikitin transformation for the *delocalized* diabatic states gives a Hamiltonian for the *localized* diabatic states, recalled hereafter

$$\mathbf{H}^{(\text{localized})} = \begin{bmatrix} H_{11} & \frac{\sqrt{2}}{2}(H_{12}+H_{13}) & \frac{\sqrt{2}}{2}(H_{13}-H_{12}) \\ \frac{\sqrt{2}}{2}(H_{12}+H_{13}) & H_{23} & \frac{H_{33}-H_{22}}{2} \\ \frac{\sqrt{2}}{2}(H_{13}-H_{12}) & \frac{H_{33}-H_{22}}{2} & -H_{23} \end{bmatrix} + \begin{bmatrix} 0 & 0 & 0 \\ 0 & \frac{H_{22}+H_{33}}{2} & 0 \\ 0 & 0 & \frac{H_{22}+H_{33}}{2} \end{bmatrix} \quad (8.1)$$

with the parameters and functions $H_{ij}(\mathbf{Q})$ defined for the LVC Hamiltonian with *delocalized* states (see eq. (7.1)).

However, the Nikitin transformation can be directly operated on the initial wavepackets, thus changing the initial state for the dynamics, without changing the diabatic states. We recall that the delocalized diabatic states D_1, D_2, and D_3 are the A_1 p3-localized and (B_2, A_1) pair of m22-localized diabatic states, respectively. The initial excitations used in chapter 7 for simulating EET were

$$\Psi_{\mathsf{B}_2}(\mathbf{Q},t=0)=\psi^{(0)}_{\mathsf{D}_0}\phi^{\mathsf{dia}}_{\mathsf{B}_2,\mathsf{m22}}=\psi^{(0)}_{\mathsf{D}_0}\begin{pmatrix}0\\1\\0\end{pmatrix}\ \text{and}\ \Psi_{\mathsf{A}_1}(\mathbf{Q},t=0)=\psi^{(0)}_{\mathsf{D}_0}\phi^{\mathsf{dia}}_{\mathsf{A}_1,\mathsf{m22}}=\psi^{(0)}_{\mathsf{D}_0}\begin{pmatrix}0\\0\\1\end{pmatrix}. \tag{8.2}$$

The simulations run from these initial states are reported again in fig. 8.1, left panels. With operating the Nikitin transformation, we keep the same definition of the Hamiltonian and of the diabatic states but have

$$\Psi_{\mathsf{L/R}}(\mathbf{Q},t=0)=\frac{\sqrt{2}}{2}\psi^{(0)}_{\mathsf{D}_0}\left(\phi^{\mathsf{dia}}_{\mathsf{B}_2,\mathsf{m22}}\pm\phi^{\mathsf{dia}}_{\mathsf{A}_1,\mathsf{m22}}\right)=\frac{\sqrt{2}}{2}\psi^{(0)}_{\mathsf{D}_0}\begin{pmatrix}0\\1\\\pm1\end{pmatrix} \tag{8.3}$$

which are now local excitation on the “left” or “right” p2 *pseudo* fragment, depending on the orientation (in the following, we talk about the pair of “L/R” and “R/L” states). The transformation is really simply a sum and difference of the delocalized states, such that the populations for these new initial states are 0:50:50 superpositions (in the view of the delocalized states). The simulations run from these locally-excited states are reported in fig. 8.1, center panels. Finally, the simulations run from the locally-excited states by directly using the local representation of the Hamiltonian (eq. (8.1)) are shown in fig. 8.1, right panels. We note that the latter two types initial states (for center and right panels) are exactly equivalent.

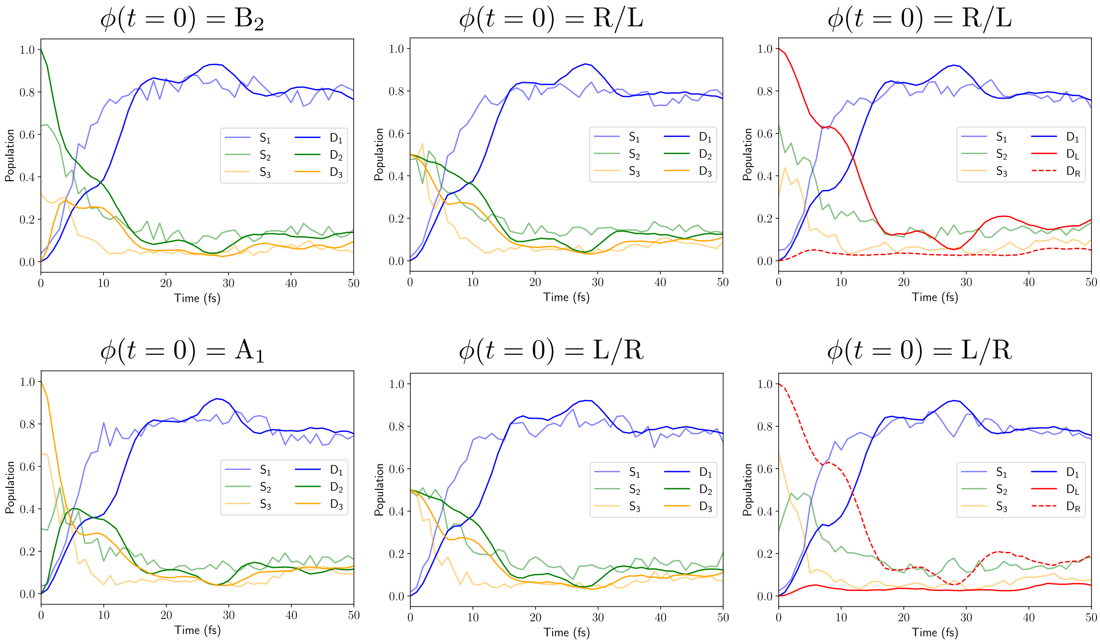

$\phi(t=0)=\mathrm{B}_2$ $\phi(t=0)=\mathrm{R/L}$ $\phi(t=0)=\mathrm{R/L}$

$\phi(t=0)=\mathrm{A}_1$ $\phi(t=0)=\mathrm{L/R}$ $\phi(t=0)=\mathrm{L/R}$

Figure 8.1: Time evolution (up to 50 fs) of the populations of the first three adiabatic and diabatic states for different initial states, in the case of a (1+3)-state 10-dimensional LVC Hamiltonian model. In the left and center panels, the pair of diabatic states for m22 are the delocalized diabatic states. In right panels, the pair of diabatic states for m22 are the localized diabatic states. The initial state $\phi(t=0)$ for the dynamics is recalled on top of each panel.

Let us stress again that the adiabatic populations are only approximately computed here (TD-DVR), hence they can not be directly compared (within numerical details) from one simulation to the other.[1]

8.1.2 Equivalence of EET from delocalized and localized excitations

For the diabatic populations, we find, as expected, that the “R/L” and “L/R” initializations yield the exact same dynamics, from both the perspective of the localized or delocalized diabatic states (center and right panels, respectively). In either of the four cases, the acceptor state D_1, localized on p3 and thus unchanged by the Nikitin transformation, exhibits the same behavior.

This is made clearer in fig. 8.2, where we show again the (delocalized and localized) diabatic populations for the initial states $\phi(t=0) = B_2$, $\phi(t=0) = B_2$ in H^{deloc}, and $\phi(t=0) = B_2$ in H^{loc}.

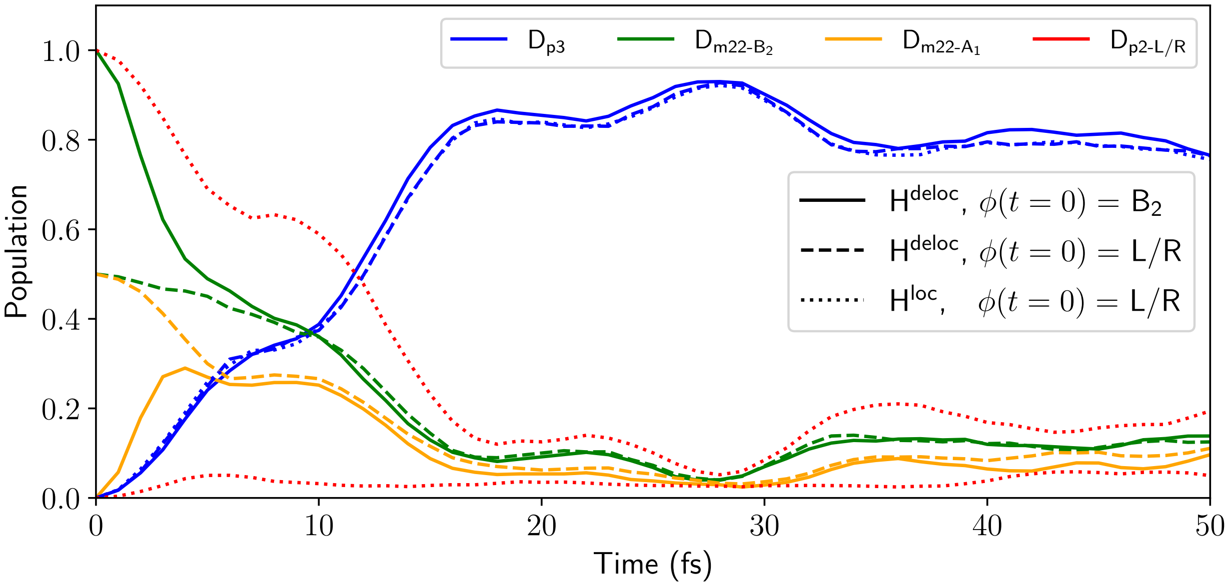

Figure 8.2: Time evolution (up to 50 fs) of the populations of the (delocalized or localized) diabatic states for different initial states, in the case of a (1+3)-state 10-dimensional LVC Hamiltonian model with all linear inter-state couplings allowed. From left to right, the initial states for the dynamics are D_1, D_2, and D_3, respectively.

We also note that the behavior of the D_2 state as transiently more populated than the D_3 state, observed in the case of delocalized excitations, is found again to some extent from the localized excitation. In fact, we note that after the first 5 fs, the populations of (D_2, D_3) are the same after a localized and a delocalized initial excitation. This is consistent with the fact that the (D_2, D_3) pair of m22-localized states are almost degenerate and strongly coupled at the FC geometry, where the dynamics is initialized. Hence, even though the initial excitation is localized, the system rapidly enters a transient regime with slightly favored population transfer for the D_2 state. Accordingly, the relaxation channel toward the acceptor state D_1 is almost unchanged.

---

[1] Preliminary results on a reduced 6-dimensional model, with usual DVR integration and no “quick” algorithm yields, as expected, the exact same adiabatic populations for the “left” and “right” initial excitations.

8.2 “Strong” coherence or not, another story of representations?

In chapter 3, we have defined the diabatic coherence between the diabatic states r and s

$$C_{rs}(t) = \langle \psi_s \,|\, \psi_r \rangle \,(t). \tag{8.4}$$

where the braket notation is defined for the integration over the nuclear degrees of freedom. In a two-level model (two electronic states), we have seen that these quantities can be simply obtained by evaluating the expectation values of the Pauli matrices. For the present case of a three-level system, such quantities would rather be evaluated by calculating the expectation values of the Gell-Mann matrices [163, 164].[2] For instance, the coherence between the diabatic states D_1 (A_1 p3-localized) and D_3 (A_1 m22-localized), for a given propagated wavepacket $|\Psi\rangle$ would be

$$\mathfrak{R}(\langle \psi_1 \,|\, \psi_3 \rangle) = \frac{1}{2} \langle \Psi \,|\, \boldsymbol{\lambda}_4 \,|\, \Psi \rangle \text{ and } \mathfrak{I}(\langle \psi_1 \,|\, \psi_3 \rangle) = \frac{i}{2} \langle \Psi \,|\, \boldsymbol{\lambda}_5 \,|\, \Psi \rangle \tag{8.5}$$

with $\boldsymbol{\lambda}_4$ and $\boldsymbol{\lambda}_5$ two of the eight Gell-Mann matrices

$$\boldsymbol{\lambda}_4 = \begin{pmatrix} 0 & 0 & 1 \\ 0 & 0 & 0 \\ 1 & 0 & 0 \end{pmatrix} \text{ and } \boldsymbol{\lambda}_5 = \begin{pmatrix} 0 & 0 & -i \\ 0 & 0 & 0 \\ i & 0 & 0 \end{pmatrix}. \tag{8.6}$$

Delocalized excitations

We start by discussing the coherences in the case of delocalized excitations, with initialized dynamics on the D_2 or D_3 states which are B_2 and A_1, respectively. We show in the first two rows of fig. 8.5 the diabatic coherences for the delocalized states with propagations initialized on the D_2 and D_3 states, respectively. Because the diabatic states and the initial states are adapted to symmetry, the coherence, evaluated *via* the simple overlap of the nuclear wavepackets, is zero at every time for states of different symmetry. As a result, we have for the delocalized excitations

$$C_{12}(t) = 0 \text{ and } C_{23}(t) = 0 \text{ (black and red lines)}. \tag{8.7}$$

On the other hand, the coherence between the diabatic states D_1 and D_3 (both A_1) has no reason to be zero by symmetry (blue line). Hence, $C_{13}(t)$ is the only non-zero off-diagonal element of the reduced-density matrix during the transfer. In particular, the coherences $C_{rs}(t)$ as functions of the population differences $P_s(t) - P_r(t)$ are shown in the last colum of the same figure. Similarly to the case of the m23 molecule, we cleardy identify two distinct regimes of the coherence C_{13} for the EET and for the oscillations in the acceptor state.

A visual aid for rationalizing the null coherence between diabatic states of different symmetry is given in fig. 8.3, panels a) or b).

---

[2] The Gell-Mann matrices are a generalization of the Pauli matrices for the three-level case.

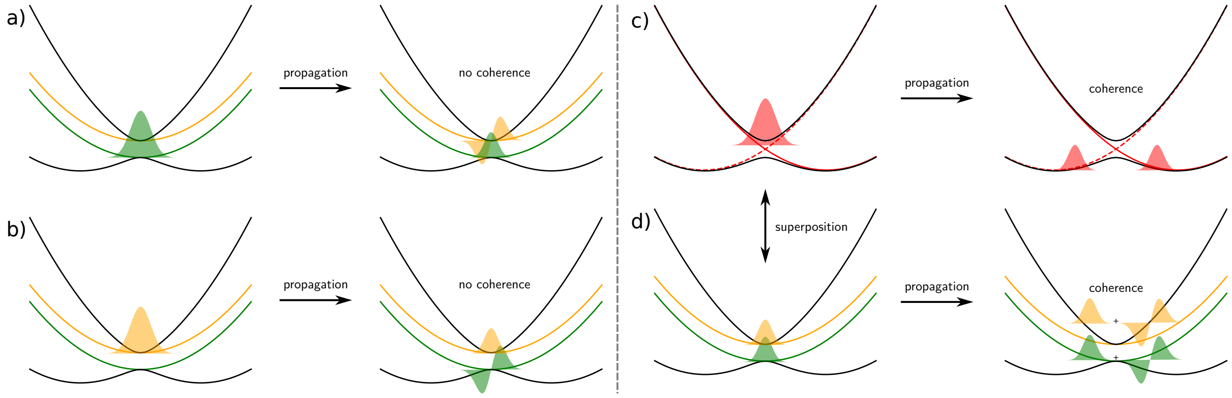

Figure 8.3: a) and b) Initial wavepackets $\Psi_{\mathsf{B}_2}(\mathbf{Q}, t = 0)$ and $\Psi_{\mathsf{A}_1}(\mathbf{Q}, t = 0)$ on pure delocalized diabatic states. c) Initial wavepacket on one of the two localized diabatic states, $\Psi_{\mathsf{L/R}}(\mathbf{Q}, t = 0)$. d) Same viewed as a superposition of the delocalized diabatic states. The coupling between the diabatic states D_2 and D_3 is non-totally symmetric, hence a change of parity for wavepackets when they transfer from one state to the other.

In any case, the initial wavepacket is totally symmetric (it is the vibrational ground state of the electronic ground state). Once projected, for instance, onto the D_2 state (of symmetry B_2), it keeps its totally-symmetrical character. However, when a part of the wavepacket starts transferring to the D_1 or the D_3 states (D_3 in the visual aid, of symmetry A_1), it changes parity (due to the non-totally symmetric couplings). There is no overlap between the nuclear wavepackets of D_2 and D_3 (or D_1), hence no coherence $C_{23}(t)$ (nor $C_{12}(t)$). In this same situation however, the nuclear wavepackets transferred to D_1 or D_3 are both non-totally symmetric and can overlap, hence a non-zero coherence $C_{13}(t)$.

Localized excitations

We show in the last two rows of fig. 8.5 the diabatic coherences for the delocalized states again, but with propagations initialized on the “left” and “right” states (obtained from eq. (8.3)). Because of the initial 50:50 preparation of the initial states, the initial coherence between the D_2 and D_3 excited states is equal to one. It rapidly decreases which is consistent with the decay of the initial superposition of the donor states in favor of the population of the acceptor state. Accordingly, the coherence between the D_1 and D_2 (or D_3) states is non-negligible in the early dynamics (instead of zero in the case of initialization on pure delocalized states). More precisely, the coherence between the acceptor (D_1) and the donor states (D_2 and D_3, initially populated with equal weights in the case of localized excitations) are very similar in variations and in amplitudes.

Similarly, a visual aid for rationalizing the non-zero coherence between diabatic states of different symmetry but with localized excitations is given in fig. 8.3, panels c) and d). We interpret the allowed non-zero coherence as due to the initial superposition which attributes nuclear wavepackets with similar parities to both D_2 and D_3 delocalized states.

8.2.1 Comparison of the coherences in localized and delocalized representations

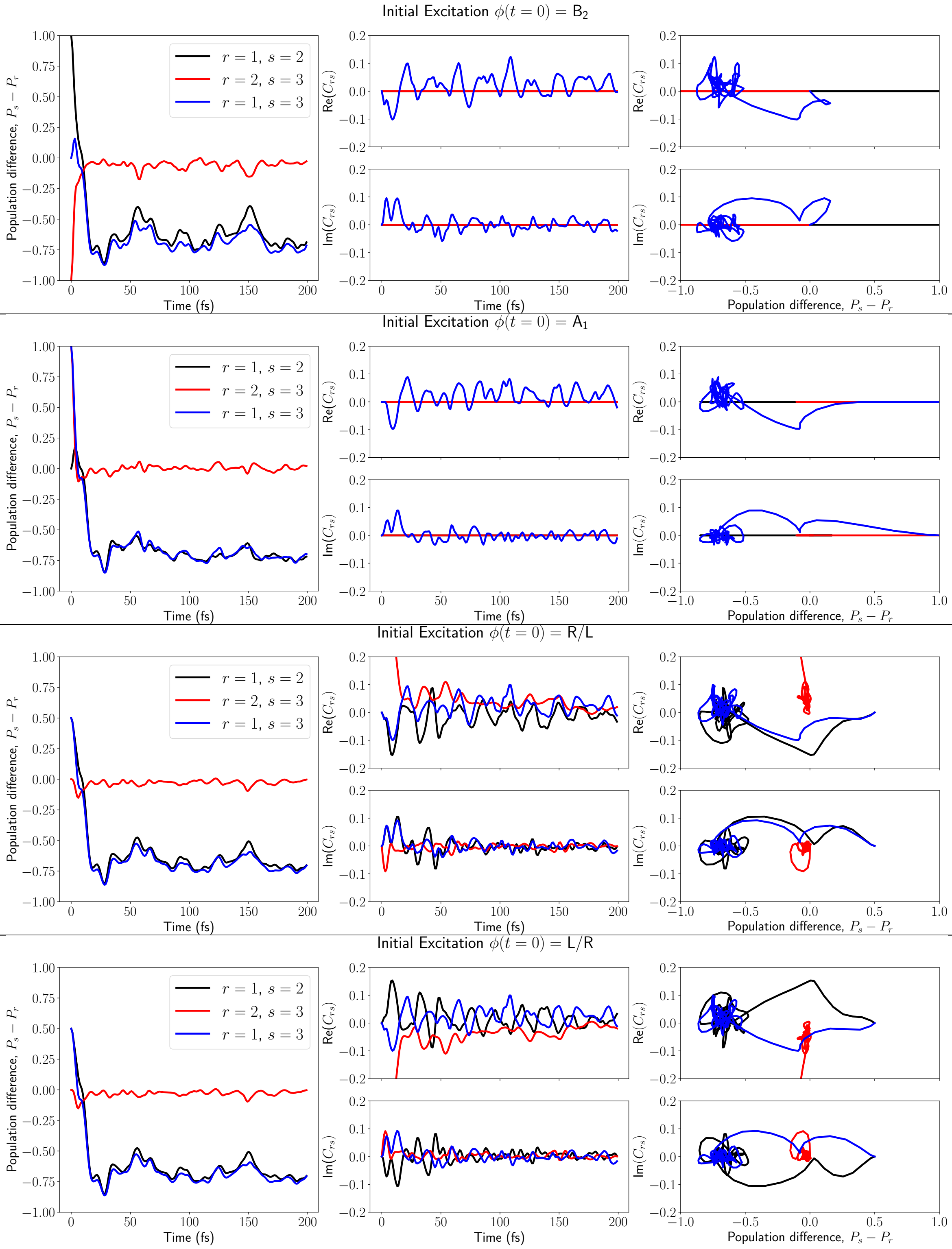

Figure 8.4: Population differences and coherences between the diabatic states $r = 1,\ s = 2$ (black), $r = 2,\ s = 3$ (red), and $r = 1,\ s = 3$ (blue). The results are given, from top to bottom panels, for initial excitations on D$_2$, D$_3$, $\frac{\sqrt{2}}{2}$(D$_2 +$ D$_3$), and $\frac{\sqrt{2}}{2}$(D$_3 -$ D$_2$), respectively.

8.2.2 Are what we call here coherences representation-dependent?

In this work, what we called diabatic coherences are quantities that depend on the representation of the electronic states. By this, we mean that the coherence between two electronic excited states for i) an initial superposition of state; or ii) an initial pure state, depends on the choice of the representation for the electronic states. We illustrated this by evaluating the coherence between states of symmetry with two limiting cases: pure states (delocalized) or superposition of states (localized). However, the superposition of the D_2 and D_3 states to form "left" and "right" states are not superpositions in the localized diabatic representations.

With the current state of our expertise on coherence, we are not able to correctly assess the physical meaning of the coherence we are measuring for pairs of diabatic states. The question of the physical meaning would be the same for the coherence between adiabatic states (briefly presented in the next section), which is simply another representation for the electronic states.

8.2.3 Toward adiabatic coherences

For the calculation of adiabatic coherences, we face the same problem as for the calculation of adiabatic populations: the size of the grid prevent the exact evaluation of high-dimensional integrals on the nuclear degrees of freedom. We briefly mention here that we extended the use of the diabatic-to-adiabatic transformation for the calculation of adiabatic populations to the calculation of the adiabatic coherences. Essentially, the calculation is the same, simply using the different indices for the electronic states.

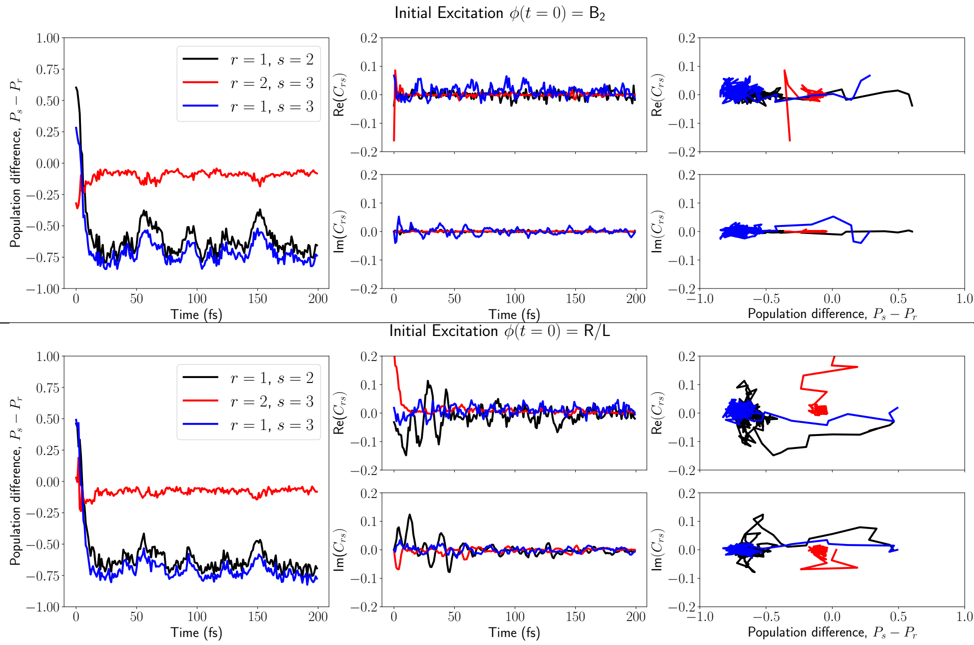

Figure 8.5: Population differences and coherences between the adiabatic states $r=1, s=2$ (black), $r=2, s=3$ (red), and $r=1, s=3$ (blue). The results are given for initial excitations on D_2 and $\frac{\sqrt{2}}{2}(\mathrm{D}_2+\mathrm{D}_3)$ it top and bottom panels, respectively.

8.3 Concluding remarks and open questions

Almost no effect of local excitations on the EET in the first dendron

To conclude, we have seen that localized excitations (simulated here by a superposition of delocalized states) on one or the other of the p2 *pseudo* fragments in the first dendron of PPE-dendrimer have the same EET dynamics than delocalized excitations. Hence, as regards the EET phenomenon, there seems to be no optimal excitation channel, and both types of excitations would result in the same light-harvesting processes.

Coherence and electronic representations

However, there are still open questions on the coherences between the electronic states. In particular, we are interested now in investigating the physical relevance of the zero-by-symmetry coherence computed between electronic states which belong to different irreducible representations. Are we missing an integral contribution in our calculation of the coherence, eq. (8.4)? Or is the coherence zero at all times t because it is zero at $t = 0$? On the other hand, we can also question the physical relevance of the non-negligible coherences obtained when considering an initial superposition of states, to simulate a local excitation $\Psi_{\mathsf{L/R}(\mathbf{Q},t=0)}$. Is this coherence only non-negligible in the representation for which the initial state is a superposition? Is it nullified when computing again the coherence in other representations, such as a localized representation or an adiabatic one?

We have not addressed these questions at the moment, but we mention that this is an active discussion. It is notably the case in the context of attochemistry, where the preparation of initial superposition of states is a central subject [165–167].

Toward electronic excitations *via* laser pulses

Finally, we mention that our present framework is well-suited for pulses study, which could serve different purposes. First, laser pulses could be used to prepare more realistically, as regards the experiments, superpositions of states. In particular, it has been applied to the symmetrically *meta*-substituted chromophore m22, to explore the feasibility of laser-controlled excitations toward symmetry-preserving or symmetry-breaking initial states [55]. We aim at reproducing these results for the first generation of dendron d223, which has also been explored recently [18].

In a second step, we would like to simulate pump-probe experiments, using two delayed laser pulses. In particular, this could also help us to disentangle the open questions of coherence, by predicting time-dependent observables and evaluating the possible effect, or not, of coherence on them. Of course, this would require further comparison with the experiments.

Chapter 9

Toward Transferable Parameters for Bottom-up Modelling of PPE-dendrimers

In part II, we simulated excitation-energy transfer (EET) in the smallest di- and tri-*meta*-substituted PPEs having an energy gradient from one branch to another. Such simulations required the characterization of the electronic excited states of the molecules and the parametrization of models for the excited-state potential energy surfaces (PESs). However, explicitly simulating the whole molecule becomes unfeasible for larger PPE-oligomers or for PPE-dendrimers such as the nano-star.

Historically, the first attempts of modelling and simulating EET in PPE-dendrimers were based on the Frenkel-exciton Hamiltonian [30] which consists in having excitation energies for each chromophore and excitonic couplings between them. In the framework of the Frenkel-exciton Hamiltonian models, the nuclear motions are in general included only *via* the definition of a harmonic bath of vibrations coupled to the localized excitons (the system).

In this chapter, we propose a strategy based on the Frenkel-exciton Hamiltonian model (viewing each exciton as an isolated fragment) supplemented by a linear vibronic coupling Hamiltonian to model the excitonic coupling (as explicitly depending on the nuclear motions). In essence, each exciton (linear *para*-substituted fragments) shall have the diabatic potential energy of the corresponding isolated fragment, and the coupling between two excitons should expand in the normal modes of the associated isolated fragments. We design and evaluate the feasibility of our methodology on one “full” extended branch of the simplified nano-star, having 2-ring, 3-ring, and 4-ring fragments connected sequentially *via* shared di-*meta*-substituted phenylenes (called b234 in the following, see fig. 9.1).

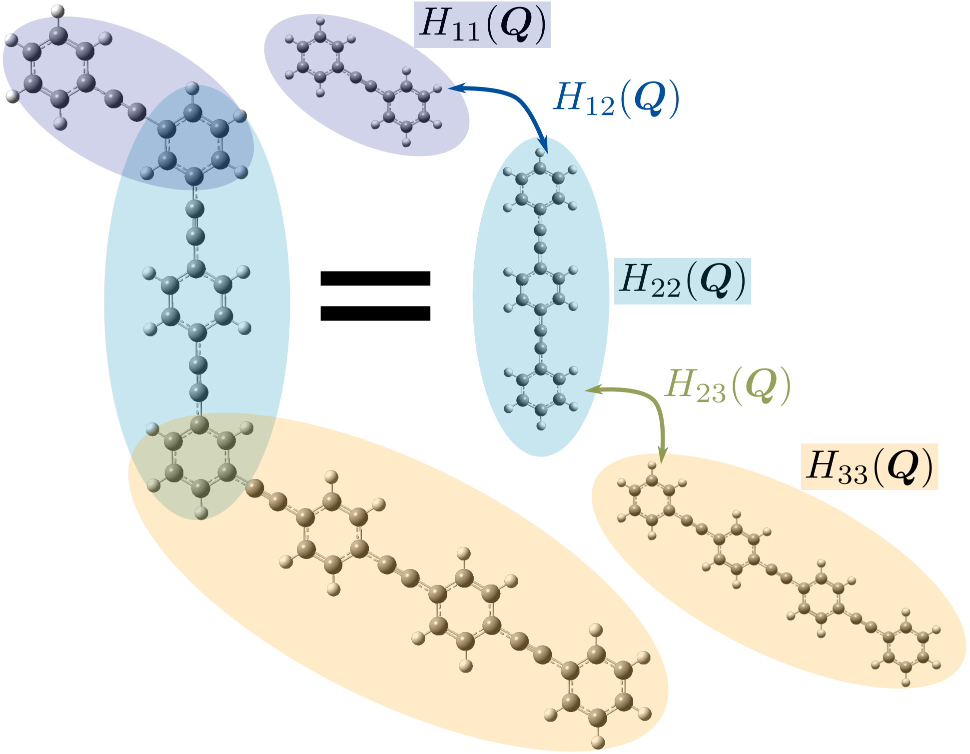

Figure 9.1: The "full" extended branch of the simplified nano-star, symbolically decomposed in three isolated linear *para*-substituted branches. This *pseudofragmentation* scheme will serve for the definition and parametrization of a model based on the Frenkel-exciton Hamiltonian.

9.1 Pre-requisites for an extended pseudofragmentation scheme

In order to use the knowledge of the isolated linear *para*-substituted PPE fragments, we must first check if the electronic excited states of the "full" extended branch are compatible with the description of local excitations on the linear *pseudo* fragments.

9.1.1 Electronic states in one of the nano-star branch

We show in fig. 9.2 the energies, transition densities and oscillator strengths for the first four vertical transitions from the Franck-Condon geometry of b234.

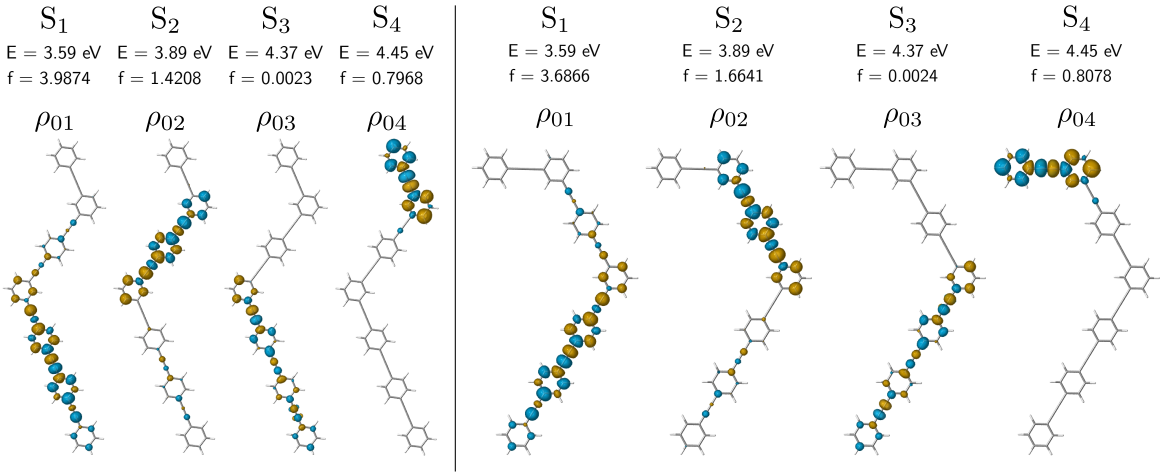

Figure 9.2: Transition densities for the first four electronic excited states at the minimum of the electronic ground state of the b234 extended branch of PPEs, for two geometry configurations ("external" and "internal" in left and right, respectively). We note here that the minima of the electronic ground states of the two configurations are separated by only 2×10^{-5} eV. In the text, we focus on the "external" configuration (left).

We identify three bright localized electronic states with non-negligible oscillator strenghts: S_1, S_2, and S_4 localized on the p4, p3, and p2 *pseudo* fragments, respectively. The electronic state S_3 is also reminiscent of a local excitation on the p4 *pseudo* fragment, but has near-zero oscillator strengths (in fact, it is comparable with the S_2 state in the isolated p4 fragment).

The three bright localized electronic states are the main motivation for modelling EET in the b234 extended branch using only knowledge from the S_1 electronic states in the isolated p4, p3, and p2 fragments. Now, a pre-requisite for comparing the nuclear motions of the isolated fragments and of the *pseudo* fragments in the "full" molecule is to be able to superimpose the isolated fragments to the molecule.

9.1.2 Alignments of isolated fragments to the "full" extended branch

To do so, we use the functions implemented in the `python` library `Procrustes` [168]. The aim of this library is to use the solutions of generalized procrustes problems to find the best rotations and permutations so as to align two distinct molecules.[1] In fig. 9.3, we show the initial inputs and outputs for our alignment procedure, which can be generalized for transforming also the normal modes of vibration (see below).

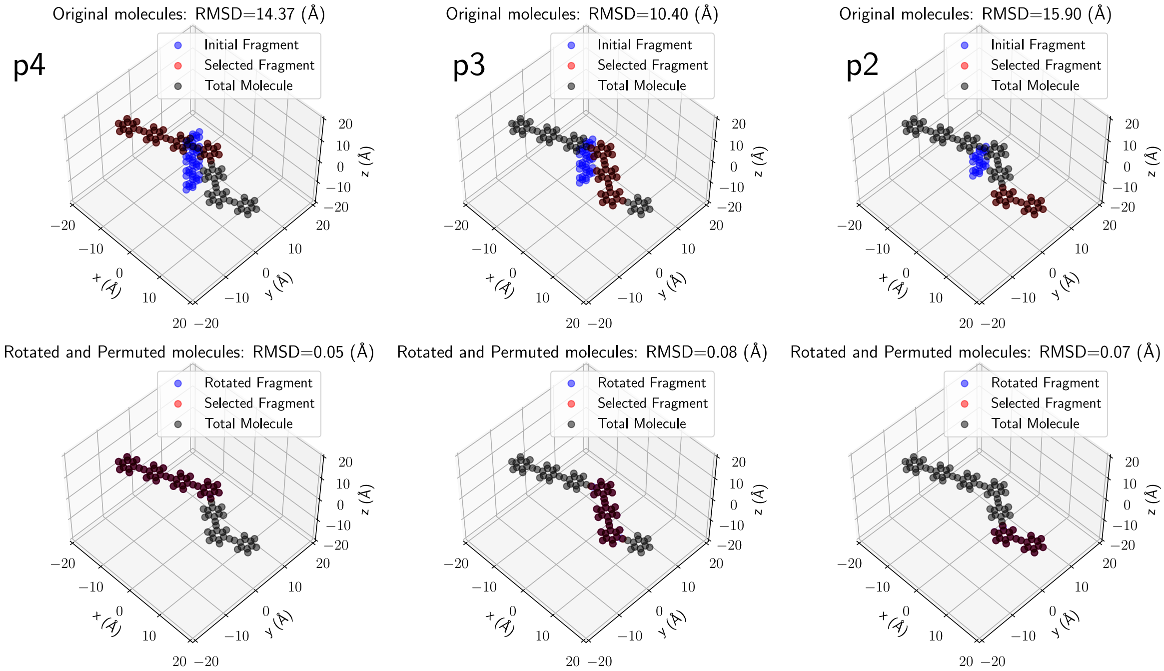

Figure 9.3: Alignment of the linear *para*-substituted PPEs with four, three, and two phenyl rings on the b234 molecule, from left to right, respectively. The molecule in black is the total molecule in which the fragments are identified. The atoms in red are the definition of the selected fragment in the total molecule. The molecule in blue is the isolated molecule to be aligned with the selected fragment.

Take-home messages

1. We identified three local excitations in the simplified nano-star extended branch, which will now be identified to the first excited excited states of the isolated p4, p3, and p2 fragments.
2. We verify that the alignement between the isolated fragments and the linear *pseudo* fragments defined in the "full" molecule is feasible.

9.2 Modelling EET with local excitations and isolated fragments

We aim to take advantage of the easily identified local excitations in the b234 molecule to build a model from the knowledge of the linear, *para*-substituted fragments only. We choose the Frenkel-exciton Hamiltonian

---

[1] Note that the procedure is some sort of optimization: our algorithm "loops" over different rotations and permutations, individually generated using the `Procrustes` library, until convergence of the root-mean-square deviation is reached.

as a basis for the model, and give it back as much information as possible from the PESs of the fragments.

9.2.1 Frenkel Hamiltonian with explicit dependence on localized modes

The conceptual formulation of the present model is a Frenkel-exciton Hamiltonian, with three excitons (the first excited state of the isolated p2, p3, and p4 fragments), as a function of the normal coordinates $\mathbf{Q} = \left(\mathbf{Q}_{\mathsf{p}n}\right)_{n=4,3,2}$

$$\mathbf{H}^{\text{Frenkel-LVC}} = \hat{T}^{\text{nu}}\mathbb{1} + \begin{bmatrix} H_{\text{p4}}(\mathbf{Q}) & H_{\text{p4--p3}}(\mathbf{Q}) & H_{\text{p4--p2}}(\mathbf{Q}) \\ H_{\text{p3--p4}}(\mathbf{Q}) & H_{\text{p3}}(\mathbf{Q}) & H_{\text{p3--p2}}(\mathbf{Q}) \\ H_{\text{p2--p4}}(\mathbf{Q}) & H_{\text{p2--p3}}(\mathbf{Q}) & H_{\text{p2}}(\mathbf{Q}) \end{bmatrix}. \tag{9.1}$$

We define the diabatic potential energies for the excitonic states

$$\begin{aligned} H_{\mathsf{p}n}(\mathbf{Q}) = E^{(1)}_{\mathsf{p}n}(\mathbf{Q}_{\mathsf{p}n} = 0) + \boldsymbol{\kappa}^{(1)}_{\mathsf{p}n} \cdot \mathbf{Q}_{\mathsf{p}n} + \frac{1}{2}\mathbf{k}^{(1)}_{\mathsf{p}_n} \cdot \mathbf{Q}^2_{\mathsf{p}_n} \text{ (modes in the excited fragment)} \\ + \sum_{m\neq n} \frac{1}{2}\mathbf{k}^{(0)}_{\mathsf{p}_m} \cdot \mathbf{Q}^2_{\mathsf{p}_m} \text{ (modes in the ground-state fragments),} \end{aligned} \tag{9.2}$$

where the excitation energy is the first excitation energy of the excited fragment, for which the energy gradients and the curvatures are used to have a realistic diabatic PES for the considered excited fragment. The curvatures with respect to the normal modes for all the other fragments are the ones of the fragments electronic ground states, and can be seen here as a harmonic "bath" to the excited fragment. The excitonic coupling, on the other hand, would be defined as

$$H_{\mathsf{p}n\text{--}\mathsf{p}m}(\mathbf{Q}) = W^{(1)}_{\mathsf{p}n\text{--}\mathsf{p}m} + \boldsymbol{\lambda}^{(1)}_{\mathsf{p}n\text{--}\mathsf{p}m} \cdot \left(a_n \mathbf{Q}_{\mathsf{p}n} + a_m \mathbf{Q}_{\mathsf{p}m}\right). \tag{9.3}$$

The very challenge of this model and this description is the definition and evaluation of the coupling $W^{(1)}_{\mathsf{p}n\text{--}\mathsf{p}m}$ and of the inter-state coupling gradient $\boldsymbol{\lambda}^{(1)}_{\mathsf{p}n\text{--}\mathsf{p}m}$. In particular, the choice and definition of the composed mode on which it is expanded

$$\mathbf{Q}_{\mathsf{p}n\text{--}\mathsf{p}m} \overset{?}{=} \left(a_n \mathbf{Q}_{\mathsf{p}n} + a_m \mathbf{Q}_{\mathsf{p}m}\right), \tag{9.4}$$

are not trivial. In particular, we will see that the most challenging part of the parametrization procedure for such a model is the definition of the "coupling modes" $\mathbf{Q}_{\mathsf{p}n\text{--}\mathsf{p}m}$.

There are now two different parametrizations and uses for the present extended Frenkel-exciton model:

- first, one can "empirically" parametrize the couplings and compare different limiting situations ("toy models" with only a constant coupling, or only a coupling gradient, symmetrical or not...). When the experiments are available and comparable to computed observables, a limiting model can be asserted or eliminated for the description of the excitonic couplings in the considered systems;
- second, one can try to use the knowledge on the isolated pairs of excitons (here di-*meta*-substituted fragments) to evaluate the coupling directly from *ab initio* calculations.

The first strategy aims at identifying the most important parameters for EET to occur, while the former aims at being predictive as regards EET. We mostly discuss the second strategy in the next sections.

9.2.2 A zeroth-order model for the excitonic coupling

The symmetrically *meta*-substituted PPE, namely m22, could be used to design a *zeroth-order* model for the variable excitonic couplings $H_{\text{p}n\text{–p}m}(\mathbf{Q})$ in PPE-oligomers. This zeroth-order model would consist in a decomposition of the coupling gradient only on the synchronous elongations in the modes of the linear *para*-substituted pn and pm fragments. The excitonic couplings would then be

$$\boldsymbol{\lambda}^{(1)}_{\text{p}n\text{–p}m} \cdot \mathbf{Q}_{\text{p}n\text{–p}m} \overset{!}{=} \frac{1}{2}\left(\boldsymbol{\kappa}^{(\text{A}_1)}_{\text{m22}} - \boldsymbol{\kappa}^{(\text{B}_2)}_{\text{m22}}\right) \cdot \mathbf{Q}_{\text{m22}} \overset{!}{=} \frac{1}{2}\left(\boldsymbol{\kappa}^{(\text{A}_1)}_{\text{m22}} - \boldsymbol{\kappa}^{(\text{B}_2)}_{\text{m22}}\right) \cdot \left(a_n \mathbf{Q}_{\text{p}n} + a_m \mathbf{Q}_{\text{p}m}\right) \tag{9.5}$$

where $=^!$ is symbolic for the approximation (and identification) of the left-hand side to the right-hand side. Our understanding is that it should also require prior average-trace and traceless separation of the 2×2 submatrix.

$$W^{(1)}_{\text{p}n\text{–p}m} = \frac{1}{2}\left(E^{(1)}_{\text{p}m} - E^{(1)}_{\text{p}n}\right). \tag{9.6}$$

From our knowledge of the m22 molecule, it should boil down to approximately $1 \times 10^{-4}\ E_{\text{h}}/(a_0\sqrt{m_e})$ of gradient coupling along the acetylenic modes which is also the order of magnitude in the m23 parametrized model. However, it would fail completely to estimate the coupling along other modes than the combined (in a synchronous way) acetylenic stretching of the two fragments linked together with the *meta* substitution, hence the "zeroth-order" label of such a parametrization.

9.2.3 Toward a realistic estimation of the excitonic coupling

In this section, we estimate the excitonic coupling by identifying it to the branching-space vectors in a without-symmetry LVC Hamiltonian model. More specifically, we propose to take into account the coupling between the fragment pn and pm *via* the inter-state coupling vector in the fragment mnm.

From the *meta*-substituted to the *para*-substituted fragments

We illustrate our strategy with the case of the excitonic coupling between the p3 and p2 *pseudo* fragments. First, the gradient of the inter-state coupling $\mathbf{h}'_{\text{m23}}$, obtained from the branching-space vectors and the position of the MECI, is re-used as the gradient of the excitonic coupling, $\boldsymbol{\lambda}^{(1)}_{\text{p}n\text{–p}m}$

$$\boldsymbol{\lambda}^{(1)}_{\text{p2–p3}} \cdot \mathbf{Q}_{\text{p2–p3}} \overset{!}{=} \frac{1}{2}\mathbf{h}'_{\text{m23}} \cdot \left(a_n \mathbf{Q}_{\text{p2}} + a_m \mathbf{Q}_{\text{p3}}\right) \tag{9.7}$$

and the collective modes (collective as regards p2 and p3) are defined as combinations of the modes of the isolated p2 and p3 fragments.

Our aim is thus to "project" the inter-state coupling onto the normal modes of the isolated p2 and p3 fragments. However, let us already stress the difficult definition of this "projection". Indeed, the inter-state coupling has $3N_{\text{m23}}$ components and the displacements for the normal modes of p2 and p3 have $3N_{\text{p2}}$ and $3N_{\text{p3}}$ components, respectively. Hence, a somehow common, intermediate but orthonormal, basis set must be built and use for this projection of quantities from the "parent" *meta*-substituted fragments onto the "child" linear *para*-substituted fragments.

A naive prior but ill-defined common “basis set” of modes

For now, we stay within an “approximate” framework where we simply “pad” the normal modes of the isolated p2 and p3 fragments with zeros on the m23 atoms that do not participate in the considered fragment. For instance, for the normal mode 56 of p2 (the acetylenic stretching)

$$\mathbf{L}_{56}^{\text{p2-in-m23}} = \left(L_{1,56}\dots, L_{i,56}, \dots, L_{3N_{\text{m23}},56}\right) \text{ with } \begin{cases} L_{i,56}^{\text{p2-in-m23}} & = L_{i,56}^{\text{p2}} \text{ if } i \text{ in the fragment p2} \\ L_{i,56}^{\text{p2-in-m23}} & = 0 \text{ otherwise} \end{cases} \tag{9.8}$$

and similarly for the modes in p3 (for instance, the normal mode 87 of p3, the synchronous acetylenic stretching). Two examples of these $3N_{\text{p2}} + 3N_{\text{p3}}$ newly defined modes are illustrated in fig. 9.4, where the child linear *para*-substituted fragments (p2, p3, and p4) have been aligned with the *meta*-substituted parent fragments (m23 and m34).

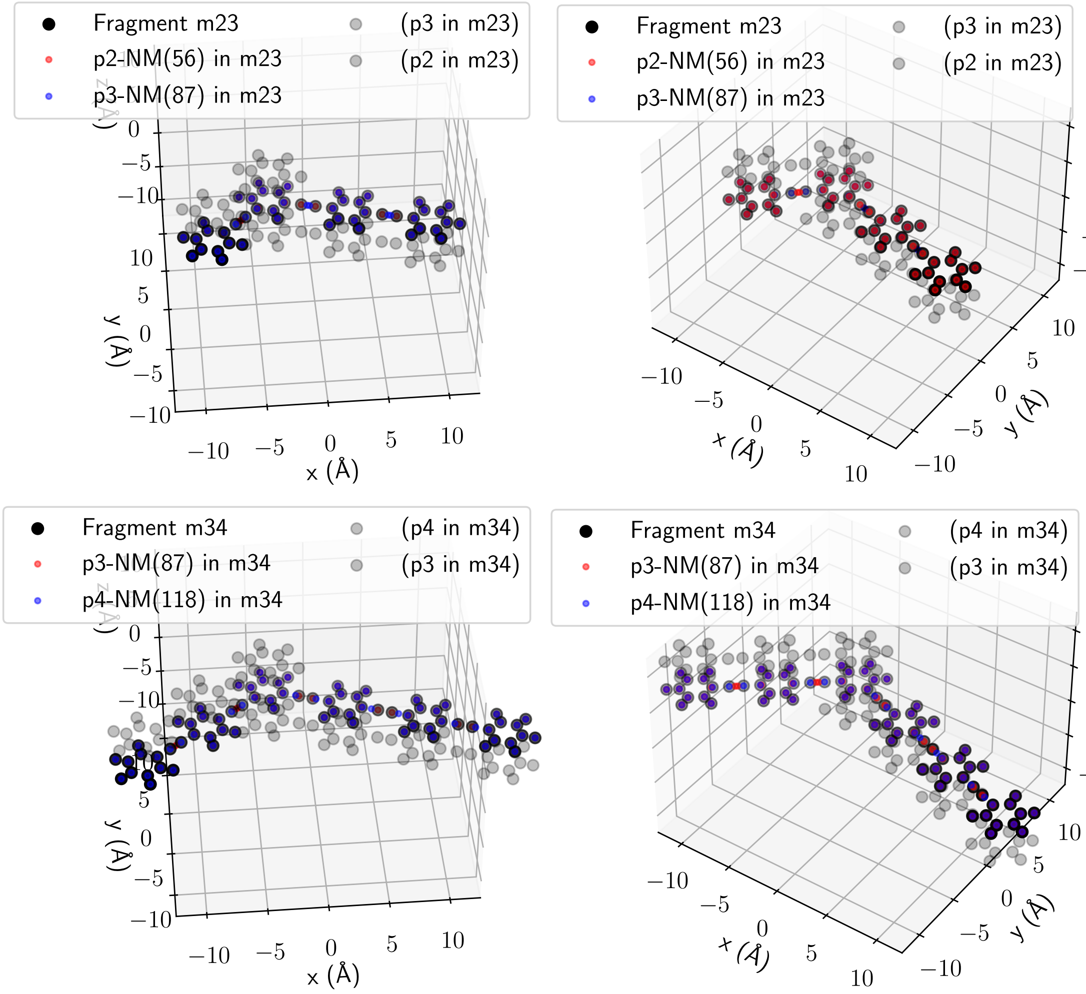

Figure 9.4: Alignment of the linear *para*-substituted PPEs with four, three, and two phenyl rings on the m23 and m34 molecules (top and bottom panels). Left and right panels are simply two different views of the same molecules and displacements. The molecule in black is the total molecule in which the fragments are identified. The transformation of the normal modes is illustrated with acetylenic displacements, computed from the isolated fragment, but applied to the atoms of the ”full” molecule (in blue and red).

The basis of p2-in-m23 and p3-in-m23 "padded" modes is not an orthogonal basis and is not directly comparable to the basis set of the normal modes of the parent fragment m23. In particular, the p2-in-m23 and p3-in-m23 modes are not orthogonal. More importantly, most of the modes have displacements on the central-phenylene ring, so that one must be careful about double-counting of nuclear displacements on the shared phenylene ring. We also note that there are more of these modes (expectedly) than there are modes of m23.

For now, let us assume (wrongly!) that we can project the normal modes of m23 into the p2-in-m23 and p3-in-m23 modes. More precisely, we compute the overlap between one mode of m23 (for instance the acetylenic mode 118) with the "padded" modes of p2 and p3. We obtain overlap tables (rectangular matrices) such as the one given in table 9.1, where we illustrated the case of the synchronous acetylenic stretching (118) and the anti-quinoidal rock-bending (114) of m23.

Table 9.1: Overlap between some normal modes of m23 with the normal modes of the isolated p2 and p3, aligned with m23. Only the five modes with the most overlap are given for each fragment.

normal mode 118 overlaps with...					
mode in p3	overlap	squared	mode in p2	overlap	squared
87	-0.992642	0.985339	60	0.189619	0.035955
88	-0.114963	0.013217	59	-0.189234	0.035810
91	-0.011286	0.000127	57	0.162140	0.026289
92	0.011275	0.000127	58	-0.161714	0.026151
89	-0.009687	0.000094	66	-0.132253	0.017491
normal mode 114 overlaps with...					
mode in p3	overlap	squared	mode in p2	overlap	squared
84	0.675256	0.455970	54	0.772456	0.596689
85	-0.446913	0.199731	53	0.321393	0.103293
82	0.307569	0.094599	52	0.299956	0.089974
83	0.307559	0.094593	55	0.297376	0.088432
86	-0.125210	0.015678	51	0.066739	0.004454

The table must be read as follows: the squared overlap of the mode 118 in m23 (p3-localized synchronous acetylenic elongation) is 0.98 with the mode 87 of p3 (synchronous acetylenic elongation) and 0.04 with the mode 60 in p2 (C-H stretching).[2] From this, it is rather clear that the modes 118-m23 and 88-p3 have analogous displacements, but again they are not similar. A second example, with important displacements on the shared central phenylene, is given with the mode 114-m23. The squared overlap

---

[2] We stress again that this squared overlap is *not* comparable to a percentage, because the basis on which it obtained is not orthogonal.

of the mode 114 in m23 (central anti-quinoidal rock-bending) is 0.46 with the mode 84 in p3 (quinoidal stretching) and 0.60 with the mode 54 in p2 (quinoidal stretching). Here, we thus understand that the rock-bending mode in m23 (which has no direct equivalent in the p3 and p2 fragments) can be seen as a sum of two modes of quinoidal stretching on the localized p3 and p2 fragments.

9.2.4 A proof of principle: dynamics in the exdented Frenkel-exciton Hamiltonian model

We hereby give our first attempt of a bottom-up modelling, for which the requirements are

- the FC geometries of the isolated p4, p3, and p2 fragments and the energy derivatives for their S_1 state;
- the S_1/S_2 MECI geometries of the isolated m23 and m34 fragments and energy derivatives of their S_1 and S_2 states;[3]
- the FC normal modes of the isolated p4, p3, p2, m23, and m34 fragments.

We choose for the primitive basis only local modes, that is, the normal modes calculated for the isolated p4, p3, and p2 branches. The selection of modes is similar to our previous choices in part II: for each fragments, we select the modes of acetylenic stretching and quinoidal stretching. Of course, the anti-quinoidal rock-bending modes are only effectively obtained when we consider the excitonic coupling, as previously derived (see again table 9.1). Herein, this consists in a selection of 15 modes in total from the linear *para*-substituted fragments.

We show the results for the propagation of mode-combined MCTDH wavepacket for the three choices of excitations (exciton p4, p3, and p2) in fig. 9.5 (from left to right, respectively).

As of now, these results cannot be fully analysed and must be discussed very carefully (we do not aim at giving general results for EET in PPE-dendrimers with the present calculations). Yet, let us comment on the main features of the time evolution of the diabatic populations in the present bottom-up simulation. First, the initially populated p4 exciton (blue lines) stays populated, and does not transfer significantly toward the other excitons, p3 and p2 (green and yellow lines), see fig. 9.5, left panels.

Next, we initialize the dynamics with the p3 exciton. It is rapidly transferred to the p4 exciton (within the first $70\,\mathrm{fs}$) but the transfer is not unidirectional, or monotonic, in the sense that the p3 exciton is populated again after this time. In particular, we see in the longer times that the p3 and p4 excitons do not stop from exchanging population. As of now, we interpret this results as a consequence of a wrong estimation of the excitonic coupling between the p3 and p4 excitons.

Finally, we set the initial wavepacket in the p2 exciton, that is the last chromophore of the extended branch. We observe a rapid transfer from the p2 to the p3 excitons, and a total decay of populations

---

[3] The S_1/S_2 MECI geometry in the m34 molecule has not been found yet. The geometry used instead is here the minimum of the S_2 state, which is rather "close" to the intersection seam ($\Delta E = 0.25\,\mathrm{eV}$)

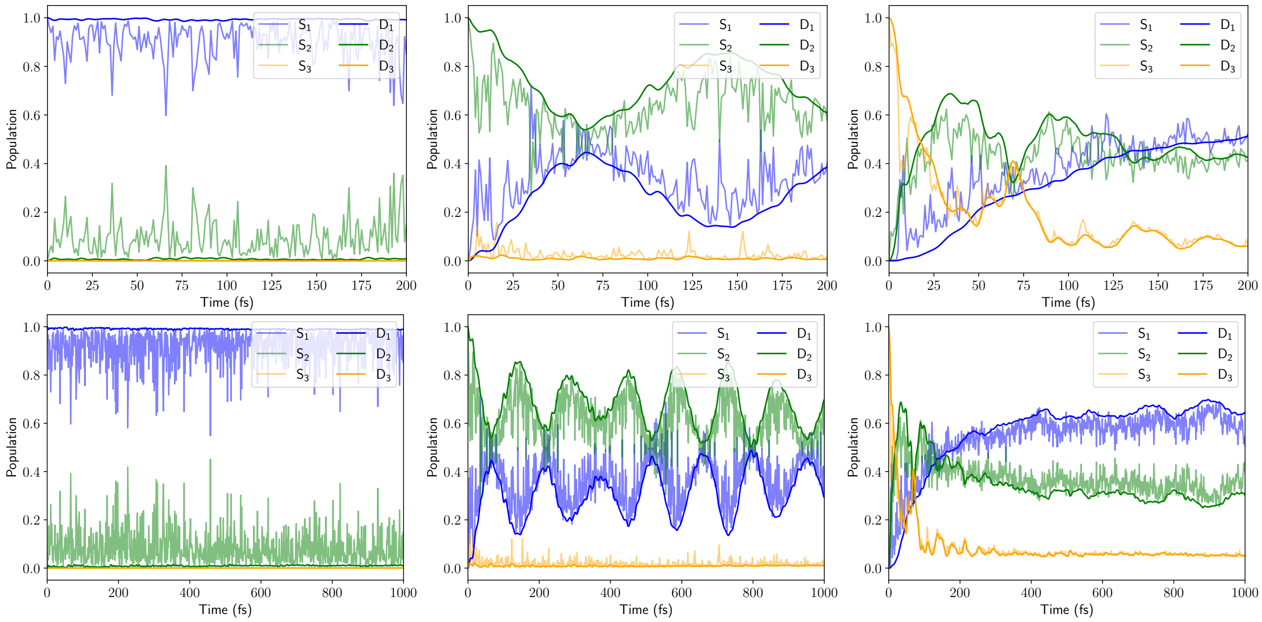

Figure 9.5: Time evolution of the diabatic and adiabatic populations (up to 200 fs and 1000 fs in top and bottom panels, respectively) for initial excitations on the diabatic state of p4, p3, and p2, from left to right, respectively.

from the p2 exciton. However, the final quantum yield is not very efficient, as a non-negligible part of the population stays trapped in the p3 exciton. Most importantly, the overall EET from the initial exciton p2 to the final exciton p4 is slow (500 fs to reach 60% of quantum yield).

9.2.5 The next step: benzene and acetylene local sites

An extension, or maybe an alternative, to this pseudofragmentation scheme based on the linear *para*-substituted fragments is a pseudofragmentation based on the local benzenes and acetylenes of the PPE-dendrimer. Previous work by Ho and Lasorne explored the calculation of the excitation energies of linear *para*-substituted fragments from an extended Hückel orbital scheme. The basic idea is to expand the excitation energy of the linear fragments, with arbitrary lengths, on the nuclear displacements associated to the acetylenes and to the benzenes. The most challenging part would now be to find transferable parameters for estimating the inter-state coupling (between linear fragments consecutively linked together *via meta*-substitution) as a function of displacements on the *connecting* benzene and on the first adjacent acetylenes.

9.3 Challenges and open questions

The challenges for the outlook of building Frenkel-LVC Hamiltonian models in a bottom-up way for the PPE-dendrimers are numerous. First, in our diabatic perspective of locally-excited electronic states, the alignment of the isolated fragments with the total extended branch is crucial, and might be not trivial.

In particular, the correspondence between the normal modes of the isolated linear fragments (or child fragments) and the modes of the total extended branch (or parent fragment) must be carefully defined. Indeed, a simple projection of the parent normal modes onto the child, localized normal modes is not directly feasible. We identify here two main questions:

- is it possible to define a generalized projection, or a generalized basis set of localized normal modes, without "double-counting" the displacements in the *meta*-substituted phenylenes for instance?
- is it possible to use such a generalized projection for transferring the parameters known for the isolated pairs of first-neighbour linear fragments to a generalized excitonic coupling gradient?

On the other hand, the question of the relevance of such modelling choices has to be addressed. In particular, are the branching-space vectors, obtained near conical intersection seams between the localized fragments, good estimates of the excitonic coupling in a Frenkel-exciton Hamiltonian? Indeed, this estimation seems to mostly provide excitonic couplings relative to the *through-bond*, Dexter-like mechanism. Can we use an analogous strategy to estimate the excitonic coupling (more likely the constant one) relative to the *through-space*, Förster-like mechanism? We hope to be able to tackle these questions in future works.

Chapter 10

General Conclusions

10.1 Historical interest for PPE-dendrimers as light-harvesting antennae

Since the 1990's, the extended dendrimers of poly(phenylene ethynylene) (PPE), and the so-called nano-star [25] on which we focussed, have drawn the attention of researchers, both experimentalists and theoreticians, for their remarkable ability for excitation-energy transfer (EET). The experiments demonstrated the additive character of the steady-state absorption spectrum and measured the quantum yield of EET, after photo-excitation of the peripheral chromophores, as close to one [32–35]. As regards modelling, Frenkel-exciton Hamiltonian models were first proposed so as to reproduce the spectroscopic features of the nano-star [29, 30]. This was further rationalized with electronic structure calculations that suggested a mechanism based on electronic excited states localized on the linear *para*-substituted fragments, hence an easily identified unidirectional energy gradient, from the peripheral to the central fragments [36, 38]. Finally, the first simulations of the excited-state dynamics following photo-excitation of the nano-star building blocks, proposed in 2009 [50–52], highlighted the role of the high-frequency acetylenic vibrations for EET in the PPE-oligomers [53].

The EET observed in PPE-oligomers is thus to be interpreted as an electronic population transfer mediated by some nuclear motions. On this ground, modelling and simulating EET in such molecules must be done as in the case of nonadiabatic processes (beyond the Born-Oppenheimer approximation), and discussed *via* the knowledge of the potential energy surfaces and nonadiabatic couplings in PPE-oligomers [18, 42]. In this thesis, we proposed among the first quantum-mechanical simulations (as regards both time-independent and time-dependent Schrödinger equations) of EET dynamics in PPE-oligomers.

In part I, we first explicited the framework we used for running nonadiabatic quantum dynamics, by defining the molecular Hamiltonian and its representations (adiabatic and diabatic). More importantly, we presented the multiconfigurational time-dependent Hartree (MCTDH) formalism that we used to quantum-mechanically propagate the nuclear wavepackets associated to the photo-excited molecules of interest.

In part II, we applied this framework to the study of the chromophores and of the units for EET in the nano-star. In both cases, vibronic coupling Hamiltonian models (linear and quadratic, up to ten degrees of freedom) were parametrized so as to account for the conical intersections in the first electronic excited states of the PPE-oligomers. The parametrization of such models was obtained by detailed analysis of the excited-state PESs (search of minima, minimum-energy conical intersections and calculation of PES-cuts). We used such models for mainly two purposes: i) producing steady-state absorption and emission spectra; and ii) evaluating the kinetics of photo-induced EET, as if it were a photochemical reaction. As regards the EET process, we showed that it was similar for asymmetrical and symmetrical PPE-oligomers (namely m23 and d223 molecules, see part II, chapters 6 and 7). It occurs, in our modelling, within $25\,\mathrm{fs}$ and with high quantum yield (about 90%). In particular, we affirm the prominent roles of the acetylenic elongations and highlighted the importance of the central-quinoidal rock-bending vibrations. We proposed a detailed analysis of the EET process, by monitoring the geometry during EET and by estimating the redistribution of the excess excitation energy in the vibrational degrees of freedom of the molecules. The feasibility of high-dimensional quantum dynamics (up to 90 degrees of freedom) was also explored, with a particular attention given to the parametrization of high-dimensional excited-state PESs and to the definition of multi-layer MCTDH trees.

Finally, in part III, chapter 9, we defined a bottom-up approach for modelling PPE-dendrimers, by defining an intermediate model between the Frenkel-exciton Hamiltonian models and the vibronic coupling Hamiltonian models. In essence, we decomposed an extended branch of the nano-star into isolated linear *para*-substituted fragments. Each one of these isolated fragments was then used to define a Frenkel-exciton in the model. The excitonic coupling was then estimated from the knowledge of the first-neighbour articulations on the *meta*-substituted phenylene, shared by two consecutive linear fragments. As of now, we only explored the feasibility of such a model but already have promising results for simulating sequential EET from the shortest to the longest fragment.

10.2 A recent renewal of interest for PPE-oligomers

PPE-oligomers have regained attention in the early 2020's, as an interesting playground for the use of nonadiabatic excited-state molecular dynamics [57, 58, 60, 61]. In particular, the EET in the asymmetrical unit have been investigated through the calculation of transient absorption pump-probe simulations [59]. The linear *para*-substituted fragments also regained interest as promising π-conjugated molecular wires [169, 170].

In this thesis, we addressed one unanswered spectroscopic question for the PPE-oligomers. We focussed in part II, chapter 5, on the symmetrically di-*meta*-substituted chromophore (namely m22), for which the absorption and the emission spectra exhibit an unusual Stokes shift and we investigated the role of symmetry for the position of the band origin in emission. We modelled the PESs of the first two electonic excited states of m22, which are a pair of strongly nonadiabatically coupled and quasi-degenerate, bright electronic states, even near the Franck-Condon region. We attributed the measured Stokes shift to an emissive contribution that has been transferred from one of the bright states to the other because of the strong coupling components along the acetylenic elongations. We raised the question of the difficult simulation of emission and fluorescence in the case of strongly nonadiabatically coupled electronic states, of which m22 seems to be an exacerbated case.

Finally, in part III, chapter 8, we started a discussion on the preparation and the importance of superposition of states, in particular in the context of localized excitations on two equivalent fragments of the molecules. We showed the small influence of local excitations on the EET process. In addition, we explored open questions as regards the physical interpretation of electronic coherences between electronic states of different symmetry, after photo-excitation of pure states or superpositions of states. Finally, we mentioned the feasibility of explicitly simulating the electronic excitations with laser pulses [18, 55], which we hope will eventually lead to the simulation of time-resolved spectroscopies.

10.3 Position of the present work in the existing literature

We show in fig. 10.1 a tentative map of the existing nonadiabatic molecular dynamics simulations on PPE-dendrimers and oligomers, for which this work is complementary.

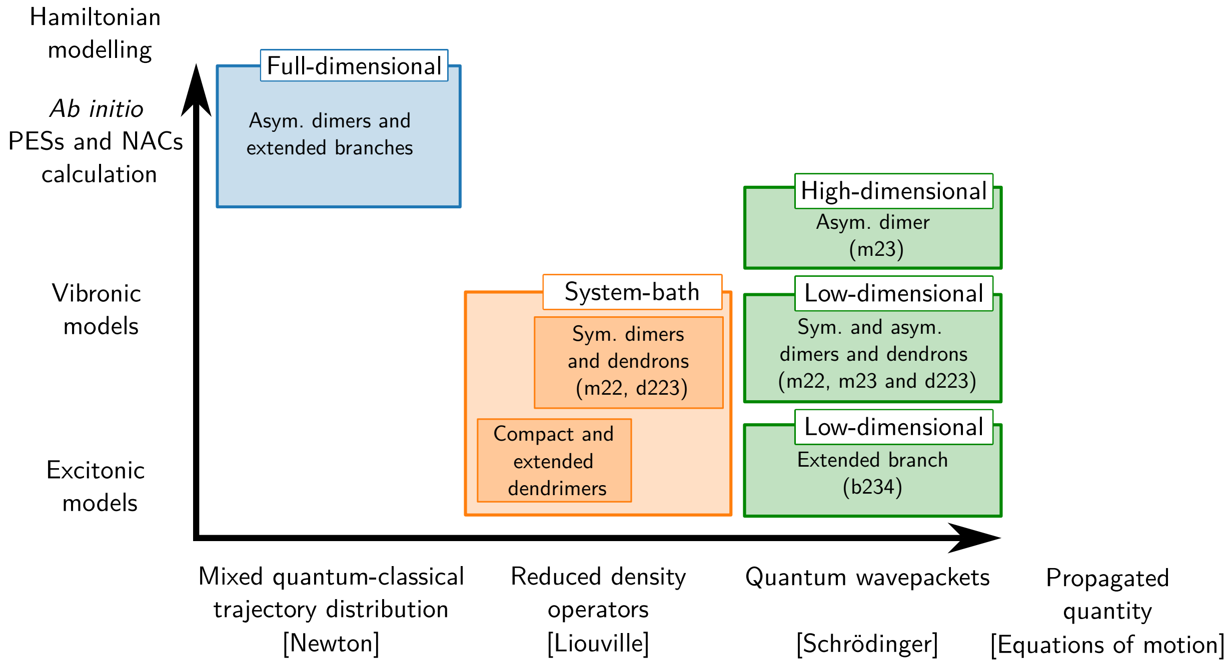

Figure 10.1: A tentative map of the existing nonadiabatic molecular dynamics simulations on PPE-dendrimers and oligomers (dimers, dendrons and extended branches), classified with respect to their propagated quantities and Hamiltonian modelling strategies. Detailed references for the different simulations are given in the text.

In blue, we mention the direct-dynamics trajectory surface hopping simulations of Fernandez-Alberti, Soler, Freixas and co-workers [50–53, 57, 60], in particular their recent simulations involving the NEXMD software [58, 61]. In orange, we first cite the seminal work of Mukamel, Chernyak, Tretiak, Minami and co-workers on the use of the phenomenological Frenkel-exciton Hamiltonian model for the description of both compact and extended dendrimers (with spectral responses and the Redfield equation) [28–31]. We also mention the work of Jaouadi, Desouter-Lecomte, Mangaud and co-workers on using reduced density operators propagation (within the context of HEOM) of effective vibronic coupling Hamiltonian models for dimers and dendrons [18, 55, 171]. Finally, the present work explored the explicit propagation of quantum wavepackets (with the MCTDH and ML-MCTDH formalisms) for PPE-oligomers. Both excitonic and vibronic Hamiltonian models have been parametrized, from low-dimensional (up to ten degrees of freedom) models for dimers, dendrons, and extended branches [154, 155] to high-dimensional (up to 90 degrees of freedom) models.

Chapitre 10

Conclusion générale

10.1 Intérêt historique pour l'EET dans les dendrimères de PPEs

Depuis les années 1990, les dendrimères étendus de poly(phénylène éthynylène) (PPE), particulièrement la *nano-star* [25] à laquelle nous nous sommes intéressés, ont attiré l'attention de chercheurs en chimie expérimentale et théorique pour leur capacité remarquable à assurer des transferts d'énergie d'excitation (EET). Les études expérimentales ont d'abord démontré le caractère additif du spectre UV-visible de la *nano-star*, et permis d'estimer le rendement quantique après photo-excitation des chromophores périphériques [32–35]. Concernant la modélisation, des modèles de Hamiltonien d'exciton de Frenkel ont été proposés pour reproduire les propriétés spectroscopiques de la *nano-star* [29, 30]. Une rationalisation de ces études phénoménologiques à l'aide de calculs de structure éléctronique a également permis de suggérer un mécanisme basé sur les excitations électroniques localisées sur les fragments linéairement *para*-substitués, avec ainsi un gradient d'énergie d'excitation unidirectionnel depuis la périphérie vers les fragments centraux [36, 38]. Enfin, les premières simulations de la dynamique des états excités suivant une photo-excitation des blocs élémentaires de PPEs, proposées en 2009 [50–52], ont démontré le rôle des vibrations acétyléniques, de haute fréquence, pour que l'EET se déroule de façon ultra-rapide [53].

L'EET observé dans les oligomères de PPEs a pu alors être interprété comme un transfert de population électronique porté par certains déplacements nucléaires. Sur cette base, la modélisation et simulation de l'EET dans de telles molécules doivent être réalisées comme s'il s'agissait d'un processus non-adiabatique (au-delà de l'approximation de Born-Oppenheimer) et discutées *via* la connaissance des surfaces d'énergie potentielle et des couplages non-adiabatiques au sein des oligomères de PPEs [18, 42]. Dans cette thèse, nous avons proposé les premières simulations quantiques (du point de vue des deux équations de Schrödinger, indépendante et dépendante du temps) de la dynamique de l'EET dans les oligomères de PPEs.

Dans la partie I, nous avons d'abord présenté le cadre de travail utilisé pour réaliser des calculs de dynamique quantique non-adiabatique, en définissant le Hamiltonien moléculaire et ses représentations (adiabatique et diabatiques). Nous avons également présenté le formalisme de Hartree multiconfigurationel dépendant du temps (MCTDH) que nous avons utilisé pour propager, de façon quantique, les paquets d'ondes nucléaires associés aux molécules d'intérêt photo-excitées.

Dans la partie II, nous avons étudié, dans ce même cadre, les chromophores de la *nano-star* et les premières unités réalisant l'EET en son sein. Dans les deux cas, des modèles de Hamiltonien de couplage vibronique (linéaire et quadratique, jusqu'à dix degrés de liberté) ont été paramétrisés de façon à prendre en compte la présence d'intersections coniques entre les premiers états électroniques des oligomères de PPEs. Ces paramétrisations sont obtenues après une étude détaillée des PESs des états excités (recherche et caractérisation de minima, d'intersections coniques d'énergie minimale, ou par des coupes de PESs). Nous avons ensuite utilisé de tels modèles pour principalement deux usages : i) produire des spectres d'absorption et d'émission stationnaire ; et ii) évaluer la cinétique de l'EET photo-induit, comme s'il s'agissait d'une réaction photochimique. Pour ce qui est du processus d'EET, nous avons montré qu'il était similaire pour les oligomères asymétriquement et symétriquement substitués (c'est à dire pour m23 et d223, voir partie II, chapitres 6 and 7). Dans nos simulations, cet EET se déroule en moins de $25\,\mathrm{fs}$ avec un rendement quantique haut (autour de 90%). En particulier, nous avons pu affirmer le rôle premier des élongations acétyléniques et nous avons souligné l'importance des modes de vibration de bascule sur le phénylène central. Nous avons proposé une analyse détaillée du processus d'EET, en suivant la géométrie de la molécule au cours de l'EET et en estimant la redistribution de l'énergie d'excitation en excès au sein des degrés de liberté vibrationnels de la molécule. Également, la faisabilité de calculs de dynamique quantique en haute dimensionalité (jusqu'à 90 degrés de liberté) a été explorée, avec une attention particulière donnée à la paramétrisation de PESs pour une telle dimensionalité et à la définition des arbres de *multi-layer* MCTDH.

Finalement, dans la partie III, chapitre 9, nous avons défini une approche ascendante pour la modélisation de dendrimères de PPEs, en définissant un modèle intermédiaire entre un Hamiltonien d'excitons de Frenkel et un Hamiltonien de couplage vibronique. En substance, nous avons décomposé une branche étendue de la *nano-star* en des fragments linéairement *para*-substitués isolés. Chacun de ces fragments isolés a alors été utilisé pour définir un exciton de Frenkel dans le modèle. Le couplage excitonique a lui été estimé en connaissance des articulations de deux fragments consécutifs, en remarquant que ces deux fragments partagent un phénylène. Pour l'instant, nous avons simplement exploré la faisabilité d'un tel modèle, mais avons déjà pu analyser des résultats prometteurs pour simuler l'EET dans des branches étendues.

10.2 Un intérêt récemment renouvelé pour les oligomères de PPEs

Les oligomères de PPEs ont retrouvé une certaine attention depuis le début des années 2020, étant vus comme des « systèmes jouets » assez intéressants pour comparer et étudier plusieurs méthodes de dynamique moléculaire non-adiabatique dans les états excités [57, 58, 60, 61]. Également, l'EET dans l'unité symétrique a été étudié à nouveau au travers de simulations d'expériences pompe-sonde, pour reproduire par exemple des spectres d'absorption transitoire dans les états excités [59]. Les fragments linéairement *para*-substitués quant a eux ont connu un nouvel intérêt comme possible fils moléculaires π-conjugés [169, 170].

Dans cette thèse, nous avons de notre côté enquêté sur une question spectroscopique jusque là sans réponse sur les oligomères de PPEs. Dans la partie II, chapitre 5, nous nous sommes intéressés au chromophore symétriquement *meta*-substitué (la molécule m22), pour lequel les spectres d'absorption et d'émission stationnaires présentent un déplacement de Stokes non-usuel. Nous avons étudié le rôle éventuel de la symétrie dans la position de la bande d'origine à l'émission, comme une possible explication de ce déplacement de Stokes. Nous avons modélisé les PESs des deux premiers états électroniques excités de m22, qui forment une paire d'états *bright* fortement couplés et quasiment dégénérés, même dans la région de Franck-Condon. Nous avons attribué le déplacement de Stokes mesuré à une contribution à l'émission due à un paquet d'ondes nucléaire qui aurait été transféré d'un des états *bright* à l'autre, à cause du couplage non-adiabatique fort, porté principalement par les élongations acétyléniques. Nous avons également posé la question de la difficile simulation de l'émission de lumière et de la fluorescence par des molécules dont les états électroniques sont fortement couplés non-adiabatiquement, pour lequel m22 semble être un cas très particulier.

Finalement, dans la partie III, chapitre 8, nous avons entamé une discussion sur la préparation et l'importance des superpositions d'états électroniques, en particulier dans le contexte d'excitations localisées sur des fragments équivalents d'une même molécule. Nous avons montré que dans le cas de d223, ces excitations localisées n'avaient que très peu d'effet sur le processus d'EET. Nous avong également exploré des questions qui nous semblaient ouvertes en ce qui concerne l'interprétation physique de la cohérence électronique entre des états de symétries différentes, après la photo-excitation d'états purs ou de superpositions d'états. Finalement, nous avons également mentionné la possibilité d'aller vers des simulations explicites des excitations électroniques depuis l'état fondamental, avec l'utilisation de pulses laser [18, 55]. Nous espérons que de telles études pourront mener à la simulation de spectroscopies résolues en temps.

10.3 Positionnement de ce travail au sein de la littérature existante

Nous montrons dans la fig. 10.1 une proposition de positionnement de différentes études de dynamique moléculaire non-adiabatique sur les oligomères et dendrimères de PPEs, pour lesquelles le présent travail est complémentaire.

En bleu, nous mentionnons les simulations de dynamique directes basées sur des ensembles de trajectoires réalisées par Fernandez-Alberti, Soler, Freixas et coll. [50–53, 57, 60], avec notamment les récentes implémentations de telles méthodes dans leur logiciel, NEXMD [58, 61]. En orange, nous citons d'abord le travail précurseur de Mukamel, Chernyak, Tretiak, Minami et coll., sur l'usage de modèles phénoménologiques

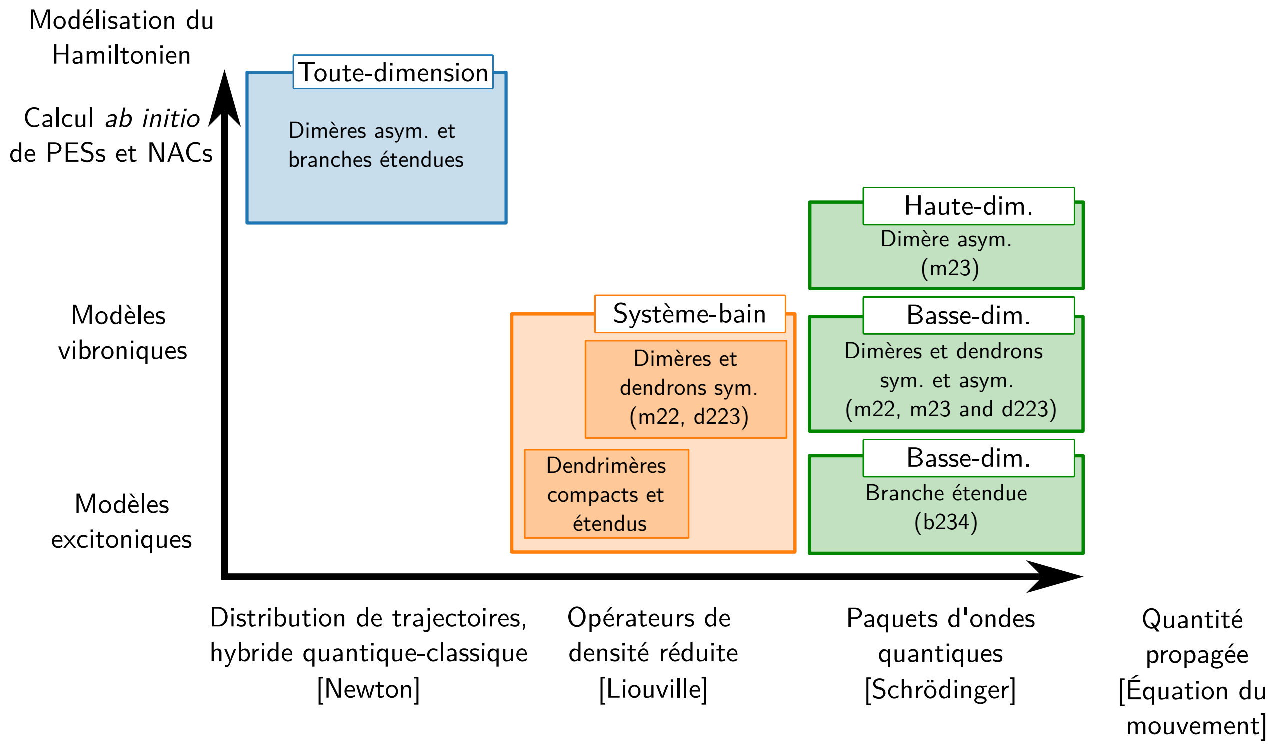

Figure 10.1 – Une proposition de carte des simulations existantes de dynamique moléculaire non-adiabatique sur les dendrimères et oligomères (dimères, dendrons et branches étendues) de PPEs, classées en fonction de la quantité propagée et de la modélisation choisie pour le Hamiltonien. Les références associées aux différentes simulations sont précisées dans le texte.

de Hamiltonien (*dit* de Frenkel) pour la description de dendrimères compacts et étendus (avec notamment des réponses spectrales et la résolution de l'équation de Redfield) [28–31]. Nous mentionnons également les travaux de Jaouadi, Desouter-Lecomte, Mangaud et coll. basés sur la propagation des opérateurs de densité réduite (avec notamment la méthode HEOM) dans le cas de modèles vibroniques effectifs, pour des dimères et des dendrons de PPEs [18, 55, 171]. Finalement, le travail développé dans ce manuscrit a été d'utiliser les outils existants de propagation exacte de paquets d'ondes (dans le formalisme MCTDH et ML-MCTDH) pour simuler l'EET dans des oligomères de PPEs. Nous avons étudié à la fois des modèles de Hamiltonien excitonique et de Hamiltonien vibronique, pour des systèmes de basse dimensionalité (jusqu'à dix degrés de libertés pour les dimères, dendrons et branches étendues) [154, 155] mais aussi pour des systèmes de haute dimensionalité (jusqu'à 90 degrés de liberté).

References

[1] X. Hu, T. Ritz, A. Damjanović, F. Autenrieth, and K. Schulten, Photosynthetic apparatus of purple bacteria, Quarterly Reviews of Biophysics, **2002**, 35 (1) 1–62.

[2] R. E. Fenna, B. W. Matthews, J. M. Olson, and E. K. Shaw, Structure of a bacteriochlorophyll-protein from the green photosynthetic bacterium Chlorobium limicola: crystallographic evidence for a trimer, Journal of Molecular Biology, **1974**, 84 (2) 231–240.

[3] D. Mendive-Tapia, E. Mangaud, T. Firmino, A. de la Lande, M. Desouter-Lecomte, H.-D. Meyer, and F. Gatti, Multidimensional quantum mechanical modeling of electron transfer and electronic coherence in plant cryptochromes: the role of initial bath conditions, The Journal of Physical Chemistry B, **2018**, 122 (1) 126–136.

[4] Y.-C. Cheng and G. R. Fleming, Dynamics of light harvesting in photosynthesis, Annual Review of Physical Chemistry, **2009**, 60 (Volume 60, 2009) 241–262.

[5] S. L. Gilat, A. Adronov, and J. M. J. Fréchet, Light harvesting and energy transfer in novel convergently constructed dendrimers, Angewandte Chemie International Edition, **1999**, 38 (10) 1422–1427.

[6] A. Adronov and J. M. J. Fréchet, Light-harvesting dendrimers, Chemical Communications, **2000**, 0 (18) 1701–1710.

[7] T. Förster, Zwischenmolekulare energiewanderung und fluoreszenz, Annalen der Physik, **1948**, 437 (1-2) 55–75.

[8] D. L. Dexter, A theory of sensitized luminescence in solids, The Journal of Chemical Physics, **1953**, 21 (5) 836–850.

[9] G. D. Scholes, X. J. Jordanides, and G. R. Fleming, Adapting the förster theory of energy transfer for modeling dynamics in aggregated molecular assemblies, The Journal of Physical Chemistry B, **2001**, 105 (8) 1640–1651.

[10] G. D. Scholes and G. R. Fleming, Energy transfer and photosynthetic light harvesting, in Adventures in Chemical Physics, **2005**, 57–129.

[11] R. D. Harcourt, G. D. Scholes, and K. P. Ghiggino, Rate expressions for excitation transfer. II. Electronic considerations of direct and through–configuration exciton resonance interactions, The Journal of Chemical Physics, **1994**, 101 (12) 10521–10525.

[12] G. D. Scholes, R. D. Harcourt, and K. P. Ghiggino, Rate expressions for excitation transfer. III. An ab initio study of electronic factors in excitation transfer and exciton resonance interactions, The Journal of Chemical Physics, **1995**, 102 (24) 9574–9581.

[13] G. D. Scholes and R. D. Harcourt, Configuration interaction and the theory of electronic factors in energy transfer and molecular exciton interactions, The Journal of Chemical Physics, **1996**, 104 (13) 5054–5061.

[14] H. v. Amerongen, L. Valkunas, and R. v. Grondelle, Photosynthetic excitons, **2000**.

[15] T. Renger, V. May, and O. Kühn, Ultrafast excitation energy transfer dynamics in photosynthetic pigment–protein complexes, Physics Reports, **2001**, 343 (3) 137–254.

[16] M. Yang and G. R. Fleming, Influence of phonons on exciton transfer dynamics: comparison of the Redfield, Förster, and modified Redfield equations, Chemical Physics, **2002**, 282 (1) 163–180.

[17] T. Firmino, E. Mangaud, F. Cailliez, A. Devolder, D. Mendive-Tapia *et al.*, Quantum effects in ultrafast electron transfers within cryptochromes, Physical Chemistry Chemical Physics, **2016**, 18 (31) 21442–21457.

[18] G. Breuil, E. Mangaud, B. Lasorne, O. Atabek, and M. Desouter-Lecomte, Funneling dynamics in a phenylacetylene trimer: Coherent excitation of donor excitonic states and their superposition, The Journal of Chemical Physics, **2021**, 155 (3) 034303.

[19] A. L. Thompson, K. M. Gaab, J. Xu, C. J. Bardeen, and T. J. Martínez, Variable electronic coupling in phenylacetylene dendrimers: the role of förster, dexter, and charge-transfer interactions, The Journal of Physical Chemistry A, **2004**, 108 (4) 671–682.

[20] H. Köppel, W. Domcke, and L. S. Cederbaum, Multimode molecular dynamics beyond the born-oppenheimer approximation, in Advances in Chemical Physics, vol. 57, **1984**, 59–246.

[21] D. R. Yarkony, Diabolical conical intersections, Reviews of Modern Physics, **1996**, 68 (4) 985–1013.

[22] W. Domcke, D. Yarkony, and H. Köppel, Conical intersections: electronic structure, dynamics & spectroscopy, no. v.15 in Advanced series in physical chemistry, **2004**.

[23] W. Domcke, D. R. Yarkony, and H. Köppel, Conical intersections: theory, computation and experiment, **2011**.

[24] Z. Xu, M. Kahr, K. L. Walker, C. L. Wilkins, and J. S. Moore, Phenylacetylene dendrimers by the divergent, convergent, and double-stage convergent methods, Journal of the American Chemical Society, **1994**, 116 (11) 4537–4550.

[25] Z. Xu and J. S. Moore, Design and synthesis of a convergent and directional molecular antenna, Acta Polymerica, **1994**, 45 (2) 83–87.

[26] E. Y. Poliakov, V. Chernyak, S. Tretiak, and S. Mukamel, Exciton-scaling and optical excitations of self-similar phenylacetylene dendrimers, The Journal of Chemical Physics, **1999**, 110 (16) 8161–8175.

[27] C. Supritz, A. Engelmann, and P. Reineker, Optical absorption in compact and extended dendrimers, Journal of Luminescence, **2005**, 111 (4) 367–381.

[28] S. Tretiak, V. Chernyak, and S. Mukamel, Localized electronic excitations in phenylacetylene dendrimers, The Journal of Physical Chemistry B, **1998**, 102 (18) 3310–3315.

[29] V. Chernyak, T. Minami, and S. Mukamel, Exciton transport in molecular aggregates probed by time and frequency gated optical spectroscopy, The Journal of Chemical Physics, **2000**, 112 (18) 7953–7963.

[30] T. Minami, S. Tretiak, V. Chernyak, and S. Mukamel, Frenkel-exciton Hamiltonian for dendrimeric nanostar, Journal of Luminescence, **2000**, 87-89 115–118.

[31] C. Wu, S. V. Malinin, S. Tretiak, and V. Y. Chernyak, Exciton scattering and localization in branched dendrimeric structures, Nature Physics, **2006**, 2 (9) 631–635.

[32] C. Devadoss, P. Bharathi, and J. S. Moore, Energy transfer in dendritic macromolecules: molecular size effects and the role of an energy gradient, Journal of the American Chemical Society, **1996**, 118 (40) 9635–9644.

[33] M. R. Shortreed, S. F. Swallen, Z.-Y. Shi, W. Tan, Z. Xu *et al.*, Directed energy transfer funnels in dendrimeric antenna supermolecules, The Journal of Physical Chemistry B, **1997**, 101 (33) 6318–6322.

[34] S. F. Swallen, R. Kopelman, J. S. Moore, and C. Devadoss, Dendrimer photoantenna supermolecules: energetic funnels, exciton hopping and correlated excimer formation, Journal of Molecular Structure, **1999**, 485-486 585–597.

[35] R. Kopelman, M. Shortreed, Z.-Y. Shi, W. Tan, Z. Xu *et al.*, Spectroscopic evidence for excitonic localization in fractal antenna supermolecules, Physical Review Letters, **1997**, 78 (7) 1239–1242.

[36] J. L. Palma, E. Atas, L. Hardison, T. B. Marder, J. C. Collings *et al.*, Electronic spectra of the nanostar dendrimer: theory and experiment, The Journal of Physical Chemistry C, **2010**, 114 (48) 20702–20712.

[37] K. M. Gaab, A. L. Thompson, J. Xu, T. J. Martínez, and C. J. Bardeen, Meta-conjugation and excited-state coupling in phenylacetylene dendrimers, Journal of the American Chemical Society, **2003**, 125 (31) 9288–9289.

[38] J. Huang, L. Du, D. Hu, and Z. Lan, Theoretical analysis of excited states and energy transfer mechanism in conjugated dendrimers, Journal of Computational Chemistry, **2015**, 36 (3) 151–163.

[39] Q. Chu and Y. Pang, Vibronic structures in the electronic spectra of oligo(phenylene ethynylene): effect of m-phenylene to the optical properties of poly(m-phenylene ethynylene), Spectrochimica Acta Part A: Molecular and Biomolecular Spectroscopy, **2004**, 60 (7) 1459–1467.

[40] S. Samori, S. Tojo, M. Fujitsuka, T. Ryhding, A. G. Fix *et al.*, Emission from regioisomeric bis(phenylethynyl)benzenes during pulse radiolysis, The Journal of Organic Chemistry, **2009**, 74 (10) 3776–3782.

[41] E. K.-L. Ho, T. Etienne, and B. Lasorne, Vibronic properties of para-polyphenylene ethynylenes: TD-DFT insights, The Journal of Chemical Physics, **2017**, 146 (16) 164303.

[42] E. K. L. Ho and B. Lasorne, Diabatic pseudofragmentation and nonadiabatic excitation-energy transfer in meta-substituted dendrimer building blocks, Computational and Theoretical Chemistry, **2019**, 1156 25–36.

[43] Y. Hirata, T. Okada, N. Mataga, and T. Nomoto, Picosecond time-resolved absorption spectrum measurements of the higher excited singlet state of diphenylacetylene in the solution phase, The Journal of Physical Chemistry, **1992**, 96 (16) 6559–6563.

[44] C. Ferrante, U. Kensy, and B. Dick, Does diphenylacetylene (tolan) fluoresce from its second excited singlet state? Semiempirical MO calculations and fluorescence quantum yield measurements, The Journal of Physical Chemistry, **1993**, 97 (51) 13457–13463.

[45] J. Saltiel and V. K. R. Kumar, Photophysics of diphenylacetylene: Light from the "dark state", The Journal of Physical Chemistry A, **2012**, 116 (43) 10548–10558.

[46] M. Krämer, U. H. F. Bunz, and A. Dreuw, Comprehensive look at the photochemistry of tolane, The Journal of Physical Chemistry A, **2017**, 121 (5) 946–953.

[47] C. Robertson and G. A. Worth, Modelling the non-radiative singlet excited state isomerization of diphenyl-acetylene: A vibronic coupling model, Chemical Physics, **2018**, 510 17–29.

[48] G. Breuil, T. Etienne, and B. Lasorne, Bright-to-dark-to-bright photoisomerisation in a forked (phenylene ethynylene) dendrimer prototype and its building blocks: a new mechanistic shortcut for excitation-energy transfer?, The European Physical Journal Special Topics, **2023**, 232 (13) 2101–2115.

[49] W. Ortiz, B. P. Krueger, V. D. Kleiman, J. L. Krause, and A. E. Roitberg, Energy transfer in the nanostar: The role of coulombic coupling and dynamics, The Journal of Physical Chemistry B, **2005**, 109 (23) 11512–11519.

[50] S. Fernandez-Alberti, V. D. Kleiman, S. Tretiak, and A. E. Roitberg, Nonadiabatic molecular dynamics simulations of the energy transfer between building blocks in a phenylene ethynylene dendrimer, The Journal of Physical Chemistry A, **2009**, 113 (26) 7535–7542.

[51] S. Fernandez-Alberti, V. D. Kleiman, S. Tretiak, and A. E. Roitberg, Unidirectional energy transfer in conjugated molecules: the crucial role of high-frequency C(triple)C bonds, The Journal of Physical Chemistry Letters, **2010**, 1 (18) 2699–2704.

[52] S. Fernandez-Alberti, A. E. Roitberg, T. Nelson, and S. Tretiak, Identification of unavoided crossings in nonadiabatic photoexcited dynamics involving multiple electronic states in polyatomic conjugated molecules, The Journal of Chemical Physics, **2012**, 137 (1) 014512.

[53] M. A. Soler, A. E. Roitberg, T. Nelson, S. Tretiak, and S. Fernandez-Alberti, Analysis of state-specific vibrations coupled to the unidirectional energy transfer in conjugated dendrimers, The Journal of Physical Chemistry A, **2012**, 116 (40) 9802–9810.

[54] S. Fernandez-Alberti, A. E. Roitberg, V. D. Kleiman, T. Nelson, and S. Tretiak, Shishiodoshi unidirectional energy transfer mechanism in phenylene ethynylene dendrimers, The Journal of Chemical Physics, **2012**, 137 (22) 22A526.

[55] A. Jaouadi, J. Galiana, E. Mangaud, B. Lasorne, O. Atabek, and M. Desouter-Lecomte, Laser-controlled electronic symmetry breaking in a phenylene ethynylene dimer: Simulation by the hierarchical equations of motion and optimal control, Physical Review A, **2022**, 106 (4) 043121.

[56] S. Fernandez-Alberti, D. V. Makhov, S. Tretiak, and D. V. Shalashilin, Non-adiabatic excited state molecular dynamics of phenylene ethynylene dendrimer using a multiconfigurational Ehrenfest approach, Physical Chemistry Chemical Physics, **2016**, 18 (15) 10028–10040.

[57] V. M. Freixas, D. Ondarse-Alvarez, S. Tretiak, D. V. Makhov, D. V. Shalashilin, and S. Fernandez-Alberti, Photoinduced non-adiabatic energy transfer pathways in dendrimer building blocks, The Journal of Chemical Physics, **2019**, 150 (12) 124301.

[58] W. Malone, B. Nebgen, A. White, Y. Zhang, H. Song *et al.*, NEXMD software package for nonadiabatic excited state molecular dynamics simulations, Journal of Chemical Theory and Computation, **2020**, 16 (9) 5771–5783.

[59] D. Hu, J. Peng, L. Chen, M. F. Gelin, and Z. Lan, Spectral fingerprint of excited-state energy transfer in dendrimers through polarization-sensitive transient-absorption pump–probe signals: On-the-fly nonadiabatic dynamics simulations, The Journal of Physical Chemistry Letters, **2021**, 12 (39) 9710–9719.

[60] V. M. Freixas, A. J. White, T. Nelson, H. Song, D. V. Makhov *et al.*, Nonadiabatic excited-state molecular dynamics methodologies: Comparison and convergence, The Journal of Physical Chemistry Letters, **2021**, 12 (11) 2970–2982.

[61] V. M. Freixas, W. Malone, X. Li, H. Song, H. Negrin-Yuvero *et al.*, NEXMD v2.0 software package for nonadiabatic excited state molecular dynamics simulations, Journal of Chemical Theory and Computation, **2023**.

[62] C. A. Mead and D. G. Truhlar, Conditions for the definition of a strictly diabatic electronic basis for molecular systems, The Journal of Chemical Physics, **1982**, 77 (12) 6090–6098.

[63] Y. Shu, Z. Varga, S. Kanchanakungwankul, L. Zhang, and D. G. Truhlar, Diabatic states of molecules, The Journal of Physical Chemistry A, **2022**, 126 (7) 992–1018.

[64] M. Desouter-Lecomte, D. Dehareng, B. Leyh-Nihant, M. T. Praet, A. J. Lorquet, and J. C. Lorquet, Nonadiabatic unimolecular reactions of polyatomic molecules, The Journal of Physical Chemistry, **1985**, 89 (2) 214–222.

[65] G. W. Richings and G. A. Worth, A practical diabatisation scheme for use with the direct-dynamics variational multi-configuration gaussian method, The Journal of Physical Chemistry A, **2015**, 119 (50) 12457–12470.

[66] G. W. Richings and G. A. Worth, Multi-state non-adiabatic direct-dynamics on propagated diabatic potential energy surfaces, Chemical Physics Letters, **2017**, 683 606–612.

[67] T. Pacher, L. S. Cederbaum, and H. Köppel, Approximately diabatic states from block diagonalization of the electronic Hamiltonian, The Journal of Chemical Physics, **1988**, 89 (12) 7367–7381.

[68] T. Pacher, H. Köppel, and L. S. Cederbaum, Quasidiabatic states from ab initio calculations by block diagonalization of the electronic Hamiltonian: Use of frozen orbitals, The Journal of Chemical Physics, **1991**, 95 (9) 6668–6680.

[69] K. Ruedenberg and G. J. Atchity, A quantum chemical determination of diabatic states, The Journal of Chemical Physics, **1993**, 99 (5) 3799–3803.

[70] G. J. Atchity and K. Ruedenberg, Determination of diabatic states through enforcement of configurational uniformity, Theoretical Chemistry Accounts, **1997**, 97 (1) 47–58.

[71] D. Simah, B. Hartke, and H.-J. Werner, Photodissociation dynamics of H2S on new coupled ab initio potential energy surfaces, The Journal of Chemical Physics, **1999**, 111 (10) 4523–4534.

[72] H. Nakamura and D. G. Truhlar, The direct calculation of diabatic states based on configurational uniformity, The Journal of Chemical Physics, **2001**, 115 (22) 10353–10372.

[73] H. Nakamura and D. G. Truhlar, Direct diabatization of electronic states by the fourfold way. II. Dynamical correlation and rearrangement processes, The Journal of Chemical Physics, **2002**, 117 (12) 5576–5593.

[74] H. Nakamura and D. G. Truhlar, Extension of the fourfold way for calculation of global diabatic potential energy surfaces of complex, multiarrangement, non-Born–Oppenheimer systems: Application to HNCO(S,S1), The Journal of Chemical Physics, **2003**, 118 (15) 6816–6829.

[75] F. Venghaus and W. Eisfeld, Block-diagonalization as a tool for the robust diabatization of high-dimensional potential energy surfaces, The Journal of Chemical Physics, **2016**, 144 (11) 114110.

[76] N. Wittenbrink, F. Venghaus, D. Williams, and W. Eisfeld, A new approach for the development of diabatic potential energy surfaces: Hybrid block-diagonalization and diabatization by ansatz, The Journal of Chemical Physics, **2016**, 145 (18) 184108.

[77] L. S. Cederbaum, H. Köppel, and W. Domcke, Multimode vibronic coupling effects in molecules, International Journal of Quantum Chemistry, **1981**, 20 (S15) 251–267.

[78] C. Cattarius, G. A. Worth, H.-D. Meyer, and L. S. Cederbaum, All mode dynamics at the conical intersection of an octa-atomic molecule: Multi-configuration time-dependent Hartree (MCTDH) investigation on the butatriene cation, The Journal of Chemical Physics, **2001**, 115 (5) 2088–2100.

[79] E. Condon, A theory of intensity distribution in band systems, Physical Review, **1926**, 28 (6) 1182–1201.

[80] E. U. Condon, Nuclear motions associated with electron transitions in diatomic molecules, Physical Review, **1928**, 32 (6) 858–872.

[81] J. Franck and E. G. Dymond, Elementary processes of photochemical reactions, Transactions of the Faraday Society, **1926**, 21 (February) 536–542.

[82] V. Barone, J. Bloino, M. Biczysko, and F. Santoro, Fully integrated approach to compute vibrationally resolved optical spectra: From small molecules to macrosystems, Journal of Chemical Theory and Computation, **2009**, 5 (3) 540–554.

[83] J. Bloino, M. Biczysko, F. Santoro, and V. Barone, General approach to compute vibrationally resolved one-photon electronic spectra, Journal of Chemical Theory and Computation, **2010**, 6 (4) 1256–1274.

[84] I. C. D. Merritt, D. Jacquemin, and M. Vacher, Nonadiabatic coupling in trajectory surface hopping: How approximations impact excited-state reaction dynamics, Journal of Chemical Theory and Computation, **2023**.

[85] B. Gonon, A. Perveaux, F. Gatti, D. Lauvergnat, and B. Lasorne, On the applicability of a wavefunction-free, energy-based procedure for generating first-order non-adiabatic couplings around conical intersections, The Journal of Chemical Physics, **2017**, 147 (11) 114114.

[86] M. R. Manaa and D. R. Yarkony, On the intersection of two potential energy surfaces of the same symmetry. Systematic characterization using a Lagrange multiplier constrained procedure, The Journal of Chemical Physics, **1993**, 99 (7) 5251–5256.

[87] M. Bearpark, M. Robb, and H. Schlegel, A direct method for the location of the lowest energy point on a potential surface crossing, **1994**.

[88] F. Sicilia, L. Blancafort, M. J. Bearpark, and M. A. Robb, New algorithms for optimizing and linking conical intersection points, Journal of Chemical Theory and Computation, **2008**, 4 (2) 257–266.

[89] S. Ruiz-Barragan, M. A. Robb, and L. Blancafort, Conical intersection optimization based on a double Newton–Raphson algorithm using composed steps, Journal of Chemical Theory and Computation, **2013**, 9 (3) 1433–1442.

[90] R. Fletcher, Practical Methods of Optimization 2e, 2e édition edn., **2000**.

[91] J. Sanz García, R. Maskri, A. Mitrushchenkov, and L. Joubert-Doriol, Optimizing Conical Intersections without Explicit Use of Non-Adiabatic Couplings, Journal of Chemical Theory and Computation, **2024**.

[92] A. Raab, G. Worth, H.-D. Meyer, and L. Cederbaum, Molecular dynamics of pyrazine after excitation to the S2 electronic state using a realistic 24-mode model Hamiltonian, The Journal of Chemical Physics, **1999**, 110 936–946.

[93] B. Gonon, B. Lasorne, G. Karras, L. Joubert-Doriol, D. Lauvergnat *et al.*, A generalized vibronic-coupling Hamiltonian for molecules without symmetry: Application to the photoisomerization of benzopyran, The Journal of Chemical Physics, **2019**, 150 (12) 124109.

[94] M. H. Beck, A. Jäckle, G. A. Worth, and H. D. Meyer, The multiconfiguration time-dependent Hartree (MCTDH) method: a Highly efficient algorithm for propagating wavepackets, Physics Reports, **2000**, 324 (1) 1–105.

[95] F. Gatti, B. Lasorne, H.-D. Meyer, and A. Nauts, Applications of quantum dynamics in chemistry, vol. 98 of *Lecture Notes in Chemistry*, **2017**.

[96] G. A. Worth, K. Giri, G. W. Richings, I. Burghardt, M. H. Beck, A. Jäckle, and H. D. Meyer, The quantics package, version 2.0, University of Birmingham: Birmingham, UK, **2020**.

[97] H. R. Larsson, B. Hartke, and D. J. Tannor, Efficient molecular quantum dynamics in coordinate and phase space using pruned bases, The Journal of Chemical Physics, **2016**, 145 (20) 204108.

[98] H. R. Larsson and D. J. Tannor, Dynamical pruning of the multiconfiguration time-dependent Hartree (DP-MCTDH) method: An efficient approach for multidimensional quantum dynamics, The Journal of Chemical Physics, **2017**, 147 (4) 044103.

[99] G. A. Worth, Accurate wave packet propagation for large molecular systems: The multiconfiguration time-dependent Hartree (MCTDH) method with selected configurations, The Journal of Chemical Physics, **2000**, 112 (19) 8322–8329.

[100] J. Coonjobeeharry, K. E. Spinlove, C. Sanz Sanz, M. Sapunar, N. Došlić, and G. A. Worth, Mixed-quantum-classical or fully-quantized dynamics? A unified code to compare methods, Philosophical Transactions of the Royal Society A: Mathematical, Physical and Engineering Sciences, **2022**, 380 (2223) 20200386.

[101] U. Manthe, A time-dependent discrete variable representation for (multiconfiguration) Hartree methods, The Journal of Chemical Physics, **1996**, 105 (16) 6989–6994.

[102] C. Lubich, From quantum to classical molecular dynamics: reduced models and numerical analysis, **2008**.

[103] M. Bonfanti, G. A. Worth, and I. Burghardt, Multi-configuration time-dependent hartree methods: From quantum to semiclassical and quantum-classical, in Quantum Chemistry and Dynamics of Excited States, **2020**, 383–411.

[104] C. Lasser and C. Su, Various variational approximations of quantum dynamics, Journal of Mathematical Physics, **2022**, 63 (7) 072107.

[105] L. Hackl, T. Guaita, T. Shi, J. Haegeman, E. Demler, and J. I. Cirac, Geometry of variational methods: dynamics of closed quantum systems, SciPost Physics, **2020**, 9 (4) 048.

[106] H. Wang and M. Thoss, Multilayer formulation of the multiconfiguration time-dependent Hartree theory, The Journal of Chemical Physics, **2003**, 119 (3) 1289–1299.

[107] U. Manthe, A multilayer multiconfigurational time-dependent Hartree approach for quantum dynamics on general potential energy surfaces, The Journal of Chemical Physics, **2008**, 128 (16) 164116.

[108] H. Wang, Multilayer multiconfiguration time-dependent Hartree theory, The Journal of Physical Chemistry A, **2015**, 119 (29) 7951–7965.

[109] J. C. Tully and R. K. Preston, Trajectory surface hopping approach to nonadiabatic molecular collisions: the reaction of H+ with D2, The Journal of Chemical Physics, **1971**, 55 (2) 562–572.

[110] M. Barbatti, Nonadiabatic dynamics with trajectory surface hopping method, WIREs Computational Molecular Science, **2011**, 1 (4) 620–633.

[111] J. C. Tully, Molecular dynamics with electronic transitions, The Journal of Chemical Physics, **1990**, 93 (2) 1061–1071.

[112] J. E. Subotnik, A. Jain, B. Landry, A. Petit, W. Ouyang, and N. Bellonzi, Understanding the surface hopping view of electronic transitions and decoherence, Annual Review of Physical Chemistry, **2016**, 67 (Volume 67, 2016) 387–417.

[113] E. J. Heller, Time-dependent approach to semiclassical dynamics, The Journal of Chemical Physics, **1975**, 62 (4) 1544–1555.

[114] E. J. Heller, Frozen Gaussians: A very simple semiclassical approximation, The Journal of Chemical Physics, **1981**, 75 (6) 2923–2931.

[115] B. Lasorne, G. A. Worth, and M. A. Robb, Excited-state dynamics, WIREs Computational Molecular Science, **2011**, 1 (3) 460–475.

[116] G. A. Worth and B. Lasorne, Gaussian wave packets and the DD-vMCG approach, in Quantum Chemistry and Dynamics of Excited States, **2020**, 413–433.

[117] B. F. E. Curchod and T. J. Martínez, Ab initio nonadiabatic quantum molecular dynamics, Chemical Reviews, **2018**, 118 (7) 3305–3336.

[118] M. Persico and G. Granucci, An overview of nonadiabatic dynamics simulations methods, with focus on the direct approach versus the fitting of potential energy surfaces, Theoretical Chemistry Accounts, **2014**, 133 (9) 1526.

[119] R. Crespo-Otero and M. Barbatti, Recent advances and perspectives on nonadiabatic mixed quantum–classical dynamics, Chemical Reviews, **2018**, 118 (15) 7026–7068.

[120] F. Agostini and E. K. U. Gross, Exact factorization of the electron–nuclear wave function: Theory and applications, in Quantum Chemistry and Dynamics of Excited States, **2020**, 531–562.

[121] A. Szabo and N. S. Ostlund, Modern quantum chemistry: Introduction to advanced electronic structure theory, **2012**.

[122] J. Toulouse, Review of approximations for the exchange-correlation energy in density-functional theory, in E. Cancès and G. Friesecke, eds., Density Functional Theory: Modeling, Mathematical Analysis, Computational Methods, and Applications, Mathematics and Molecular Modeling, **2023**, 1–90.

[123] P. Hohenberg and W. Kohn, Inhomogeneous electron gas, Physical Review, **1964**, 136 (3B) B864–B871.

[124] W. Kohn and L. J. Sham, Self-consistent equations including exchange and correlation effects, Physical Review, **1965**, 140 (4A) A1133–A1138.

[125] A. D. Becke, A multicenter numerical integration scheme for polyatomic molecules, The Journal of Chemical Physics, **1988**, 88 (4) 2547–2553.

[126] C. Lee, W. Yang, and R. G. Parr, Development of the Colle-Salvetti correlation-energy formula into a functional of the electron density, Physical Review B, **1988**, 37 (2) 785–789.

[127] A. D. Becke, A new mixing of Hartree–Fock and local density-functional theories, The Journal of Chemical Physics, **1993**, 98 (2) 1372–1377.

[128] A. D. Becke, Density-functional thermochemistry. III. The role of exact exchange, The Journal of Chemical Physics, **1993**, 98 (7) 5648–5652.

[129] P. J. Stephens, F. J. Devlin, C. F. Chabalowski, and M. J. Frisch, Ab initio calculation of vibrational absorption and circular dichroism spectra using density functional force fields, The Journal of Physical Chemistry, **1994**, 98 (45) 11623–11627.

[130] A. D. Becke, Density-functional thermochemistry. IV. A new dynamical correlation functional and implications for exact-exchange mixing, The Journal of Chemical Physics, **1996**, 104 (3) 1040–1046.

[131] A. D. Becke, Density-functional thermochemistry. V. Systematic optimization of exchange-correlation functionals, The Journal of Chemical Physics, **1997**, 107 (20) 8554–8560.

[132] H. Iikura, T. Tsuneda, T. Yanai, and K. Hirao, A long-range correction scheme for generalized-gradient-approximation exchange functionals, The Journal of Chemical Physics, **2001**, 115 (8) 3540–3544.

[133] T. Yanai, D. P. Tew, and N. C. Handy, A new hybrid exchange–correlation functional using the Coulomb-attenuating method (CAM-B3LYP), Chemical Physics Letters, **2004**, 393 (1) 51–57.

[134] J.-D. Chai and M. Head-Gordon, Systematic optimization of long-range corrected hybrid density functionals, The Journal of Chemical Physics, **2008**, 128 (8) 084106.

[135] M. Casida and M. Huix-Rotllant, Progress in time-dependent density-functional theory, Annual Review of Physical Chemistry, **2012**, 63 (1) 287–323.

[136] E. K. U. Gross and N. T. Maitra, Introduction to TDDFT, in M. A. Marques, N. T. Maitra, F. M. Nogueira, E. Gross, and A. Rubio, eds., Fundamentals of Time-Dependent Density Functional Theory, Lecture Notes in Physics, **2012**, 53–99.

[137] R. Van Leeuwen, Key concepts in time-dependent density-functional theory, International Journal of Modern Physics B, **2001**, 15 (14) 1969–2023.

[138] C. Cohen-Tannoudji, B. Diu, and F. Laloë, Quantum mechanics, volume 2: Angular momentum, spin, and approximation methods, 2e édition edn., **2020**.

[139] M. E. Casida, Time-dependent density functional response theory for molecules, in Recent Advances in Density Functional Methods, vol. Volume 1 of *Recent Advances in Computational Chemistry*, **1995**, 155–192.

[140] X. Blase, I. Duchemin, and D. Jacquemin, The Bethe–Salpeter equation in chemistry: Relations with TD-DFT, applications and challenges, Chemical Society Reviews, **2018**, 47 (3) 1022–1043.

[141] X. Blase, I. Duchemin, D. Jacquemin, and P.-F. Loos, The Bethe–Salpeter equation formalism: From physics to chemistry, The Journal of Physical Chemistry Letters, **2020**, 11 (17) 7371–7382.

[142] M. J. Frisch, G. W. Trucks, H. B. Schlegel, G. E. Scuseria, M. A. Robb *et al.*, Gaussian 16 Revision A.03, **2016**.

[143] C. Adamo and D. Jacquemin, The calculations of excited-state properties with Time-Dependent Density Functional Theory, Chemical Society Reviews, **2013**, 42 (3) 845–856.

[144] R. Ditchfield, W. J. Hehre, and J. A. Pople, Self-consistent molecular-orbital methods. IX. An extended Gaussian-type basis for molecular-orbital studies of organic molecules, The Journal of Chemical Physics, **1971**, 54 (2) 724–728.

[145] W. J. Hehre, R. Ditchfield, and J. A. Pople, Self—consistent molecular orbital methods. XII. Further extensions of Gaussian—type basis sets for use in molecular orbital studies of organic molecules, The Journal of Chemical Physics, **1972**, 56 (5) 2257–2261.

[146] P. C. Hariharan and J. A. Pople, The influence of polarization functions on molecular orbital hydrogenation energies, Theoretica chimica acta, **1973**, 28 (3) 213–222.

[147] T. Clark, J. Chandrasekhar, G. W. Spitznagel, and P. V. R. Schleyer, Efficient diffuse function-augmented basis sets for anion calculations. III. The 3-21+G basis set for first-row elements, Li–F, Journal of Computational Chemistry, **1983**, 4 (3) 294–301.

[148] H. B. Schlegel, Optimization of equilibrium geometries and transition structures, Journal of Computational Chemistry, **1982**, 3 (2) 214–218.

[149] J. Liu and W. Liang, Analytical Hessian of electronic excited states in time-dependent density functional theory with Tamm-Dancoff approximation, The Journal of Chemical Physics, **2011**, 135 (1) 014113.

[150] J. Liu and W. Liang, Analytical approach for the excited-state Hessian in time-dependent density functional theory: Formalism, implementation, and performance, The Journal of Chemical Physics, **2011**, 135 (18) 184111.

[151] R. Sarkar, M. Boggio-Pasqua, P.-F. Loos, and D. Jacquemin, Benchmarking TD-DFT and wave function methods for oscillator strengths and excited-state dipole moments, Journal of Chemical Theory and Computation, **2021**, 17 (2) 1117–1132.

[152] F. Santoro, R. Improta, A. Lami, J. Bloino, and V. Barone, Effective method to compute Franck-Condon integrals for optical spectra of large molecules in solution, The Journal of Chemical Physics, **2007**, 126 (8) 084509.

[153] F. Santoro, A. Lami, R. Improta, J. Bloino, and V. Barone, Effective method for the computation of optical spectra of large molecules at finite temperature including the Duschinsky and Herzberg–Teller effect: The Qx band of porphyrin as a case study, The Journal of Chemical Physics, **2008**, 128 (22) 224311.

[154] J. Galiana and B. Lasorne, On the unusual Stokes shift in the smallest PPE dendrimer building block: Role of the vibronic symmetry on the band origin?, The Journal of Chemical Physics, **2023**, 158 (12) 124113.

[155] J. Galiana and B. Lasorne, Excitation energy transfer and vibronic relaxation through light-harvesting dendrimer building blocks: A nonadiabatic perspective, The Journal of Chemical Physics, **2024**, 160 (10) 104104.

[156] V. D. Kleiman, J. S. Melinger, and D. McMorrow, Ultrafast dynamics of electronic excitations in a light-harvesting phenylacetylene dendrimer, The Journal of Physical Chemistry B, **2001**, 105 (24) 5595–5598.

[157] J. S. Melinger, Y. Pan, V. D. Kleiman, Z. Peng, B. L. Davis, D. McMorrow, and M. Lu, Optical and photophysical properties of light-harvesting phenylacetylene monodendrons based on unsymmetrical branching, Journal of the American Chemical Society, **2002**, 124 (40) 12002–12012.

[158] L. Alfonso-Hernandez, S. Athanasopoulos, S. Tretiak, B. Miguel, A. Bastida, and S. Fernandez-Alberti, Vibrational energy redistribution during donor–acceptor electronic energy transfer: Criteria to identify subsets of active normal modes, Physical Chemistry Chemical Physics, **2020**, 22 (33) 18454–18466.

[159] D. Mendive-Tapia, T. Firmino, H.-D. Meyer, and F. Gatti, Towards a systematic convergence of Multi-Layer (ML) Multi-Configuration Time-Dependent Hartree nuclear wavefunctions: The ML-spawning algorithm, Chemical Physics, **2017**, 482 113–123.

[160] D. Mendive-Tapia and H.-D. Meyer, Regularizing the MCTDH equations of motion through an optimal choice on-the-fly (i.e., spawning) of unoccupied single-particle functions, The Journal of Chemical Physics, **2020**, 153 (23) 234114.

[161] F. Montorsi, D. Aranda, M. Garavelli, F. Santoro, and F. Segatta, Spectroscopy from quantum dynamics: a mixed wave function/analytical line shape functions approach, Theoretical Chemistry Accounts, **2023**, 142 (11) 108.

[162] D. Mendive-Tapia, H.-D. Meyer, and O. Vendrell, Optimal mode combination in the multiconfiguration time-dependent hartree method through multivariate statistics: Factor analysis and hierarchical clustering, Journal of Chemical Theory and Computation, **2023**, 19 (4) 1144–1156.

[163] M. Gell-Mann, The eightfold way: a theory of strong interaction symmetry, in The Eightfold Way, **2000**.

[164] B. Lasorne, On the use of Lie group homomorphisms for treating similarity transformations in nonadiabatic photochemistry, Advances in Mathematical Physics, **2014**, 2014 1–14.

[165] G. J. Halász, A. Perveaux, B. Lasorne, M. A. Robb, F. Gatti, and Vibók, Coherence revival during the attosecond electronic and nuclear quantum photodynamics of the ozone molecule, Physical Review A, **2013**, 88 (2) 023425.

[166] I. C. D. Merritt, D. Jacquemin, and M. Vacher, Attochemistry: Is controlling electrons the future of photochemistry?, The Journal of Physical Chemistry Letters, **2021**, 12 (34) 8404–8415.

[167] T. Tran, A. Ferté, and M. Vacher, Simulating attochemistry: Which dynamics method to use?, The Journal of Physical Chemistry Letters, **2024** 3646–3652.

[168] F. Meng, M. Richer, A. Tehrani, J. La, T. D. Kim, P. W. Ayers, and F. Heidar-Zadeh, Procrustes: A python library to find transformations that maximize the similarity between matrices, Computer Physics Communications, **2022**, 276 108334.

[169] J. Valdiviezo and J. L. Palma, Molecular rectification enhancement based on conformational and chemical modifications, The Journal of Physical Chemistry C, **2018**, 122 (4) 2053–2063.

[170] R. Suzuki, K. Chiba, S. Tanaka, and K. Okuyama, Electronic spectra of jet-cooled 1,4-bis(phenylethynyl)benzene: Strength in -electron conjugation and two large-amplitude torsional motions, The Journal of Chemical Physics, **2024**, 160 (2) 024301.

[171] A. Jaouadi, E. Mangaud, and M. Desouter-Lecomte, Re-exploring control strategies in a non-Markovian open quantum system by reinforcement learning, Physical Review A, **2024**, 109 (1) 013104.

[172] J. N. Harvey, M. Aschi, H. Schwarz, and W. Koch, The singlet and triplet states of phenyl cation. A hybrid approach for locating minimum energy crossing points between non-interacting potential energy surfaces, Theoretical Chemistry Accounts, **1998**, 99 (2) 95–99.

Appendix A

Optimization of Minimum-Energy Conical Intersections

In this appendix, we give additional details as regards the strategies used in this work to optimize minimum-energy conical intersection (MECI) geometries.

Two main strategies have been applied and implemented in home-made interfaces for the `Gaussian16` package. Both are based on energy derivatives only and do not require the explicit knowledge of the derivative coupling vector.

A.1 Projected seam gradient and numerical branching space

The first one is strongly inspired from the implementations of Harvey, Sicilia, Ruiz-Barragan and their co-workers [88, 89, 172], which are inspired from the original work of Bearpark [87]. We implemented a version of the algorithms of Harvey and of Sicilia (with and without energy switch, respectively) with a numerical evaluation of the branching space. This numerical evaluation of the branching space is obtained *via* the diagonalization of the Hessian of the squared (halved) energy difference

$$\mathbf{K}_{\mathsf{SED}} = 2\Delta V\left(\frac{\mathbf{K}_2 - \mathbf{K}_1}{2}\right) + 2\left(\mathbf{g}^{\mathsf{ad}}\mathbf{g}^{\mathsf{ad},\mathsf{T}}\right) \tag{A.1}$$

which yields two eigenvectors associated to non-zero eigenvalues, $\mathbf{u}_1$ and $\mathbf{u}_2$. The choice of the gradient seam would then be, at the locus of a conical intersection, the projection of the gradient average s on the intersection space

$$\mathbf{g}_{\mathsf{IS}} = \mathbf{P}_{\mathsf{IS}}\mathbf{s} \tag{A.2}$$

with

$$\mathbf{P}_{\mathsf{IS}} = \mathbb{1} - \mathbf{u}_1\mathbf{u}_1^{\mathsf{T}} - \mathbf{u}_2\mathbf{u}_2^{\mathsf{T}} \tag{A.3}$$

and

$$\mathbf{P}_{\mathsf{BS}} = \mathbf{u}_1\mathbf{u}_1^{\mathsf{T}} + \mathbf{u}_2\mathbf{u}_2^{\mathsf{T}}. \tag{A.4}$$

From this point, the algorithms we implemented are very similar to the ones of Harvey and Sicilia

- for a Harvey-like optimization, the effective gradient (composed gradient, CG) for the optimization is

  $$\mathbf{g}_{\mathsf{CG}} = \mathbf{g}_{\mathsf{IS}} + \mathbf{f}(\mathbf{g}^{\mathsf{ad}}). \tag{A.5}$$

  and the displacement is computed as a quasi-Newton step using a BFGS update for the Hessian. We call this a “CG” algorithm in the following. The variants for the definitions of the function-vector $\mathbf{f}$ are given in eq. (2.105).

- for a Sicilia-like optimization, the effective gradient for the optimization and the calculated displacements depend on the closeness to the CoIn seam
  - if $\Delta E > \Delta E_{\mathsf{switch}}$, the step is similar to the Harvey-like optimization (composed gradient eq. (A.5) and a unique quasi-Newton step)

- if $\Delta E \leq \Delta E_{\mathsf{switch}}$, the step is divided into two displacements (composed step, CS); one following the gradient of the seam eq. (A.2) with the associated quasi-Newton step and one following directly the gradient difference.

We call this a "CG-CS" algorithm in the following.

The most obvious disadvantage of our implementation of these algorithms is the requirement of the Hessians for computing the numerical branching-space vectors. Furthermore, such an approximation of the branching space is ill-defined at "true" conical intersections, that is numerically degenerate states ($\Delta E < 10^{-7}\,E_{\mathsf{h}}$).

A.2 Lagrange multipliers and updated branching space

The second strategy is based on the use of a Lagrange multiplier to satisfy the $\Delta E = 0$ constraint during the optimization. We implemented a version of a very recent algorithm proposed by Joubert-Doriol and co-workers, where they designed their algorithm as a method without any explicit use of the derivative coupling (exact or approximate) [91]. In particular, we were interested here in their new single Lagrange Multiplier (SLM) algorithm, for which we implemented a home-made version.

Details about the SLM algorithm can be find in the original paper [91]. In essence, the displacements from one step to another of the optimization are computed using

- the Hessian for the average energy (updated with a BFGS algorithm using the gradient average);
- the Hessian for the squared energy difference (updated with a BFGS algorithm using the gradient difference);
- the Lagrange multiplier, updated using the two previously mentioned Hessians, the gradient average and the gradient difference.

The branching space is not directly necessary for the calculation of the new displacements at each step, hence the branching-space vectors have not to be known explicitly. The advantage is here twofold. First, similarly to our modified implementations of the CG and CG-CS algorithms (appendix A.1), there is no need for the explicit knowledge of the derivative coupling vector, making the optimization feasible for all electronic structure methods (as long as the energy gradients can be obtained). Second, and this is a tremendous advantage, there is no need of computing the adiabatic excited-state Hessians at each step (unlike what was presented in appendix A.1).

A.3 The difficult approach of the seam in m34

All three algorithms (CG, CG-CS, and SLM) failed to optimize the S_1/S_2 MECI geometry in the case of the m34 molecule (3-ring and 4-ring *meta*-substituted *pseudo* fragments, $N_{\mathsf{atoms}} = 72$). In particular, up to now, all the optimizations led to an absurd drift in the energy of the ground state ($8\,$eV above the minimum of the electronic ground state at step 90, and accordingly same for all the excited-state energies). These energy drifts are consistent with the absurd geometries obtained, which correspond to the breaking of some cumulenic bonds between acetylenes and phenylenes. In particular, the electronic states have completely lost the LE character of the initially targeted states (and the associated conical intersection).

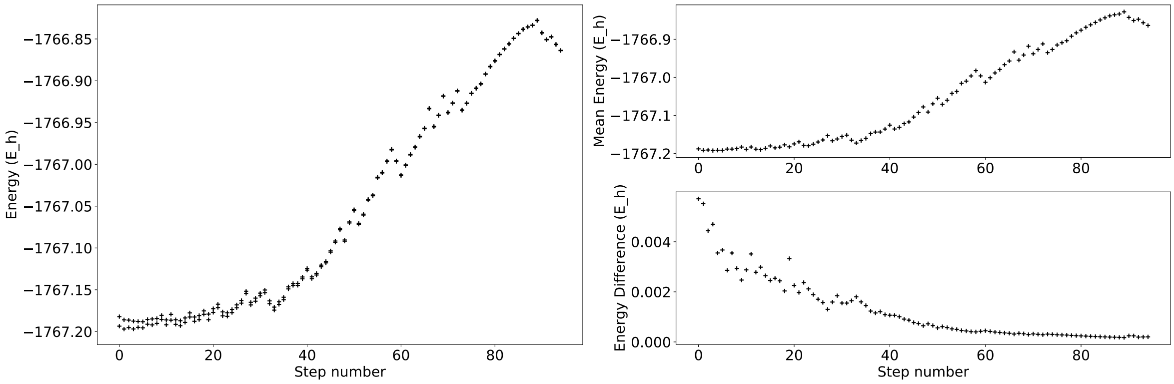

Figure A.1: Results of an attempt of MECI optimization, using the SLM algorithm [91], for the $\mathrm{S}_1/\mathrm{S}_2$ conical intersection in the m34 molecule ($N_{\text{atoms}} = 72$). Left, energies (in E_{h}) of the first and second adiabatic states during optimization; right, energy average and energy difference (in E_{h}) between the first and second adiabatic states during optimization.

It is more likely that the present algorithms are not adapted to so many degrees of freedom. In particular, the update of the Hessians might be problematic in the current state of the implementation (in Cartesian coordinates rather than in internal coordinates). Also, we still have to investigate the characters of the first two electronic excited states of such a *meta*-conjugation of 3-ring and 4-ring *pseudo* fragments, to better estimate the possibility for this MECI to exist in the $\mathrm{S}_1/\mathrm{S}_2$ manifold of m34.

A.4 Choice of the algorithm for the different molecules

We give in table A.1 the outcome of the three algorithms (CG, CG-CS, and SLM) for different PPE-oligomers. We did not exhaustively tested all the algorithms nor all the variants (convergence criteria, maximum displacements...) on each molecule.

In our experience, the approach of the CoIn seam was relatively easy with the three algorithms in the case of electronic states with different symmetry (for instance, A_1 and B_2 in the case of m22, or d223). On the other hand, finding the seam in the case of electronic states with same symmetry was much more complicated. To some extent, the CG-CS algorithm was able to better optimize the MECI geometry (for m23 for instance), which we attributed to a more stable conservation of the small energy difference once the CoIn seam was reached. In either case, our latests attempts were much more successful using the SLM algorithm (see fig. A.2 for a selection of successful optimizations, as opposed to the ones of m34)

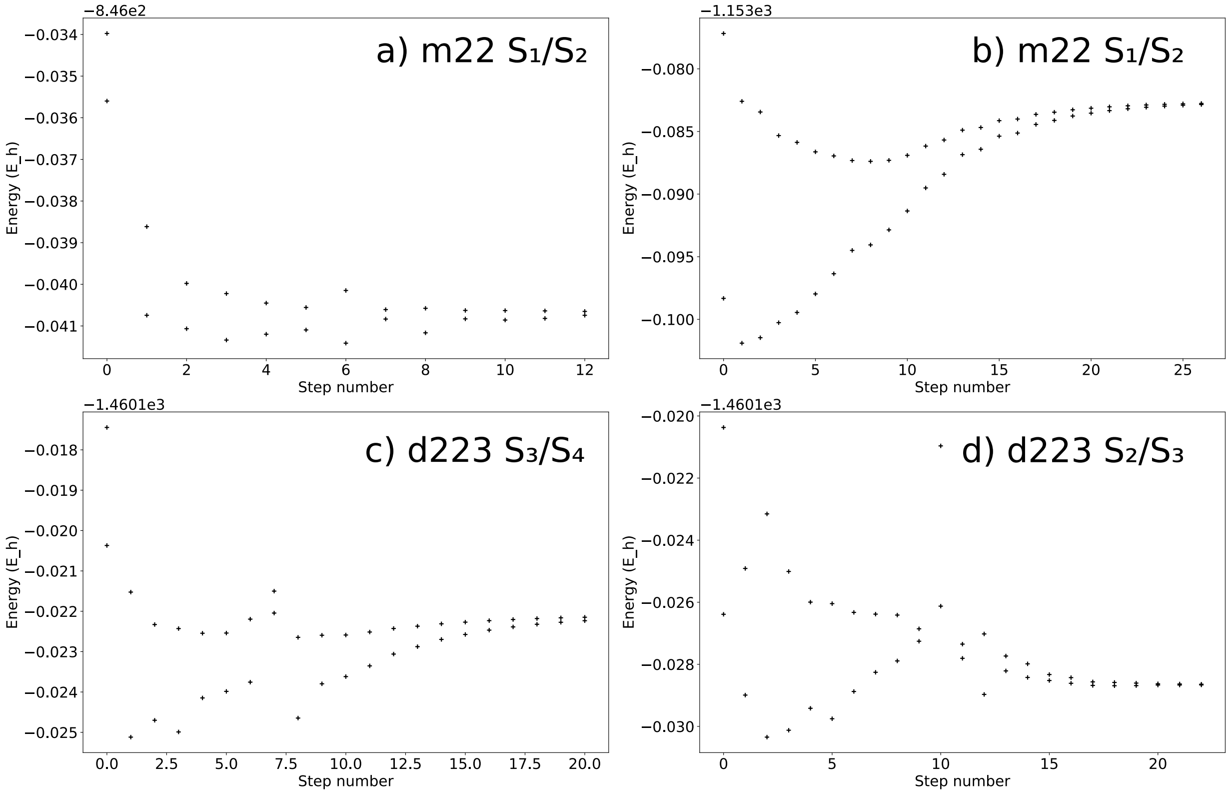

Figure A.2: Results of MECI optimization, using the SLM algorithm [91], for a) the S_1/S_2 MECI of m22; b) the S_1/S_2 MECI of m23; c) the S_3/S_4 MECI of d223; d) the S_2/S_3 MECI of d223. Energies are given in E_h.

Table A.1: Outcome of the three algorithms (composed gradient, mixed composed gradient/composed step, and SLM) for different PPE-oligomers and conical intersections.

Molecule, CoIn / Algo.	CG [172]	CG-CS [88]	SLM [91]
m22 S_1/S_2	converged	converged	converged
m23 S_1/S_2	X	converged	converged
m34 S_1/S_2	X	X	X
d222 S_1/S_2	converged	not tested	converged
d222 S_2/S_3	not tested	not tested	converged
d223 S_1/S_2	not tested	converged	converged
d223 S_2/S_3	not tested	converged	converged
d223 S_3/S_4	converged	not tested	converged

Appendix B

Parameters for Vibronic Coupling Hamiltonian Models

In this appendix, we give the numerical parameters for the definition of the vibronic coupling Hamiltonian models used throughout this work, which have been encoded in the operator format of `Quantics`. All the parameters except the energies are given in mass-weighted atomic units. In particular,

- the first-order parameters are given in $\frac{E_\mathrm{h}}{a_0\sqrt{m_e}}$ (gradients of the energies or of the couplings, κ_i, λ_i, or h'_i);
- the second-order parameters are given in $\frac{E_\mathrm{h}}{a_0^2 m_e}$ (curvatures k_i, mode-mixing couplings γ_{ij} or μ_{ij}).

B.1 C_{2v} symmetrically *meta*-substituted PPE (m22)

B.1.1 (1+2)-state 3-dimensional LVC and QVC models [global fit]

Table B.1: LVC parameters obtained upon fitting *ab initio* calculations. The diabatic energies at the reference point are $E^{(1)} = 4.405\,\text{eV}$ and $E^{(2)} = 4.380\,\text{eV}$.

LVC							
Mode i	Symmetry	$k_i^{(0)}$	$k_i^{(1)}$	$k_i^{(2)}$	$\kappa_i^{(1)}$	$\kappa_i^{(1)}$	λ_i
81	A_1	0.00056900	0.00004764	0.00005004	-0.00037632	-0.00015483	0.0
87	B_2	0.00011627	0.00010051	0.00010055	0.0	0.0	0.00074566
88	A_1	0.00011636	0.00010737	0.00010805	0.00077356	0.00089401	0.0

Table B.2: QVC parameters obtained upon fitting *ab initio* calculations. The diabatic energies at the reference point are $E^{(1)} = 4.407\,\text{eV}$ and $E^{(2)} = 4.379\,\text{eV}$.

LVC							
Mode i	Symmetry	$k_i^{(0)}$	$k_i^{(1)}$	$k_i^{(2)}$	$\kappa_i^{(1)}$	$\kappa_i^{(1)}$	λ_i
81	A_1	0.00056900	0.00004751	0.00004981	-0.00038974	-0.00015231	0.0
87	B_2	0.00011627	0.00010156	0.00009792	0.0	0.0	0.00065516
88	A_1	0.00011636	0.00010737	0.00010795	0.00079081	0.00089479	0.0
QVC							
$\gamma_{81,88}^{(1)}$		-0.00000259					
$\gamma_{81,88}^{(2)}$		-0.00000052					
$\mu_{87,81}$		-0.00000108					
$\mu_{87,88}$		-0.00001187					

B.1.2 (1+2)-state 10-dimensional LVC model [global fit]

Table B.3: LVC parameters for the (1+2)-state 10-dimensional [global fit] of m22. The diabatic energies at the reference point are $E^{(1)} = 4.4293\,$eV and $E^{(2)} = 4.4734\,$eV.

Mode i	Symmetry	$k_i^{(0)}$	$k_i^{(1)}$	$k_i^{(2)}$	$\kappa_i^{(1)}$	$\kappa_i^{(2)}$	λ_i
50	A$_1$	0.00002184	0.00002133	0.00002099	0.00009210	0.00012980	0.0
53	B$_2$	0.00002196	0.00002220	0.00002135	0.0	0.0	0.00008370
54	A$_1$	0.00002197	0.00002186	0.00002189	-0.00011530	-0.00009514	0.0
75	A$_1$	0.00004509	0.00004333	0.00004528	-0.00009890	0.00004805	0.0
81	A$_1$	0.00005690	0.00005583	0.00004959	-0.00015338	-0.00036253	0.0
84	B$_2$	0.00005873	0.00004876	0.00006576	0.0	0.0	-0.00041519
85	A$_1$	0.00005944	0.00005789	0.00005365	-0.00030346	-0.00019885	0.0
86	B$_2$	0.00005958	0.00005509	0.00005472	0.0	0.0	0.00008113
87	B$_2$	0.00011627	0.00011131	0.00011828	0.0	0.0	-0.00082134
88	A$_1$	0.00011636	0.00011424	0.00011757	0.00096955	0.00086032	0.0

B.2 $\mathrm{C_s}$ asymmetrically *meta*-substituted PPE (m23)

B.2.1 (1+2)-state 8-dimensional LVC model [mixed global/local fit]

Table B.4: LVC parameters for the (1+2)-state 8-dimensional model of m23. The diabatic energies at the reference point are $E^{(1)} = 3.8766\,\mathrm{eV}$ and $E^{(2)} = 4.4520\,\mathrm{eV}$.

Mode	Symmetry	$k_i^{(0)}$	$k_i^{(1)}$	$k_i^{(2)}$	$\kappa_i^{(1)}$	$\kappa_i^{(2)}$	h'_i
111	A’	0.00005691	0.00005649	0.00005014	-0.00014338	-0.00030371	0.00009640
114	A’	0.00005873	0.00005760	0.00004286	0.00030431	-0.00031251	-0.00011256
115	A’	0.00005925	0.00005640	0.00005875	-0.00033673	-0.00010607	-0.00003386
116	A’	0.00005951	0.00005888	0.00005307	0.00005883	0.00019169	0.00003792
117	A’	0.00005994	0.00005612	0.00005941	0.00034508	0.00003239	0.00000969
118	A’	0.00011557	0.00011414	0.00010996	-0.00100405	-0.00010761	0.00006847
119	A’	0.00011623	0.00009186	0.00009662	-0.00010674	0.00022954	0.00014127
120	A’	0.00011634	0.00011389	0.00009228	-0.00018406	-0.00102473	-0.00013513

B.3 C_{2v} symmetrically tri-*meta*-substituted PPE (d223)

B.3.1 (1+3)-state 10-dimensional LVC models [global fit with all couplings]

Table B.5: LVC parameters for the (1+2)-state 10-dimensional [global fit] of d223. The diabatic energies at the reference point are $E^{(1)} = 3.8598\,$eV, $E^{(2)} = 4.3897\,$eV, and $E^{(3)} = 4.4693\,$eV. All couplings have been allowed (as long as they are adapted to symmetry).

Mode i	Symmetry	$k_i^{(0)}$	$k_i^{(1)}$	$k_i^{(2)}$	$k^{(3)}$	$\kappa_i^{(1)}$
143	A_1	0.00005768	0.00005792	0.00005910	0.00004407	0.00025597
144	B_2	0.00005768	0.00007126	0.00004395	0.00005217	0.0
145	A_1	0.00005924	0.00005664	0.00005932	0.00005930	0.00036978
146	A_1	0.00005945	0.00005929	0.00005745	0.00005692	-0.00002453
147	B_2	0.00005948	0.00006306	0.00004852	0.00005937	0.0
148	A_1	0.00005991	0.00005701	0.00005979	0.00005917	0.00036151
149	A_1	0.00011563	0.00011651	0.00011486	0.00010813	0.00099516
150	A_1	0.00011632	0.00010519	0.00011405	0.00009544	0.00024767
151	B_2	0.00011642	0.00012159	0.00010656	0.00010746	0.0
152	A_1	0.00011653	0.00011554	0.00011504	0.00011252	0.00019448

Mode i	Symmetry	$\kappa_i^{(2)}$	$\kappa_i^{(3)}$	$\lambda_i^{(12)}$	$\lambda_i^{(23)}$	$\lambda_i^{(13)}$
143	A_1	-0.00013105	-0.00028946	0.0	0.0	0.00021350
144	B_2	0.0	0.0	0.00033478	-0.00042812	0.0
145	A_1	0.00002533	0.00003181	0.0	0.0	-0.00000099
146	A_1	-0.00027012	-0.00015984	0.0	0.0	-0.00000274
147	B_2	0.0	0.0	-0.00018869	-0.00013984	0.0
148	A_1	0.00000496	0.00002201	0.0	0.0	-0.00008968
149	A_1	0.00007889	0.00008465	0.0	0.0	0.00017465
150	A_1	-0.00015918	-0.00015696	0.0	0.0	0.00039799
151	B_2	0.0	0.0	0.00021486	-0.00076213	0.0
152	A_1	0.00090028	0.00080972	0.0	0.0	0.00016269

B.3.2 (1+3)-state 10-dimensional LVC models [global fit without H_{13} coupling]

Table B.6: LVC parameters for the (1+2)-state 10-dimensional [global fit] of d223. The diabatic energies at the reference point are $E^{(1)} = 3.8598\,\text{eV}$, $E^{(2)} = 4.3897\,\text{eV}$, and $E^{(3)} = 4.4693\,\text{eV}$. The parameters are obtained with setting all the couplings $\lambda_i^{(13)}$ to zero.

Mode i	Symmetry	$k_i^{(0)}$	$k_i^{(1)}$	$k_i^{(2)}$	$k^{(3)}$	$\kappa_i^{(1)}$
143	A_1	0.00005768	0.00005279	0.00005910	0.00004919	0.00024191
144	B_2	0.00005768	0.00007126	0.00004395	0.00005217	0.0
145	A_1	0.00005924	0.00005664	0.00005932	0.00005930	0.00036978
146	A_1	0.00005945	0.00005929	0.00005745	0.00005692	-0.00002453
147	B_2	0.00005948	0.00006306	0.00004852	0.00005937	0.0
148	A_1	0.00005991	0.00005626	0.00005979	0.00005991	0.00036028
149	A_1	0.00011563	0.00011162	0.00011486	0.00011302	0.00097347
150	A_1	0.00011632	0.00009054	0.00011405	0.00011009	0.00022132
151	B_2	0.00011642	0.00012159	0.00010656	0.00010746	0.0
152	A_1	0.00011653	0.00011261	0.00011504	0.00011545	0.00020321

Mode i	Symmetry	$\kappa_i^{(2)}$	$\kappa_i^{(3)}$	$\lambda_i^{(12)}$	$\lambda_i^{(23)}$	$\lambda_i^{(13)}$
143	A_1	-0.00013105	-0.00027539	0.0	0.0	0.0
144	B_2	0.0	0.0	0.00033478	-0.00042812	0.0
145	A_1	0.00002533	0.00003181	0.0	0.0	0.0
146	A_1	-0.00027012	-0.00015984	0.0	0.0	0.0
147	B_2	0.0	0.0	-0.00018869	-0.00013984	0.0
148	A_1	0.00000496	0.00002323	0.0	0.0	0.0
149	A_1	0.00007889	0.00010634	0.0	0.0	0.0
150	A_1	-0.00015919	-0.00013061	0.0	0.0	0.0
151	B_2	0.0	0.0	0.00021486	-0.00076213	0.0
152	A_1	0.00090028	0.00080099	0.0	0.0	0.0